# STRAIN HARDENING CEMENTITIOUS COMPOSITES: MATERIAL DEVELOPMENT, PERFORMANCE CHARACTERIZATION, STRUCTURAL, AND 3D PRINTING APPLICATIONS

EDITED BY: Kequan Yu, Jinlong Pan, Jian Zhou, Yingwu Zhou, Xiangming Zhou and Yan Zhuge

PUBLISHED IN: Frontiers in Materials

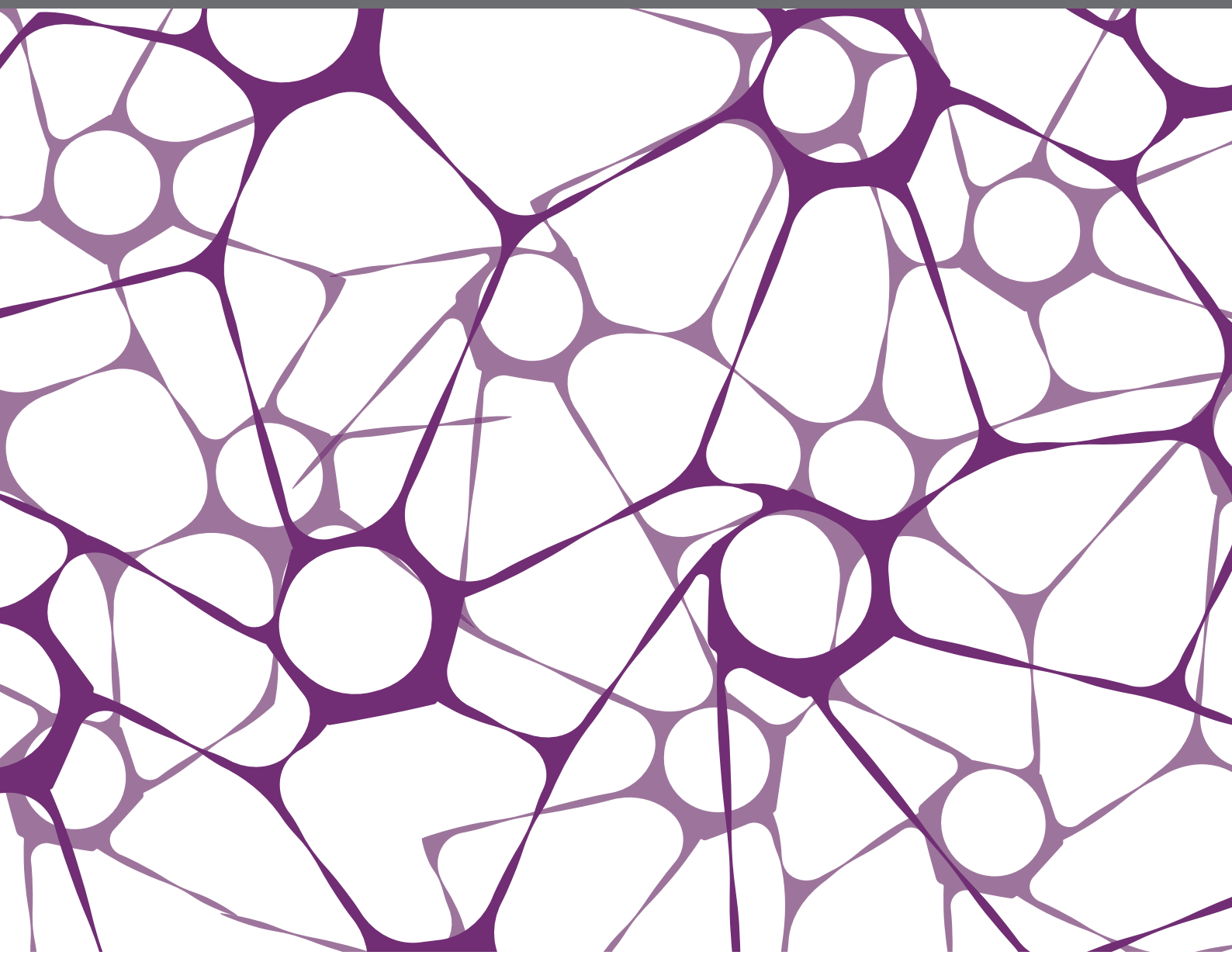

frontiers Research Topics

# frontiers



ISSN 1664-8714
ISBN 978-2-88976-168-5
DOI 10.3389/978-2-88976-168-5

## About Frontiers

Frontiers is more than just an open-access publisher of scholarly articles: it is a pioneering approach to the world of academia, radically improving the way scholarly research is managed. The grand vision of Frontiers is a world where all people have an equal opportunity to seek, share and generate knowledge. Frontiers provides immediate and permanent online open access to all its publications, but this alone is not enough to realize our grand goals.

## Frontiers Journal Series

The Frontiers Journal Series is a multi-tier and interdisciplinary set of open-access, online journals, promising a paradigm shift from the current review, selection and dissemination processes in academic publishing. All Frontiers journals are driven by researchers for researchers; therefore, they constitute a service to the scholarly community. At the same time, the Frontiers Journal Series operates on a revolutionary invention, the tiered publishing system, initially addressing specific communities of scholars, and gradually climbing up to broader public understanding, thus serving the interests of the lay society, too.

## Dedication to Quality

Each Frontiers article is a landmark of the highest quality, thanks to genuinely collaborative interactions between authors and review editors, who include some of the world's best academicians. Research must be certified by peers before entering a stream of knowledge that may eventually reach the public - and shape society; therefore, Frontiers only applies the most rigorous and unbiased reviews.
Frontiers revolutionizes research publishing by freely delivering the most outstanding research, evaluated with no bias from both the academic and social point of view. By applying the most advanced information technologies, Frontiers is catapulting scholarly publishing into a new generation.

## What are Frontiers Research Topics?

Frontiers Research Topics are very popular trademarks of the Frontiers Journals Series: they are collections of at least ten articles, all centered on a particular subject. With their unique mix of varied contributions from Original Research to Review Articles, Frontiers Research Topics unify the most influential researchers, the latest key findings and historical advances in a hot research area! Find out more on how to host your own Frontiers Research Topic or contribute to one as an author by contacting the Frontiers Editorial Office: frontiersin.org/about/contact

# STRAIN HARDENING CEMENTITIOUS COMPOSITES: MATERIAL DEVELOPMENT, PERFORMANCE CHARACTERIZATION, STRUCTURAL, AND 3D PRINTING APPLICATIONS

Topic Editors:
**Kequan Yu,** Tongji University, China
**Jinlong Pan,** Southeast University, China
**Jian Zhou,** Hebei University of Technology, China
**Yingwu Zhou,** Shenzhen University, China
**Xiangming Zhou,** Brunel University London, United Kingdom
**Yan Zhuge,** University of South Australia, Australia

**Citation:** Yu, K., Pan, J., Zhou, J., Zhou, Y., Zhou, X., Zhuge, Y., eds. (2022). Strain Hardening Cementitious Composites: material development, performance characterization, structural, and 3D printing applications. Lausanne: Frontiers Media SA. doi: 10.3389/978-2-88976-168-5

# Table of Contents

frontiers in Materials

ORIGINAL RESEARCH
published: 08 April 2021
doi: 10.3389/fmats.2021.673752

# Tensile Performance of High Ductility Cementitious Composites With Recycled Powder From C&D Waste

*Jing Ji[1,2], Huayu Song[1], Liangqin Jiang[1], Hongguo Ren[3]*, Yunfeng Zhang[1,2] and Yingchun Liu[1,2]*

[1] Heilongjiang Key Laboratory of Disaster Prevention, Mitigation and Protection Engineering, Northeast Petroleum University, Daqing, China, [2] Key Laboratory of Earthquake Engineering and Engineering Vibration, Institute of Engineering Mechanics, China Earthquake Administration, Harbin, China, [3] Handan Key Laboratory of Building Physical Environment and Regional Building Protection Technology, School of Architecture and Art, Hebei University of Engineering, Handan, China

The effects of recycled powder (RP) on hydration, micro-structures, compressive strength and tensile properties of high-ductility cementitious composites (HDCC) were studied. Three mass ratios of RP ranging from 10, 30 to 60% were employed to partially replace the cement. The hydration kinetics of RP-amended matrix was measured to investigate the influence of RP on the cementitious hydration process and the phase development was quantified by the thermal gravimetric analysis. Mechanical properties, including the compressive and tensile properties of HDCCs were obtained at 28 days. The morphology of reinforced polyethylene fiber at the fracture surface was obtained by the environmental scanning electron microscope (SEM) analysis.

**Keywords: high-ductility cementitious composites, micro-structures, mechanical properties, tensile performance, recycled powder**

OPEN ACCESS

***Edited by:***
*Kequan Yu,*
*Tongji University, China*

***Reviewed by:***
*Shuai Fang,*
*South China University of Technology, China*
*Jie Xiao,*
*Guangdong University of Technology, China*

****Correspondence:***
*Hongguo Ren*
*renhongguo771126@163.com*

***Specialty section:***
*This article was submitted to Structural Materials, a section of the journal Frontiers in Materials*

***Received:*** *28 February 2021*
***Accepted:*** *16 March 2021*
***Published:*** *08 April 2021*

***Citation:***
*Ji J, Song H, Jiang L, Ren H, Zhang Y and Liu Y (2021) Tensile Performance of High Ductility Cementitious Composites With Recycled Powder From C&D Waste. Front. Mater. 8:673752. doi: 10.3389/fmats.2021.673752*

## INTRODUCTION

Recycled powder (RP) with the particle size smaller than 150 μm is a byproduct during the concrete (clay brick) crushing process. It is estimated that RP accounts for roughly 20% of the entire concrete and clay brick waste (Sun et al., 2017). These tiny grains should be properly utilized to avoid the potential pollution to the air and underground water (Xiao et al., 2016).

Over the past decades, quite a few researches have been conducted to investigate the effects of alternative cementitious materials to the mechanical properties of concrete (Li et al., 2007, 2009; Yang et al., 2007; Zhang and Zhang, 2018; Wang et al., 2019). In recent years, RP was utilized to substitute a fraction of cement in the mixture as a supplementary cementitious material like fly ash and metakaolin. It was revealed that the RP would speed up hydration at the early age while reducing total hydration heat release (Liu et al., 2014). On the basis of the micro-mechanics designing theory, the coarse aggregate in the high-ductility cementitious composites (HDCC) mixture should be removed and the sand/binder ratio was largely diminished in HDCC to ensure good fiber dispersion and thus a satisfactory strain capacity with a strain-hardening phenomenon (Yu et al., 2017, 2018; Ding et al., 2018; Ji et al., 2019). The elimination of coarse aggregate and the reduction in the sand amount consequently raised the amount of cement in HDCC. However, it is noticed that higher cement dosage in HDCC, on one hand, increased the manufacturing cost; on the other hand, led to soaring heat of hydration and lager autogenous shrinkage of HDCC, which adversely reduced the compressive and tensile performance of HDCC.

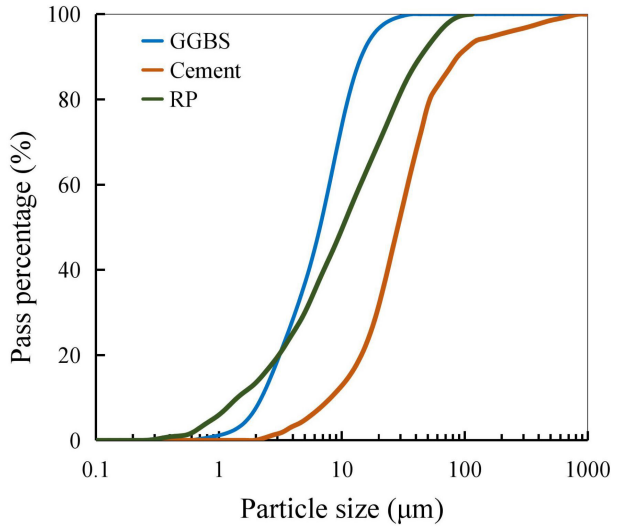


**FIGURE 1 |** Particle size distributions of the component.

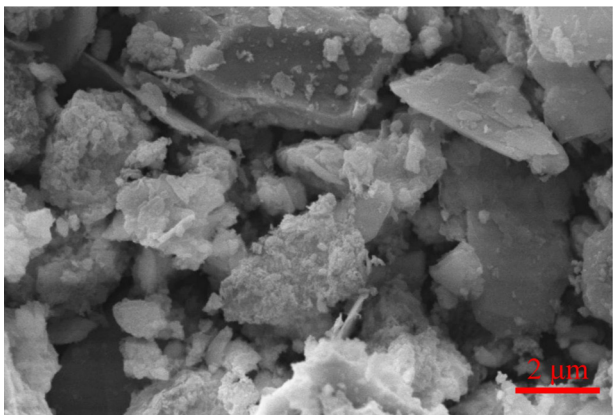


**FIGURE 2 |** Morphology of RP particles.

Thus, the aim of this paper is to utilize the RP to partially replace the cement in HDCC, which could significantly reduce the amount of cement. The impact of RP particles on mechanical performance of HDCC, including the tensile and compressive performance was then discussed. The microstructures of RP-amended HDCC, including the hydration heat, thermal gravimetric analysis, and morphology of polyethylene fiber, were also investigated.

## TEST PREPARATION

### Raw Materials and Mix Proportions

The HDCC was consisted of three parts: cementitious binder, aggregate, and reinforced fiber. 42.5R type I Cement, ground granulated blast slag (GGBS), and RP were used as the binder constituents for HDCC. GGBS and SF particles were considered as the pozzolanic components, which would accelerate the development of hydrated calcium silicate (C-S-H). RP was utilized to partly substitute the cement owing to its potential pozzolanic function (Liu et al., 2017). The silica sand with the particle diameter of 70–120 meshes was used as the aggregate. The sand/binder ratio was controlled at a low value to ensure the fiber dispersion. The gradation curves of cementitious materials and silica sand are given in **Figure 1**. The diameter and length of PE fiber are 24 μm and 18 mm, respectively. The tensile strength and Young's modulus of PE fiber are 2,400 MPa and 100 GPa and its elongation at breakage is 2–3%. Finally, a high-range superplasticizer was effectively employed to preserve the mixture flowability at a relatively small water/cementitious binder ratio.

Tiny particles of silica fume, RP and GGBS could densify of the matrix by filling the large pores, strengthen sand-paste interface and thus enhance the matrix strength. RP particles were gathered from a recycled factory, which crushed the construction wastes including both concrete and clay bricks. 85% RP particles had a size lower than 45 μm, within which 42% particles were lower than 10 μm. The fine particles were beneficial to the strength development of matrix because of the apparent filling effect (Yu et al., 2020).

**Figure 2** shows the morphology of RP particles, which has the similar irregular shapes to that of GGBS. The thermal gravimetric analysis of RP shows a trough around 680–720°C, exhibiting a decarbonization of $CaCO_3$ at this temperature range with the escape of $CO_2$.

The four mixture proportions of HDCC are given in **Table 1**. Three replacement ratios of RP to cement dosage up to 60% by mass (10, 30, and 60%) were employed. The water/binder ratio of all the four mixtures was fixed at 0.36. The mixture was named as HDCC-RP-A, where A denotes as the mass ratio of RP. The fiber mass in all the mixtures was 19.4 kg/m$^3$, representing a 2% volume.

### Experimental Preparation

A TAM air calorimeter was utilized to measure the hydration heat of HDCC matrix following the instruction of ASTM C1702-09a ASTM International (2008). A fixed volume of each matrix (around 0.1 L) mixed at room temperature was rapidly put into the ampule and kept in the chamber for 72 h. TGA/DTG analysis was conducted by Mettlery Toled TGA/SDTA 852 balance. Each dry-slice sample around 12 mg was ground into fine powder and heated from 20 to 1,000°C at a fixed rate of 10°C/min.

The full-range tensile stress-strain relationship of HDCC under uniaxial tension was determined by the plain dumbbell-shaped specimen (as shown in **Figure 3**) according to JSCE specification [16]. The dimensions of dumbbell-shaped specimen are shown in **Figure 4** with a cross-section of 30 mm × 13 mm and the gauge length of 80 mm. For each case from HDCC-Reference to HDCC-RP-60%, four dumbbell specimens were cast and tested to obtain their tensile properties at 28 days. The dumbbell geometry could ensure the distribution of majority cracks in the gauge length to allow a more reliable measurement of tensile strain. Cube specimens with edge length of 50 mm were prepared for the compression test at 28 days. The detailed

**TABLE 1 |** Mix properties of HDCC.

| Mixture types (kg/m$^3$) | Cement (kg/m$^3$) | RP (kg/m$^3$) | GGBS (kg/m$^3$) | Silica sand (kg/m$^3$) | Water (kg/m$^3$) | PE fiber (kg/m$^3$) | HRWR (kg/m$^3$) | W/Binder |
|---|---|---|---|---|---|---|---|---|
| HDCC-reference | 600 | – | 400 | 600 | 360 | 19.4 | 5 | 0.36 |
| HDCC-RP-10% | 540 | 60 | 400 | 600 | 360 | 19.4 | 5 | 0.36 |
| HDCC-RP-30% | 420 | 180 | 400 | 600 | 360 | 19.4 | 5 | 0.36 |
| HDCC-RP-60% | 240 | 360 | 400 | 600 | 360 | 19.4 | 5 | 0.36 |

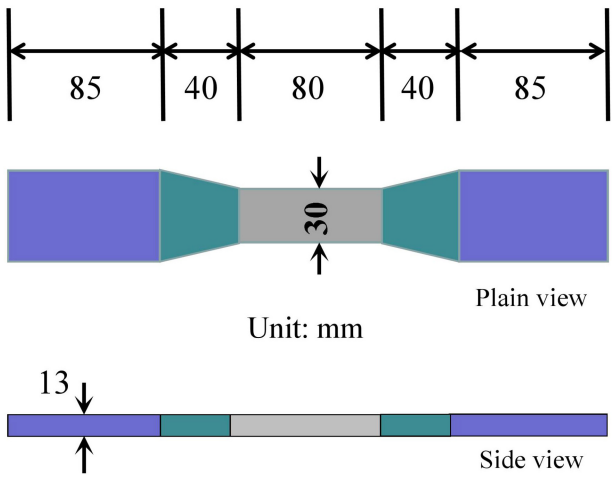


**FIGURE 3 |** Dimensions of dumbbell specimens.

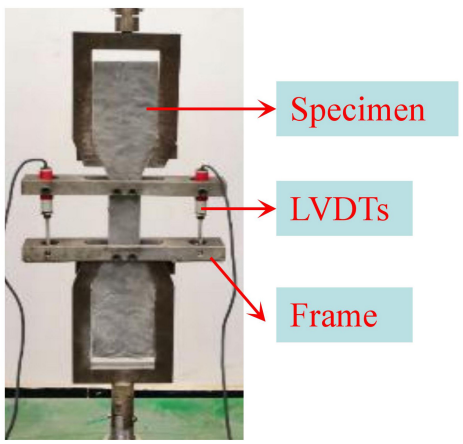


**FIGURE 4 |** Test setup of uniaxial tensile test.

experimental program of compressive and tensile tests is listed in **Table 2**.

## Experimental Setup and Procedure

**Figure 4** shows the setup of uniaxial tensile test. The alignment of whole setup was specially adjusted before loading to avoid the eccentric loading. The tensile loading speed was kept at 0.5 mm/min according to Japan Society of Civil Engineers [JSCE] (2008) with a 50 N preloading. The loading capacity of test machine is 50 kN. A light-weight frame holding two symmetrically installed transducers (LVDTs) was attached to the dumbbell-shaped

**TABLE 2 |** Test program of HDCC with different replacement ratios of RP.

| Mixture proportions | Compressive test | |
|---|---|---|
| | test | Tensile |
| HDCC-RP-Reference to HDCC-RP-60% | 5 | 4 |
| | 5 | 4 |

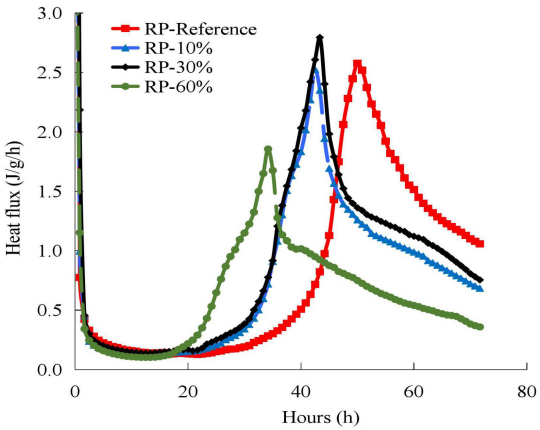


**FIGURE 5 |** Hydration evolution of HDCC.

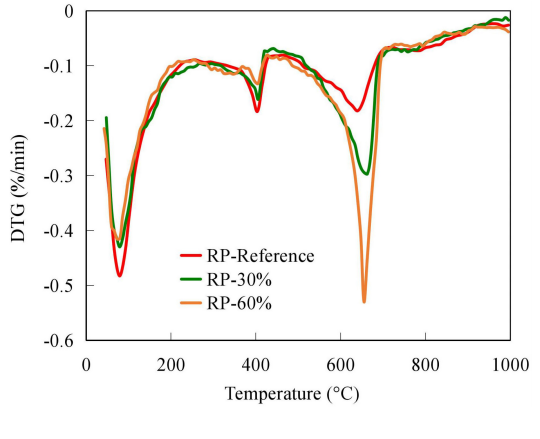


**FIGURE 6 |** DTG analysis of HDCC.

specimen to determine the displacement of specimen under tension. The tensile strain capacity of HDCC was calculated by the average reading of two LVDTs.

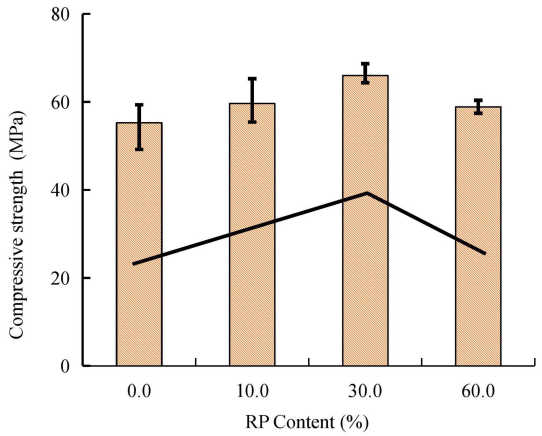


**FIGURE 7 |** Compressive strength of HDCCs.

# RESULTS AND DISCUSSION

## Isothermal Calorimetry

The isothermal calorimetry was utilized to measure the hydration evolution of HDCC matrices under different RP contents, i.e., the replacement ratio from 10 to 60% of cement. **Figure 5** shows the normalized heat flux under unit weight of binder material. The addition of RP accelerates the hydration rate and it is demonstrated that the dormant period of HDCC-RP-60% matrix was shortest due to the existence of $CaCO_3$ as the main compound of RP, which is considered to act as the accelerating seeds to the formation of tricalcium silicate ($C_3S$) (Nehdi et al., 1996). The hydration activity of the four HDCC matrices mainly happened in the first 72 h, after which it decreased generally with curing age. The heat flux peak of HDCC matrices generally declined with the RP content (**Figure 5**), while the peaks of RP-10% and RP-30% were comparable to or even higher than that of the reference matrix.

## Phase Development Analysis

The DTG results of HDCC matrices with different RP replacement ratios at 28d were shown in **Figure 6**. Three

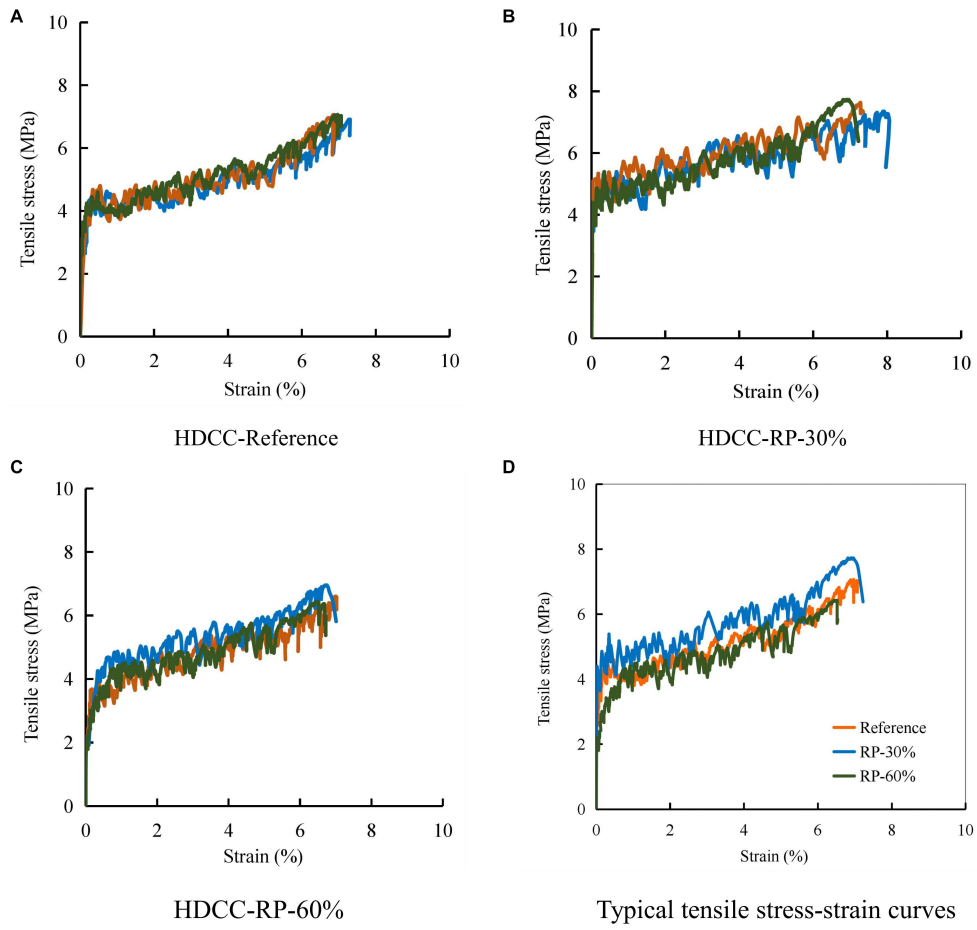


**FIGURE 8 |** Tensile stress-strain curves of HDCCs. **(A)** HDCC-Reference. **(B)** HDCC-RP-30%. **(C)** HDCC-RP-60%. **(D)** Typical tensile stress-strain curves.

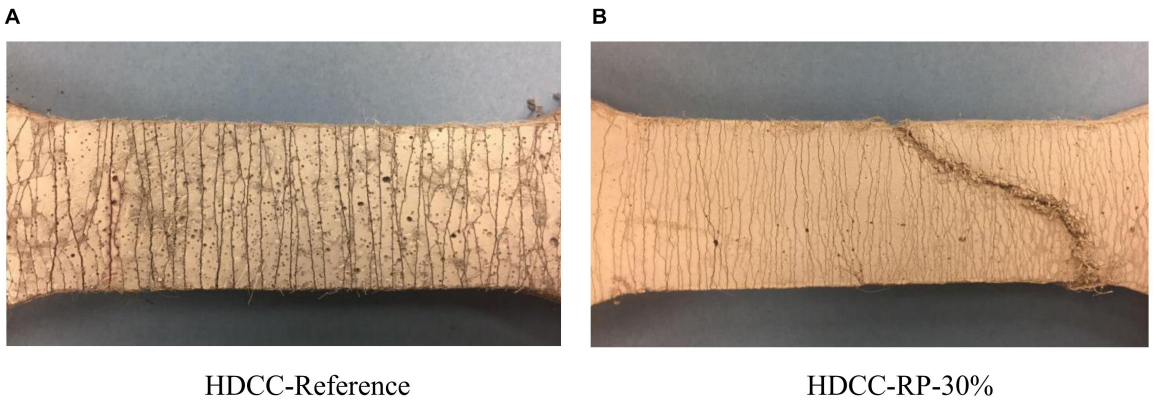


**FIGURE 9 |** Crack pattern of HDCCs. **(A)** HDCC-Reference. **(B)** HDCC-RP-30%.

significant peaks could be observed: the first peak is around 200°C, mainly related to the dehydration of ettringite; the second peak around 450°C is the dehydroxylation of $Ca(OH)_2$; and the third peak around 500–800°C is the decarbonization of $CaCO_3$ (Huang et al., 2017).

The peaks of $CaCO_3$ in different matrices increased significantly with the larger amount of RP, while the peak of $Ca(OH)_2$ of HDCC-RP-60% was lower than those of HDCC-Reference and HDCC-RP-30% at 28d due to the significant reduction in cement and the potential pozzolanic reaction of RP in HDCC-RP-60%.

## Compressive Properties of HDCCs

**Figure 7** displays the compression strength of HDCCs at 28d. The average strength value of reference specimen was 55.23 MPa and it raised to 66.0 MPa at the replacement ratio of 30%. The strength evolution of RP-amended HDCCs indicated that an appropriate amount of RP would promote the compression strength owing to its pozzolanic and filler effect. However, excessive RP, which meant an excessive replacement of cement up to 60% would damage the compressive strength to some extent and compressive strength of HDCC-RP-60% is 58.45 MPa.

## Tensile Stress-Strain Curves and Tensile Properties

**Figure 8** displays the tensile stress-strain relationships of HDCCs with different RP replacement ratios. The HDCC specimens in four cases show a robust strain-hardening performance. The tensile peak stress of HDCC-Reference was 7.00 MPa, which was close to the value of HDCC-RP-10% but lower than that of HDCC-RP-30% (i.e., 7.57 MPa). Moreover, the addition of RP did not sacrifice the tensile strain capacity of RP-HDCCs even up to the RP content of 60%.

**Figure 9** shows the crack distribution of HDCC specimens at the unloading stage. The average crack numbers are 37, 42, 43, and 48 for HDCC-RP-Reference, HDCC-RP-10%, HDCC-RP-30%, and HDCC-RP-60%, respectively. The cracks evenly spread along the gauge length with an average crack spacing of 2.16 mm for HDCC-RP-Reference, 1.86 mm for HDCC-RP-30% and 1.67 mm for HDCC-RP-60%, respectively. The mixing of RP boosted the crack development leading to a larger crack number and consequently a smaller the crack spacing, which may be due to the increase in interfacial stress between fiber and matrix.

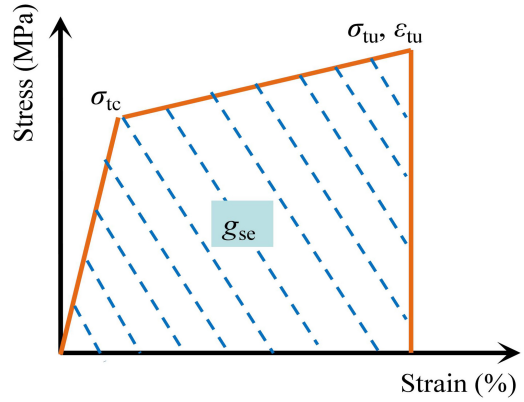


**FIGURE 10 |** Tensile parameters of HDCCs (Ding et al., 2018).

The tensile parameters including the initial cracking stress $\sigma_{tc}$, peak stress $\sigma_{tu}$, strain capacity and strain energy $g_{se}$ are shown in **Figure 10**. Detailed definitions of these parameters could be referred to Ding et al. (2018).

**Figure 11** summarizes the tensile parameters of HDCCs under different replacement ratios. The peak stress $\sigma_{tu}$ increased generally from 7.0 MPa of HDCC-RP-Reference to 7.09 MPa of HDCC-RP-10%, and then to 7.57 MPa of HDCC-RP-Reference-30%. It is noticed that the $\sigma_{tu}$ of HDCC-RP-60% (6.66 MPa) was only 5.5% lower than that of the HDCC-RP-Reference. The high replacement ratio of cement by RP did not compromise the strength development of HDCC, but significantly increased its greenness and reduced its impact on the environment. The initial stress $\sigma_{tc}$ shared a similar tendency with the $\sigma_{tu}$ of HDCCs (see in **Figure 11A**).

The addition of RP had positive influence on the tensile strain capacity up to the replacement ratio of 30% due to the

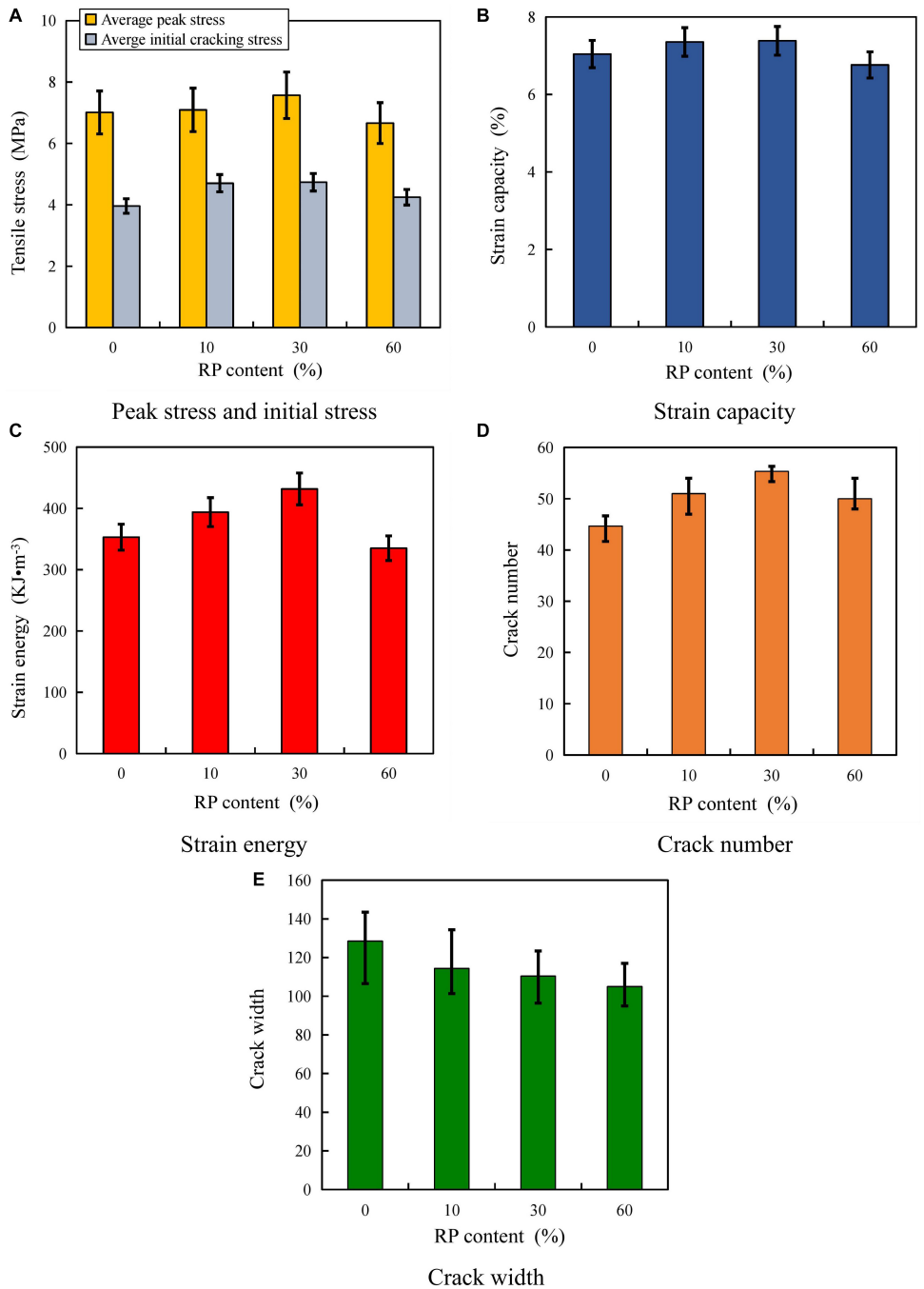


**FIGURE 11 |** Tensile parameters of HDCCs with different RP replacement ratios. **(A)** Peak stress and initial stress. **(B)** Strain capacity. **(C)** Strain energy. **(D)** Crack number. **(E)** Crack width.

enhancement of interfacial stress (see in **Figure 11B**). However, a further increase of the RP content up to 60% slightly weakened the strain capacity of HDCC-RP-60%, which could be attributed to the smaller crack width in HDCC-RP-60% (see in **Figure 11E**). The strain energy $g_{se}$, kept almost constant to HDCC-RP-30% at around 430 kJ/m$^3$ and then decreased apparently to 335 kJ/m$^3$ of HDCC-RP-60% due to the combination of lower $\sigma_{tu}$ and $\varepsilon_{tu}$. The $g_{se}$ of HDCC was significantly greater than those of conventional fiber-reinforced concrete and ultra-high performance concrete at the range of 50–100 kJ/m$^3$ (Wille et al., 2011).

In addition, it is interpreted from **Figures 11D,E** that the reduction in $\varepsilon_{tu}$ of HDCC-RP-60% was the result of finer crack width of RP-amended HDCCs. The RP particle size was smaller than that of cement particle, which would help to establish a

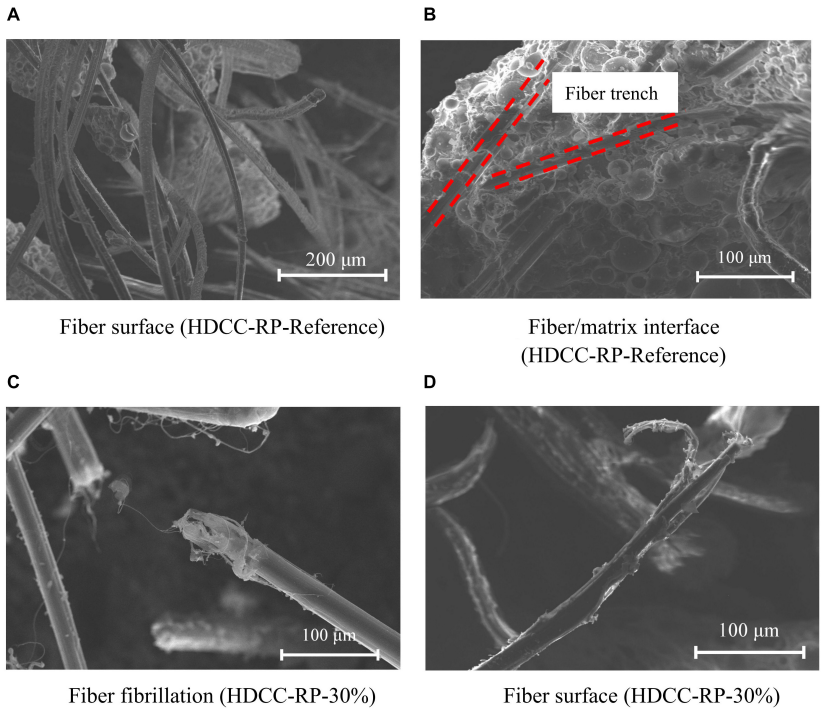


**FIGURE 12 |** Morphology of HDCCs. **(A)** Fiber surface (HDCC-RP-Reference). **(B)** Fiber/matrix interface (HDCC-RP-Reference). **(C)** Fiber fibrillation (HDCC-RP-30%). **(D)** Fiber surface (HDCC-RP-30%).

denser matrix, leading to tinier crack width. It is calculated that the average crack width of HDCC-RP-60% was around 120 μm, which was close to that of PVA-ECC (Li, 2003).

## Morphology of Fiber in HDCC

**Figure 12** shows the morphology of fibers and fiber/matrix interface of HDCC-RP-Reference and HDCC-RP-30% by scanning electron microscope (SEM) observation. The SEM samples were taken from the ruptured surface of the dumbbell specimens. The majority of PE fibers were stretched out of the HDCC matrix with a blunt end (see in **Figure 12A**) or slightly damaged (see in **Figure 12C**). However, the fibers of HDCC-RP-30% were damaged more severely and led to a higher tensile strength (see in **Figure 12D**).

# CONCLUSION

The impact of RP on hydration, phase development, compressive strength and tensile properties of HDCC were studied in the present research. Three replacement ratios of RP ranging from 10, 30 to 60% were employed. The detailed conclusions are listed as follows.

(1) The addition of RP accelerates the hydration rate and it is demonstrated that the dormant period of HDCC-RP-60% matrix was shortest due to the existence of $CaCO_3$ as the main compound of RP, which is considered to act as the accelerating seeds. The peaks of $CaCO_3$ in different matrices increased significantly with the larger amount of RP. However, the peaks of $Ca(OH)_2$ decreased with higher RP contents due to the significant reduction in cement.

(2) All the HDCC mixtures demonstrated a robust strain-hardening performance with evenly distributed cracks. The peak tensile stress and compressive strength of HDCCs increased with RP replacement ratio up to 30% due to a combination of pozzolanic and filler effect and these strengths decreased afterward. The crack number increased with RP contents, while the strain capacity of HDCC-RP-60% decreased slightly due to its the tinier crack width. The morphology of PE fiber of the tested specimen was investigated by the SEM analysis. The optimal replacement ratio of RP for future practical application is suggested for 30% provided with the similar particle size of current research, when the mechanical performance is considered.

# DATA AVAILABILITY STATEMENT

The raw data supporting the conclusions of this article will be made available by the authors, without undue reservation.

# AUTHOR CONTRIBUTIONS

JJ, HS, and LJ were responsible for designing the experiment scheme, test execution, data analysis, and writing the original manuscript. HR was responsible for guiding the experiment scheme and revision of the manuscript. YZ and YL participated

in the experimental scheme design. All authors contributed to the article and approved the submitted version.

## FUNDING

The authors are grateful for the financial support received from the National Natural Science Foundation of China (grant no. 51178087); The Natural Science Foundation of Heilongjiang Province (grant no. LH2020E018); Opening Fund for Key Laboratory of The Ministry of Education for Structural Disaster and Control of Harbin Institute of Technology (grant no. HITCE201908); Scientific Research Fund of Institute of Engineering Mechanics, China Earthquake Administration (grant no. 2020D07), and Northeast Petroleum University Guided Innovation Fund (grant no. 2020YDL-02).

## REFERENCES

ASTM International (2008). *ASTM Technical Committee Members and Staff Attend Concrete Industry Event in Colombia*. ASTM Standardization News: West Conshohocken, PA, 36.

Ding, Y., Yu, J. T., Yu, K. Q., and Xu, S. L. (2018). Basic mechanical properties of ultra-high ductility cementitious composites: from 40 MPa to 120 MPa. *Compos. Struct.* 185, 634–645. doi: 10.1016/j.compstruct.2017.11.034

Huang, W., Kazemi-Kamyab, H., Sun, W., and Scrivener, K. L. (2017). Effect of cement substitution by limestone on the hydration and microstructural development of ultra-high performance concrete (UHPC). *Cem. Concr. Comp.* 77, 86–101. doi: 10.1016/j.cemconcomp.2016.12.009

Japan Society of Civil Engineers [JSCE] (2008). *Recommendations for Design and Construction of High Performance Fiber Reinforced Cement Composites with Multiple Fine Cracks*. Tokyo: Japan Society of Civil Engineers, 1–16.

Ji, J., Yu, D. Y., Jiang, L. Q., Xu, Z. C., Liu, Y. C., and Zhang, S. L. (2019). Effect of post-fire curing on the compressive properties of fire-damaged ultra-high toughness cementitious composites. *J. Test. Eval.* 47, 140–152.

Li, H., Xiao, H. G., and Ou, J. P. (2007). Effect of compressive strain on electrical resistivity of carbon black-filled cement-based composites. *Cem. Concr. Comp.* 28, 824–828. doi: 10.1016/j.cemconcomp.2006.05.004

Li, H., Xu, S., and Leung, C. K. (2009). Tensile and flexural properties of ultra-high toughness cemontious composite. *J. Wuhan Univ. Technol.* 24, 677–683. doi: 10.1007/s11595-009-4677-5

Li, V. C. (2003). On engineered cementitious composites (ECC). *J. Adv. Concr. Technol.* 1, 215–230.

Liu, J. C., Tan, K. H., and Zhang, D. (2017). Multi-response optimization of post-fire performance of strain hardening cementitious composite. *Cem. Concr. Comp.* 80, 80–90. doi: 10.1016/j.cemconcomp.2017.03.001

Liu, Q., Tong, T., Liu, S., Yang, D., and Yu, Q. (2014). Investigation of using hybrid recycled powder from demolished concrete solids and clay bricks as a pozzolanic supplement for cement. *Constr. Build. Mater.* 73, 754–763. doi: 10.1016/j.conbuildmat.2014.09.066

Nehdi, M., Mindess, S., and Aitcin, P. C. (1996). Optimization of high strength limestone filler cement mortars. *Cem. Concr. Res.* 26, 883–893. doi: 10.1016/0008-8846(96)00071-3

Sun, Z., Liu, F., Tong, T., Qi, C., and Yu, Q. (2017). Hydration of Concrete Containing Hybrid Recycled Demolition Powders. *J. Mater. Civil Eng.* 29:04017037. doi: 10.1061/(asce)mt.1943-5533.0001842

Wang, Y., Wei, L., Yu, J., and Yu, K. (2019). Mechanical properties of high ductile magnesium oxychloride cement-based composites after water soaking. *Cem. Concr. Comp.* 97, 248–258. doi: 10.1016/j.cemconcomp.2018.12.028

Wille, K., Naaman, A., and Montesinos, G. (2011). Ultra-high performance concrete with compressive strength exceeding 150 MPa (22 ksi): a simpler way. *J. ACI Mater.* 108, 46–54.

Xiao, J., Ma, Z., and Ding, T. (2016). Reclamation chain of waste concrete: a case study of Shanghai. *Waste Manage.* 48, 334–343. doi: 10.1016/j.wasman.2015.09.018

Yang, E. H., Yang, Y., and Li, V. C. (2007). Use of high volumes of fly ash to improve ECC mechanical properties and material greenness. *J. ACI Mater.* 104, 620–628.

Yu, J., Li, H. D., Leung, C. K., Lin, X., Lam, J. Y., Sham, I. M., et al. (2017). Matrix design for waterproof engineered cementitious composites (ECCs). *Constr. Build. Mater.* 139, 438–446. doi: 10.1016/j.conbuildmat.2017.02.076

Yu, K. Q., Lu, Z. D., Dai, J. G., and Shah, S. P. (2020). Direct tensile properties and stress–strain model of UHP-ECC. *J. Mater. Civil Eng.* 32:04019334. doi: 10.1061/(asce)mt.1943-5533.0002975

Yu, K., Li, L., Yu, J., Wang, Y., Ye, J., and Xu, Q. (2018). Direct tensile properties of engineered cementitious composites: a review. *Constr. Build. Mater.* 165, 346–362. doi: 10.1016/j.conbuildmat.2017.12.124

Zhang, Z., and Zhang, Q. (2018). Matrix tailoring of engineered cementitious composites (ECC) with non-oil-coated, low tensile strength PVA fiber. *Constr. Build. Mater.* 161, 420–431. doi: 10.1016/j.conbuildmat.2017.11.072

**Conflict of Interest:** The authors declare that the research was conducted in the absence of any commercial or financial relationships that could be construed as a potential conflict of interest.

frontiers in Materials

ORIGINAL RESEARCH
published: 02 August 2021
doi: 10.3389/fmats.2021.711872

# Development of Engineered Cementitious Composites Using Sea Sand and Metakaolin

*Qiyao Yao[1], Zuo Li[1], Chenyu Lu[1], Linxin Peng[1,2,3], Yuejing Luo[4,5] and Xiaodan Teng[1,2,3]**

[1]School of Civil Engineering and Architecture, Guangxi University, Nanning, China, [2]Key Laboratory of Disaster Prevention and Structural Safety of Ministry of Education, Guangxi University, Nanning, China, [3]Guangxi Key Laboratory of Disaster Prevention and Engineering Safety, Guangxi University, Nanning, China, [4]Hualan Design & Consulting Group, Nanning, China, [5]Guangxi Transportation Science & Technology Group CO., LTD, Nanning, China*

The present study investigates the possibility of using sea sand, instead of silica sand, in producing engineered cementitious composites (ECCs) and the optimal mix proportion, mechanical behavior, and erosive effect of chloride ions on sea sand ECCs (SECCs). Nine groups of SECC specimens were prepared based on the orthogonal test design, and these cured for the uniaxial tensile, uniaxial compression, and fracture energy tests. The roundness and sphericity of sea sand and silica sand were quantified by digital microscopy. The microstructure and composition of SECCs were characterized by scanning electron microscopy (SEM) and X-ray diffraction (XRD). The mix proportions of SECCs with a tensile strain capacity more than 2% and a compressive strength more than 60 MPa were obtained. The factor analysis of these serial tests revealed that the contents of both fly ash and sea sand have a significant effect on the compressive strength and tensile strain capacity of SECCs. The fracture energy test revealed that the matrix fracture toughness of SECCs significantly increases with the increase in sea sand content. The XRD analysis revealed that the addition of metakaolin can enhance the ability of SECCs to bind chloride ions, and with the increase in chloride ion content, the ability of SECCs to bind chloride ions would improve. The results of the present study provide further evidence of the feasibility of using sea sand in the production of ECCs, in order to meet the requirements of diverse concrete components on ductility and durability.

**Keywords: sea sand, engineered cementitious composites, orthogonal test, SEM, XRD, Friedel's salt**

OPEN ACCESS

***Edited by:***
*Kequan Yu,*
*Tongji University, China*

***Reviewed by:***
*Rui Zhong,*
*Southeast University, China*
*Shao-Bo Kang,*
*Chongqing University, China*
*Yao Ding,*
*Chongqing University, China*

****Correspondence:***
*Xiaodan Teng*
*xdteng@gxu.edu.cn*

***Specialty section:***
*This article was submitted to Structural Materials, a section of the journal Frontiers in Materials*

***Received:*** *19 May 2021*
***Accepted:*** *30 June 2021*
***Published:*** *02 August 2021*

***Citation:***
*Yao Q, Li Z, Lu C, Peng L, Luo Y and Teng X (2021) Development of Engineered Cementitious Composites Using Sea Sand and Metakaolin. Front. Mater. 8:711872. doi: 10.3389/fmats.2021.711872*

## INTRODUCTION

Engineered cementitious composites (ECCs) are a novel structural material with high resistance to crack and damage and were originally proposed by Li and Leung (Li and Leung, 1992). With the addition of fibers, the tensile strain–hardening characteristic of more than 2% ultimate tensile strain can be obtained, which is approximately 200 times that for ordinary concrete. Excellent crack control, good resistance to wear and spalling, provides ECCs great potentials in the replacement of mainstream building materials (Li et al., 2003; Kojima et al., 2004; ECC Technology Network, 2005; Rokogo and Kanda, 2005; Li and Xu, 2009; Zhong, et al., 2021). However, the aggregate used by ECCs is generally fine silica sand, which is priced at 20–30 times more than untreated sea sand (price varies by region). This high cost limits ECCs' large-scale production and further application in the construction industry. Therefore, it is a promising approach to use sea sand in the place of fine silica sand, in order to reduce the cost of production.

In addition, the preparation of ECCs by sea sand not only saves costs but also eliminates the time-consuming problem of transporting silica sand from inland to coastal areas, thereby shortening the construction period. Huang et al. (Huang et al., 2020a) discussed the feasibility of producing seawater sea sand ECCs (SS-ECCs) by compressive tests and direct tensile tests, and the results indicated that seawater and sea sand slightly increase the compressive strength by 12% and marginally decrease the tensile strength by 6% and tensile strain capacity by 18%. Furthermore, some scholars (Huang et al., 2020b; Huang et al., 2021; Yu et al., 2021) comprehensively investigated the influence of sea sand size, polyethylene fiber length, and fiber volume dosage on the mechanical performance and crack characteristics of SS-ECCs. They proposed a probabilistic method to analyze the reliability of the tensile strain capacity of SS-ECCs, a five-dimensional representation to assess the overall performance of SS-ECCs, and a probabilistic model to describe the stochastic nature and evolution of crack width. Yao et al. (Yao et al., 2022) used sea sand to partially replace silica sand, in combination with BFRP bars, in order to greatly improve the tensile strength of SECCs. Although the effect of sea sand on the mechanical behavior of ECCs has been previously examined, until recently, few data hinted at the importance of chloride ions and the negative effects on the mechanical property of SECCs.

In terms of replacing silica sand with sea sand, the high content of chloride ions in sea sand would corrode the reinforcement. In the present study, metakaolin was added to alleviate the erosive impact of chloride ions, and the comprehensive effects of the amount of fly ash and sea sand on the mechanical properties of SECCs were investigated, according to the orthogonal test design method and the typical ECC design basis (Li, 2012). Analysis of variance (ANOVA) and range analysis were performed on the data through uniaxial tensile and uniaxial compression tests, in order to obtain the optimal fit ratio for tensile strain capacity and compressive strength. The roundness and sphericity of sand were quantified using a digital microscope to distinguish the grain morphology of sea sand from that of the silica sand matrix. Scanning electron microscopy (SEM) and X-ray diffraction (XRD) were used to analyze the mechanism of factor action from a microscopic viewpoint and the chemical composition. In addition, the influence of matrix fracture toughness on the tensile properties of SECCs was investigated using the fracture energy test. The present study would provide reference for further research on the engineering applications of SECC proportion design, contributing to the establishment of the balance between the economy and material properties.

## MATERIALS AND METHODS

In the replacement of silica sand with sea sand, there is concern that the high content of chloride ions in sea sand would corrode the steel reinforcement. There are two binding forms of chloride ions in cement-based materials. One is physical adsorption, that is, chloride ions are adsorbed on the surface of the C-S-H gel. However, the binding force is relatively weak, making it easy to be damaged due to the conversion of the adsorbed chloride ions into free chloride ions (Wang et al., 2013). The other form is chemical binding. Previous studies (Ben-Yair, 1974) have revealed that, in the case of mixed chloride ions, chloride ions would react with the cement hydration product $Ca(OH)_2$ to generate $CaCl_2$ and subsequently react with $C_3A$ in the cement to generate Friedel's salt. The chemical reaction is as follows:

$$Ca(OH)_2 + 2Cl- \rightarrow CaCl_2 + 2OH-, \quad (1)$$

$$C_3A + CaCl_2 + 10H_2O \rightarrow C_3A \cdot CaCl_2 \cdot 10H_2O. \quad (2)$$

The above chemical reaction shows that the binding of chloride ions is mainly due to the formation of Friedel's salt, and the amount of chloride ions that are bound usually increases with an increment in the effectiveness of the $Al_2O_3$ content in cementitious materials. Compared with various supplementary cementitious materials (silica powder, slag, and fly ash), metakaolin (45% $Al_2O_3$) has the highest binding rate of chloride ions (Thomas et al., 2012). As the content of $Al_2O_3$ in the matrix increases (the content of $C_3A$ increases in the matrix), the equilibrium equation **(2)** of the chemical reaction moves to the right. That is, as the metakaolin content increases, the binding rate of chloride ions also increases. Furthermore, metakaolin can refine the pore structure of concrete, reduce chloride ion transport channels, and improve chloride ion penetration resistance (Zeng et al., 2015). However, the $Al_2O_3$ content in cement is merely approximately 5–12%, while metakaolin can reach as high as 40%. Therefore, metakaolin was added in the present experiment to bind the chloride ion and refine the pore structure.

In addition, after the replacement of silica sand with sea sand, which is generally a medium-size sand, the increase in aggregate particle size would lead to more tortuous crack paths (Li, 2012). Thus, the matrix fracture toughness ($K_m$) would not be conducive to multiple cracks. Considering that $K_m$ in the matrix decreases with the increase in fly ash content (Turk and Nehdi, 2018), the investigators attempted to increase the fly ash content to reduce the fracture toughness ($K_m$) of the matrix, thereby maintaining the ductility of the SECC.

## Orthogonal Experimental Design

The orthogonal test is a mathematical method for conducting multifactorial tests based on statistical principles and the orthogonal theory (Statistics group of institute of mathematics

**TABLE 1 |** Test factors and levels.

| Levels | Factors | | |
|---|---|---|---|
| | Sea sand (A) | Metakaolin (B) | Fly ash (C) |
| 1 | 0.6 | 0.12 | 1.2 |
| 2 | 0.8 | 0.16 | 2.2 |
| 3 | 1 | 0.2 | 3.2 |

*Note: The component fractions are presented by weight; factor A represents sea sand/aggregate, factor B represents metakaolin/binder, and factor C represents fly ash/cement.*

**TABLE 2 |** Mix proportions of SECCs.

| Mix ID | Cement | Fly ash | Metakaolin | Silica sand | Sea sand | Water | Fiber (%) (volume) |
|---|---|---|---|---|---|---|---|
| 1 | 1 | 1.2 | 0.12 | 0.338 | 0.507 | 0.626 | 2 |
| 2 | 1 | 2.2 | 0.16 | 0.489 | 0.734 | 0.907 | 2 |
| 3 | 1 | 3.2 | 0.20 | 0.641 | 0.961 | 1.188 | 2 |
| 4 | 1 | 2.2 | 0.12 | 0.242 | 0.967 | 0.896 | 2 |
| 5 | 1 | 3.2 | 0.16 | 0.317 | 1.270 | 1.177 | 2 |
| 6 | 1 | 1.2 | 0.20 | 0.175 | 0.699 | 0.648 | 2 |
| 7 | 1 | 3.2 | 0.12 | 0 | 1.572 | 1.166 | 2 |
| 8 | 1 | 1.2 | 0.16 | 0 | 0.859 | 0.637 | 2 |
| 9 | 1 | 2.2 | 0.20 | 0 | 1.237 | 0.918 | 2 |

*Note: The component fractions are presented by weight.*

CAS, 1975). The orthogonal test selects sufficient representative samples from the full-scale test, according to orthogonality, in order to analyze the relationship between factors and results. The representative samples have the characteristics of uniform dispersion and neat comparison, which is the main method for the fractional factor analysis design. In the present study, the orthogonal test was used to determine the optimal mix proportion. The orthogonal test is widely used in research works and can handle complex issues with significantly lower cost and less time (Bai et al., 2009).

In the present study, the experimental factors to be considered were sea sand content (factor A), metakaolin content (factor B), and fly ash content (factor C). The basis of the orthogonal test is the orthogonal table, and according to the number of different factors or values, different orthogonal tables are selected. The test factors and levels are presented in **Table 1**. The $L_9(3^4)$ orthogonal table (Gao et al., 2019) was applied for the present study. The mix proportions used in the orthogonal test are presented in **Table 2**.

## Raw Materials and Specimen Preparation

SECCs comprise ordinary Portland cement [Class P.O 42.5, Guangxi, China (General Administration of Quality Supervision, Inspection and Quarantine of the People's Republic of China, 2007)], fly ash (aggregate size 13 μm, Class I, Henan, China), metakaolin (aggregate size 6.5 μm, Henan, China), fine silica sand (aggregate size 106 μm, Jiangsu, China), sea sand (chloride content 0.21%, fineness modulus 2.43, and shell particle content 4.4%; the grading curve is presented in **Figure 1**; Philippines), water, polycarboxylate superplasticizer (water reducing rate 25%, Anhui, China), and 2% (volume %) polyvinyl alcohol fiber (the physical and mechanical characteristics are presented in **Table 3**; Kuraray, Japan). The average aggregate diameter used in this study is the average length diameter $D_l$. By adding the diameters of all the aggregates of the sample and dividing them by the total number of aggregate diameters, the average diameter of the aggregates obtained is equal to the arithmetic mean of the diameters of all the particles and is called the average length diameter $D_l$. (Zhang et al., 2000). The chemical composition of cement, fly ash, and metakaolin is presented in **Table 4**. The grading curves for fly ash, metakaolin, and silica sand were determined by particle size analysis (PSA), as shown in **Figure 1**. The sand-to-binder and water-to-binder ratios were 0.36 and 0.27, respectively. The dose of the water-reducing agent was adjusted according to the consistency of the mixture during mixing. The adjustment principle was that the slump of the mixture should reach 200 ± 10 mm.

The uniaxial compression compressive strength of SECCs was measured using cubes, with a dimension of 70.70 mm × 70.70 mm × 70.70 mm, which has been widely used in China (Ministry of Industry and Information of the People's Republic of China, 2018). Then, a 400 mm × 100 mm × 15 mm rectangular plate was used for the tensile test (Li et al., 2001). Four 2 mm thick aluminum plates were pasted at the two ends of the plate specimen to reduce the potential stress concentration caused by the clamping part.

The mixing procedure was initiated by dry mixing of cement, metakaolin, sea sand, fly ash, and fine silica sand using a standard mortar mixer for 2 min (140 rpm). Afterward, the water and water reducer were added to the dry components (stirred at 285 rpm for 5 min), and the PVA fibers were slowly mixed while stirring at 285 rpm for 5 min. Then, the specimens were shaken for 1 min after pouring and

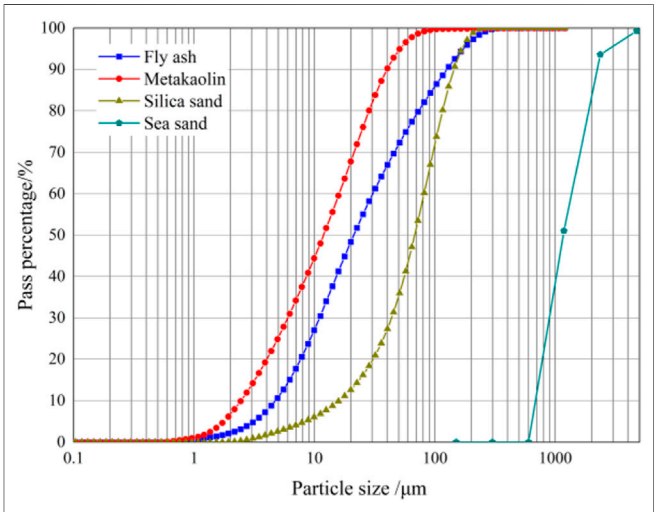


**FIGURE 1 |** Particle size distribution of fly ash, metakaolin, silica sand, and sea sand.

**TABLE 3 |** Physical and mechanical characteristics of the PVA fiber.

| Length (mm) | Diameter (μm) | Tensile strength (MPa) | Elongation (%) | Elastic modulus (GPa) | Density (g/cm$^3$) |
|---|---|---|---|---|---|
| 12 | 39 | 1,620 | 7 | 42.8 | 1.3 |

**TABLE 4 |** Chemical composition of cement, fly ash, and metakaolin (%).

| Material | CaO | $SiO_2$ | $Al_2O_3$ | $Fe_2O_3$ | MgO | $SO_3$ | $Na_2O$ | $K_2O$ | $TiO_2$ | $P_2O_5$ | LOI[a] |
|---|---|---|---|---|---|---|---|---|---|---|---|
| Cement | 63.21 | 18.48 | 6.74 | 3.45 | 3.24 | 3.16 | 0.171 | 0.533 | 0.35 | 0.158 | 3.33 |
| Fly ash | 2.58 | 32.54 | 24.76 | 4.92 | 0.397 | 1.17 | 0.523 | 0.589 | 0.717 | 0.251 | 1.15 |
| Metakaolin | 0.04 | 53.29 | 43.11 | 0.68 | 0.22 | 0.11 | 0.44 | 0.42 | 0.28 | 0.52 | 1.35 |

[a]*Note: LOI, loss on ignition at 1,000°C.*

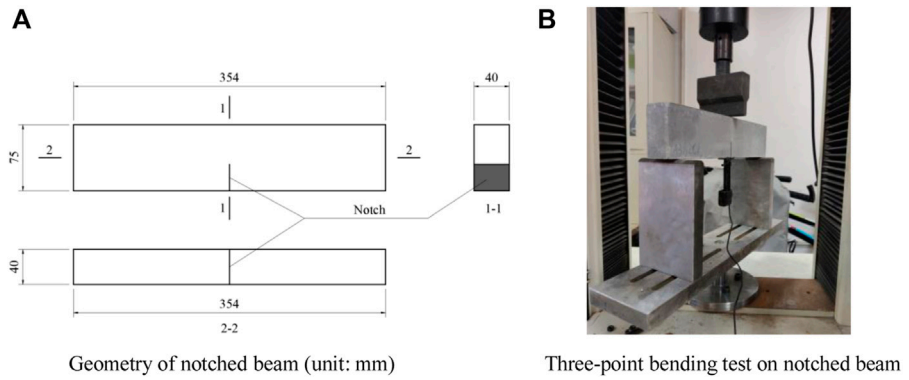


**FIGURE 2 |** Notched beam size and loading method. **(A)** Geometry of the notched beam (unit: mm). **(B)** Three-point bending test on the notched beam.

allowed to stand for 24 h in an environment with a temperature of 25 ± 3°C and a relative humidity of 65 ± 2%. Next, the specimens were stored at a relative humidity of 95 ± 5% and a temperature of 20 ± 2°C, at the age of 28 days. Three specimens were prepared for each proportion used for the tensile test, and three specimens were prepared for each proportion used for the compressive test. The tensile tests were conducted using a microcomputer-controlled electro-hydraulic servo universal testing machine. In the tensile test, the loading method was displacement controlled, and the loading rate was 0.20 mm/min. In the compression test, the loading rate was 0.30 MPa/s.

In order to determine the influence of the fracture toughness of the matrix on the tensile property of SECCs, a three-point bending test on the notched beam was conducted according to ASTM E399-12 (ASTM, 2009). The specimen size was 354 mm × 75 mm × 40 mm. Before the test, a 30.0 mm deep notch was cut at the middle bottom of the specimen, as shown in **Figure 2A**. During the test, a clip extensometer was used to measure the crack mouth opening displacement (CMOD), with a loading rate of 0.05 mm/min. The loading details are presented in **Figure 2B**.

# RESULTS AND DISCUSSIONS

## Uniaxial Tensile Performance

### Test Results

The ultimate tensile stress and ultimate tensile strain of SECCs are listed in **Table 5**. The ultimate tensile strain of SECCs with different mix proportions ranges between 0.38 and 2.4%. The tensile specimen with more than 15% difference compared to the average value was eliminated based on the experimental standard (Ministry of Industry and Information of the People's Republic of China, 2018). The stress–strain curves of the two tensile tests are presented in **Figure 3**. It can be observed from the stress–strain curve that all mixtures exhibited distinct strain-hardening characteristics. Followed by cracking, the bridging capacity of the fiber restricts further crack propagation, and the fluctuation of stress on the curve reflects the generation of multiple cracking behaviors on the specimen surface. In order to scientifically analyze the influence of various factors on SECCs, range analysis and variance analysis were performed on the data in **Table 5**. The null column in the table is actually a comprehensive column of uninvestigated interactions and other unknown influencing factors, which can reflect the errors caused by random factors.

**TABLE 5 |** Results of the uniaxial tensile test of SECCs.

| Mix ID | Factors | | | | Ultimate tensile stress (MPa) | | Ultimate tensile strain (%) | |
|---|---|---|---|---|---|---|---|---|
| | A (sea sand) | B (metakaolin) | C (fly ash) | Null column | First trial | Second trial | First trial | Second trial |
| 1 | 1 (0.6) | 1 (0.12) | 1 (1.2) | 1 | 4.58 | 4.46 | 0.91 | 0.94 |
| 2 | 1 (0.6) | 2 (0.16) | 2 (2.2) | 2 | 3.88 | 2.98 | 0.55 | 0.60 |
| 3 | 1 (0.6) | 3 (0.20) | 3 (3.2) | 3 | 3.48 | 2.99 | 2.40 | 2.10 |
| 4 | 2 (0.8) | 1 (0.12) | 2 (2.2) | 3 | 3.32 | 2.56 | 0.67 | 0.69 |
| 5 | 2 (0.8) | 2 (0.16) | 3 (3.2) | 1 | 2.76 | 2.63 | 1.29 | 1.20 |
| 6 | 2 (0.8) | 3 (0.20) | 1 (1.2) | 2 | 3.84 | 3.33 | 0.39 | 0.38 |
| 7 | 3 (1.0) | 1 (0.12) | 3 (3.2) | 2 | 3.08 | 3.61 | 0.83 | 0.84 |
| 8 | 3 (1.0) | 2 (0.16) | 1 (1.2) | 3 | 3.36 | 3.13 | 0.42 | 0.43 |
| 9 | 3 (1.0) | 3 (0.20) | 2 (2.2) | 1 | 3.25 | 2.67 | 0.69 | 0.65 |

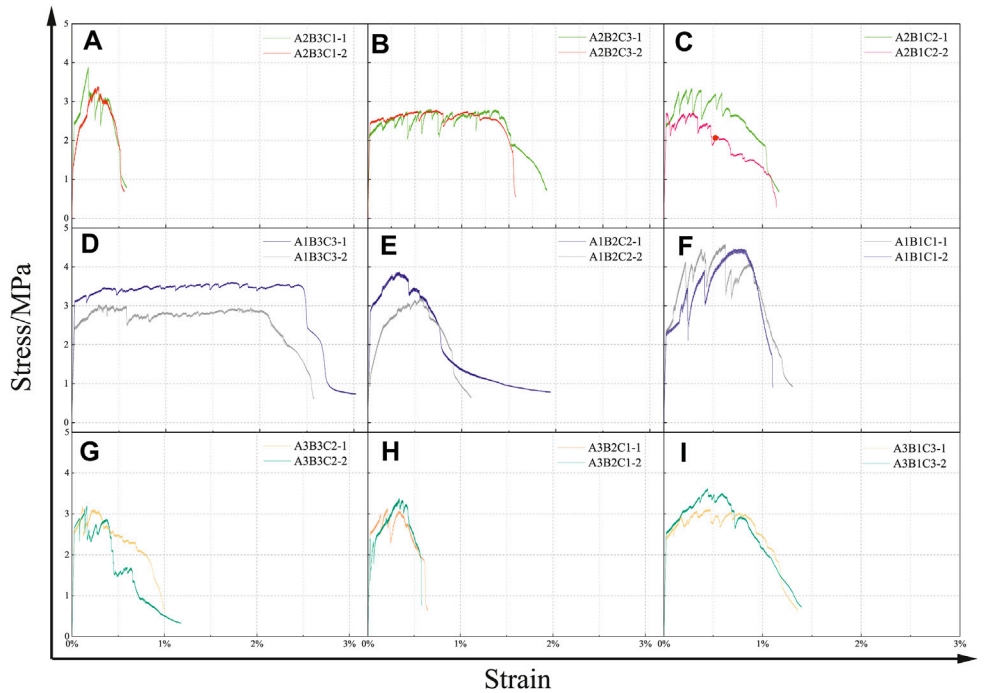


**FIGURE 3 |** Tensile stress–strain curves of SECCs. **(A)**: A2B3C1; **(B)**: A2B2C3; **(C)**: A2B1C2; **(D)**: A1B3C3; **(E)**: A1B2C2; **(F)**: A1B1C1; **(G)**: A3B3C2; **(H)**: A3B2C1; **(I)**: A3B1C3.

**TABLE 6 |** Range analysis of the uniaxial tensile test of SECCs.

| | Factors | $k_1$ | $k_2$ | $k_3$ | $R$ | Order of factors | Optimal mix proportion |
|---|---|---|---|---|---|---|---|
| Ultimate tensile stress | A | 3.73 | 3.07 | 3.18 | 0.66 | C > A > B | A1B1C1 |
| | B | 3.60 | 3.12 | 3.26 | 0.48 | | |
| | C | 3.78 | 3.11 | 3.09 | 0.69 | | |
| Ultimate tensile strain | A | 1.25 | 0.77 | 0.64 | 0.61 | C > A > B | A1B3C3 |
| | B | 0.81 | 0.75 | 1.10 | 0.35 | | |
| | C | 0.58 | 0.64 | 1.44 | 0.87 | | |

## Range Analysis

Range analysis can quickly and intuitively analyze the primary and the secondary order of influencing factors and obtain the optimal mix proportion of SECCs. Range analysis was carried out, and the analysis results for ultimate tensile stress are presented in **Table 6**. The order of influence of each factor on ultimate tensile stress is fly

ash content > sea sand content > metakaolin content, and the optimal mix proportion is A1B1C1. It can be observed from the optimal proportion that the ultimate tensile stress was the greatest when the content of sea sand and fly ash was the lowest. This is because a lower $K_m$ is attained with the increase in fly ash (Li, 2012), and the decrease in $K_m$ resulted in the decrease in tensile strength. The addition of sea sand also reduced the ultimate tensile stress, but its influence was less than that of fly ash. However, the matrix fracture toughness $K_m$ of the ECC matrix increased with the increase in aggregate particle size. This can be attributed to the fact that an increase in aggregate size can lead to fiber reunion, which prevents fibers from performing well in bridging (Li and Li, 2013), ultimately leading to the reduction in ultimate tensile strength. In the present study, digital microscopy was used to quantify the particle morphology of sea sand and silica sand, in order to determine whether there are morphological factors other than particle size that affect the mechanical properties of SECCs. The reason for the minimal effect of metakaolin on the ultimate tensile stress of SECCs is that although metakaolin can refine the pore structure and improve the tensile strength of SECCs to a certain extent, it mainly plays the role of binding the chloride ion in the matrix. Furthermore, this has the least amount in the matrix. Therefore, this has a minimal effect on the ultimate tensile stress of SECCs.

According to the range analysis of the ultimate tensile strain, the order of influence of each factor on the ultimate tensile strain is also fly ash content > sea sand content > metakaolin content, and the optimal mix proportion is A1B3C3. This is because as the content of fly ash increases, the chemical bonding of the fiber/matrix interface decreases, and the frictional bonding increases (Yang, 2007). In particular, the interface bond would be helpful for the fiber pull-out failure, rather than the fiber tensile failure, in the matrix. Furthermore, the increase in fly ash would reduce the matrix fracture toughness $K_m$. Both trends are conducive to the development of multiple cracks in SECCs and improving the ductility. In order to further confirm this result, the destruction of fibers in specimens was observed using a scanning electron microscope after unloading. The range analysis results revealed that the enhancement amplitude for matrix fracture toughness by sea sand (when the content was 0.6) was less than the reduction amplitude for matrix fracture toughness by fly ash (when FA/C was 3.2). However, when the sea sand content was ≥0.8, the increase of matrix fracture toughness for sea sand was greater than the decrease of matrix fracture toughness for fly ash. In general, the ultimate tensile strain generally decreases with the increase in sea sand content. In addition, with the same amount of sea sand, the higher the content of fly ash, the better the ductility, which is consistent with the previous discussion.

## Analysis of Particle Morphology

The critical issue to be addressed for the SECC mix proportion design is to satisfy both the strength and energy criteria (Li, 2012). The strength criterion must initially be met when microcracks are generated. That is, the first cracking strength controlled by the matrix fracture toughness should be less than the fiber bridging capacity $\sigma_0$ at any given potential crack surface:

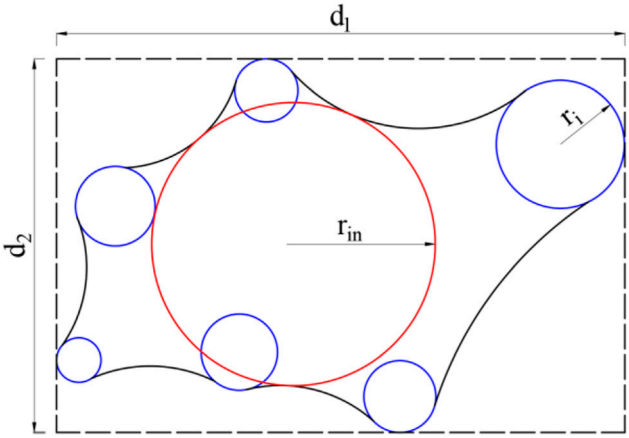


**FIGURE 4 |** Geometric features of sand particles.

$$\sigma_{cr} < \sigma_0 \ . \tag{3}$$

In addition, the energy criterion must be satisfied. The flat crack propagation mode requires an energy balance, that is, the work performed by the tensile load applied on the matrix $\sigma_{ss}\delta_{ss}$ must be equal to the energy required to break down the toughness of the crack-tip material $J_{tip}$ and the energy required to open the fiber bridging crack from 0 to $\delta_{ss}$:

$$\sigma_{ss}\delta_{ss} - \int_0^{\delta_{ss}} \sigma(\delta)\mathrm{d}\delta = J_{tip}, \tag{4}$$

where

$$J_{tip} = \frac{K_m^2}{E_c}, \tag{5}$$

where $E_c$ refers to Young's modulus of the matrix, and the left side of **Eq. 4** is called the complementary energy. When $\sigma(\delta)$ reaches the bridging stress $\sigma_0(\delta_0)$, the complementary energy reaches the maximum value:

$$J_b' \equiv \sigma_0\delta_0 - \int_0^{\delta_0} \sigma(\delta)\mathrm{d}\delta. \tag{6}$$

In order to achieve steady-state cracking, the following is necessary:

$$J_b' > J_{tip}. \tag{7}$$

As an important ingredient for typical ECCs, sand has an important impact on the basic mechanical properties, workability, shrinkage rate, and material cost of materials (Li, 2011). A larger aggregate particle size increases the sinuosity of the crack propagation and matrix fracture toughness $K_m$ (Li, 2012). This is not conducive to flat crack propagation necessary for ECCs and can cause fiber reunion, resulting in the insufficient fiber bridging capacity of flat cracks (Li and Li, 2013). Wu et al. (Wu et al., 2019) explored the influence of the morphological parameters of sand on the mechanical performance of ECCs and determined the morphological parameters (including particle

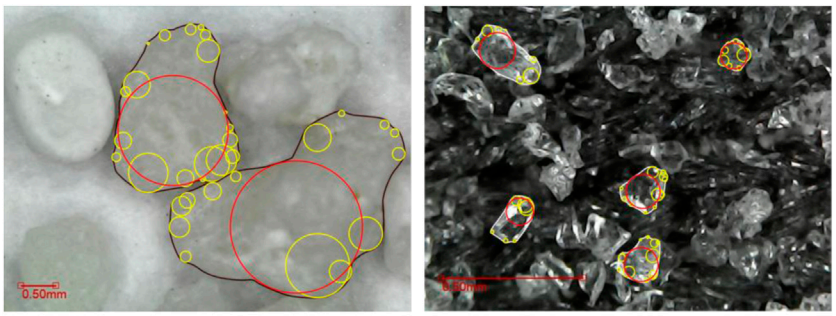


**FIGURE 5 |** Schematic diagram for the roundness and sphericity calculation of **(A)** sea sand and **(B)** silica sand.

roundness and sphericity) of river sand using image analysis and computer algorithms.

Wadell and Hakon (Wadell, 1932; Wadell, 1933) first proposed the use of roundness to describe the sharpness of particle corners. As shown in **Figure 4**, $r_{in}$ refers to the radius of the maximum inscribed circle, $r_i$ refers to the radius of the $i$th inscribed circle, and $n$ refers to the total number of corner circles. The roundness of sand particles is defined as the ratio between the average radius of the curvature at the particle corners and the maximum radius of the inner circle in the following equation:

$$R = \frac{\sum_{i=1}^{n} \frac{r_i}{n}}{r_{in}}. \tag{8}$$

$R$ ranges from 0 to 1. The rounder the sand, the closer the value of R to 1. The sphericity of sand particles describes the approximation degree of the projected area of particles to a circle (Krumbein and Sloss, 1951) as the ratio of the particle width $d_2$ to the particle length $d_1$ in **Eq. 9**. For the sphericity of spherical particles, $S$ is equal to 1. For elongated particles, $S \ll 1$:

$$S = \frac{d_1}{d_2}. \tag{9}$$

Under a digital microscope, the sphericity and roundness of silica sand and sea sand are calculated, as shown in **Figure 5**. The yellow circle represents the inner circle of the sand corners, while the red circle represents the maximum inner circle of the sand particles. A total of 100 complete sand particles were randomly selected from the electronic images of these two kinds of sand, and the roundness and sphericity were calculated and averaged. It can be observed from the calculation results that the sphericity and roundness of these two kinds of sand are not significantly different, and the main difference lies in the particle size and main component. The average particle size of sea sand is 0.42 mm, while the average particle size of silica sand is 0.10 mm. In addition, the main components of sea sand are $SiO_2$ and $CaCO_3$, while the main component of silica sand is $SiO_2$. Therefore, the difference in aggregate morphology between sea sand and silica sand has minimal impact on the fracture toughness of the SECC matrix. This is consistent with the previous discussion that the influence of aggregates on the ultimate tensile stress and ultimate tensile strain of SECCs mainly lies in the particle size.

## Morphology Analysis

After the uniaxial tensile test, the sections of each group of specimens, with a size of 15 mm × 15 mm × 10 mm, were taken out using a small cutting machine. A Phenom scanning electron microscope was used for observation, under an accelerating voltage of 15 kV.

On the microscopic observation of SECC failure surfaces with different mix proportions, the destruction of fibers in different proportions could be clearly observed. In the present study, the tensile failure sections of A1B1C3, A3B2C1, and A2B2C3 were analyzed with the classical ratio of M45 (Singh et al., 2019) as the control. The SEM test results are presented in **Figure 6**.

According to the SEM observations, the fibers in the matrix had tensile failure, regardless of the content of sea sand for SECCs. This was attributable to the fact that, in the energy criterion, in order to fully play the role of the bridging fiber in the matrix, the bond strength of the fiber/matrix should be moderate. That is, if the bond strength is lower, the fiber tension–softening phenomenon would occur, while if the bond strength is higher, the possibility of fiber rupture would increase, thereby reducing $J_b'$, which is not conducive to multiple cracks. Besides, the increase of fly ash content can reduce the chemical bonding strength at the fiber/matrix interface (Li, 2012). The fly ash content of the SECC matrix varies in different mix proportions; therefore, the chemical bond strength of the fiber/matrix interface is different.

The ductility of SECCs is significantly influenced by the fracture toughness of the matrix. In order to determine the influence of different sea sand content on the fracture toughness of the SECC matrix, the three-point bending test of the notched beam was carried out. The results are summarized in **Table 7**. The fracture toughness $K_m$ is calculated according to **Eqs. 10**, **11** (Yu et al., 2018). The load–CMOD curve is presented in **Figure 7A**. As shown in **Figure 7B**, the content of sea sand has a significant influence on $K_m$:

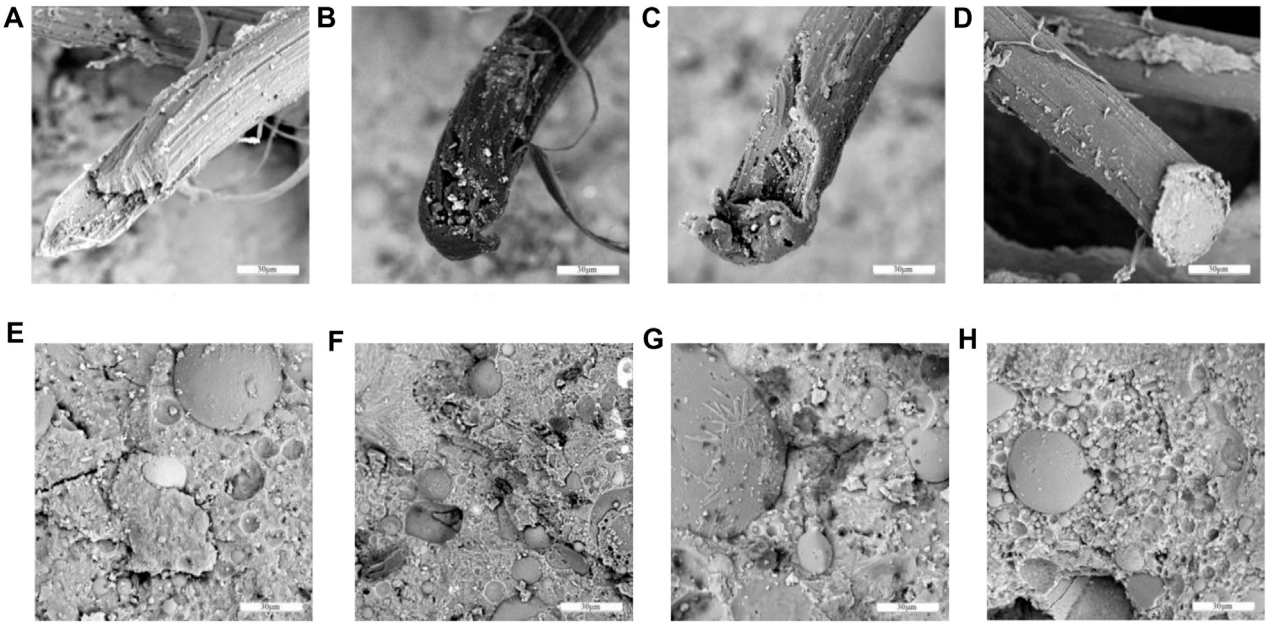


**FIGURE 6 |** SEM images of the microstructure on the fracture surface of ECCs: **(A)** and **(E)** represent A1B3C3, **(B)** and **(F)** represent A2B2C3, **(C)** and **(G)** represent A3B2C1, and **(D)** and **(H)** represent M45.

**TABLE 7 |** Fracture toughness of the mixture.

| Mixture ID | CMOD (mm) | Mass (kg) | Peak load (kN) | Fracture toughness $K_m$ (MPa·m$^{1/2}$) |
|---|---|---|---|---|
| A3B2C1 | 0.027 | 2.11 | 0.578 | 0.508 |
| A2B2C3 | 0.023 | 2.07 | 0.523 | 0.475 |
| A1B3C3 | 0.027 | 1.94 | 0.493 | 0.447 |

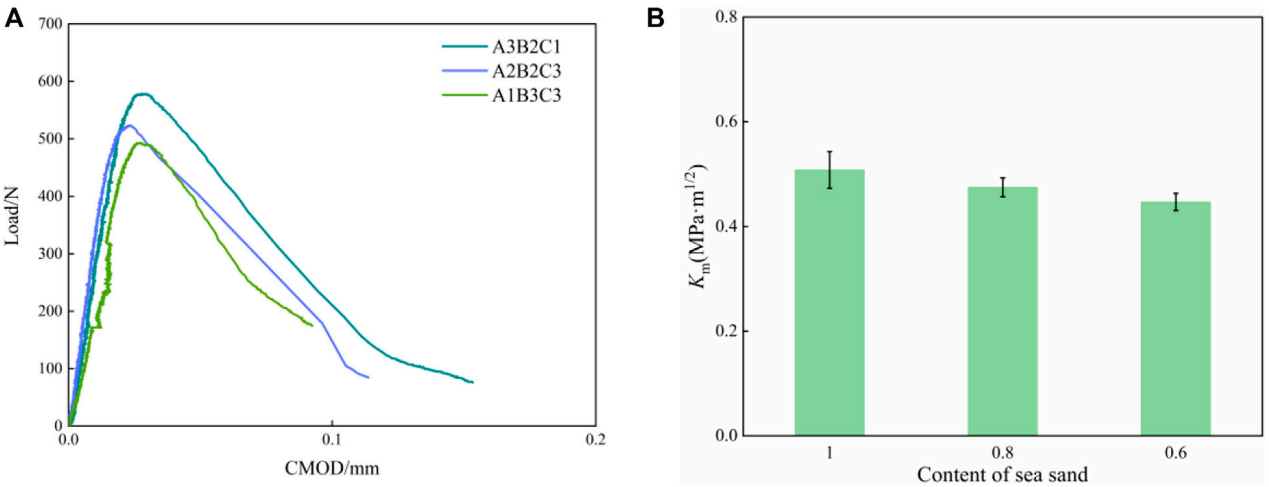


**FIGURE 7 | (A)** Load–CMOD curve of specimens and **(B)** $K_m$ of the mixture under the three-point bending load.

**TABLE 8 |** Analysis of variance for the ultimate tensile stress test.

| Factors | Sum of squared deviations | Degrees of freedom | Variance | F critical value | F value | Significance |
|---|---|---|---|---|---|---|
| A | 1.48 | 2 | 0.74 | $F_{0.1}(2,11) = 2.86$ | 5.00 | (*) |
| B | 0.73 | 2 | 0.36 | $F_{0.05}(2,11) = 3.98$ | 2.47 | |
| C | 1.86 | 2 | 0.93 | $F_{0.01}(2,11) = 7.21$ | 6.31 | * |
| $S_{e1}$ | 0.33 | 2 | 0.17 | — | — | — |
| $S_{e2}$ | 1.29 | 9 | 0.14 | — | — | — |
| $S_e$ | 1.63 | 11 | 0.15 | — | — | — |

*Note: (*), the change in the factor level has a certain influence on the test.*
**The change in the factor level has a significant influence on the test.*

**TABLE 9 |** Analysis of variance for the ultimate tensile strain test.

| Factors | Sum of squared deviations | Degrees of freedom | Variance | F critical value | F value | Significance |
|---|---|---|---|---|---|---|
| A | 1.23 | 2 | 0.61 | $F_{0.1}(2,11) = 2.86$ | 7.56 | ** |
| B | 0.42 | 2 | 0.21 | $F_{0.05}(2,11) = 3.98$ | 2.61 | — |
| C | 2.79 | 2 | 1.39 | $F_{0.01}(2,11) = 7.21$ | 17.16 | ** |
| $S_{e1}$ | 0.84 | 2 | 0.42 | — | — | — |
| $S_{e2}$ | 0.05 | 9 | 0.01 | — | — | — |
| $S_e$ | 0.89 | 11 | 0.08 | — | — | — |

***Note: The change in the factor level has a highly significant influence on the test.*

$$K_m = \frac{1.5\left(F_Q + \frac{mg}{2} \times 10^{-2}\right) \times 10^{-3} \cdot S \cdot a_0^{\frac{1}{2}}}{th^2} f(\alpha), \tag{10}$$

$$f(\alpha) = \frac{1.99 - \alpha(1-\alpha)\left(2.15 - 3.93\alpha + 2.7\alpha^2\right)}{(1+2\alpha)(1-\alpha)^{\frac{3}{2}}}, \alpha = \frac{a_0}{h}. \tag{11}$$

The matrix fracture toughness significantly increases with the increase in sea sand content. This is not conducive to the realization of the energy criterion and leads to the excessive rupture number of the fiber. In contrast, for M45 without sea sand, more fibers were observed in the SEM images for pull-out failure, while few fibers had tensile failure.

Fly ash has three effects in the matrix: microaggregate effect, activity effect, and morphological effect (Yan, 2007). In the SEM images, fly ash particles with a complete grain shape and smooth surface (not involved in the secondary hydration reaction) and fly ash particles attached to the C-S-H gel (already involved in the secondary hydration reaction) could be clearly observed. With the increase in fly ash content, the amount of fly ash without the secondary hydration reaction increases. This significantly improves the pore structure and compactness of the matrix. In addition, the C-S-H gel formed by fly ash participating in the secondary hydration reaction was closely bound to the fly ash. When the matrix was damaged, the fly ash took the hydration products away from the matrix, leaving spherical holes on the fractured surface. Although the increase in fly ash content can reduce the chemical bonds of the fiber/matrix and increase the friction bonds (Yang, 2007), it would still be difficult to balance the improvement of matrix fracture toughness caused by the addition of sea sand. Thus, in ECCs mixed with sea sand, all fibers had tensile failure. However, the ultimate tensile strain of A1B3C3 with the highest fly ash content and the least sea sand content could still reach 2%. This is consistent with the previous discussion that both the increase in interfacial bonds and decrease in fracture toughness of the matrix contribute to the improvement of the ductility of ECCs.

## Variance Analysis

Variance analysis can distinguish the differences in test results due to the changes in factor levels from differences due to fluctuations in error. The variance analysis for the ultimate tensile stress and ultimate tensile strain test results for SECCs is presented in **Tables 8, 9**. It can be observed in **Table 8** that fly ash content is the main factor that affects ultimate tensile stress, and sea sand content merely has a certain influence on ultimate tensile stress. Furthermore, it can be observed in **Table 9** that the content of fly ash and sea sand had a significant influence on the ultimate tensile strain and that the content of fly ash had a more significant influence. However, the change in metakaolin content had no significant influence on the ultimate tensile strength and ultimate tensile strain of SECCs. This is consistent with the results of the range analysis, which shows that the orthogonal analysis result is reasonable.

## Compressive Performance

### Test Results

The compressive strength test results for SECCs are presented in **Table 10**. The compressive strength for SECCs in the nine groups with different mixing proportions ranged between 37.81 and 64.66 MPa. All tested SECCs met the requirements for the design strength grade.

### Range Analysis

The range analysis for the SECC compressive test data was carried out, and the results are presented in **Table 11**. The order of factors

**TABLE 10 |** Results of the compressive strength test for SECCs.

| Mix ID | Factors | | | | Compressive strength (MPa) |
|---|---|---|---|---|---|
| | A (sea sand) | B (metakaolin) | C (fly ash) | Null column | Trial |
| 1 | 1 (0.6) | 1 (0.12) | 1 (1.2) | 1 | 58.38 |
| 2 | 1 (0.6) | 2 (0.16) | 2 (2.2) | 2 | 45.73 |
| 3 | 1 (0.6) | 3 (0.20) | 3 (3.2) | 3 | 37.95 |
| 4 | 2 (0.8) | 1 (0.12) | 2 (2.2) | 3 | 46.75 |
| 5 | 2 (0.8) | 2 (0.16) | 3 (3.2) | 1 | 37.81 |
| 6 | 2 (0.8) | 3 (0.20) | 1 (1.2) | 2 | 51.50 |
| 7 | 3 (1.0) | 1 (0.12) | 3 (3.2) | 2 | 43.67 |
| 8 | 3 (1.0) | 2 (0.16) | 1 (1.2) | 3 | 64.66 |
| 9 | 3 (1.0) | 3 (0.20) | 2 (2.2) | 1 | 47.75 |

**TABLE 11 |** Range analysis for the compressive strength test of SECCs.

| | Factors | k1 | $k_2$ | $k_3$ | R | Order of factors | Optimal mix proportion |
|---|---|---|---|---|---|---|---|
| Compressive strength | A | 47.35 | 45.35 | 52.03 | 6.67 | C > A > B | A3B2C1 |
| | B | 49.60 | 49.40 | 45.73 | 3.87 | | |
| | C | 58.18 | 46.74 | 39.81 | 18.37 | | |

that affect the compressive strength is fly ash content > sea sand content > metakaolin content, and the optimal proportion is A3B2C1. The content of fly ash was also the main factor that affected the compressive strength of SECCs. An appropriate content of fly ash can promote the secondary hydration of cement and fill pores, in order to improve the strength. However, if the fly ash is increased, the amount of cement per unit volume decreases, the effective water-to-cement ratio to control the hydration reaction increases, and the early compressive strength of the material decreases (Fu and Cai, 2019). Therefore, when the content of sea sand is the same, the compressive strength of SECCs decreases with the increase in fly ash content.

Furthermore, sea sand is a secondary factor that affects the compressive strength of SECCs. This can be attributed to the fact that sea sand has a higher density due to the composition of shell particles, which is calcium carbonate. Although calcium carbonate has no gelation, shell particles are strong and durable, which reduce the porosity, to some extent (Xiao et al., 2017). Therefore, the increase of sea sand content contributes to the improvement of the compressive strength of SECCs. The influence of the change in metakaolin content on the tensile performance and compressive performance of SECCs cannot be observed from the range analysis and variance analysis. Therefore, the present study analyzed the action of metakaolin from the chemical point of view.

## X-Ray Diffraction Pattern Analysis

Considering that it is difficult to obtain the effect of metakaolin on the basic mechanical properties of SECCs with the orthogonal test and that it is also difficult to observe Friedel's salt in the SEM images, SECC samples that were aged for 28 days were used for the XRD analysis of the nine mixed proportions, in order to demonstrate chemical reactions (**Eqs. 1**, **2**) and the change in metakaolin content. The samples were crushed and ground in mortar. Then, anhydrous ethanol was added during grinding to stop hydration. After grinding to cement fineness, the samples were collected and dried in an oven at 50 ± 5°C, in order to prevent the hydration products from decomposition at high temperature. Next, the powder samples were analyzed using an X-ray diffractometer (Rigaku D/MAX 2500V, Japan) with a scanning speed of 4°/min and a test range of 5°–60°. The generation of Friedel's salt was observed.

The XRD test patterns for the nine groups of SECC and M45 are presented in **Figure 8**. The diffraction characteristic peaks for Friedel's salt were $d$ = 7.78, 3.88, 3.76, 2.85, 2.41, and 1.69 Å ($2\theta$ = 11.35°, 22.86°, 23.64°, 31.32°, 37.21°, and 53.91°). According to the diffraction pattern, the main crystal components in SECCs were ettringite (AFt), calcium carbonate, Friedel's salt, unhydrated tricalcium silicate and dicalcium silicate, calcium hydroxide, and silica dioxide, while calcium carbonate and Friedel's salt were not present in M45.

### *Effects of Sulfate Ions on Phase Composition*

In the case of mixing chloride ions in sea sand, $C_3A$ in the matrix reacts with the chloride ion to form Friedel's salt in the cement hydration process, and the use of sulfate in the cementation material (the $SO_3$ content in cement was the highest, 3.16%) would cause competition between the sulfate ion and the chloride ion for $C_3A$. However, in the hydration process of cement mixed with chloride ions, it has been generally considered that the $C_3A$ phase preferentially reacts with sulfate ions to form AFt until the sulfate ions are exhausted, and subsequently, Friedel's salt is generated (Wang et al., 2013). Hence, the peak value of AFt in the diagram was not obvious. Furthermore, the addition of various mineral admixtures reduced the absolute production amount of AFt. If the fly ash content is increased, the cement content decreases, and the sulfate ions in the matrix on the whole

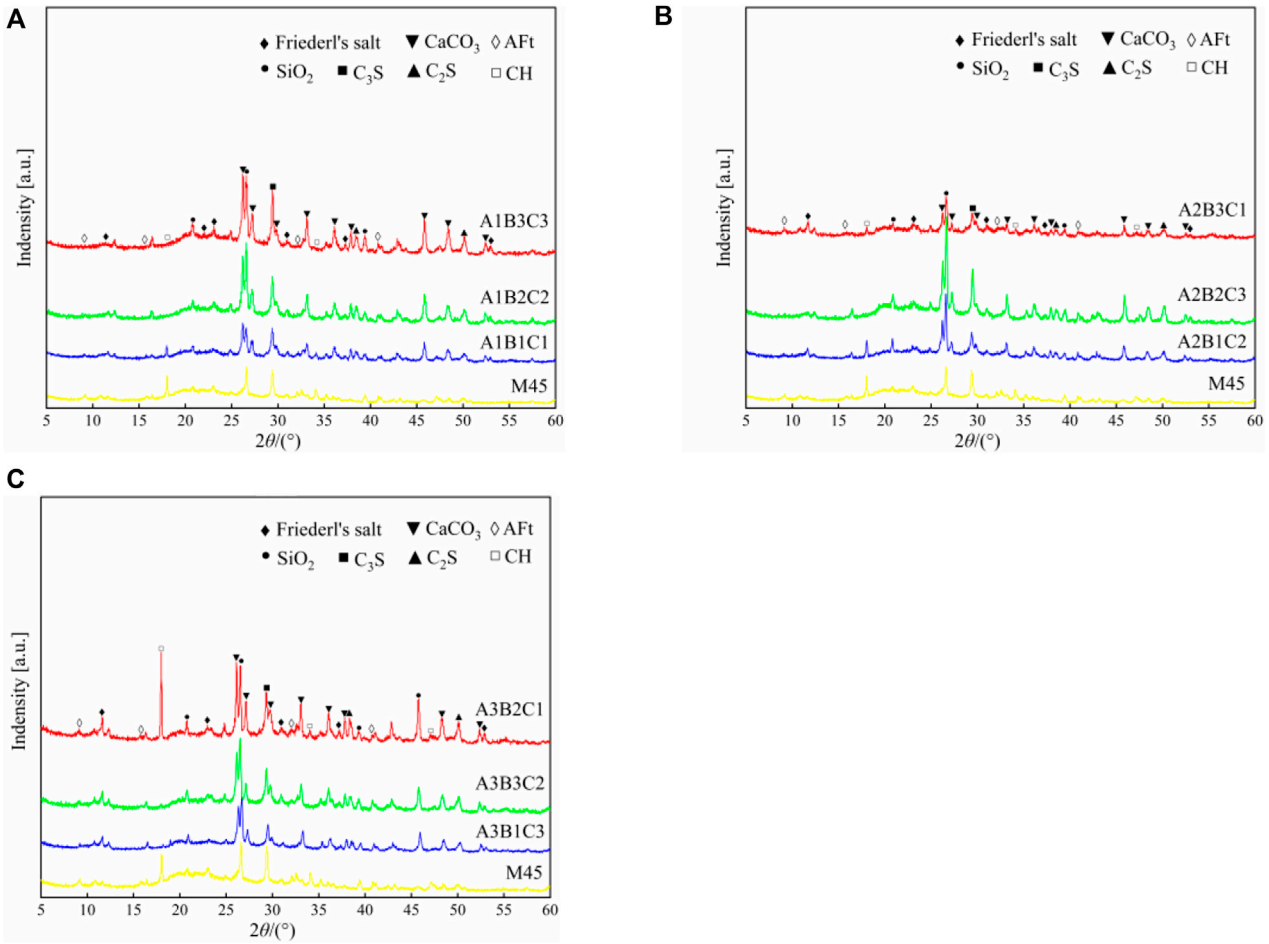


**FIGURE 8 |** X-ray diffraction pattern for SECC and M45.**(A)**: The sea sand content is 60%; **(B)**: The sea sand content is 80%; **(C)**: The sea sand content is 100%.

also decrease. Therefore, in the proportion with the least fly ash content (FA/C = 1.2), the peak value of AFt was the most obvious.

***Analysis of Causes Affecting the Production of Friedel's Salt***

It can be observed from **Figures 8A–C** that the diffraction peak intensity of Friedel's salt increases with the increase in sea sand content. Therefore, the increase of sea sand content (i.e., the increase in chloride ion content) increases the content of Friedel's salt. This can be attributed to the fact that metakaolin and fly ash both contain a significant amount of $C_3A$, which can fully react with the chloride ions in sea sand to form Friedel's salt (Wang et al., 2013). Therefore, if the chloride ion content is increased, the content of Friedel's salt also increases. In addition, in the initial stage of mixing, the chloride ion at the far end of the surface of sea sand is dissolved in the solution, at the interface between sea sand and cement paste. In the later stage of mixing, along with the hydration of cement, the chloride ions near the surface of sea sand would gradually spread outward, with sea sand as the center. Some of free chloride ions formed Friedel's salt with hydration products, while the other parts were distributed around the aggregate or adsorbed by the C-S-H gel (Xing et al., 2006). Therefore, the diffraction peak of Friedel's salt was not obvious for the proportion with less sea sand content (less chloride ion content). However, the chloride ion mainly reacts with metakaolin to produce Friedel's salt (Wang et al., 2013), thereby affecting the mechanical properties of SECCs. In the present study, the curing time was short, and Friedel's salt content generated by the reaction was small. Hence, it was difficult to observe the macro effect of metakaolin.

## Variance Analysis

The variance analysis for the SECC compressive strength test results is presented in **Table 12**. As illustrated in **Table 12**, the content of both sea sand and fly ash had influences on the SECC compressive strength. Fly ash was still the main factor that affected the compressive strength, and the influence of sea sand content was less than that of fly ash. Furthermore, there was no significant difference in the influence of metakaolin content on compressive strength. The variance analysis result was consistent with the range analysis result. Hence, the orthogonal analysis result is reasonable.

# CONCLUSION

In the present study, range and variance analysis, XRD analysis, and SEM analysis were applied to investigate the SECC uniaxial

**TABLE 12 |** Analysis of variance for the compressive strength test.

| Factors | Sum of squared deviations | Degrees of freedom | Variance | F critical value | F value | Significance |
|---|---|---|---|---|---|---|
| A | 70.37 | 2 | 35.19 | $F_{0.1}(2,2) = 9.00$ | 17.24 | (a) |
| B | 28.44 | 2 | 14.22 | $F_{0.05}(2,2) = 19.0$ | 6.97 | — |
| C | 516.33 | 2 | 258.16 | $F_{0.01}(2,2) = 99.0$ | 126.52 | ** |
| $S_e$ | 12.24 | 2 | 6.12 | — | — | — |

*Note: (a), the change in the factor level has a certain influence on the test.*
***The change in the factor level has a highly significant influence on the test.*

tensile and compressive performances. The following conclusions were obtained.

The ultimate tensile strain of SECCs was 0.38–2.40%, the ultimate tensile stress of SECCs was 2.56–4.58 MPa, and the compressive strength of SECCs was 37.81–64.66 MPa. The content of fly ash and sea sand had a highly significant positive effect on ultimate tensile strain. Furthermore, the fly ash content had a highly significant negative effect on compressive strength, and the ultimate tensile stress and compressive strength were less affected by the sea sand content.

For the parameter ranges, the content of fly ash and sea sand almost completely determined the ductility of SECCs. The increase in fly ash content significantly increased the ductility of SECCs. The decrease of cement content and the increase of fly ash content led to the decrease of SECC compressive strength. Furthermore, the ultimate tensile strain decreased with the increase in sea sand content, and by observation and calculation using a digital microscope, sea sand and silica sand had similar sphericity and roundness, except for the difference in particle size and chemical composition. Moreover, the fracture energy test revealed that the matrix fracture toughness of SECCs significantly increased with the increase in sea sand content.

Although the content of metakaolin had minimal influence on the basic mechanical properties of SECCs in the test, which could contribute to the lack of curing time and the incomplete reaction of $C_3A$ in metakaolin with the chloride ion in sea sand, Friedel's salt could be observed in the XRD analysis, and this content increased with the increase in sea sand content (chloride ion content). Therefore, metakaolin is indispensable for binding chloride ions in the SECC matrix to improve durability.

In the SECC uniaxial tensile test, it could be observed from the SEM test that the fiber failure mode was tensile failure. Finally, the mixed proportions of group 3 (FA/C was 3.2, the sea sand content was 0.6, and the metakaolin content was 0.2) and group 8 (FA/C was 1.2, the sea sand content was 1, and the metakaolin content was 0.16) were recommended for SECCs, based on the results of the present study.

In the present study, more economical, site-specific, and durable SECC proportions were obtained while maintaining the ductility of SECCs at more than 2%. Depending on the engineering application, the proportion of high ductility (ultimate tensile strain 2.4%, compressive strength 37.95 MPa, and ultimate tensile stress 3.48 MPa) or high compressive strength (compressive strength 64.66 MPa, ultimate tensile strain 0.42%, and ultimate tensile stress 3.36 MPa) can be selected, which can meet the tensile strain capacity, corrosion resistance, or strength requirements of practical constructions.

## DATA AVAILABILITY STATEMENT

The original contributions presented in the study are included in the article/supplementary material, and further inquiries can be directed to the corresponding author.

## AUTHOR CONTRIBUTIONS

QY designed the experiment and involved in data analysis. QY and XT investigated the data and wrote the manuscript. QY, ZL, CL, and XT performed the methodology. QY, ZL, CL, and XT revised the manuscript. XT involved in funding acquisition and project administration.

## FUNDING

The authors are grateful for the financial support provided by the China Postdoctoral Science Foundation (No. 2018M633298), the National Natural Science Foundation of China (Nos. 51738004, 51878186, 11962001), the Innovation Project of Guangxi Graduate Education (No. YCSW2019048), the National Key Research and Development Program (No. 2019YFC1511103), and the Guangxi Innovation-driven Major Project (No. GuiKe AA18118055).

## REFERENCES

ASTM (2009). Standard Test Method for Linear-Elastic Plane-Strain Fracture Toughness KIC of Metallic Materials. New York: ASTM International, E399–09.

Bai, W., Zhang, J., Yan, P., and Wang, X. (2009). Study on Vibration Alleviating Properties of Glass Fiber Reinforced Polymer concrete through Orthogonal Tests. *Mater. Des.* 30 (4), 1417–1421. doi:10.1016/j.matdes.2008.06.028

Ben-Yair, M. (1974). The Effect of Chlorides on concrete in Hot and Arid Regions. *Cement Concrete Res.* 4 (3), 405–416. doi:10.1016/0008-8846(74)90106-9

ECC Technology Network (2005). *Repair of Mitaka Dam*. Available at: http://www.engineeredcomposites.com/Applications/mitaka dam.html (Accessed April 6, 2020).

Fu, B. Q., and Cai, X. R. (2019). Effect of Large Amount Fly Ash on Properties of High Toughness Fiber Reinforced Cementitious Composites. *Concrete* (08), 88–91. doi:10.3969/j.issn.1002-3550.2019.08.020

Gao, N., Gao, J., Hu, X. L., Xu, X. X., Sun, R. J., and Lu, Q. (2019). Mix Proportion Design of UHTCC Based on Orthogonal Test. *Concrete* 000 (006), 55–60. doi:10.3969/j.issn.1002-3550.2019.06.013

General Administration of Quality Supervision, Inspection and Quarantine of the People's Republic of China. (2007). Common Portland Cement. Beijing: Standards Press of China, GB 175–2007.

Huang, B.-T., Wu, J.-Q., Yu, J., Dai, J.-G., and Leung, C. K. (2020a). High-strength Seawater Sea-Sand Engineered Cementitious Composites (SS-ECC): Mechanical Performance and Probabilistic Modeling. *Cement and Concrete Composites* 114, 103740. doi:10.1016/j.cemconcomp.2020.103740

Huang, B.-T., Yu, J., Wu, J.-Q., Dai, J.-G., and Leung, C. K. (2020b). Seawater Sea-Sand Engineered Cementitious Composites (SS-ECC) for marine and Coastal Applications. *Composites Commun.* 20, 100353. doi:10.1016/j.coco.2020.04.019

Huang, B.-T., Wu, J.-Q., Yu, J., Dai, J.-G., Leung, C. K. Y., and Li, V. C. (2021). Seawater Sea-Sand Engineered/strain-Hardening Cementitious Composites (ECC/SHCC): Assessment and Modeling of Crack Characteristics. *Cement Concrete Res.* 140, 106292. doi:10.1016/j.cemconres.2020.106292

Kojima, S., Sakata, N., and Kanda, T. (2004). Application of Direct Sprayed ECC for Retrofitting Dam Structure Surface Application for Mitaka-Dam. *Concrete J.* 42, 135–139.

Krumbein, W. C., and Sloss, L. L. (1951). Stratigraphy and Sedimentation. *Soil Sci.* 71 (5), 401. doi:10.1097/00010694-195105000-00019

Li, M., and Li, V. C. (2013). Rheology, Fiber Dispersion, and Robust Properties of Engineered Cementitious Composites. *Mater. Struct.* 46 (3), 405–420. doi:10.1617/s11527-012-9909-z

Li, Q. H., and Xu, S. L. (2009). Performance and Application of Ultra High Toughness Cementitious Composite: A Review. *Eng. Mech.* 26, 23–67.

Li, V. C. (2011). *Engineered Cementitious Composites (ECC)-material, Structural, and Durability Performance Concrete Construction Engineering Handbook*. Boca Raton: CRC Press

Li, V. C. (2012). Tailoring ECC for Special Attributes: A Review. *Int. J. Concr Struct. Mater.* 6 (3), 135–144. doi:10.1007/s40069-012-0018-8

Li, V. C., Fischer, G., Kim, Y., Lepech, M. D., Qian, S., Weimann, M., et al. (2003). Durable Link Slabs for Jointless Bridge Decks Based on Strain-Hardening Cementitious Composites. *Deterioration*.

Li, V. C., and Leung, C. K. Y. (1992). Steady-State and Multiple Cracking of Short Random Fiber Composites. *J. Eng. Mech.* 118 (11), 2246–2264. doi:10.1061/(asce)0733-9399(1992)118:11(2246)

Li, V. C., Wang, S. X., and Wu, C. (2001). Tensile Strain-Hardening Behavior or Polyvinyl Alcohol Engineered Cementitious Composite (PVA-ECC). *ACI Mater. J.* 98, 483–492. doi:10.1089/apc.2006.20.829

Ministry of Industry and Information of the People' s Republic of China (2018). *Standard Test Method for the Mechanical Properties of Ductile Fiber Reinforced Cementitious Composites*. Beijing, China: China Building Materials Press. JC/T 2461-2018

Rokogo, K., and Kanda, T. (2005). *Proceedings of International Workshop on HPFRCC in Structural Applications*. Bagneux: RILEM Publications SARL.

Singh, M., Saini, B., and Chalak, H. D. (2019). Performance and Composition Analysis of Engineered Cementitious Composite (ECC) - A Review. *J. Building Eng.* 26, 100851. doi:10.1016/j.jobe.2019.100851

Statistics group of institute of mathematics CAS (1975). *Orthogonal Tests*. Beijing, China: People's Education Press.

Thomas, M. D. A., Hooton, R. D., Scott, A., and Zibara, H. (2012). The Effect of Supplementary Cementitious Materials on Chloride Binding in Hardened Cement Paste. *Cement Concrete Res.* 42 (1), 1–7. doi:10.1016/j.cemconres.2011.01.001

Turk, K., and Nehdi, M. L. (2018). Coupled Effects of limestone Powder and High-Volume Fly Ash on Mechanical Properties of ECC. *Construction Building Mater.* 164 (MAR.10), 185–192. doi:10.1016/j.conbuildmat.2017.12.186

Wadell, H. (1932). Volume, Shape, and Roundness of Rock Particles. *J. Geology.* 40 (5), 443–451. doi:10.1086/623964

Wadell, H. (1933). Sphericity and Roundness of Rock Particles. *J. Geology.* 41 (3), 310–331. doi:10.1086/624040

Wang, X. G., Shi, C. J., He, F. Q., Yuan, Q., Wang, D. H., Huang, Y., et al. (2013). Chloride Binding and its Effects on Microstructure of Cement-Based Materials. *J. Chin. Ceram. Soc.* 41 (2), 187–198. doi:10.7521/j.issn.0454-5648.2013.02.11

Wu, H.-L., Yu, J., Zhang, D., Zheng, J.-X., and Li, V. C. (2019). Effect of Morphological Parameters of Natural Sand on Mechanical Properties of Engineered Cementitious Composites. *Cement and Concrete Composites* 100, 108–119. doi:10.1016/j.cemconcomp.2019.04.007

Xiao, J., Qiang, C., Nanni, A., and Zhang, K. (2017). Use of Sea-Sand and Seawater in concrete Construction: Current Status and Future Opportunities. *Construction Building Mater.* 155 (30), 1101–1111. doi:10.1016/j.conbuildmat.2017.08.130

Xing, F., Liu, J., Dong, B., and Huo, Y. (2006). Combination Procedure and Mechanism of Sea Sand Type Chloride Ions with Cement Materials. *J. Southeast Univ. (Natural Sci. Edition)* 36, 167–172.

Yan, P. (2007). Mechanism of Fly Ash's Effects during Hydration Process of Composite Binder. *J. Chin. Ceram. Soc.* 35, 167–171.

Yang, E. H. (2007). *Designing Functionalities into ECC Materials via Micromechanics. [dissertation]. [Michigan]*. Beijing, China: University of Michigan.

Yao, Q. Y., Lu, C. Y., Peng, L. X., Teng, X. D., and Luo, Y. J. (2022). Experimental Study on Tensile and Bending Properties of Sea Sand ECC Reinforced by BFRP Bars under Chloride Salt Erosion. *Acta Materiae Compositae Sinica*. doi:10.13801/j.cnki.fhclxb.20210426.005

Yu, J., Huang, B.-T., Wu, J.-Q., Dai, J.-G., and Leung, C. K. Y. (2021). "Tensile and Compressive Performance of High-Strength Engineered Cementitious Composites (ECC) with Seawater and Sea-Sand," in *Fibre Reinforced Concrete: Improvements and Innovations. BEFIB 2020. RILEM Bookseries*. Editors P. Serna, A. Llano-Torre, J. R. Martí-Vargas, and J. Navarro-Gregori (Cham: Springer), Vol. 30, 1034–1041. doi:10.1007/978-3-030-58482-5_91

Yu, K.-Q., Yu, J.-T., Dai, J.-G., Lu, Z.-D., and Shah, S. P. (2018). Development of Ultra-high Performance Engineered Cementitious Composites Using Polyethylene (PE) Fibers. *Construction Building Mater.* 158, 217–227. doi:10.1016/j.conbuildmat.2017.10.040

Zeng, J. J., Wang, S. N., Fan, Z. H., and Xiong, J. B. (2015). Improvement Effect and Mechanism of Metakaolin on marine concrete Chloride Penetration Resistance. *J. Wuhan Univ. Technology* 37, 22–28. doi:10.3963/j.issn.1671-4431.2015.04.005

Zhang, M., Weng, Z., Huang, Z., and Pan, Z. (2000). Characterization of Statistical Average Particle Size and Particle Size Distribution. *Polym. Mater. Sci. Eng.* 16 (005), 1–4. doi:10.3321/j.issn:1000-7555.2000.05.001

Zhong, R., Zhang, F., Poh, L. H., Wang, S., Le, H. T. N., and Zhang, M.-H. (2021). Assessing the Effectiveness of UHPFRC, FRHSC and ECC against High Velocity Projectile Impact. *Cement and Concrete Composites* 120, 104013. doi:10.1016/j.cemconcomp.2021.104013

**Conflict of Interest:** The author YL was employed by Guangxi Transportation Science & Technology Group CO., LTD., and now by Hualan Design & Consulting Group.

The remaining authors declare that the research was conducted in the absence of any commercial or financial relationships that could be construed as a potential conflict of interest.

**Publisher's Note:** All claims expressed in this article are solely those of the authors and do not necessarily represent those of their affiliated organizations, or those of the publisher, the editors and the reviewers. Any product that may be evaluated in this article, or claim that may be made by its manufacturer, is not guaranteed or endorsed by the publisher.

frontiers in Materials

ORIGINAL RESEARCH
published: 23 August 2021
doi: 10.3389/fmats.2021.727273

# Experimental Research on Compressive and Shrinkage Properties of ECC Containing Ceramic Wastes Under Different Curing Conditions

*Yan Xiong*[1,2], *Yi Yang*[1], *Shuai Fang*[1]*, *Di Wu*[3] *and Yingfeng Tang*[4]

[1]School of Civil Engineering and Transportation, South China University of Technology, Guangzhou, China, [2]State Key Laboratory of Subtropical Building Science, South China University of Technology, Guangzhou, China, [3]Earthquake Engineering Research and Test Center, Guangzhou University, Guangzhou, China, [4]Guangzhou Pearl River Foreign Investment Architectural Design Institute Co. Ltd, Guangzhou, China

Engineered cementitious composites (ECCs) suffer from high shrinkage and low early strength due to large dosage of cementitious materials and slow hydration of fly ash. This study aims to improve compressive properties and reduce drying shrinkage of ECC using ceramic wastes and hydrothermal curing. Experimental results have indicated that ceramic polishing powder (CPP) and recycled ceramic sand (RCS) exert opposite effect on the compressive strength of ECC. Hydrothermal-cured ECC enhances elasticity modulus and compressive strength and reduces later drying shrinkage as compared with that under standard curing. A CPP dosage of 35% and a hydrothermal curing regime with a temperature of 70°C and age of 7 days are recommended for the engineering application of ECC.

**Keywords: ECC, compressive property, shrinkage, ceramic waste, curing condition**

OPEN ACCESS

***Edited by:***
*Kequan Yu,*
*Tongji University, China*

***Reviewed by:***
*Li Yazhao,*
*Nanyang Technological University, Singapore*
*Dan Meng,*
*Nanyang Technological University, Singapore*

***Correspondence:**
*Shuai Fang*
*fangshuai@scut.edu.cn*

***Specialty section:***
*This article was submitted to Structural Materials, a section of the journal Frontiers in Materials*

***Received:*** *18 June 2021*
***Accepted:*** *28 July 2021*
***Published:*** *23 August 2021*

***Citation:***
*Xiong Y, Yang Y, Fang S, Wu D and Tang Y (2021) Experimental Research on Compressive and Shrinkage Properties of ECC Containing Ceramic Wastes Under Different Curing Conditions. Front. Mater. 8:727273. doi: 10.3389/fmats.2021.727273*

## INTRODUCTION

Compared with common cement-based materials, the engineered cementitious composite (ECC) has excellent ductility, impact strength, and fracture resistance (Li, 2003). It exhibits strain-hardening and multiple cracking behaviors with ultimate strain exceeding 3% under uniaxial tension (Li et al., 2001). Because of these significant advantages, ECC has become increasingly popular in the field of civil engineering. However, ECC produces large drying shrinkage due to the high content of cementitious materials. Its 28-day shrinkage strain can reach up to 1,200–1,800 με (Gao et al., 2018). Such large shrinkage causes high tensile stress and even cracks in ECC, which degrades the stiffness and resistance to penetration. When ECC is utilized as the repairing and connecting material, the shrinkage weakens the bond between the ECC and the substrate (Li and Li, 2006). The high dosage of fly ash in ECC even causes low early strength, which leads to long curing time and slow turnover of formwork. In addition, the cementitious materials and quartz sand increase the cost of ECC. The above-mentioned shortcomings hinder the application of ECC in engineering.

High-temperature curing, including steam curing and hydrothermal curing, can effectively activate pozzolanic reaction and elevate the early hydration degree of cementitious materials. More hydration products generate on the surface of cementitious particles, which makes the microstructure denser (Hanehara et al., 2001). As a result, the early strength of cement-based

materials is significantly improved. The high-temperature curing also shortens the curing time and production cycle, speeds up the turnover of the mold, and improves the production efficiency (Wu et al., 2017; Liu et al., 2020). Studies have demonstrated that steam curing improves the bond performance of the fiber-cement matrix interface. The strength and fracture energy of the interface show an upward trend with increasing curing age (Zhu et al., 2011; Wei, 2017). Besides the mechanical properties, the shrinkage of concrete can be reduced by high-temperature curing (Richard and Cheyrezy, 1995).

Ceramic polishing powder (CPP) is a by-product from grinding and polishing processes of ceramic tile production. Benefited by the small particle size and glass phase, CPP has high pozzolanic activity, which makes it an ideal substitute to replace cement or fly ash (Ay and Ünal, 2000; Wang et al., 2011). Wang et al. (2012) found that CPP as an admixture can exert secondary hydration effect, refine the pore structure of the hardened cement paste, and inhibit the alkali-aggregate reaction. Li et al. (2019a) indicated that addition of CPP by 20 vol% can reduce the cement content by 33% and increase 7-day and 28-day compressive strength by 85% at least. In addition, CPP can effectively improve chloride resistance of the mortar (Li et al. 2020), substantially decrease autogenous shrinkage of cement paste (Li et al. 2019b), and improve the frost resistance of the mortar (Cao et al., 2014).

In addition as a substitute for cement, qualified hardness and good wear resistance enable ceramic wastes to act as aggregates. Using recycled ceramic sand (RCS) as a replacement to partial sand can lead to various enhancements in the compressive strength, abrasion resistance, workability, resistance to chloride-ion corrosion of concrete, and reduction in the shrinkage of the mortar (Binici, 2007; López et al., 2007; Liu et al., 2015; Nie et al., 2015). However, it was also found that RCS slightly deteriorated workability and compressive strength of masonry mortar and recycled concrete in other studies. This was attributed to high water absorption, slightly low density, and rough surface of the RCS than river sand (Wu et al., 2008). The influence of RCS on mechanical properties of cementitious composites needs to be studied further.

The annual emission of ceramic wastes in China has exceeded 18 million tons. The wastes from Foshan account for one fifth of the national emission (Cai et al., 2011; Wang et al., 2019). However, most of the ceramic wastes are disposed by means of stacking in the open, without any treatment or utilization. The waste particles and dust pollute air, groundwater, and soil, which arouses public concern (Xu et al., 2013). Application of ceramic wastes in ECC is an appropriate method to deal with the wastes from the perspective of economics and environment.

As mentioned above, high-temperature curing can increase early strength and reduce drying shrinkage of cementitious materials. CPP and RCS have great potential to be mineral admixtures and aggregates, respectively. The application of ceramic wastes in ECC will produce additional economic and environmental benefits. This study, therefore, was intended to improve the compressive and shrinkage performance of ECC using ceramic wastes and hydrothermal curing. To this aim, ECC specimens containing ceramic wastes were first cured under various conditions and then subjected to compressive and drying shrinkage tests. The effects of curing conditions and ceramic waste dosages were investigated.

# EXPERIMENTAL PROGRAM

## Materials and Mix Proportions

The materials used in the production of the ECC mixture consisted of cementitious materials, aggregates, fibers, and additives.

### Cementitious Materials

Class 42.5R ordinary Portland cement and Class F fly ash were used as the binders of the control mixture. The fly ash had a specific surface area of 362 $m^2$/kg. CPP was utilized as an alternative to fly ash. The chemical composition of cement, fly ash, and CPP is presented in **Table 1**. Similar to fly ash, CPP was mainly composed of aluminosilicate. The residue on the 45 μm sieve of cement, fly ash, and CPP was 10.2, 11.2, and 3.1%, respectively, which meets the requirement as cementitious materials. The particle sizes of the cementitious materials are illustrated in **Figure 1**. CPP had fineness between that of cement and fly ash.

### Aggregates

Quartz sand and RCS with the size of about 100 mesh were used as the aggregates of ECC. As illustrated in **Figure 2**, RCS was obtained by crushing and milling ceramic tile fragments and configuration according to the gradation of quartz sand. The microtopography of both aggregates was taken using a scanning electron microscope. Both RCS and quartz sand had sharp edges and rough surfaces, while there were more large particles and chippings in the former (**Figure 3**). This is also verified by the size distribution of aggregates in **Figure 1**. RCS particles had close median size while wider distribution than quartz sand.

### Fibers

The fibers used were polyvinyl alcohol (PVA) fibers and basalt fibers (**Figure 4**). Detailed properties of the fibers are summarized in **Table 2**.

### Additives

A superplasticizer with a water reducing rate of 20% and a hydroxypropyl methyl cellulose-based thickener were used to improve the workability of ECC in this study.

### Mix Proportions

As shown in **Table 3**, a total of three mixture proportions were adopted. P0 was the control mixture without any ceramic waste. P1 replaced half of fly ash by CPP. P1S1 further replaced half of quartz sand by RCS based on P1. The constant water-binder ratio of 0.35, the PVA fiber dosage of 1.5vol%, and the basalt fiber dosage of 0.5vol% were kept for all mixtures (Tang, 2020).

**TABLE 1 |** Chemical composition of the cementitious materials (%).

| Materials | $SiO_2$ | $Al_2O_3$ | $Fe_2O_3$ | CaO | MgO | $SO_3$ | $K_2O$ | $Na_2O$ | $Cl^-$ | Loss on ignition |
|---|---|---|---|---|---|---|---|---|---|---|
| Cement | 19.57 | 7.69 | 2.39 | 59.21 | 2.84 | 2.45 | 0.59 | — | 0.06 | 3.20 |
| Fly ash | 53.97 | 31.15 | 4.16 | 4.01 | 1.01 | 0.73 | 2.04 | — | 0.13 | 2.67 |
| CPP | 69.04 | 16.92 | 0.77 | 1.43 | 1.38 | — | 2.17 | 2.17 | 0.58 | 2.93 |

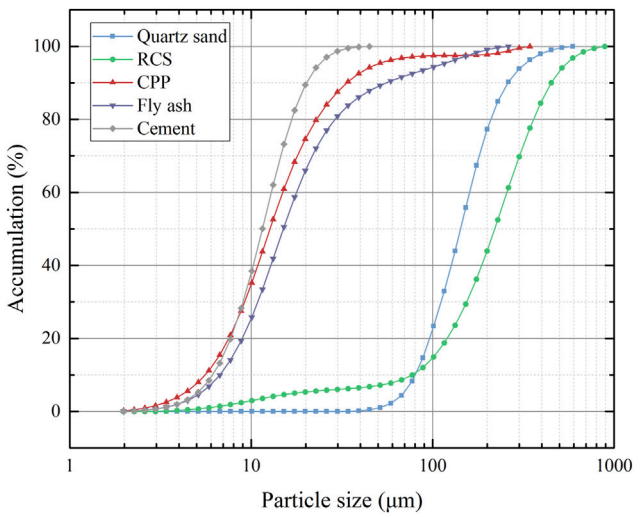


**FIGURE 1 |** Size distribution of cementitious materials and aggregates.

## Preparation of Specimens

Cementitious materials, aggregates, and thickener were first mixed for about 3–4 min. Water and superplasticizer were then added and mixed for the next 2–3 min until the mixture was homogeneous. Basalt fibers and PVA fibers were added with an interval of 1 minute to avoid clustering. The mixture was then mixed at high speed for three additional minutes.

The fresh mixture was cast into molds and compacted on a vibrating table. The specimens were subsequently placed indoors for 24 h with a polyethylene film on them.

## Curing Conditions

After reaching the age of 24 h, the specimens were removed from the moulds and subjected to various curing schemes. Five curing schemes, including standard curing and four hydrothermal ones, were adopted (**Table 4**). The temperature and relative humidity for the standard curing were set according to the Chinese standard GB/T 17671-1999 (SBQTS, 1999). For the hydrothermal curing, the specimens were immersed in a hot water controller equipped with a thermostat. The upper temperature of hydrothermal curing was set at 70°C, according to the Chinese standards GB/T 31387-2015 (AQSIQ and SAC, 2015) and JG/T 565–2018 (MHURD, 2018). Hydrothermal cured specimens were cooled down to room temperature before compression and shrinkage tests.

## Axial Compression Tests

Axial compression tests were carried on ECC specimens with reference to the Chinese standards CECS 13-2009 CECS (2009) and JGJ/T 70-2009 (MHURD, 2009). In consideration of the loading capacity of the testing machine, cylindrical specimens

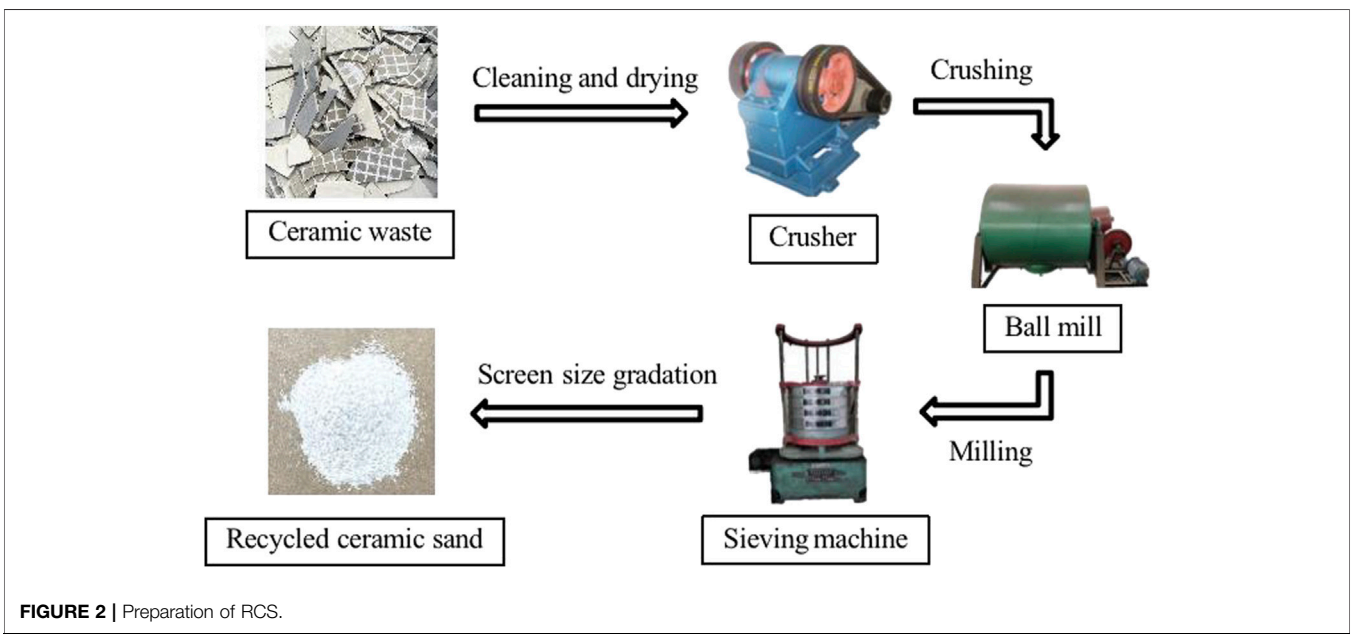


**FIGURE 2 |** Preparation of RCS.

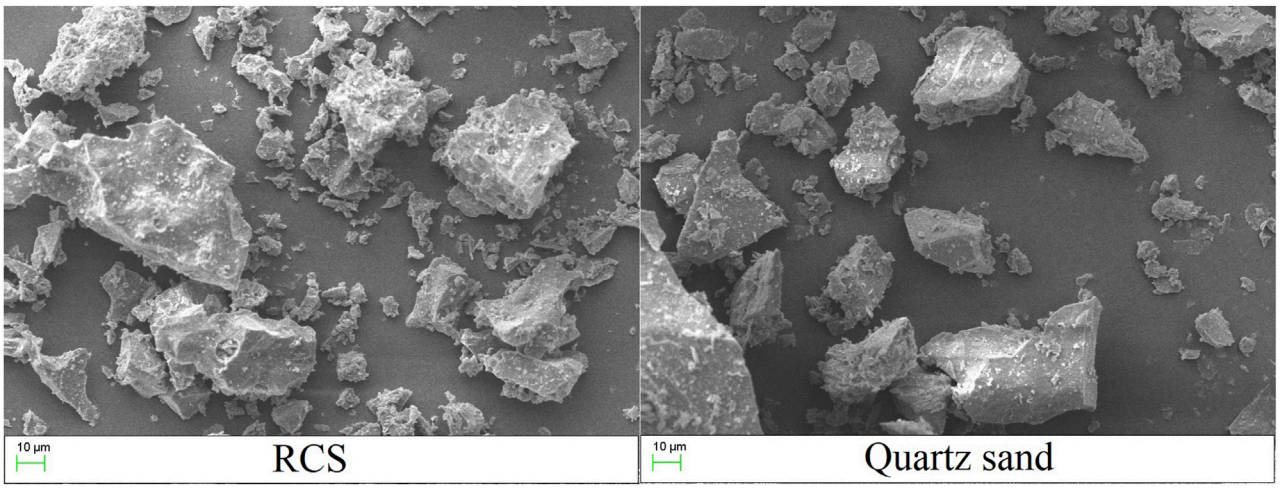


**FIGURE 3 |** Scanning electron microscope images of RCS and quartz sand.


**FIGURE 4 |** Images of PVA fibers and basalt fibers.

**TABLE 2 |** Material properties of fibers.

| Fiber | Density (g/cm$^3$) | Diameter (μm) | Length (mm) | Tensile strength (MPa) | Elastic modulus (GPa) | Elongation (%) |
|---|---|---|---|---|---|---|
| PVA fiber | 1.30 | 40 | 12 | 1,560 | 41 | 6.50 |
| Basalt fiber | 2.65 | 17 | 9 | 2,750 | 90.1 | 2.92 |

**TABLE 3 |** Mix proportions of ECC (kg/m$^3$).

| Mixture ID | Cement | Fly ash | CPP | Quartz sand | RCS | Water | Superplasticizer | Thickener |
|---|---|---|---|---|---|---|---|---|
| P0 | 323.2 | 754.2 | 0 | 355.5 | 0 | 377.1 | 1.26 | 0.54 |
| P1 | 323.2 | 377.1 | 377.1 | 355.5 | 0 | 377.1 | 1.91 | 0.54 |
| P1S1 | 323.2 | 377.1 | 377.1 | 177.8 | 177.8 | 377.1 | 1.91 | 0.54 |

**TABLE 4 |** Description of curing schemes.

| Test ID | Curing method | Temperature (°C) | Time |
|---|---|---|---|
| H2D0 | Standard curing | 20 | 7 days for shrinkage test and 28 days for compressive test |
| H5D3 | Hydrothermal curing | 50 | 3 days |
| H5D7 | Hydrothermal curing | 50 | 7 days |
| H7D3 | Hydrothermal curing | 70 | 3 days |
| H7D7 | Hydrothermal curing | 70 | 7 days |

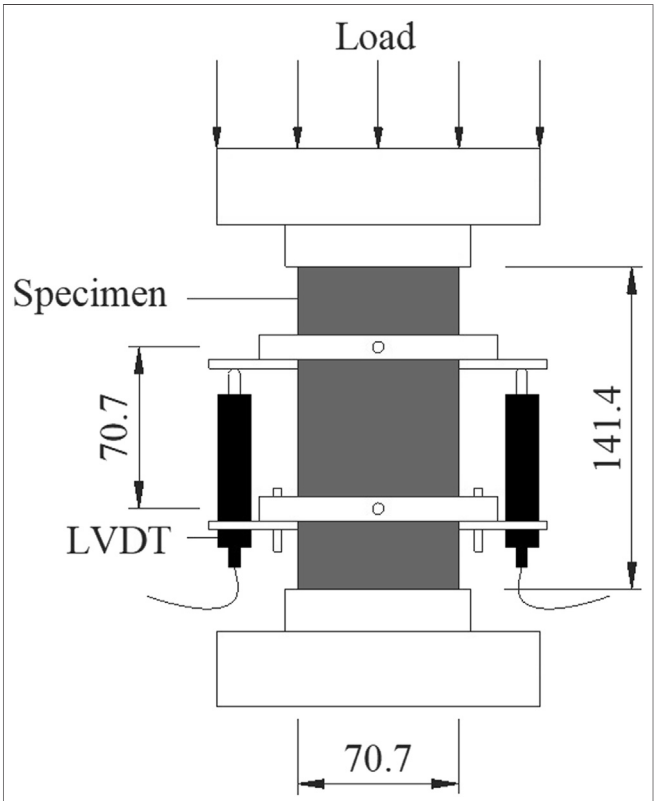


**FIGURE 5 |** Schematic view of the compression test (unit: mm).

with a height of 141.4 mm and a diameter of 70.7 mm were employed. Three specimens were prepared for each mix proportion under each curing scheme. Before the test, gypsum was used to cap both ends of the specimens to level. As shown in **Figure 5**, a pair of LVDTs was installed in the middle of the specimens with a gauge length of 70.7 mm to measure axial deformation. Axial load with a rate of 0.5 mm/min was applied using an electrohydraulic servo tester. The loads and axial deformation were recorded synchronously with a data acquisition instrument. The elastic modulus of ECC specimens was calculated based on the specification in the Chinese standard JGJ/T 70-2009 (MHURD, 2009).

## Shrinkage Tests

Drying shrinkage of ECC after curing was tested in accordance with JGJ/T 70–2009 (MHURD, 2009). Prismatic specimens for the shrinkage test had dimensions of 40 mm × 40 mm × 160 mm.

**FIGURE 6 |** Failure mode of specimens after the compression test.

After curing, the initial length of specimens was recorded. The specimens were then placed in an environmental chamber under a temperature of 20°C and a relative humidity of 60%. The shrinkage values were recorded on the 7th, 14th, 21st, and 28th day of the test.

# RESULTS AND DISCUSSION

## Compressive Properties

**Figure 6** shows the failure mode of specimens after axial compression. It was evident that the cracks were mostly diagonal. The existence of fibers prevented specimens from peeling off. This is linked to the bridging effect of fibers which limits the development of cracks and improves the ductility of ECC (Lin et al., 2019). The incorporation of ceramic waste and the hydrothermal curing resulted in little change on the failure mode of ECC.

The stress–strain relationships of specimens under axial compression are plotted in **Figure 7**. As compared with standard cured specimens, hydrothermal cured ones exhibited much higher stiffness and peak stress, but slightly less peak strain.

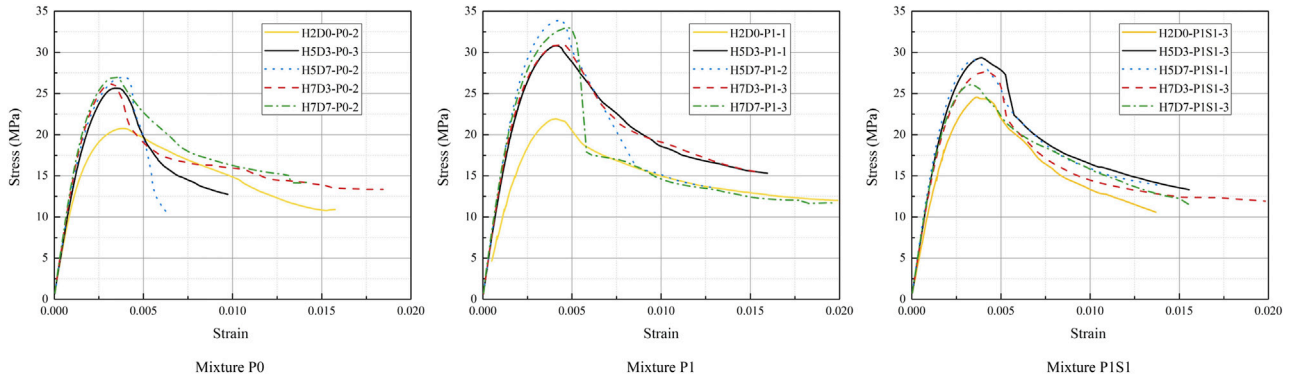


**FIGURE 7 |** Stress–strain relationships of ECC specimens under compression.

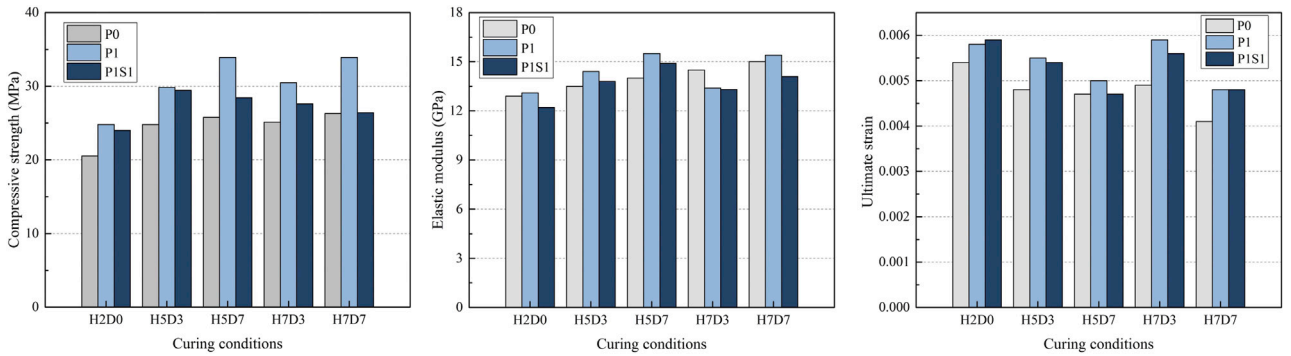


**FIGURE 8 |** Compressive strength, elastic modulus, and peak strain of ECC.

Mixture P1 showed the highest compressive strength, followed by P1S1, while P0 ranked last.

The effect of ceramic wastes and curing conditions on the compressive properties of ECC is illustrated in **Figure 8**. Under the standard curing, the replacement of fly ash by CPP increased the compressive strength of P1 specimens by 21%, which is benefited by the finer particles and higher pozzolanic activity of CPP. Previous studies have indicated that CPP can effectively reduce the porosity of matrix, thereby increasing the compressive strength (Tang, 2020; Li et al., 2021; Xiong et al., 2021). CPP also slightly improved the ultimate strain of ECC. This can be explained by the findings of Kulovaná et al. (2016) that a proper amount of CPP was able to enhance the effective fracture toughness of concrete. High fracture toughness raised the threshold for propagation of cracks and thus increased the peak strain of CPP-incorporated ECC.

The replacement of quartz sand by RCS, however, slightly reduced the compressive strength and elastic modulus of the P1S1 specimens, as compared to P1 ones. This phenomenon is mainly ascribed to increasing porosity caused by deteriorative workability of fresh RCS-incorporated mixture. RCS is characterized by higher water absorption than natural aggregate. This reduces actual water for mixing while increases the viscosity of the fresh mixture. The viscous mixture is difficult to be compacted and results in porous microstructures after hardening. The previous mercury intrusion porosimetry results indicated that complete replacement of quartz sand by RCS increased total porosity of matrix by 9.3% (Tang, 2020). In addition, ceramic tiles have Moh's hardness between 4 and 5, which is lower than that of 7 in quartz (Chen, 2017). The inferior hardness affects the performance of RCS under compression.

After hydrothermal curing, ECC specimens elevated both compressive strength and elastic modulus while decreased peak strain. The ranking of the three formulas was approximately the same as that under standard curing, but the gap widened among them. Hydrothermal curing accelerated hydration of the cementitious materials, which magnified the differences in compressive properties (Fathy and Sun, 2014; Gonzalez-Corominas et al., 2016; Huang et al., 2016). Increasing curing temperature to 50°C significantly improved compressive performance of P0 and P1 specimens. When it further increased to 70°C, scarcely any effect was observed. Extension of hydrothermal curing increased elastic modulus while reduced strain capacity of ECC. The long hydrothermal curing also exhibited positive influence in the compressive strength of P0 and P1 specimens, except P1S1 ones. The compressive strength of P1S1 under curing schemes H5D7 and H7D7 was 28.44 and 26.40 MPa, a little lower than that

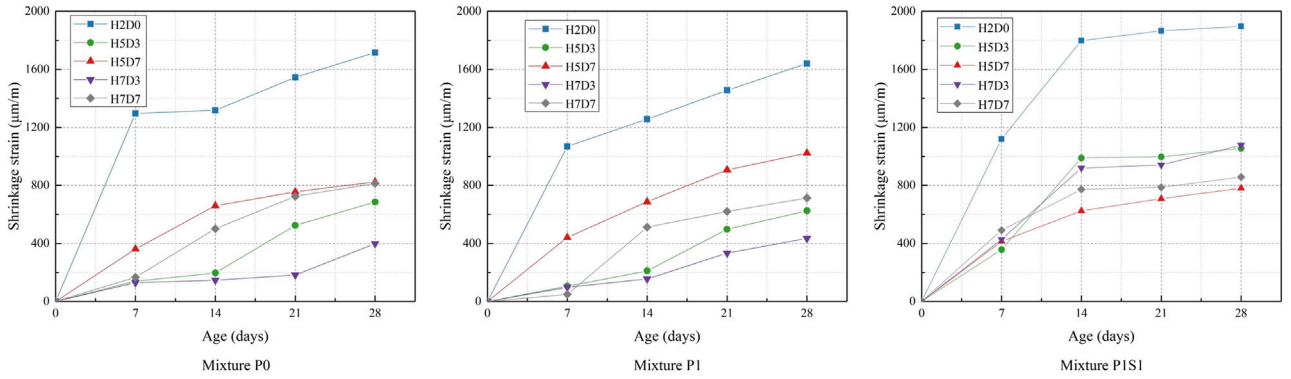


**FIGURE 9 |** Drying shrinkage of ECC.

of 29.44 and 27.60 MPa under curing schemes H5D3 and H7D3, respectively. The slight deterioration in compressive strength is ascribed to the negative effect of hydrothermal curing on the soundness of RCS. It was found that immersion of RCS in hot water with 70°C for 3 days increased the crushing index of RCS by 14.6% in the preliminary test. The hydrothermal curing schemes of H5D7 and H7D7 are recommended for CPP-incorporated mixture with the consideration of compressive performance of ECC.

## Shrinkage Properties

Variation of shrinkage strain with ages is illustrated in **Figure 9**. After the curing, shrinkage grew fast in the first 7 days while slowed down after 14 days. Experimental results showed that replacement of fly ash by CPP had little effect on the shrinkage of ECC, while the incorporation of RCS increased the shrinkage of ECC. This is attributed to the difference in hydration rates between CPP and the fine particles in RCS. The particle size less than 45 μm provided CPP with excellent hydration activity. Most of the shrinkage was achieved in CPP-incorporated specimens during the curing period. However, the fine particles in the RCS were much larger than CPP. This part of fine RCS particles had an activity index of 69, which was lower than that of 91 in CPP (Tang, 2020). This demonstrates a medium hydration activity of the fine RCS particles, which resulted in slow hydration and continuous shrinkage after curing.

Hydrothermal curing can effectively reduce later drying shrinkage of all three mixtures. Compared with the standard curing, hydrothermal schemes H5D3, H5D7, H7D3, and H7D7 reduced 28-day shrinkage of mixture P0 by 60, 52, 77, and 53% while reduced that of mixture P1 by 62, 38, 74, and 57%, respectively. The later shrinkage of P0 and P1 decreased as the curing temperature increased. Higher temperature can promote hydration and strengthen microstructure, which reduces the later shrinkage strain of ECC (Richard and Cheyrezy, 1995). P0 and P1 specimens increased their shrinkage with increasing curing time. Extension of curing promoted hydration of cementitious materials. As one of the hydration products, more adsorbed water grew in the capillaries of the hardened matrix. When the specimens are exposed to dry environment, the adsorbed water evaporated, resulting in shrunk matrix induced by capillary stress (Huang, 2006). However, the shrinkage strain of P1S1 was found to decrease with increasing curing time, opposite to that of P0 and P1. The reason seemed to be linked to the internal curing of RCS. The low apparent density and high water absorption enabled RCS outstanding ability to store water. Long curing time benefited the water storage of RCS and continuous release of water to the surrounding matrix, which relieved the drying shrinkage (Liu and Liu, 2012).

# CONCLUSION

In this study, the effect of ceramic wastes and curing conditions on compressive and shrinkage properties of ECC was researched. After standard and hydrothermal curing, ECC specimens were subjected to the axial compression test and dry shrinkage test, respectively. Based on the experimental results, the following conclusions are drawn.

CPP was qualified for effective alternative to fly ash in ECC. Replacement of half fly ash by CPP increased the compressive strength by 20% at least and exerted positive influence in the elastic modulus and peak strain of ECC. CPP had little impact on the drying shrinkage of ECC.

RCS degraded the compressive performance and increases later drying shrinkage of ECC. The preparation technique should be improved to smooth RCS particles.

Hydrothermal curing effectively improved strength development and later volume stability of ECC. CPP-incorporated ECC can increase compressive strength by 37% while decrease 28-day drying shrinkage by 38% at least. Elevating curing temperatures was beneficial to the later volume stability. Extension of curing contributed to the compressive performance of ECC.

It is recommended to cure CPP-incorporated ECC under a hydrothermal environment with a temperature of 70°C for 7 days.

## DATA AVAILABILITY STATEMENT

The raw data supporting the conclusions of this article will be made available by the authors, without undue reservation.

## AUTHOR CONTRIBUTIONS

YX: methodology, data interpretation, funding acquisition, project administration, resources, supervision, validation, and writing—review and editing. YY: data curation, investigation, visualization, and writing—original draft. SF: conceptualization, data interpretation, formal analysis, investigation, methodology, visualization, and writing—review and editing. DW: project administration, resources, supervision, and validation. YT: conceptualization, data curation, data interpretation, investigation, validation, and writing—original draft. All authors contributed to the article and approved the submitted version.

## FUNDING

This work was supported by the National Natural Science Foundation of China (Project Nos. 51878298 and 51778160), Natural Science Foundation of Guangdong Province of China (Project No. 2021A1515012606), Science and Technology Program of Guangdong Province of China (Project No. 2018B02028003), and State Key Laboratory of Subtropical Building Science International Cooperation Open Project of China (Project No. 2019ZA05).

## ACKNOWLEDGMENTS

The technical support from the State Key Laboratory of Subtropical Building Science is gratefully acknowledged.

## REFERENCES

AQSIQ and SAC (General Administration of Quality Supervision, Inspection and Quarantine of the People's Republic of China), and SAC (Standardization Administration of the People's Republic of China) (2015). *GB/T 31387-2015: Reactive Powder Concrete*(in Chinese). Beijing: Standards Press of China.

Ay, N., and Ünal, M. (2000). The Use of Waste Ceramic Tile in Cement Production. *Cem. Concr. Res.* 30, 497–499. doi:10.1016/S0008-8846(00)00202-7

Binici, H. (2007). Effect of Crushed Ceramic and Basaltic Pumice as fine Aggregates on Concrete Mortars Properties. *Construct. Build. Mater.* 21, 1191–1197. doi:10.1016/j.conbuildmat.2006.06.002

Cai, X., Xi, X., Shui, A., Wu, T., Chen, J., Jian, R., et al. (2011). Study on Preparation of High-Strength-Lightweight Building Materials with Porcelain Polishing Waste. *B. Chin. Ceram. Soc.* 30, 955–959. (in Chinese). doi:10.16552/j.cnki.issn1001-1625.2011.04.023

Cao, C., Wang, G., Liu, S., He, X., and Nie, Y. (2014). Effect of Ceramic Polishing Powder and Polypropylene Fiber on Properties of Mortar. *B. Chin. Ceram. Soc.* 33, 1354–1359. doi:10.16552/j.cnki.issn1001-1625.2014.06.063 CNKI:SUN:GSYT.0.2014-06-020 (in Chinese).

CECS (China Association for Engineering Construction Standardization) (2009). *CECS 13–2009: Standard Test Methods for Fiber Reinforced Concrete*. (in Chinese). Beijing: China Planning Press.

Chen, X. C. (2017). Discussion on Moh's Hardness Testing Method of Ceramic Tiles. *Foshan Ceram.* 27, 44–47. (in Chinese). doi:10.3969/j.issn.1006-8236.2017.06.013

Fathy, S., and Sun, W. (2014). Influence of Different Curing Regimes on the Microstructure and Macro Performance of UHPFRCC. *J. Southeast. Univ.* 30, 348–352. doi:10.3969/j.issn.1003-7985.2014.03.017

Gao, S., Wang, Z., Wang, W., and Qiu, H. (2018). Effect of Shrinkage-Reducing Admixture and Expansive Agent on Mechanical Properties and Drying Shrinkage of Engineered Cementitious Composite (ECC). *Construct. Build. Mater.* 179, 172–185. doi:10.1016/j.conbuildmat.2018.05.203

Gonzalez-Corominas, A., Etxeberria, M., and Poon, C. S. (2016). Influence of Steam Curing on the Pore Structures and Mechanical Properties of Fly-Ash High Performance Concrete Prepared with Recycled Aggregates. *Cem. Concr. Compos.* 71, 77–84. doi:10.1016/j.cemconcomp.2016.05.010

Hanehara, S., Tomosawa, F., Kobayakawa, M., and Hwang, K. (2001). Effects of Water/powder Ratio, Mixing Ratio of Fly Ash, and Curing Temperature on Pozzolanic Reaction of Fly Ash in Cement Paste. *Cem. Concr. Res.* 31, 31–39. doi:10.1016/S0008-8846(00)00441-5

Huang, D., Wang, G., Lu, S., Li, H., and Zhu, M. (2016). Hydration Activity of Ceramic Polishing Powder at Hydrothermal Conditions. *B. Chin. Ceram. Soc.* 35, 561–567. (in Chinese). doi:10.16552/j.cnki.issn1001-1625.2016.02.046

Huang, Y. (2006). *Study on Correlation of Drying Shrinkage between Cement Mortar and Concrete*. [Master's thesis]. [Nanjing]: Nanjing University of Technology. doi:10.7666/d.d023861

Kulovaná, T., Vejmelková, E., Keppert, M., Rovnaníková, P., Keršner, Z., and Černý, R. (2016). Mechanical, Durability and Hygrothermal Properties of Concrete Produced Using Portland Cement-Ceramic Powder Blends. *Struct. Concrete.* 17, 105–115. doi:10.1002/suco.201500029

Li, M., and Li, V. C. (2006). Behavior of ECC/Concrete Layered Repair System Under Drying Shrinkage Conditions/Das Verhalten Eines Geschichteten Instandsetzungssystems aus ECC und Beton Unter der Einwirkung von Trocknungsschwinden. *J. Restor. Build. Monum.* 12, 143–160. doi:10.1515/rbm-2006-6040

Li, V. C., Wang, S., and Wu, C. (2001). Tensile Strain-Hardening Behavior of Polyvinyl Alcohol Engineered Cementitious Composite (PVA-ECC). *ACI Mater. J.* 98, 483–492. doi:10.1089/apc.2006.20.82910.14359/10851

Li, L. G., Zhuo, Z. Y., Zhu, J., Chen, J. J., and Kwan, A. K. H. (2019a). Reutilizing Ceramic Polishing Waste as Powder Filler in Mortar to Reduce Cement Content by 33% and Increase Strength by 85%. *Powder Technol.* 355, 119–126. doi:10.1016/j.powtec.2019.07.043

Li, L. G., Zhuo, Z. Y., Zhu, J., and Kwan, A. K. H. (2020b). Adding Ceramic Polishing Waste as Paste Substitute to Improve Sulphate and Shrinkage Resistances of Mortar. *Powder Tech.* 362, 149–156. doi:10.1016/j.powtec.2019.11.117

Li, L. G., Zhuo, Z. Y., Kwan, A. K. H., Zhang, T. S., and Lu, D. G. (2020). Cementing Efficiency Factors of Ceramic Polishing Residue in Compressive Strength and Chloride Resistance of Mortar. *Powder Tech.* 367, 163–171. doi:10.1016/j.powtec.2020.03.050

Li, L. G., Ouyang, Y., Zhuo, Z.-Y., and Kwan, A. K. H. (2021). Adding Ceramic Polishing Waste as Filler to Reduce Paste Volume and Improve Carbonation and Water Resistances of Mortar. *Aben* 2, 3. doi:10.1186/s43251-020-00019-2

Li, V. C. (2003). On Engineered Cementitious Composites (ECC). *Act* 1, 215–230. doi:10.3151/jact.1.215

Lin, J.-X., Song, Y., Xie, Z.-H., Guo, Y.-C., Yuan, B., Zeng, J.-J., et al. (2020). Static and Dynamic Mechanical Behavior of Engineered Cementitious Composites with PP and PVA Fibers. *J. Build. Eng.* 29, 101097. doi:10.1016/j.jobe.2019.101097

Liu, F., and Liu, J. (2012). Experimental Study on the Internal Curing Effect of Recycled Ceramic Sand in Mortar. *Concrete* 11, 102–103. (in Chinese). doi:10.3969/j.issn.1002-3550.2012.11.034

Liu, J., Liu, F., and Zhang, C. (2015). Dry Shrinkage of Recycled Ceramic Mixed Sand Mortar. *China Concr. Cem. Prod.* 04, 54–58. (in Chinese). doi:10.19761/j.1000-4637.2015.04.014

Liu, Z., Hu, J., Weng, Z., Wang, Y., and Xie, Y. (2020). Research Progress on the Effect of Steam Curing on the Performance of Cementitious Materials. *Concrete* 04, 9–13. (in Chinese). doi:10.3969/j.issn.1002-3550.2020.04.003

López, V., Llamas, B., Juan, A., Morán, J. M., and Guerra, I. (2007). Eco-efficient Concretes: Impact of the Use of White Ceramic Powder on the Mechanical Properties of Concrete. *Biosyst. Eng.* 96, 559–564. doi:10.1016/j.biosystemseng.2007.01.004

MHURD (Ministry of Housing and Urban-Rural Development of the People's Republic of China) (2009). *JGJ/T 70-2009: Standard for Test Method of Basic Properties of Construction Mortar* (in Chinese). Beijing: China Architecture & Building Press.

MHURD (Ministry of Housing and Urban-Rural Development of the People's Republic of China) (2018). *JG/T 565-2018: Standard for Quality Management of Precast Concrete Member Fabricated in the Plant* (in Chinese). Beijing: Standards Press of China.

Nie, Y., Liu, X., Peng, Y., Li, X., and Yang, X. (2015). Performance Study of Recycled Masonry Mortar Produced with Reclaimed Ceramic Tiles. *J. Hunan Univ. Nat. Sci. Ed.* 30, 67–71. (in Chinese). doi:10.13582/j.cnki.1672-9102.2015.01.011

Richard, P., and Cheyrezy, M. (1995). Composition of Reactive Powder Concretes. *Cem. Concr. Res.* 25, 1501–1511. doi:10.1016/0008-8846(95)00144-2

SBQTS (State Bureau of Quality and Technical Supervision)(1999). *GB/T 17671-1999: Test Method for Fluidity of Cement Mortar* (in Chinese). Beijing: Standards Press of China.

Tang, Y. (2020). Experimental Study on ECC Mechanical Properties of Hybrid Fibers Containing Ceramic Waste under Different Curing Conditions. [Master's thesis]. Guangzhou: Guangzhou University. (in Chinese). doi:10.27040/d.cnki.ggzdu.2020.000502

Wang, G. X., Xu, K. J., Zhu, M. Q., and Tian, B. (2011). Pozzolanic Activity of Ceramic Polishing Powder as Cementitious Material. *Msf* 675-677, 135–138. doi:10.4028/www.scientific.net/MSF.675-677.135

Wang, G., Tan, L., Nie, Y., and Tian, X. (2012). Effect of Ceramic Polishing Powder on the Chloride Permeability of Concrete. *B. Chin. Ceram. Soc.* 31, 1564–1570. (in Chinese). doi:10.16552/j.cnki.issn1001-1625.2012.06.012

Wang, S., Wang, C., Wang, Y., Zhang, X., and Chen, Y. (2019). Production and Reutilization of Ceramic Waste. *J. Ceram.* 40, 710–717. (in Chinese). doi:10.13957/j.cnki.tcxb.2019.06.002

Wei, Y. (2017). Mechanical Properties of PVA Fiber/Cement-Matrix Interface and Their Effects on Tensile Properties of SHCC. [Master's thesis]. Wuhan: Wuhan University of Technology, 809307. CNKI:CDMD:2.1019 (in Chinese) .

Wu, X., Li, Y., and Yang, J. (2008). Masonry Mortar and Concrete Producing with Recycled Ceramic Aggregate Producing. *Concr.* 0, 50–52. (in Chinese). doi:10.3969/j.issn.1002-3550.2008.09.017

Wu, Z., Shi, C., and He, W. (2017). Comparative Study on Flexural Properties of Ultra-high Performance Concrete with Supplementary Cementitious Materials under Different Curing Regimes. *Construct. Build. Mater.* 136, 307–313. doi:10.1016/j.conbuildmat.2017.01.052

Xiong, Y., Xu, G., Wu, D., Fang, S., and Tang, Y. (2021). Investigation of Using the Ceramic Polishing brick Powder in Engineered Cementitious Composites. *J. Build. Eng.* 43, 102489. doi:10.1016/j.jobe.2021.102489

Xu, Z., Wei, J., Li, F., Gao, P., Chen, Y., and Yu, Q. (2013). Utilizing Ceramic Waste for Autoclaved Aerated Concrete. *New Build. Mater.* 40, 48–51. (in Chinese). doi:10.3969/j.issn.1001-702X.2013.01.015

Zhu, Y., Yang, Y., Gao, X., and Deng, H. (2011). Effect of Curing Temperature on the Mechanical Properties of Engineered Cementitious Composites. *J. Shenzhen Univ. (Sci. Eng.).* 28, 72–77. (in Chinese). doi:10.3969/j.issn.1000-2618.2011.01.011

**Conflict of Interest:** YT is employed by Guangzhou Pearl River Foreign Investment Architectural Design Institute Co. Ltd.

The remaining authors declare that the research was conducted in the absence of any commercial or financial relationships that could be construed as a potential conflict of interest.

**Publisher's Note:** All claims expressed in this article are solely those of the authors and do not necessarily represent those of their affiliated organizations, or those of the publisher, the editors and the reviewers. Any product that may be evaluated in this article, or claim that may be made by its manufacturer, is not guaranteed or endorsed by the publisher.

frontiers in Materials

ORIGINAL RESEARCH
published: 13 September 2021
doi: 10.3389/fmats.2021.704207

# Seismic Performance of Ni-Ti SMA Wires Equipped in the Spatial Skeletal Structure

*Yang Liu*[1,2,3]*, *Tao Yang*[1,4], *Binbin Li*[2,4,5], *Bo Liu*[5], *Wentao Wang*[6] *and Sheliang Wang*[5]

[1]School of Urban Planning and Municipal Engineering, Xi'an Polytechnic University, Xi'an, China, [2]State Key Laboratory of Green Building in Western China, Xi'an University of Architecture and Technology, Xi'an, China, [3]The Key Laboratory of Well Stability and Fluid and Rock Mechanics in Oil and Gas Reservoir of Shaanxi Province, Xi'an Shiyou University, Xi'an, China, [4]Key Laboratory of Structure Engineering and Earthquake Resistance, Ministry of Education (XAUAT), Xi'an, China, [5]College of Civil Engineering, Xi'an University of Architecture and Technology, Xi'an, China, [6]Department of Civil and Environmental Engineering, University of Michigan, Ann Arbor, MI, United States

Nickel Titanium (Ni-Ti) Shape Memory Alloy (SMA) can be used to limit response of structure during external disturbances such as large seismic events. This paper presents a seismic performance study of Ni-Ti SMA wires equipped in the spatial skeletal structure. First, an improved Graesser-Cozzarelli (G-C) numerical constitutive model of the Austenitic phase of NiTi SMA wire is established. By contrast, the model based on uniaxial cyclic loading experimental tests is demonstrated as feasibility and validity. Next, a method consisting of a three-layer steel spatial skeletal structure model equipped with SMA wires is employed for simulation and experimental tests. According to the obtained constitutive numerical model, the simulation program of vibration control is written to simulate the effect of vibration control of seismic EL-centro wave. Furthermore, a shaking table experimental test was designed to verify the vibration control effect under the same action of seismic EL-centro wave. By comparison of the results of the numerical simulation and shaking table test, dynamic responses of the displacement and acceleration for different floors with control and without control was concluded. The superior superelastic properties of SMA wires used in passive control are investigated and the correctness of the constitutive numerical model are verified as well. The results show that such a comprehensive analysis integrates seismic-resistant behavior of Ni-Ti SMA wires in this type of structure. Besides, proposed method has broad application prospects to address the issues in passive control field of building structures.

**Keywords: spatial skeletal structure, Ni-Ti SMA wire, numerical constitutive model, shake table tests, seismic control performance**

OPEN ACCESS

***Edited by:***
*Xiangming Zhou,*
*Brunel University London,*
*United Kingdom*

***Reviewed by:***
*Pavlo Maruschak,*
*Ternopil Ivan Pului National Technical University, Ukraine*
*Peng Zhang,*
*National Natural Science Foundation of China, China*

***Correspondence:**
*Yang Liu*
*yangliu@xpu.edu.cn*

***Specialty section:***
*This article was submitted to Structural Materials, a section of the journal Frontiers in Materials*

***Received:*** *02 May 2021*
***Accepted:*** *02 August 2021*
***Published:*** *13 September 2021*

***Citation:***
*Liu Y, Yang T, Li B, Liu B, Wang W and Wang S (2021) Seismic Performance of Ni-Ti SMA Wires Equipped in the Spatial Skeletal Structure. Front. Mater. 8:704207. doi: 10.3389/fmats.2021.704207*

## INTRODUCTION

In recent years, more and more earthquake disasters have damaged various houses and buildings and their auxiliary facilities. Damaged construction projects of municipal facilities will threaten people's lives, e.g., the Indian Ocean earthquake and tsunami (2004), Wenchuan earthquake (2008), etc. Spatial skeletal structure, the first barrier against earthquakes, is widely employed as the primary in building and bridge structures to undertake most of the external forces. Therefore, the mechanical properties of the spatial skeletal structure to seismic performance is especially crucial to building structures. Popular seismic design philosophy basically allows new materials to prevent or reduce

seismic forces against earthquakes by civil engineers. However, the permanent residual deformation and damage makes it almost impossible for building structure to serve continuously, which has rendered huge economic losses. How to design and reconstruct structures to make them available to use continuously after repairs or adjustments has become one of the concentrations of seismic engineering. One strategy is to apply superelastic shape memory alloys (SMAs) in structures. (Ozbulut and Hurlebaus, 2010; Mertmann et al., 2011; Wang and Wu, 2011; Mohd Jani et al., 2014).

Shape memory alloy (SMA) is one of smart materials and contains Nickel Titanium (Ni-Ti) based alloys, Cu-based alloys, and FeMnSi-based alloys, etc. (Wang and Wu, 2011; Mertmann et al., 2011; Ozbulut et al., 2011; Gurubrahmam et al., 2019). SMAs have many superior properties, e.g., high hysteretic responses, excellent superelastic behavior, fine shape memory effect, good fatigue resistance, and well controllable mechanical properties. They have inspired interest from researchers for its recovery of inelastic deformations upon removing load applied. It is well known that such features are determined by its thermo-elastic martensite transformation, and martensite reorientation and detwinning (Yu et al., 2014; Liu et al., 2020). Theories and structural applications of SMAs have been studied and published. Brinson (1993) proposed a comprehensive one-dimensional constitutive law for SMAs, which introduced a separation of the martensite fraction internal variable into stress-induced and temperature-induced components into the model. Chausov et al. (2016) studied the processes of deformation and fracture of high-strength titanium alloys under impact-oscillatory loading and dynamic non-equilibrium, and the research revealed that significant microstructural refinement of the alloy was observed after the impact-oscillatory loading. Ren et al. (2007) studied the modeling of the hysteretic behavior of superelastic SMA wires using the improved Graesser' model. Li et al. (2019) summarized an enormous number of constitutive models to describe the super-elastic effect and experimentally investigated the hysteretic behavior of super-elastic Ni-Ti SMA bars under quasi-static conditions. Mirzaeifar et al. (2013) proposed a closed-form solution for bending analysis of shape memory alloy (SMA) beams. Jung et al. (2013) investigated the deformation behavior of a composite panel as a function of the different composite geometric parameters of the shape memory alloy wire.

Recently, in order to explore all potential applications of SMAs, a reliable model that describes highly complex behavior of the material has been pursued by many researchers. Here Liu et al. (2020) proposed an improved 1D Graesser-Cozzarelli (G-C) model for predicting the hysteretic responses of the super-elastic SMAs at various strain rates and strain amplitudes. The simplified model is to improve efficiency and quality of SMA wires in structural vibration control. It is noted that in room temperature, the improved G-C model is fully focused on the loading conditions at a specified strain amplitude and strain rate. In previous studies, the superelastic SMAs have been widely employed in vibration control, structural strengthening and repair, and new damper devices (Graesser and Cozzarelli, 1992; Alam et al., 2007; Ozbulut and Hurlebaus, 2010; Ozbulut et al., 2011; Wang and Wu, 2011; Choi et al., 2018; Preciado et al., 2018; Hamdaoui et al., 2019; Mirzai et al., 2019). And the methods have been developed to dissipate the energy in structural engineering. Ghassemieh et al. (2012) verified a novel approach to reduce the vulnerability of reinforced concrete shear wall structures by using the SMA wires. Romano and Tannuri (2009) presented a developed cooling system actuator based on the Seebeck–Peltier effect to improve its dynamic response using a SMA wire. Boroschek et al. (2007) conducted a shaking table test that has a model of three-story structures that armed copper-based SMA dampers. Yan et al. (2013) designed a SMA wire energy dissipater. It is applied in a steel frame structure model to passively reduce dynamic responses of the steel frame structure. Parulekar et al. (2012) made an analytical study of a supporting steel structure of dump tanks with and without SMA dampers. Jia et al. (2019) proposed a new system including the advantage of SMA and inerter elements. In such cases, the SMA damping inerter is a robust system for mitigating structural vibration. Cladera et al. (2014) present a state of the knowledge of existing studies and applications of SMAs in distinguishing their properties: superelasticity, shape memory, and damping. Sayyaadi and Zakerzadeh (2012) studied the position control of shape memory alloy actuator which is based on the generalized Prandtl–Ishlinskii inverse model.

The superelastic properties of Ni-Ti SMA are the capacity of high hysteretic responses and excellent superelastic behavior under dynamic loading. They can be used to dissipate energy and reduce displacement of the structure. However, there are some challenges in that the prior vibration control research still lacks studies on relationship between SMA hysteresis response and passive control effect for shaking table test model experiments.

Given the fact that the mentioned studies have limitations, in this paper, a numerical constitutive model of the Austenitic phase of Ni-Ti SMA wire was established. It is based on the uniaxial cyclic loading experimental tests and the improved G-C constitutive model. In this research, simulation and experimental tests were included by a three-layer steel frame structure model equipped SMA wires. According to the obtained constitutive numerical model, the simulation program of vibration control is written to simulate the effect of vibration control of EL-centro wave (Niazi, 1986). Furthermore, a shaking table experimental test was designed to verify the vibration control effect of the assembled SMA wires. It is under the action of seismic EL-centro wave and the correctness of the simulated vibration control. The primary objective of this paper was to study the damping effect of SMA wires and the correctness of constitutive numerical model. By comparison, the superior superelastic properties of SMA wires used in passive control and the correctness of the constitutive numerical model is verified.

# METHODS FOR MODELLING AND ANALYZING

## Model of Super-Elastic SMA Wires

The superelasticity, which refers to the ability of undergoing large elastic deformation, is a unique property of SMAs. Under the

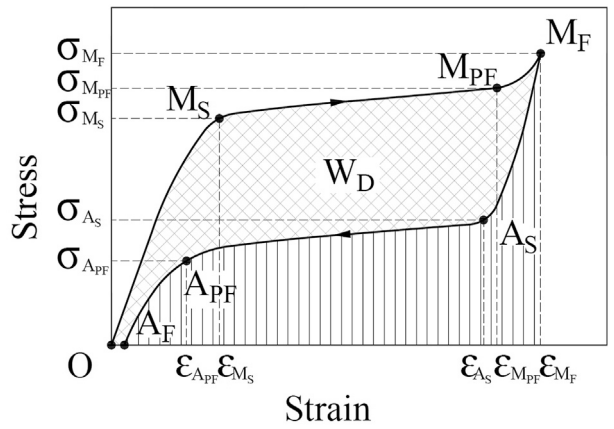


**FIGURE 1 |** Typical hysteretic stress-strain curve of SMA wires.

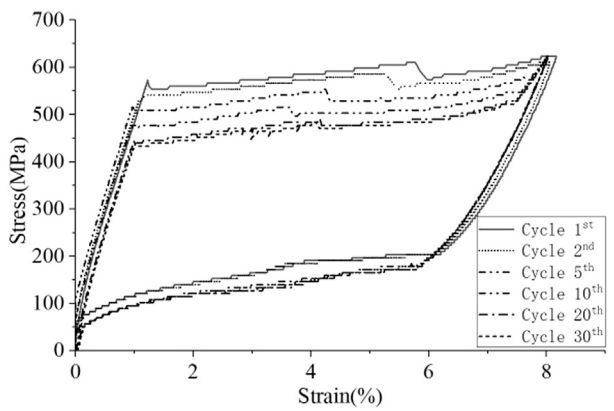


**FIGURE 2 |** The hysteretic curves of various cycles.

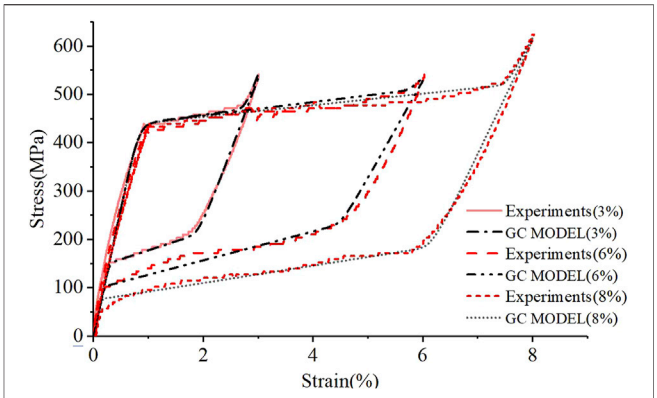


**FIGURE 3 |** Comparison between experiments and GC model with various strain amplitudes.

condition of ambient temperature $T > T_{A_F}$($T_{A_F}$ is temperature above which the microstructure is fully austenitic), the stress-strain model of SMA wire is shown as the bold black solid curve in **Figure 1** (Ozbulut and Hurlebaus, 2010; Liu et al., 2020). The material is initially in the austenitic phase as shown in the segment of O-$M_S$. When the SMA is under increasing tensile stress, the material enters into the phase of transformation from austenite to martensite. It is shown in the stress plateau segment of $M_S$-$M_{PF}$ in the figure. Subsequently, the stress continues to increase beyond the $M_{PF}$ point and enters the hardening martensite stage until it reaches the end of Point $M_F$. At this point, the stress and the strain both reach their maximum value and the SMA enters the unloading stress stage. The austenitic phase is shown in the segment of $M_F$-$A_S$. When the tensile stress continues to decrease, the material transforms from martensite to austenite, as shown in the stress plateau segment of $A_S$-$A_{PF}$ in the figure. With the stress decreasing beyond the $A_{PF}$ point to zero, it comes to the austenite stage until it reaches the end of point $A_F$. As **Figure 1** shows, the area of a typical hysteretic stress-strain path curve is the dissipated energy per cycle ($W_D$). The parameter $W_D$ is used to evaluate the energy-dissipation performance of the SMAs. In this study, only the phenomenological mechanical property is discussed in different uniaxial cyclic loading peak strain and loading speed in ambient temperature.

Considering the significant influence of strain amplitude and strain rate, Liu et al. (2020) obtained a more accurate constitutive model based on G-C (Graesser-Cozzarelli) model with ambient temperature $T > T_{A_F}$ ($T_{A_F}$ is temperature above which the microstructure is fully austenitic). For the loading stage, the equations that describe improved G-C model are as follows:

$$\dot{\sigma} = (1 - s(\varepsilon))E_{OM_S}\left[\dot{\varepsilon} - |\dot{\varepsilon}|\left|\frac{\sigma - \beta}{\sigma_{M_S}}\right|^{n-1}\left(\frac{\sigma - \beta}{\sigma_{M_S}}\right)\right] + s(\varepsilon)E_{M_{PF}M_F}\dot{\varepsilon} \quad (1)$$

$$\beta = E_{OM_S}h_a\left(\varepsilon - \frac{\sigma}{E_{OM_S}}\right) \quad (2)$$

$$s(\varepsilon) = \frac{\tanh\left(g\left(|\varepsilon| - \varepsilon_{M_{PF}}\right)\right) + 1}{2} \quad (3)$$

$$h_a = \frac{E_{OM_S}}{E_{OM_S} - E_{M_SM_{PF}}} \quad (4)$$

For the unloading stage, the equations that describe improved G-C model are as follows:

$$\dot{\sigma} = E_{M_FA_S}\left[\dot{\varepsilon} - |\dot{\varepsilon}|\left|\frac{\sigma - \beta}{\sigma_{A_S}}\right|^{n-1}\left(\frac{\sigma - \beta}{\sigma_{A_S}}\right)\right] \quad (5)$$

$$\beta = E_{M_FA_S}h_m\left(\varepsilon - \frac{\sigma}{E_{M_FA_S}} + f_T\tanh\left(\overline{a}\varepsilon\right)\right) \quad (6)$$

$$h_m = \frac{E_{M_FA_S}}{E_{M_FA_S} - E_{A_SA_{PF}}} \quad (7)$$

The $\tanh(x)$ is the error function expressed as:

$$\tanh(x) = 1 - \frac{2}{1 + e^{2x}} \quad (8)$$

where $\sigma$ and $\varepsilon$ are the uniaxial stress and the uniaxial strain respectively; $\sigma_{M_S}$ is the initiation stress for the forward transformation; $\sigma_{A_S}$ is the initiation stress for the reverse transformation; $E_{OM_S}$ is the deformation modulus of austenite;

**TABLE 1 |** Simulation parameters of SMA wires.

| Strain amplitudes (%) | Stage conditions | Simulation parameters |
|---|---|---|
| 3 | loading stage | $E_{OM_S}$ = 53000.5 MPa, $E_{M_{PF}M_F}$ = 30,000 MPa,$\sigma_{M_S}$ = 440.89 MPa, $h_a$ = 0.03, $\varepsilon_{M_{PF}}$ = 0.0272, g = 1,000, $n$ = 10 |
|  | unloading stage | $f_T$ = 0.114, $E_{M_FA_S}$ = 53000.5 MPa, $\sigma_{A_S}$= 152.00 MPa,$h_m$ = 0.075, $\overline{a}$ = 254.366 |
| 6 | loading stage | $E_{OM_S}$ = 53000.5 MPa, $E_{M_{PF}M_F}$ = 10,000 MPa, $\sigma_{M_S}$ = 440.89 MPa, $h_a$ = 0.027, $\varepsilon_{M_{PF}}$ = 0.0571, g = 1,000, $n$ = 10 |
|  | unloading stage | $f_T$ = 0.114, $E_{M_FA_S}$ = 53000.5 MPa, $\sigma_{A_S}$ = 440.89 MPa,$h_m$ = 0.027, $\overline{a}$ = 254.366 |
| 8 | loading stage | $E_{OM_S}$ = 53000.5 MPa, $E_{M_{PF}M_F}$ = 20,000 MPa, $\sigma_{M_S}$ = 440.89 MPa, $h_a$ = 0.023, $\varepsilon_{M_{PF}}$ = 0.0748, g = 1,000, $n$ = 10 |
|  | unloading stage | $f_T$ = 0.114, $E_{M_FA_S}$ = 53000.5 MPa, $\sigma_{A_S}$ = 77 MPa,$h_m$ = 0.035, $\overline{a}$ = 254.366 |

**TABLE 2 |** Comparison results at various strain amplitudes.

| Strain amplitudes (%) | Dissipated energy per cycle (MJ·m−3/cycle) |  | Error percentage (%) |
|---|---|---|---|
|  | Experimental test | Improved G-C model | Improved G-C model |
| 3 | 4.65 | 4.59 | −1.27 |
| 6 | 13.19 | 13.42 | 1.76 |
| 8 | 20.91 | 21.55 | 3.10 |

$E_{M_SM_{PF}}$ is the loading modulus of the mixed phase; $E_{M_{PF}M_F}$ is the deformation modulus of detwinned martensite; $h_a$ is a coefficient that adjusts the stiffness of the stress plateau; $E_{M_FA_S}$ is the unloading modulus of the mixed phase; $\varepsilon_{M_{PF}}$ is the completion strain for the forward transformation; $n$ is the material coefficients that adjust the corner sharpness of the hysteretic curve; $f_T$ is a coefficient that describes the phase state of SMAs at various temperatures; $h_m$ is a coefficient that adjusts the stiffness of the stress plateau at the unloading stage; $\overline{a}$ is an adjustment coefficient.

In previous studies, Binshan et al. (2017) conducted a uniaxial cyclic loading test on superelastic Ni-Ti SMA wire at laboratory temperature (20 ± 3°C). The diameter of specimens is 1.0 mm with composition Ti-51% at Ni and the phase-transition temperature is −13°C. To stabilize the material's behavior and to eliminate the accumulation of residual strain, all specimens that were used in tests had been cyclically loaded 30 times at 3, 6, and 8% of peak strain with a strain rate at $4.5 \times 10^{-3}$, $1.5 \times 10^{-2}$, $3.0 \times 10^{-2}$, and $4.5 \times 10^{-2}$/sec respectively.

As **Figure 2** shows, it is the hysteretic curves of various cycles from 1st to 30th under the condition of 8% strain amplitude with strain rate $4.5 \times 10^{-3}\ \mathrm{s}^{-1}$. **Figure 3** presents the comparison of the hysteretic curves between tests and improved G-C model of axial strain-amplitude-strain- rate-dependent model at $4.5 \times 10^{-3}$ in austenitic phase for SMA wires. With the improved G-C model, the simulated parameters were shown in **Table 1** under a different strain amplitude with strain rate $4.5 \times 10^{-3}\ \mathrm{s}^{-1}$.

To make further quantitative analysis, area surrounded by each stress-strain hysteresis loop ($W_D$) between the predictions of improved G-C model and the experimental test were compared. **Table 2** shows the comparison results of different strain amplitudes. It shows that the improved model can substantially reduce the error percentage of the dissipated energy per cycle ($W_D$). The maximum error percentage of the improved G-C model is less than 3.10%, which can meet the demand of engineering calculating precision. By contrast, the improved model can accurately predict the actual energy dissipation at different strain rates.

## Dynamic Equations of Seismic Control

According to Newton's second law of motion and the basic principles of structural dynamics, the equation of motion for the structure equipped with austenite SMA wire passive control system shown in **Figure 3** that is subjected to earthquake excitation was:

$$\begin{aligned}&[M]\{\ddot{u}(t)\} + [C]\{\dot{u}(t)\} + [K]\{u(t)\}\\&\quad = [G][M]\left\{-\ddot{u}_g(t)\right\} + [L]\{F(t)\}\end{aligned} \tag{9}$$

where $[M]$, $[C]$, and $[K]$ are the structure's mass matrix, damping matrix, and stiffness matrix respectively; $\{\ddot{u}(t)\}$, $\{\dot{u}(t)\}$, and $\{u(t)\}$ are respectively the acceleration, the velocity, and the displacement of the structure's nodes relative to the ground motion; $[G]$ is the position distribution matrix of earthquake excitation; $\{-\ddot{u}_g(t)\}$ is the acceleration of ground motion under earthquake excitation; $[L]$ is cable node placement position matrix of the SMA wires; and $[F(t)]$ is the passive control force imposed on the structure's nodes by SMA wire cable. In the test, the direction of simulated seismic vibration was along the X axis. As a result, we can get the following formula:

$$F(t) = \begin{cases}\sigma \cdot A \cdot \cos\theta_{ijk}\,; & \varepsilon > 0\\ 0 & ; \quad \varepsilon \le 0\end{cases} \tag{10}$$

where $\theta_{ijk}$ is the direction angle between the SMA wire inhaul cable $C_{J^i_{XYZ}J^j_{XYZ}}$ connecting the nodes and coordinate axis (X, Y, or Z); $C_{J^i_{XYZ}J^j_{XYZ}}$ is the cable that joins the nodes$J^i_{XYZ}$ and $J^j_{XYZ}$, for example, in the study their four cables $C_{J_{001}J_{111}}$, $C_{J_{011}J_{121}}$, $C_{J_{110}J_{200}}$, $C_{J_{120}J_{210}}$ as shown in **Figure 4B**. $J_{XYZ}$ represents node number of the frame structure, subscript x, y, and z, each letter represents the node's position number on each axis respectively. $\sigma$, $\varepsilon$, and $A$ are respectively the tensile stress, tensile strain, and area of section of the SMA wire inhaul cable connecting the structure node i as shown in **Figure 4B**. The number in the coordinate system represents the coordinate system number.

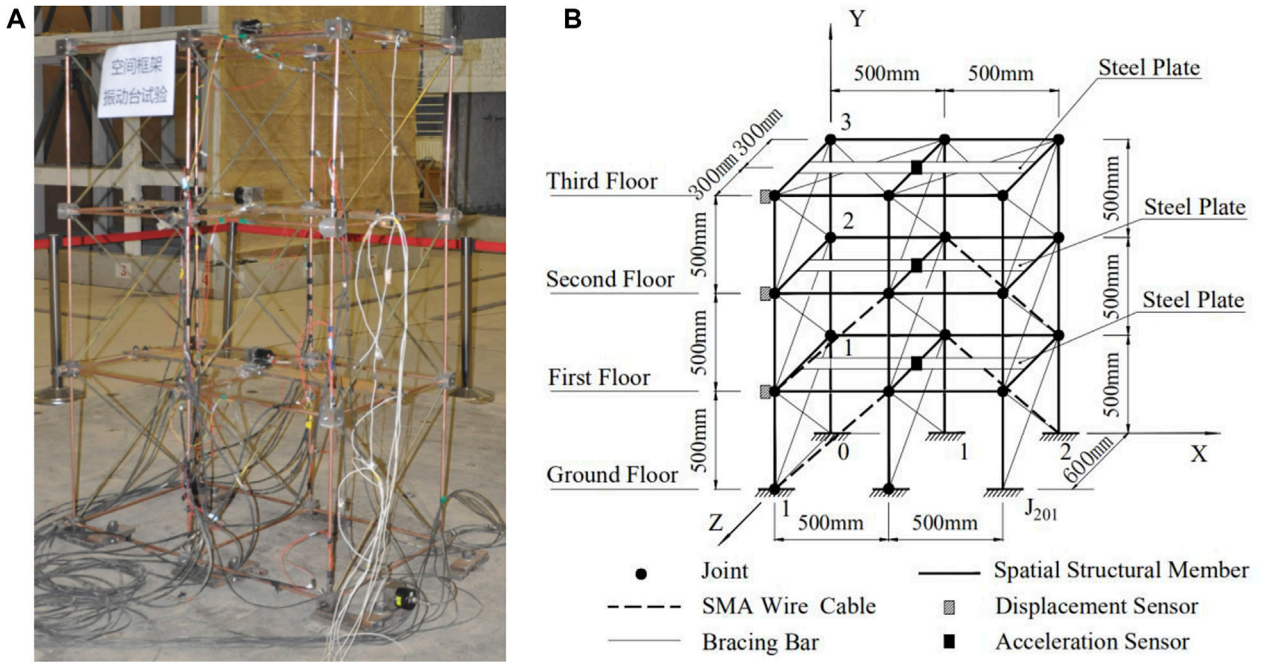


**FIGURE 4 |** Experimental model of spatial skeletal structure: **(A)** real model, **(B)** schematic model and sensors.

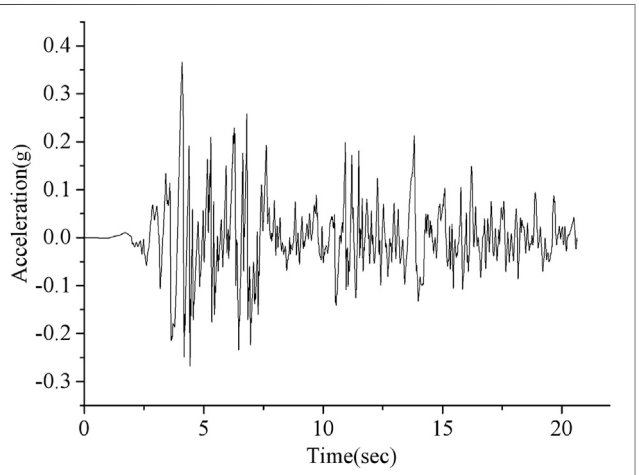


**FIGURE 5 |** Time-acceleration curve of El Centro earthquake.

## SIMULATION AND EXPERIMENT

### Material and Test Model

In this study, the stresses were mainly considered in characteristic test at room temperature (20 ± 3°C). All SMA wire specimens were provided by Xi'an Saite Metal Materials Development Co., Ltd. The diameter of SMA wire is 1.0 mm with composition Ti-51% at Ni as mentioned in *Model of Super-Elastic SMA Wires*. The phase-transition temperature $T_{A_F}$ is −13°C provided by the manufacturer. Tests and optimized constitutive model of SMA wire were discussed in the previous sections. This section presents seismic control performance of optimization for improved G-C constitutive model. Here, numerical simulation experiment was used to study the control effects of a space frame structure model with the optimized model of SMA wire. Then a shaking table test was conducted to verify the correctness of the simulation. An experimental model is designed. It is a 2-span and 3-layer space frame structure with the shorter edge of 600 mm (Z direction), the longer edge of 1,000 mm (X direction), and the layer height h of 500 mm (Y direction) in plane dimension as shown in **Figure 4**. For installation convenience, each node was designed as installing and connecting holes with a 1 kg steel mass block. And a 12 kg steel plate is arranged on each floor as the floor weight. All spatial structural members adopt Q235B (ISO: Fe360D) steel pipes with an external diameter of 10 mm and wall thickness of 1.2 mm, the material elasticity modulus of 206 GPa, Poisson's ratio of 0.3 and density of $7.85\times10^3$ kg/m$^3$. In the shaking table test and the numerical simulation experiment, Wave of EL Centro earthquake (1940) was defined as earthquake simulate excitation as shown in **Figure 5**. Only horizontal seismic action was considered in this study with the direction of simulated seismic vibration along the *X* axis. By comparison, four austenite Ni-Ti SMA wire cables are selected to study the effect of the control simulation at last in the test model. The austenite Ni-Ti SMA wire cables as flexible supporting members were installed on the structure as shown in **Figure 4**. The joints $J_{001}$ $J_{011}$, and $J_{021}$ were armed with displacement sensors in the same vertical plane of the spatial skeletal structure. And

acceleration sensors armed in the center of the plane of each floor are shown in **Figure 4B**.

## Simulation

Dynamic time history analysis on the spatial skeletal structure equipped with SMA wire passive control system is conducted. Computation program based on **Eqs 9**, **10** prepared by MATLAB® is used. Considering the vibration reduction efficiency and economy, four SMA wire inhaul cables were selected for comparison study between simulation and experiment under the same layout condition. The SMA wire inhaul cables arrangement are shown in **Figure 4**, and the corresponding cables are $C_{J_{001}J_{111}}$, $C_{J_{011}J_{121}}$, $C_{J_{110}J_{200}}$, and $C_{J_{120}J_{210}}$respectively.

In this study, wave of EL Centro earthquake was selected as earthquake simulate excitation, using 20 s of time period, 0.02 s of step pace, and 200 gal of peak acceleration amplitude as shown in **Figure 5**.

Wave loading direction was uniaxial along direction X. The joints $J_{001}$ $J_{011}$, and $J_{021}$ were selected as monitoring points for displacement in the same vertical plane of the spatial skeletal structure. And each midpoint of spatial structural members was selected as monitoring points of acceleration.

As is show in **Eq. 9**, the dynamic analysis program of the structure was written by MATLAB® language to vibration response of the structure. Firstly, results of improved G-C model were obtained. And the improved G-C model superelastic stress-strain models were saved in the form of data structure by using the save command. Stepwise integration method is a more effective dynamic analysis method in structural analysis. Here the newmark-β algorithm program (Krause and Walloth, 2012; Yuchuan et al., 2019) was used for dynamic analysis of spatial model structure with SMA wire passive control system to solve the dynamic equation. It is shown in **Eq. 8**, where the control force $[F(t)]$ can be obtained by using the improved G-C model.

In numerical simulation, the following two hypotheses were made in calculating and analyzing the earthquake response. First, all the mass is concentrated at the nodes of each floor. Second, the change of temperature of SMA wire inhaul cable was ignored in the test, i.e., it was assumed that the initial working temperature of each inhaul cable $T_{0j}$ will not change on the section of inhaul cable and the length direction, since it remains constant temperature $T_{0j} \geq T_{A_F}$. Last, the seismic response, the acceleration response, and displacement response were obtained. Results were analyzed by simulation for no control and optimized control of the model structures.

## Experimental Test Apparatus and Procedure

Experimental test apparatus. The shaking table test was carried out on a 4 m × 4 m simulated seismic vibration table designed and manufactured by MTS in the structural engineering and seismic laboratory of Xi'an University of Architecture and Technology in China. The data acquisition system was LMS SCADAS III data acquisition system made by LMS® company. And PCB® acceleration sensor and Harbin 891 displacement sensor were installed as shown in **Figure 4B**. Other main test equipments were chosen as dynamic resistance strain acquisition system, small dynamic strain recorder, and type 891 8-wire amplifier. Experimental model of spatial skeletal structure was shown in **Figure 4** as the same as the model of emulation. **Figure 4A** is experimental model with SMA wire cable on the vibration table. **Figure 4B** is a schematic diagram of sensor layout including displacement sensors and acceleration sensors.

Experimental test procedure. In this test, the input direction of the seismic wave is still uniaxial along the X direction as **Figure 4B** shown by the MTS® vibration table.

1) In the uncontrolled condition (there were no cables in $J_{001}J_{111}$, $J_{011}J_{121}$, $J_{110}J_{200}$, and $J_{120}J_{210}$ respectively):

First, the white noise excitation for a duration of 120 s was excited before the experimental test to estimate the dynamic properties of the model in the uncontrolled condition. Second, in the uncontrolled condition, 100 gal peak acceleration excitation was input respectively as shown in **Figure 4**. And after the excitation test, the white noise excitation was excited again. Then, 200 gal peak acceleration excitation was input. At the same time, the test data, the acceleration, and displacement response were detected and recorded.

2) In the controlled condition (there were SMA wires of cables in $J_{001}J_{111}$, $J_{110}J_{200}$, and $J_{120}J_{210}$ respectively):

All the experimental procedures are the same as the previous uncontrolled condition above. The white noise excitation, acceleration excitation was excited, and the data of acceleration and were detected and recorded.

# TEST RESULTS AND DISCUSSION

## Results of Simulation Dynamic Response

Under simulated ground motion load, acceleration and displacement values of each layer reflect the seismic performance of the structure. The characteristics of Ni-Ti SMA wire was tested and phase kinetics model was predicted in *Methods for Modelling and Analyzing*. This section discusses the effect of the strategy for position and force control realized for a three-floor space truss armed with Ni-Ti SMA wires, and the main results are shown in **Figures 6**, **7** with the EL Centro earthquake wave. For natural frequencies of the structure, the time history curves of acceleration were draw from the tests of the white noise excitation in shaking table test. Then the data were analyzed by the method of Fourier transform frequency response function. The natural frequencies of the structure was 2.4 Hz of every floor without control. The natural frequencies of the structure with control were respectively 4.16 Hz of first floor, 4.34 Hz of second floor, and 4.32 Hz of third floor. The natural frequencies of the structure were changed and the natural frequency of the structure increases. The stiffness of the structure increases after equipped Ni-Ti SMA wire as the bracing cable.

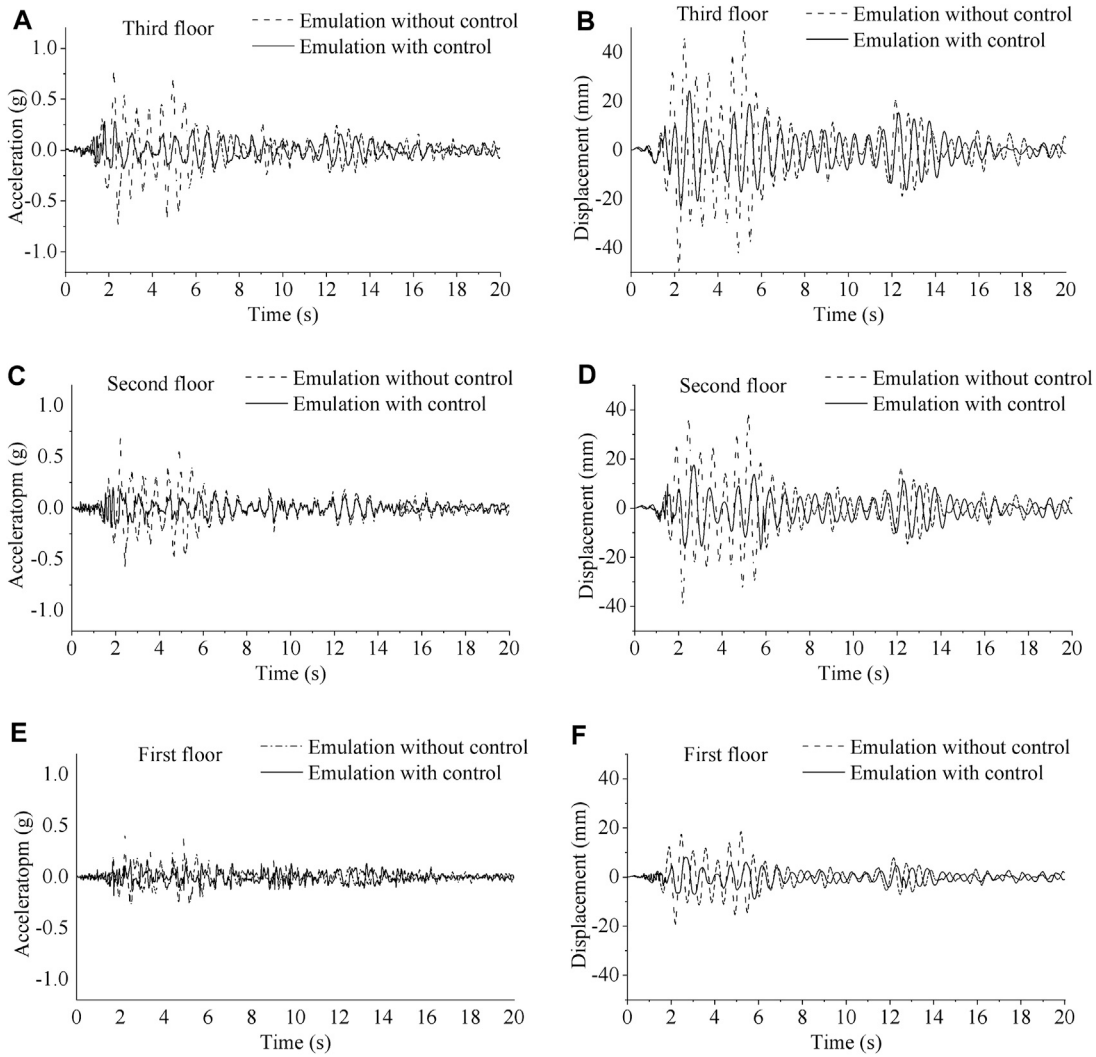


**FIGURE 6 |** Time history curve of displacement response and acceleration response on model structure in emulation: **(A)** acceleration response on the third floor, **(B)** displacement response on the third floor, **(C)** acceleration response on the second floor, **(D)** displacement response on the second floor, **(E)** acceleration response on the first floor, and **(F)** displacement response on the first floor.

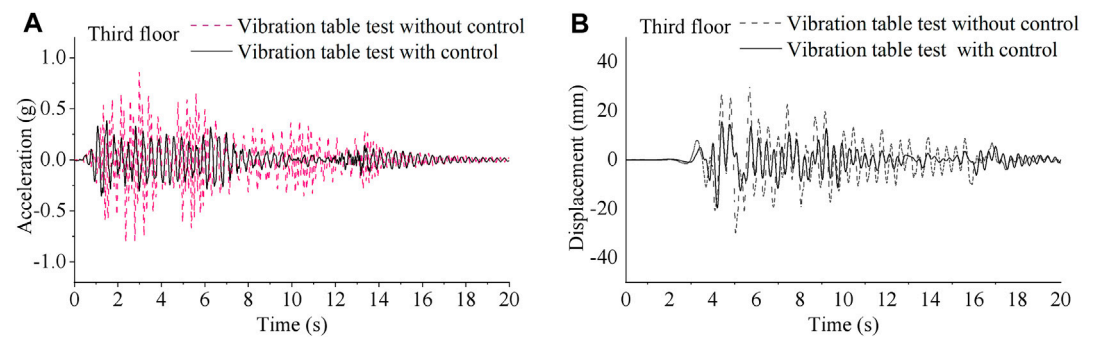


**FIGURE 7 |** Time history curve of displacement response and acceleration response on experimental model structure in vibration table test: **(A)** acceleration response on the third floor, and **(B)** displacement response on the third floor.

**TABLE 3 |** Comparison of displacement and peak acceleration with or without control.

| EL-centro wave | Floor | Peak displacement (mm) | | $\alpha_1$ (%) | Peak acceleration (g) | | $\alpha_2$ (% |
|---|---|---|---|---|---|---|---|
| | | Without control | Control | | Without control | Control | |
| 100 gal | First | 9.121 | 6.821 | 25 | 0.201 | 0.098 | 51 |
| | Second | 19.120 | 14.210 | 26 | 0.300 | 0.133 | 56 |
| | Third | 24.141 | 15.120 | 37 | 0.381 | 0.171 | 55 |
| 200 gal | First | 19.210 | 8.910 | 54 | 0.400 | 0.190 | 53 |
| | Second | 37.110 | 17.501 | 53 | 0.590 | 0.210 | 64 |
| | Third | 48.100 | 24.700 | 49 | 0.730 | 0.280 | 62 |

The vibration displacement at the bottom of the base column was the same as that of the surface of the shaking table. The motion of the first floor was consistent with that of the shaking table. As shown in **Figure 6**, with the increase of floors, the corresponding acceleration and displacement becomes more obvious. As shown in **Figures 6A–F** were time history curve of emulated displacement response and acceleration response of the model structure for the 200 gal peak acceleration excitation. As shown in **Figure 6**, as the floors increase, the corresponding acceleration becomes more pronounced. As shown in **Figure 6C**, the time-history acceleration curves at the second floor. It shows that the acceleration amplitude of the spatial skeletal structure armed with Ni-Ti SMA wires was approximately 64% lower than that of no control. As shown in **Figure 6D**, the time-history displacement curves of second floor, the displacement amplitude of the spatial skeletal structure with control was approximately 53% lower than that of without control. Unlike the second floor, the acceleration amplitude decreased by 62% and the displacement amplitude decreased by 49% compared with the control and non-control in the third floor. It was deduced that the toughness of structure and the passive damping of Ni-Ti SMA wires both played an important role to reduce the vibration of the three floor frame structure. As **Table 3** showns $\alpha_1$ is control effect of peak displacement and $\alpha_2$ control effect of peak acceleration between control and without control. The control effect of peak displacement and acceleration in 200 gal excited were better than 100 gal.

## Results of Vibration Table Test

With 100/200 gal EL Centro seismic wave input, the time-history curves of displacement and acceleration of each monitoring point in the frame structure equipped with SMA are shown in **Figure 4B**. As shown in **Figure 7**, vibration table test results of third floor for the 200 gal peak acceleration excitation was obtained. **Figure 7A** is third floor time-acceleration curve. In contrast, the model dissipates seismic energy mainly by the third floor. **Figure 7B** is third floor time-displacement curve. The displacement amplitude of third floor was approximately 30 mm without control, and 19 mm with control. The acceleration amplitude of third floor was approximately 0.72 g without control and 0.38 g with control.

Obviously, the SMA wire inhaul cables play a passive damping role under the vibration load. The inhaul cables bear the displacement movement of the position with the different strain amplitudes and strain rates in tests. They are stretched and unloaded to consumes energy and absorb vibration in the spatial skeletal structure.

By comparison of earthquake responses during simulation and vibration table test, it was obvious that the passive austenite Ni-Ti SMA wires worked better than the no-control one. The analysis results showed that the emulation and the experimental results of the structure's earthquake response peak values are basically in agreement on the trend, indicating the feasibility of SMA wire passive control emulation by MATLAB® and applicability of the improved G-C model.

The mechanical behavior of spatial skeletal structures made of Ni-Ti SMA alloys has been investigated. It shows reversible martensitic transformations and the associated effects of transformation plasticity and shape memory when simulating seismic loading modes.

# CONCLUSION

This study focused on the mechanical properties and seismic performance of Ni-Ti SMA wire. A new numerical constitutive model of the Austenitic phase of Ni-Ti SMA wire was established. And the correctness of the model was verified by simulation and shaking table test. The following conclusions are reached:

1) The improved G-C models are stable and precise with a different strain amplitude and strain rate of Ni-Ti SMA wires in austenite state. The simulation parameters were calculated by the test data with different strain amplitudes and loading stages at room temperature. The improved model can accurately predict the actual energy dissipation at different strain rates.
2) The natural frequencies of the structure were changed with Ni-Ti SMA bracing cable. When the natural frequency of the structure increases, the stiffness of the structure increases after equipped Ni-Ti SMA wire as the bracing cable.
3) In emulation, the dynamic time history analysis on the spatial skeletal structure equipped with SMA wire passive control system showed that the control effect of peak displacement and acceleration in 200 gal excited performed better than 100 gal. The improved G-C model, a representative phenomenology-based model describing the deformation behavior of shape memory alloys under alternating loads, is stable and precise.

It is still noted that the improved G-C constitutive model for SMA bars is available to the uniaxial cyclic loading experimental tests at different strain amplitudes and loading rates. The study was the result of macroscopic

representation at room temperature. In subsequent studies, the change factors such as temperature change, velocity, deformation rate, and the aging of the material will be fully considered.

## DATA AVAILABILITY STATEMENT

The original contributions presented in the study are included in the article/supplementary material, further inquiries can be directed to the corresponding author.

## AUTHOR CONTRIBUTIONS

YL, TY, BiL, WW, BoL, and SW contributed to conception and design of the study. YL and SW conceived and designed the method. TY and BiL conducted the tests and measured the data. BoL organized the database. YL and WW wrote the first draft of the manuscript. All authors contributed to manuscript revision, read, and approved the submitted version.

## FUNDING

The work was financially supported by the Opening Fund of State Key Laboratory of Green Building in Western China (LSKF202116), key laboratory of well stability and fluid and rock mechanics in Oil and gas reservoir of Shaanxi Province, Xi'an Shiyou University (No. WSFRM20200102001), Science and Technology Plan Project of Yulin (CXY-2020-053), Innovation Capability Support Program of Shaanxi (NO.2020PT-038), Key Lab of Structural Engineering and Earthquake Resistance, Ministry of Education (XAUAT) (KL-SEER-ME -202003), and National Natural Science Foundation of China (No.51678480).

## REFERENCES

Alam, M. S., Youssef, M. A., and Nehdi, M. (2007). Utilizing shape memory alloys to enhance the performance and safety of civil infrastructure: a review. *Can. J. Civ. Eng.* 34, 1075–1086. doi:10.1139/l07-038

Binshan, Y., Sheliang, W., Tao, Y., and Yujiang, F. (2017). BP Neural Netwok Constitutive Model Based on Optimization with Genetic Algorithm for SMA. *ACTA METALLURGICA SINICA* 53 (2), 248–256.

Boroschek, R. L., Farias, G., Moroni, O., and Sarrazin, M. (2007). Effect of SMA Braces in a Steel Frame Building. *J. Earthquake Eng.* 11, 326–342. doi:10.1080/13632460601125763

Brinson, L. C. (1993). One-Dimensional Constitutive Behavior of Shape Memory Alloys: Thermomechanical Derivation with Non-constant Material Functions and Redefined Martensite Internal Variable. *J. Intell. Mater. Syst. Structures* 4 (2), 229–242. doi:10.1177/1045389x9300400213

Chausov, M., Maruschak, P., Pylypenko, A., and Markashova, L. (2016). Enhancing plasticity of high-strength titanium alloys VT 22 under impact-oscillatory loading. *Phil. Mag.*, 1–11. doi:10.1080/14786435.2016.1262973

Choi, E., Mohammadzadeh, B., Kim, D., and Jeon, J.-S. (2018). A new experimental investigation into the effects of reinforcing mortar beams with superelastic SMA fibers on controlling and closing cracks. *Composites B: Eng.* 137, 140–152. doi:10.1016/j.compositesb.2017.11.017

Cladera, A., Oller, E., and Ribas, C. (2014). Pilot Experiences in the Application of Shape Memory Alloys in Structural Concrete. *J. Mater. Civil Eng.* 26 (11), 1–10. doi:10.1061/(asce)mt.1943-5533.0000974

Ghassemieh, M., Mostafazadeh, M., and Sadeh, M. S. (2012). Seismic control of concrete shear wall using shape memory alloys. *J. Intell. Mater. Syst. Structures* 23 (5), 535–543. doi:10.1177/1045389x12436731

Graesser, E. J., and Cozzarelli, F. A. (1992). Shape-Memory Alloys as New Materials for Aseismic Isolation. *J. Eng. Mech.* 117 (11), 2590–2608.

Hamdaoui, Karim., Benadla, Zahira., Chitaoui, H., and Benallal, M. E. (2019). Dynamic behavior of a seven century historical monument reinforced by shape memory alloy wires. *Smart Structures Syst.* 23 (4), 337–345.

Jia, Y., Li, L., Wang, C., Lu, Z., and Zhang, R. (2019). A novel shape memory alloy damping inerter for vibration mitigation. *Smart Mater. Structures* (28), 1–12. doi:10.1088/1361-665x/ab3dc8

Jung, B.-S., Kong, J.-P., Li, N., Kim, Y.-M., Kim, M.-S., Ahn, S.-H., et al. (2013). Numerical simulation and verification of a curved morphing composite structure with embedded shape memory alloy wire actuators. *J. Intell. Mater. Syst. Structures* 24 (1), 89–98. doi:10.1177/1045389x12459588

Gurubrahmam, K., Baburam, K. G. e. a., Kumar, A., and Gara, D. K. (2019). A short review on constitutive modelling of the shape memory alloys-1. *Ijmperd* 9 (4), 849–858. doi:10.24247/ijmperdaug201987

Krause, R., and Walloth, M. (2012). Presentation and comparison of selected algorithms for dynamic contact based on the Newmark scheme. *Appl. Numer. Math.* 62, 1393–1410. doi:10.1016/j.apnum.2012.06.014

Li, C., Zhou, Z., and Zhu, Y. (2019). A uniaxial constitutive model for NiTi shape memory alloy bars considering the effect of residual strain. *J. Intell. Mater. Syst. Structures* 30 (8), 1163–1177. doi:10.1177/1045389x19835932

Liu, B., Li, B., Wang, S., Liu, Y., Yang, T., and Zhou, Y. (2020). A 1D strain-amplitude- and strain-rate-dependent model of super-elastic shape memory alloys for structural vibration control. *Structures* 25, 426–435. doi:10.1016/j.istruc.2020.03.028

Mertmann, M., Oswald, W., Steegmueller, R., and Schuessler, A. (2011). Study on Thermomechanical Treatment, Mechanical Properties and Fatigue of Nitinol Superelastic Thin Sheet. *J. Mater. Eng. Perform.* 20 (4-5), 787–792. doi:10.1007/s11665-011-9891-6

Mirzaeifar, R., DesRoches, R., Yavari, A., and Gall, K. (2013). On superelastic bending of shape memory alloy beams. *Int. J. Sol. Structures* 50 (10), 1664–1680. doi:10.1016/j.ijsolstr.2013.01.035

Mirzai, N. M., Attarnejad, R., and Hu, J. W. (2019). Enhancing the seismic performance of EBFs with vertical shear link using a new self-centering damper. *INGEGNERIA SISMICA* XXXV (4), 57–76.

Mohd Jani, J., Leary, M., Subic, A., and Gibson, M. A. (2014). A review of shape memory alloy research, applications and opportunities. *Mater. Des. (1980-2015)* 56, 1078–1113. doi:10.1016/j.matdes.2013.11.084

Niazi, M. (1986). Inferred displacements, velocities and rotations of a long rigid foundation located at el centro differential array site during the 1979 imperial valley, california, earthquake. *Earthquake Engng. Struct. Dyn.* 14, 531–542. doi:10.1002/eqe.4290140404

Ozbulut, O. E., Hurlebaus, S., and Desroches, R. (2011). Seismic Response Control Using Shape Memory Alloys: A Review. *J. Intell. Mater. Syst. Structures* 22 (14), 1531–1549. doi:10.1177/1045389x11411220

Ozbulut, O. E., and Hurlebaus, S. (2010). Neuro-fuzzy Modeling of Temperature-and Strain-rate-dependent Behavior of NiTi Shape Memory Alloys for Seismic Applications. *J. Intell. Mater. Syst. Structures* 21 (8), 837–849. doi:10.1177/1045389x10369720

Parulekar, Y. M., Reddy, G. R., Vaze, K. K., Guha, S., Gupta, C., Muthumani, K., et al. (2012). Seismic response attenuation of structures using shape memory alloy dampers. *Struct. Control. Health Monit.* 19 (1), 102–119. doi:10.1002/stc.428

Preciado, A., Ramirez-Gaytan, A., Gutierrez, N., Vargas, D., Manuel Falcon, J., and Ochoa, G. (2018). Nonlinear earthquake capacity of slender old masonry structures prestressed with steel. *FRP NiTi SMA tendons, Steel Compos. Structures* 26 (2), 213–226.

Ren, W., Li, H., and Song, G. (2007). A one-dimensional strain-rate-dependent constitutive model for superelastic shape memory alloys. *Smart Mater. Struct.* 16 (1), 191–197. doi:10.1088/0964-1726/16/1/023

Romano, R., and Tannuri, E. A. (2009). Modeling, control and experimental validation of a novel actuator based on shape memory alloys. *Mechatronics* 19, 1169–1177. doi:10.1016/j.mechatronics.2009.03.007

Sayyaadi, H., and Zakerzadeh, M. R. (2012). Position control of shape memory alloy actuator based on the generalized Prandtl-Ishlinskii inverse model. *Mechatronics* 22 (7), 945–957. doi:10.1016/j.mechatronics.2012.06.003

Wang, Q., and Wu, N. (2011). A review on structural enhancement and repair using piezoelectric materials and shape memory alloys. *Smart Mater. Structures* 21, 1–24. doi:10.1088/0964-1726/21/1/013001

Yan, S., Niu, J., Mao, P., Song, G., and Wang, W. (2013). Experimental Research on Passive Control of Steel Frame Structure Using SMA Wires. *Math. Probl. Eng.* 2013, 1–13. doi:10.1155/2013/416282

Yu, C., Kang, G., and Kan, Q. (2014). Crystal plasticity based constitutive model of NiTi shape memory alloy considering different mechanisms of inelastic deformation. *Int. J. Plasticity* 54, 132–162. doi:10.1016/j.ijplas.2013.08.012

Yuchuan, F., Zhao, C., Hongye, Y., and Wen, B. (2019). Dynamic load identification algorithm based on Newmark-β and self-filtering. *Proc. Inst. Mech. Eng. C: J. Mech. Eng. Sci.* 234, 96–107. doi:10.1177/0954406219869981

**Conflict of Interest:** The authors declare that the research was conducted in the absence of any commercial or financial relationships that could be construed as a potential conflict of interest.

**Publisher's Note:** All claims expressed in this article are solely those of the authors and do not necessarily represent those of their affiliated organizations, or those of the publisher, the editors and the reviewers. Any product that may be evaluated in this article, or claim that may be made by its manufacturer, is not guaranteed or endorsed by the publisher.

## NOMENCLATURE

$E_{OM_S}$ is the deformation modulus of austenite

$E_{M_SM_{PF}}$ is the loading modulus of the mixed phase

$E_{M_{PF}M_F}$ is the deformation modulus of detwinned martensite

$E_{M_FA_S}$ is the unloading modulus of the mixed phase

$f_{\mathrm{T}}$ is a coefficient that describes the phase state of SMAs at various temperatures

$h_{\mathrm{a}}$ is a coefficient that adjusts the stiffness of the stress plateau

$h_{\mathrm{m}}$ is a coefficient that adjusts the stiffness of the stress plateau at the unloading stage

$n$ is the material coefficients that adjust the corner sharpness of the hysteretic curve

$\mathbf{T_{A_F}}$ (austenitic completion temperature at 0 stress) is temperature above which the microstructure is fully austenitic

$\mathbf{T_{A_F}}$ (austenitic completion temperature at 0 stress) is temperature above which the microstructure is fully austenitic

$\mathrm{W_D}$ is the dissipated energy per cycle

$\varepsilon_{M_{PF}}$ is the completion strain for the forward transformation

$\sigma_{M_S}$ is the initiation stress for the forward transformation

$\sigma_{A_S}$ is the initiation stress for the reverse transformation.

frontiers in Materials

ORIGINAL RESEARCH
published: 29 October 2021
doi: 10.3389/fmats.2021.752720

# Feasibility of Using the Hollow Glass Microsphere to Develop Lightweight CAC-GGBFS-Blended Strain-Hardening Cementitious Composites

*Wei Fan*[1], *Yan Zhuge*[1]*, *Xing Ma*[1], *Christopher W.K. Chow*[1], *Nima Gorjian*[2] *and Yue Liu*[1]

[1]UniSA STEM, Scarce Resources and Circular Economy (ScaRCE), University of South Australia, Adelaide, SA, Australia, [2]South Australian Water Corporation, Adelaide, SA, Australia

Strain hardening cementitious composites (SHCCs) with superior tensile strength and ductility have been utilized as an effective repair material. A corrosion-resistant binder, calcium aluminate cement (CAC)–ground granulated blast-furnace slag (GGBFS) blends, has been introduced into SHCC to expand its application in the concrete sewage network rehabilitation. As a repair material, the lightweight property is particularly favorable as it can broaden its functionality. This article presents a study on developing a novel lightweight CAC-GGBFS-blended SHCC using hollow glass microsphere (HGM), namely, HGMLW-SHCCs. The fine silica sand content was substituted with HGM at 25, 50, 75, and 100 vol % in HGMLW-SHCC. We examined flowability, density, uniaxial compressive behavior, direct tensile behavior, and pseudo strain-hardening indices. Microstructure analysis was also conducted to understand the meso-scale behavior of this new lightweight composite. The newly developed HGMLW-SHCC had a 28-day density of only 1756 kg/m$^3$. Compressive and tensile strengths were determined in the range of 62.80–49.39 MPa and 5.81–4.19 MPa, respectively. All mixtures exhibited significant strain-hardening behavior. Even though the increased HGM content negatively affected the tensile strength of HGMLW-SHCC, it had a positive effect on its ductility. In addition, HGM can reduce crack width and tensile stress fluctuations significantly. The results showed that HGM was a promising material for producing strong and lightweight corrosion-resistant SHCCs to be used as a retrofitting material in the wastewater industry.

**Keywords: strain hardening, lightweight concrete, calcium alumina cement, mechanical property, hollow glass microsphere, polyethylene fiber**

OPEN ACCESS

***Edited by:***
*Kequan Yu,*
*Tongji University, China*

***Reviewed by:***
*Jun-Jie Zeng,*
*Guangdong University of Technology, China*
*Bo-Tao Huang,*
*Hong Kong Polytechnic University, China*

***Correspondence:**
*Yan Zhuge*
*yan.zhuge@unisa.edu.au*

***Specialty section:***
*This article was submitted to Structural Materials, a section of the journal Frontiers in Materials*

***Received:*** *03 August 2021*
***Accepted:*** *20 September 2021*
***Published:*** *29 October 2021*

***Citation:***
*Fan W, Zhuge Y, Ma X, Chow CWK, Gorjian N and Liu Y (2021) Feasibility of Using the Hollow Glass Microsphere to Develop Lightweight CAC-GGBFS-Blended Strain-Hardening Cementitious Composites. Front. Mater. 8:752720. doi: 10.3389/fmats.2021.752720*

**Abbreviations:** SHCC, strain hardening cementitious composite; HGMLW-SHCC, hollow glass microsphere incorporated lightweight SHCC; SEM, scanning electron microscopy; $J_b$, complementary energy; EDX, energy dispersive X-ray spectroscopy; $J_{tip}$, crack tip toughness; HGM, hollow glass microsphere; $K_m$, matrix fracture toughness; CAC, calcium aluminate cement; PSH, index of pseudo strain-hardening; GGBFS, ground granulated blast-furnace slag; $E_m$, Young's modulus of the matrix; PE, Polyethylene; $\sigma_c$, initial matrix cracking strength; HPMC, hydroxypropyl methyl cellulose; $\sigma_0$, fiber bridging strength; PCE, polycarboxylates; $\sigma_{ss}$, steady-state crack stress; XRD, X-ray diffraction; $\sigma_{flu-max}$, maximum stress fluctuation; XRF, X-ray fluorescence.

## INTRODUCTION

Concrete sewerage pipe has been used extensively ascribed to its high strength, versatility, and cost efficiency (Song et al., 2021). However, sewerage pipes made of concrete are widely subjected to microbial-induced concrete corrosion (MICC), which causes pipe structural degradation such as mass loss, surface cracking, and reinforcement corrosion. As the sewer infrastructures are usually buried deep underground, and the traditional excavation method will cause substantial economic loss to the society; therefore, it is necessary to develop an innovative trenchless technology to repair these valuable assets.

Calcium aluminate cement (CAC)-based mortar lining has been adopted for sewerage pipe rehabilitation Two decades ago (El-Hemaly et al., 2008), the brittleness nature of the mortar material is prone to crack easily under tension load, particularly when repairing the pipe crown and invert. To improve the durability and mechanical properties of the CAC mortar lining material, the authors have taken a pilot step to tailor this material into a high performance fiber-reinforced cementitious material, namely, PE fiber-reinforced CAC-ground granulated blast-furnace slag (GGBFS)-blended strain hardening cementitious composite (SHCC) (Fan et al., 2020; Fan et al., 2020). This newly developed cementitious composite can achieve 5% tensile strain capacity with only 1% PE fiber reinforcement, with an excellent strain-hardening behavior under tension. The PE fiber-reinforced CAC-GGBFS-blended SHCC can produce multiple cracks distributed evenly with a small, tiny crack width usually less than 100 μm; this unique behavior makes it outperform the conventional cement mortar lining materials that failed from macro single cracking under tensile loading (Sheta et al., 2021). With the distinctive properties of high ductility and durability (Yu et al., 2018), SHCCs are found to be used in a broad range of applications, from repair to retrofit virgin and corroded reinforced concrete structural elements (Shang et al., 2019). As a lining material to be sprayed onto the corroded pipe wall, lightweight property will be greatly favored. However, the lightweight property of this new composite has not yet been achieved. The PE fiber-reinforced CAC-GGBFS-blended SHCC has a density of 2,140 kg/m$^3$ while a structural lightweight concrete usually has a compressive strength over 17 MPa and a unit density less than 1920 kg/m$^3$ (213R-14 2014). The additional load will make an adverse impact to the rehabilitated structures and limit the *in-situ* application of the repair material. Therefore, the lightweight property is greatly preferred and favored, and efforts must be made to further develop the PE fiber-reinforced CAC-GGBFS-blended SHCC with the lightweight characteristic.

A common method for producing lightweight SHCC is to incorporate lightweight aggregates. A lightweight environmental-friendly filler material, hollow glass microsphere (HGM), has been widely used as a filler material for sand replacement in cement-based composites (Wang et al., 2019; Al-Gemeel et al., 2018; Aslani and Wang 2019). HGM is a dimension-controlled hollow spherical shape particle with air encapsulated by a thin glass enclosure of sphere. The HGM material is widely available with a bulk density ranging from 120 kg/m$^3$ to 490 kg/m$^3$ and the particle size is about 81 μm and less. Compared to the popular lightweight fly ash cenosphere materials, the use of HGM can offer a lower density and improve the greenness of the cementitious composite as it contains a significant amount of recycled glass (Wang et al., 2019; Meddah, 2019; Aslani et al., 2021). Hence, by replacing silica aggregates with HGM, an SHCC with more sustainable effect can be produced.

Wang and Li (2003) developed a group of lightweight SHCCs with hollow glass bubbles, expanded perlite, air bubbles, and polymeric microform. It was found that due to the relatively small size and closed-shell structure, glass bubbles were found to be the most promising lightweight filler for SHCCs by reaching an average density of 1450 kg/m$^3$ with a high tensile strain capacity of 4.24%. Zhuge et al. (2014) replaced 10% volume of cement with HGM in fiber-reinforced cementitious composites; the compressive strength was slightly decreased with a 6% reduction of density. Al-Gemeel et al. (2018) also discovered similar results, compressive and flexural strengths were decreased, but the flowability was increased with the use of 10% volume of HGM. Chen et al. (2021) investigated HGM incorporated ultralightweight cement composites by examining their mechanical properties, durability, and the additional HGM influence on the microstructures. The results showed that the HGM incorporated lightweight composite had a density ranging from 778 to 948 kg/m$^3$ on day-1 and a compressive strength ranging from 22.9 to 33.1 MPa at 28 days. A design concept of developing UHP-SHCC by using HGMs has been proposed by Yu et al. (2017) and Lu et al. (2021). The results indicated that the compressive strength is over 120 MPa and the air-dried density is only about 1800 kg/m$^3$, indicating the inclusion of HGMs would be a promising material for lightweight composites. Aslani and Wang (2019) developed a lightweight fiber-reinforced cementitious composite with three different kinds of HGMs to substitute the fly ash content at 40 and 60% by weight, the density was reduced by 10% and the compressive strength was decreased by 3%. Oreshkin et al. (2016) reported that the addition of HGMs also improved the dispersion of fibers and the flowability of the mixture. Martín et al. (2021) further studied the HGM–cement paste interaction. The results showed that the HGMs can not only act as a lightweight aggregate material but also contribute as a SCM by interacting with cement initially as nucleation agents and then as pozzolanic materials. Apart from the mechanical property, the sulfuric acid resistance can also be improved with the addition of HGM (Zhang et al., 2018), which suits the need for sewerage environment.

Thus, to better utilize recycle glass resources and develop a lightweight high-performance repair material, this article first attempts to use the HGM to fully replace fine silica sand in CAC-GGBFS-blended SHCC. To optimize the mix design, different volume fractions of HGMs (V = 0, 25, 50, 75, and 100%) were added into the lightweight HGMLW-SHCC mixture. The polyethylene (PE) fiber with a low volume fraction of 1% was utilized to achieve a high tensile strain capacity. A series of experimental programs including mechanical properties and microstructure of HGMLW-SHCCs were investigated. The flowability and density of HGMLW-SHCCs were first

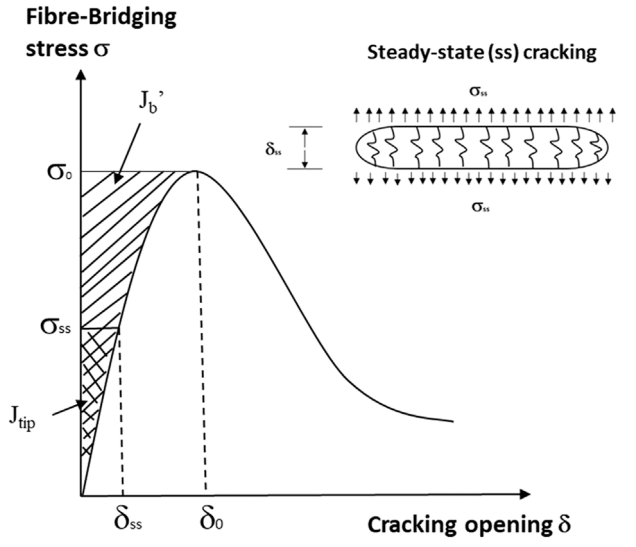


**FIGURE 1 |** Typical relationship curve of SHCC.

measured and followed with the compressive strength being measured at 1, 7, and 28 days. To date, research on direct tensile behavior of HGM-incorporated SHCCs is still quite limited, thus, a comprehensive tensile stress–strain relationship was investigated at 28 days after curing. The tensile strength of the lightweight HGMLW-SHCC is more than 6 MPa and its tensile strain capacity goes up to 8%. The pseudo strain-hardening (PSH) indices for all the HGMLW-SHCC mixtures were calculated to check the ductility. In addition, microstructure analysis of scanning electron microscopy (SEM) and energy dispersive X-ray spectroscopy (EDX) imaging were conducted to study the relationship between micromechanical behaviors and micromechanical performance (Liu et al., 2021).

## THE MICROMECHANICS-BASED DESIGN THEORY OF THE SHCC

The design of an HGMLW-SHCC with robust tensile strain-hardening behavior relies on the understanding of micromechanical interactions between fiber, matrix, and fiber–matrix interface as the addition of HGM will increase the porosity of the CAC-GGBFS-blended cementitious matrix and lower the matrix toughness $K_m$. To quantify the toughness of the HGMLW-SHCC, a micromechanical-based model was used (Kanda and Li, 2002). In this analytic toolset, two PSH indices (Kanda and Li, 1998) should be verified to ensure achieving the steady propagation of multiple cracking initiated from the HGMLW-SHCC (Yu et al., 2018).

1. First, the strength index $PSH_s$, defined as the ratio of the fiber bridging stress $\sigma_0$ to the initial matrix cracking stress $\sigma_c$ (**Figure 1**). $\sigma_c$ should be lowered than $\sigma_0$. $\sigma_c$ is calculated by the matrix fracture toughness $K_m$ and preexisting internal flaw size $a_{0,}$ and $\sigma_0$ was determined based on the single-crack tensile test in *Interpretation of micromechanical analysis*.
2. Second, the energy index $PSH_e$, defined as the ratio of the fiber bridging complementary energy Jb' to the crack tip toughness Jtip. Jtip must be less than Jb', i.e., $J_{tip} = K_m^2/E_m \le \sigma_o\delta_o - \int_0^{\delta_O}\sigma(\delta)d\delta = J_b^{'}$, where $\sigma(\delta)$ represents the bridging stress $\sigma_0$ versus crack opening $\delta$ curve. $K_m$ is the fracture toughness and $E_m$ is the elastic modulus of the matrix. $E_m$ can be obtained from the direct tensile test and $K_m$ can be calculated by the three-point bending test on notched beams and calculated by the following equations (Xu and Reinhardt, 1999):

$$K_m = \frac{1.5\left(F_Q + \frac{mg}{2}\times 10^{-2}\right)\times 10^{-3}\cdot S\cdot a_0^{\frac{1}{2}}}{th^2} f(\alpha),$$

$$f(\alpha) = \frac{1.99 - \alpha(1-\alpha)\left(2.15 - 3.93\alpha + 2.7\alpha^2\right)}{(1+2\alpha)(1-\alpha)^{3/2}}, \alpha = \frac{a_0}{h}.$$

$F_Q$ is the peak load applied on the matrix; m represents the mass of the beam matrix sample; g stands for the gravitational acceleration as 9.81 m/s$^2$; S is span of the beam sample under the three-point bending test; a0 is the notch depth of the matrix beam sample; t and h are the width and thickness of the matrix beam sample, respectively and $f(\alpha)$ is the shape parameter of the matrix beam sample. Existing studies (Kanda and Li, 1998; Liu et al., 2021) revealed that for a polyethylene (PE) fiber-reinforced SHCC, the $PSH_s$ value should be over 1.2 and the $PSH_e$ value should be higher than 3 to achieve a high strain-hardening performance.

## EXPERIMENTAL PROGRAM

### Materials and Mix Design

HGMLW-SHCC is designed with the CAC-GGBFS-blended cementitious material, fine silica sand, HGM, water, PE fiber, and polycarboxylate-based superplasticizer; the mixture design is tabulated in **Table 1**. The mixture ID is named by the varying volume ratios of HGM to replace sand with the percentage number. HGMLW-SHCC-0 is used as a reference mixture without adding HGM, then the fine aggregate was partially replaced with HGM from 25 to 100%. Rapid hardened CAC ISTRA 40 and GGBFS were used as the binder in this study. The fine aggregates utilized in this study has a specific gravity of 2.65, the maximum grain size was 185 μm, and the mean size was 126 μm. The lightweight additive used in this study was Sphericel 110P8 HGM with a maximum grain size of 25 μm and mean size of 15 μm and an average particle density of 1,100 kg/m$^3$ and crushing strength of 68.95 MPa. The addition of HGM contributes to the achievement of a low density to the composites. The physical properties of Sphericel 110P8 are provided in **Table 2**. To impart the high ductility, a high fiber aspect ratio (Lf (18 mm)/df (20 μm) = 900), high tensile strength (3,000 MPa) polyethylene (PE) fiber with a volume fraction of 1% was used to increase the fiber–matrix interface area which improves the fiber bridging capacity. To maintain the flowability of the mixture, a viscosity agent hydroxypropyl

**TABLE 1 |** Mix design of HGMLW-SHCC (kg/m$^3$).

| Mixture ID | Binder | | Filler | | Water | HPMC[a] | PCE[b] | PE fiber (1% vol) | W/b |
|---|---|---|---|---|---|---|---|---|---|
| | Cement | GGBFS | Fine sand | HGM | | | | | |
| **HGMLW-SHCC-0 (Control mix** | 480 | 720 | 594 | 0 | 370 | 0.5 | 1.0 | 10 | 0.3 |
| **HGMLW-SHCC-25** | 480 | 720 | 445 | 62 | 370 | 0.5 | 1.0 | 10 | 0.3 |
| **HGMLW-SHCC-50** | 480 | 720 | 296 | 124 | 370 | 0.5 | 1.0 | 10 | 0.3 |
| **HGMLW-SHCC-75** | 480 | 720 | 148 | 185 | 370 | 0.5 | 1.0 | 10 | 0.3 |
| **HGMLW-SHCC-100** | 480 | 720 | 0 | 246 | 370 | 0.5 | 1.0 | 10 | 0.3 |

[a]*Hydroxypropyl methyl cellulose.*
[b]*Powder polycarboxylates superplasticizer and water to binder ratio.*

**TABLE 2 |** Specification of HGM 110P8 powder.

| Properties | HGM 110P8 |
|---|---|
| **Specific gravity** | 1.1 |
| **Bulk density (g/cm$^3$)** | 0.49 |
| **Particle size distribution (μm)** | 2–25 |
| **Particle mean size (μm)** | 15 |
| **Maximum working pressure (MPa)** | 68.98 |

**TABLE 3 |** XRF results and loss of ignition (LOI) of ingredients.

| Chemical content (wt%) | CAC (%) | GGBFS (%) | HGM (%) |
|---|---|---|---|
| **CaO** | 37.72 | 45.78 | 5.41 |
| **$SiO_2$** | 4.67 | 32.20 | 54.53 |
| **$Al_2O_3$** | 37.85 | 12.58 | < 0.01 |
| **MgO** | 0.48 | 5.34 | 0.452 |
| **$Fe_2O_3$** | 16.48 | 0.475 | 0.077 |
| **$Na_2O$** | 0.155 | 0.24 | 25.717 |
| **$TiO_2$** | 1.89 | 0.66 | < 0.01 |
| **$K_2O$** | 0.15 | 0.397 | 0.077 |
| **$Cr_2O_3$** | 0.127 | 0.003 | 0.006 |
| **LOI**[a] | 0.64 | 2.32 | 3.73 |

[a]*Loss on ignition.*

methylcellulose (HPMC) and a powder type polycarboxylates (PCE) superplasticizer were both found necessary in HGMLW-SHCC mixtures for achieving adequate workability. The chemical composition of HGM, CAC, and GGBFS were quantitatively analyzed by X-Ray fluorescence (XRF) as shown in **Table 3**. In addition to the chemical element analysis, the mineral compounds were also investigated by X-ray diffraction (XRD) measurements as shown in **Figure 2A**. XRD analysis results revealed that CAC was well crystalline while HGM was completely amorphous. Gradation curves of all the ingredients are shown in **Figure 2B**. It should be noted that the flowability of mixtures was affected considerably with the increasing content of HGM.

## Mixing Procedure and Specimen Preparation

It is critical to mix and make the PE fiber uniformly dispersed to achieve optimal material performances. All HGMLW-SHCC mixtures were mixed in a Hobart mixer with 10-L capacity. The solid ingredients including the CAC, GGBFS, silica sand, and HGM were first dry mixed at the speed of 140 rpm for 1 min. Then premixed water with HPMC and PCE powder was added into the mixture and mixed at the speed of 140 rpm for 6 min then 420 rpm for 2 min until the homogenous and consistent state was achieved. PE fibers were then gradually added into the mixture and mixed at the speed of 140 rpm first until the fibers were uniformly dispersed then turned to the speed of 420 rpm for 2 min. Finally, the mixture was poured into steel molds and covered with plastic sheets. All the specimens were demolded after 24 h and then cured in air at the temperature of 23°C and relative humidity (RH) of 98% until the age of 28 days.

## Testing Procedure

### Physical Properties

The physical properties were first investigated. The flowability of the fresh HGMLW-SHCC in a different mixture design was examined with the mini-slump test, also known as spread-flow tests. A mini-slump cone was used to fill with the mortar, located in the center of the flat plate. Second, the mini-slump cone was lifted carefully in 5 seconds to allow a free spread of the mortar mixture for 3 minutes. The diameter of the spread was measured and averaged in two perpendicular directions. Then, the spread value was calculated by the subtraction of the two-average value between the diameters and the cone bottom. Details of the tests can be found in Nematollahi and Sanjayan (2014). A relative slump ($T_P$) can be calculated as:

$$\Gamma_P = \left(\frac{D_1}{D_0}\right)^2 - 1,$$

where $D_1$ is the average value of the two orthogonal diameters of the mixture and $D_0$ is the diameter of the cone bottom.

Apart from examining the flowability of the HGMLW-SHCC, it is also significant to avoid the damage of 110P8 HGM during mixing to provide lightweight to the composite. Therefore, harden-state density measurement was conducted to discover the damage of 110P8 HGM during mixing. The tested density was compared with the estimated value based on the specific gravity of all ingredients and mix proportions.

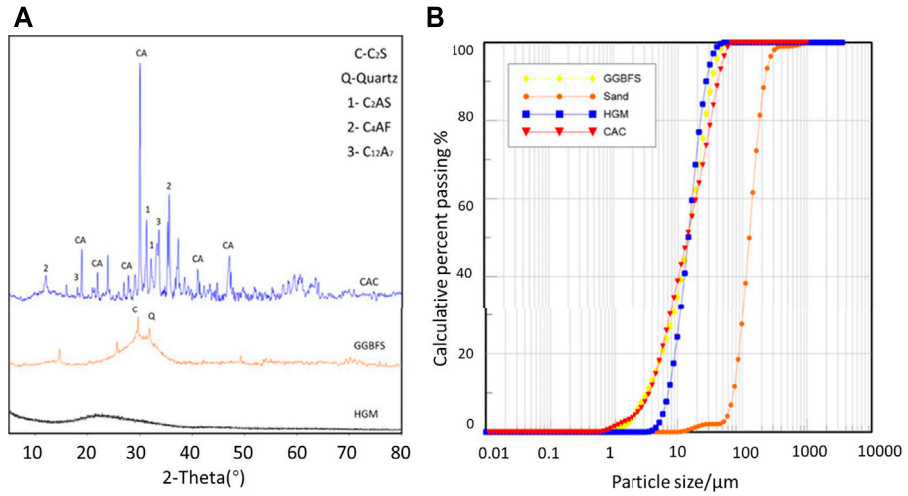


**FIGURE 2 | (A)** XRD patterns and **(B)** Particle size distributions of cementitious materials and HGM.

### Mechanical Tests

A series of mechanical tests were conducted to evaluate the influence of HGM content on the mechanical properties of HGMLW-SHCC. The uniaxial compressive strength of HGMLW-SHCC was measured according to ASTM C109 (2008), at least three 50 mm cubes were tested at the age of 1, 7 and 28 days after curing and the mean value was recorded. The test was conducted by a load-controlled testing machine with a capacity of 1,500 kN with a load control rate of 50 kN/min under a quasi-static condition.

As recommended by the JSCE (Japan Society of Civil Engineers, 2008), dog bone–shaped specimens were used to measure the tensile behavior of HGMLW-SHCC, a constant loading rate was operated at 0.5 mm/min as a displacement control. Two linear variable displacement transducers (LVDTs) with a gauge length of 80 mm were attached on both sides of the dog-bone specimen to measure the elongation; the testing setup and specimen geometry are shown in **Figure 3**.

To discover the impact of HGM on the fracture toughness of the HGMLW-SHCC cementitious matrix, the three-point bending test was executed on 40 × 40 × 160 $mm^3$ notched beams. Beams were prepared based on the mixture proportions but without adding the fibers. As depicted in **Figure 3B**, a 12 mm notch was cut on the bottom surface of the midspan by using a small electronic diamond saw. The test was conducted with a loading rate of 1 mm/min according to the RILEM FMC-50 method (Belysheva et al., 1990). A clip-on extensometer was installed on the lateral surface to measure the crack opening displacement as shown in **Figure 3B**.

The single-crack tensile test was performed to investigate the effect of HGM content on the fiber-bridging capacity. Dog-bone specimens were notched around the four faces in the midheight of the specimen before cutting using a saw blade (thickness of 0.4 mm) to promote the formation of a single crack after 28 days curing. The notches depth were 2 and 6.5 mm in two perpendicular directions at the cross section which is shown in **Figure 3C**. The single-crack tensile test was conducted on the same instrument as uniaxial tensile tests. The loading speed was set to 1 mm/min and the crack openings were measured by using an Instron extensometer.

### Microstructure Analysis

To have a further understanding of the interaction between the PE fiber and the cementitious matrices with different HGM content, the microstructures analysis was conducted using scanning electron microscopy (SEM) and energy-dispersive X-ray spectroscopy (EDX) mapping analysis. Nail-sized samples were taken from the fractured specimen of the dog-bone specimen after the tensile test then oven-dried at 40°C for 24 h (Liu et al., 2021).

## RESULTS AND DISCUSSION

### Flowability

Flowability results of each fresh HGMLW-SHCC mixture are graphically presented in **Figure 4A**. The spread-flow test was characterized by a relative slump value. As expected, the relative slump value experienced a 15% increase when fine silica aggregates were 100% replaced by the lightweight HGM. These results may be ascribed to the lubricating effect of the spherical-shaped HGM particles. Neither segregation nor bleeding in the mixtures was observed, and all the mixtures showed good cohesion and homogeneity.

### Density

The harden-state density of the HGMLW-SHCC is an important indicator of the HGM particle survival rate. If a certain portion of the HGM particle is broken while mixing, the harden-state density measured will be expected to achieve

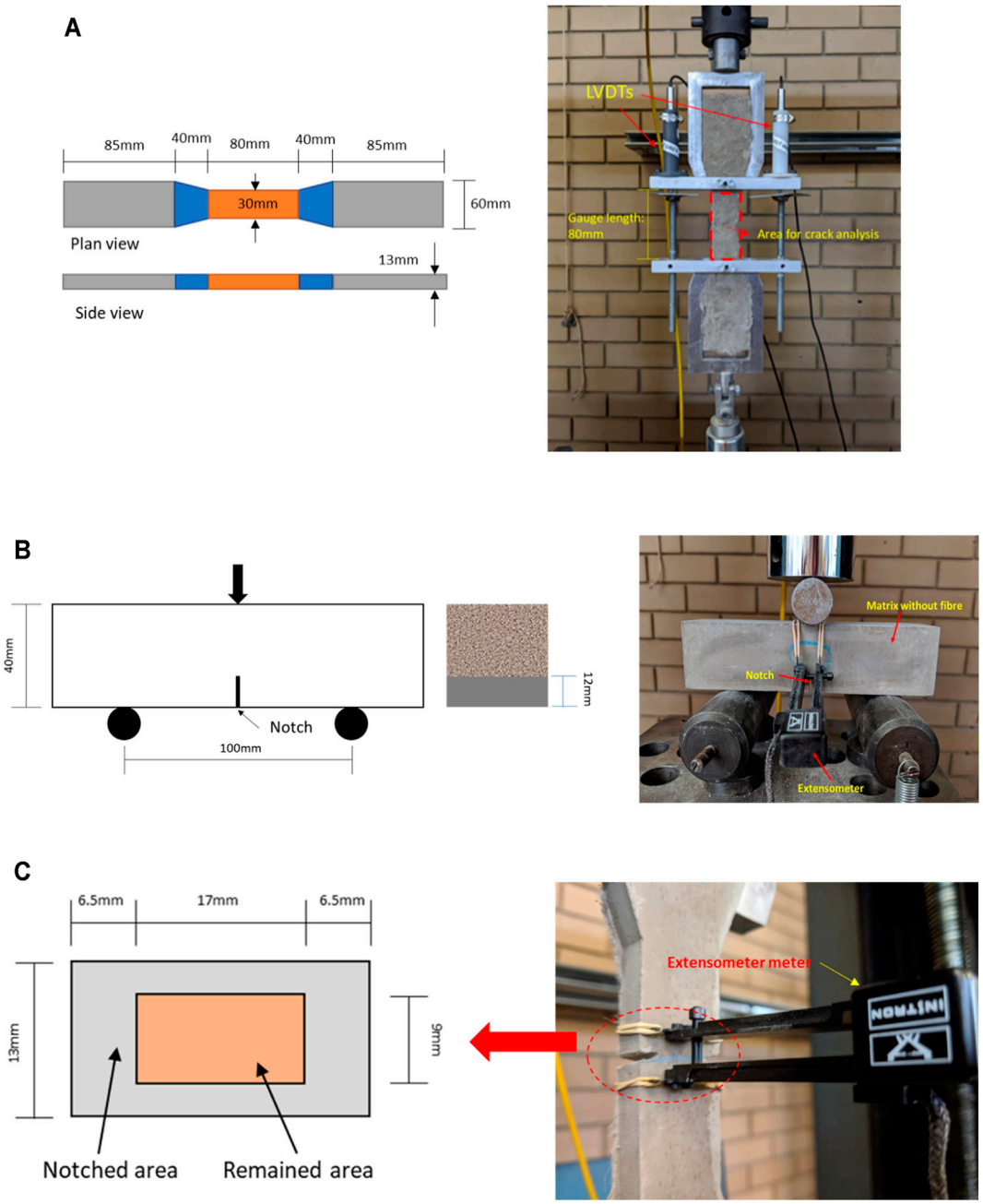


**FIGURE 3 | (A)** Direct tensile test setup: **(B)** Matrix toughness test setup; **(C)** Single crack tension test setup.

a much higher value than the targeted density estimated from the mix proportion. The harden-state density of the HGMLW-SHCC was measured after curing for 28 days; the reported density was the average of six cube samples from the same batch of mix. ACI Committee 213 recommends that density less than 1920 kg/m$^3$ can be referred as lightweight concrete (213R-14, 2014; Standard, 2008). The measured densities with standard deviation and theoretically calculated densities of each mixture are plotted in **Figure 4B**. Measured densities decreased with the increasing amount of HGM. Lightweight properties were achieved when the HGM substitution rate exceeded 50%. All measured densities exhibited 3–5% lower than theoretically calculated density, which indicated that the HGMLW-SHCC was porous, and most glass balls remained unbroken.

## Compressive Behavior

The average compressive strength results of HGMLW-SHCC at 1, 7, and 28 days were summarized in **Figure 4C**. CAC is known for

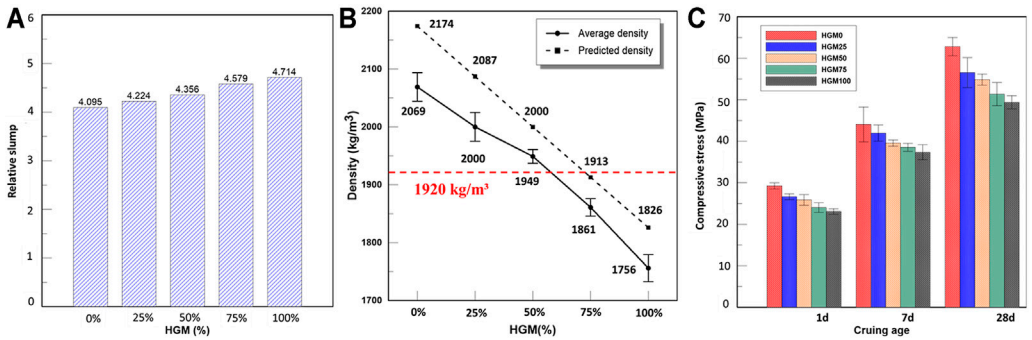


**FIGURE 4 | (A)** Relative slump value: **(B)** 28 days density: and **(C)** Compressive strength of HGMLQ W-SHCC.

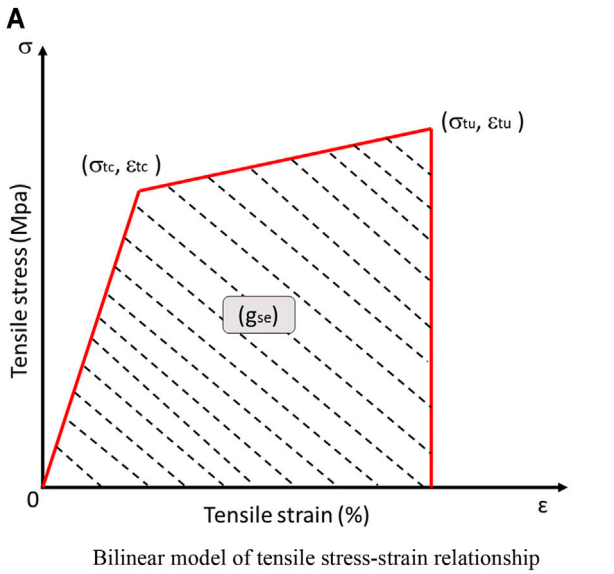


**FIGURE 5 | (A)** Bilinear model of tensile stress-strain relationship. **(B)** Average results of tensile stress-strain curves of HGMLW-SHCC.

rapid setting as a repair material, so it is critical to investigate the effect of the HGM content on the early strength of HGMLW-SHCC. All HGMLW-SHCC mixtures achieved over 40% of 28-day compressive strength on the first day of curing, exhibiting that HGM had a minor effect on early strength growth. Based on the compressive strength results, it can be seen that HGM degraded the composite strength as the compressive strength decreased with the increasing content of HGM. The compressive strength decreased by 10% when the HGM content was increased by 25%. The reduction trends of each curing age showed that replacing silica sand with HGM did not significantly affect the hydration process since HGM has a similar chemical composition to sand. It should be noted that HGMLW-SHCC 100 achieved a compressive strength of 49.39 MPa in 28 days; even though it is 22% less than the benchmark (control group), the strength is strong enough to be used as a repair material for concrete sewerage but adds more sustainability and durability.

## Tensile Properties

### Tensile Stress–Strain Curve

To understand the failure of HGMLW-SHCC, the typical tensile stress–strain curve can be classified into three stages: start with an ascending linear stage, then a strain-hardening stage, and finally descend with a strain-softening stage. The growth of strain capacity is attributed to the increase of crack number and the crack width of SHCC remains constant during the strain-hardening process. The critical parameters representing the tensile properties of HGMLW-SHCC, including the initial cracking strength ($\sigma_{tc}$), the peak tensile strength ($\sigma_{tu}$), the strain capacity at peak stress ($\varepsilon_{tu}$), and the energy absorption capacity ($g_{se}$) are highlighted in **Figure 5A**. The strain energy density was calculated with the integral area underneath the ascending branch of the stress–strain curves as described in the formula below (Yu et al., 2020):

$$g_{se} = \int_0^{\varepsilon_{tu}} \sigma(\varepsilon) d\varepsilon.$$

The corresponding average experimental stress–strain curves of HGMLW-SHCC specimens with different HGM portions are compared in **Figure 5B**. Three specimens were tested for each

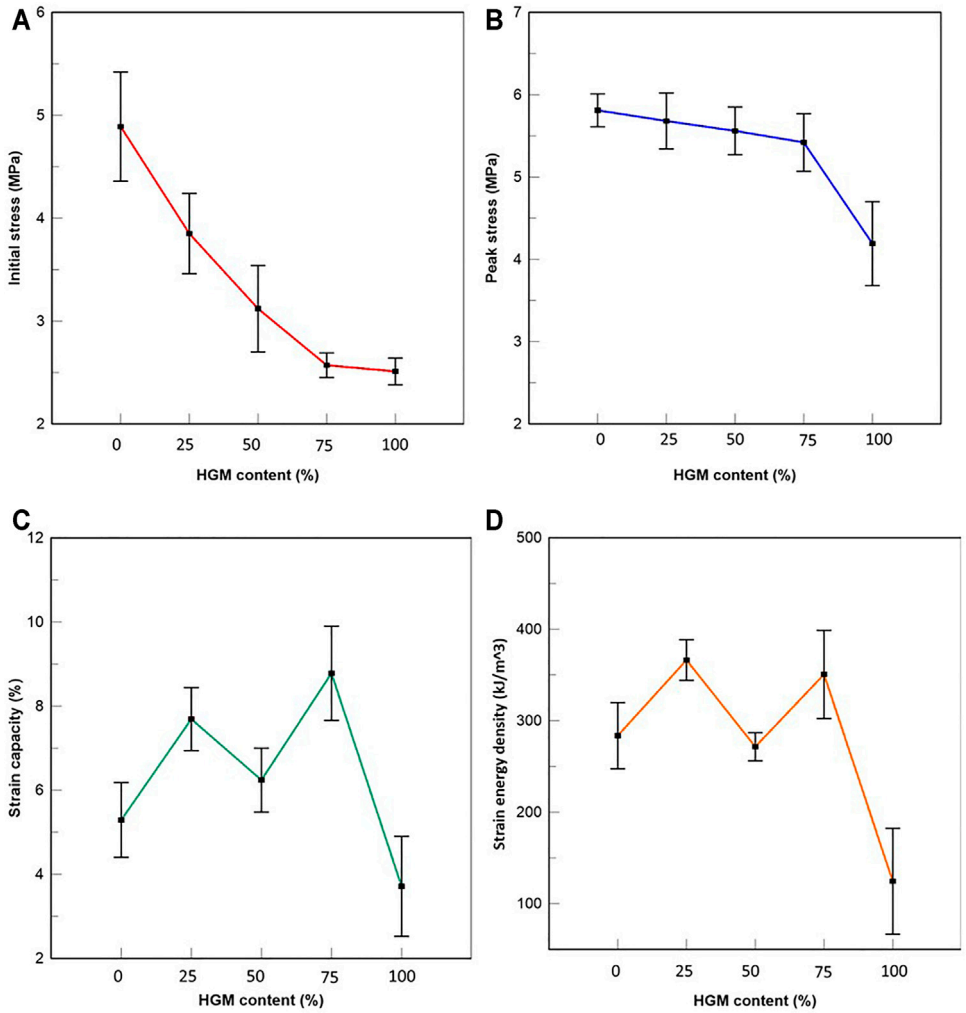


**FIGURE 6** | **(A)** Initial stress of HGMLW-SHCC. **(B)** Peak stress of HGMLW-SHCC. **(C)** Strain capacity of HGMLW-SHCC. **(D)** Strain energy of HGMLW-SHCC.

mixture and an average curve was obtained and highlighted from the test results. All specimens with different mix proportions show an apparent tensile strain-hardening phenomenon. The average tensile strain of the reference mixture HGMLW-SHCC 0 achieved 5.29%. After the substitution of sand with HGM to 25, 50, 75, and 100%, the average tensile strain varied to 7.69, 6.24, 8.78, and 3.71%, respectively. The corresponding strain energy in the reference mixture HGMLW-SHCC 0 was 283.6 KJ $m^{-3}$. HGMLW-SHCC 25 and HGMLW-SHCC 75 achieved even higher strain energy than the reference mixture after adding HGM, with the value of 366.3 KJ $m^{-3}$ and 350.5 KJ $m^{-3}$, respectively.

The four tensile parameters mentioned previuosly are presented in **Figure 6**. Similar to the compressive strength, the initial cracking stress and peak stress were decreased as the HGM substitution rate increased. The average initial cracking stress dropped about 50% from 4.89 to 2.51 MPa, while the peak stress only dropped 27% from 5.81 to 4.19 MPa when the HGM volume rate rose from 0 to 100%. It can be noted that only when the HGM substitution rate reaches 100%, the initial stress and peak stress as well as strain capacity reduced remarkably; the tensile strain capacities of all other three mixtures with HGM addition (up to 75%) went up to an average of 6%. It can be seen that for up to 75% HGM replacement, even the peak stress was reduced slightly and the strain capacity as well as the strain energy absorption were increased. The introduction of HGM had negative impact on the stress but little effect on the tensile strain capacity, which may be attributed to the lubrication effect causing better fiber dispersion.

## Crack Characteristics

The tensile properties of HGMLW-SHCC can be reflected by the cracking behavior to a certain extent. The detailed values of crack number, average crack width, and average crack spacing after unloading of HGMLW-SHCC are shown in **Figure 7A–C**. The characteristic of the cracks after failure, for e.g., the number of cracks ($N_c$), the average crack width ($w_c$), and the average crack spacing ($s_c$), is determined by the

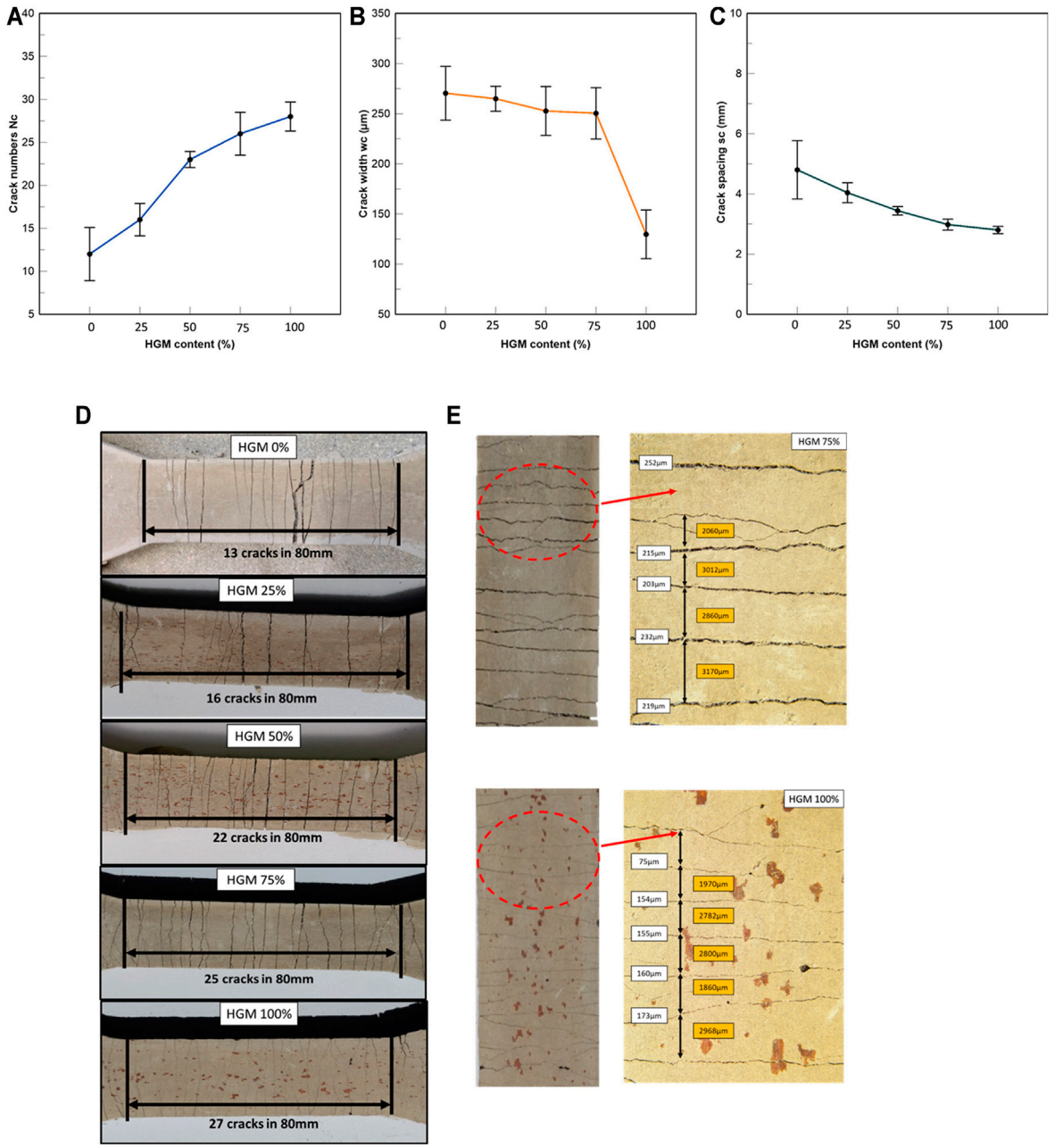


**FIGURE 7** | **(A)** Crack numbers. **(B)** Crack width. **(C)** Crack spacing. **(D)** Crack patterns. **(E)** Microscopic observation of the cracks.

crack pattern. The number of cracks ($N_c$) of the specimen was counted by visually observing on both sides of the specimen. Most of the microcracks were found that went through the entire section of the specimen. The average crack width ($w_c$) and crack spacing were then calculated based on the formula below:

Crack width. $\delta L/Nc$

Crack spacing = $(\delta L + L)/Nc$

As shown in **Figure 7D**, all samples were shown significant multiple cracks, irrespective of the HGM amount, cracks were saturated over the gauge length without localization. The number of cracks increased from 13 to 27 as the HGM content increased. Smaller crack widths were found when more HGM was adopted, this phenomenon is possibly owing to the better fiber dispersion behavior due to HGM as well as the spherical HGM can lessen crack propagation by reducing the tortuosity of the fracture path along the interface between the HGM and cementitious matrices. All the cracks are finely distributed with an average spacing from 2.8 to 4.8 mm. The cracking behavior of HGMLW-SHCC 75 and HGMLW-SHCC 100 were further observed under microscopic

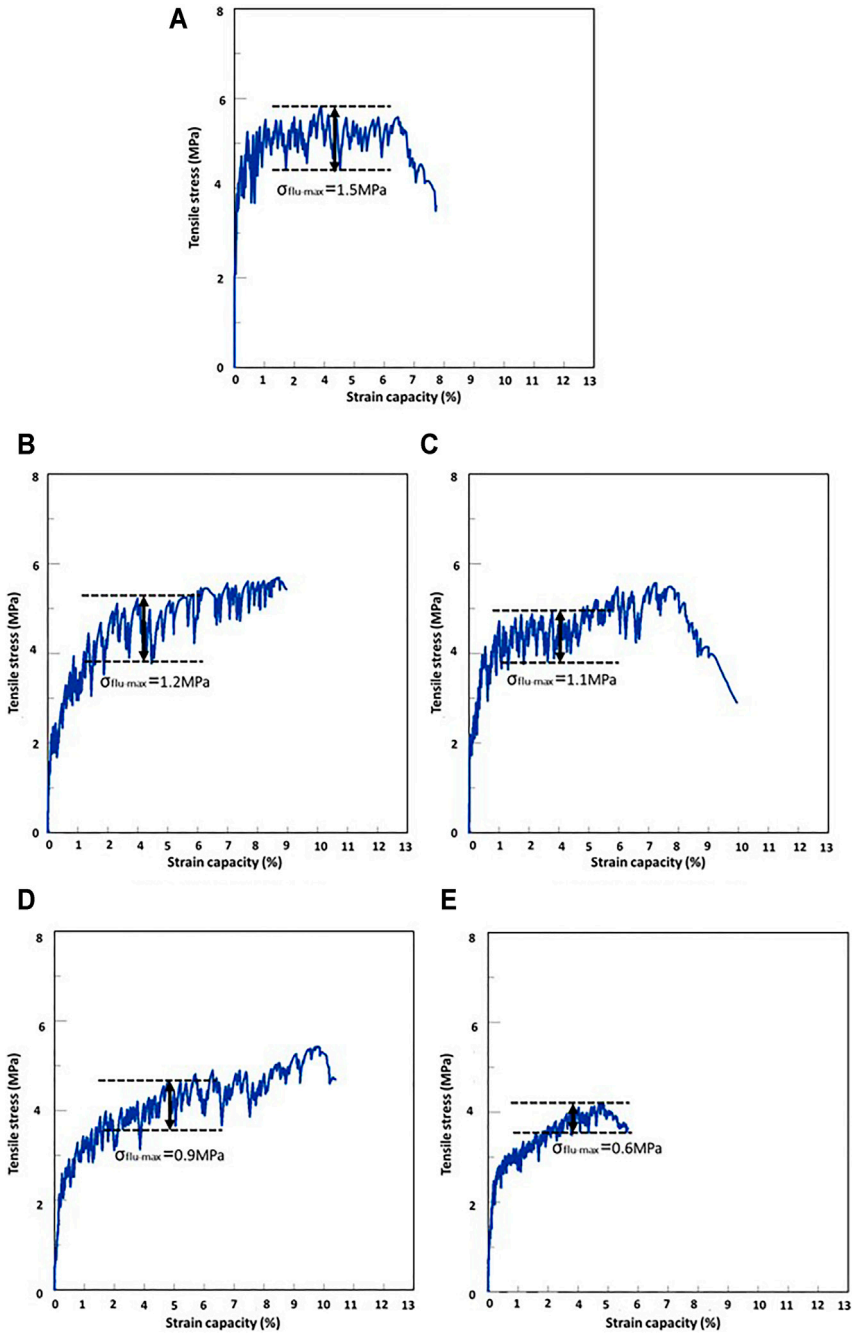


**FIGURE 8** | **(A)** HGMLW-SHCC 0, **(B)** HGMLW-SHCC 25, **(C)** HGMLW-SHCC 50, **(D)** HGMLW-SHCC 75, **(E)** HGMLW-SHCC 100.

examination for comparison. Average crack width $w_c$ and average crack spacing $s_c$ were shown in **Figure 7E**. It is obvious that incorporating HGM in SHCC can effectively minimize the crack width, thus, increase the durability of the material.

## Stress Fluctuation

Much like other SHCCs, a stress fluctuation was observed under the direct tensile test during the strain-hardening part, which has negative effects on the stability of the structures. PE fiber offers great stress fluctuation due to its hydrophobicity nature, which caused the interfacial friction between the PE fibers and the cementitious matrix to be weaker during cracking. **Figure 8** shows the result of average tensile behavior of all the mixtures with the value of maximum stress fluctuations $\sigma_{flu\text{-}max}$. It can be seen that the addition of HGM can be beneficial to reduce stress fluctuation. The degree of stress fluctuation decreased as the HGM content increased, from 1.5 MPa of HGMLW-SHCC 0–0.6 MPa of HGMLW-SHCC 100. Due to the addition of

**TABLE 4 |** Fracture toughness of HGMLW-SHCC.

| Mixture ID | Mass (kg) | $F_Q$ (kN) | $E_m$ (GPa) | $K_m$ (MPa·m$^{1/2}$) | $J_{tip}$ (J/m$^2$) |
|---|---|---|---|---|---|
| **HGMLW-SHCC-0** | 0.527 ± 0.05 | 0.66 ± 0.25 | 17.56 ± 0.69 | 0.331 ± 0.010 | 12.23 ± 0.35 |
| HGMLW-SHCC-25 | 0.509 ± 0.02 | 0.61 ± 0.18 | 15.40 ± 1.65 | 0.306 ± 0.012 | 9.08 ± 0.16 |
| HGMLW-SHCC-50 | 0.496 ± 0.06 | 0.57 ± 0.03 | 13.48 ± 1.03 | 0.286 ± 0.002 | 9.06 ± 0.10 |
| HGMLW-SHCC-75 | 0.474 ± 0.08 | 0.49 ± 0.16 | 10.28 ± 0.08 | 0.246 ± 0.003 | 6.88 ± 0.13 |
| HGMLW-SHCC-100 | 0.448 ± 0.04 | 0.42 ± 0.08 | 10.04 ± 0.05 | 0.211 ± 0.005 | 5.43 ± 0.08 |

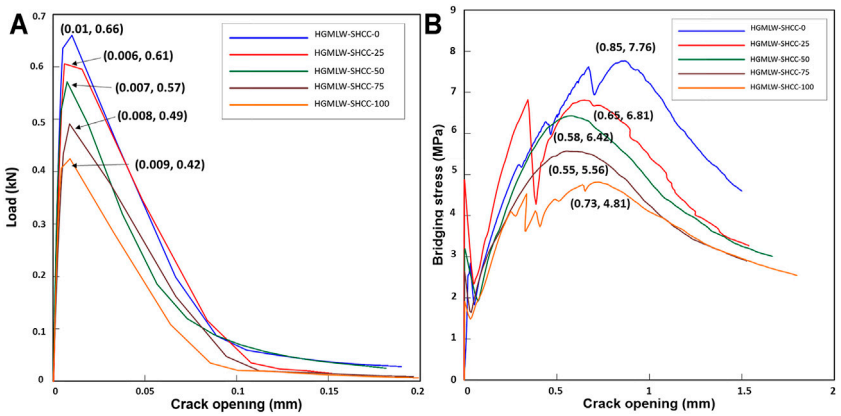


**FIGURE 9 |** Average results of **(A)** of crack mouth opening displacement; **(B)** Single-crack tensile test.

**TABLE 5 |** Single-crack tensile test results and PSH indices.

| Mixture ID | HGMLW-SHCC-0 | HGMLW-SHCC-25 | HGMLW-SHCC-50 | HGMLW-SHCC-75 | HGMLW-SHCC-100 |
|---|---|---|---|---|---|
| $\sigma_0$ (MPa) | 7.76 ± 0.25 | 6.81 ± 0.13 | 6.42 ± 0.07 | 5.56 ± 0.54 | 4.81 ± 0.28 |
| $\delta_0$ (mm) | 0.85 ± 0.06 | 0.65 ± 0.09 | 0.58 ± 0.12 | 0.55 ± 0.07 | 0.73 ± 0.05 |
| $J_b'$ (J/m$^2$) | 1,249.2 ± 22.7 | 1,095.5 ± 24.3 | 1,032.8 ± 26.2 | 893.6 ± 21.5 | 572.3 ± 20.2 |
| $PSH_s$ ($\sigma_0/\sigma_c$) | 1.58 ± 0.09 | 1.76 ± 0.08 | 1.91 ± 0.06 | 2.05 ± 0.07 | 2.16 ± 0.03 |
| $PSH_e$ ($J_b'/J_{tip}$) | 102.1 ± 3.6 | 120.6 ± 11.2 | 113.9 ± 5.1 | 129.8 ± 10.7 | 105.3 ± 3.5 |

HGM, the strength of the matrix reduces the small stress fluctuation caused by the interfacial stress between the PE fiber and the matrix.

## Interpretation of Micromechanical Analysis

**Table 4** shows the results of the matrix toughness test on the notched plain mortar beam samples. The peak load $F_Q$ and the mass m of each sample were summarized first. The fracture toughness $K_m$, Young's modulus $E_m$, and matrix fracture energy $J_{tip}$ were then evaluated. The peak load versus crack mouth opening displacement (CMOD) relationship was plotted in **Figure 9A**, where most of the load-displacement curves were tested with fully descending branches. The results are summarized in **Table 4**. It is obvious that the $K_m$ and $E_m$ decreased with the additional amount of HGM, owing to the adverse effect of HGM to the compressive strength of HGMLW-SHCC. The fracture energy $J_{tip}$ dropped from 6.27 J/m$^2$ to 4.45 J/m$^2$ as the introduction of HGM resulted in a lower matrix strength. The tensile stress-crack opening displacement curves of the notched HGMLW-SHCC sample results are presented in **Figure 9B**. It can be found that the peak bridging stress reduced as the HGM content increased. $\sigma_0$, $\delta_0$, $J_b'$, and the calculated pseudo strain-hardening ($PSH_s$ and $PSH_e$) index are listed in **Table 5**. It can be seen that the $PSH_s$ ($\sigma_c/\sigma_0$) value increased from 1.58 to 2.16 when the HGM replacement rate increased from 0 to 100%; this is due to the reduction in matrix cracking strength. All the mixtures showed a $PSH_s$ value larger than 1.2, which is corresponding to the steadily initiated cracks on the HGMLW-SHCC samples. Then, the $PSH_e$ ($J_b'/J_{tip}$) was calculated based on the complementary energy $J_b'$ and the matrix fracture energy $J_{tip}$.

All mixtures showed a relatively high $PSH_e$ value, even with 100% HGM replacement. The $PSH_e$ value of HGMLW-SHCC 100 is more than 35 times higher than the

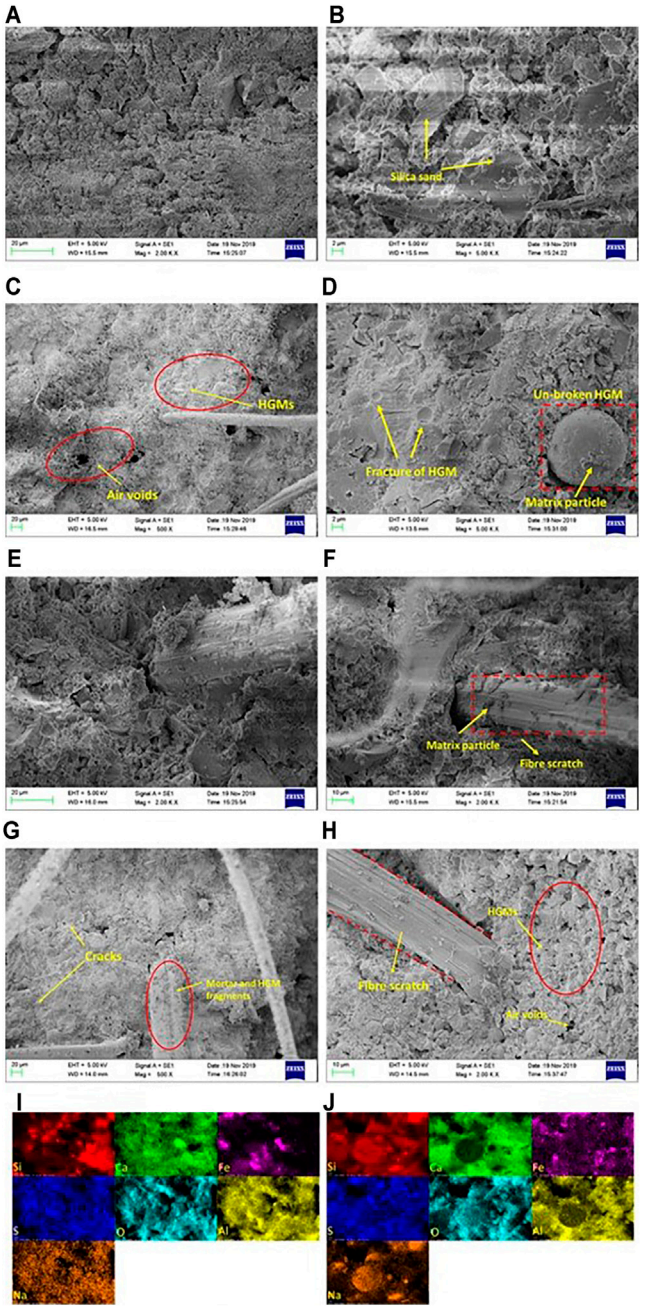


**FIGURE 10 | (A)** SEM image of HGMLW-SHCC0; **(B)** High magnification on SE M image of HGML W-SHCC 0: **(C)** SEM image of HGML W-SHOC 0: **(G)** and **(H)** PE fiber–matrix interface HGMLW-SHCC 100; **(I)** and **(J)** Detection of individual elemental phases by EDS.

recommended threshold value of 3 (Kanda and Li, 2002); therefore, the criterion of energy is compiled as well as a significant strain-hardening behavior was achieved.

## SEM-EDX Mapping

**Figure 10A–D** shows the SEM images of HGMLW-SHCC. For comparison, two specimens with 0 and 100% volume fractions of HGM were tested. **Figure 10A** indicates that the HGMLW-SHCC 0 mixture is dense and homogeneous, and no apparent air voids were observed. **Figure 10C** shows some air voids on the surface of the mortar. The number of air voids increased with increasing HGM content. These results indicate that the spherical particles of HGM induced more air voids in the matrix, which benefit the lightweight property of the end product. **Figure 10D** captured the smooth spherical shape of unbroken HGM with some attached pastes, attributing to a slight degree of pozzolanic reaction. Please note that HGM or silica sand was identified based on EDS mapping analysis (see **Figure 10I,J**).

**Figure 10E–H** shows the interaction of the PE fiber with blended cementitious matrix in samples of HGMLW-SHCC 0 and HGMLW-SHCC 100. **Figure 10E,F** showed that HGMLW-SHCC 0 has some residual mortar paste left on the surface of the PE fiber, indicating a good bonding strength between the PE fiber and HGMLW-SHCC 0 matrix. **Figure 10G,H** showed a relatively clean and smooth surface of PE fibers in HGMLW-SHCC 100, which may result from a weak fiber–matrix bond. These results could be attributed to the fact that the introduction of HGM into the cementitious matrix loosens the surrounding matrix, as shown in **Figure 10H**.

**Figure 10I,J** compare the exact distribution of various elemental phases in the samples with or without HGM addition. The elemental mapping results indicated that the calcium from hydration products was homogeneously distributed throughout the selected region in **Figure 10I**. Whereas **Figure 10J** shows the mapped region assigned to the HGM particle was rich in Si and Na, and the absence of Ca revealed that the HGM remained unreacted in the cementitious composite.

## CONCLUSION

This experimental study took a pilot step to develop a lightweight SHCC by using HGM. Based on the theory of micromechanics, HGMLW-SHCC with significant strain-hardening behavior was developed. A series of mechanical and microstructural tests were conducted and the results can be summarized as follows:

1. The introduction of HGM to the PE fiber-reinforced CAC-GGBFS-blended SHCC improves the flowability and greatly reduces the density from 2069 kg/m$^3$ to 1756 kg/m$^3$, meets the requirement of lightweight concrete.
2. The compressive strength of HGMLW-SHCC reduced after adding HGM but it still achieved almost 50 MPa when fully replaced for sand. All mixtures exhibited significant strain-hardening behavior with a maximum strain capacity up to 8.78%, almost 50% higher than the reference mixture group. Tensile strength was reduced insignificantly even the HGM content increased up to 75%; tensile stress fluctuations as well as crack width were all benefited.
3. Both $PSH_s$ and $PSH_e$ indices of the designed HGMLW-SHCC have fully satisfied the recommended values in the relevant

literature, which ensures a high strain-hardening behavior of HGMLW-SHCC.

4. SEM images captured the smooth spherical shape of unbroken HGM particles. HGM shell remains intact with CAC-GGBFSA-blended matrix after 28 days of moist curing, which means that little or no interaction between the microspheres and the cementitious matrix. EDX element mapping analysis further proves HGM remained unreacted in the cementitious composite.

## DATA AVAILABILITY STATEMENT

The raw data supporting the conclusions of this article will be made available by the authors, without undue reservation.

## AUTHOR CONTRIBUTIONS

FW performed the data curation, formal analysis, methodology, and wrote the first draft. YZ contributed to conception and design and supervision. YL contributed to the microstructure analysis. All authors contributed to manuscript revision, read, and approved the submitted version.

## ACKNOWLEDGMENTS

The first author would like to acknowledge the University of South Australia Postgraduate Research Award and Research Training Program scholarships for his PhD study. The authors would like to thank the staff at the UniSA laboratory—Tim Golding, Henry Senko, and Shane Kakko, for their assistance during the experimental work. The authors are grateful for the donation of slag from Independent Cement and Lime; the donation of hollow microspheres from Potters Asia Pacific (Australia) to be used in this study.

## REFERENCES

213R-14, ACI (2014). Guide for Structural Lightweight-Aggregate Concrete, ACI COMMITTEE REPORT. Available at http://www.uomisan.edu.iq/library/admin/book/68340626265.pdf.

Al-Gemeel, A. N., Zhuge, Y., and Youssf, O. (2018). Use of Hollow Glass Microspheres and Hybrid Fibres to Improve the Mechanical Properties of Engineered Cementitious Composite. *Construction Building Mater.* 171, 858–870. doi:10.1016/j.conbuildmat.2018.03.172

Aslani, F., and Wang, L. (2019). Development of Strain-Hardening Lightweight Engineered Cementitious Composites Using Hollow Glass Microspheres. *Struct. Concrete* (April), 1–16. doi:10.1002/suco.201900096

Aslani, F., Dehghani, A., and Wang, L. (2021). The Effect of Hollow Glass Microspheres, Carbon Nanofibers and Activated Carbon Powder on Mechanical and Dry Shrinkage Performance of Ultra-lightweight Engineered Cementitious Composites. *Construction Building Mater.* 280, 122415. doi:10.1016/j.conbuildmat.2021.122415

Belysheva, G. V., Egorochkin, A. N., Sennikov, P. G., Lopatin, M. A., and Voronenkov, V. V. (1990). UV-spectroscopic Study of Complex Formation by Certain Cycloolefins with Tetracyanoethylene and Molecular Iodine. *Russ. Chem. Bull.* 39 (6), 1181–1184. doi:10.1007/bf00962380

Chen, F., Cheng, S., Zhang, G., Chen, S., and Yang, R. (2021). Development of Ultralightweight Cement Composites with Low Density and High-specific Strength Using Hollow Glass Microspheres. *J. Mater. Civil Eng.* 33 (6), 1–9. doi:10.1061/(asce)mt.1943-5533.0003739

El-Hemaly, S. A. S., Abdallah, H. A. M., Abadir, M. F., and El Sersy, H. H. (2008). Evaluation of the Internal High Alumina Cement Mortar Lining of Ductile Cast Iron Pipes Used in Sewage Transportation. *Mater. Des.* 29 (6), 1280–1283. doi:10.1016/j.matdes.2007.05.001

Fan, W., Zhuge, Y., Ma, X., Chow, C. W. K., Gorjian, N., Oh, J.-A., et al. (2020). Durability of Fibre-Reinforced Calcium Aluminate Cement (CAC)-Ground Granulated Blast Furnace Slag (GGBFS) Blended Mortar after Sulfuric Acid Attack. *Materials* 13 (17), 3822. doi:10.3390/ma13173822

Fan, W., Zhuge, Y., Ma, X., Chow, C. W. K., and Gorjian, N. (2020). Strain Hardening Behaviour of PE Fibre Reinforced Calcium Aluminate Cement (CAC) - Ground Granulated Blast Furnace (GGBFS) Blended Mortar. *Construction Building Mater.* 241, 118100. doi:10.1016/j.conbuildmat.2020.118100

JapanSociety of Civil Engineers (2008) Recommendations for Design and Construction of High Performance Fiber Reinforced Cement Composites with Multiple Fine Cracks (HPFRCC). *Concrete Engineereing Ser* 82, 6–10. Testing MethodAvailable at http://www.jsce.or.jp/committee/concrete/e/index.html

Kanda, T., and Li, V. C. (1998). Multiple Cracking Sequence and Saturation in Fiber Reinforced Cementitious Composites. *Concrete Res. Tech.* 9(2), 19–33. doi:10.3151/crt1990.9.2_19

Kanda, T., and Li, V. C. (2002). New Micromechanics Design Theory for Pseudostrain Hardening Cementitious Composite. *J. Eng. Mech.* 125 (4), 373–381. doi:10.1061/(asce)0733-9399(1999)125:4(373)

Liu, Y., Zhuge, Y., Chow, C. W. K., Keegan, A., Ma, J., Hall, C., et al. (2021). Cementitious Composites Containing Alum Sludge Ash: An Investigation of Microstructural Features by an Advanced Nanoindentation Technology. *Construction Building Mater.* 299 (July), 124286. doi:10.1016/j.conbuildmat.2021.124286

Liu, Y., Zhuge, Y., Chow, C. W. K., Keegan, A., Pham, P. N., Li, D., et al. (2021). The Potential Use of Drinking Water Sludge Ash as Supplementary Cementitious Material in the Manufacture of Concrete Blocks. *Resour. Conservation Recycling* 168, 105291. doi:10.1016/j.resconrec.2020.105291

Lu, J.-X., Shen, P., Zheng, H., Ali, H. A., and Poon, C. S. (2021). Development and Characteristics of Ultra High-Performance Lightweight Cementitious Composites (UHP-LCCs). *Cement Concrete Res.* 145 (September 2020), 106462. doi:10.1016/j.cemconres.2021.106462

Martín, C. M., Scarponi, N. B., Villagrán, Y. A., Manzanal, D. G., and Piqué, T. M. (2021). Pozzolanic Activity Quantification of Hollow Glass Microspheres. *Cement and Concrete Composites* 118 (February)103981. doi:10.1016/j.cemconcomp.2021.103981

Nematollahi, B., and Sanjayan, J. (2014). Effect of Different Superplasticizers and Activator Combinations on Workability and Strength of Fly Ash Based Geopolymer. *Mater. Des.* 57, 667–672. doi:10.1016/j.matdes.2014.01.064

Oreshkin, D., Semenov, V., and Rozovskaya, T. (2016). Properties of Light-Weight Extruded Concrete with Hollow Glass Microspheres. *Proced. Eng.* 153, 638–643. doi:10.1016/j.proeng.2016.08.214

Seddik Meddah, M. (2019).Use of Waste Window Glass as Substitute of Natural Sand in Concrete Production, *IOP Conf. Ser. Mater. Sci. Eng.* 603 3 IOP Publishing, 032011. doi:10.1088/1757-899X/603/3/032011

Shang, X. Y., Jiang, T., Li, L. Z., and Zhou, D. (2019). Strengthening of RC Structures by Using Engineered Cementitious Composites: A Review. *Sustainability (Switzerland)* 11 (12). doi:10.3390/su11123384

Sheta, A., Ma, X., Zhuge, Y., ElGawady, M. A., Mills, J. E., Singh, A., et al. (2021). Structural Performance of Novel Thin-Walled Composite Cold-Formed Steel/PE-ECC Beams. *Thin-Walled Structures* 162 (February), 107586. doi:10.1016/j.tws.2021.107586

Song, Y., Chetty, K., Garbe, U., Wei, J., Bu, H., O'moore, L., et al. (2021). A Novel Granular Sludge-Based and Highly Corrosion-Resistant Bio-Concrete in Sewers. *Sci. Total Environ.* 791, 148270. doi:10.1016/j.scitotenv.2021.148270

Standard, A. S. T. M. (2008). *ASTM C109-Standard Test Method for Compressive Strength of Hydraulic Cement Mortars*. West Conshohocken, PA,US: " ASTM International

Wang, L., Aslani, F., Hajirasouliha, I., and Roquino, E. (2019). Ultra-Lightweight Engineered Cementitious Composite Using Waste Recycled Hollow Glass Microspheres. *J. Clean. Prod.* 33(6) 119331. doi:10.1016/j.jclepro.2019.119331

Wang, S., and Li, V. C. (2003), 27 Lightweight Engineered Cementitious Composites (ECC). In PRO 30: 4th International RILEM Workshop on High Performance Fiber Reinforced Cement Composites (HPFRCC 4), Michigan: RILEM Publications, 379

Xu, S., and Reinhardt, H. W. (1999). Determination of Double-K Criterion for Crack Propagation in Quasi-Brittle Fracture Part II: Analytical Evaluating and Practical Measuring Methods for Three-Point Bending Notched Beams. *Int. J. Fracture* 98 (2), 151–177. Available at: http://link.springer.com/article/10.1023/A:1018740728458. doi:10.1023/a:1018740728458

Yu, K.-Q., Yu, J.-T., Dai, J.-G., Lu, Z.-D., and Shah, S. P. (2018). Development of Ultra-high Performance Engineered Cementitious Composites Using Polyethylene (PE) Fibers. *Construction Building Mater.* 158, 217–227. doi:10.1016/j.conbuildmat.2017.10.040

Yu, K., Ding, Y., Liu, J., and Bai, Y. (2020). Energy Dissipation Characteristics of All-Grade Polyethylene Fiber-Reinforced Engineered Cementitious Composites (PE-ECC). *Cement and Concrete Composites* 106 (October 2019), 103459. doi:10.1016/j.cemconcomp.2019.103459

Yu, K., Wang, Y., Yu, J., and Xu, S. (2017). A Strain-Hardening Cementitious Composites with the Tensile Capacity up to 8 %. *Construction Building Mater.* 137, 410–419. doi:10.1016/j.conbuildmat.2017.01.060

Yu, K., Li, L., Yu, J., Xiao, J., Ye, J., and Wang, Y. (2018). Feasibility of Using Ultra-high Ductility Cementitious Composites for Concrete Structures without Steel Rebar. *Eng. Structures* 170, 11–20. doi:10.1016/j.engstruct.2018.05.037

Zhang, W., Yao, X., Yang, T., Liu, C., and Zhang, Z. (2018). Increasing Mechanical Strength and Acid Resistance of Geopolymers by Incorporating Different Siliceous Materials. *Construction Building Mater.* 175, 411–421. doi:10.1016/j.conbuildmat.2018.03.195

Zhuge, Yan., Shen, C. J., Lu, G. X., Hesse, G., Chen, S., and Ruan, D. (2014). "Material Properties and Impact Resistance of a New Lightweight Engineered Cementitious Composite," in In: 23rd Australasian Conference on the Mechanics of Structures and Materials (ACMSM 23), Byron Bay, Australia, Dec 2014, 9–12.

**Conflicts of Interest:** Author NG is employed by South Australian Water Corporation.

The remaining authors declare that the research was conducted in the absence of any commercial or financial relationships that could be construed as a potential conflict of interest.

**Publisher's Note:** All claims expressed in this article are solely those of the authors and do not necessarily represent those of their affiliated organizations, or those of the publisher, the editors, and the reviewers. Any product that may be evaluated in this article, or claim that may be made by its manufacturer, is not guaranteed or endorsed by the publisher.

frontiers in Materials

ORIGINAL RESEARCH
published: 05 November 2021
doi: 10.3389/fmats.2021.783176

# Surface-Functionalized Nanocelluloses as Viscosity-Modifying Agents in Engineered Cementitious Composites

*Long Liang[1,2], Junlei Yang[3], Guowei Lv[3], Zhen Lei[3], Xiurong Li[2] and Qiaoling Liu[1,2,4]**

[1]School of Civil Engineering, Shandong Jianzhu University, Jinan, China, [2]Engineering Research Institute of Appraisal and Strengthening of Shandong Jianzhu University CO., LTD, Jinan, China, [3]Shandong Luqiao Group CO., LTD, Jinan, China, [4]Key Laboratory of Building Structural Retrofitting and Underground Space Engineering of Ministry of Education, Jinan, China

This study investigated the feasibility of using nanofibrilliated celluloses (CNF) (0.1% by weight of binder materials) with three oxidation degrees, no oxidation (NCNF), low oxidation (LCNF), and high oxidation (HCNF), as a viscosity-modifying agent (VMA) to develop polyethylene fiber (PE)-engineered cementitious composites (ECC). Attenuated total reflection-Fourier transform infrared (ATR-FTIR), dynamic light scattering (DLS), and zeta potential were performed to characterize the properties of the CNF with different oxidation degrees. More stable CNF suspensions could be obtained due to the increasing oxidation degree. Rheology tests showed that CNF replacing VMA could modify the plastic viscosity and yield stress of the fresh matrices. With increasing the oxidation degree of CNF, a significant enhancement was seen for the rheological parameters. It was conducted that CNF could increase the compressive strength, the tensile stress, the nominal flexural strength, and the fracture toughness compared with ECC using VMA, and much higher oxidation degrees yielded higher enhancements (HCNF > LCNF > NCNF). ECC using CNF to replace VMA also achieved ultra-high ductility behavior with the tensile strain of over 8% and the saturated multiple cracking pattern. These finds were supplemented by thermal gravimetric analysis (TGA), which showed that the degree of hydration increased with increasing CNF surface oxidation degree. Additionally, the morphology images of PE fibers were observed by scanning electron microscope (SEM).

**Keywords: polyethylene fibers, engineered cementitious composites, nanofibrilliated celluloses, rheology, ultra-high ductility, fracture toughness**

OPEN ACCESS

***Edited by:***
*Kequan Yu,*
*Tongji University, China*

***Reviewed by:***
*Xiaodan Teng,*
*Guangxi University, China*
*Haoliang Wu,*
*Hong Kong University of Science and Technology, Hong Kong SAR, China*

****Correspondence:***
*Qiaoling Liu*
*lql263@163.com*

***Specialty section:***
*This article was submitted to Structural Materials, a section of the journal Frontiers in Materials*

***Received:*** *25 September 2021*
***Accepted:*** *11 October 2021*
***Published:*** *05 November 2021*

***Citation:***
*Liang L, Yang J, Lv G, Lei Z, Li X and Liu Q (2021) Surface-Functionalized Nanocelluloses as Viscosity-Modifying Agents in Engineered Cementitious Composites. Front. Mater. 8:783176. doi: 10.3389/fmats.2021.783176*

## INTRODUCTION

Engineered cementitious composites (ECC) are a type of cement-based materials with high ductility, which belongs to the range of fiber-reinforced cementitious composites (FRC). ECC was developed by using binder materials and fine aggregates, mixing with chopped fibers of about 2% volume, and designed according to the theory of fracture mechanics and micromechanics, so as to achieve the high ductility of cement-based materials (Li, 2019). Polyvinyl alcohol (PVA) fibers are used mostly to prepare ECC, which can usually achieve ultimate tensile stress of 3–5 MPa and tensile strain of 1%–5% (Yang et al., 2007; Wu et al., 2018; Zhang et al., 2020). Due to the hydrophilicity of the surface of PVA fibers, a strong chemical bond will be formed between fibers and matrices. When cracks appear under the tensile load, the load is

transferred from PVA fibers to the surrounding matrices, and fibers rupture easily due to the existence of the chemical bond during the debonding process of PVA fibers. The energy generated by the ruptures of fibers is less than that generated by the sliding friction of fibers (Pereira et al., 2012), weakening the bridging ability of PVA fibers, thereby limiting the improvement of the strength and ductility of ECC. Recently, using high-strength and high-elastic modulus polyethylene (PE) fibers to develop ECC has become a hot topic (Yu et al., 2017, 2018; Li et al., 2019). Compared with PVA fibers, the surface of PE fibers is hydrophobic and has higher nominal tensile strength and nominal tensile modulus of elasticity, and then PE fibers embedded in matrices have a higher bridging ability (Wang et al., 2020b), breaking through the limitations of PVA-ECC. The strain-hardening characteristics of ECC are attributed to the bridging effect of fibers, and the uniform dispersion of fibers in matrices is an important prerequisite to achieve this excellent property. The rheological properties of the fresh ECC matrices affect strongly the fiber dispersion uniformity, and it is necessary for combining rheology with ECC micro-design theory to achieve the high ductility of cementitious composites (Li and Li, 2013).

Recently, nanotechnology, an advanced field in science and technology, has been transforming into the field of cement-based materials. Various types of nanomaterials have been applied for improving the mechanical and durability of cement-based materials. Nanofibrilliated celluloses (CNF), as a nature-based resource, are prevailing in reinforcing composite materials (Kang et al., 2018). It is expected to provide a new idea for developing eco-friendly high-performance cement-based materials. CNF is generated by attacking amorphous regions of celluloses (from plant and tree resources), and it has several characteristics such as high aspect ratio, high surface area, low density, and high stiffness compared with other nanomaterials. The properties of CNF composites depend partly on the chemical functionalized surface of CNF (Klemm et al., 2011); a lot of alternate surface chemistries can be obtained due to the difference in the method of degradation, such as sulfate ester, hydroxyl, and acetyl. Additionally, plenty of hydroxyl groups exist on the surface of CNF produced by mechanical methods, and these can be converted to carboxylate groups using TEMPO-mediated oxidation treatments (Xu et al., 2014). On the basis of the surface chemistries of CNF, it is proven that CNF has the ability to modify the rheological properties of cement-based materials (Hisseine et al., 2018a; Montes et al., 2020), and improves the mechanical properties (Hisseine et al., 2018b; Ez-zaki et al., 2021).

Viscosity-modifying agent (VMA) based on cellulose ethers, such as hydroxyethylmethyl cellulose (HEC) or hydroxypropylmethyl cellulose (HPMC), is commonly used to improve the workability and stability of the fresh concrete mixture. In terms of ECC, VMA as an admixture was added to adjust the rheological properties of the fresh matrices for achieving a uniform dispersion of fibers in previous studies (Wang et al., 2020a; Wang et al., 2020b) considering that CNF also can impact the rheological performance of the fresh paste, and it is reported that CNF results in the enhancement of the microstructure and mechanical properties of cement-based materials (Ghahari et al., 2020; Hisseine et al., 2020). In this study, CNF, regarded as an alternative to common VMA, was used to develop and reinforce ECC. The effect of the different surface chemistries, oxidation degrees, of CNF on the performances of ECC was compared. CNF with three oxidation degrees, including no oxidation (NCNF), low oxidation (LCNF), and high oxidation (HCNF), was selected, and the properties of CNF were characterized by attenuated total reflection-Fourier transform infrared (ATR-FTIR), particle size distribution, and zeta potential. A constant CNF content of 0.1% by weight of binder materials was set to produce ECC. The rheological behavior was performed by using the plastic viscosity and yield stress of the fresh ECC matrices, conforming to the Modified Bingham model. A series of mechanical tests consisting of compressive strength, tensile properties, and fracture properties were evaluated at 28 days. In addition, thermal gravimetric analysis (TGA) was conducted to quantify the degrees of hydration of matrices at 28 days.

# MATERIALS AND METHODS

## Materials

### Basic Materials

Ordinary Portland cement (OPC) 52.5 grade, fly ash (FA), and silica fume (SF) were adopted as binder materials, and **Table 1** summarizes their chemical compositions. The quartz sand with a particle size of no more than 0.21 mm was selected as the fine aggregate. The particle size distributions of OPC, FA, SF, and sand are shown in **Figure 1**. Polyethylene (PE) fibers were added to reinforce matrices, and the nominal properties of PE fibers were as follows: the diameter and length were 24 μm and 18 mm, respectively, with a density of 970 kg/m$^3$. The tensile strength and elastic modulus were 2,900 MPa and 116 GPa, respectively, and the elongation was 2%–3%. Polycarboxylate superplasticizer (SP) was used to adjust the workability of the fresh mixtures. VMA-based hydroxypropylmethylcellulose (HPMC) was introduced to promote the dispersion of fibers.

### Surface Functionalized Nanofibrillated Celluloses

Nanofibrillated celluloses (CNFs), extracted from pulps, with different surface oxidation degrees were provided by the Shengquan Group Company, Jinan, China, and they were divided into no oxidation, low oxidation degree, and high oxidation degree. The CNF was a colloidal suspension form with a solid content of 0.6%.

## Mixture Proportions and Procedures

The mixture proportions were designed and listed in **Table 2**. Each mixture proportion was named ECC-0.1xCNF, where x represents the oxidation degree, dividing into H (high oxidation degree), L (low oxidation degree), and N (no oxidation). CNF was added to matrices at the same content of 0.1% by the total weight of binder materials. To more uniformly disperse the CNF suspensions in the mortar, they must be homogenized in advance by magnetic stirring and ultrasonic dispersion in water (Cao et al., 2016).

Dry materials including OPC, FA, SF, and sand were mixed for 2 min. For ECC-Ref, water and SP were gradually added into the dry materials and mixed for another 8 min. VMA was needed to add into the fresh matrices and mixed continually

**TABLE 1 |** Chemical compositions of binder materials (%).

| Material | $SiO_2$ | CaO | $Al_2O_3$ | $Fe_2O_3$ | $SO_3$ | MgO | $K_2O$ |
|---|---|---|---|---|---|---|---|
| Ordinary Portland cement (OPC) | 21.2 | 60.3 | 3.2 | 3.98 | 2.55 | 1.53 | 0.75 |
| Fly ash (FA) | 53.4 | 8.12 | 24.21 | 4.36 | 0.45 | 0.84 | 1.02 |
| Silica fume (SF) | 98.24 | 0.35 | 1.52 | 0.77 | — | 1.06 | 1.54 |

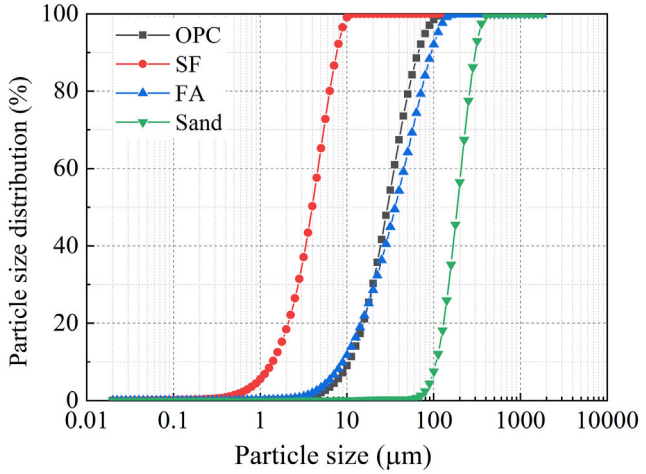


**FIGURE 1 |** Particle size distribution of ordinary Portland cement (OPC), silica fume (SF), fly ash (FA), and sand.

for 2 min. For ECC-CNF, water, SP, and CNF suspensions were added into the dry materials and mixed for another 8 min. Then, the fresh matrices reached a homogeneous condition. Finally, PE fibers were slowly poured into the mixture, and quickly mixed until fibers were uniformly dispersed. The fresh ECC was cast into molds and demolded after 48 h. All specimens were cured in water at a temperature of 20 ± 2°C until 28 days.

# Tests

## Attenuated Total Reflection-Fourier Transform Infrared (ATR-FTIR)

CNF suspensions should be dried into a thin film. ATR-FTIR analyses of CNF were conducted using the iS50 FT-IR spectrometer (ThermoFisher Scientific, United States). FTIR spectra were recorded in the wavenumber range of 4,000–450 $cm^{-1}$ with a resolution of 4 $cm^{-1}$ and 32 scans.

## Particle Size Distribution and Zeta Potential

Base on the dynamic light scattering (DLS), the particle size distribution and zeta potential were conducted by a zetasizer nano series instrument (Malvern, United Kingdom). The CNF suspensions were dispersed ultrasonically before tests, and the solid content was 0.3%. Then, the sample was analyzed under the following conditions: water refractive index 1.3328, viscosity 0.8827 cP, and temperature 25°C.

## Scanning Electron Microscope

SEM was taken to observe the morphology and surface of PE fibers, and samples for SEM were prepared from the fractured section of tensile tests.

## Rheology

The rheological properties of the fresh ECC matrices (no fiber) were measured with a rotary rheometer (Kinexus, Malvern, United Kingdom) kept at a constant temperature of 25 ± 0.1°C. A vane spindle with a 25-mm-diameter cup cylinder rheometer was installed (see **Figure 2A**. The fresh matrices were injected into the cup, and a 1-mm gap was set between the spindle and the bottom cup. In the test program from **Figure 2B**, samples went first through pre-shearing to reach the same original state. Then the sample was kept for 30 s to get a stable condition. Finally, the shear rate increased linearly from 0.1 to 100 $s^{-1}$ in 60 s and then decreased linearly to 0.1 $s^{-1}$ in another 60 s.

## Thermogravimetric Analysis

TGA was carried out with a TGA/SDTA 851 instrument (Mettler Toledo). Approximately 30 mg of hardened matrices at 28 days were ground into fine powders and heated from 30°C to 1,000°C in a nitrogen atmosphere at a constant rate of 10°C/min.

## Compressive Strength

The 28-day compressive strength was measured using 70.7-mm cubes, and the compression tests were conducted on a 3,000-kN servo-hydraulic testing machine under a loading rate of 1 MPa/s.

**TABLE 2 |** Mixture proportions.

| Mixture ID | Binder | | | Water | Sand | VMA | CNF (%) | SP (%) | Fiber (%) |
|---|---|---|---|---|---|---|---|---|---|
| | OPC | FA | SF | | | | | | |
| ECC-Ref | 0.5 | 0.4 | 0.1 | 0.22 | 0.3 | 0.03% | 0 | 0.4 | 2 |
| ECC-0.1HCNF | 0.5 | 0.4 | 0.1 | 0.22 | 0.3 | 0 | 0.1 | 0.4 | 2 |
| ECC-0.1LCNF | 0.5 | 0.4 | 0.1 | 0.22 | 0.3 | 0 | 0.1 | 0.4 | 2 |
| ECC-0.1NCNF | 0.5 | 0.4 | 0.1 | 0.22 | 0.3 | 0 | 0.1 | 0.4 | 2 |

*Note: binder, water, and sand are mass fraction; the percentage of viscosity modifying agent (VMA), nanofibrilliated celluloses (CNF), and HRWR is by weight of binder; fiber is by volume of composites.*

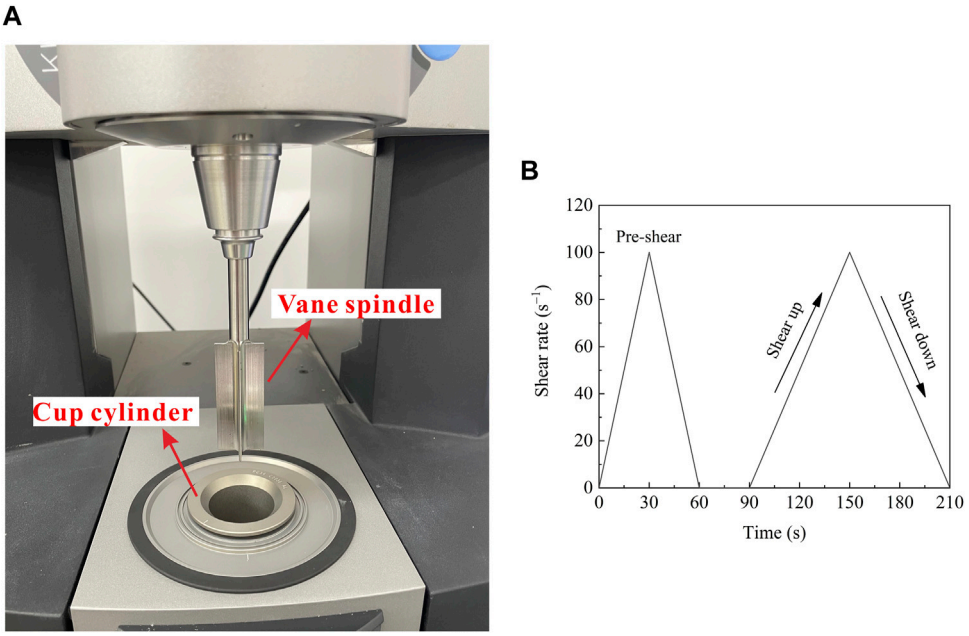


**FIGURE 2 |** Rheology test. **(A)** Rheometer; **(B)** Test program.

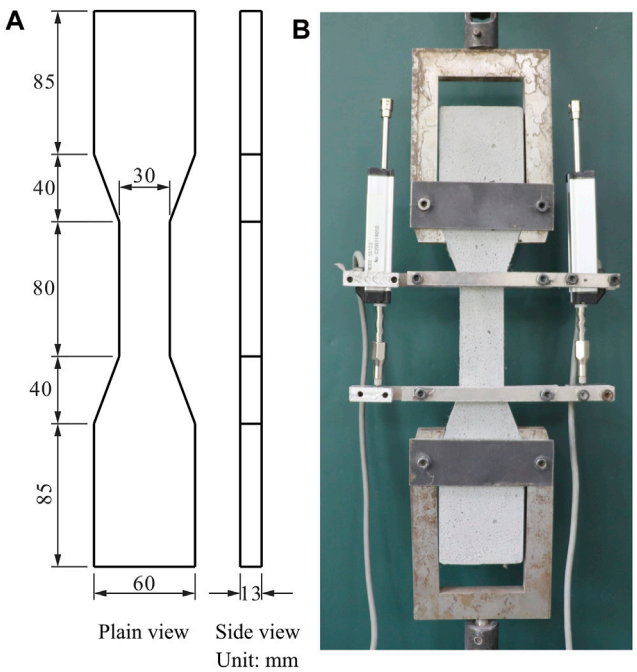


**FIGURE 3 |** ECC tensile test. **(A)** Dimensions of a dogbone-shaped specimen. **(B)** Test setup.

### Tensile Test

The dogbone-shaped specimens were adopted to obtain the uniaxial direct tensile strain–stress curves of ECC (Kanakubo et al., 2005), and the dimensions of the dogbone-shaped specimens and test setup are shown in **Figure 3**. The tensile tests were conducted under a loading rate of 0.5 mm/min. Two extensometers fixed on the middle part with a gauge length of 80 mm were used to measure the elongation of specimens. According to the tensile strain–stress curves, the first cracking stress σtc, ultimate tensile stress $\sigma_{tp}$, tensile strain $\varepsilon_{tu}$, crack number $n_c$, crack width $w_c$, and crack spacing $d_c$ were obtained to evaluate the tensile properties of ECC.

### Fracture Test

According to RILEM TC50-FMC (RILEM, 1985), the prismatic beams of 40 mm × 40 mm × 160 mm were prepared for three-point bending tests. To investigate the fracture effect, a notch with a width of 2 mm and a depth of 10 mm was cut in the middle span of the specimens. The fracture tests were conducted with the span support of 100 mm and a loading rate of 1 mm/min. A clip-gauge was used to measure the crack mouth opening displacement (CMOD). **Figure 4** depicts the test setup and specimen size.

## RESULTS

## Nanofibrilliated Celluloses Properties

### Surface Structure of Nanofibrilliated Celluloses

**Figure 5** shows the FTIR spectra of the different CNFs (Li et al., 2015). The band near 3,300 cm$^{-1}$ is assigned to the vibration stretching of O–H from hydroxyl groups. The band at 2,887 cm$^{-1}$ is assigned to the symmetric and asymmetric stretching of C–H from $CH_2$ groups related to the cellulose structure. The band at 1,590 cm$^{-1}$ is strongly related to the antisymmetric stretching of COO– from carboxylic acid salts, which represents the

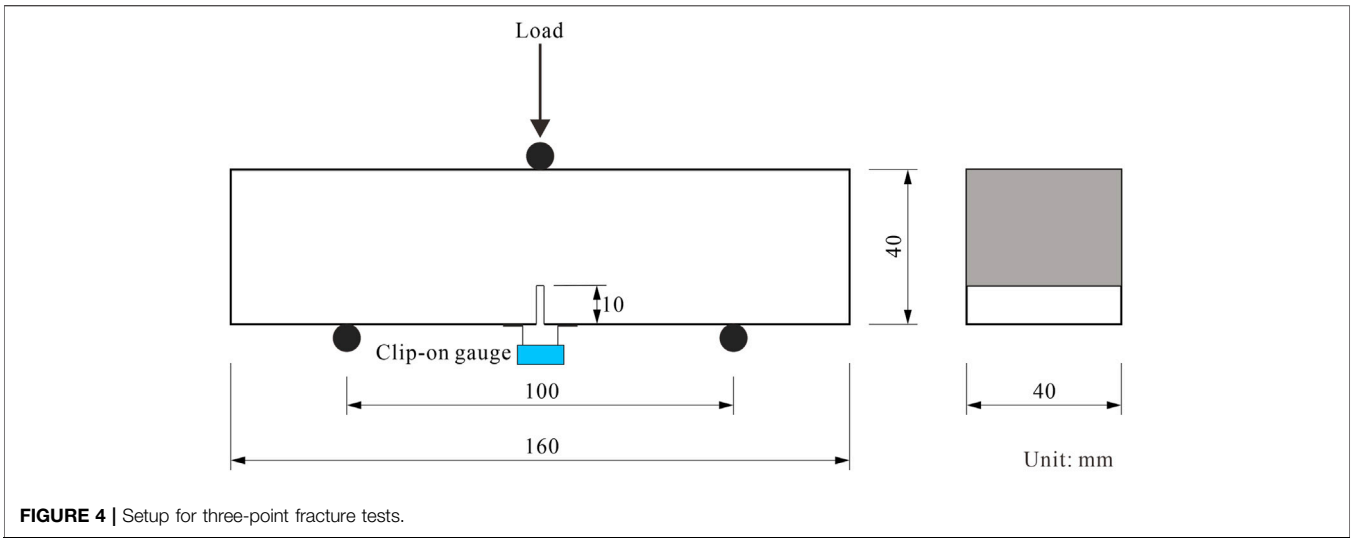


**FIGURE 4 |** Setup for three-point fracture tests.

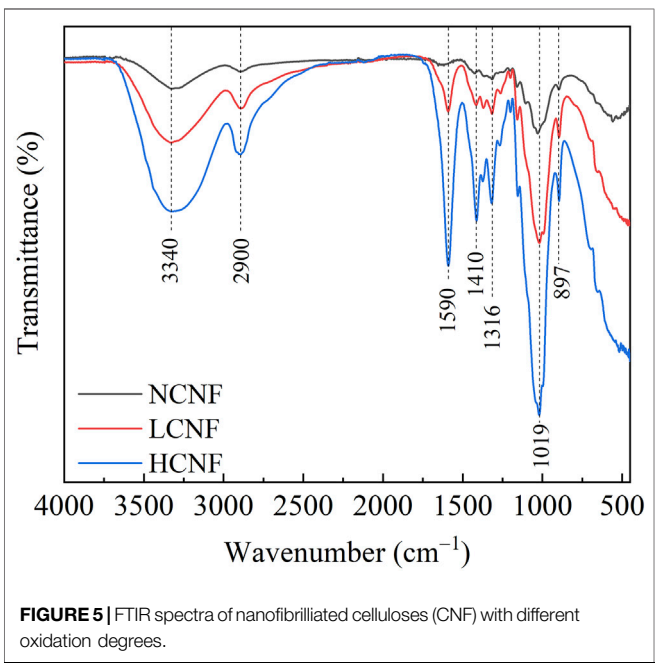


**FIGURE 5 |** FTIR spectra of nanofibrilliated celluloses (CNF) with different oxidation degrees.

introduction of carboxylate groups oxidized on the surface structure of CNF. HCNF with a higher degree of oxidation had a higher intensity of the COO– band at 1,590 cm$^{-1}$ compared with LCNF, while the peak of NCNF at 1,590 cm$^{-1}$ was absent, which determined the oxidation degree order of HCNF > LCNF > NCNF. Moreover, the hydrophilicity of CNF was determined on the carboxylate and hydroxyl groups.

### Particle Size Distribution and Zeta Potential

The dynamic light scattering (DLS) method could quantitatively obtain rough results of the particle size distribution for CNF fibrils (Benini et al., 2018), as shown in **Figure 6A**. It can be seen that the average particle size of CNF gradually decreased from 3,218.49 to 244.78 nm due to the higher oxidation degree. For DLS analysis, the measured particle size is the hydrodynamic diameter of suspensions (Benini et al., 2018), and then aggregated particles might result in a higher value of particle size. Therefore, the decreasing particle size of CNF oxidized might be attributed to the improved dispersion in water. It should be noted that HCNF and LCNF had much lower values of zeta potential (NCNF > LCNF > HCNF), indicating the higher effect of oxidation degree on the stability of CNF suspensions. As shown in **Figure 6B**, after static for 7 days, the HCNF suspension showed high stability, and the LCNF suspension appeared slightly stratified, while NCNF displayed severe precipitation phenomenon, which was ascribed to the surface zeta potential. For the negative value of zeta potential, lower values illustrated that there existed sufficient mutual repulsion, thus, leading to high colloidal stability, and such a similar trend has been reported (Seta et al., 2020).

## Rheological Properties of the Fresh Engineered Cementitious Composites Matrices (Constant Superplasticizer)

**Figure 7** shows the rheological behavior of the fresh matrices. As can be seen from **Figure 7**, all the fresh matrices exhibited a shear-thinning behavior, showing that the shear viscosity decreased with the increase in shear rate. The yield stress and plastic viscosity were determined by using the Modified Bingham model (expressed in **Eq. 1**) (Yahia and Khayat, 2001) that represents an idealized type of fluid that could fit the shear rate–shear stress curves of cement-based materials, and the fitting results showed quite good correlations with a coefficient of $R^2 > 0.99$.

$$\tau = \tau_0 + \mu\gamma + c\gamma^2 \quad (1)$$

where $\tau$ is the shear stress, $\gamma$ is the shear rate, $\tau_0$ is the yield stress, $\mu$ is the plastic viscosity, and $c$ is the regression coefficient.

The fresh matrices for no VMA (with no VMA, no CNF, and 0.4% SP) showed the lowest plastic viscosity and yield

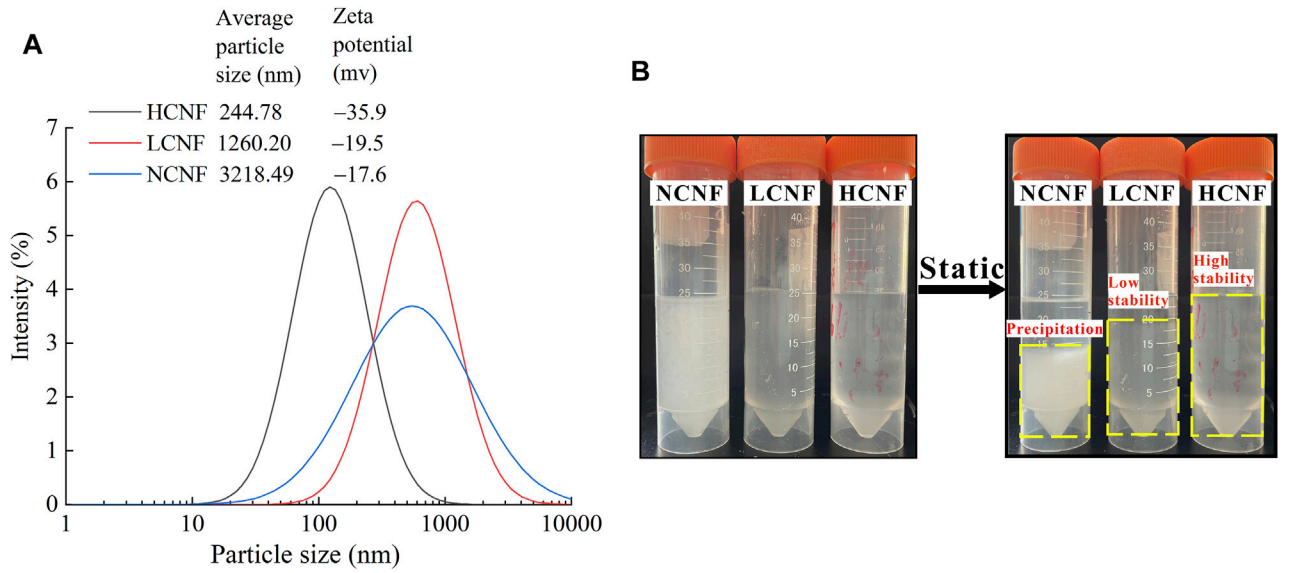


**FIGURE 6 | (A)** Particle size distribution and zeta potential and **(B)** stability of CNF suspensions.

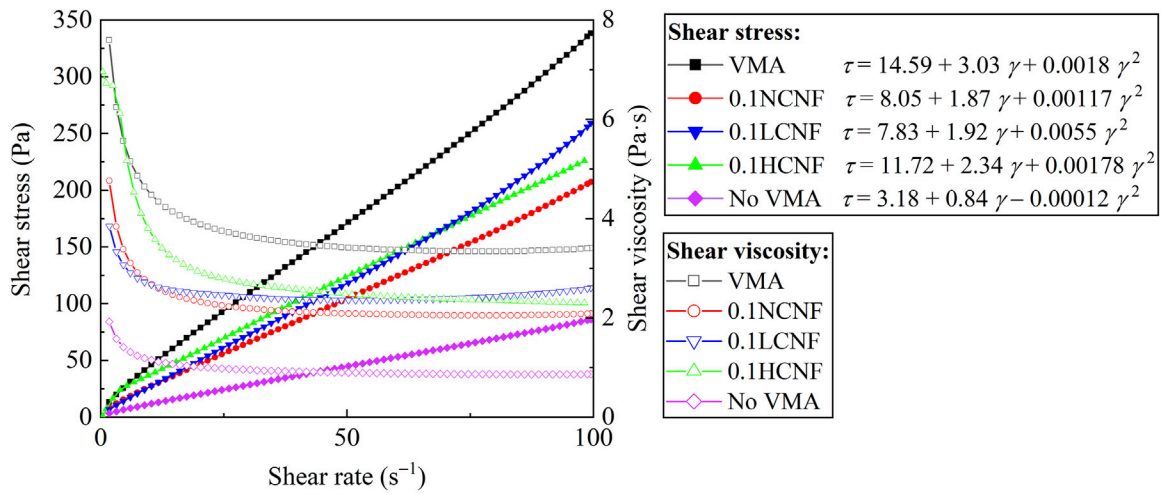


**FIGURE 7 |** Shear stress and shear viscosity curves of the fresh matrices.

stress of 0.84 Pa·s and 3.18 Pa, respectively. Adding VMA enhanced the plastic viscosity to 3.03 Pa·s by 3.6 times to promote the dispersion of fibers, and the yield stress increased to 14.59 Pa by 4.6 times. In comparison, the incorporation of three types of CNF also increased the plastic viscosity and yield stress to varying degrees. HCNF, LCNF, and NCNF increased the plastic viscosity to 2.34, 1.92, and 1.87 Pa·s, respectively, and these corresponded to increases by 2.8 times, 2.3 times, and 2.2 times, respectively. The yield stress increased to 8.05, 7.83, and 11.70 Pa, respectively, by 2.5 times, 2.5 times, and 3.7 times, respectively. When the CNF content was set to 0.1%, the effect of HCNF on the rheological properties of the fresh matrices was more significant.

The modifying rheological properties mechanism of VMA could be explained as its water retention and adsorption on cement (Pourchez et al., 2006), and that of CNF might be similar. The hydrophilicity of CNF determined its water-absorbed capacity, and HCNF with a higher density of carboxylate groups had more absorbed water. Meanwhile, a lower surface zeta potential of HCNF enhanced the adsorption between CNF and cement, hence, increasing the resistance to deformation of the fresh matrices. Therefore, these results proved the feasibility of using CNF as VMA.

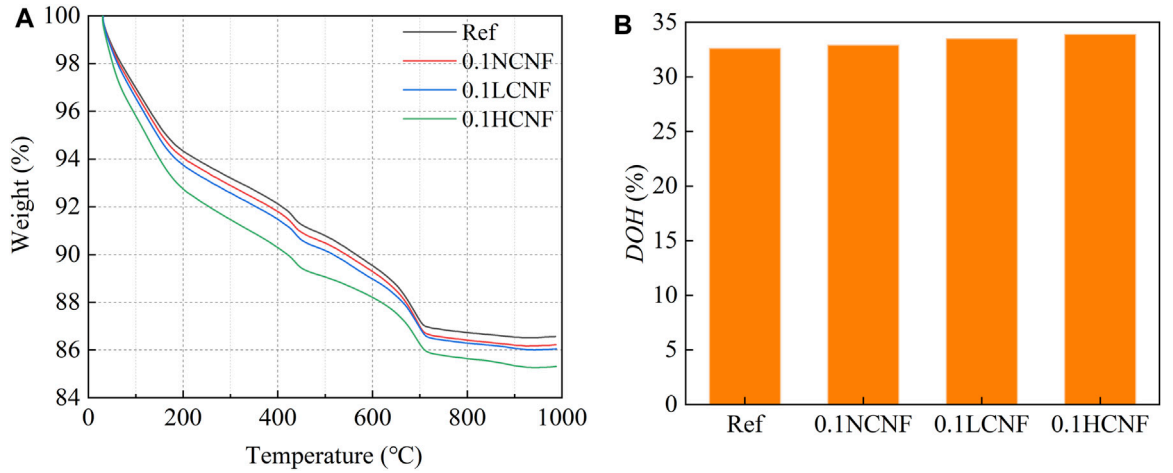


**FIGURE 8 |** TGA results. **(A)** Weight loss. **(B)** Hydration degree of cement.

## Thermogravimetric Analysis

**Figure 8A** illustrates the thermogravimetric analysis (TGA) results of ECC matrices at 28 days. The weight loss of the non-evaporable water at 105°–1,000°C (Nassiri et al., 2021) could be calculated from the TGA curves. The degree of hydration (DOH) was assessed by normalizing the non-evaporable water content to the assumption maximum hydration value of 0.23 g/g unhydrated cement (Cao et al., 2015), as described by **Eq. 2**.

$$DOH = \frac{W_{NEW}}{0.23}, \quad W_{NEW} = W_{loss} - CO_{loss} \tag{2}$$

where $W_{NEW}$ is the weight loss of non-evaporable water at 105°–1,000°C, $W_{loss}$ is the total weight loss of samples at 105°–1,000°C, and $CO_{loss}$ is the weight loss of decarbonization at 600°–780°C.

The results of DOH are summarized in **Figure 8B**. NCNF, LCNF, and HCNF showed higher DOH than Ref, and the improvement in DOH might be attributed to a short-circuit diffusion mechanism proposed by Cao et al. (2015). The zeta potential for NCNF, LCNF, and HCNF was −17.6 , −19.5, and −35.9 mv, respectively, so CNF had a trend to absorb the surface of cement particles (+1.1 mv). At later ages of hydration, more water might be transported into the unhydrated cement core by the CNF channel, resulting in more hydration products. Meanwhile, HCNF with a higher oxidation degree more strongly tended to adhere to cement particles, thus, giving the highest DOH.

## Engineered Cementitious Composite Compressive Strength

**Figure 9** shows the results of the 28-day compressive strength. Compared with ECC-Ref for only 60 MPa, CNF with different DOs could always enhance the compressive strength to 65.1, 74.0, and 81.4 MPa, of ECC-0.1NCNF, ECC-0.1LCNF, and ECC-0.1HCNF, respectively, and the peak increase was found in ECC-0.1HCNF by 35.7%, indicating that a higher DO favor an increase in the compressive strength of ECC. The enhancement in the compressive strength of ECC by adding CNF could be due to the acceleration of hydration degrees of cement at 28 days.

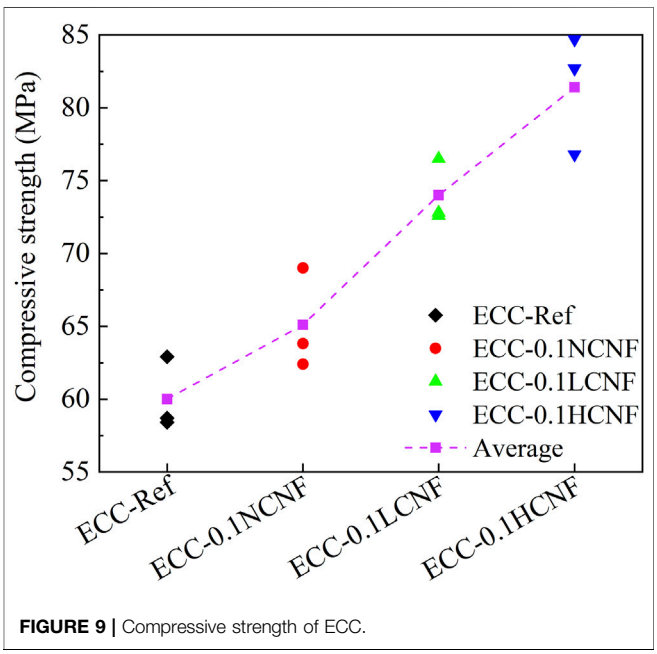


**FIGURE 9 |** Compressive strength of ECC.

## Engineered Cementitious Composite Tensile Properties

**Figure 10** illustrates the tensile strain curves of ECC with different types of CNF, and the key tensile parameters are summarized in **Table 3**. It is clearly shown that all specimens exhibited obvious strain-hardening behavior. **Figure 11A** shows the saturated multiple cracking pattern observed in a typical specimens. The tensile strain capacity of all groups could reach over 8%, which was attributed to

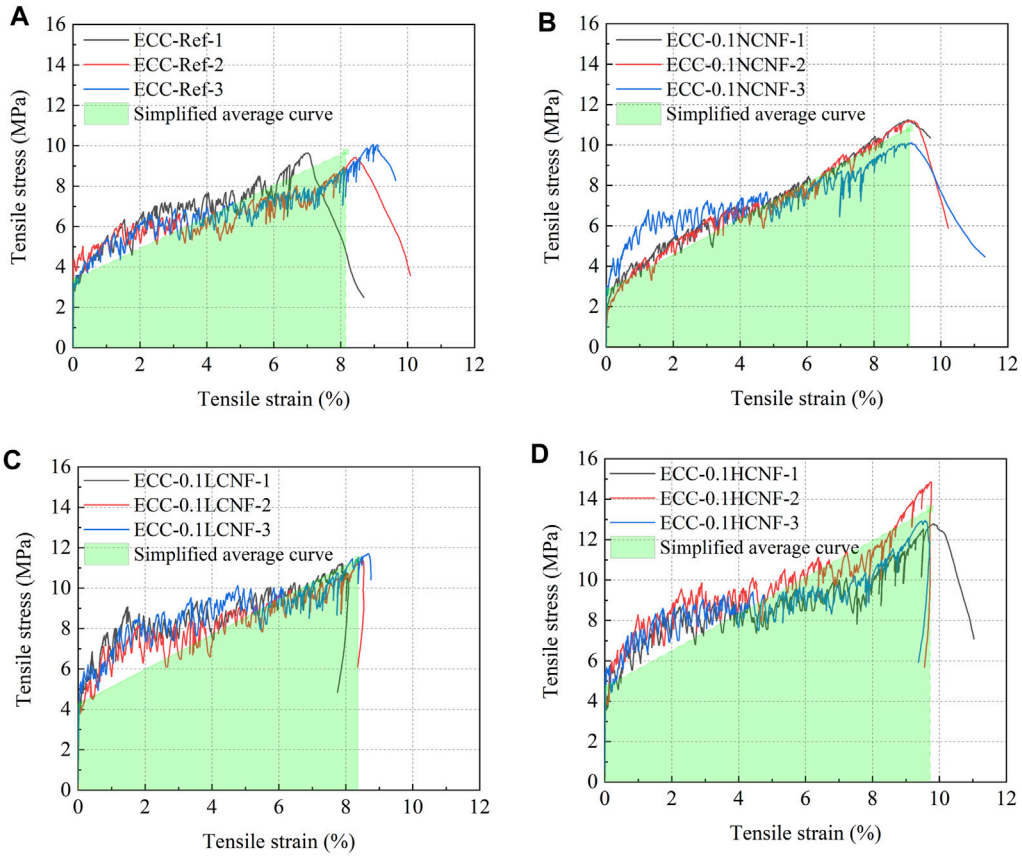


**FIGURE 10 |** Tensile strain–stress curves of ECC. **(A)** Ref; **(B)** 0.1% content of CNF of no oxidation; **(C)** 0.1% content of CNF of low oxidation degree; **(D)** 0.1% content of CNF of high oxidation degree.

**TABLE 3 |** Tension test results of engineered cementitious composites (ECC).

| Mixture ID | $\sigma_{tc}$ (MPa) | $\sigma_{tp}$ (MPa) | $\varepsilon_{tu}$ (%) | $g_{se}$ (KJ/m$^3$) | $n_c$ | $w_c$ (μm) | $d_c$ (mm) |
|---|---|---|---|---|---|---|---|
| ECC-0CNF | 3.37 ± 0.24 | 9.71 ± 0.27 | 8.15 ± 0.82 | 538 ± 51 | 70 ± 5 | 107.56 ± 2.60 | 1.44 ± 0.14 |
| ECC-0.1NCNF | 2.79 ± 0.31 | 10.84 ± 0.53 | 9.06 ± 0.05 | 638 ± 14 | 69 ± 3 | 120.38 ± 5.62 | 1.45 ± 0.06 |
| ECC-0.1LCNF | 4.25 ± 0.13 | 11.43 ± 0.20 | 8.35 ± 0.34 | 707 ± 37 | 71 ± 4 | 111.21 ± 12.11 | 1.44 ± 0.14 |
| ECC-0.1HCNF | 4.70 ± 0.57 | 13.53 ± 0.94 | 9.72 ± 0.11 | 880 ± 43 | 71 ± 5 | 131.98 ± 5.10 | 1.49 ± 0.06 |

the saturated multiple crack distribution. As shown in **Figure 11B**, during the multiple cracking, the tensile stress dropped when a new crack appeared. Compared with ECC-Ref, the process of strain-hardening behavior for ECC-0.1HCNF was far more fluctuant, and that for ECC-0.1NCNF was more stable.

**Figure 12** compares the tensile behavior parameters, the first cracking stress, peak stress, tensile strain, and strain energy, of all groups. As shown in **Figure 12A**, for ECC-Ref, prepared using VMA, the first cracking stress and the peak stress were 3.37 and 9.71 MPa, respectively. Using LCNF and HCNF created a higher first cracking stress and peak stress. HCNF led to 39.5% and 39.3% increases in the first cracking stress of 4.70 MPa and peak stress of 13.53 MPa over those of ECC-Ref, and LCNF led to 26.1% and 17.7% increases in those. NCNF posed a negative effect on the first cracking stress, decreasing by 17.2%, but increased the peak stress by 11.6%. As shown in **Figure 12B**, ECC-Ref, ECC-0.1NCNF, ECC-0.1LCNF, and ECC-0.1HCNF exhibited ultra-high tensile strain capacities of 8.15%, 9.06%, 8.35%, and 9.72%, respectively. In addition, the strain energy dissipation showed a similar trend with the peak stress. ECC prepared using CNF to replace VMA achieved similarly ultra-high ductility. High strength and high ductility are associated with the high bridging capacity provided by the PE fibers and a lower bond between the PE fibers and matrices. On the other hand, when the SP content was set at the same value of 0.4%, the plastic viscosity of the fresh matrices for NCNF, LCNF, and HCNF was 1.87, 1.92, and 2.34 Pa·s, respectively, showing lower values than that for VMA of 3.03 Pa·s. It is

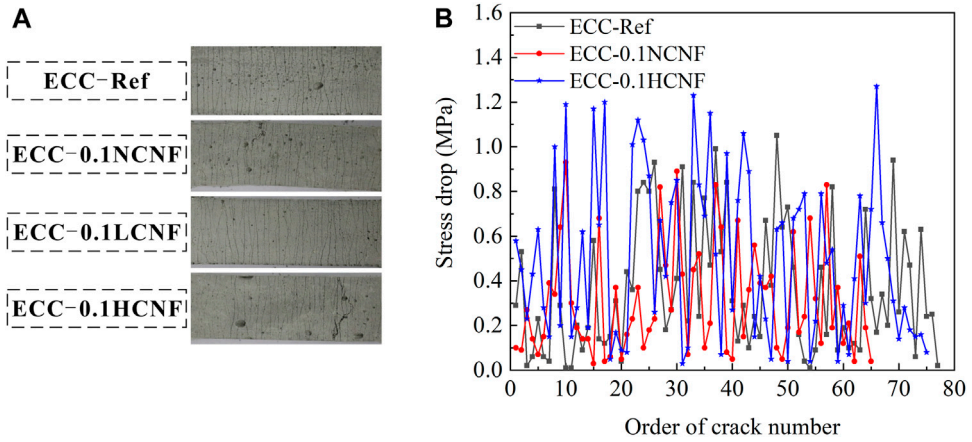


**FIGURE 11 |** Typical crack patterns of ECC. **(A)** Crack distribution. **(B)** Stress drops.

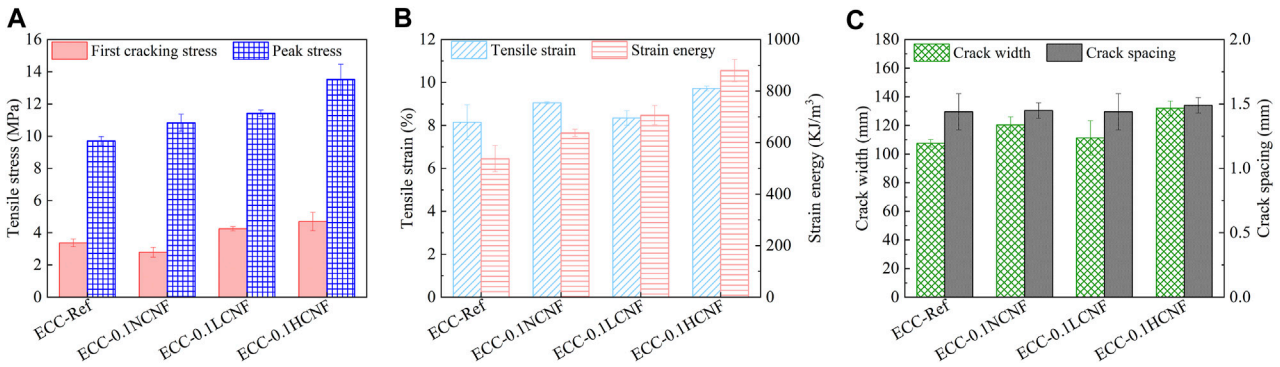


**FIGURE 12 |** Tensile behavior parameters. **(A)** First cracking stress and peak stress. **(B)** Tensile strain and strain energy. **(C)** Crack width and crack spacing.

noted that the crack number was all close to the value of 70, which caused the differences in the crack width and the crack spacing (see **Figure 12C**). This range for the plastic viscosity all might be suitable for achieving the uniform fiber dispersion. The crack width of ECC introducing CNF was slightly higher than ECC-Ref. The crack width of all specimens was limited to less than 150 μm, exhibiting the excellent ability in the crack width-controlled characteristic (Yu et al., 2017).

Introducing LCNF or HCNF increased the initial cracking stress up to 4.25 MPa for ECC-0.1LCNF and 4.70 MPa for ECC-0.1HCNF and the tensile stress up to 11.43 MPa for ECC-0.1LCNF and 13.53 MPa for ECC-0.1HCNF. These indicated that oxidized CNF exerted a positive effect on the enhancement in the initial cracking stress and tensile stress, and the improvement by 39.5% and 39.3% due to the adding of HCNF was higher than that by 26.1% and 17.7% due to the adding of LCNF.

## Engineered Cementitious Composite Fracture Properties

**Figure 13** shows the load–CMOD curves of ECC. All groups showed a strong fracture-hardening behavior. In terms of ECC, the nominal flexural strength $\sigma_n$ is introduced and calculated using **Eq. 3**.

$$\sigma_n = \frac{c_n F_n}{bd} \tag{3}$$

where $c_n$ is the coefficient correlated to the geometric dimensions by **Eq. 4**, and Fn is the peak load.

$$c_n = \frac{3s}{2d\left[1 - (\alpha/d)^2\right]} \tag{4}$$

The ability in the crack resistance can be quantitatively evaluated on the fracture toughness, and the fracture toughness $K_{IC}$ is determined using a simplified method (Xu and Reinhardt, 2000). Based on the load–CMOD curves, the fracture toughness is calculated by **Eq. 5**.

$$K_{IC} = \frac{3F_n s}{2bd^2}\sqrt{a_c} f(V_h) \tag{5}$$

where $f(V_h)$ is the empirical formula for stress factor, as described in **Eq. 6**, and $a_c$ is the critical effective crack length, as shown in **Eq. 7**.

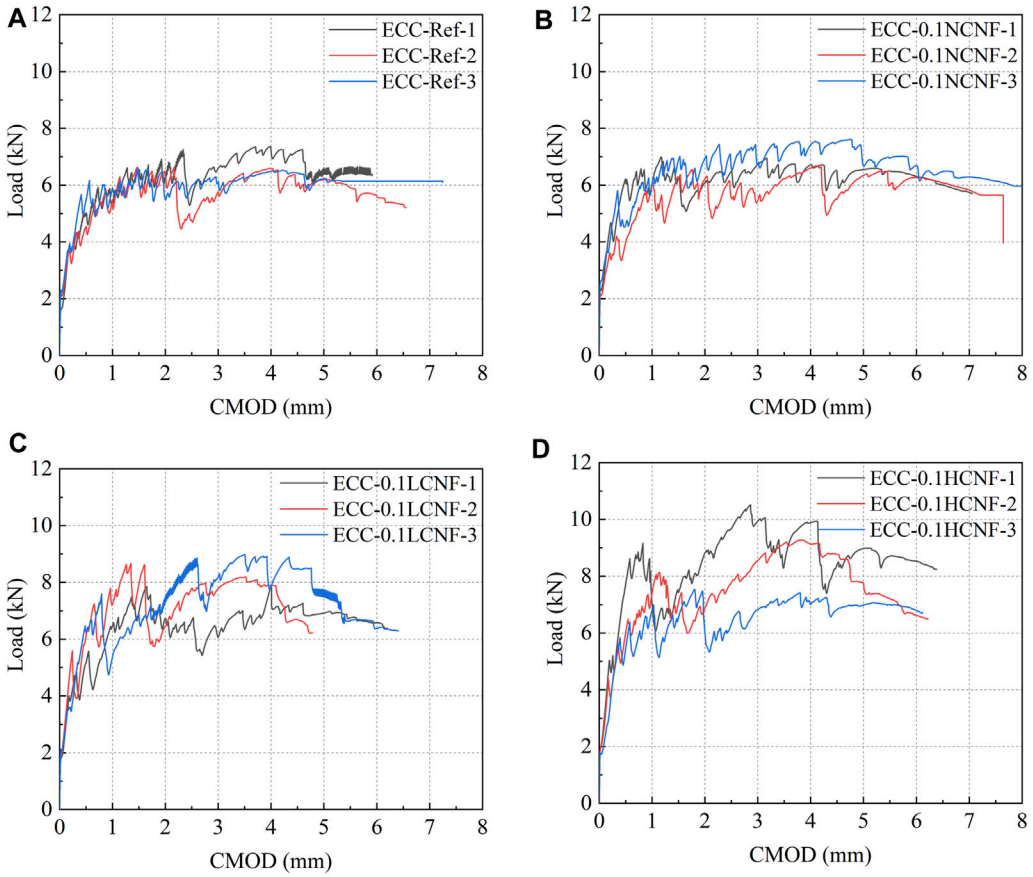


**FIGURE 13 |** Load–CTOD curves of ECC. **(A)** Ref; **(B)** 0.1% content of CNF of no oxidation; **(C)** 0.1% content of CNF of low oxidation degree; **(D)** 0.1% content of CNF of high oxidation degree.

$$f(V_h) = \frac{1.99 - V_h(1 - V_h)(2.15 - 3.93V_h + 2.7V_h^2)}{(1 + 2V_h)(1 - V_h)^{3/2}}, V_h = \frac{a + h_0}{d + h_0} \tag{6}$$

$$a_c = \frac{2}{\pi}(d + h_0)\arctan\sqrt{\frac{bE \cdot CMOD}{32.6F_n} - 0.1135} - h_0 \tag{7}$$

where $E$ is the elastic modulus and calculated based on the linear elastic stage in the load-CMOD curve, as expressed in **Eq. 8**.

$$E = \frac{F_i}{b \cdot CMOD_i}\left[3.7 + 32.6\tan^2\left(\frac{\pi}{2}V_h\right)\right] \tag{8}$$

**Table 4** lists the calculated results of the fracture toughness $K_{IC}$, the peak load $F_n$, and fracture energy $G_f$. Compared with ECC-Ref, it can be observed that the nominal flexural strength for ECC-0.1NCNF, ECC-0.1LCNF, and ECC-0.1HCNF increased by 4.4%, 22.7%, and 34.4%, respectively, which indicated that CNF improved the frictional strength between fibers and matrices. The addition of NCNF, LCNF, and HCNF also enhanced the fracture toughness from 6.03 to 6.30, 7.38, and 8.08 MPa·m$^{1/2}$, respectively, and this corresponded to the enhancements of 4.5%, 20.3%, and 34.0%, respectively. In addition, the fracture-hardening stage of CNF was much larger than that of Ref, thus, leading to the increases in the fracture energy by 4%–27.7%, which was attributed to much stronger PE fiber-bridging capacity. The larger enhancement in the nominal flexural strength, fracture energy, and fracture toughness for ECC-0.1HCNF could be achieved than that for other ECC.

## Scanning Electron Microscope Observation of Polyethylene Fibers

**Figure 14** displays the morphology images of PE fibers in ECC, including ECC-Ref, ECC-0.1NCNF, and ECC-0.1HCNF. Fibers were embedded and bonded in matrices, contributing to ultra-high tensile strain capacity. It can be observed that most of the fibers were pulled out from matrices, and the hydration products adhered to the surface of the fibers. There was a likely trend in ECC-Ref,

**TABLE 4 |** Results of fracture parameters of ECC.

| Mixture ID | $F_n$ (kN) | $\sigma_n$ (MPa) | *CMOD* (mm) | $G_f$ (KN·m) | $K_{IC}$ (MPa·m$^{1/2}$) |
|---|---|---|---|---|---|
| ECC-0CNF | 6.78 ± 0.33 | 16.95 ± 0.83 | 4.22 ± 0.27 | 23.28 ± 0.89 | 6.03 ± 0.29 |
| ECC-0.1NCNF | 7.08 ± 0.39 | 17.70 ± 0.98 | 4.03 ± 0.66 | 24.21 ± 5.29 | 6.30 ± 0.35 |
| ECC-0.1LCNF | 8.32 ± 0.42 | 20.80 ± 1.05 | 3.95 ± 0.34 | 26.65 ± 3.18 | 7.38 ± 0.37 |
| ECC-0.1HCNF | 9.11 ± 1.22 | 22.78 ± 3.05 | 4.10 ± 0.17 | 29.74 ± 3.21 | 8.08 ± 1.08 |

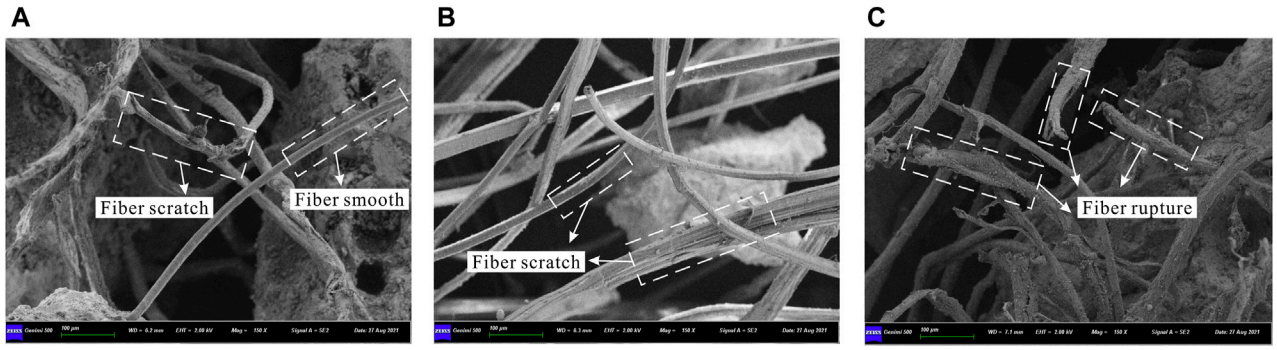


**FIGURE 14 |** SEM images of polyethylene (PE) fibers in ECC. **(A)** ECC-Ref; **(B)** ECC-0.1NCNF; **(C)** ECC-0.1HCNF.

ECC-0.1NCNF, and ECC-0.1HCNF that the surface of fibers appeared smooth and scratched, and the end of the pulled-out fibers ruptured.

## CONCLUSION

This study investigated the feasibility of using CNF as VMA to develop ECC. CNF at 0.1% content with three different oxidation degrees, such as no oxidation, low oxidation degree, and high oxidation degree, namely, NCNF, LCNF, and HCNF, respectively, was used to replace VMA. The micro-scale and macro-scale performances of ECC-Ref, ECC-0.1NCNF, ECC-0.1LCNF, and ECC-0.1HCNF were evaluated. The major conclusions supported that CNF presented a great potential to develop ECC as VMA and reinforcing agent, as follows:

1) Compared with NCNF, LCNF and HCNF with higher surface carboxylate group content had much better stability in water. The high stability of HCNF suspensions was attributed to the higher electrostatic repulsion due to the lower zeta potential.
2) CNF has a significant effect on modifying the rheological properties like VMA. The yield stress and plastic viscosity of the fresh ECC matrices could slightly increase with higher oxidation degrees of CNF, which was traced back to the higher water absorbed capacity of higher carboxylate group contents.
3) NCNF, LCNF, and HCNF increased the cement degree of hydration at 28 days, and the effect of HCNF on the hydration appeared to be higher than that of LCNF and NCNF. HCNF was more easily capable of adhering to the surface of cement particles, becoming the channel to transport more water for the later hydration.
4) CNF with different surface oxidation degrees could effectively improve the mechanical properties compared with ECC-Ref. The compressive strength and the tensile stress increased due to the addition of NCNF, LCNF, and HCNF. The higher oxidation degree of CNF, the greater strength it could increase. The tensile strain capacity for ECC-Ref, ECC-0.1NCNF, ECC-0.1LCNF, and ECC-0.1CNF could all achieve over 8% with the saturated multiple cracking pattern, and the crack widths were all less than 150 μm.
4) The addition of NCNF, LCNF, and HCNF enhanced the fracture properties, including the nominal flexural strength, the fracture energy, and the fracture toughness, and higher enhancements were found with the increasing CNF oxidation degree. This proved that CNF could improve the fiber bridging capacity and the crack resistance of PE fibers.

Although a series of experiments were carried out in the current study, demonstrating the potential of CNF to allow viscosity modifying and nano-reinforcing in ECC, the mechanisms of the reinforced effect still need to be further investigated. Moreover, the long-term performance of CNF in ECC also should be considered in future research.

## DATA AVAILABILITY STATEMENT

The original contributions presented in the study are included in the article/Supplementary Material. Further inquiries can be directed to the corresponding author.

## AUTHOR CONTRIBUTIONS

Conceptualization, LL and QL; methodology, QL; validation, QL; formal analysis, LL; investigation, JY, GL, and ZL; resources, QL; data curation, LL and XL; writing—original draft preparation, LL and JY; writing—review and editing, QL; supervision, QL; funding acquisition, QL. All authors have read and agreed to the published version of the manuscript.

## FUNDING

This research was funded by the National Natural Science Foundation of China (grant nos. 52038006, 52078282, and 51908339), the China Academy of Engineering Consulting Project "Research on Development Strategy and Key Technologies of Bamboo Construction Sector in China towards 2035" (no. 2018-ZCQ-06), and the Program for Changjiang Scholars and Innovative Research Team from the University of China (grant no. IRT_17R69).

## REFERENCES

Benini, K. C. C. D. C., Voorwald, H. J. C., Cioffi, M. O. H., Rezende, M. C., and Arantes, V. (2018). Preparation of Nanocellulose from Imperata Brasiliensis Grass Using Taguchi Method. *Carbohydr. Polym.* 192, 337–346. doi:10.1016/j.carbpol.2018.03.055

Cao, Y., Zavaterri, P., Youngblood, J., Moon, R., and Weiss, J. (2015). The Influence of Cellulose Nanocrystal Additions on the Performance of Cement Paste. *Cement and Concrete Composites* 56, 73–83. doi:10.1016/j.cemconcomp.2014.11.008

Cao, Y., Zavattieri, P., Youngblood, J., Moon, R., and Weiss, J. (2016). The Relationship between Cellulose Nanocrystal Dispersion and Strength. *Construction Building Mater.* 119, 71–79. doi:10.1016/j.conbuildmat.2016.03.077

Ez-zaki, H., Riva, L., Bellotto, M., Valentini, L., Garbin, E., Punta, C., et al. (2021). Influence of Cellulose Nanofibrils on the Rheology, Microstructure and Strength of Alkali Activated Ground Granulated Blast-Furnace Slag: a Comparison with Ordinary Portland Cement. *Mater. Struct.* 54, 1–18. doi:10.1617/s11527-020-01614-5

Ghahari, S., Assi, L. N., Alsalman, A., and Alyamaç, K. E. (2020). Fracture Properties Evaluation of Cellulose Nanocrystals Cement Paste. *Materials* 13, 2507. doi:10.3390/ma13112507

Hisseine, O. A., Basic, N., Omran, A. F., and Tagnit-Hamou, A. (2018a). Feasibility of Using Cellulose Filaments as a Viscosity Modifying Agent in Self-Consolidating concrete. *Cement and Concrete Composites* 94, 327–340. doi:10.1016/j.cemconcomp.2018.09.009

Hisseine, O. A., Omran, A. F., and Tagnit-Hamou, A. (2018b). Influence of Cellulose Filaments on Cement Paste and concrete. *J. Mater. Civ. Eng.* 30, 1–14. doi:10.1061/(ASCE)MT.1943-5533.0002287

Hisseine, O. A., Soliman, N. A., Tolnai, B., and Tagnit-Hamou, A. (2020). Nano-engineered Ultra-high Performance concrete for Controlled Autogenous Shrinkage Using Nanocellulose. *Cement Concrete Res.* 137, 106217. doi:10.1016/j.cemconres.2020.106217

Kanakubo, T., Shimizu, K., Katagiri, M., Kanda, T., Fukuyama, H., and Rokugo, K. (2005). Tensile Characteristics Evaluation of DFRCC Round Robin Test Results by JCI-TC. in International RILEM Workshop on High Performance Fiber Reinforced Cementitious Composites in Structural Applications Honolulu, Hawaii: RILEM Publications SARL, 27–36. doi:10.1617/2912143942.004

Kang, X., Kuga, S., Wang, C., Zhao, Y., Wu, M., and Huang, Y. (2018). Green Preparation of Cellulose Nanocrystal and its Application. *ACS Sust. Chem. Eng.* 6, 2954–2960. doi:10.1021/acssuschemeng.7b02363

Klemm, D., Kramer, F., Moritz, S., Lindström, T., Ankerfors, M., Gray, D., et al. (2011). Nanocelluloses: A New Family of Nature-Based Materials. *Angew. Chem. Int. Ed.* 50, 5438–5466. doi:10.1002/anie.201001273

Li, B., Xu, W., Kronlund, D., Määttänen, A., Liu, J., Smått, J.-H., et al. (2015). Cellulose Nanocrystals Prepared via Formic Acid Hydrolysis Followed by TEMPO-Mediated Oxidation. *Carbohydr. Polym.* 133, 605–612. doi:10.1016/j.carbpol.2015.07.033

Li, L., Cai, Z., Yu, K., Zhang, Y. X., and Ding, Y. (2019). Performance-based Design of All-Grade Strain Hardening Cementitious Composites with Compressive Strengths from 40 MPa to 120 MPa. *Cement and Concrete Composites* 97, 202–217. doi:10.1016/j.cemconcomp.2019.01.001

Li, M., and Li, V. C. (2013). Rheology, Fiber Dispersion, and Robust Properties of Engineered Cementitious Composites. *Mater. Struct.* 46, 405–420. doi:10.1617/s11527-012-9909-z

Li, V. C. (2019). *Engineered Cementitious Composites (ECC): Bendable concrete for Sustainable and Resilient Infrastructure*, : SpringerLink. doi:10.1007/978-3-662-58438-5

Montes, F., Fu, T., Youngblood, J. P., and Weiss, J. (2020). Rheological Impact of Using Cellulose Nanocrystals (CNC) in Cement Pastes. *Construction Building Mater.* 235, 117497. doi:10.1016/j.conbuildmat.2019.117497

Nassiri, S., Chen, Z., Jian, G., Zhong, T., Haider, M. M., Li, H., et al. (2021). Comparison of Unique Effects of Two Contrasting Types of Cellulose Nanomaterials on Setting Time, Rheology, and Compressive Strength of Cement Paste. *Cement and Concrete Composites* 123, 104201. doi:10.1016/j.cemconcomp.2021.104201

Pereira, E. B., Fischer, G., and Barros, J. A. O. (2012). Direct Assessment of Tensile Stress-Crack Opening Behavior of Strain Hardening Cementitious Composites (SHCC). *Cement Concrete Res.* 42, 834–846. doi:10.1016/j.cemconres.2012.03.006

Pourchez, J., Peschard, A., Grosseau, P., Guyonnet, R., Guilhot, B., and Vallée, F. (2006). HPMC and HEMC Influence on Cement Hydration. *Cement Concrete Res.* 36, 288–294. doi:10.1016/j.cemconres.2005.08.003

RILEM (1985). Determination of the Fracture Energy of Mortar and concrete by Means of Three-point bend Tests on Notched Beams, *Materials and Struc.* 18, 287–290. doi:10.1007/BF02472918

Seta, F. T., An, X., Liu, L., Zhang, H., Yang, J., Zhang, W., et al. (2020). Preparation and Characterization of High Yield Cellulose Nanocrystals (CNC) Derived from ball Mill Pretreatment and Maleic Acid Hydrolysis. *Carbohydr. Polym.* 234, 115942. doi:10.1016/j.carbpol.2020.115942

Wang, Y., Jian, X., Yu, J., Ye, J., and Dong, F. (2020a). Development of gypsum-based Composites with Tensile Strain-hardening Characteristics. *J. Am. Ceram. Soc.* 103, 7115–7126. doi:10.1111/jace.17419

Wang, Y., Liu, F., Yu, J., Dong, F., and Ye, J. (2020b). Effect of Polyethylene Fiber Content on Physical and Mechanical Properties of Engineered Cementitious Composites. *Construction Building Mater.* 251, 118917. doi:10.1016/j.conbuildmat.2020.118917

Wu, H.-L., Zhang, D., Ellis, B. R., and Li, V. C. (2018). Development of Reactive MgO-Based Engineered Cementitious Composite (ECC) through Accelerated Carbonation Curing. *Construction Building Mater.* 191, 23–31. doi:10.1016/j.conbuildmat.2018.09.196

Xu, Q., Li, W., Cheng, Z., Yang, G., and Qin, M. (2014). TEMPO/NaBr/NaClO-mediated Surface Oxidation of Nanocrystalline Cellulose and its Microparticulate Retention System with Cationic Polyacrylamide. *BioResources* 9, 994–1006. doi:10.15376/biores.9.1.994-1006

Xu, S., and Reinhardt, H. W. (2000). A Simplified Method for Determining Double-K Fracture Parameters for Three-point Bending Tests. *Int. J. Fract.* 104, 181–209. doi:10.1023/A:1007676716549

Yahia, A., and Khayat, K. H. (2001). Analytical Models for Estimating Yield Stress of High-Performance Pseudoplastic Grout. *Cement Concrete Res.* 31, 731–738. doi:10.1016/S0008-8846(01)00476-8

Yang, E. H., Yang, Y., and Li, V. C. (2007). Use of High Volumes of Fly Ash to Improve ECC Mechanical Properties and Material Greenness. *Mj* 104, 620–628. doi:10.14359/18966

Yu, K.-Q., Yu, J.-T., Dai, J.-G., Lu, Z.-D., and Shah, S. P. (2018). Development of Ultra-high Performance Engineered Cementitious Composites Using

Polyethylene (PE) Fibers. *Construction Building Mater.* 158, 217–227. doi:10.1016/j.conbuildmat.2017.10.040

Yu, K., Wang, Y., Yu, J., and Xu, S. (2017). A Strain-Hardening Cementitious Composites with the Tensile Capacity up to 8%. *Constr. Build. Mater.* 137, 410–419. doi:10.1016/j.conbuildmat.2017.01.060

Zhang, D., Jaworska, B., Zhu, H., Dahlquist, K., and Li, V. C. (2020). Engineered Cementitious Composites (ECC) with limestone Calcined clay Cement (LC3). *Cement and Concrete Composites* 114, 103766. doi:10.1016/j.cemconcomp.2020.103766

**Conflict of Interest:** LL, QL, and XL were employed by the Engineering Research Institute of Appraisal and Strengthening of Shandong Jianzhu University Co., LTD. JY, GL, and ZL were employed by the Shandong Luqiao Group Co., Ltd.

**Publisher's Note:** All claims expressed in this article are solely those of the authors and do not necessarily represent those of their affiliated organizations, or those of the publisher, the editors, and the reviewers. Any product that may be evaluated in this article, or claim that may be made by its manufacturer, is not guaranteed or endorsed by the publisher.

frontiers in Materials

ORIGINAL RESEARCH
published: 17 November 2021
doi: 10.3389/fmats.2021.775188

# Effect of Fibre Types on the Tensile Behaviour of Engineered Cementitious Composites

*Mingzhang Lan*[1]*, *Jian Zhou*[2] *and Mingfeng Xu*[2]*

[1]College of Materials Science and Engineering, Beijing University of Technology, Beijing, China, [2]School of Civil and Transportation Engineering, Hebei University of Technology, Tianjin, China

Engineered cementitious composite (ECC) is a group of ultra-ductile fibre-reinforced cementitious composites, characterised by high ductility and moderate content of short discontinuous fibre. The unique tensile strain-hardening behaviour of ECC results from a deliberate design based on the understanding of micromechanics between fibre, matrix, and fibre–matrix interface. To investigate the effect of fibre properties on the tensile behaviour of ECCs is, therefore, the key to understanding the composite mechanical behaviour of ECCs. This paper presents a study on the fibre-bridging behaviour and composite mechanical properties of ECCs with three types of fibres, including oil-coated polyvinyl alcohol (PVA) fibre, untreated PVA fibre, and polypropylene (PP) fibre. The experimental result reveals that various fibres with different properties result in difference in the fibre-bridging behaviour and composite mechanical properties of ECCs. The difference in the composite mechanical properties of ECCs with different fibres was interpreted by analysing the fibre-bridging behaviour.

**Keywords: engineered cementitious composites, tensile behaviour, fibre-bridging behaviour, polyvinyl alcohol fibre, polypropylene fibre**

OPEN ACCESS

***Edited by:***
*Antonio Caggiano, Darmstadt University of Technology, Germany*

***Reviewed by:***
*Yading Xu, Delft University of Technology, Netherlands*
*Bo-Tao Huang, Hong Kong Polytechnic University, Hong Kong SAR, China*

***Correspondence:**
*Mingzhang Lan*
*lanmingzhang@bjut.edu.cn*
*Mingfeng Xu*
*xumingfeng@hebut.edu.cn*

***Specialty section:***
*This article was submitted to Structural Materials, a section of the journal Frontiers in Materials*

***Received:*** *13 September 2021*
***Accepted:*** *13 October 2021*
***Published:*** *17 November 2021*

***Citation:***
*Lan M, Zhou J and Xu M (2021) Effect of Fibre Types on the Tensile Behaviour of Engineered Cementitious Composites. Front. Mater. 8:775188. doi: 10.3389/fmats.2021.775188*

## INTRODUCTION

By deliberate design based on the understanding of micromechanics between fibre, matrix, and fibre–matrix interface, engineered cementitious composite (ECC) exhibits unique strain-hardening behaviour (Li, 2003). Under tensile load, ECC shows tensile strain-hardening behaviour and develops tensile strain capacity in the range of 3–7%, compared to 0.01–0.05% for ordinary concrete and fibre-reinforced concrete (FRC). **Figure 1** illustrates the difference in the typical tensile stress–strain curves of ordinary concrete, FRC, and ECC (Fischer and Li, 2003). Ordinary concrete is a brittle material, and crack formation is followed by a sudden loss of load carrying capacity. Although tensile strength and fracture toughness are enhanced, to some extent, by adding fibre, FRC is, nevertheless, a quasi-brittle material, showing strain-softening single-cracking behaviour under tension. On the contrary, ECC has a metal-like feature. After the first crack forms in ECC, tensile load-carrying capacity rises as strain increases, through multiple-cracking process with tight crack width control. The crack width of ECC is self-controlled to below 100 μm without the presence of steel reinforcement, which is much smaller than the typical crack width observed in ordinary concrete and FRC (Weimann and Li, 2003; Xiao et al., 2021; Xiong et al., 2021).

The unique tensile strain-hardening behaviour and tight crack width control of ECC result from an elaborate design using micromechanics model to tailor the interaction between fibre, matrix, and fibre–matrix interface (Li, 1993). The fibre-bridging properties play a crucial role on the tensile

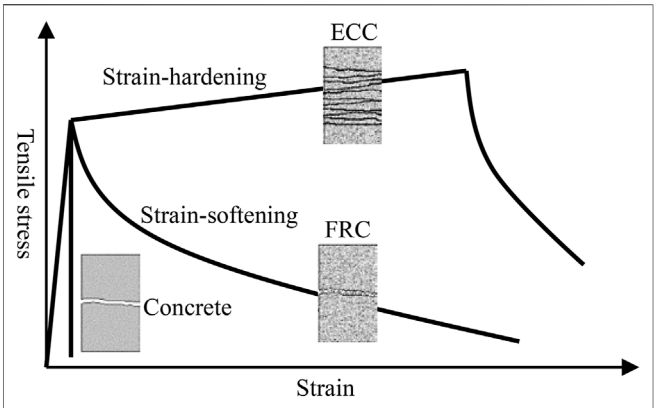


**FIGURE 1 |** Typical tensile stress-strain curves of concrete, FRC, and ECC (Fischer and Li, 2003).

strain-hardening behaviour of ECC. When ECC is loaded in tension, the matrix starts to crack in its weakest cross-section. The fibre crossing this crack takes over the tensile load. Thanks to the engineered steady-state cracking behaviour, the fibre in this crack can carry an increasing load, which generates new cracks at other sites (Li and Leung, 1992). By repeating this process, ECC exhibits tensile strain-hardening multiple-cracking behaviour.

Several types of fibre have been used to produce ECC, and their properties are summarised in **Table 1**. The first version of ECC was made of high-modulus polyethylene (PE) fibre in the mid-1990s (Li et al., 1995; Li et al., 1996). Reinforced with 1.5% by volume of high-modulus PE fibre, PE-ECC exhibits tensile strain capacity ranging from 4 to 7%, tensile strength over 5.5 MPa, and compressive strength over 60 MPa. The PE fibre enables the ECC with superior mechanical properties. Therefore, PE-ECC with various features was developed, such as the PE-ECC prepared with seawater and sea sand with non-corrosion function (Huang et al., 2021), the PE-ECC prepared with artificial fine aggregates that reduces the industrial burden on the environment (Xu L.-Y. et al., 2021), the PE-ECC with ultra high dectility as a noval and resilient fireproof coating (Cai et al., 2021), and the PE/steel fibre-ECC with compressive strength over 210 MPa for complex and severe service environments (Huang, et al., 2021b). Considering the large crack width of PE-ECC due to the hydrophobic nature of PE fibre, and the high cost of the PE fibre, studies moved on for alternatives. In the early 2000s, Li and his co-workers have successfully developed a group of ECCs with polyvinyl alcohol (PVA) fibre, costing one-eight of the high-modulus PE fibre (Li et al., 2001). Since the surface of PVA fibre is hydrophilic, ordinary PVA fibre tends to rupture instead of pullout of a cementitious matrix due to the strong chemical bond with matrix, and this has a negative effect on the tensile ductility of ECC. The interfacial properties between PVA fibre and matrix were, therefore, tailored by applying 1.2% by weight of oil coating on the fibre surface (Li et al., 2002). ECC with the oil-coated PVA fibre exhibits tensile strain capacity of 3–5% and tensile strength of 4–5 MPa (Li et al., 2001). After Li's work, many ECC materials with oil-coated PVA fibre have been developed in many institutions (Kim et al., 2003; Wang and Li, 2006; Kim et al., 2007; Yang et al., 2007; Zhang et al., 2009; Zhou et al., 2010). In recent years, several researchers have developed ECC materials with non-oil-coated PVA fibre, which exhibit comparable composite properties as oil-coated-PVA ECC (Ma et al., 2015; Pan et al., 2015; Said et al., 2015; Meng et al., 2017; Zhang and Zhang, 2018). Yang (2008) and Felekoglu et al. (2014) have developed a group of ECCs with high-tenacity polypropylene (PP) fibre. The high-tenacity PP fibre consists of a high strength core made of high molecular weight PP resin and an engineered sheath with/without surface coating (De Lhoneux et al., 2002). The high-tenacity PP fibre has a tensile strength of 850 MPa, about twice as high as that of ordinary PP fibre. ECC with the tenacity PP fibre showed multiple-cracking behaviour under tensile load and had tensile strain capacity over 4%, while the ultimate tensile strength was below 2.5 MPa, much lower than that of PE-ECC and PVA-ECC. Tosun-Felekoglu and Felekoglu (2013) have tried to develop ECC with ordinary PP fibre. Although their specimens showed deflection-hardening multiple-cracking behaviour under a four-point bending load, further studies are still needed to prove whether the composite has the strain-hardening multiple-cracking feature. Recently, a novel ECC with basalt fibre, an inorganic fibre, has been developed by Xu M. et al. (2021). Basalt fibre-ECCs show a tensile strain capacity of 0.4–0.9%, and an average crack width is <8 μm, about one order of magnitude smaller than typical ECCs prepared with PVA, PP, or PE fibres.

This paper aims to investigate the mechanical properties of ECCs with different PVA and PP fibres and to reveal the effect of fiber types and properties on uniaxial tensile and fibre bridging properties of ECCs. First, the framework of the ECC micromechanics design guidelines is briefly reviewed. The mix design and experimental program are then described. The experimental results of uniaxial tensile tests, loaded crack width measurement, and bending and compressive tests are presented. The results of uniaxial tensile tests using notched specimens are also reported to estimate the bridging properties

**TABLE 1 |** Properties of fibre used in ECC.

| Type of fibre | Diameter $d$ (μm) | Length $l$ (mm) | Tensile strength $f_t$ (MPa) | Modulus of elasticity $E$ (GPa) | Elongation $\Delta l$ (%) |
|---|---|---|---|---|---|
| PE (Li et al., 1996) | 38 | 12.7 | 3000 | 120 | 3.1 |
| PVA (Li et al., 2001) | 39 | 8 or 12 | 1620 | 42.8 | 6.0 |
| PP (Yang, 2008) | 12 | 6 or 12 | 850 | 11.6 | 21 |
| Basalt (Xu et al., 2021b) | 14.1 | 9 | 2230 | 85.8 | 2.85 |

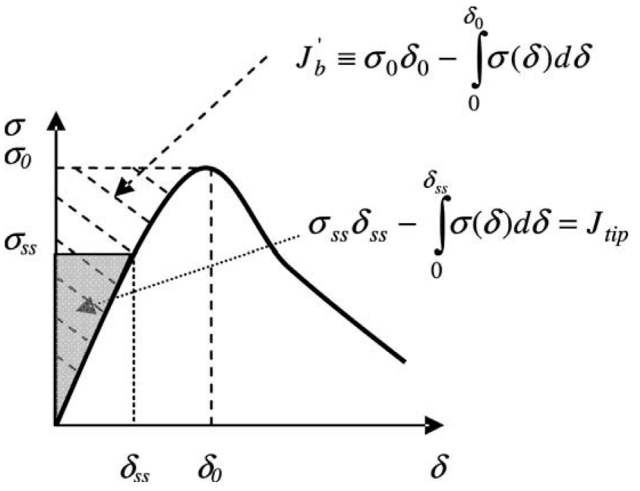


**FIGURE 2 |** Typical bridging stress-crack opening σ(δ) curve for steady-state crack propagation. Hatched area represents complimentary energy $J_b'$. Shaded area represents crack tip toughness $J_{tip}$ (Li and Leung, 1992).

between fibre and matrix. Last, the comparison between the tensile properties of ECCs made of different fibres is discussed from the point of view of ECC micromechanics.

## ECC MICROMECHANICS

The ECC micromechanics model was established by Li and Leung in the early 1990s (Li and Leung, 1992) and has been successfully used in ECC material design by many researchers (Li et al., 1995; Li et al., 2001; Li et al., 2002; Wang and Li, 2006; Yang et al., 2007; Zhou et al., 2010; Ranade et al., 2013). The ECC micromechanics model links macroscale composite properties (tensile strength and strain capacity) to micromechanical properties (fibre-bridging parameters) based on the fundamental understanding of the mechanical interactions among fibre, matrix, and fibre–matrix interface. The scale linking represents the ECC material design philosophy: to understand the microscale behaviour and to tailor the micromechanical properties are the keys to designing targeted composite properties. The ECC micromechanics model consists of two guiding concepts, i.e., energy criterion and strength criterion.

### Energy Criterion

The fundamental requirement for strain hardening and multiple cracking is that the cracks develop steady-state crack propagation rather than Griffith-type crack propagation (Li and Leung, 1992). Steady-state crack propagation refers to as that a crack increases in length at constant steady-state cracking stress $\sigma_{ss}$ while maintaining a constant crack opening $\delta_{ss}$. Marshall and Cox (1988) employed the J-integral method and proposed a general solution for the condition of steady-state crack propagation:

$$J_{tip} = \sigma_{ss}\delta_{ss} - \int_0^{\delta_{ss}} \sigma(\delta)d\delta \quad (1)$$

where $J_{tip}$ is the crack tip toughness, and $\delta_{ss}$ is the crack opening corresponding to the steady-state cracking stress $\sigma_{ss}$.

**Equation 1** expresses the energy balance (energy demanded and supplied to crack tip) per unit crack advance during steady-state crack propagation, as schematically illustrated in **Figure 2**. The right-hand side of **Eq. 1** can be interpreted as the net energy input by external work (first term) minus the energy consumed by the bridging elements at the crack tip propagation zone from 0 to $\delta_{ss}$ (second term), which is referred to as the complementary energy and represents the shaded area in **Figure 2**. The maximum complementary energy $J_b'$ occurs when the stress reaches the maximum fibre bridging strength $\sigma_0$ in this crack and represents the hatched area in **Figure 2**, as follow:

$$J_b' = \sigma_0\delta_0 - \int_0^{\delta_0} \sigma(\delta)d\delta \quad (2)$$

where $\delta_0$ is the crack opening corresponding to the maximum fibre bridging strength $\sigma_0$.

In order to ensure steady-state crack propagation, the energy criterion requires that the available crack-driving, i.e., energy maximum complementary energy $J_b'$, should be greater than the energy required for crack propagation, i.e., crack tip toughness $J_{tip}$:

$$J_b' \geq J_{tip} \quad (3)$$

### Strength Criterion

The strength criterion determines the initiation of cracks and requires that the matrix tensile cracking strength $\sigma_c$ should be lower than the maximum fibre bridging strength $\sigma_0$.

$$\sigma_c < \sigma_0 \quad (4)$$

where the matrix tensile cracking strength $\sigma_c$ is determined by the matrix fracture toughness and the pre-existing flaw size, such as air voids.

## MATERIALS AND METHODS

### Materials

One single cementitious matrix was used in this study, and the mix proportion is given in **Table 2**. The matrix was made of ordinary Portland cement, fly ash, and silica fume mixed with water at the water-to-powder ratio of 0.175. A polycarboxylate superplasticiser was also added to adjust the fresh properties of the mixtures until the flowability of the mixtures reached 190 ± 5 mm. Flowability test was conducted according to ASTM C 1437 (ASTM C 1437, 2007).

Two PVA fibres and one PP fibre were used in the experimental program, and their properties are given in **Table 3**. Fibre "PVA1" was the 1.2 w% oil-coated PVA fibre

**TABLE 2 |** Mix composition of the matrix.

| Portland cement (kg/m$^3$) | Fly ash (kg/m$^3$) | Silica fume (kg/m$^3$) | Water (kg/m$^3$) | Superplasticiser (kg/m$^3$) |
|---|---|---|---|---|
| 263.9 | 1,407.5 | 88.0 | 307.9 | 8.2–10.3 |

**TABLE 3 |** Properties of the three fibres used in this study.

| Fibre | Diameter *d* (μm) | Length *l* (mm) | Tensile strength $f_t$ (MPa) | Elastic modulus *E* (GPa) | Elongation at break $\Delta l$ (%) |
|---|---|---|---|---|---|
| PVA1 | 39 | 12 | 1,620 | 42.8 | 6.0 |
| PVA2 | 15 | 12 | 1,500 | 40 | 6.8 |
| PP | 20 | 12 | **530** | 7.1 | 26.0 |

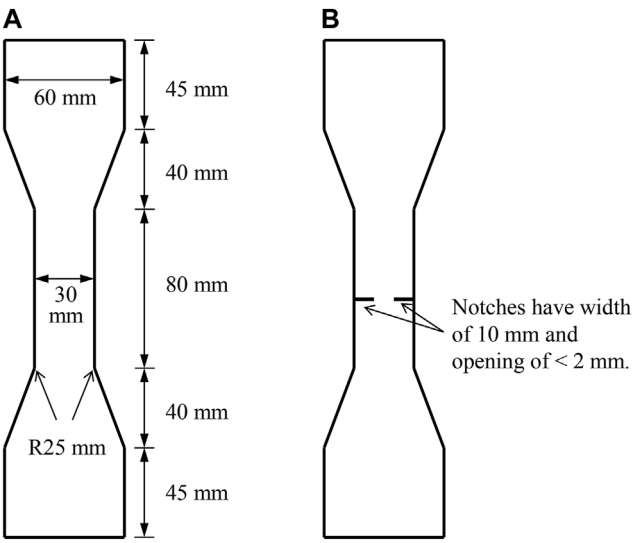


**FIGURE 3 |** Dogbone-shape specimen **(A)** and notched dogbone-shape specimen **(B)**.

with a surface oil coating of 1.2% by weight, and this fibre has been widely used in the studies on PVA-ECCs. Fibres "PVA2" and "PP" were ordinary PVA fibre and PP fibre manufactured by Chinese manufacturers. The tensile strength and elastic modulus of PVA1 fibre are higher than those of PVA2 fibre, while the diameter of the former is much larger than the latter. PP fibre has a relatively lower tensile strength and elastic modulus than two PVA fibres. The elongation ratio at break of PP fibre is considerably high.

The effect of fibre content on the macroscale composite properties and microscale fibre-bridging properties of the composites was studied. Considering a typical PVA fibre content in ECCs is 2% by volume, the composites with 1, 1.5, 2, and 2.5% by volume of PVA1 fibre and PVA2 fibre were prepared. According to the strength criterion, a larger amount of PP fibre should be used, since PP fibre has a lower tensile strength and thereof a lower bridging strength in PP-ECC (Kanda and Li, 1999). PP fibre contents of 2, 2.5, 3, and 4% by volume were investigated.

## Mixing, Casting, and Curing

Powder materials, water, and admixtures were first mixed in a 5-L mixer at a low speed for 1 min and at high speed for another 2 min. Then, fibre was evenly added within 1 min during low-speed mixing. Last, mixing is continued at high speed for another 2 min.

Prism specimens with the dimension of 160 mm × 40 mm × 40 mm were prepared for compression and three-point bending tests. Dogbone-shape specimens were prepared for uniaxial tension tests, recommended by the Japan Society of Civil Engineers (Yokota et al., 2008). Half of the dogbone-shape specimens (as shown in **Figure 3** left) were used to evaluate the composite tensile properties, and another half of dogbone-shape specimens with two 10-mm-wide notches (as shown in **Figure 3**, right) were used to evaluate the fibre-bridging properties. The specimens were cured in a climate chamber with a temperature of 20°C and relative humidity above 95% for 24 h. After demoulded, the specimens were sealed in a plastic bag and cured in a room with a temperature of 20°C until the age of 28 days.

## Compression and Three-Point Bending Tests

The prism specimens were sawn into two pieces evenly, used for compression tests. Compression tests were conducted under load control with a loading speed of 2,400 N/ s. The loaded area was 40 mm × 40 mm. Six specimens were tested for each mixture, and the compressive strength was calculated by averaging the results of the six measurements.

The rest prism specimens were used in three-point bending tests for evaluating the flexural strength. The support span was 100 mm, and the load point was at the mid of support span. The test was conducted under load control with a loading speed of 50 N/ s. Three specimens were tested for each mixture, and the flexural strength was calculated by averaging the results of the three measurements.

## Uniaxial Tension Test

Uniaxial tensile tests were conducted with the dogbone-shape specimens for investigating the tensile properties of the composites and the notched dogbone-shape specimens for

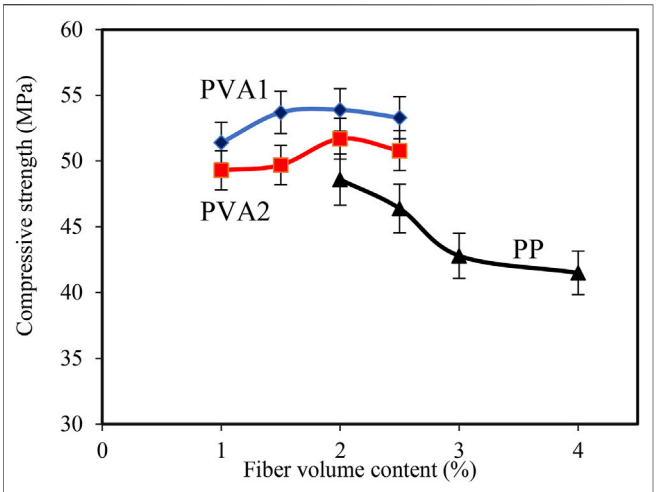


**FIGURE 4 |** Compressive strength of the composites with PVA1 fibre, PVA2 fibre and PP fibre at 28 days.

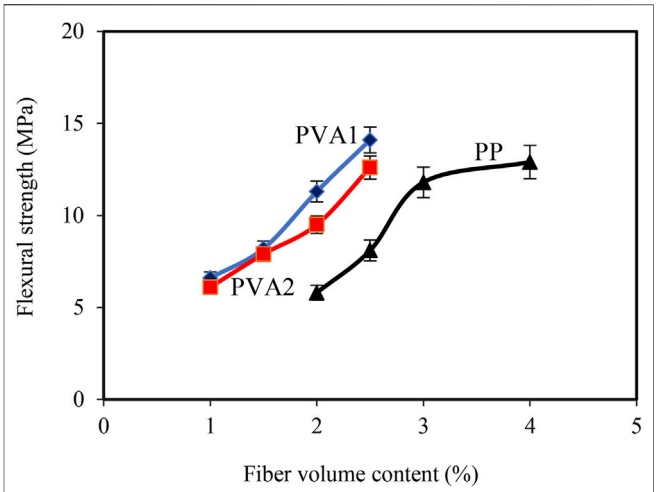


**FIGURE 5 |** Flexural strength of the composites with PVA1 fibre, PVA2 fibre, and PP fibre at 28 days.

investigating the fibre-bridging properties. The test procedure was the same for the two types of specimens. Two ends of the specimens were placed in two wedge clamp chucks. The upper and lower clamps were connected to the loading device with a pin joint and a fixed joint, respectively. One extensometer with a precision of 1 μm was attached on the specimen to measure the deformation, and the gauge length was 80 mm. The tests were conducted under displacement control with a loading speed of 0.004 mm/ s. The experimental results of each composite are calculated by averaging the data of six specimens.

## Loaded Average Crack Width

Loaded average crack width was measured on the dogbone-shape specimens after uniaxial tension tests. The number of cracks within gauge length along the central axis was accounted under a microscope with a magnification of × 100. The average crack number $N$ of each specimen was calculated by averaging the number of cracks on both sides. Since ECC deforms several hundred times larger than the matrix, the elastic deformation of the matrix contributes little to the overall deformation of the composites. Therefore, the overall tensile deformation can be simply considered as the sum of crack openings. Accordingly, the average crack width $w_c$ can be calculated by dividing the measured tensile deformation at the peak load $\Delta l$ by the average crack number $N$:

$$w_c = \frac{\Delta l}{N} \tag{5}$$

# EXPERIMENTAL RESULTS

## Compressive and Flexural Strengths

**Figures 4**, **5** give the 28-days compressive and flexural strengths of the composites with PVA1 fibre, PVA2 fibre, and PP fibre. In general, given the same fibre content, the composites with PVA1 fibre exhibited slightly higher compressive and flexural strengths than the composites with PVA2 fibre and the composites with PP fibre exhibited the lowest compressive and flexural strengths.

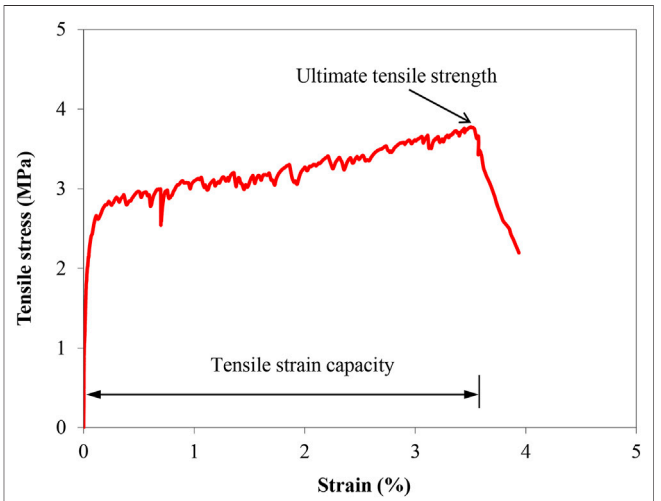


**FIGURE 6 |** Typical tensile stress-strain curve of the composites obtained from uniaxial tensile tests with dogbone-shape specimens.

As PVA fibre content increased from 1 to 2.5% by volume, the compressive strength of the composites with PVA1 fibre and PVA2 fibre first increased and then decreased, and the former ranges from 51.4 to 53.9 MPa and the latter ranges from 49.3 to 51.7 MPa. The increase in the PP fibre content from 2 to 4% by volume caused a decrease in the compressive strength of the composites with PP fibre from 48.6 to 41.5 MPa. The increase in the content of the three fibres all resulted in an increase in flexural strength of the composites. The flexural strength of the composites with PVA1 fibre increased from 6.6 to 11.4 MPa, that of the composites with PVA2 fibre increased from 6.1 to 12.6

**TABLE 4 |** Uniaxial tensile test results of the composites with the three fibres at 28 days.

| Type of fibre | Fibre content (vol. %) | Ultimate tensile strength (MPa) | Tensile strain capacity (%) | Loaded average crack width $w_c$ (μm) |
|---|---|---|---|---|
| PVA1 | 1 | 3.42 ± 0.18 | 0.66 ± 0.32 | 192.6 ± 7.6 |
| | 1.5 | 3.79 ± 0.15 | 2.05 ± 0.22 | 141.9 ± 18.7 |
| | 2 | 4.10 ± 0.12 | 3.48 ± 0.32 | 101.3 ± 9.3 |
| | 2.5 | 4.41 ± 0.18 | 4.10 ± 0.38 | 95.1 ± 8.3 |
| PVA2 | 1 | 3.03 ± 0.19 | 0.29 ± 0.25 | 103.4 ± 15.3 |
| | 1.5 | 3.49 ± 0.22 | 1.70 ± 0.33 | 68.7 ± 5.0 |
| | 2 | 3.82 ± 0.13 | 3.25 ± 0.40 | 46.3 ± 5.5 |
| | 2.5 | 4.00 ± 0.15 | 3.65 ± 0.47 | 43.9 ± 4.0 |
| PP | 2 | 2.43 ± 0.28 | 0.01 ± 0.004 | – |
| | 2.5 | 2.90 ± 0.20 | 1.94 ± 0.26 | 327.0 ± 42.9 |
| | 3 | 3.31 ± 0.14 | 3.14 ± 0.32 | 153.4 ± 13.5 |
| | 4 | 3.59 ± 0.22 | 3.94 ± 0.36 | 126.9 ± 10.4 |

MPa, and that of the composites with PP fibre increased from 5.8 to 12.9 MPa.

## Tensile Properties

**Figure 6** shows a typical tensile stress–strain curve of the composites obtained from uniaxial tensile tests with dogbone-shape specimens. The maximum tensile stress in tensile stress–strain curves is defined as ultimate tensile strength, and the corresponding strain is defined as tensile strain capacity.

**Supplementary Figures SA1–SA3** in Appendix show the tensile stress–strain curves of the composites with PVA1 fibre, PVA2 fibre, and PP fibre at 28 days. **Table 4** summaries the experimental results of ultimate tensile strength, tensile strain capacity, and loaded average crack width of the composites. Except the composite with 2% by volume of PP fibre, the rest composites exhibited strain-hardening multiple-cracking behaviour. As fibre content increased, the composites with PVA1 fibre, PVA2 fibre, and PP fibre showed more pronounced strain-hardening multiple-cracking behaviour, manifested as increasing tensile strain capacity and decreasing average crack width. An acceptable strain-hardening multiple-cracking behaviour of the composites was achieved, when PVA fibre content was not lower than 1.5% or PP fibre content was not lower than 2.5%, preferably 2% or 3%, respectively.

Given the same fibre content, the composites with PVA1 fibre exhibited higher ultimate tensile strength and greater tensile strain capacity than the composites with PVA2 fibre, while the average crack width in the former was more than two times larger than that in the latter. For instance, with 2% by volume of PVA fibre, the former had an ultimate tensile strength of 4.1 MPa, tensile strain capacity of 3.5%, and average crack width of 101.3 μm, and the latter had an ultimate tensile strength of 3.8 MPa, tensile strain capacity of 3.3%, and average crack width of 46.3 μm. Compared to the composites with the two PVA fibres, the composites with PP fibre exhibited a lower ultimate tensile strength, comparable tensile strain capacity, and larger average crack width.

## Fibre-Bridging Properties

To interpret the tensile properties of the composites, the bridging properties between fibre and matrix were investigated by using uniaxial tension test with notched specimens. **Figure 7** shows a typical fibre bridging stress–crack opening curves of the composites obtained from uniaxial tensile tests with notched dogbone-shape specimens. Matrix cracking strength is the tensile stress at the cracking of the matrix, and it relates to the tensile strength of the matrix. Fibre-bridging strength is the maximum tensile stress after cracking.

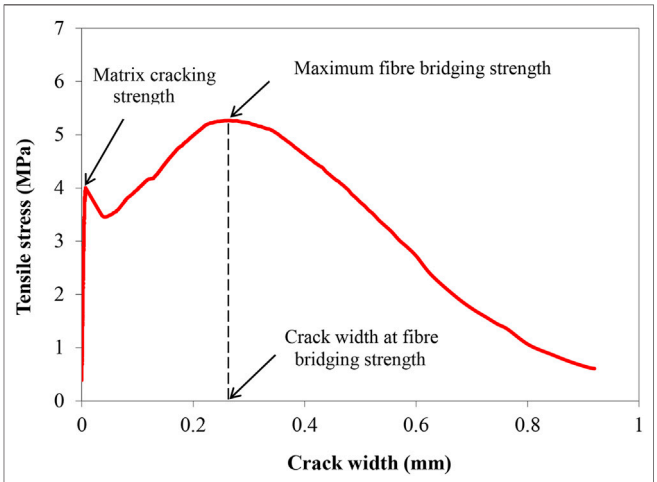


**FIGURE 7 |** Fibre bridging stress-crack opening curves of the composites obtained from uniaxial tensile tests with notched dogbone-shape specimens.

**Supplementary Figures SA4–SA6** in Appendix give the fibre bridging stress–crack opening curves of the composites with PVA1 fibre, PVA2 fibre, and PP fibre at 28 days. **Table 4** summarises the experimental results of matrix cracking strength, fibre-bridging strength, and crack opening at fibre-bridging strength. The mixture with 2% by volume of PP fibre had a matrix cracking strength higher than the maximum fibre bridging strength. After the matrix cracks, the external load, which needs to exceed matrix cracking strength, must be higher than the maximum fibre bridging strength. Consequently, fibres in the crack cannot hold this external load, and the matrix exhibits single-cracking behaviour. On the contrary, the rest

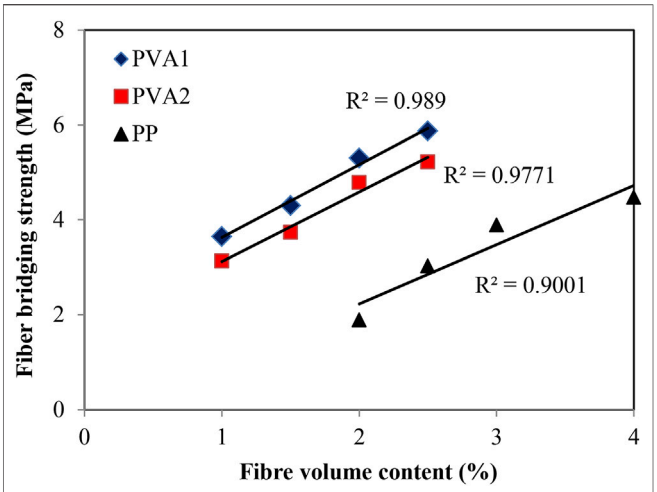


**FIGURE 8 |** Relation of maximum fibre bridging strength to fibre content.

mixtures had a matrix cracking strength lower than maximum fibre bridging strength; after cracking, fibres in the cracks can hold the load higher than the matrix cracking strength and generate subsequent cracking.

The increase in fibre content led to no obvious negative influence on matrix cracking strength and a more pronounced increase in maximum fibre bridging strength. As shown in **Figure 8**, the fibre-bridging strength of the composites fell around to the fitting line, exhibiting a relationship that is close to linear to the content of three types of fibres, respectively. The experimental results also reveal that fibre content has no obvious influence on the crack opening at the maximum fibre bridging strength.

Given the same fibre content, the composites with PVA1 fibre exhibited similar matrix cracking strength and higher maximum fibre bridging strength than the composites with PVA2, while the crack opening at the fiber-bridging strength of the former was roughly two times larger than that of the latter. Compared to the composites with the two PVA fibres, the composites with PP fibre exhibited a lower matrix cracking strength and maximum fibre bridging strength and significantly larger crack opening at maximum fibre bridging strength.

In the condition that fibres are randomly oriented and pullout (rather than fibre rupture) are expected, the key parameters of the fibre bridging properties, the maximum fibre bridging strength $\sigma_0$, and the crack opening corresponding to the maximum fibre bridging strength $\delta_0$, can be expressed as in **Eqs 6**, **7**; (Li, 1992).

$$\sigma_0 = \frac{1}{2} g \tau V_f \frac{L_f}{d_f} \tag{6}$$

$$\delta_0 = \frac{\tau L_f^2}{E_f d_f (1 + \eta)} \tag{7}$$

where $g$ is the snubbing factor; $\tau$ is the fibre/matrix frictional bond strength; $L_f$, $d_f$, and $E_f$ are the fibre volume fraction, length, diameter, and Young's modulus, respectively. $\eta = (V_f E_f)/(V_m E_m)$, where $V_m$ and $E_m$ are the matrix volume fraction and Young's modulus, respectively. From the above two equations, it can be seen that the maximum fibre bridging strength $\sigma_0$ and its corresponding crack opening $\delta_0$ are determined by the fibre properties, such as its diameter, length, elastic modulus, and fibre/matrix bonding. In this study, the large diameter of PVA1 seems to negatively affect $\sigma_0$, while the rest fibre properties overwhelmed and finally generated a relatively high bridging strength. Although the smaller diameter of PVA2 facilitates the bridging strength, a lower bridging strength was still obtained, due to its oil coating that reduces the fibre/matrix frictional bond (Yang, 2008). For PP fibre, its hydrophobic surface (Zhang et al., 2020) is not beneficial to the high fibre/matrix frictional bond or the high bridging strength as well. This does not mean that the oil coating or hydrophobic surface is undesirable. When considering fibre rupture, oil coating and hydrophobic surface contribute to preventing fibres from rupture and therefore a high ductility.

## DISCUSSION

The test results included in the previous section show that the composites with two PVA fibres and one PP fibre, up to a certain fibre content, can all exhibit multiple-cracking behaviour and tensile strain-hardening behaviour. Different fibres have led to different composite tensile properties and fibre-bridging properties. In this section, the relation of composite tensile properties and fibre-bridging behaviour is discussed from the point of view of ECC micromechanics reported in ***ECC Micromechanics***.

As expressed in **Eq. 4**, the strength criterion requires that the matrix tensile cracking strength $\sigma_c$ should be lower than the maximum fibre bridging strength $\sigma_0$, and as expressed in **Eq. 3**, the energy criterion requires that the fracture energy of matrix $G_m$ should be lower than the maximum complementary energy $J_b'$. These two criteria ensure the occurrence of multiple-cracking behaviour and tensile strain-hardening behaviour. The intensity of multiple cracking and the tensile ductility are, however, determined by the uniformity of the composites, in particular pre-existing flaw size distribution and fibre distribution. Due to the randomness nature of pre-existing flaw size and fibre distribution in composites, large margins between $\sigma_0$ and $\sigma_c$ and between $J_b'$ and $J_{tip}$ are preferred for saturated multiple cracking and high tensile ductility. The strain-hardening indexes are, therefore, defined to quantitatively evaluate the margins:

$$SH_{strength} = \frac{\sigma_0}{\sigma_c} \tag{8}$$

$$SH_{erengy} = \frac{J_b'}{J_{tip}} \tag{9}$$

The matrix tensile cracking strength $\sigma_c$ and the maximum fibre bridging strength $\sigma_0$ were estimated using uniaxial tension test with notched specimens, as given in **Table 5**. At small fibre content, appropriate for ECC, $J_{tip}$ approached the matrix fracture energy $G_m$. $G_m$ was calculated with matrix fracture toughness $K_m$ and elastic modulus $E_m$ in the term of $K_m^2/E_m$, where $K_m$ was estimated using three-point bending test with notched beam

**TABLE 5 |** Bridging properties between the three fibres and matrix at 28 days.

| Type of fibre | Fibre content (vol. %) | Matrix cracking strength $\sigma_c$ (MPa) | Fibre bridging strength $\sigma_0$ (MPa) | Crack opening at maximum fibre bridging strength $\delta_0$ (μm) |
|---|---|---|---|---|
| PVA1 | 1 | 3.14 ± 0.19 | 3.65 ± 0.30 | 253.3 ± 10.7 |
| | 1.5 | 3.29 ± 0.37 | 4.30 ± 0.18 | 261.7 ± 13.7 |
| | 2 | 3.44 ± 0.25 | 5.33 ± 0.25 | 260.3 ± 14.8 |
| | 2.5 | 3.74 ± 0.33 | 5.86 ± 0.22 | 267.3 ± 8.2 |
| PVA2 | 1 | 2.91 ± 0.27 | 3.13 ± 0.18 | 128.0 ± 11.4 |
| | 1.5 | 3.38 ± 0.31 | 3.76 ± 0.22 | 125.3 ± 7.2 |
| | 2 | 3.70 ± 0.13 | 4.79 ± 0.15 | 134.1 ± 7.6 |
| | 2.5 | 3.60 ± 0.20 | 5.21 ± 0.14 | 132.6 ± 17.8 |
| PP | 2 | 2.55 ± 0.22 | 1.90 ± 0.20 | 505.0 ± 29.0 |
| | 2.5 | 2.60 ± 0.27 | 3.03 ± 0.18 | 516.8 ± 30.7 |
| | 3 | 2.79 ± 0.33 | 3.88 ± 0.27 | 528.1 ± 28.3 |
| | 4 | 2.51 ± 0.37 | 4.48 ± 0.15 | 515.6 ± 14.9 |

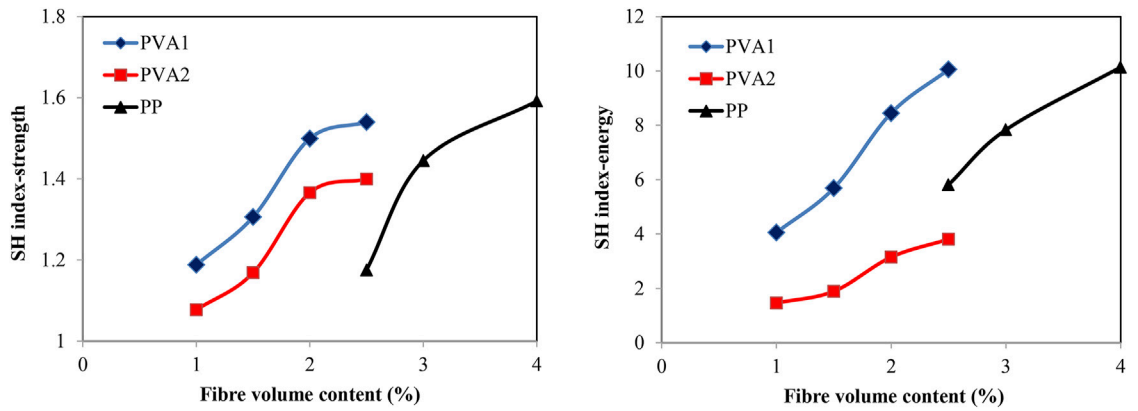


**FIGURE 9 |** Strain-hardening indexes of the ECCs with different fibres.

specimens and was estimated using uniaxial tension test. The one single matrix used in the composites with three types of fibres had fracture energy of 28.2 J/ $m^2$. $J_b'$ can be calculated by **Eq. 2** with the fibre bridging stress–crack opening curves given in ***Fibre-Bridging Properties***.

Among the composites with three types of fibres, only the composite with 2% PP fibre has a $SH_{strength}$ below 1, and the strength criterion is, therefore, not satisfied. This explains why the composite with 2% PP fibre did not exhibit strain-hardening and multiple-cracking behaviour, while the rest of the composites did. **Figure 9** gives the strain-hardening indexes $SH_{strength}$ and $SH_{energy}$ of the composites with different fibres (except the one with 2% PP fibre). For the three types of fibres, as the fibre content increases, both the strain-hardening indexes $SH_{strength}$ and $SH_{energy}$ increase. This agrees with the observation in tensile tests that the increased fibre content led to more pronounced strain-hardening multiply-cracking behaviour.

The previous study suggested that PE fibre–ECCs need to have strain-hardening indexes $SH_{strength}$ and $SH_{energy}$ over 1.2, and three to produce good strain-hardening behaviour (Kanda and Li, 1998). For PVA fibre–ECCs, $SH_{strength}$ is, however, required to be >1.45 due to lower tensile strength and higher interfacial bonds of PVA fibre compared with PE fibre (Li et al., 2002). As shown in **Figure 10**, the experimental results of this study reveal that for a strain capacity of 3%, the $SH_{strength}$ of 1.45 also applies to PVA1 fibre, which is the same fibre as used in Li et al. (2002). For PVA2 fibre, this value is about 1.2, close to the value for PE fibres; while for PP fibre, this value is 1.45. The values of $SH_{energy}$ for PVA1, PVA2, and PP fibres are 8, 3, and 8, respectively.

The crack opening at maximum fibre bridging strength $\delta_0$ is a parameter often used to describe the fibre-bridging properties. Once composite cracks under tension, the tensile load is transferred from matrix to fibres within the crack through fibre–matrix interfaces. When the crack width is smaller than $\delta_0$, the interfaces can carry higher load, due to the slip-hardening behaviour of PE, PVA, and PP fibres within matrix. This process eventually leads to strain-hardening and multiple-cracking behaviour of composites. When the crack width is beyond $\delta_0$, fibres are gradually pulled out of matrix, the load-carrying capacity of the interfaces declines, and composite fails.

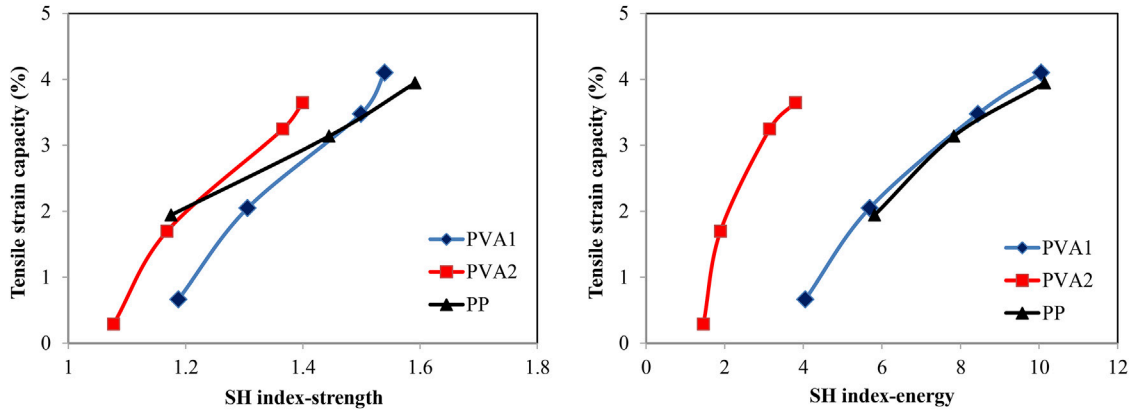


**FIGURE 10 |** Relation of tensile strain capacity to strain-hardening indexes.

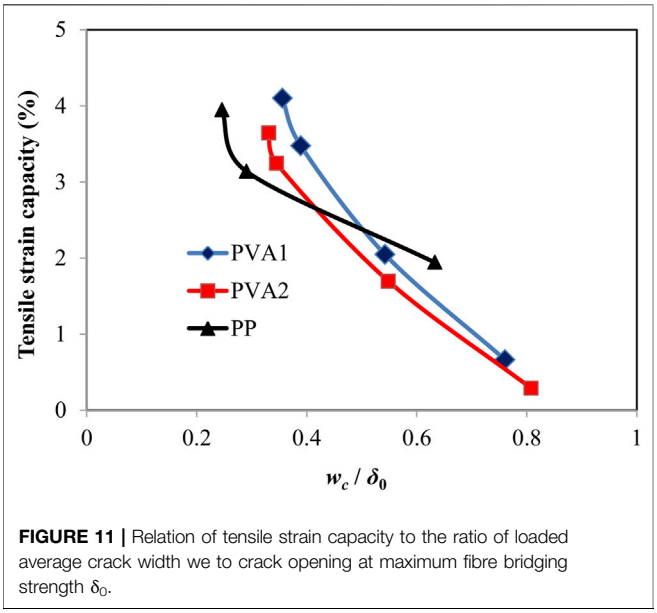


**FIGURE 11 |** Relation of tensile strain capacity to the ratio of loaded average crack width we to crack opening at maximum fibre bridging strength $\delta_0$.

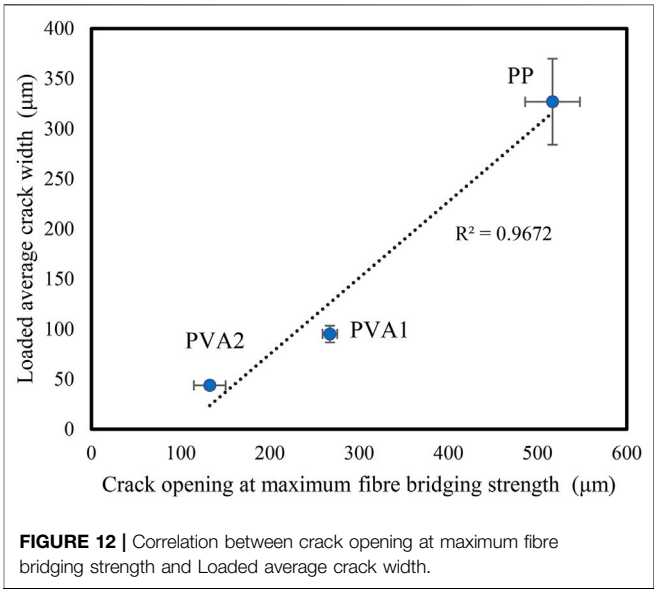


**FIGURE 12 |** Correlation between crack opening at maximum fibre bridging strength and Loaded average crack width.

Therefore, during strain-hardening stage, all cracks in ECCs must be smaller than $\delta_0$. Like strength and energy criteria, a large margin between $\delta_0$ and crack width $w_c$, which means a lower $w_c/\delta_0$ ratio, is preferred for a higher tensile ductility, as shown in **Figure 11**.

Besides, the trends of ultimate tensile strength and average crack width of ECC with different fibre types can be traced back to the fibre bridging properties. For ECC with PVA1, PVA2, and PP fibres at 2.5% fibre content, the crack opening at the maximum fibre bridging strength increases in the order of the PVA1 fibre, the PVA2 fibre, and the PP fibre. As can be seen in **Figure 12**, the average loaded crack width of the ECC composites with the three fibres increased in the same order. **Figure 13** shows the ultimate tensile strength plotted against the maximum fibre bridging strength. The linear correction between the maximum fibre bridging strength and the ultimate tensile strength was evident. This implies that the ultimate tensile strength is largely governed by the variation of the maximum fibre bridging strength, which evolves with fibre types.

## CONCLUSION

The paper presents the effect of fibre types on the compressive and tensile properties (macroscale) and the fibre-bridging properties (mesoscale) of ECC. Based on the experimental results and discussion, the following conclusions can be drawn:

1) Up to a certain fibre content, the composites with ordinary PVA fibre or PP fibre all exhibit strain-hardening multiple-cracking behaviour under uniaxial tensile load. Fibre volume contents of exceeding 1.5 and 2.5%, preferably 2 and 3%, are required for the composites with the PVA fibre and the PP fibre for a good ductility, respectively.

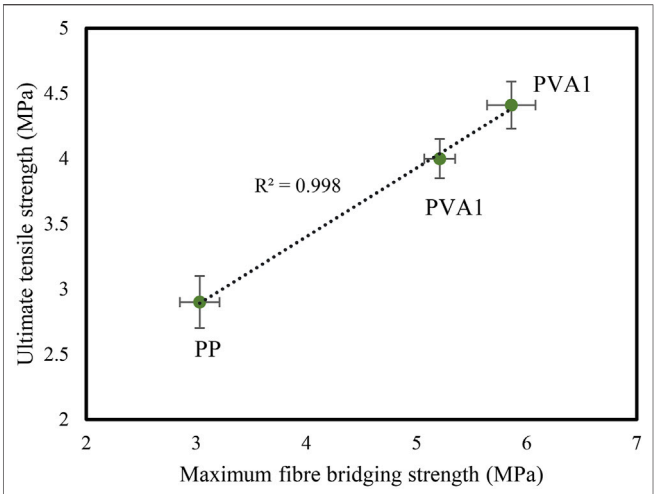


**FIGURE 13 |** Correlation between maximum fibre bridging strength and ultimate tensile strength.

2) Given the fibre volume content of 2%, the composites with the oil-coated PVA fibre (39 μm in diameter) exhibit greater tensile strain capacity but fewer cracks with larger average crack width than the composites with the ordinary PVA fibre (15 μm in diameter). The former also has a higher compressive, tensile, and flexural strength than the latter.
3) The composites with 3% by volume of the ordinary PP fibre have lower tensile strain and less cracks with larger average crack width than those with 2% by volume of two PVA fibres. Beyond peak tensile load, the former shows a slower loss of tensile load carrying capacity than the latter, i.e., the former has a long "tail" in tensile stress–strain curves. The former also has a lower compressive, tensile, and flexural strength than the latter.
4) In tensile load–crack opening curves, the cracking opening at peak load of the composites increases in the order of the ordinary PVA fibre, the oil-coated PVA fibre, and the ordinary PP fibre. This explains why the average loaded crack width of the composites with the three fibres increases in the same order.
5) The tensile strain capacities of the composites with the three fibres show good correlation to the two strain-hardening indexes. However, the critical values of strain-hardening indexes for producing good strain-hardening behaviour are different for different fibres.
6) The tensile strain capacities of the composites with the three fibres also show good correlation to the ratio of loaded average crack width to crack opening at maximum fibre bridging strength. Like strength and energy criteria, a large margin between and crack width is preferred for high tensile ductility.

## DATA AVAILABILITY STATEMENT

The raw data supporting the conclusions of this article will be made available by the authors, without undue reservation.

## AUTHOR CONTRIBUTIONS

ML contributed to the design, investigation, and writing of the original draft. JZ contributed to the writing–review and funding acquisition. MX contributed to the conception and data curation. All authors contributed to manuscript revision and read and approved the submitted version.

## FUNDING

The authors gratefully acknowledge the financial support of the National Natural Science Foundation of China (No. 51878238).

## SUPPLEMENTARY MATERIAL

The Supplementary Material for this article can be found online at: https://www.frontiersin.org/articles/10.3389/fmats.2021.775188/full#supplementary-material

## REFERENCES

ASTM, C 1437 (2007). *Standard Test Method for Flow of Hydraulic Cement Mortar*. West Conshohocken, PA: ASTM International.

Cai, Z., Liu, F., Yu, J., Yu, K., and Tian, L. (2021). Development Of Ultra-High Ductility Engineered Cementitious Composites As A Novel And Resilient Fireproof Coating. *Construction Building Mater.* 288, 123090. doi:10.1016/j.conbuildmat.2021.123090

De Lhoneux, B., Kalbskopf, R., Kim, P., Li, V. C., Lin, Z., Vidts, D., Wang, S., and Wu, H. C. (2002). "Development of High Tenacity Polypropylene Fibres for Cementitious Composites," in Proceedings of the JCI International Workshop on Ductile Fibre Reinforced Cementitious Composites (DFRCC) - Application and Evaluation, Takayama, Japan, Oct. 2002, 121–132.

Felekoglu, B., Tosun-Felekoglu, K., Ranade, R., Zhang, Q., and Li, V. C. (2014). Influence of Matrix Flowability, Fiber Mixing Procedure, and Curing Conditions on the Mechanical Performance of HTPP-ECC. *Composites B: Eng.* 60, 359–370. doi:10.1016/j.compositesb.2013.12.076

Fischer, G., and Li, V. C. (2003). Deformation Behavior of Fibre-Reinforced Polymer Reinforced Engineered Cementitious Composite (ECC) Flexural Members under Reversed Cyclic Loading Conditions. *Struct. J.* 100 (1), 25–35. doi:10.14359/12436

Huang, B.-T., Weng, K.-F., Zhu, J.-X., Xiang, Y., Dai, J.-G., and Li, V. C. (2021b). Engineered/strain-hardening Cementitious Composites (ECC/SHCC) with an Ultra-high Compressive Strength over 210 MPa. *Composites Commun.* 26, 100775. doi:10.1016/j.coco.2021.100775

Huang, B.-T., Wu, J.-Q., Yu, J., Dai, J.-G., Leung, C. K. Y., and Li, V. C. (2021a). Seawater Sea-Sand Engineered/strain-Hardening Cementitious Composites (ECC/SHCC): Assessment and Modeling of Crack Characteristics. *Cement Concrete Res.* 140, 106292. doi:10.1016/j.cemconres.2020.106292

Kanda, T., and Li, V. C. (1998). Multiple Cracking Sequence and Saturation in Fiber Reinforced Cementitious Composites. *Concrete Res. Tech.* 9 (2), 19–33. doi:10.3151/crt1990.9.2_19

Kanda, T., and Li, V. C. (1999). Effect Of Fiber Strength And Fiber-Matrix Interface On Crack Bridging In Cement Composites. *J. Eng. mech.* 125 (3), 290–299. doi:10.1061/(ASCE)0733-9399(1999)125:3(290)

Kim, J.-K., Kim, J.-S., Ha, G. J., and Kim, Y. Y. (2007). Tensile and Fiber Dispersion Performance of ECC (Engineered Cementitious Composites) Produced with Ground Granulated Blast Furnace Slag. *Cement Concrete Res.* 37 (7), 1096–1105. doi:10.1016/j.cemconres.2007.04.006

Kim, Y. Y., Kong, H. J., and Li, V. C. (2003). Design of Engineered Cementitious Composite Suitable for Wet-Mixture Shotcreting. *Mater. J.* 100 (6), 511–518. doi:10.14359/12958

Li, V. C. (1992). Postcrack Scaling Relations for Fiber Reinforced Cementitious Composites. *J. Mater. Civil Eng.* 4 (1), 41–57. doi:10.1061/(asce)0899-1561(1992)4:1(41)

Li, V. C. (1993). From Micromechanics to Structural Engineering. *Doboku Gakkai Ronbunshu* 1993 (471), 1–12. doi:10.2208/jscej.1993.471_1

Li, V. C., and Leung, C. K. Y. (1992). Steady-State and Multiple Cracking of Short Random Fiber Composites. *J. Eng. Mech.* 118 (11), 2246–2264. doi:10.1061/(asce)0733-9399(1992)118:11(2246)

Li, V. C., Mishra, D. K., and Wu, H.-C. (1995). Matrix Design for Pseudo-strain-hardening Fibre Reinforced Cementitious Composites. *Mater. Structures* 28 (10), 586–595. doi:10.1007/bf02473191

Li, V. C. (2003). On Engineered Cementitious Composites (ECC). *Act* 1 (3), 215–230. doi:10.3151/jact.1.215

Li, V. C., Wang, S., and Wu, C. (2001). Tensile Strain-Hardening Behavior of Polyvinyl Alcohol Engineered Cementitious Composite (PVA-ECC). *Mater. J.* 98 (6), 483–492. doi:10.14359/10851

Li, V. C., Wu, H. C., and Chan, Y. W. (1996). Effect of Plasma Treatment of Polyethylene Fibres on Interface and Ementitious Composite Properties. *J. Am. Ceram. Soc.* 79 (3), 700–704. doi:10.1111/j.1151-2916.1996.tb07932.x

Li, V. C., Wu, H. C., Wang, S., Ogawa, A., and Saito, T. (2002). Interface Tailoring for Strain-Hardening Polyvinyl Alcohol-Engineered Cementitious Composite (PVA-ECC). *Mater. J.* 99 (5), 463–472. doi:10.14359/12325

Ma, H., Qian, S., Zhang, Z., Lin, Z., and Li, V. C. (2015). Tailoring Engineered Cementitious Composites with Local Ingredients. *Construction Building Mater.* 101, 584–595. doi:10.1016/j.conbuildmat.2015.10.146

Marshall, D. B., and Cox, B. N. (1988). A J-Integral Method for Calculating Steady-State Matrix Cracking Stresses in Composites. *Mech. Mater.* 7 (2), 127–133. doi:10.1016/0167-6636(88)90011-7

Meng, D., Huang, T., Zhang, Y. X., and Lee, C. K. (2017). Mechanical Behaviour of a Polyvinyl Alcohol Fibre Reinforced Engineered Cementitious Composite (PVA-ECC) Using Local Ingredients. *Construction Building Mater.* 141, 259–270. doi:10.1016/j.conbuildmat.2017.02.158

Pan, Z., Wu, C., Liu, J., Wang, W., and Liu, J. (2015). Study on Mechanical Properties of Cost-Effective Polyvinyl Alcohol Engineered Cementitious Composites (PVA-ECC). *Construction Building Mater.* 78, 397–404. doi:10.1016/j.conbuildmat.2014.12.071

Ranade, R., Li, V. C., Stults, M. D., Heard, W. F., and Rushing, T. S. (2013). Composite Properties of High-Strength, High-Ductility Concrete. *ACI Mater. J.* 110 (4), 413–422. doi:10.14359/51685788

Said, S. H., Razak, H. A., and Othman, I. (2015). Flexural Behavior of Engineered Cementitious Composite (ECC) Slabs with Polyvinyl Alcohol Fibers. *Construction Building Mater.* 75, 176–188. doi:10.1016/j.conbuildmat.2014.10.036

Tosun-Felekoglu, K., and Felekoglu, B. (2013). Effects of Fiber-Matrix Interaction on Multiple Cracking Performance of Polymeric Fiber Reinforced Cementitious Composites. *Composites Part B: Eng.* 52, 62–71. doi:10.1016/j.compositesb.2013.03.043

Wang, S., and Li, V. C. (2006). High-early-strength Engineered Cementitious Composites. *ACI Mater. J.* 103 (2), 97. doi:10.14359/15260

Weimann, M. B., and Li, V. C. (2003). Hygral Behavior of Engineered Cementitious Composites (ECC)/Vergleich der hygrischen Eigenschaften von ECC mit Beton. *Restoration of Buildings and Monuments* 9 (5), 513–534. doi:10.1515/rbm-2003-5791

Xiao, J., Long, X., Ye, M., Jiang, H., Liu, L., and Zhai, K. (2021). Experimental Study of Bond Behavior between Rebar and PVA-Engineered Cementitious Composite (ECC) Using Pull-Out Tests. *Front. Mater.* 8, 633404. doi:10.3389/fmats.2021.633404

Xiong, Y., Yang, Y., Fang, S., Wu, D., and Tang, Y. (2021). Experimental Research on Compressive and Shrinkage Properties of ECC Containing Ceramic Wastes under Different Curing Conditions. *Front. Mater.* 8, 727273. doi:10.3389/fmats.2021.727273

Xu, L.-Y., Huang, B.-T., and Dai, J.-G. (2021). Development of Engineered Cementitious Composites (ECC) Using Artificial fine Aggregates. *Construction Building Mater.* 305, 124742. doi:10.1016/j.conbuildmat.2021.124742

Xu, M., Song, S., Feng, L., Zhou, J., Li, H., and Li, V. (2021). Development of basalt Fiber Engineered Cementitious Composites and its Mechanical Properties. *Construction Building Mater.* 266, 121173. doi:10.1016/j.conbuildmat.2020.121173

Yang, E.-H. (2008). *Designing Added Functions in Engineered Cementitious Composites*. Michigan (IL): University of Michigan.

Yang, E.-H., Yang, Y., and Li, V. C. (2007). Use of High Volumes of Fly Ash to Improve ECC Mechanical Properties and Material Greenness. *ACI Mater. J.* 104 (6), 620–628. doi:10.14359/18966

Yokota, H., Rokugo, K., and Sakata, N. (2008). "JSCE Recommendations for Design and Construction of High Performance Fibre Reinforced Cement Composite with Multiple fine Cracks," in *High Performance Fibre Reinforced Cement Composites* (Tokyo, Japan: Springer).

Zhang, D., Yu, J., Wu, H., Jaworska, B., Ellis, B. R., and Li, V. C. (2020). Discontinuous Micro-fibers as Intrinsic Reinforcement for Ductile Engineered Cementitious Composites (ECC). *Composites Part B: Eng.* 184, 107741. doi:10.1016/j.compositesb.2020.107741

Zhang, J., Gong, C., Guo, Z., and Zhang, M. (2009). Engineered Cementitious Composite with Characteristic of Low Drying Shrinkage. *Cement Concrete Res.* 39 (4), 303–312. doi:10.1016/j.cemconres.2008.11.012

Zhang, Z., and Zhang, Q. (2018). Matrix Tailoring of Engineered Cementitious Composites (ECC) with Non-oil-coated, Low Tensile Strength PVA Fiber. *Construction Building Mater.* 161, 420–431. doi:10.1016/j.conbuildmat.2017.11.072

Zhou, J., Qian, S., Sierra Beltran, M. G., Ye, G., van Breugel, K., and Li, V. C. (2010). Development of Engineered Cementitious Composites with limestone Powder and Blast Furnace Slag. *Mater. Struct.* 43 (6), 803–814. doi:10.1617/s11527-009-9549-0

**Conflict of Interest:** The authors declare that the research was conducted in the absence of any commercial or financial relationships that could be construed as a potential conflict of interest.

**Publisher's Note:** All claims expressed in this article are solely those of the authors and do not necessarily represent those of their affiliated organizations, or those of the publisher, the editors and the reviewers. Any product that may be evaluated in this article, or claim that may be made by its manufacturer, is not guaranteed or endorsed by the publisher.

frontiers in Materials

ORIGINAL RESEARCH
published: 17 November 2021
doi: 10.3389/fmats.2021.769579

# Tensile Behavior of Hybrid Fiber-Reinforced Ultra-High-Performance Concrete

*Jiayue Li and Zongcai Deng**

*The Key Laboratory of Urban Security and Disaster Engineering, Ministry of Education, Beijing University of Technology, Beijing, China*

Thirty dog bone-shaped specimens were tested to study the effects of steel fiber mixed with seven kinds of non-metallic fibers on the tensile properties of ultra-high-performance concrete (UHPC). Through experiments and micromorphological analysis, the effects of hybrid fibers on the compressive strength, tensile strength, peak strain, fracture energy, and characteristic length of UHPC were analyzed. The results showed that the hybrid fiber-reinforced UHPC showed good ductile failure characteristics, which reflected the good crack resistance and toughening effect of different fibers. The tensile stress–strain curves of UHPC with different hybrid fibers can be divided into two parts: ascending section and softening section, and the softening section was greatly affected by the type and content of fibers. Basalt fiber with a diameter of 0.02 mm had the most obvious strengthening effect on UHPC, and polyvinyl alcohol fiber with a diameter of 0.2 mm and length of 8 mm had the best toughening effect. The mixing of steel fiber and non-metallic fiber cannot only reduce the preparation cost but also improve the fracture energy and toughness of UHPC.

**Keywords: hybrid fiber, ultra-high-performance concrete, tensile behavior, fracture energy, microstructures**

OPEN ACCESS

***Edited by:***
*Kequan Yu,*
*Tongji University, China*

***Reviewed by:***
*Xing-yan Shang,*
*Shandong Jianzhu University, China*
*Ru Mu,*
*Hebei University of Technology, China*

****Correspondence:***
*Zongcai Deng*
*dengzc@bjut.edu.cn*

***Specialty section:***
*This article was submitted to Structural Materials, a section of the journal Frontiers in Materials*

***Received:*** *02 September 2021*
***Accepted:*** *06 October 2021*
***Published:*** *17 November 2021*

***Citation:***
*Li J and Deng Z (2021) Tensile Behavior of Hybrid Fiber-Reinforced Ultra-High-Performance Concrete. Front. Mater. 8:769579. doi: 10.3389/fmats.2021.769579*

## INTRODUCTION

Ultra-high-performance concrete (UHPC) should not only have ultra-high compressive strength but also have good tensile properties, crack resistance, and toughness. The brittleness of ultra-high strength concrete increases obviously, and how to reduce its brittleness and improve its ability to resist fracture after a crack is very important (He et al., 2021). The effective way to improve the tensile properties and toughness of UHPC is usually to use high-performance fiber toughening technology (Kim et al., 2018). Steel fiber has the function of strengthening and toughening, but adding more steel fiber will increase the cost and reduce the workability of UHPC. When the crack width is small, the crack resistance and reinforcement effect of steel fiber is obvious. When the deformation is large, the steel fiber slides obviously, and the toughening effect is reduced (Deng et al., 2020), while the coarse non-metallic fibers play an obvious role in improving the deformation capacity of UHPC. Steel fibers and non-metallic fibers are mixed with complementary advantages, and give full play to the strengthening and toughening effects of fibers of different varieties and sizes, improve the fracture energy of UHPC, reduce the preparation cost, and promote the development of UHPC preparation technology and engineering application.

Kobayashi et al. (1982) first proposed the concept of hybrid fiber, that is, steel fiber and polypropylene (PE) fiber were mixed into concrete. In the later researches, most researchers studied the mechanical properties of hybrid fiber-reinforced concrete under different loading modes by changing the types and the fiber volume fraction of the hybrid fiber. The types of

hybrid fiber can be mainly divided into three categories, namely, steel–steel hybrid fiber, steel–polymer hybrid fiber, and polymer–polymer hybrid fiber (Guo et al., 2019).

In recent years, there are many reports on steel–steel hybrid fiber concrete. Park et al. (2012) investigated the effect of steel fiber on the tensile properties of ultra-high-performance hybrid fiber concrete (UHP-HFRC). The results showed that the overall shape of the tensile stress–strain curve of UHP-HFRC mainly depended on the type of macrofiber, although the addition of microfiber was conducive to strain hardening and multiple cracking behaviors. Chun et al. (2019) discussed the impact of mixed use of macro- and microsteel fibers on the pullout and tensile properties of UHPC. Kazim et al. (Turk et al., 2021) studied the effects of macro- and microsteel fiber mixing with different volume contents on the mechanical properties of self-compacting concrete. The test results showed that the hybrid-reinforced concrete specimen showed excellent ductility compared with the single macrosteel fiber-reinforced concrete specimen. Chang et al. (2020) found that the compressive strength and flexural strength of hybrid steel fiber-reinforced sulfoaluminate cement-based reactive powder concrete were effectively improved with an increase in the content of steel fibers. Steel fibers, as a kind of fiber that are seeing great attention worldwide, are widely studied by many researchers since they can improve the toughness of concrete (Kim et al., 2011; Yoo et al., 2017; Fantilli et al., 2018; Yoo et al., 2020). There are also many reports about polymer–polymer hybrid fibers (Ahmed et al., 2011; Silva et al., 2013; Pan et al., 2015; Banyhussan et al., 2016; Gong et al., 2020; Sükrü et al., 2020; Turk et al., 2021).

As we all know, steel fiber has the effect of strengthening and toughening, but adding more steel fibers will increase the production cost and reduce the workability. Recent research works reported that non-metallic fibers could also be used in UHPC instead of steel fibers (Kang et al., 2016). However, the addition of non-metallic fibers alone may reduce the workability of UHPC and expand the crack width, although it will improve the tensile ductility. Steel fiber and non-metallic fiber are mixed and complementary, to give full play to the strengthening and toughening effects of fibers of different varieties, different scales, and different stress stages. Rashiddadash et al. (2014) found that hybrid fiber-reinforced concrete with 0.75% steel fibers and 0.25% PE fibers had higher toughness indexes, modulus of rupture, and impact resistance than other hybrid mixtures. Kang et al. (2016) studied the effects of the mixed combination of 0.2-mm-diameter steel fiber and microfibers on the mechanical properties of UHPC. The test results showed that the combination of high-strength synthetic fiber (such as PE fiber) and steel fiber can improve the tensile properties of UHPC, and basalt fiber can effectively improve the tensile strength of UHPC. In the same year, Kang (Kang et al., 2016) proposed a method to improve the tensile ductility and control crack width of UHPC, and to examine the effect of artificial flaws and fiber hybridization on the tensile behavior of UHPC. Kim et al. (2019) investigated several factors affecting the efficiency of mixing steel fiber and PE fiber to improve the compressive strength and tensile properties of UHPC. The tensile strength also decreased with the increase in PE fiber content, and the strain capacity and energy absorption capacity per unit volume increased significantly after adding PE fiber. Yoo et al. (2019) considered three different types of steel fibers and four different replacement ratios of steel fibers to PE fibers, and high-energy absorbent ultra-high-performance hybrid steel and PE fiber-reinforced concrete were successfully developed at a 2% fiber volume fraction. Tran et al. (2021) examined the use of polyamide fibers in improving strain rate sensitivity and impact tensile resistance of hybrid ultra-high-performance fiber-reinforced concrete. Li et al. (2020) investigated the flexural performance of a hybrid polyethylene–steel fiber-reinforced ultra-high-performance concrete. In addition, scholars also studied multi-wall carbon nanotube (CNT) (Yoo et al., 2018), bagasse fiber (Tian et al., 2015), and polyvinyl alcohol (PVA) fiber (Yu et al., 2021). At present, different scholars have carried out a lot of research on hybrid fiber concrete, but the types of fibers need to be expanded. In addition, there are a few studies on hybrid reinforcement of UHPC with coarse and fine fibers.

In this paper, steel fibers were mixed with polyolefin (PP) fiber, PVA fiber, polyester (PET) fiber, and basalt fiber (BF). Through the direct tensile test, the contribution of hybrid fiber to the improvement of UHPC tensile properties was studied, and the tensile properties of UHPC reinforced by different varieties and sizes were compared. The test results will provide a reference for selecting fiber varieties, determining fiber geometry, and preparing high-toughness UHPC.

# EXPERIMENTAL PROGRAM

## Materials

The raw materials used in the test include the following: The cement is P.O. 52.5 ordinary Portland cement. The $SiO_2$ content of the silica fume is 95%, and the ignition loss at 950°C is 1%. The mineral powder is S95 granulated blast furnace slag powder. The diameter of quartz sand is 0.18–2 mm. Superplasticizer is added to get the appropriate workability. Mixing water is the daily water. The mix proportion of the UHPC matrix is shown in **Table 1**.

The steel fiber used to prepare UHPC was copper-plated and endless hook-shaped steel fiber and its mechanical parameters are listed in **Table 2**. To study the strengthening and toughening effect of different hybrid fiber-reinforced UHPC, different kinds of non-metallic fibers were added to the steel fiber–UHPC system: PP fiber, PVA fiber, PET fiber, and BF fiber.

All non-metal fibers were named in the form A-b-c, where A represented the fiber type, b represented the fiber length, and c represented the fiber diameter. For example, the PP-40-0.6 represented that the non-metal fiber selected for the hybrid fiber-reinforced UHPC was PP fiber, with a length of 40 mm and a diameter of 0.6 mm. The photos of non-metal fiber are shown in **Figure 1**.

**TABLE 1 |** Mix proportion of ultra-high-performance concrete (UHPC) matrix.

| Cement | Silica fume | Mineral powder | Quartz sand | Water | Superplasticizer |
|---|---|---|---|---|---|
| 556 | 101 | 354 | 1,213 | 182 | 11 |

**TABLE 2 |** Steel fiber properties.

| Type | Length/mm | Diameter/mm | Aspect ratio | Tensile strength/MPa | Elastic modulus/GPa |
|---|---|---|---|---|---|
| CW01–0.2/13 | 13 | 0.2 | 65 | 2,850 | 210 |

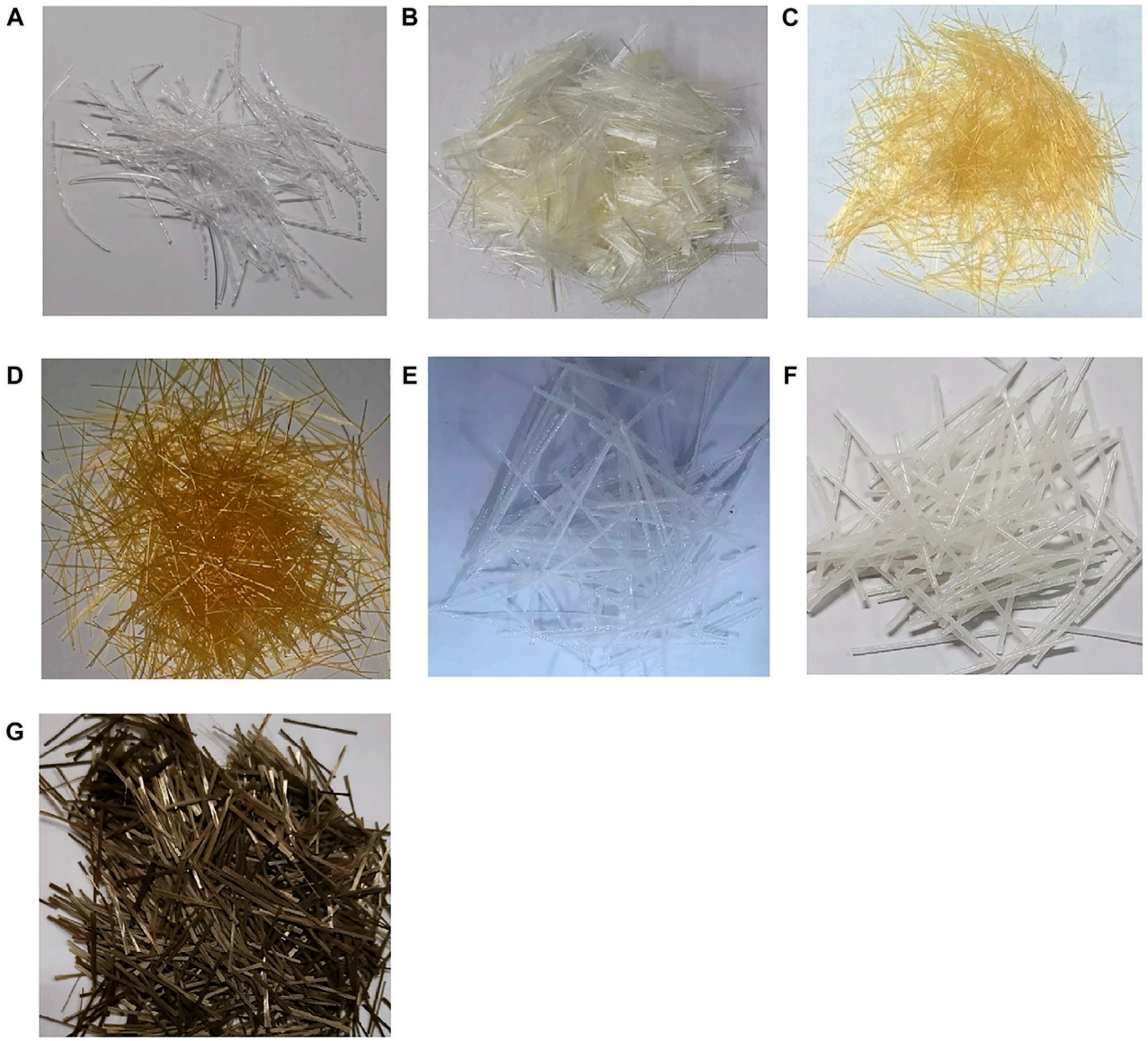


**FIGURE 1 |** Photos of non-metallic fibers. **(A)** PP-40-0.6, **(B)** PVA-12-0.04, **(C)** PVA-8-0.2, **(D)** PVA-12-0.2, **(E)** PET-30-0.75, **(F)** PET-30-0.9, and **(G)** BF-12-0.02.

**TABLE 3 |** Performance parameters of different fibers.

| Type | Length/mm | Diameter/mm | Elastic modulus/GPa | Tensile strength/MPa | Density/(kg/m$^3$) | Fine or coarse |
|---|---|---|---|---|---|---|
| PP-40-0.6 | 40 | 0.6 | 8 | 650 | 910 | Coarse |
| PVA-12-0.04 | 12 | 0.04 | 40 | >1,600 | 1,640 | Fine |
| PVA-8-0.2 | 8 | 0.2 | 35 | >1,500 | 1,640 | Coarse |
| PVA-12-0.2 | 12 | 0.2 | 39 | >1,600 | 1,640 | Coarse |
| PET-30-0.75 | 30 | 0.75 | 8 | 380 | 1,380 | Coarse |
| PET-30-0.9 | 30 | 0.9 | 8 | 380 | 1,380 | Coarse |
| BF-12-0.02 | 12 | 0.02 | 90 | 2,300 | 2,650 | Fine |

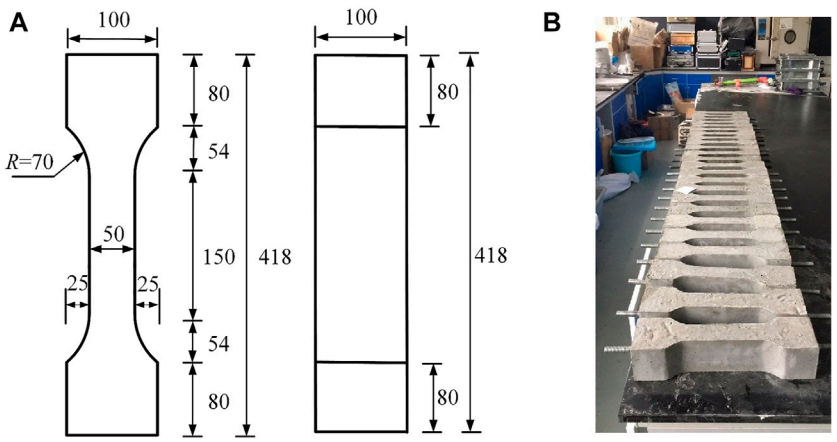


**FIGURE 2 |** Tensile specimens. **(A)** Dimensions of tensile specimens. **(B)** Photos of tensile specimens.

**TABLE 4 |** Specimen details.

| Specimen ID | $v_{f1}$/% | Non-metallic fiber type | $v_{f2}$/% | Number of identical specimens |
|---|---|---|---|---|
| S0 | 0 | — | — | 3 |
| S1.3 | 1.3 | — | — | 3 |
| S1.8 | 1.8 | — | — | 3 |
| S1.3PP0.5-40 | 1.3 | PP-40-0.6 | 0.5 | 3 |
| S1.3PVA0.5-12a | 1.3 | PVA-12-0.04 | 0.5 | 3 |
| S1.3PVA0.5-8 | 1.3 | PVA-8-0.2 | 0.5 | 3 |
| S1.3PVA0.5–12 b | 1.3 | PVA-12-0.2 | 0.5 | 3 |
| S1.3PET0.5-30a | 1.3 | PET-30-0.75 | 0.5 | 3 |
| S1.3PET0.5-30b | 1.3 | PET-30-0.9 | 0.5 | 3 |
| S1.3B0.5-12 | 1.3 | BF-12-0.02 | 0.5 | 3 |

*Note.* $v_{f1}$ *represented the steel fiber volume content;* $v_{f2}$ *represented the non-metallic fiber volume content.*

The mechanical parameters of non-metallic fibers are listed in **Table 3**. Referring to the Chinese standard: technical specification for fiber-reinforced concrete structures (CECS 38:2004) (CECS 38:2004, 2004), it was considered that a fiber diameter less than 0.1 mm was fine fiber, and a fiber diameter greater than 0.1 mm was coarse fiber.

## Design of Experiment

A total of 10 groups of specimens were designed, including 7 groups of hybrid fiber-reinforced UHPC specimens, 2 groups of single-doped steel fiber UHPC specimens, and 1 group of non-fiber UHPC specimens. The specimen was the dog bone shape (GB/T 50081-2019, 2019; T/CBMF 37-2018, 2018; Zhao et al., 2019; Cai et al., 2021; Yu et al., 2021), as shown in **Figure 2**, and the details of the specimens are shown in **Table 4**. The fiber volume content of all hybrid fiber-reinforced UHPC specimens was maintained at 1.8% (steel fiber:1.3%, non-metallic fiber: 0.5%), and three parallel specimens were poured for each group of specimens. When each group of specimens was casting, three UHPC cubes (100 mm × 100 mm × 100 mm)

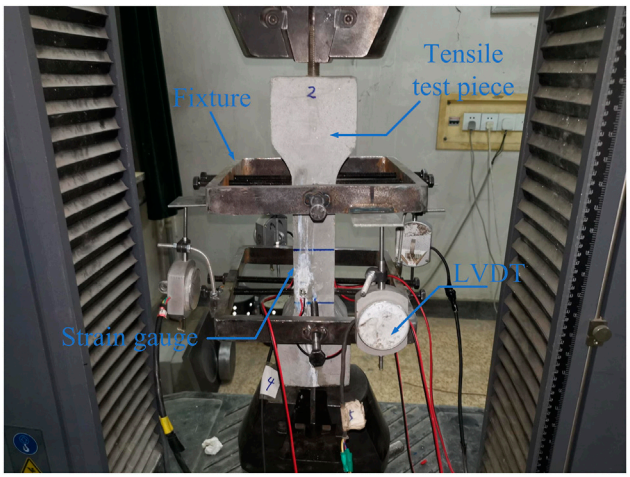


**FIGURE 3 |** Test setup.

were poured to obtain the compressive strength ($f_{cu}$). All the specimens and UHPC cubes were placed in a normal temperature environment and cured until the test.

According to the type of fiber mixed in UHPC, the hybrid fiber-reinforced UHPC specimens were named Sx-Ay-z, where S represented steel fiber, x represented steel fiber volume content; A represented the non-metallic fiber type, y represented the non-metallic fiber volume content, and z represented the non-metallic fiber length. In particular, PVA fibers with a length of 12 mm and PET fibers in this experiment had the same fiber length but different diameters. Therefore, the name of the specimen was distinguished by a and b, and a was the one with finer fiber diameter. For example, the S1.3PET0.5-30a that represented the steel fiber volume content was 1.3%, PET fiber volume content was 0.5%, the length was 30 mm, and the diameter was 0.75 mm.

The single-doped steel fiber specimen was named Sx, where S represented steel fiber, and x represented the steel fiber volume content. For example, the S1.3 that represented steel fiber volume content was 1.3%. Since three parallel specimens were poured in each group, the parallel specimens were distinguished by /1, /2, and /3. For example, the three parallel test specimens of S1.3 were named S1.3/1, S1.3/2, and S1.3/3 in turn.

## Instrumentation and Test Procedure

All specimens were tested using the 300-kN MTS testing machine. To accurately measure the deformation of the specimen, a steel loading and fixing system was designed for the experiment. Four linear variable differential transducers (LVDTs) were arranged on the surface of the specimen to measure the axial deformation of the specimen over a gauge length of 150 mm. Two concrete strain gauges were arranged to assist in measuring the axial strain of the specimen. The loading was conducted by displacement control with a rate of 0.15 mm/min, and the test setup is shown in **Figure 3**.

# RESULTS AND DISCUSSION

## Failure Modes

Taking the specimen S1.3PET0.5-30a as an example, the typical failure mode is shown in **Figure 4**. At the initial stage of loading, the specimen did not have obvious change. With the loading continuing, the specimens would crack at the weak section of the weak position. After the specimen cracked, the UHPC at the cracked site gradually withdrew from work, the deformation continued to increase, and the cracks continued to develop around the specimen. At this time, the geometric centroid and force of the specimen were not in a straight line, eccentric tension occurred, and the UHPC on the other side may produce compressive stress at the moment. With the development of deformation, the two ends of the main crack continue to expand

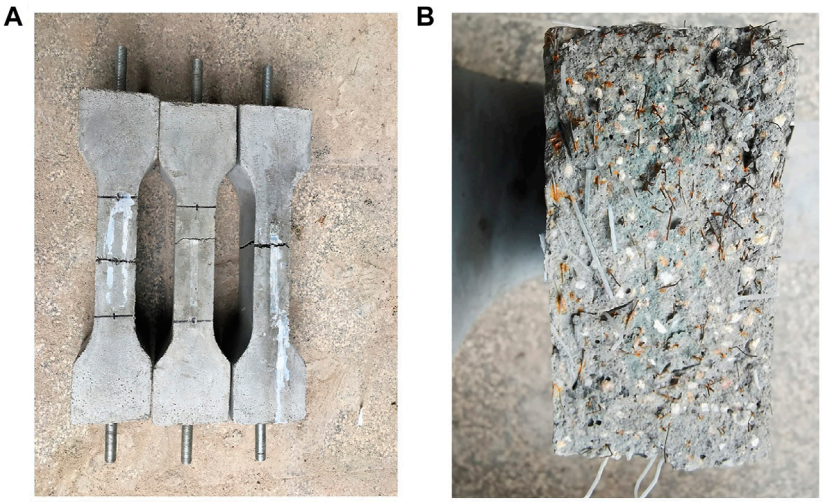


**FIGURE 4 |** Typical failure mode. **(A)** Failure mode of specimen. **(B)** Fracture failure state of specimens.

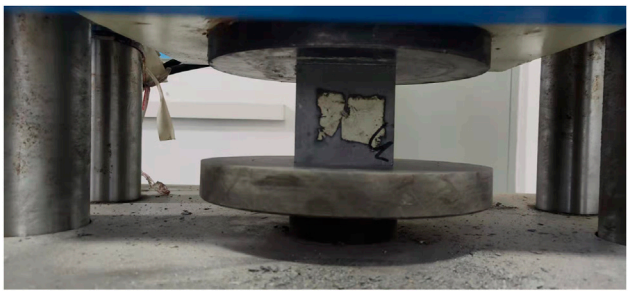

**FIGURE 5 |** Test setup for compressive strength.

and extend, and the specimen showed full cross-section tension until the bearing capacity was lost. After the specimen was cracked, the specimen made a "crack" sound, and the tensile stress fluctuated immediately. The sound was produced by the fibers being continuously pulled out, which reflected the bridging effect of the fibers.

It was worth noting that the failure mode of the plain UHPC specimen without fiber was different from that of the fiber-reinforced UHPC specimen. When the plain UHPC specimen was loaded to the peak tensile strength, the full section was suddenly divided into two parts, and the failure had no ductility.

The tensile properties of different hybrid fiber-reinforced UHPC were also different: the specimens mixed with PVA fiber or BF fiber with high elastic modulus and high aspect ratio (length/diameter) had a long process from loading to cracking, especially the specimens that had obvious strain-hardening characteristics before cracking, and the failure process of the specimens was slow. PP fiber and PET fiber with low elastic modulus and low aspect ratio can effectively reduce the later crack propagation rate.

## Effect of Hybrid Fiber on Compressive Properties of Ultra-High-Performance Cement

All UHPC cubes (100 mm × 100 mm×100 mm) were tested for compressive strength with a 2,000-kN MTS testing machine, and the test setup is shown in **Figure 5**. The loading was conducted with stress control with a rate of 1.0 MPa/s. At the end of the test, the plain UHPC without fiber was suddenly broken at the peak load with a fragmentation, showing the characteristics of brittle failure. On the contrary, hybrid fiber-reinforced UHPC still maintained good integrity after failure, reflecting the bridging effect of fibers.

The average cube compressive strength $f_{cu}$ of UHPC in each group is listed in **Table 5**. The compressive strength of UHPC increased by 26.1% and 32.4% when the steel fiber content increased from 0 to 1.3% and 1.8%, respectively, indicating that steel fiber had a significant reinforcing effect on UHPC. This was because steel fibers were randomly distributed in the UHPC. When the UHPC was deformed under compression, the tension of the steel fibers would indirectly increase the compressive strength of UHPC. In addition, the steel fiber also changed the failure mode of the UHPC. The plain UHPC specimen was crushed when it was damaged, while the UHPC with steel fibers still had good integrity when it was damaged, which also reflected the bridging effect of fiber.

Compared with the single-doped steel fiber specimen S1.8, the compressive strength of some hybrid fiber-reinforced UHPC specimens were reduced, and only the compressive strength of specimens S1.3PP0.5-40 and S1.3PET0.5-30b did not decrease. It showed that with the addition of non-metal fibers, the compressive strength of UHPC may be reduced. The reasons may be that the fibers of different types and sizes were dispersed in the UHPC matrix, resulting in uneven distribution of mixed fibers in the UHPC matrix and increasing some original defects.

## Effect of Hybrid Fiber on Tensile Properties of Ultra-High-Performance Concrete

### Tensile Stress–Strain Curve

To compare the differences of tensile properties of different types of fiber-reinforced UHPC, the typical tensile stress–strain curves of each group of specimens are shown in **Figure 6**. Due to the large ultimate deformation of hybrid fiber-reinforced UHPC, to more intuitively compare the differences in the whole failure process of different specimens, the process from loading to cracking of each group of specimens was enlarged and placed at the upper right of **Figure 6**. The tensile stress–strain curves of different hybrid fiber-reinforced UHPC can be divided into two

**TABLE 5 |** Average values of test results.

| Specimen ID | $f_{cu}$/MPa | $\sigma_p$/MPa | $\varepsilon_p/\mu\varepsilon$ | $E_t$/GPa | $G_F$/(N/m) | $L_{ch}$/mm |
|---|---|---|---|---|---|---|
| S1.3PP0.5-40 | 121.44 | 4.27 | 121 | 36.89 | 13,724.29 | 27,767.88 |
| S1.3PVA0.5-12a | 101.15 | 5.13 | 254 | 42.32 | 28,054.24 | 45,112.80 |
| S1.3PVA0.5-8 | 108.14 | 4.74 | 192 | 37.23 | 31,447.36 | 52,109.94 |
| S1.3PVA0.5-12 b | 106.15 | 4.95 | 116 | 55.83 | 22,206.54 | 50,598.56 |
| S1.3PET0.5-30a | 108.30 | 5.07 | 139 | 44.50 | 23,771.44 | 41,152.82 |
| S1.3PET0.5-30 b | 119.79 | 4.18 | 85 | 40.21 | 12,638.43 | 29,085.37 |
| S1.3B0.5-12 | 107.26 | 5.44 | 189 | 45.12 | 16,586.55 | 25,288.75 |
| S0 | 91.51 | 4.16 | 101 | 36.91 | — | — |
| S1.3 | 115.35 | 4.73 | 109 | 38.60 | 10,954.26 | 18,899.4 |
| S1.8 | 121.13 | 5.21 | 110 | 40.53 | 32,602.58 | 48,680.29 |

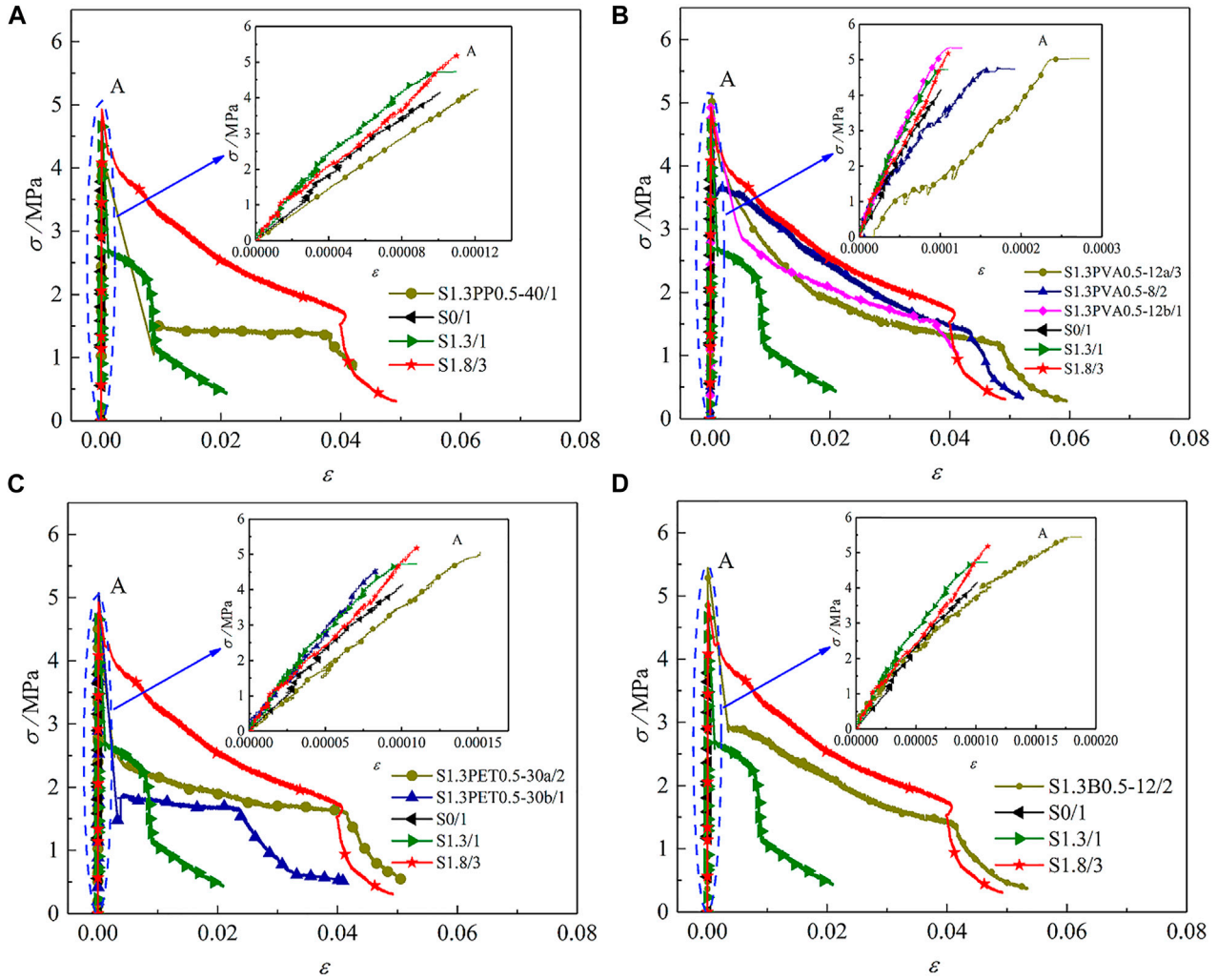


**FIGURE 6 |** Tensile stress–strain curve. **(A)** S1.3PP0.5. **(B)** S1.3PVA0.5. **(C)** S1.3PET0.5. **(D)** S1.3B0.5.

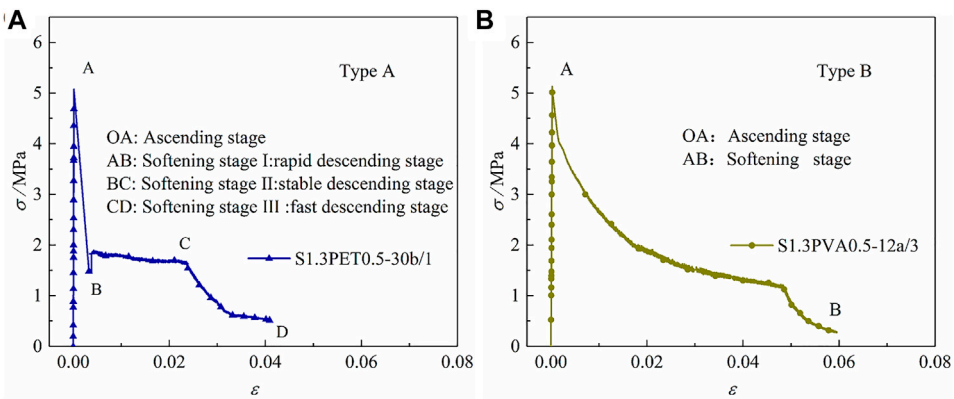


**FIGURE 7 |** Two types of strain-softening ultra-high-performance concrete (UHPC) tensile complete curves. **(A)** Type A. **(B)** Type B.

parts: ascending and softening branches. Due to the different types and volume content of fibers, the tensile stress–strain curves can be divided into two different types (Type A and Type B). The ascending branches of the tensile curve of the two types of strain-softening UHPC were similar, and the softening branches were different, as shown in **Figure 7**.

Type A: generally, the tensile stress–strain curve of UHPC with low fiber content or hybrid steel fiber and long or coarse non-metallic fiber. It can be divided into four stages: 1) Ascending stage: The relationship between stress and strain is approximately linear until microcracks appear in the specimen. At this stage, the single-doped steel fiber or hybrid fiber effectively reduces the possibility of stress concentration in the matrix. When the tensile stress increases to the initial crack stress, microcracks appear in the component, the cracked UHPC loses its bearing capacity, and the fibers crossing the cracks begin to play a role. Generally, some microfibers have low elastic modulus but have a large number, which can significantly inhibit the development of early microcracks. Compared with ordinary concrete, the generation and expansion of initial cracks of fiber concrete are delayed; 2) Softening stage I: rapid descending stage. After the specimen reaches the tensile strength, it cracks, and the bearing capacity decreases rapidly. This kind of curve often shows that the fiber content is low, or the steel fiber is mixed with long or coarse non-metallic fibers, and these fibers begin to play a bridging role gradually after the specimen cracks. Therefore, the bearing capacity of the specimen decreases suddenly at the moment of cracking. This stage is closely related to the type and content of fiber in the specimen. When the fiber content or type is appropriate, the bearing capacity of the specimen decreases only slightly. On the contrary, the bearing capacity of the specimen will decrease greatly; 3) Softening stage II: stable descending stage. At this stage, with the increase in crack width, the fibers between cracks, especially some macrofibers, begin to play a bridging role. The fiber is well bonded with the matrix, which can effectively delay and prevent the expansion of cracks, improve the toughness of the matrix, and maintain the stability of bearing capacity; 4) Softening stage III: fast descending stage. As the fibers are continuously pulled out or broken, the fiber-bridging effect is gradually weakened, and the bearing capacity of the specimen decreases rapidly with the increase in specimen deformation.

Type B: generally, the UHPC tensile stress–strain curve with high fiber content or hybrid steel fiber and fine non-metallic fiber. It can be roughly divided into two stages: 1) Ascending stage, which is similar to the ascending section of type A. Since microfibers can inhibit the development of early microcracks, strain hardening is more likely to occur before specimen cracking than type A. 2) Softening stage: After the specimen is cracked, the fibers between the cracks effectively play a bridging role to control the extension of macrocracks, and the bearing capacity does not decrease rapidly. Compared with the tensile stress–strain curve of type A, the softening section is gentler and shows good toughness.

It can be seen from the tensile stress–strain curve of the hybrid PP fiber in **Figure 6A** that the coarse PP fiber had little effect on the ascending stage, but the tensile peak strain was slightly increased. After the specimen S1.3PP0.5-40 cracked, the tensile stress dropped significantly. The reason was that the diameter of the PP fiber was too coarse, and the effect of controlling the expansion of microcracks before cracking was not obvious. When the specimen was cracked, the PP fibers between the cracks cannot immediately play a bridging role, so the stress decreased. Compared with the single-doped steel fiber specimen S1.3, the descending stage of the specimen S1.3PP0.5-40 was gentler, and the toughening effect was obvious.

It can be seen from the tensile stress–strain curve of hybrid PVA fiber in **Figure 6B** that before cracking, the specimens S1.3PVA0.5-12a, S1.3PVA0.5-8, and S1.3PVA0.5-12b had obvious strain-hardening characteristics, reflecting the good crack resistance of PVA fiber. Among them, fiber PVA-12-0.04 had the best crack resistance, followed by PVA-8-0.2, and PVA-12-0.2 was inferior. The reason was that the diameter of the three PVA fibers was relatively small, and the elastic modulus was medium. Before cracking, they can effectively delay the development of microcracks, improve the crack resistance of the specimen, and improve the tensile strength of the specimen, which had an obvious effect of strengthening the crack resistance. Compared with specimen S1.3, the descending section of the specimens S1.3PVA0.5-12a, S1.3PVA0.5-8, and S1.3PVA0.5-12b was gentle, and the ultimate deformation was large. The reason was that there were hydroxyl groups on the surface of the PVA fiber, which was well bonded with the UHPC matrix and which can effectively control the development of macrocracks, reflecting the good toughening effect of the PVA fiber.

It can be seen from the tensile stress–strain curve of hybrid PET fiber in **Figure 6C** that before cracking, specimen S1.3PET0.5-30a had strain-hardening characteristics, while specimen S1.3PET0.5-30b had no strain hardening characteristics. After cracking, the descending section of S1.3PET0.5-30a was gentle, and the ultimate strain was large, which reflected the good crack resistance and toughening effect of fiber PET-30-0.75. The tensile stress of specimen S1.3PET0.5-30b decreased greatly after cracking, and the descending section was also relatively gentle, which also reflected the crack resistance and toughening effect of the fiber PET-30-0.9. A comprehensive comparison found that the crack resistance and toughening effect of the fiber PET-30-0.9 were weaker than that of the fiber PET-30-0.75. The reason was that the diameter of the fiber PET-30-0.9 was too thick, and the number of fibers per unit cross-sectional area was too small. Therefore, it was suggested that the diameter of fiber PET should not exceed 0.75 mm.

It can be seen from the tensile stress–strain curve of hybrid BF fiber in **Figure 6D** that before cracking, the specimen S1.3B0.5-12 had obvious strain-hardening characteristics, and the tensile strength had been significantly improved. At the moment of cracking, the bearing capacity decreased obviously, and then the descending section was gentle. It can be seen that the BF fiber had a fine diameter and high elastic modulus, which has an obvious strengthening and toughening effect.

To better quantitatively compare the differences in tensile properties of each group of specimens, the strength corresponding to the peak point was taken as the tensile strength ($\sigma_p$), and its corresponding strain was taken as the

peak strain ($\varepsilon_p$). Take the slope of the connecting line between 5% and 50% of the maximum stress in the ascending stage of the tensile stress–strain curve of the specimen as the elastic modulus ($E_t$). To evaluate the performance differences of the different specimens after cracking, fracture energy ($G_F$) was defined to characterize the energy absorption capacity of the specimens and characteristic length ($L_{ch}$) to characterize the brittleness of the specimens. All the above results were the average values of the same group of parallel specimens, and the results are listed in **Table 5**.

## Effect of Hybrid Fiber on Tensile Strength

The tensile strength $\sigma_p$ of UHPC in each group is listed in **Table 5**. When the steel fiber content increased from 0 to 1.3% and 1.8%, the tensile strength of UHPC increased by 13.70% and 25.24% respectively, indicating that the tensile strength of UHPC can be significantly improved by adding steel fibers. In addition, the addition of steel fibers also changed the brittle failure characteristics of the plain UHPC. After the peak tensile strength, the descending section of specimen S1.8 was gentler than that of S1.3. This was because the steel fibers played a great role before and during the cracking of UHPC. The steel fiber exerted its bridging function and continuously transmitted the stress to the surrounding matrix so that the matrix can continue to work under the stress after it was cracked, which cannot only increase the tensile stress but also improve the ability to resist tensile deformation.

Compared with S1.3, the tensile strength of S1.3PP0.5-40 and S1.3PET0.5-30b decreased by 9.73% and 11.63%, respectively, and the tensile strength of S1.3PVA0.5-12a, S1.3PVA0.5-8, S1.3PVA0.5-12b, S1.3PET0.5-30a, and S1.3B0.5-12 increased by 8.46%, 0.03%, 4.65%, 7.19%, and 15.01%, respectively. Generally speaking, microfibers can effectively prevent the development of microcracks, and macrofibers can effectively prevent the development of cracks after macrocracks appeared (Fantilli et al., 2017; Stahli and Mier 2007). Therefore, some fine fibers such as PVA-12-0.04 and BF-12-0.02 had an obvious enhancement effect on the matrix. Some coarse fibers such as PP-40-0.6 and PET-30-0.9 cannot prevent the development of microcracks well before the specimen cracked, so the tensile strength of the specimen was significantly reduced.

The tensile strength of the specimen hybrid with three different sizes of PVA fiber and steel fiber was improved. The reinforcement effect of the two PVA fibers with a length of 12 mm was better than that of the PVA fiber with a length of 8 mm. The length of fiber PVA-12-0.04 and PVA-12-0.2 was the same as 12 mm, but the diameter of fiber PVA-12-0.04 was only 0.04 mm, so its reinforcement effect was the best.

Among all the hybrid fiber-reinforced UHPC specimens, the tensile strength of specimen S1.3B0.5-12 was the highest, even higher than that of specimen S1.8, indicating that the reinforcement effect of fiber BF-12-0.02 was the best among all non-metallic fibers because its minimum diameter was only 0.02 mm, and its elastic modulus was the highest among all non-metallic fibers. Therefore, selecting fine fibers with high elastic modulus was the most effective way to improve the tensile strength of materials.

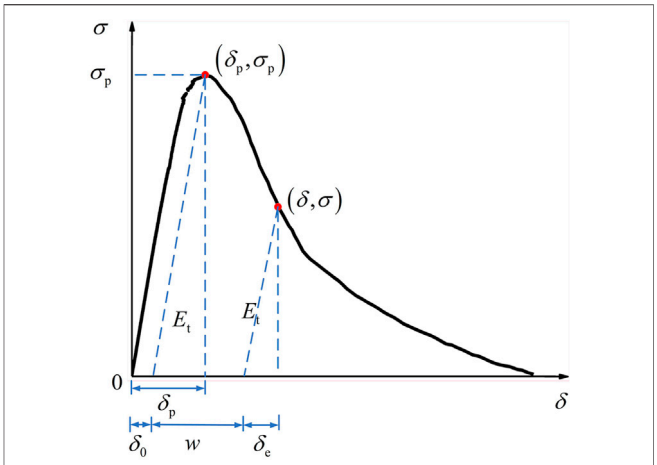


**FIGURE 8 |** Schematic diagram of UHPC tensile stress–total deformation curve.

## Effect of Hybrid Fiber on Peak Strain

The peak strain $\varepsilon_p$ of UHPC in each group is listed in **Table 5**. When the steel fiber content increased from 0 to 1.3% and 1.8%, the peak strain of UHPC was close.

Compared with S1.8, the peak strain of S1.3PET0.5-30b decreased by 22.73%, and the peak strain of S1.3PP0.5-40, S1.3PVA0.5-12a, S1.3PVA0.5-8, S1.3PVA0.5-12b, S1.3PET0.5-30a, and S1.3B0.5-12 increased by 10.00%, 110.00%, 74.55%, 5.45%, 26.36%, and 71.81%, respectively. Similar to the effect of hybrid fibers on tensile strength, in general, microfibers can effectively prevent the development of microcracks, and macrofibers can effectively prevent the development of cracks after macrocracks appeared (Fantilli et al., 2017; Stahli and Mier 2007).

For three different sizes of PVA fiber and steel fiber hybrid-reinforced UHPC specimens, the peak strain of specimens S1.3PVA0.5-12a, S1.3PVA0.5-8, and S1.3PVA0.5-12b decreased in turn. The reason was that the diameter of fiber PVA-12-0.04 was only 0.04 mm, and the number of fibers contained in the unit cross-sectional area was the largest, which also reflected the contribution of micro-fibers to slowing down the initiation and development of microcracks.

Compared with S1.3PET0.5-30a, the peak strain of S1.3PET0.5-30b decreased by 38.85%. The same reason was that the diameter of fiber PET-30-0.9 was too coarse, and the number of fibers contained in the section of the same area reduced, resulting in a decrease in peak strain.

In all fiber hybrid-reinforced UHPC tensile specimens, PVA-12-0.04, PVA-8-0.2, and BF-12-0.02 had a significant increase in peak strain because these three fibers had fine diameter, high elastic modulus, and excellent enhancement effect.

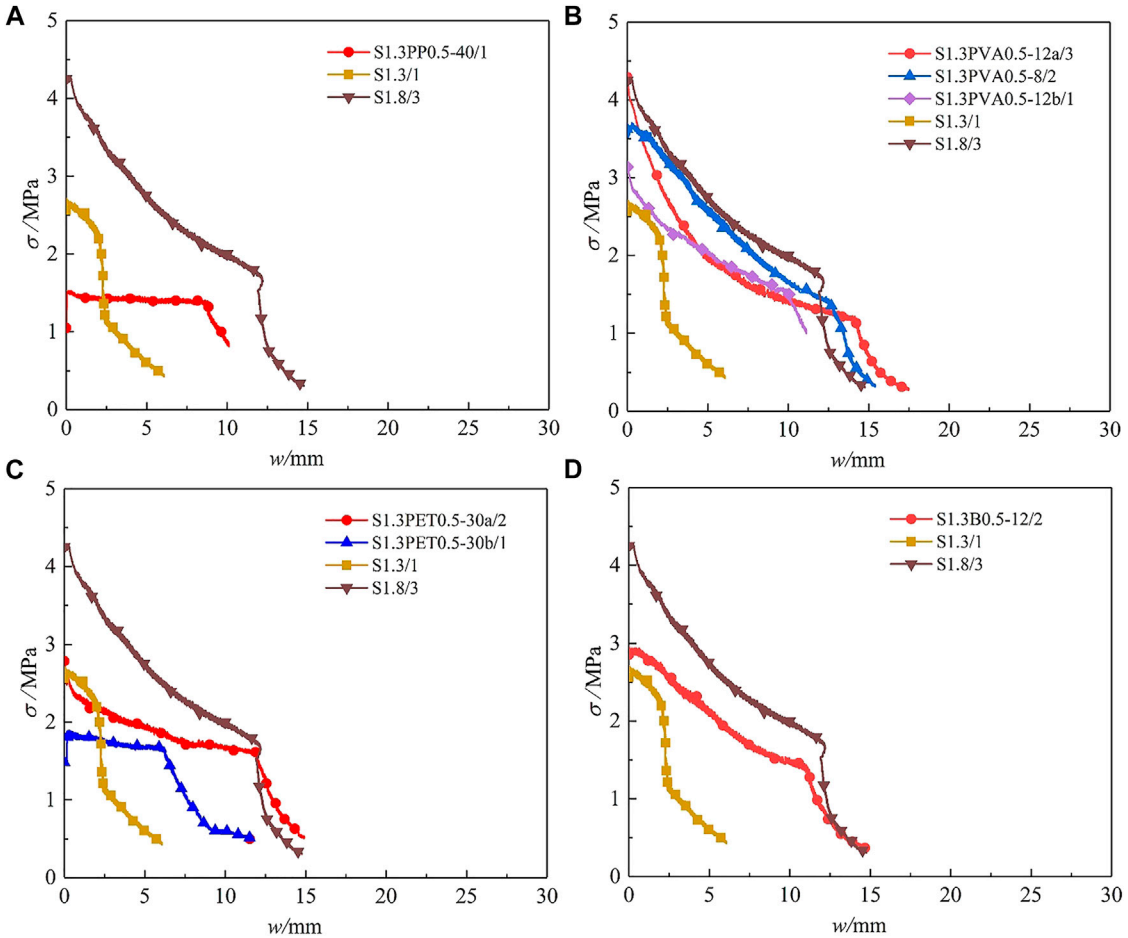


**FIGURE 9 |** Tensile stress-crack width curve. **(A)** S1.3PP0.5. **(B)** S1.3PVA0.5. **(C)** S1.3PET0.5. **(D)** S1.3B0.5.

## Tensile Stress-Crack Width Curve

Based on the assumption that the specimen does not crack before peak load, and the residual deformation does not increase after the peak load, the schematic diagram of UHPC tensile stress–total deformation curve is shown in **Figure 8**, and the total deformation $\delta$ (Deng et al., 2009) of hybrid fiber-reinforced UHPC in the tensile process is:

$$\delta = \delta_e + \delta_0 + w \tag{1}$$

where $w$ is the macrocrack width, and $\delta_e$ and $\delta_0$ are the elastic deformation and residual deformation outside the fracture zone of the specimen, respectively, and then:

$$\delta_e = \frac{\sigma l}{E_t} \tag{2}$$

$$\delta_e^0 = \frac{\sigma_p l}{E_t} \tag{3}$$

$$\delta_0 = \delta_p - \delta_e^0 \tag{4}$$

where $\sigma$ and $\sigma_p$ are the axial tensile stress and the peak stress, respectively, $\delta_p$ and $\delta_e^0$ are the total deformation and elastic deformation corresponding to peak stress, respectively, $E_t$ is the elastic modulus, and $l$ is the gauge distance of the specimen.

The crack propagation width $w$ is independent of the length of the specimen, and there is no macrocrack before the maximum load (Deng et al., 2009). According to **Eq. 1**, the $w$ is:

$$w = \delta - \delta_e - \delta_0 \tag{5}$$

The tensile stress–crack width curves are shown in **Figure 9**. Different hybrid fiber-reinforced UHPC had significant differences due to the different characteristics of non-metal fibers. To better evaluate the difference in tensile stress–crack width curves of different tensile specimens, the evaluation index of fracture energy ($G_F$) was introduced (see the *Effect of hybrid fibers on fracture energy* section for details).

## Effect of Hybrid Fibers on Fracture Energy

Fracture energy $G_F$ (Deng et al., 2009) is the energy consumed to form cracks per unit area, that is, the ratio of the area under the tensile stress–crack width curves to the cross-sectional area of the specimen, and

$$G_F = \int_0^{w_f} \sigma(w)\mathrm{d}w \quad (6)$$

The fiber-reinforced UHPC had large deformation. To compare the toughness differences of different specimens more accurately, it was uniformly taken that the load was reduced to 20% of the cracking load. The calculation results of the fracture energy of the different specimens are listed in **Table 5**. The fracture energy value reflected the energy consumed by UHPC during the fracture process. The greater the fracture energy, the greater the energy consumed by UHPC during the fracture process, and the more significant the crack resistance effect of the fiber.

Plain UHPC specimen S0 had a brittle fracture, and the fracture energy was not considered. The fracture energy of UHPC increased by 197.62% when the content of steel fiber was increased from 1.3% to 1.8%, indicating that steel fiber had a significant toughening effect on UHPC.

Compared with the single-doped steel fiber specimen S1.3, the fracture energies of S1.3PP0.5-40, S1.3PVA0.5-12a, S1.3PVA0.5-8, S1.3PVA0.5-12b, S1.3PET0.5-30a, S1.3PET0.5-30b, and S1.3B0.5-12 increased by 25.29%, 156.10%, 187.07%, 102.72%, 117.01%, 15.37%, and 53.88%, respectively. The steel fiber content of all hybrid fiber-reinforced UHPC was 1.3%, and the fracture energy was significantly improved by adding non-metallic fiber of fiber content 0.5%, which showed that the steel fiber and non-metallic fiber were mixed with complementary advantages and gave full play to the strengthening and toughening effects of fibers of different varieties and sizes. In general, long fibers can more effectively limit the development of macrocracks than short fibers, to improve the ductility of UHPC and achieve the effect of toughening. In the test, the fibers PVA-12-0.04, PVA-8-0.2, PVA-12-0.2, PET-30-0.75, and BF-0.02 all showed good toughening effects.

The fracture energy of the specimens S1.3PVA0.5-8, S1.3PVA0.5-12a, and S1.3PVA0.5-12b decreased sequentially in three different sizes of PVA fiber and steel fiber hybrid-reinforced UHPC specimens, which showed that among the three types of PVA fibers, fiber PVA-8-0.2 had the best toughening effect, followed by PVA-12-0.04, and PVA-12-0.2 was the worst.

Compared with the specimen S1.3PET0.5-30a, the fracture energy of S1.3PET0.5-30b was reduced by 47.99%. The reasons were also that the diameter of fiber PET-30-0.9 was too thick, the number of fibers contained in the section of the same area was reduced, and the bonding force between the fiber and the matrix was reduced, resulting in the decrease in fracture energy.

Compared with other non-metallic fibers, the fracture energy of all steel fiber–PVA hybrid fiber-reinforced UHPC was very high, indicating that PVA fiber had a good toughening effect due to its relatively high elastic modulus, tensile strength, and excellent dispersion. In addition, the fracture energy of the specimen S1.3PET0.5-30a was also higher, which reflected the good toughening effect of the fiber PET-30-0.75.

The fracture energy of all hybrid fiber-reinforced UHPC was lower than that of specimen S1.8, indicating that steel fiber played an important role in strengthening and toughening in the whole process of specimen tension. However, high steel fiber content would increase the cost and reduce the workability. When the crack width of steel fiber was small, the crack resistance and reinforcement effect were obvious. When the deformation was large, the steel fiber would slip obviously, and the toughening effect was reduced. Through the above test results, it can be found that the hybrid of steel fiber and non-metallic fiber can complement the advantages of each other, give full play to the strengthening and toughening effect of different varieties and different sizes of fibers, not only improve the fracture energy and toughness of UHPC but also reduce the preparation cost, and promote the development of UHPC preparation technology and engineering application.

### Characteristic Length

The characteristic length $L_{ch}$ (Deng et al., 2009) proposed by Hillerborg is usually used to express the brittle fracture performance of concrete, and

$$L_{ch} = \frac{E_t G_F}{(f_t)^2} \quad (7)$$

where the units of $L_{ch}$ and $E_t$ are mm and GPa, respectively, and the units of $G_F$ and $f_t$ are N/m and MPa, respectively. The smaller the $L_{ch}$, the more brittle the material.

The calculation results of the characteristic lengths of different specimens are listed in **Table 5**. The plain UHPC specimen S0 had a brittle fracture, and the characteristic length was not considered. In the specimens with single steel fiber, when the content of steel fiber increased from 1.3% to 1.8%, the characteristic length of UHPC increased by 222.73%, which showed that steel fiber had a significant toughening effect on UHPC and reduced the brittleness of the material.

Compared with the specimen S1.3, the characteristic lengths of the specimens S1.3PP0.5-40, S1.3PVA0.5-12a, S1.3PVA0.5-8, S1.3PVA0.5-12b, S1.3PET0.5-30a, S1.3PET0.5-30b, and S1.3B0.5-12 were increased by 64.83%, 167.80%, 209.33%, 200.36%, 17.36%, 259.39%, and 50.12%, respectively. The average characteristic length of ordinary mortar was 110 mm, the average characteristic length of ordinary concrete and polypropylene fiber concrete were 600 and 650 mm, respectively, the characteristic length of engineered cementitious composite (ECC) was between 1,405 and 3,461 mm (Deng et al., 2009), and the characteristic length of hybrid fiber-reinforced UHPC was between 19,700.21 and 60,542.86 mm, which reflected the good toughness of hybrid fiber-reinforced UHPC. The reason was that hybrid fiber had good crack control ability, delayed the development of cracks, and prevented the extension of macrocracks.

## Superficial Microstructure Characteristics of Different Fibers

The observation results of the microstructure morphology of UHPC by scanning electron microscope (SEM) is shown in

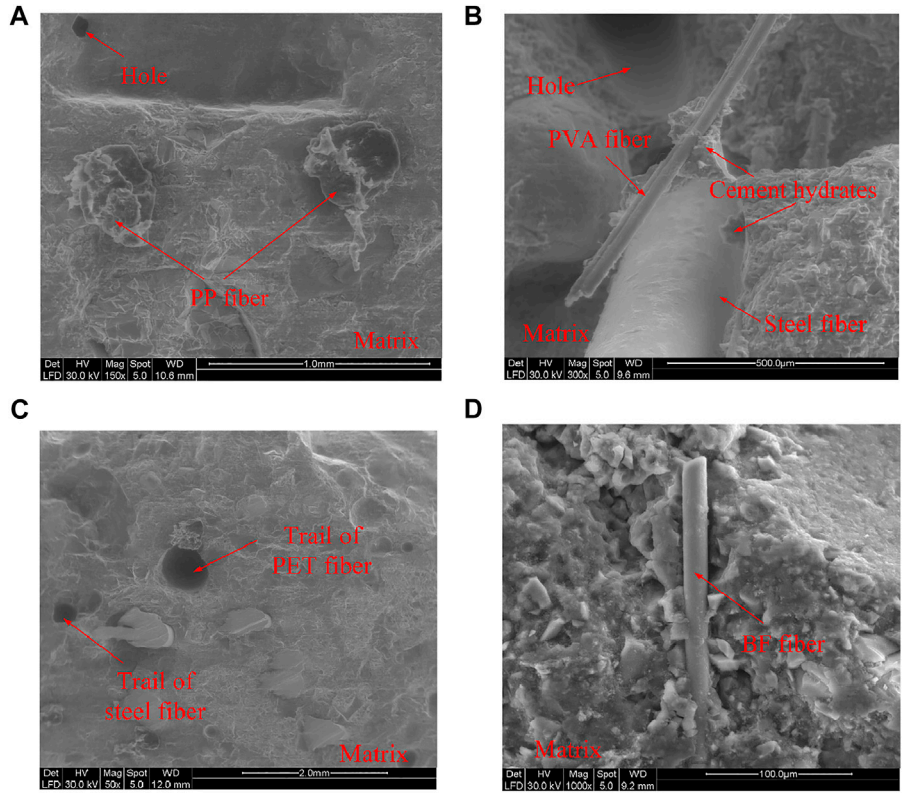


**FIGURE 10 |** (SEM) observations of matrix and different fiber interfaces in UHPC. **(A)** PP fiber. **(B)** PVA fiber. **(C)** PET fiber. **(D)** BF fiber.

**Figure 10**. Due to the low water/binder ratio, the hardened UHPC matrix was quite dense. In **Figure 10A**, the PP fibers were fully bonded with the matrix, giving full play to the bridging effect in the failure process, and delaying the expansion of local macrocracks. In **Figure 10B**, the steel fiber had a smooth surface and a small number of hydration products on the surface, which meant that the interfacial bonding strength between the matrix and the steel fiber was weak. The weaker bond strength and the higher tensile strength of steel fibers made it easier for steel fibers to pull out rather than rupture. PVA fiber had good hydrophilicity, and a large number of hydration products can be observed on the surface of the PVA fiber. These hydration products ensured better adhesion between PVA fiber and the UHPC matrix. In the early stage of failure, the PVA microfiber can effectively play the bridging role and delay the further development of microcracks. With the increase inf specimen deformation, microcracks became macrocracks. Because of its thicker diameter and longer length, steel fiber can effectively prevent the propagation of macrocracks and improve the ductility of materials until most of the steel fibers were pulled out. In **Figure 10C**, because of its large size, the PET fiber was similar to the PP fiber, mainly bridging macrocracks, and finally, most PET fibers were pulled out or ruptured. In **Figure 10D**, BF fibers were well wrapped by the UHPC matrix, which showed that BF fiber and UHPC matrix had a strong mechanical bite effect, closely bonded, and give full play to the bridging effect. In addition, BF fiber had the most obvious reinforcing effect because of its fine diameter and high elastic modulus.

## CONCLUSION

In this paper, 10 groups of tensile specimens were designed, including 7 groups of hybrid fiber-reinforced UHPC specimens, 2 groups of single-doped steel fiber UHPC specimens, and 1 group of plain UHPC specimens. Seven kinds of non-metallic fiber and steel fiber were selected to carry out experimental research and theoretical analysis on different kinds, different diameters, and different lengths of non-metallic fiber–steel fiber hybrid-reinforced UHPC. The main conclusions are as follows:

1) The addition of different non-metallic fibers would reduce the compressive strength of UHPC. The reason may be that fibers of different types and sizes were dispersed unevenly in the UHPC matrix, adding to some of the original defects.
2) Hybrid fiber-reinforced UHPC tensile specimens can still bear the load after cracking, showing good ductile failure characteristics, reflecting the good crack resistance and toughening effect of different fibers.
3) The tensile stress–strain curves of UHPC with different hybrid fibers can be divided into two parts: ascending

section and softening section. Among them, the softening section was greatly affected by the type and content of fiber.

4) Some microfibers such as PVA-12-0.04 and BF-12-0.02 had an obvious reinforcing effect on the UHPC matrix, the tensile strength and peak strain of the specimen were improved. Fiber BF-12-0.02 had a fine diameter and high elastic modulus, and the reinforcement effect was the most significant.
5) Compared with the single-doped steel fiber specimen S1.3, the fibers PVA-12-0.04, PVA-8-0.2, PVA-12-0.2, PET-30-0.75, and BF-12-0.02 were added respectively, the fracture energy of the specimen was increased by 53.88%–187.07%, which reflected its good toughening effect. Among the three PVA fibers of different sizes, the fiber PVA-8-0.2 had the best toughening effect; the diameter of the coarse PET fiber should not be greater than 0.75 mm; too coarse a diameter can reduce the bonding force between fiber and matrix reducing the fracture energy.
6) The hybrid of steel fiber and non-metallic fiber can complement the advantages of each other, give full play to the strengthening and toughening effects of different varieties and sizes of fibers, not only improve the fracture energy and toughness of UHPC but also reduce the preparation cost, and promote the development of UHPC preparation technology and engineering application.

## DATA AVAILABILITY STATEMENT

The original contributions presented in the study are included in the article/Supplementary Material. Further inquiries can be directed to the corresponding author.

## AUTHOR CONTRIBUTIONS

JL conceptualized the study, formulated the methodology, performed the software and formal analysis, conducted data curation, and wrote and prepared the original draft. ZD reviewed and edited the manuscript, supervised the study, was in charge of the project administration, and acquired the funding. All authors have read and agreed to the published version of the manuscript.

## FUNDING

This research was performed under a grant from the Beijing Municipal Education Committee funding project (Grant No. KZ201810005008).

## ACKNOWLEDGMENTS

The authors would like to thank the Beijing Municipal Education Committee funding project (No. KZ201810005008) for supporting the present work.

## REFERENCES

Ahmed, S. F. U., and Mihashi, H. (2011). Strain Hardening Behavior of Lightweight Hybrid Polyvinyl Alcohol (PVA) Fiber Reinforced Cement Composites. *Mater. Struct.* 44, 1179–1191. doi:10.1617/s11527-010-9691-8

Banyhussan, Q. S., Yıldırım, G., Bayraktar, E., Demirhan, S., and Şahmaran, M. (2016). Deflection-hardening Hybrid Fiber Reinforced concrete: the Effect of Aggregate Content. *Construction Building Mater.* 125, 41–52. doi:10.1016/j.conbuildmat.2016.08.020

Cai, Z., Liu, F., Yu , J., Yu, K., and Tian, L. (2021). Development of ultra-high ductility engineered cementitious composites as a novel and resilient fireproof coating. Construction Building Mater 288, 123090. doi:10.1016/j.conbuildmat.2021.123090

Chang, J., Cui, K., and Zhang, Y. (2020). Effect of Hybrid Steel Fibers on the Mechanical Performances and Microstructure of Sulphoaluminate Cement-Based Reactive Powder concrete. *Construction Building Mater.* 261, 120502. doi:10.1016/j.conbuildmat.2020.120502

Chun, B., and Yoo, D.-Y. (2019). Hybrid Effect of Macro and Micro Steel Fibers on the Pullout and Tensile Behaviors of Ultra-high-performance concrete. *Composites B: Eng.* 162, 344–360. doi:10.1016/j.compositesb.2018.11.026

Deng, F., Xu, L., Chi, Y., Wu, F., and Chen, Q. (2020). Effect of Steel-Polypropylene Hybrid Fiber and Coarse Aggregate Inclusion on the Stress-Strain Behavior of Ultra-high Performance concrete under Uniaxial Compression. *Compos. Structures* 252, 112685. doi:10.1016/j.compstruct.2020.112685

Deng, Z., Xue, H., Li, P., and Zhang, P. (2009). Uniaxial Tensile Mechanical Properties of High Ductile Fiber Reinforced Cementitious Composites. *J. Beijing Univ. Tech.* 35 (9), 1204–1208. (In Chinese).

Fantilli, A. P., Kwon, S., Mihashi, H., and Nishiwaki, T. (2018). Synergy Assessment in Hybrid Ultra-high Performance Fiber-Reinforced concrete (UHP-FRC). *Cement and Concrete Composites* 86, 19–29. doi:10.1016/j.cemconcomp.2017.10.012

Gong, T., Curosu, I., Liebold, F., Vo, D. M. P., Zierold, K., Maas, H.-G., et al. (2020). Tensile Behavior of High-Strength, Strain-Hardening Cement-Based Composites (HS-SHCC) Reinforced with Continuous Textile Made of Ultra-high-molecular-weight Polyethylene. *Materials.* 13, 5628. doi:10.3390/ma13245628

Guo, H., Tao, J., Chen, Y., Li, D., Jia, B., and Zhai, Y. (2019). Effect of Steel and Polypropylene Fibers on the Quasi-Static and Dynamic Splitting Tensile Properties of High-Strength concrete. *Construction Building Mater.* 224, 504–514. doi:10.1016/j.conbuildmat.2019.07.096

He, J., Chen, W., Zhang, B., Yu, J., and Liu, H. (2021). The Mechanical Properties and Damage Evolution of UHPC Reinforced with Glass Fibers and High-Performance Polypropylene Fibers. *Materials* 14, 2455. doi:10.3390/ma14092455

Kang, S., Choi, J., Koh, K., Lee, K., and Lee, B. (2016). Hybrid Effects of Steel Fiber and Microfiber on the Tensile Behavior of Ultra-high Performance concrete. *Compos. Struct.* 145, 37–42. doi:10.1016/j.compstruct.2016.02.075

Kang, S., Lee, K., Choi, J., Lee, Y., Felekoglu, B., and Lee, B. (2016). Control of Tensile Behavior of Ultra-high Performance concrete through Artificial Flaws and Fiber Hybridization. *Int. J. Concr. Struct. Mater.* 10 (3), 33–41. doi:10.1007/s40069-016-0155-6

Kim, D. J., Park, S. H., Ryu, G. S., and Koh, K. T. (2011). Comparative Flexural Behavior of Hybrid Ultra High Performance Fiber Reinforced concrete with Different Macro Fibers. *Construction Building Mater.* 25, 4144–4155. doi:10.1016/j.conbuildmat.2011.04.051

Kim, M.-J., Kim, S., and Yoo, D.-Y. (2018). Hybrid Effect of Twisted Steel and Polyethylene Fibers on the Tensile Performance of Ultra-high-performance Cementitious Composites. *Polymers* 10, 879. doi:10.3390/polym10080879

Kim, M., Yoo, D., and Yoon, Y. (2019). Effects of Geometry and Hybrid Ratio of Steel and Polyethylene Fibers on the Mechanical Performance of Ultra-high-

performance Fiber-Reinforced Cementitious Composites. *J. Mater. Res. Technol.* 8 (2), 1835–1848. doi:10.1016/j.jmrt.2019.01.001

Kobayashi, K., and Cho, R. (1982). Flexural Characteristics of Steel Fibre and Polyethylene Fibre Hybrid-Reinforced concrete. *Composites* 13, 164–168. doi:10.1016/0010-4361(82)90054-4

Li, Y., Yang, E., and Tan, K. (2020). Flexural Behavior of Ultra-high Performance Hybrid Fiber Reinforced concrete at the Ambient and Elevated Temperature. *Constr. Build. Mater.* 250, 118487. doi:10.1016/j.conbuildmat.2020.118487

Özkan, Ş., and Demir, F. (2020). The Hybrid Effects of PVA Fiber and basalt Fiber on Mechanical Performance of Cost Effective Hybrid Cementitious Composites. *Construction Building Mater.* 263, 120564. doi:10.1016/j.conbuildmat.2020.120564

Pan, Z., Wu, C., Liu, J., Wang, W., and Liu, J. (2015). Study on Mechanical Properties of Cost-Effective Polyvinyl Alcohol Engineered Cementitious Composites (PVA-ECC). *Construction Building Mater.* 78, 397–404. doi:10.1016/j.conbuildmat.2014.12.071

Park, S. H., Kim, D. J., Ryu, G. S., and Koh, K. T. (2012). Tensile Behavior of Ultra High Performance Hybrid Fiber Reinforced concrete. *Cement and Concrete Composites* 34 (2), 172–184. doi:10.1016/j.cemconcomp.2011.09.009

Rashiddadash, P., Ramezanianpour, A., and Mahdikhani, M. (2014). Experimental Investigation on Flexural Toughness of Hybrid Fiber Reinforced concrete (HFRC) Containing Metakaolin and Pumice. *Constr. Build. Mater.* 51, 313–320. doi:10.1016/j.conbuildmat.2013.10.087

Silva, E. R., Coelho, J. F. J., and Bordado, J. C. (2013). Strength Improvement of Mortar Composites Reinforced with Newly Hybrid-Blended Fibres: Influence of Fibres Geometry and Morphology. *Construction Building Mater.* 40, 473–480. doi:10.1016/j.conbuildmat.2012.11.017

Stahli, P., and Mier, J. (2007). Manufacturing, Fibre Anisotropy and Fracture of Hybrid Fibre concrete. *Eng. Fract. Mech.* 74, 223–242. doi:10.1016/j.engfracmech.2006.01.028

Standard for test methods of concrete physical and mechanical properties GB/T 50081-2019 (2019). Beijing, China: China Architecture and Building Press.

Technical specification for fiber reinforced concrete structures CECS (2004). Beijing, China: Planning Press.

Tian, H., Zhang, Y., Ye, L., and Yang, C. (2015). Mechanical Behaviours of green Hybrid Fibre-Reinforced Cementitious Composites. *Constr. Build. Mater.* 95, 152–163. doi:10.1016/j.conbuildmat.2015.07.143

Tran, T., Tran, N., and KIm, D. (2021). Enhancing Impact Resistance of Hybrid Ultra-high-performance Fiber-Reinforced Concretes through Strategic Use of Polyamide Fibers. *Constr. Build. Mater.* 271, 121562. doi:10.1016/j.conbuildmat.2020.121562

Turk, K., Bassurucu, M., and Bitkin, R. (2021). Workability, Strength and Flexural Toughness Properties of Hybrid Steel Fiber Reinforced SCC with High-Volume Fiber. *Constr. Build. Mater.* 266, 120944. doi:10.1016/j.conbuildmat.2020.120944

Yoo, D.-Y., Kim, M. J., Kim, S.-W., and Park, J.-J. (2017). Development of Cost Effective Ultra-high-performance Fiber-Reinforced concrete Using Single and Hybrid Steel Fibers. *Construction Building Mater.* 150, 383–394. doi:10.1016/j.conbuildmat.2017.06.018

Yoo, D.-Y., Sohn, H.-K., Borges, P. H. R., Fediuk, R., and Kim, S. (2020). Enhancing the Tensile Performance of Ultra-high-performance concrete through Strategic Use of Novel Half-Hooked Steel Fibers. *J. Mater. Res. Tech.* 9 (3), 2914–2925. doi:10.1016/j.jmrt.2020.01.042

Yoo, D., and Kim, M. (2019). High Energy Absorbent Ultra-high-performance concrete with Hybrid Steel and Polyethylene Fibers[J]. *Constr. Build. Mater.* 209, 354–363. doi:10.1016/j.conbuildmat.2019.03.096

Yoo, D., Kim, S., and Lee, S. (2018). Self-sensing Capability of Ultra-high-performance concrete Containing Steel Fibers and Carbon Nanotubes under Tension. *Sens. Actuators, A.* 276, 125–136. doi:10.1016/j.sna.2018.04.009

Yu, J., Zhang, H., and Qi, Y. (2021). Uniaxial Tensile Test and Numerical Simulation of Hybrid Fiber Reinforced concrete. *IOP Conf. Ser. Earth Environ. Sci.* 643, 012066. doi:10.1088/1755-1315/643/1/012066

Yu, K., McGee, W., Ng, T., Zhu, H., and Li, V. (2021). 3D-printable engineered cementitious composites (3DP-ECC): Fresh and hardened properties. *Cem. Concr. Res.* 143, 106388. doi:10.1016/j.cemconres.2021.106388

Zhao, J., Shi, H., and Lu, X. (2019). *Basic properties and test methods of ultra-high performance concrete*. Beijing: China: Building Materials Press.

**Conflict of Interest:** The authors declare that the research was conducted in the absence of any commercial or financial relationships that could be construed as a potential conflict of interest.

**Publisher's Note:** All claims expressed in this article are solely those of the authors and do not necessarily represent those of their affiliated organizations, or those of the publisher, the editors, and the reviewers. Any product that may be evaluated in this article, or claim that may be made by its manufacturer, is not guaranteed or endorsed by the publisher.

frontiers in Materials

ORIGINAL RESEARCH
published: 30 November 2021
doi: 10.3389/fmats.2021.691342

# Analysis of Biaxial Mechanical Properties and Failure Criterion of Self-Compacting Concrete

*Jun Zhang*[1]*, *Chen Li*[1], *Congxiang Zhu*[1] and *Zhiqing Zhao*[2]

[1]School of Architecture, Yangzhou Polytechnic Institute, Yangzhou, China, [2]School of Art and Architecture, Global Institute of Software Technology, Suzhou, China

Biaxial compression-compression, biaxial tension-compression and compression-shear tests were carried out on self-compacting concrete (SCC) using the rock true triaxial machine and compression-shear hydraulic servo machine to explore the biaxial mechanical properties of SCC. The failure modes and stress-strain curves of SCC under different loading conditions were obtained through experiment. Based on the comparison with the biaxial loading test data of ordinary concrete, the following conclusions are drawn: the failure modes and failure mechanisms under biaxial compression-compression and biaxial tension-compression are similar between SCC and ordinary concrete. Under compression-shear loading, the oblique cracks formed on the lateral surface of the specimen parallel to the shear direction gradually increased and the friction marks on the shear failure section were gradually deepened with the increase of axial compression ratio. The development trend of the stress-strain curve in the principal stress direction was not related to the lateral stress. Under the influence of lateral compressive stress, the principal compressive stress of SCC was increased by 55.78% on average; under biaxial tension-compression, the principal tensile stress of SCC had a maximum reduction of 62.79%; and under the compression-shear action, the shear stress of SCC had a maximum increase of 3.35 times. Compared with the biaxial stress test data of ordinary concrete, it can be seen that the lateral compressive stress had a more significant effect on the principal stress of SCC under biaxial loading. Subsequently, the strength criterion equations of SCC under biaxial loading were proposed based on the principal stress space and octahedral space stress respectively, which have shown good applicability in practice.

**Keywords: self-compacting concrete, biaxial compression-compression, biaxial tension-compression, compression-shear, experimental study, strength criterion**

OPEN ACCESS

***Edited by:***
*Yingwu Zhou,*
*Shenzhen University, China*

***Reviewed by:***
*Zehra Canan Girgin,*
*Yıldız Technical University, Turkey*
*Biao Hu,*
*Shenzhen University, China*
*Yu Zheng,*
*Dongguan University of Technology, China*

***Correspondence:**
*Jun Zhang*
*zhangjun@ypi.edu.cn*

***Specialty section:***
*This article was submitted to Structural Materials, a section of the journal Frontiers in Materials*

***Received:*** *06 April 2021*
***Accepted:*** *01 October 2021*
***Published:*** *30 November 2021*

***Citation:***
*Zhang J, Li C, Zhu C and Zhao Z (2021) Analysis of Biaxial Mechanical Properties and Failure Criterion of Self-Compacting Concrete. Front. Mater. 8:691342. doi: 10.3389/fmats.2021.691342*

## 1 INTRODUCTION

Self-compacting concrete (SCC) is a type of high-fluid concrete which can be compacted in engineering applications without applying vibration. It is characterized by the advantages of good workability, high durability and strength, and ability to effectively optimize the construction environment. Particularly, for the excellent applicability in structures with difficulties in construction and pouring, SCC has shown promising research values and engineering application prospects (Zhao et al., 2015; Lazniewska-Piekarczyk, 2016; Pajak et al., 2019; Kandasamy and Kothandaraman 2020; Wang et al., 2020).

To date, the studies on SCC at home and abroad were generally carried out from the perspectives of concrete mix ratio, durability, mechanical properties and structural engineering applications. Okamura and Ozawa (1995) and Dinakar and Manu (2014) proposed the fixed sand volume method and full-calculation method for computing the mix ratio of SCC, respectively. Reiterman et al. (2019) analyzed the influence of different admixture components on the frost resistance of concrete and examined the related mechanisms. Anne-Mieke and de Schutter (2005) analyzed the creep performance of SCC and found that the environment had an important effect on the creep performance. According to Asteris and Kolovos (2019), the compressive and tensile strengths of SCC were similar to those of ordinary concrete at the same water-cement ratio, and the elastic modulus of SCC was similar to that of ordinary concrete at the same strength grade. Klaus and Yvette (2005) investigated the pull-out properties of steel fibers in SCC. Zhu et al. (2001) analyzed the structural applications of SCC and reported a high level of homogeneity. The research on the mechanical properties of SCC is usually conducted by applying conventional loading methods, i.e., compression, tension and flexural resistance. However, in actual concrete structures, concrete is often subjected to multiaxial stress states (Yu et al., 2018a; Ren et al., 2018; Xu et al., 2020). Among the studies on the multiaxial mechanical properties of concrete, the conventional triaxial loading machine is the most commonly used test method, but unfortunately, this machine cannot satisfy the loading conditions with unequal confining pressures. Therefore, the results obtained would be different from the actual engineering conditions, making it difficult to perform multiaxial tensile loading experiment. Comparatively, the true triaxial machine can satisfy multiaxial loading conditions with unequal confining pressures by eliminating the defects of the conventional triaxial machine, so that the results are more consistent with the actual engineering states (Chi et al., 2014; Shi et al., 2014; Yu et al., 2018b). By performing true triaxial experiment, Kupfer (1973) examined the biaxial mechanical properties of concrete and proposed the corresponding strength criterion equation. Fujikake et al. (2000) analyzed the multiaxial mechanical properties of concrete from the perspective of loading strain rate. Guo (1997) studied the multiaxial mechanical properties of concrete and discussed the related stress mechanism by considering different loading paths and loading methods. He and Song (2010) and Shang and Song (2013) investigated the multiaxial mechanical properties of different types of concrete by taking into account the effects of different environmental factors and proposed the corresponding strength criterion and constitutive relation respectively. The changing amplitude of multiaxial mechanical properties under the action of lateral compressive stress is mainly related to the type and composition characteristics of the concrete (Shi et al., 2014).

Since the composition and pouring method of SCC are different from those of ordinary concrete, it may have a certain impact on the changing amplitude of the principal stress of SCC under the action of lateral compressive stress. Regarding the literature on the multiaxial mechanical properties of SCC, Fantilli et al. (2011) used a conventional triaxial machine to examine the multiaxial compressive properties of SCC containing fibers and analyzed the effects of different confining pressures and fiber contents on the triaxial compressive strength and ductility. Mohamed et al. (2019) carried out an experimental study on the mechanical properties of self-compacting steel fiber concrete under biaxial loading by applying the biaxial loading technique; based on the experiment results, they proposed the biaxial failure criterion of self-compacting steel fiber concrete at different steel fiber contents. Zamri et al. (2020) investigated the multiaxial stress state of self-compacting steel fiber concrete in concrete beams and analyzed the stress mechanism of steel fiber in the multiaxial stress state. The existing research on the multiaxial mechanical properties of SCC still has deficiencies, especially when the true triaxial loading method was adopted. Moreover, concrete is not only subjected to multiaxial tension and compression in real-world structures, some structures such as concrete gravity dams, reinforced concrete deep beams and airport roads may also be subjected to multiaxial shear stress conditions. Relevant research has been conducted on the multiaxial shear stress mode of ordinary concrete, but not yet on SCC. A compressive investigation on the multiaxial mechanical properties of SCC can therefore contribute to a better understanding of its multiaxial stress characteristics, so as to facilitate the rational design and control of SCC in practical applications to avoid waste in the usage of materials or safety problems due to insufficient usage of materials. In view of this, the experimental study on the multiaxial mechanical properties of SCC has important significance and practical values.

This paper mainly aims to examine the mechanical properties of SCC under biaxial loading by considering different axial compression ratios. The true triaxial testing machine and the material compression-shear hydraulic servo machine were used to carry out biaxial compression-compression, biaxial tension-compression and compression-shear loading tests respectively. From the experiment, the failure modes and stress-strain curves under different loading conditions were obtained. Then, by extracting the characteristic values from the stress-strain curves and comparing with the biaxial loading test data of ordinary concrete, the biaxial mechanical properties of SCC were analyzed in detail and the corresponding failure criterion equations were proposed. The findings of this study are of great significance to the calculation and applications of SCC in engineering practice.

# 2 EXPERIMENT PROGRAM

## 2.1 Specimen Design

This experimental study was conducted using specimens of Grade SCC30. Of the various raw materials, the cement is ordinary Portland cement P.O 42.5; the coarse aggregates are natural gravel aggregates with the particle size ranged 4–16 mm; the fine aggregates are natural river sands with a fineness modulus of 2.5 and an apparent density of 2650 kg/m$^3$. Considering the specific characteristics of SCC, a certain amount of fly ash

powders and high-efficiency water reducer (i.e., naphthalenesulfonic acid formaldehyde condensate water reducer) were added into the concrete mixture to improve the overall performance. When the proportion of water reducer is around 1% of the cement content, the water reduction efficiency is about 20%. The mix ratio of SCC specimens was determined according to the "Technical specification for application of self-compacting concrete" (JGJ/T 283-2012). Specifically, each cubic meter of concrete contains 300 kg of cement, 123 kg of water, 865 kg of coarse aggregates, 781 kg of fine aggregates, 200 kg of fly ash and 3.20 kg of water reducer.

The pouring method of SCC in this study was different from that of ordinary concrete and was determined according to the "Technical specification for application of self-compacting concrete" (JGJ/T 283-2012) in this study. The specific process is as follows: 1) pour the cement, fine aggregates and mineral powders into the mixer according to the specified ratio for initial stirring; 2) pour water and water reducer into the mixture for the second round of stirring; 3) after stirring evenly, pour coarse aggregates into the mixture for the third round of stirring; 4) after stirring evenly, pour the mixture into mold and demold after 24 h; 5) place the specimen into the standard curing room for 28 days before the experiment.

The SCC mixture in this study was a newly prepared mixture. Its working performance was tested according to the European EFNACR2005 standard. The test results of the slump expansion and L-groove pass rate indicated that the specimens used in the experiment met the relevant requirements specified by EFNACR2005 Grade II SCC and had good working properties.

## 2.2 Loading Program

The biaxial loading program in this study mainly considered three loading methods: biaxial compression-compression, biaxial tension-compression and compression-shear. The biaxial compression-compression and biaxial tension-compression loading methods are composed of eight different lateral compressive stress values (0, 2, 4, 6, 8, 10, 12 and 14 MPa) and were applied by the constant lateral loading mode. That is, the lateral compressive stress was applied first to load the confining pressure. When the lateral stress reached the pre-specified value, the compressive stress in the principal direction (or the principal tensile stress/shear stress) was loaded until failure. The multiaxial compression-shear loading method is composed of eight different axial compression ratios (ξ) which were determined by the uniaxial compressive strength $f_c$ of SCC in this study (0, 3, 6, 9, 12, 15, 20 and 30%$f_c$). Its loading process is similar to that of biaxial compression-compression and biaxial tension-compression. By referencing to the related literature (Dinakar and Manu, 2014) and the machine restrictions, the SCC specimens were designed to be 100 mm × 100 mm × 100 mm cubes in this study. The biaxial loading methods are shown in **Figure 1**. In view of the randomness and discreteness of concrete materials, three specimens were prepared and tested for each loading condition, and the mean values were calculated for analysis.

The biaxial compression-compression loading method is shown in **Figure 1A**. Firstly, the lateral compressive stress was applied in the X direction to exert the confining pressure through the force control loading method at the rate of 0.05 MPa/s. After the load reached the designed confining pressure, the principal compressive stress was then applied in the Z direction through the displacement control loading method at the rate of 0.8 mm/min. The biaxial tension-compression loading method was similar to earlier related studies. Firstly, the lateral compressive stress was applied in the Z direction at the same loading rate as biaxial compression-compression. After the load reached the designed confining pressure, the split load was applied in the X direction, so as to form the tensile stress in the Y direction and eventually the biaxial tension-compression loading condition. The detailed loading method is shown in **Figure 1B**. The loading rate of principal tensile stress is the same as that of the principal compressive stress of biaxial compression-compression, which met the loading requirements of the experiment (Tschegg et al., 2015; Yu et al., 2019).

The multiaxial compression-shear loading method is shown in **Figure 1C**, and the load was applied by the constant lateral loading method. Specifically, the axial load was applied first at the loading rate of 0.05 MPa/s, and after the axial load reached the specified axial compression ratio, the shear load would be applied. The shear load was applied using the displacement control method at the rate of 0.8 mm/min until the specimen failed and the shear load became stable.

Biaxial compression-compression and biaxial tension-compression were loaded using a rock true triaxial machine (**Figure 2A**). This machine has three loading actuators that are perpendicular to one another, and each loading actuator is equipped with independent load sensors and a deformation measuring device. The sensitivity and error range of the load sensors meet the corresponding test requirements. The biaxial tension-compression load exerts a confining pressure in the Z direction and the split-tensile instrument exerts a split-tensile load in the X direction, so as to realize the loading program as shown in **Figure 2B**. In this study, the SCC biaxial compression-compression and biaxial tension-compression test methods have been evaluated according to the EN/ASTM standards. Combined with the true triaxial biaxial compression-compression and biaxial tension-compression test methods in the relevant literature, the methods adopted are able to obtain the load and deformation parameter values in the loading process to satisfy the specified research needs (Chi et al., 2014; He and Song, 2018).

The compression-shear loading of SCC was applied by a material compression-shear hydraulic servo machine. This machine is equipped with independent load sensors and displacement sensors in the axial direction and transverse shear direction. The error ranges of the load sensors and displacement sensors are compliant with the corresponding test requirements. The loading equipment is shown in **Figure 2C**. The compression-shear test equipment used in this study is able to eliminate the rotation effect and bending effect in the compression-shear testing process, so as to meet the specific test requirements (Yu et al., 2018a).

When applying the multiaxial load on the concrete specimen, it is necessary to implement anti-friction measures on the confining pressure surface, because the friction between the confining pressure surface and the contact surface of the specimen has a significant impact on the load measurement of the principal stress direction. If anti-friction measures were not taken, the obtained load results in the principal stress direction

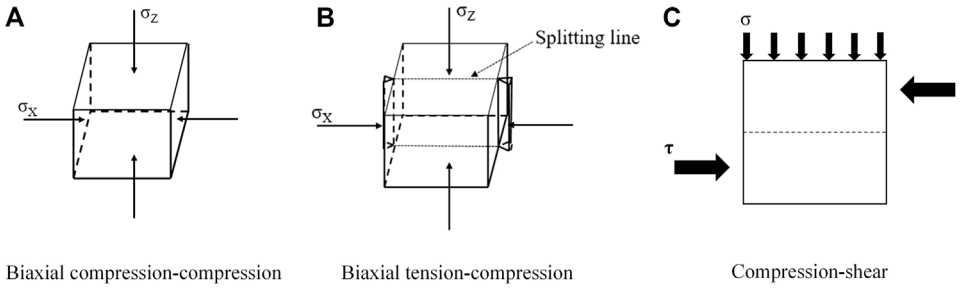


**FIGURE 1 |** Biaxial loading schematic diagram of SCC. **(A)** Biaxial compression-compression. **(B)** Biaxial tension-compression. **(C)** Compression-shear.

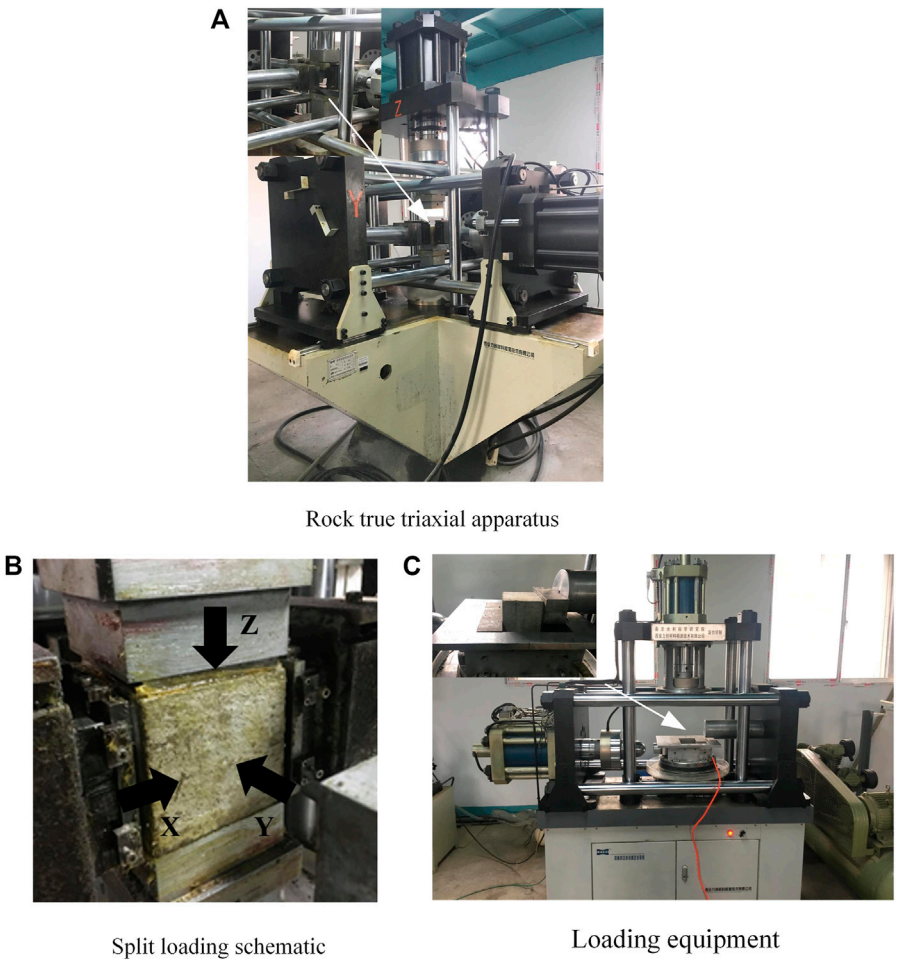


**FIGURE 2 |** Experiment equipment and loading method. **(A)** Rock true triaxial apparatus. **(B)** Split loading schematic. **(C)** Loading equipment.

would be subjected to the friction effect and might be twice or even several times larger than the actual results. By referencing to the related literature on the biaxial compression-compression and biaxial tension-compression tests, the combination of three-layer PTFE film and mechanical butter was adopted as the anti-friction measure (i.e., an appropriate amount of mechanical butter was applied between the film layer and layer, between the film and the specimen loading surface, and between the film and the equipment loading surface) in this study to meet the test requirements (He and Song, 2010; Shang and Song, 2013). For the multiaxial compression-shear loading method, rolling balls were generally used to control the impact of friction on the test results. The experiment program aforementioned can be simplified into a flowchart as shown in **Figure 3**.

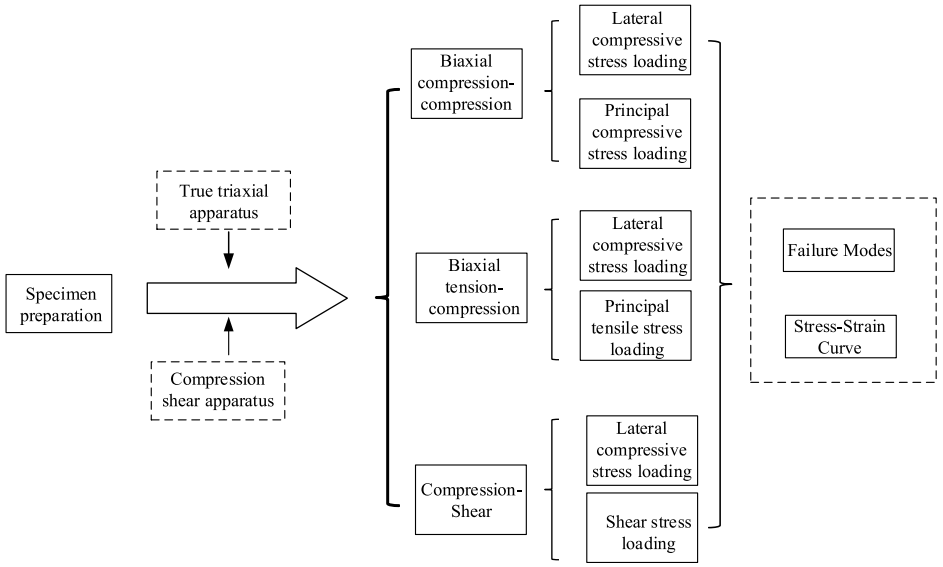


**FIGURE 3 |** The biaxial loading experiment program of SCC.

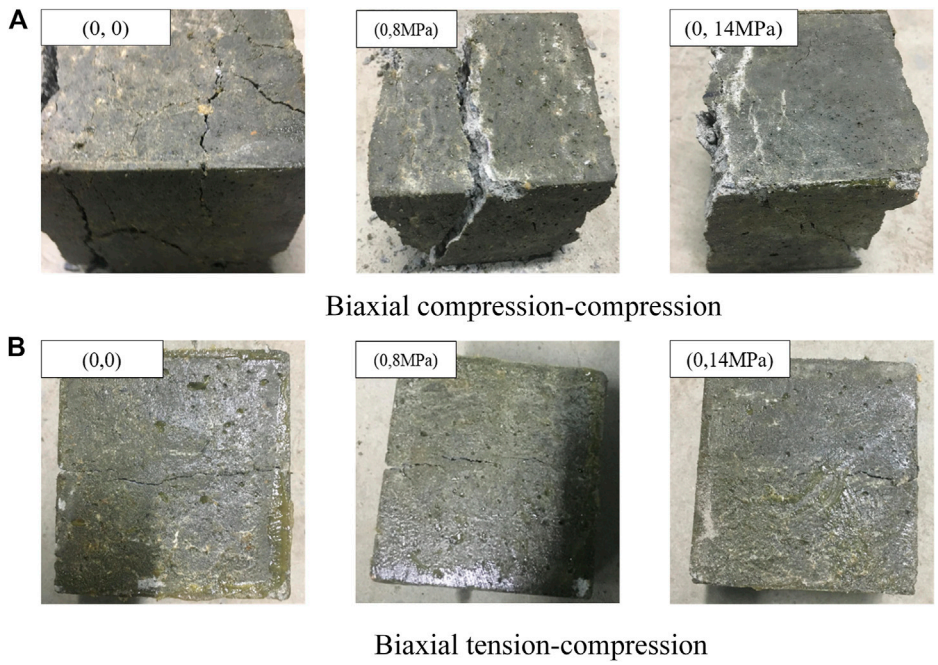


**FIGURE 4 |** SCC failure modes under biaxial loading. **(A)** Biaxial compression-compression. **(B)** Biaxial tension compression.

# 3 ANALYSIS OF TEST RESULTS

## 3.1 Failure Mode

According to the experiment program described above, the rock true triaxial machine and the material compression-shear hydraulic servo machine were used to obtain the failure modes of SCC under different loading conditions. Then, the influences of different loading conditions on the mechanical properties of SCC were examined by analyzing the failure modes of the specimens from a macroscopic perspective. In view of space limitation, this paper chose the lateral compressive stresses of 0, 8 and 14 MPa as the examples for the analysis of biaxial compression-compression and biaxial tension-compression loading conditions, and chose the axial compression ratios of 0, 6, 15 and 30% as the examples for the analysis of the compression-shear failure mode, as shown in **Figures 4–6**.

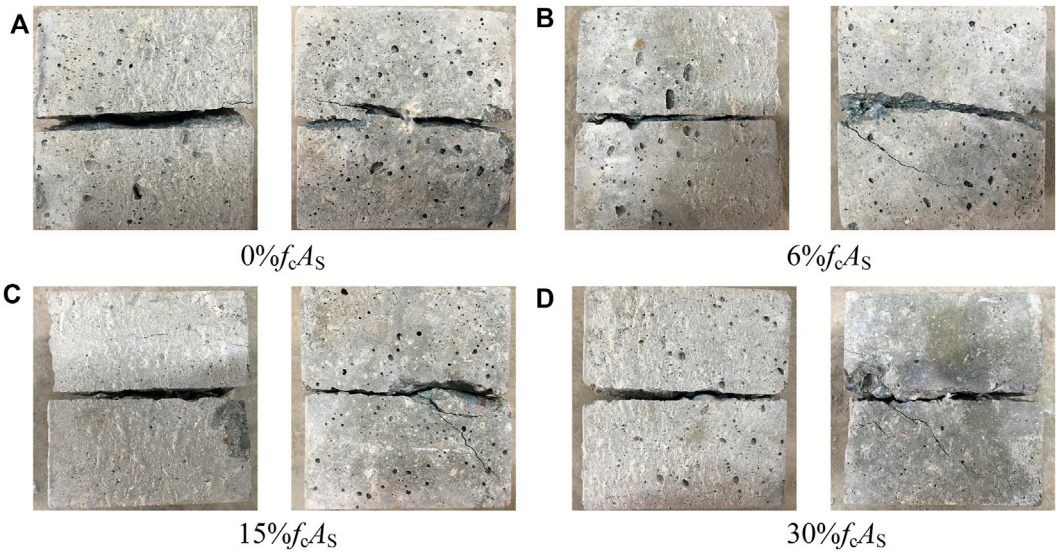


**FIGURE 5 |** Shear failure modes of SCC under different axial loads. **(A)** 0%fcAS. **(B)** 6%fcAS. **(C)** 15%fcAS. **(D)** 30%fcAS.

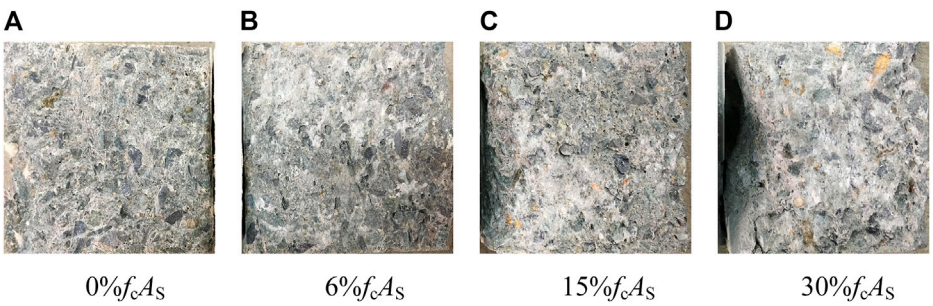


**FIGURE 6 |** Failure modes on the shear failure section of SCC under different axial loads. **(A)** 0%fcAS. **(B)** 6%fcAS. **(C)** 15%fcAS. **(D)** 30%fcAS.

**Figure 4A** shows the biaxial compression-compression failure mode of SCC. When the lateral compressive stress was 0 MPa, the specimen formed a penetrating-crack failure mode with the cracks evenly distributed on the non-loading surface. When the lateral stress was small, the biaxial compression-compression failure mode of SCC was similar to the failure mode under 0 MPa lateral stress. As the lateral compression stress increased, the specimen would gradually develop and form a flaky splitting failure mode. When the lateral compressive stress was increased to 8 MPa, the SCC specimen would begin to show a flaky failure mode. With the further increase of the lateral compressive stress, the number of flaky blocks increased continuously, and more concrete blocks would fall off from the specimen. When the lateral compressive stress was further increased to 14 MPa, the failure mode as shown in **Figure 4A** (0, 14 MPa) was generated. Correspondingly, there were a large amount of flaky blocks falling off from the surface of the specimen and the integrity of the specimen was weakened. The mechanism of biaxial compression-compression failure of SCC can be explained as follows. First, the axial compressive stress formed a tensile strain in the vertical direction of the non-loading surface under the action of the Poisson's ratio effect. When the lateral compressive stress was small, the lateral loading surface was mainly subjected to tensile strain, and the specimen would eventually form the failure mode similar to that under uniaxial compression. When the lateral compressive stress was large, the vertical direction of the lateral loading surface of the specimen would form a compressive strain, and only the vertical direction of the non-loading surface would form a tensile strain. Eventually, the specimen would develop the flaky splitting failure mode. The pattern of this failure mode is similar to that of ordinary concrete under biaxial compression-compression, but the difference is that, when the lateral compressive stress is large, the flaky failure of ordinary concrete is basically vertical, while that of SCC shows an oblique development pattern. The biaxial tension-compression failure mode of SCC is shown in **Figure 4B**. Under different lateral compressive stresses, all the SCC specimens showed a splitting failure mode, and a penetrating and basically straight fracture line was formed. The specimens were broken into two parts after failure, and the failure mode was

not related to the value of the lateral compressive stress. For the specific failure mechanism, when the splitting direction of the SCC specimen reached the ultimate tensile strain, the tensile fracture failure mode would occur. According to the relevant literature, the biaxial tension-compression failure mode of ordinary concrete showed a similar pattern and development trend to that of SCC (Guo 1997; Yu et al., 2019).

**Figure 5** shows the failure modes on the specimen surfaces perpendicular to the shear loading direction and parallel to the loading direction of SCC respectively under different axial compression ratios. The failure line perpendicular to the shear direction was of a straight pattern, which was mainly caused by the loading action of the upper and lower shear boxes of the test machine. This failure mode was not affected by the axial compression ratio. The shear fracture line parallel to the shear direction showed a fluctuating pattern compared to that of the vertical loading direction. This is mainly due to the fact that the specimen would form initial cracks under the loading action of the upper and lower shear boxes. As the shear load increased, the cracks would develop along the shear direction through the weak areas in the mortar and coarse aggregates. Since these weak areas were not completely in a straight line, eventually, the failure mode as shown in **Figure 5** was formed. At the same time, as the axial compression ratio increased, the number of oblique cracks on the lateral surface of the specimen that is parallel to the shear loading direction would gradually grow. This is because when shear failure occurred, oblique cracks could be easily formed on the lateral surface parallel to the shear direction affected by the shear failure section, especially when the axial load was large. With the increase of the axial load, the number of oblique cracks would gradually increase, exhibiting a more obvious damage.

**Figure 6** shows the failure modes on the shear failure section of SCC under different axial compression ratios. When the axial compression ratio was 0, the failure section of the specimen was relatively flat and smooth. When the axial compression ratio began to increase, obvious friction marks would be observed on the shear failure section and a certain amount of concrete slags were generated. As the axial compression ratio increased further, the friction marks on the shear failure section became more obvious and more concrete slags would be generated along with the falling-off of some concrete blocks.

## 3.2 Stress-Strain Curve

The load and deformation data was captured by the load sensors and deformation sensors of the rock true triaxial machine and the material compression-shear hydraulic servo machine. The data of biaxial compression-compression stress was determined by the ratio of the load data acquired from the load sensors to the stress area on the specimen loading surface. The strain data was determined by the ratio of the displacement data acquired from the displacement sensors to the height of the specimen in the loading direction. The data of biaxial tensile-compressive stress was calculated through the load stress conversion equation under split-tensile loading as stipulated in the "Standard for test method of mechanical properties on ordinary concrete" (GB/T 50081-2002). The strain data was determined by the ratio of the deformation data acquired from the displacement sensors in the splitting direction to the height of the specimen in the loading direction. It is noteworthy that the strain data under split-tensile loading in this paper was the nominal strain data rather than the actual tensile strain data of SCC. This paper only aims to examine and analyze the stress characteristic value and stress failure criterion, with no intention to perform quantitative analysis on the strain characteristic value. Therefore, the use of nominal strain data had little effect on the qualitative analysis of the development trend of the stress-strain curve. The shear stress-strain curves of SCC under different axial compression ratios were obtained by the compression-shear hydraulic servo machine. Shear stress refers to the ratio of the shear load to the area of the shear section, and shear strain refers to the ratio of the displacement in the shear direction to the length of the specimen parallel to the shear direction. The principal compressive stress-strain curve and tensile stress-strain curve of SCC under biaxial compression-compression and biaxial tension-compression obtained based on the aforementioned stress and strain data are shown in **Figures 7–9** respectively.

It can be seen from **Figure 7** that the principal compressive stress-strain curve of SCC under biaxial compression-compression had good continuity and smoothness. The development trend of the principal compressive stress-strain curve could be divided into three stages: the elastic stage (i.e., the stress of SCC increased linearly with the increase of strain), the elastoplastic stage (i.e., the stress no longer increased linearly but showed a reduced increasing amplitude with the increase of strain), and the declining stage (i.e., the strain maintained an increasing trend, but the stress began to decrease after reaching its peak value). The development trend of the principal compressive stress-strain curve had no relation with the lateral compressive stress. Compared with ordinary concrete, SCC exhibited obvious brittle failure characteristics. From the overall trend, it can be observed that the principal compressive stress of SCC under lateral compressive stress was higher than that without lateral compressive stress, indicating that the lateral compressive stress had a significant effect on the principal compressive stress. As shown in **Figure 7**, the biaxial compression stress-strain curve was curved to a certain extent in the initial stage. This is mainly because, in the initial stage of loading (for an extremely short period of time), there was a very small gap between the loading surface of equipment and the surface of specimen when the two were just in contact and the specimen had a very small deflection. After the gap was eliminated by compression, the stress-strain curve would show a straight pattern. This curving section of the stress-strain relation basically does not affect the accuracy of the maximum stress value of SCC under different confining pressures.

**Figure 8** shows the principal tensile stress-strain curve of SCC under biaxial tension-compression. The development trend of the principal tensile stress-strain curve under biaxial tension-compression was similar to that under the uniaxial split-tension loading condition, which could be divided into two stages: the elastic stage (i.e., the stress increased linearly with the increase of deformation) and the declining stage (i.e., after the stress reached its peak value, it would decline rapidly to 0 and the specimen would exhibit obvious brittle failure characteristics).

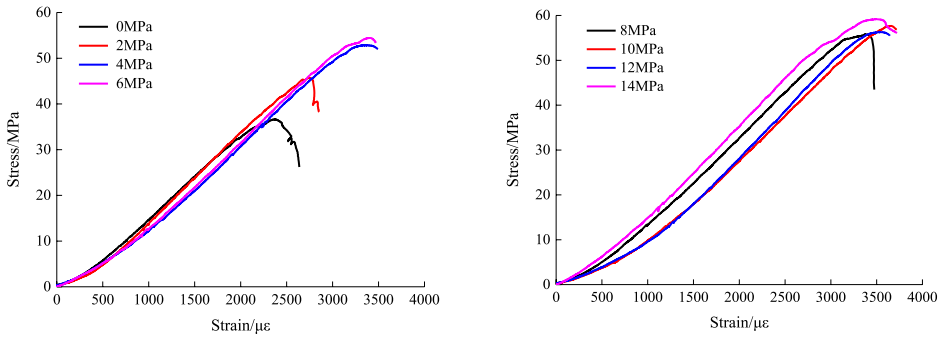


**FIGURE 7 |** The principal compressive stress-strain curve of SCC under biaxial compression-compression.

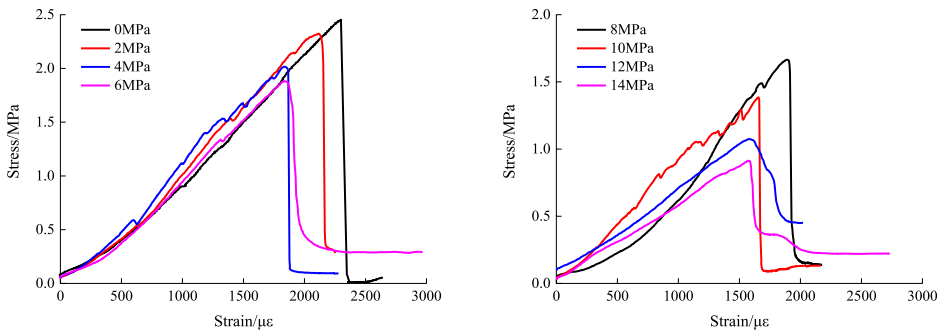


**FIGURE 8 |** The principal compressive stress-strain curve of SCC under biaxial tension-compression.

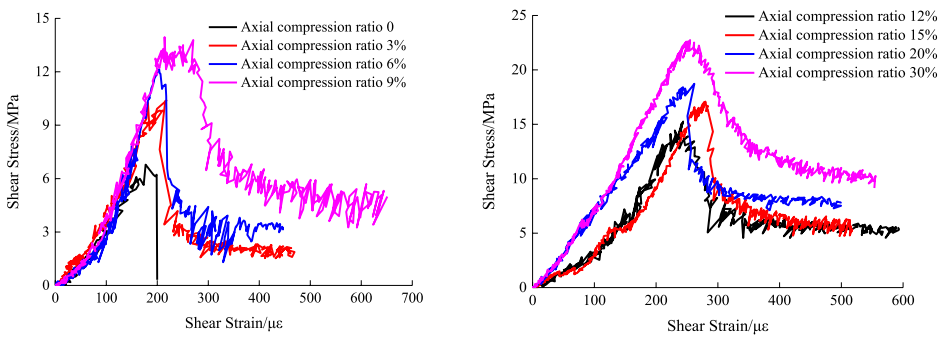


**FIGURE 9 |** Shear stress-strain curves of SCC under different axial compression ratios.

From the development trend, it can be seen that the lateral compressive stress had no effect on the principal tensile stress-strain curve. As the lateral compressive stress increased, the principal tensile stress decreased gradually.

**Figure 9** shows the shear stress-strain curves of SCC under different axial compression ratios. When the axial compression ratio was 0, the shear stress-strain curve could be divided into two stages: the elastic ascending stage and the direct declining stage. When the axial compression ratio began to increase, the development trend of the shear stress-strain curve became obviously different, that is, there was an obvious stress balance stage after the elastic ascending stage and the declining stage, during which the shear stress remained basically unchanged. In the elastic ascending stage, the shear stress was mainly formed by the Van der Waals force, the chemical adhesive force and the mechanical bite force on the shear section of the concrete specimen. More specifically, in the early phase of the elastic ascending stage, the shear stress was mainly formed by the Van der Waals force and the chemical adhesive force on the shear section, while in the late phase of the elastic ascending stage, the shear stress was mainly formed by the chemical adhesive force and the mechanical bite force on the shear section. In the

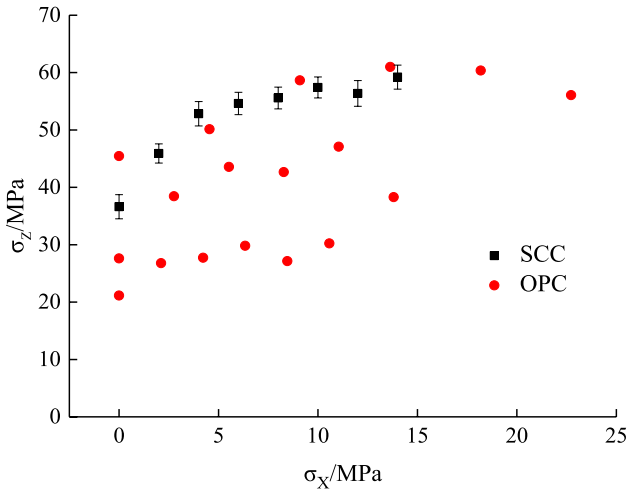


**FIGURE 10 |** The principal compressive stress and lateral compressive stress of SCC.

declining stage of the shear stress-strain curve, the shear stress was mainly caused by the mechanical bite force and the friction force on the shear section. In the stress balance stage of the shear stress-strain curve, the shear stress was mainly formed by the friction force between the shear failure sections. According to a preliminary analysis of **Figure 9**, it can be found that the shear stress and residual stress of SCC increased significantly with the increase of the axial compression ratio.

## 3.3 Analysis of Characteristic Values

### 3.3.1 Analysis of Stress Characteristic Values

The principal stress peak values were extracted from the principal compressive stress-strain curve under biaxial compression-compression, the principal tensile stress-strain curve under biaxial tension-compression and the stress-strain curve under compression-shear loading as shown in **Figures 7–9**, respectively, in order to analyze the influence of lateral compressive stress on the principal stress. Considering the discreteness of the test data and the accuracy of the analysis results, error bars were added to the principal stress data. The midpoint of the error bar was the average of the principal stress values of the three parallel SCC specimens for each loading condition. The length of the error bar was the degree of discreteness of the principal stress of each loading condition. In this study, the average discreteness percentage of the principal compressive stress under biaxial compression-compression was 3.89%, and that of the principal tensile stress under biaxial tension-compression was 6.70%. Referring to the test specifications on the concrete mechanical properties, the analysis requirements were satisfied.

In order to compare with ordinary concrete, a comparative study was carried out between the biaxial loading test data of SCC in this study and the biaxial loading test data of three different strength grades (C30, C40 and C50) of ordinary concrete obtained from the relevant literature (Yu et al., 2019). On the basis of **Figures 7**, **8**, the relations between the principal compressive stress under biaxial compression-compression (principal tensile stress), the shear stress under compression-shear, and the lateral compressive stress of SCC were obtained, as shown in **Figures 10**, **11**.

According to **Figures 10**, **11**, the lateral compressive stress had a significant impact on the principal compressive stress of SCC under biaxial compression-compression. With the increase of the lateral compressive stress, the principal compressive stress under biaxial compression-compression showed a more significant increase than the uniaxial compressive stress. When the lateral compressive stress was 0 MPa, the principal compressive stress of SCC was 36.62 MPa. When the lateral compressive stress was increased to 14 MPa, the principal compressive stress was increased to 59.17 MPa accordingly, suggesting an average increase of 55.78% compared with the uniaxial compressive condition. This is because the mechanical bite force between mortar and coarse aggregates, and between coarse aggregates and coarse aggregates of SCC, were increased with the increase of lateral compressive stress, which eventually led to an increase in the principal compressive stress. Comparatively, under biaxial compression-compression, the average increase in the principal compressive stress of ordinary concrete C30, C40 and C50 affected by the lateral compressive stress was 32.88, 48.75 and 28.63% respectively. With respect to the overall development trend, the lateral compressive stress had a more significant impact on the principal compressive stress of SCC than on that of ordinary concrete under biaxial compression-compression. The similarities between SCC and ordinary concrete are that: when the lateral compressive stress ratio was less than 0.2, the principal compressive stress of both SCC and ordinary concrete changed significantly under the action of lateral compressive stress; when the lateral compressive stress ratio was greater than 0.2, the principal compressive stress of SCC changed stably, suggesting a similar changing trend to that of the principal compressive stress of ordinary concrete affected by the lateral compressive stress under biaxial compression-compression applied through the proportional loading mode (Guo, 1997).

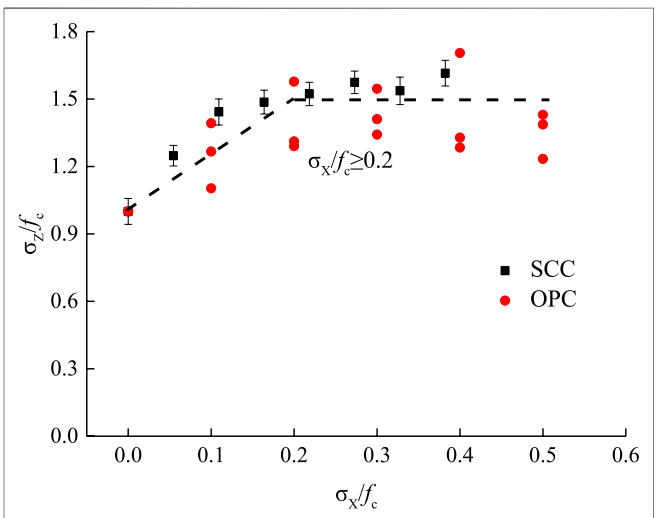


**FIGURE 11 |** The ratio of principal compressive stress and the ratio of lateral compressive stress of SCC.

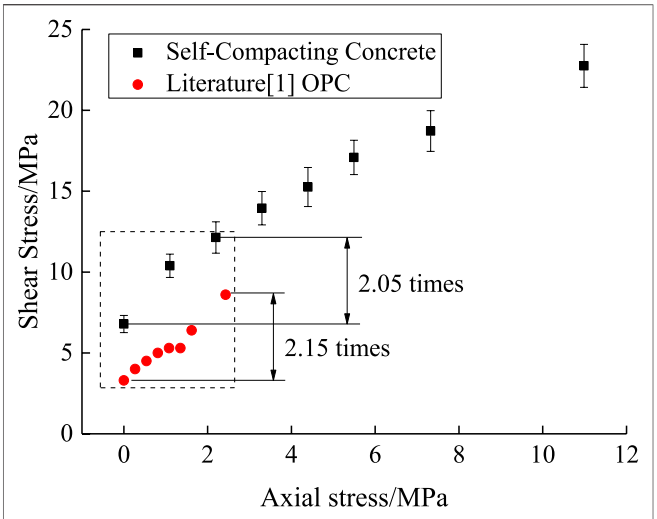


**FIGURE 12 |** The relation between the axial action and shear action of SCC under different axial compression ratios.

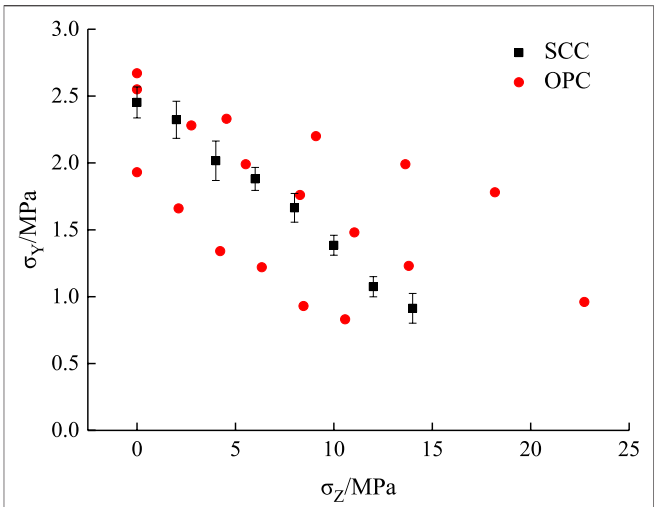


**FIGURE 13 |** The principal tensile stress and lateral compressive stress of SCC.

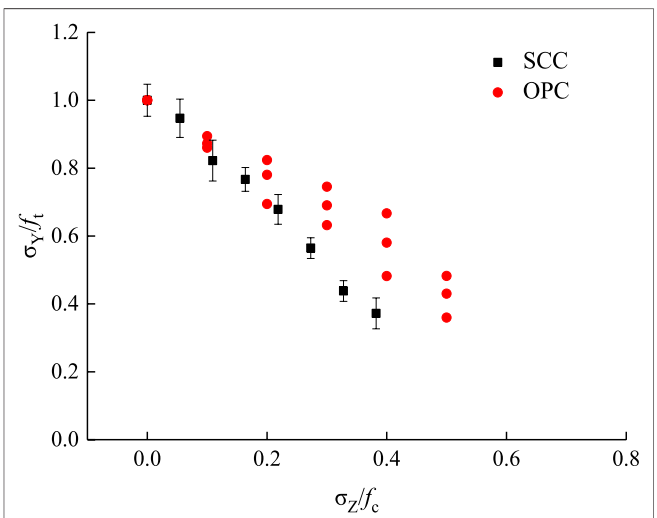


**FIGURE 14 |** The ratio of principal tensile stress and the ratio of lateral compressive stress of SCC.

According to **Figure 12**, when the axial compression ratio was 0, the shear stress of SCC was 6.79 MPa. As the axial compression ratio increased, the shear stress of SCC began to increase gradually. When the axial compression ratio was 9%, the corresponding shear stress was increased to 13.95 MPa, which was 2.05 times higher than that under the axial compression ratio of 0%. Comparatively, the shear stress of ordinary concrete at the axial compression ratio of 9% was increased by 2.15 times relative to the working condition of 0% axial compression ratio. There is basically a similar trend between SCC and ordinary concrete. When the axial compression ratio was 30%, the shear stress of SCC was increased to 22.75 MPa, which was 3.35 times higher than that under the working condition of 0% axial compression ratio.

**Figures 13**, **14** present the changing trend of the principal tensile stress of SCC affected by the lateral compressive stress under biaxial tension-compression. As the lateral compressive stress increased, the principal tensile stress decreased gradually. When the lateral compressive stress was 0 MPa, the principal tensile stress of SCC was 2.45 MPa. When the lateral compressive stress was 14 MPa, the principal tensile stress was decreased to 0.91 MPa, suggesting a decrease of 62.79%. This is mainly because the lateral compressive stress formed a tensile strain in the principal tensile stress direction affected by the Poisson's ratio effect. With the increase of the lateral compressive stress, the tensile strain formed in the principal tensile stress direction would increase gradually. When the principal tensile stress began to apply, the specimen would reach its ultimate tensile strain first and then gradually decrease; eventually, the principal tensile stress would decrease with the further increase of the lateral compressive stress. An earlier study (Yu et al., 2019) reported that the principal tensile stress of ordinary concrete C30, C40 and C50 under biaxial tension-compression was reduced by 51.81, 41.96 and 33.33% respectively under the influence of the lateral compressive stress. It can be seen that the lateral compressive stress had a more significant impact on the principal tensile stress of SCC than on that of ordinary concrete under biaxial tension-compression.

In order to eliminate the impact of different compressive strengths on the test results, the test results were preprocessed by the dimensionless method before analysis. According to **Figure 15**, the increase in the shear stress of SCC affected by the axial compression ratio was similar to that of ordinary concrete. As the axial compression ratio increased, the increasing amplitude of shear stress under the influence of axial compression ratio decreased gradually. This is mainly because the SCC specimen tended to enter the elastoplastic stage under a large axial load. Accordingly, the internal micro-cracks in the specimen began to expand, and the increasing

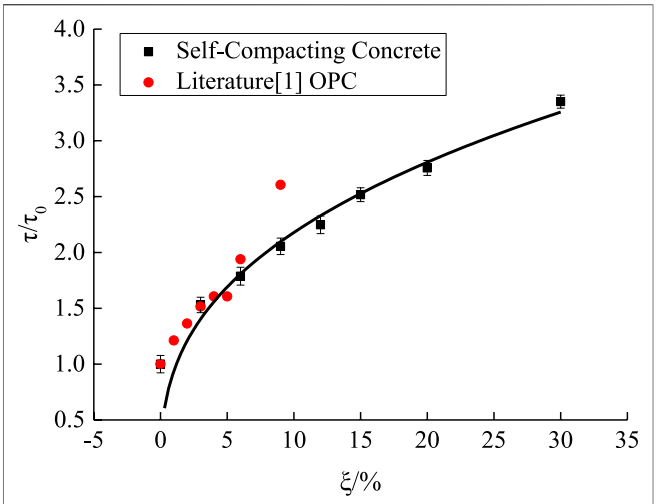


**FIGURE 15 |** The relation between the axial action and shear action of SCC under different axial compression ratios.

amplitude of the shear stress would start decreasing at this moment. By considering the development trend of the relation between the axial compression ratio and the shear stress increase factor ($\tau/\tau_0$), the two were speculated to form a power function relation, as shown in **Eq. 1**.

$$\frac{\tau}{\tau_0} = a \times \xi^b \tag{1}$$

According to the test data in this study, mathematical regression analysis was performed using **Eq. 1** and the results are shown in **Eq. 2** and **Figure 15**. It can be seen that the proposed equation for the relation between the axial compression ratio and the shear stress increase factor of SCC had good applicability to the quantitative stress analysis under the multiaxial compression-shear loading condition.

$$\frac{\tau}{\tau_0} = 0.93801 \times \xi^{0.36602} \quad R^2 = 0.9807 \tag{2}$$

For the stress mechanism under multiaxial compression-shear, the axial loading effect significantly increased the mechanical bite force and friction force between the shear sections of SCC, that is, the shear load gradually increased with the increase of the axial load. When the axial load had increased to the threshold level, the increasing amplitude of shear load would begin to decline. This is because when the axial load was large, the initial internal damage of SCC would evolve greatly and the crack damage would develop rapidly. Consequently, the Van der Waals force and chemical adhesive force on the shear section would be weakened. However, since the axial load would significantly increase the mechanical bite force and friction force between the shear sections, when the axial load reached the threshold value, the increasing amplitude of shear load under the influence of axial compression ratio would start declining with the further increase of the axial load.

The residual stress is mainly formed by the mutual friction between the shear failure sections of the specimen, which can be determined by the friction coefficient between the axial load and the shear failure section. In this study, the residual stress was determined based on the shear stress-strain curve of SCC using the same method as described in the relevant literature (Yu et al., 2018a). The relations between the axial load and the residual load of SCC under different axial compression ratios were obtained as shown in **Supplementary Figure S1**.

Yu et al. (2018a) examined the residual stress of ordinary concrete under the multiaxial compression-shear loading condition and found that the friction coefficient between the shear failure sections of ordinary concrete was 1.46. According to the test data in this study, the relation between the axial load and residual load of SCC was obtained, as shown in **Supplementary Figure S1**. It can be seen that with the increase of the axial load, the residual load of SCC on the shear failure section increased gradually. Based on the test data of SCC under the multiaxial compression-shear loading condition, the friction coefficient of SCC on the shear failure section was calculated by performing mathematical regression analysis, which was 1.107, lower than that of ordinary concrete.

## 4 FAILURE CRITERION

For the multiaxial compression-shear loading method, the shear stress and compressive stress were usually converted into the first principal stress, the second principal stress and the third principal stress through **Eqs 3–5**, in order to analyze the development trend of the multiaxial compressive-shear strength of SCC.

$$\sigma_1 = \frac{\sigma}{2} + \sqrt{\left(\frac{\sigma}{2}\right)^2 + \tau^2} \tag{3}$$

$$\sigma_2 = 0 \tag{4}$$

$$\sigma_3 = \frac{\sigma}{2} - \sqrt{\left(\frac{\sigma}{2}\right)^2 + \tau^2} \tag{5}$$

### 4.1 Plane stress space

For the biaxial loading method of ordinary concrete, Kupfer (1973) put forward the biaxial compression-compression and biaxial tension-compression strength criterion equations under the proportional loading method based on regression analysis of massive experimental data and literature data, as shown in **Eqs 6**, **7**.

$$\left(\frac{\sigma_Z}{f_c} + \frac{\sigma_X}{f_c}\right)^2 - \frac{\sigma_Z}{f_c} - 3.65\frac{\sigma_X}{f_c} = 0 \tag{6}$$

Where: $\sigma_X$ and $\sigma_Z$ refer to the lateral compressive stress in the X direction and the principal compressive stress in the Z direction, respectively (unit: MPa); $f_c$ refers to the uniaxial compressive stress (unit: MPa).

$$\frac{\sigma_Y}{f_t} + 0.8\frac{\sigma_Z}{f_c} = 1 \tag{7}$$

Where: $\sigma_Y$ and $\sigma_Z$ refer to the principal tensile stress in the Y direction and the lateral compressive stress in the Z direction, respectively (unit: MPa); $f_t$ refers to the uniaxial split-tensile stress (unit: MPa).

There has been extensive literature on the analysis of the biaxial stress mode of ordinary concrete under constant lateral loading. It has been argued that the Kupfer strength criterion is relatively conservative in predicting the strength relation under constant lateral loading, which is mainly attributed to the loading method itself, as different loading paths may have a significant impact on the concrete strength criterion. Based on the Kupfer strength criterion, the strength criterion equation of ordinary concrete under the constant lateral loading method was proposed, which showed good applicability to ordinary concrete structures (Yu et al., 2019). According to the analysis of the effect of lateral compressive stress on the principal compressive stress (principal tensile stress) of SCC, the biaxial compression-compression and biaxial tension-compression strength criterion equations for SCC were proposed, as shown in **Eqs 8**, **9**. Meanwhile, a comparative analysis was performed by referring to the test data and the strength criterion of ordinary concrete under the biaxial stress loading method (Yu et al., 2019).

$$\left(\frac{\sigma_Z}{f_c}+\frac{\sigma_X}{f_c}\right)^2+a\frac{\sigma_Z}{f_c}+b\frac{\sigma_X}{f_c}=0 \tag{8}$$

$$\frac{\sigma_Y}{f_t}+c\frac{\sigma_Z}{f_c}=1 \tag{9}$$

Based on the biaxial compression-compression and biaxial tension-compression test data of SCC related to the strength criterion equations as shown in **Eqs 8**, **9**, the biaxial compression-compression and biaxial tension-compression strength criterion equations of SCC were established using mathematical software, as shown in **Eqs 10**, **11** and **Supplementary Figures S2, S3**.

$$\left(\frac{\sigma_Z}{f_c}+\frac{\sigma_X}{f_c}\right)^2-1.01\frac{\sigma_Z}{f_c}-6.43\frac{\sigma_X}{f_c}=0 \tag{10}$$

$$\frac{\sigma_Y}{f_t}+1.614\frac{\sigma_Z}{f_c}=1 \tag{11}$$

From **Eqs 10**, **11**, it can be seen that the biaxial compression-compression and biaxial tension-compression strength criterion equations of SCC proposed based on the Kupfer criterion had good applicability. In addition, according to **Supplementary Figures S2, S3**, the biaxial strength criterion equation of ordinary concrete under constant lateral loading appeared to be conservative in predicting the strength of SCC, that is, the lateral compressive stress had a stronger impact on the principal stress of SCC under biaxial loading than on that of ordinary concrete.

Thus, the multiaxial compression-shear test data of SCC in this paper was converted into the principal stress data using **Eqs 3**–**5**. By comparing with the multiaxial compression-shear test data of ordinary concrete (Yu et al., 2018a), the development trend of the strength of SCC in the plane stress space was obtained, as shown in **Supplementary Figure S4**.

It can be seen from **Supplementary Figure S4** that, with the increase of the first principal stress, the third principal stress of SCC decreased gradually and showed a development trend and changing amplitude similar to those of ordinary concrete. Further, by comparing the principal stress space failure criterion of ordinary concrete under multiaxial compression-shear (Yu et al., 2018a) with the test data of SCC in this paper, the results as shown in **Eq. 12** and **Supplementary Figure S4** were obtained.

$$\frac{\sigma_3}{f_c}=-0.69545\times\left(\frac{\sigma_1}{f_c}\right)-0.03828 \tag{12}$$

According to **Supplementary Figure S4**, the principal stress space failure criterion proposed by Yu et al. (2018a) had deficiencies in predicting the multiaxial compression-shear strength of SCC. When the dimensionless value of the first principal stress was less than 0.4, the principal stress space failure criterion of ordinary concrete would lead to a predicted value that is higher than actual. On the contrary, when the dimensionless value of the first principal stress was higher than 0.4, the principal stress space failure criterion of ordinary concrete would lead to a conservative prediction. In view of the situation above, the multiaxial compression-shear failure criterion equation of SCC was proposed based on **Eq. 11**, as shown in **Eq. 13**.

$$\frac{\sigma_3}{f_c}=a\times\left(\frac{\sigma_1}{f_c}\right)+b \tag{13}$$

The multiaxial compression-shear test data of SCC in this paper was converted into the first principal stress and the third principal stress values. Then, the failure criterion equation of SCC was obtained by performing mathematical regression analysis using **Eq. 13**, as shown in **Eq. 14** and **Supplementary Figure S4**.

$$\frac{\sigma_3}{f_c}=-0.49193\times\left(\frac{\sigma_1}{f_c}\right)-0.11716\ \ R^2=0.97845 \tag{14}$$

According to **Eq. 14** and **Supplementary Figure S4**, the multiaxial compression-shear failure criterion equation of SCC proposed based on the plane stress space had good applicability to engineering practice and could effectively demonstrate the development trend of the strength of SCC under the multiaxial compression-shear loading condition. Compared with ordinary concrete, the third principal stress of SCC showed a smoother changing curve under the influence of the first principal stress.

## 4.2 Octahedral Space Stress

For the examination of the multiaxial stress strength criterion of concrete, the method of using octahedral space stress expression to describe the multiaxial strength pattern has wide applicability in practice (Ottosen 1977). According to the multiaxial stress octahedral space stress of concrete, the failure criterion equation of SCC was established as shown in **Eqs 15**, **16**.

$$\frac{\tau_{oct}}{f_c} = a_1 + b_1\frac{\sigma_{oct}}{f_c} \tag{15}$$

$$\frac{\tau_{oct}}{f_c} = a_2\left(\frac{\sigma_{oct}}{f_c}\right)^2 + b_2\frac{\sigma_{oct}}{f_c} + c_2 \tag{16}$$

Where, the expression of normal stress $\sigma_{oct}$ is shown in **Eq. 17**, and the expression of shear stress $\tau_{oct}$ is shown in **Eq. 18**.

$$\sigma_{oct} = \frac{\sigma_X + \sigma_Y + \sigma_Z}{3} \tag{17}$$

$$\tau_{oct} = \frac{1}{3}\sqrt{(\sigma_Z - \sigma_X)^2 + (\sigma_X - \sigma_Y)^2 + (\sigma_Y - \sigma_Z)^2} \tag{18}$$

The biaxial loading test data of SCC in this paper was converted into the normal stress $\sigma_{oct}$ and shear stress $\tau_{oct}$ through **Eqs 17**, **18** respectively. Then, the octahedral space stress strength criterion of SCC was obtained by performing mathematical regression analysis based on **Eqs 15**, **16** using mathematical software, as shown in **Supplementary Figure S5**.

Based on the octahedral stress space failure criterion equations as shown in **Eqs 15**, **16**, the expressions of biaxial failure criterion of SCC under biaxial loading were obtained by performing mathematical regression analysis on the biaxial loading test data, as shown in **Supplementary Figure S5** and **Eqs 19–22**.

SCC:

$$\frac{\tau_{oct}}{f_c} = -0.94918 - 0.07097\frac{\sigma_{oct}}{f_c} \quad R^2 = 0.96185 \tag{19}$$

$$\frac{\tau_{oct}}{f_c} = 0.86531\left(\frac{\sigma_{oct}}{f_c}\right)^2 - 1.47159\frac{\sigma_{oct}}{f_c} - 0.04776 \quad R^2 = 0.97778 \tag{20}$$

OPC:

$$\frac{\tau_{oct}}{f_c} = -0.05591 - 1.07862\frac{\sigma_{oct}}{f_c} \quad R^2 = 0.9914 \tag{21}$$

$$\frac{\tau_{oct}}{f_c} = 0.29666\left(\frac{\sigma_{oct}}{f_c}\right)^2 - 1.21882\frac{\sigma_{oct}}{f_c} - 0.05843 \quad R^2 = 0.99422 \tag{22}$$

According to the analysis on the octahedral space stress strength criterion of SCC under biaxial loading as shown in **Supplementary Figure S5**, the primary strength criterion equation and the secondary strength criterion equation established for octahedral space stress could effectively reflect the development trend of the strength of SCC under biaxial loading. Compared with the octahedral space stress strength criterion of ordinary concrete, the strength criterion equation of SCC had a greater similarity to that of ordinary concrete under biaxial tension-compression. Under biaxial compression-compression, the difference in the strength criterion equation between SCC and ordinary concrete gradually appeared. Meanwhile, it can be seen from **Supplementary Figure S5** that the lateral compressive stress had a more significant impact on the principal stress of SCC under biaxial loading than that on ordinary concrete.

The plane stress space strength criterion and the octahedral space stress strength criterion of SCC proposed in this paper are two independent and different expressions, with different applicability in the real world. The plane stress space is a special form of expression form for the principal stress space. The principal stress space is constituted based on the first principal stress, the second principal stress and the third principal stress. Under the biaxial loading method, one of the principal stresses is zero, that is, a plane stress space is formed. The strength criterion obtained through the plane stress space has high intuitiveness, and the expression is relatively simple. Corresponding, its applicability is low and is only suitable for biaxial loading and tension/compression-shear loading conditions. For the octahedral space stress, an equal inclined plane is formed on the three principal stress axes through the space evolution of the principal stresses, and the stresses formed on this inclined plane are the normal stress and shear stress (i.e., the octahedral space stress). The failure criterion obtained in this way has high applicability, not only suitable for biaxial loading and tensile/compression shear loading, but also for triaxial loading conditions. The envelope surface of the strength criterion can be simplified by means of the meridian.

Compared with ordinary concrete, the biaxial compressive stress-strain curve of SCC shows more obvious brittleness characteristics. Meanwhile, the lateral stress has a more significant influence on the biaxial stress of SCC than that on ordinary concrete, and the failure criterion meridian of SCC is significantly higher than that of ordinary concrete. The failure criterion of SCC is obviously different from that of ordinary concrete. In the subsequent construction of the elastoplastic damage constitutive model, SCC also shows different characteristics from ordinary concrete. SCC has the advantages of high compactness, strong durability and good working performance. Its composition indicates a certain level of commonality. In this study, the lateral stress shows a more significant effect on the principal stress of SCC under biaxial loading than that on ordinary concrete. This is mainly attributed to the concrete composition, as the compactness of SCC is higher than that of ordinary concrete. Thus, it is proposed that the compactness of concrete needs to be further improved by optimizing the mix ratio design in order to achieve better multiaxial mechanical properties.

## 5 CONCLUSION

According to the test data of biaxial compression-compression, biaxial tension-compression and compression-shear in this paper, the failure modes, the principal stress-strain curves and the principal stress values of SCC under different loading conditions were obtained. Then, by comparing with the corresponding test data of ordinary concrete under biaxial loading, the following conclusions are drawn:

1) The lateral compressive stress has a significant impact on the failure mode of SCC under biaxial compression-compression. When the lateral compressive stress is small, the failure mode is similar to that of uniaxial compression. When the lateral compressive stress is large, the specimen shows an oblique flaky failure mode. The failure modes of all the specimens under biaxial tension-compression are split failure, suggesting no relationship with the lateral compressive stress. This failure pattern is basically similar to that of ordinary concrete under

biaxial loading. With respect to the multiaxial compression-shear failure mode of SCC, the shear failure line of the specimen perpendicular to the direction of shear loading is of a straight pattern and is not related to the axial compression ratio. As the axial compression ratio increases, the oblique cracks on the lateral surface of the specimen that is parallel to the direction of shear loading begin to increase gradually, and meanwhile, the friction marks on the shear fracture section are gradually deepened.

2) The development trend and pattern of the principal stress-strain curve of SCC under biaxial loading are similar to those of uniaxial loading, and are not affected by the lateral compressive stress. The lateral compressive stress has a significant impact on the principal compressive stress and principal tensile stress of biaxial compression-compression and biaxial tension-compression. When a lateral compressive stress is applied, the principal compressive stress of SCC is obviously increased compared with that under uniaxial compression, while the principal tensile stress decreases gradually as the lateral compressive stress increases. Compared with the ordinary concrete under biaxial loading, the lateral compressive stress has a more significant impact on the principal stress of SCC.
3) As the axial compression ratio increases, the shear stress and residual stress of SCC increase significantly. When the axial compression ratio is large, the increasing amplitude of shear stress will slow down gradually with the further increase of the axial compression ratio. According to the analysis of residual stress, the friction coefficient of SCC on the shear failure section is lower than that of ordinary concrete.
4) Based on the plane stress space and the octahedral space stress, the strength criterion equations of SCC under biaxial loading were proposed using the data in this study. The proposed strength criterion equations are shown to have good applicability in engineering practice. In addition, according to the changing curve of the octahedral stress space strength criterion equation, it can be seen that the strength criterion equation of SCC is similar to that of ordinary concrete under biaxial tension-compression, but under biaxial compression-compression, the difference in the strength criterion equation between the two will gradually appear. The univariate quadratic failure criterion has higher applicability than the linear expression, and meanwhile, the envelope curve of the compression-shear multiaxial failure criterion of SCC is higher than that of ordinary concrete.

## DATA AVAILABILITY STATEMENT

The original contributions presented in the study are included in the article/**Supplementary Material**, further inquiries can be directed to the corresponding author.

## AUTHOR CONTRIBUTIONS

JZ contributed to the conception and research method of the study. CL was responsible for testing and organizing the database. CZ performed the statistical analysis. JZ and ZZ wrote the first draft of the manuscript. All authors contributed to manuscript revision and read and approved the submitted version.

## FUNDING

This research was funded by the General projects of natural science research in Colleges and universities of Jiangsu Province (20KJD560001). The authors gratefully acknowledge the financial support.

## ACKNOWLEDGMENTS

The authors would like to express sincere thanks to natural science research in Colleges and universities of Jiangsu Province.

## SUPPLEMENTARY MATERIAL

The Supplementary Material for this article can be found online at: https://www.frontiersin.org/articles/10.3389/fmats.2021.691342/full#supplementary-material

**Supplementary Figure S1** | The relations between the axial load and residual load of SCC under different axial compression ratios.

**Supplementary Figure S2** | Biaxial compression-compression strength criterion of SCC.

**Supplementary Figure S3** | Biaxial tension-compression strength criterion of SCC.

**Supplementary Figure S4** | Failure criterion of SCC in the plane stress space.

**Supplementary Figure S5** | The octahedral space stress strength criterion of SCC under biaxial loading.

## REFERENCES

Anne-Mieke, P., and de Schutter, G. (2005). "Creep and Shrinkage of Self-Compacting concrete," in *Proceedings of 1st International Symposium on Design, Performance and Use of Self-Consolidating Concrete*. Editors Z Yu, C Shi, and K Khayat (Paris: RILEM Publication SARL), 329–336.

Asteris, P. G., and Kolovos, K. G. (2019). Self-Compacting Concrete Strength Prediction Using Surrogate Models. *Neural Comput. Appl.* 31 (1), 409–424. doi:10.1007/s00521-017-3007-7

Chi, Y., Xu, L., Mei, G., Hu, N., and Su, J. (2014). A Unified Failure Envelope for Hybrid Fibre Reinforced concrete Subjected to True Triaxial Compression. *Compos. Structures* 109 (6), 31–40. doi:10.1016/j.compstruct.2013.10.054

Dinakar, P., and Manu, S. N. (2014). Concrete Mix Design for High Strength Self-Compacting Concrete Using Metakaolin-ScienceDirect. *Mater. Des.* 60 (1), 661–668. doi:10.1016/j.matdes.2014.03.053

Fantilli, A. P., Vallini, P., and Chiaia, B. (2011). Ductility of Fiber-Reinforced Self-Consolidating Concrete under Multi-Axial Compression. *Cement and Concrete Composites* 33 (4), 520–527. doi:10.1016/j.cemconcomp.2011.02.007

Fujikake, K., Mori, K., Uebayashi, K., Ohno, T., and Mizuncr, J. (2000). Dynamic Properties of Concrete Materials with High Rates of Tri-Axial Compressive Loads. *Structures Mater.* 48, 511–522. doi:10.2495/SU000471

Guo, Z. (1997). *Strength and Deformation of concrete: Experimental Foundation and Constitutive Relationship*. Beijing: Tsinghua University Press, 166–167.

He, Z.-J., and Song, Y.-P. (2010). Triaxial Strength and Failure Criterion of Plain High-Strength and High-Performance concrete before and after High Temperatures. *Cement Concrete Res.* 40 (1), 171–178. doi:10.1016/j.cemconres.2009.08.024

Kandasamy, S., and Kothandaraman, S. (2020). Influence of Controlled Permeable Formwork Liner on Surface Quality of Self Compacting concrete. *Construction Building Mater.* 260, 119756. doi:10.1016/j.conbuildmat.2020.119756

Klaus, H., and Yvette, K. (2005). "Pull-out Behavior of Steel Fibers in Self Compacting concrete," in *Proceedings of 1st International Symposium on Design, Performance and Use of Self-Consolidating Concrete*. Editors Z Yu, C Shi, and K H Khayat (Paris: RILEM Publication SARL), 523–532.

Kupfer, H. B. (1973). Behavior of Concrete under Biaxial Stresses. *J. Eng. Mech. Division ASCE* 66 (8), 853–866. doi:10.1061/jmcea3.0001789

Lazniewska-Piekarczyk, B. (2016). Investigations on the Relationship between Porosity and Strength of Admixtures Modified High Performance Self-Compacting Concrete. *J. civil Eng. Manag.* 22 (2), 520–528. doi:10.3846/13923730.2014.897978

Mohamed, R. N., Zamri, N. F., Elliott, K. S., Rahman, A. B. A., and Bakhary, N. (2019). Steel Fibre Self-Compacting Concrete under Biaxial Loading. *Construction Building Mater.* 224, 255–265. doi:10.1016/j.conbuildmat.2019.07.076

Okamura, H., and Ozawa, K. (1995). Mix Design for Self–Compacting Concrete. *Concrete Libr. JSCE* 25 (6), 107–120.

Ottosen, N. S. (1977). A Failure Criterion for Concrete. *J. Engrg. Mech. Div.* 103 (4), 527–535. doi:10.1061/jmcea3.0002248

Pajak, M., Janiszewski, J., and Kruszka, L. (2019). Laboratory Investigation on the Influence of High Compressive Strain Rates on the Hybrid Fibre Reinforced Self-Compacting Concrete. *Construction Building Mater.* 227 (10), 116687. doi:10.1016/j.conbuildmat.2019.116687

Reiterman, P., Holčapek, O., Zobal, O., and Keppert, M. (2019). Freeze-thaw Resistance of Cement Screed with Various Supplementary Cementitious Materials. *Rev. Adv. Mater. Sci.* 58, 66–74. doi:10.1515/rams-2019-0006

Ren, Y., Yu, Z., Huang, Q., and Ren, Z. (2018). Constitutive Model and Failure Criterions for Lightweight Aggregate Concrete: A True Triaxial Experimental Test. *Construction Building Mater.* 171, 759–769. doi:10.1016/j.conbuildmat.2018.03.219

Shang, S., and Song, Y. (2013). Dynamic Biaxial Tensile–Compressive Strength and Failure Criterion of Plain Concrete. *Construction Building Mater.* 40 (40), 322–329. doi:10.1016/j.conbuildmat.2012.11.012

Shi, L., Wang, L., Song, Y., and Shen, L. (2014). Dynamic Multiaxial Strength and Failure Criterion of Dam Concrete. *Construction Building Mater.* 66 (1), 181–191. doi:10.1016/j.conbuildmat.2014.05.076

Tschegg, E. K., Schneemayer, A., Merta, I., and Rieder, K. A. (2015). Energy Dissipation Capacity of Fibre Reinforced Concrete under Biaxial Tension-Compression Load. Part I: Test Equipment and Work of Fracture. *Cement and Concrete Composites* 62, 195–203. doi:10.1016/j.cemconcomp.2015.07.002

Wang, J., Dai, Q., Si, R., Ma, Y., and Guo, S. (2020). Fresh and Mechanical Performance and Freeze-Thaw Durability of Steel Fiber-Reinforced Rubber Self-Compacting Concrete (SRSCC). *J. Clean. Prod.* 277, 123180. doi:10.1016/j.jclepro.2020.123180

Xu, D., Chen, Z., and Zhou, C. (2020). Seismic Performance of Recycled Concrete Filled Circular Steel Tube Columns. *Front. Mater.* 7, 612059. doi:10.3389/fmats.2020.612059

Yu, Z., Qiao, H., Xie, X., and Lu, B. (2018b). Comparative Study on Compressive-Shear Behavior of Ordinary Concrete and Lightweight Aggregate Concrete. *Mater. Rep.* 32 (24), 4269–4275. doi:10.11896/j.issn.1005-023X.2018.24.011

Yu, Z., Sun, X., and Li, F. (2019). Experimental Analysis and Failure Criterion of Plain Concrete Subjected to Biaxial Loading under Fixed Lateral Loading. *Adv. Civil Eng.* 2019, 7059475. doi:10.1155/2019/7059475

Yu, Z., Huang, Q., Xie, X., and Xiao, N. (2018a). Experimental Study and Failure Criterion Analysis of Plain Concrete Under Combined Compression-Shear Stress. *Construction Building Mater.* 179, 198–206. doi:10.1016/j.conbuildmat.2018.05.242

Zamri, N. F., Mohamed, R. N., and Ibrahim, I. S. (2020). The Fibre Shear Supplement of Precast Beam-Half Joints Using Steel Fibre Self-Compacting concrete. *Mater. Today Proc.* 39, 988–992. doi:10.1016/j.matpr.2020.04.577

Zhao, H., Sun, W., Wu, X., and Gao, B. (2015). The Properties of the Self-Compacting Concrete with Fly Ash and Ground Granulated Blast Furnace Slag mineral Admixtures. *J. Clean. Prod.* 95, 66–74. doi:10.1016/j.jclepro.2015.02.050

Zhu, W., Gibbs, J. C., and Bartos, P. J. M. (2001). Uniformity of *In Situ* Properties of Self-Compacting Concrete in Full-Scale Structural Elements. *Cement and Concrete Composites* 23 (1), 57–64. doi:10.1016/s0958-9465(00)00053-6

**Conflict of Interest:** The authors declare that the research was conducted in the absence of any commercial or financial relationships that could be construed as a potential conflict of interest.

**Publisher's Note:** All claims expressed in this article are solely those of the authors and do not necessarily represent those of their affiliated organizations, or those of the publisher, the editors and the reviewers. Any product that may be evaluated in this article, or claim that may be made by its manufacturer, is not guaranteed or endorsed by the publisher.

frontiers in Materials

ORIGINAL RESEARCH
published: 13 December 2021
doi: 10.3389/fmats.2021.807900

# Influence of Calcined Bauxite Aggregate on the Resistance of Cement Composites Subjected to Small Caliber Deformable Projectile Impact

*Fengling Zhang*[1] *and Rui Zhong*[2]*

[1]*Department of Civil and Environmental Engineering, National University of Singapore, Singapore, Singapore,* [2]*Engineering Research Center of Safety and Protection of Explosion and Impact of Ministry of Education, School of Civil Engineering, Southeast University, Nanjing, China*

This paper presents an experimental investigation on the influence of calcined bauxite aggregate (CBA) on the resistance of cement composites subjected to small caliber deformable projectile impact at a designed velocity of 400 m/s. The deformable projectile was made from copper with a purity of 99.5% and a diameter of 8.0 mm. Compared to mixtures with conventional coarse granite aggregate and/or siliceous fine aggregate, the incorporation of either fine or coarse CBA or their combination is beneficial in reducing the depth of penetration (DOP), equivalent crater diameter (CD), and crater volume (CV) caused by deformable projectile impact. CBA is found to be more effective in controlling the DOP and CV in comparison to the CD. Replacing of conventional aggregate with CBA leads to more severe damage to the projectiles (e.g., projectile length reduction, diameter increase, and mass loss). Relative effective hardness is an effective indicator to the deformation potential and penetration capacity of a deformable projectile to impact cement composites incorporating CBA.

**Keywords: calcined bauxite, cement composites, projectile impact, penetration depth, crater**

OPEN ACCESS

***Edited by:***
*Kequan Yu,*
*Tongji University, China*

***Reviewed by:***
*Shaoqin Ruan,*
*Zhejiang University, China*
*Fei Zhou,*
*Tongji University, China*

****Correspondence:***
*Rui Zhong*
*cerzhong@seu.edu.cn*

***Specialty section:***
*This article was submitted to Structural Materials, a section of the journal Frontiers in Materials*

***Received:*** *02 November 2021*
***Accepted:*** *19 November 2021*
***Published:*** *13 December 2021*

***Citation:***
*Zhang F and Zhong R (2021) Influence of Calcined Bauxite Aggregate on the Resistance of Cement Composites Subjected to Small Caliber Deformable Projectile Impact. Front. Mater. 8:807900. doi: 10.3389/fmats.2021.807900*

## INTRODUCTION

The resistance of cement composites subjected to extreme loadings, such as high-velocity projectile impact (HVPI), has been a research topic of much attention (Li et al., 2005; Zhang et al., 2005; Dancygier et al., 2007; Máca et al., 2014; Wu et al., 2015a; Kong et al., 2017; Zhang et al., 2021a; Zhang and Zhong, 2021; Zhong et al., 2021). It is increasingly recognized that besides compressive strength, the resistance of cement composites to HVPI is also significantly affected by aggregate (Yankelevsky, 2017). The experimental study by Zhang et al. (2005) reported that the inclusion of coarse granite aggregate (GA) into cement composites decreases the depth of penetration (DOP) as well as the equivalent crater diameter (CD). A similar phenomenon is also observed in (Werner et al., 2013; Wu et al., 2015b). Wu et al. (2015a) investigated the influence of coarse aggregate type (basalt and corundum), size (65–75 mm, 35–45 mm, and 5–20 mm), and volume fraction (45% and 30%). It was found that the use of stronger, harder, and larger size and higher volume fraction coarse aggregate is beneficial for the resistance of concrete subjected to HVPI. The positive influence of coarse aggregate is also confirmed in (Dancygier and Yankelevsky, 1999; Bludau et al., 2006; Dancygier et al., 2007;

**TABLE 1 |** Physical and mechanical properties of GA and CBA.

| Type | Crushing value | Elastic modulus | Compressive strength | Specific gravity | Hardness |
|---|---|---|---|---|---|
| GA | 32.7% | 65.0 GPa | 238.5 MPa | 2.65 | 21.1 HRC, 93.7 HR15T |
| CBA | 8.0% | 240.0 GPa | N.A. | 3.20 | 51.6 HRC, 96.7 HR15T |

*Note: The aggregate crushing value was determined according to BS 812–110 (British Standards BS 812-110, 1990). The elastic modulus was measured using Ø75 × 130-mm cylindrical specimen for GA whereas it was estimated using $E = [V^2\rho(1+\nu)(1-2\nu)]/(1-\nu)$ for CBA where $V$, $\rho$ and $\nu$ are the velocity of ultrasonic pulse, density and Poisson's ratio of CBA, respectively. The compressive strength was determined using Ø75 × 130-mm cylindrical specimen for GA and is not available for CBA owing to the difficulties in obtaining sufficiently large test specimen. The specific gravity was determined according to ASTM C127 (ASTM C127, 2015). The hardness was measured based on HRC and HR15T scales, respectively, according to the procedures described in (Zhang et al., 2020b).*

**TABLE 2 |** The mixture proportions of cement composites.

| Mixture designation | | *w/b* | Fine aggregate (sand) | Coarse aggregate | Mixture proportions (kg/m$^3$) | | | | | | |
|---|---|---|---|---|---|---|---|---|---|---|---|
| | | | | | Water | Cement | Silica fume | Fine aggregate (sand) | Coarse aggregate | Steel fiber | Superplasticizer |
| Mortar | M-0.60-S | 0.60 | Siliceous | — | 330 | 549 | — | 1288 | — | 39 (0.5% by volume) | 0 |
| | M-0.28-S | 0.28 | | | 231 | 751 | 75 | 1288 | — | | 4.3 |
| | M-0.17-S | 0.17 | | | 168 | 901 | 90 | 1288 | — | | 12.7 |
| | M-0.60-B | 0.60 | Bauxite | — | 330 | 549 | – | 1567 | — | | 0 |
| | M-0.28-B | 0.28 | | | 231 | 751 | 75 | 1567 | — | | 3.6 |
| | M-0.17-B | 0.17 | | | 168 | 901 | 90 | 1567 | — | | 15.9 |
| Concrete | C-0.28-SG | 0.28 | Siliceous | Granite | 139 | 450 | 45 | 772 | 946 | 39 (0.5% by volume) | 10.0 |
| | C-0.28-SB | 0.28 | | Bauxite | 139 | 450 | 45 | 772 | 1142 | | 6.0 |
| | C-0.28-BB | 0.28 | Bauxite | Bauxite | 139 | 450 | 45 | 939 | 1142 | | 5.7 |

Wu et al., 2015b; Wang et al., 2016; Zhong et al., 2021). Apart from coarse aggregate, the inclusion of siliceous fine aggregate into cement composites could also lead to improved resistance to some extent such as decreasing the DOP (Dancygier et al., 2007; Wang et al., 2016; Zhong et al., 2021). A recent study by Wang et al. (2016) found that the DOP appears to reduce with the increase of effective hardness which is calculated based on the hardness and volume proportion of matrix and coarse aggregate.

Zhang et al. (2020a) investigated the HVPI resistance of cement composites characterized with a wide range of compositions and compressive strengths ranging from 34.2 to 220.2 MPa. It was identified that the effective hardness is a critical parameter governing the DOP since it characterizes the overall contribution of fine and coarse aggregate as well as matrix. Zhong et al. (2021) compared the HVPI resistance of a variety of advanced concretes, including ultra-high performance concrete (UHPC), fiber reinforced high strength concrete (FRHSC) and engineered cementitious composites (ECC). In contrast to the relatively small projectiles used in (Zhang et al., 2020a), sufficiently large caliber projectiles were used to avoid potentially biased results due to the presence of coarse aggregate. The beneficial effect of coarse aggregate was observed and a close correlation between the effective hardness and DOP was identified. To sum up, the incorporation of aggregate is beneficial for the resistance of cement composites to HVPI. However, these studies focused on the performance of cement composites subjected to non-deformable projectile impact.

Due to its high strength and hardness [compressive strength in excess of 2000 MPa and Moh's hardness of approximately 9.5 (Wu et al., 2015a)], the use of calcined bauxite aggregate (CBA) in cement composites indeed resulted in substantially improved mechanical properties and resistance to HVPI as reported in our earlier work (Zhang et al., 2021b). Nevertheless, non-deformable projectiles were used in that study. The effect of CBA on the resistance of cement composites subjected to HVPI using deformable projectile is not clear. However, there are practical issues warranting a better understanding of such effect. Aircraft engine missile attack is an important concern in the design of nuclear power plant containments, skyscrapers and critical bridges as pointed by Kœchlin and Potapov (2009). The aircraft engine missile can be equivalently treated as a deformable projectile in these cases as reported in (Kœchlin and Potapov, 2009; Riedel et al., 2010; Zhang et al., 2018).

In contrast to the extensive investigations on the behavior of cement composites subjected to non-deformable HVPI, only a limited number of experimental studies are devoted to deformable HVPI (Gold et al., 1996; Nia et al., 2014; Kong et al., 2017; Feng et al., 2018). Furthermore, among those limited studies, focus was placed on the influence of striking velocity. Kong et al. (2017) explored the influence of striking velocities ranging from 510 to 1850 m/s and observed three penetration regimes with increasing impact velocities: rigid penetration, deformable penetration without eroding, and eroding penetration regimes. To the best knowledge of the

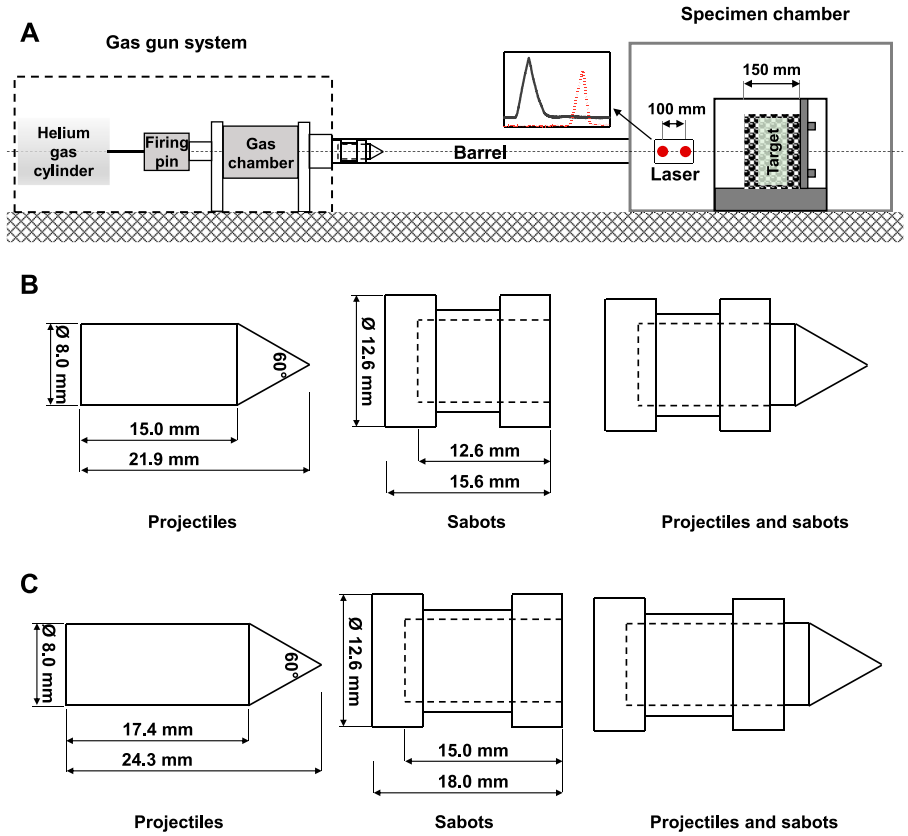


**FIGURE 1 |** Schematic of **(A)** HVPI test setup, **(B)** copper, and **(C)** steel projectile and their sabot.

**TABLE 3 |** Properties of copper and steel used for different projectiles.

| Type | Yield strength[a] | Ultimate strength[a] | Elastic modulus[a] | Poisson's ratio[a] | Density[a] | Hardness |
|---|---|---|---|---|---|---|
| Copper | 275 MPa | 290 MPa | 115 GPa | 0.34 | 8,940 kg/m$^3$ | ~42 HRB[a], 78.4 HR15T[b] |
| Steel | 2150–2200 MPa | 2950–3100 MPa | 210 GPa | 0.30 | 7,700 kg/m$^3$ | 60–62 HRC[a], 97.2 HR15T[b] |

[a]*Provided ay the supplier.*
[b]*Determineb in our laboratory.*

authors, the influence of coarse aggregate on cement composites subjected to deformable HVPI is far from well understood and relevant experimental studies are rarely reported.

This study is a continuation of our earlier work to unveil the influence of CBA (both fine and coarse) on the resistance of cement composites subjected to the impact of deformable projectiles. The cement composites investigated in this study include six mortars and three concretes with unconfined Ø100 × 200-mm cylindrical compressive strengths ranging from 37.9 to 210.2 MPa. The dimension of the specimens for the HVPI test is 300 × 170 × 150-mm. Conical-nosed deformable projectiles were made from copper weighting 7.8 g and with a diameter of 8.0 mm. The designed striking velocity is 400 m/s.

The damage of cement composites induced by the HVPI is quantified based on the depth of penetration (DOP), equivalent crater diameter (CD), and crater volume (CV), while the damage of projectiles is characterized based on the length reduction ($\gamma_l$), diameter increase ($\gamma_d$), and mass loss ($\gamma_m$). The results of our earlier work (Zhang et al., 2021b), where the same array of cement composites, impacted by non-deformable projectiles having the same mass, diameter, and target striking velocity, are also included for comparison purpose.

# MATERIAL AND METHODS

## Materials

CBA utilized in this study possesses an 83.4% aluminium oxide ($Al_2O_3$) content and a specific gravity of 3.20. Conventional aggregates utilized include siliceous fine aggregate with a fineness modulus of 2.70 and a specific gravity of 2.63, as well as coarse granite aggregate (GA) with a specific gravity of 2.65 and a maximum aggregate size of 10 mm. **Table 1** compares the physical and mechanical properties of the coarse CBA and GA.

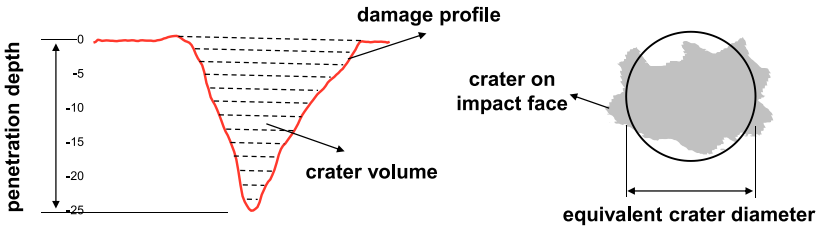


**FIGURE 2 |** Illustration on the measurement of DOP, CD, and CV.

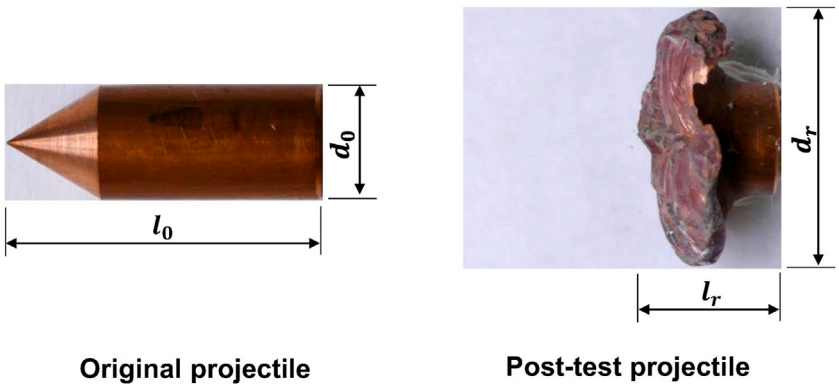


**FIGURE 3 |** Original and residual length and diameter measurement of a copper projectile.

Based on the significantly lower aggregate crushing value (32.7% vs. 8.0% for GA and CBA, respectively), which is defined as the percentage by weight of the crushed material obtained when the aggregates are subjected to a specific load (British Standards BS 812-110, 1990), it is reasonable to assume that the compressive strength of GA is lower compared to that of CBA. In addition, the CBA exhibits both higher hardness and elastic modulus than that of the GA (**Table 1**). Detailed comparisons between these two aggregates can be found in our earlier work (Zhang et al., 2021b). To minimize the effect of aggregate gradation, as-received CBAs were sieved and tailored to achieve similar particle size distributions as conventional aggregates. CEM I 52.5N ordinary Portland cement was utilized for all mixtures. Microsilica Grade 940U silica fume from Elkem was utilized. Steel fibers were provided by Bekaert with a diameter of 0.16 mm and a length of 13 mm. ADVA 181N polycarboxylate-based superplasticizer supplied by GCP Applied Technologies was utilized in some mixtures for workability improvement purpose.

## Mixture Design and Specimen Preparation

**Table 2** provides the mixture proportions of all mixtures investigated in this study. The water to binder (*w/b*) ratio was varied from 0.17 to 0.60 to achieve different compressive strength levels. The designation of mixtures starts with a letter followed by a numerical number. The letters M and C represent mortar and concrete, respectively. The following number indicates the *w/b* ratio. The mixture designation ends with one or two letters for the type of used aggregate. For mortars, no coarse aggregate is used and thus there is only one ending letter. S and B stand for siliceous sand and fine CBA, respectively. For concretes, there are two ending letters with the first and the second letters indicate the type of fine and coarse aggregate, respectively. For example, C-0.28-SG means the concrete mixture has a *w/b* ratio of 0.28 and both siliceous sand and coarse GA are used. All of the cement composites incorporated a 0.5% volume fraction of steel fibers in order to alleviate the specimen splitting after the HVPI tests and to facilitate a consistent damage characteristics measurement (Zhang et al., 2021b). A Hobart mixer was utilized for mixing mortars and a pan mixer was utilized for mixing concretes. Dry materials (cement, silica fume, fine or coarse aggregate) were firstly dry-mixed for 1–2 min, followed by the addition of water (Cai et al., 2021). A proper amount of superplasticizer was then added to improve the workability of mortar and concrete mixtures. Lastly, steel fibers were added by hand once the mixture turned fluid. All the specimens were covered with plastic sheets and left in laboratory after casting, demolded after 1 day and stored in a fog room for additional 6 days. Thereafter, all the specimens were left in the laboratory at an ambient temperature of approximately 30°C until testing at an age of around 91 days.

## Test Methods

At the age of HVPI tests, the compressive strengths and elastic moduli of different mixtures were determined using Ø100 × 200-mm cylindrical specimens following the ASTM C39 (ASTM C39, 2017) and ASTM C469 (ASTM C469, 2014), respectively. The Rockwell hardness was measured using 100-mm length cubic

**TABLE 4 |** Summary of the DOP, CD, and CV in cement composites subjected to copper and steel projectile impact.

| Mixture | | w/b | Fine aggregate (sand) | Coarse aggregate | Compressive strength (MPa) | Elastic modulus (GPa) | Effective hardness (HR15T) | Copper projectile impact | | | | | | Steel projectile impact | | | | | |
|---|---|---|---|---|---|---|---|---|---|---|---|---|---|---|---|---|---|---|---|
| | | | | | | | | Type of projectile damage | Striking velocity (m/s) | DOP (mm) | Normalized DOP ($\times10^{-3}$ mm/(m/s)) | CD (mm) | CV ($\times10^{-1}$ ml) | Type of projectile damage | Striking velocity (m/s) | DOP (mm) | Normalized DOP ($\times10^{-3}$ mm/(m/s)) | CD (mm) | CV ($\times10^{-1}$ ml) |
| Mortars | M-0.60-S | 0.60 | Siliceous | — | 37.9±0.2 | 21.5±0.7 | 46.2 | Deformable | 395.1±15.6 | 19.7±2.6 | 49.6±4.6 | 66.9±5.5 | 130.3±27.8 | Non-deformable | 412.3±10.5 | 30.8±1.5 | 74.6±1.7 | 66.2±6.3 | 122.3±24.8 |
| | M-0.28-S | 0.28 | | | 93.4±1.4 | 36.7±0.4 | 69.3 | Deformable | 403.2±0.0 | 10.0±1.2 | 24.8±2.9 | 48.8±0.4 | 48.3±4.5 | Non-deformable | 396.8±0.0 | 15.8±0.7 | 39.7±1.8 | 59.3±2.2 | 79.0±4.6 |
| | M-0.17-S | 0.17 | | | 146.9±1.4 | 49.5±0.7 | 76.2 | Deformable | 410.1±12.0 | 6.6±1.4 | 16.0±3.1 | 40.4±5.9 | 23.3±9.8 | Non-deformable | 409.2±11.0 | 12.4±1.1 | 30.2±1.9 | 55.8±2.7 | 68.0±13.1 |
| | M-0.60-B | 0.60 | Bauxite | — | 45.0±0.3 | 30.1±0.5 | 50.1 | Deformable | 427.4±3.7 | 18.3±1.8 | 42.8±3.9 | 56.2±3.5 | 61.3±13.7 | Non-deformable | 426.1±2.1 | 27.6±2.1 | 64.8±4.8 | 60.7±3.2 | 99.0±5.0 |
| | M-0.28-B | 0.28 | | | 120.0±2.4 | 56.8±1.2 | 74.2 | Deformable | 431.1±3.7 | 8.5±0.9 | 19.6±1.9 | 44.9±0.8 | 42.7±7.6 | Non-deformable | 420.3±9.2 | 12.7±0.9 | 30.1±1.4 | 53.9±1.5 | 64.3±8.7 |
| | M-0.17-B | 0.17 | | | 190.9±3.4 | 77.7±2.1 | 80.0 | Deformable | 405.5±8.2 | 3.9±0.7 | 9.6±1.5 | 26.4±1.2 | 12.3±1.5 | Non-deformable | 425.6±4.7 | 11.6±1.6 | 27.1±3.4 | 51.8±5.9 | 59.8±19.5 |
| Concretes | C-0.28-SG | 0.28 | Siliceous | Granite | 118.1±3.4 | 46.7±0.2 | 80.2 | Deformable | 409.0±4.2 | 7.6±0.3 | 18.6±0.6 | 41.7±3.9 | 24.3±7.6 | Non-deformable | 411.2±11.8 | 11.2±2.9 | 27.1±6.1 | 50.4±5.4 | 55.3±8.8 |
| | C-0.28-SB | 0.28 | | Bauxite | 156.0±6.7 | 82.3±3.0 | 85.6 | Deformable | 425.6±7.0 | 5.4±1.3 | 12.7±2.8 | 36.5±2.9 | 20.5±11.8 | Deformable | 426.8±4.8 | 10.4±2.2 | 24.3±5.0 | 52.1±2.9 | 54.8±7.2 |
| | C-0.28-BB | 0.28 | Bauxite | Bauxite | 210.2±2.2 | 108.8±0.5 | 87.0 | Deformable | 427.4±4.2 | 3.9±1.0 | 9.0±2.4 | 26.7±2.6 | 6.3±3.3 | Deformable | 431.0±2.4 | 8.7±1.8 | 20.2±4.1 | 49.2±5.8 | 44.2±14.4 |

*Note that 1) DOP is the depth of penetration, CD is the equivalent crater diameter, CV is the crater volume, and 2) experimental results are expressed as average value ± standard deviation as at least three specimens are tested for each mixture.*

**TABLE 5 |** Summary of the $\gamma_l$, $\gamma_d$, and $\gamma_m$ of copper and steel projectiles after HVPI tests.

| Mixture | | w/b | Fine aggregate (sand) | Coarse aggregate | Compressive strength (MPa) | Copper projectile impact | | | | | Steel projectile impact | | | | |
|---|---|---|---|---|---|---|---|---|---|---|---|---|---|---|---|
| | | | | | | Type of projectile damage | Striking velocity (m/s) | Normalized $\gamma_l$ ($\times10^{-5}$/(m/s)) | Normalized $\gamma_d$ ($\times10^{-5}$/(m/s)) | Normalized $\gamma_m$ ($\times10^{-5}$/(m/s)) | Type of projectile damage | Striking velocity (m/s) | Normalized $\gamma_l$ ($\times10^{-5}$/(m/s)) | Normalized $\gamma_d$ ($\times10^{-5}$/(m/s)) | Normalized $\gamma_m$ ($\times10^{-5}$/(m/s)) |
| Mortars | M-0.60-S | 0.60 | Siliceous | — | 37.9±0.2 | Deformable | 395.1±15.6 | 12.5±2.9 | 17.7±1.7 | 1.3±0.1 | Non-deformable | 412.3±10.5 | — | — | — |
| | M-0.28-S | 0.28 | | | 93.4±1.4 | Deformable | 403.2±0.0 | 56.3±11.4 | 90.3±4.5 | 1.6±0.2 | Non-deformable | 396.8±0.0 | 2.3±0.8 | 0.0±0.0 | 1.1±0.0 |
| | M-0.17-S | 0.17 | | | 146.9±1.4 | Deformable | 410.1±12.0 | 110.9±15.5 | 231.2±37.4 | 1.8±0.1 | Non-deformable | 409.2±11.0 | 4.1±1.4 | 0.0±0.0 | 1.3±0.1 |
| | M-0.60-B | 0.60 | Bauxite | — | 45.0±0.3 | Deformable | 427.4±3.7 | 38.6±0.2 | 66.7±2.1 | 1.5±0.3 | Non-deformable | 426.1±2.1 | — | — | — |
| | M-0.28-B | 0.28 | | | 120.0±2.4 | Deformable | 431.1±3.7 | 96.4±19.6 | 201.4±11.6 | 1.9±0.2 | Non-deformable | 420.3±9.2 | 3.7±1.6 | 0.0±0.0 | 1.6±0.1 |
| | M-0.17-B | 0.17 | | | 190.9±3.4 | Deformable | 405.5±8.2 | 146.9±22.6 | 388.5±18.1 | 5.9±0.1 | Non-deformable | 425.6±4.7 | 6.0±0.9 | 0.0±0.0 | 1.7±0.2 |
| Concretes | C-0.28-SG | 0.28 | Siliceous | Granite | 118.1±3.4 | Deformable | 409.0±4.2 | 92.6±17.4 | 246.8±7.2 | 2.3±0.2 | Non-deformable | 411.2±11.8 | 4.5±1.6 | 0.0±0.0 | 1.1±0.1 |
| | C-0.28-SB | 0.28 | Siliceous | Bauxite | 156.0±6.7 | Deformable | 425.6±7.0 | 109.0±9.9 | 301.9±22.4 | 3.7±1.9 | Deformable | 426.8±4.8 | 17.5±2.6 | 0.0±0.0 | 5.6±1.1 |
| | C-0.28-BB | 0.28 | Bauxite | Bauxite | 210.2±2.2 | Deformable | 427.4±4.2 | 147.3±24.7 | 400.8±15.6 | 7.6±1.2 | Deformable | 431.0±2.4 | 25.1±3.4 | 0.0±0.0 | 9.4±1.3 |

*Note that 1) $\gamma_l$ is the projectile length reduction, $\gamma_d$ is the projectile diameter increase, $\gamma_m$ is the projectile mass loss, and 2) experimental results are expressed as average value ± standard deviation as at least three specimens are tested for each mixture.*

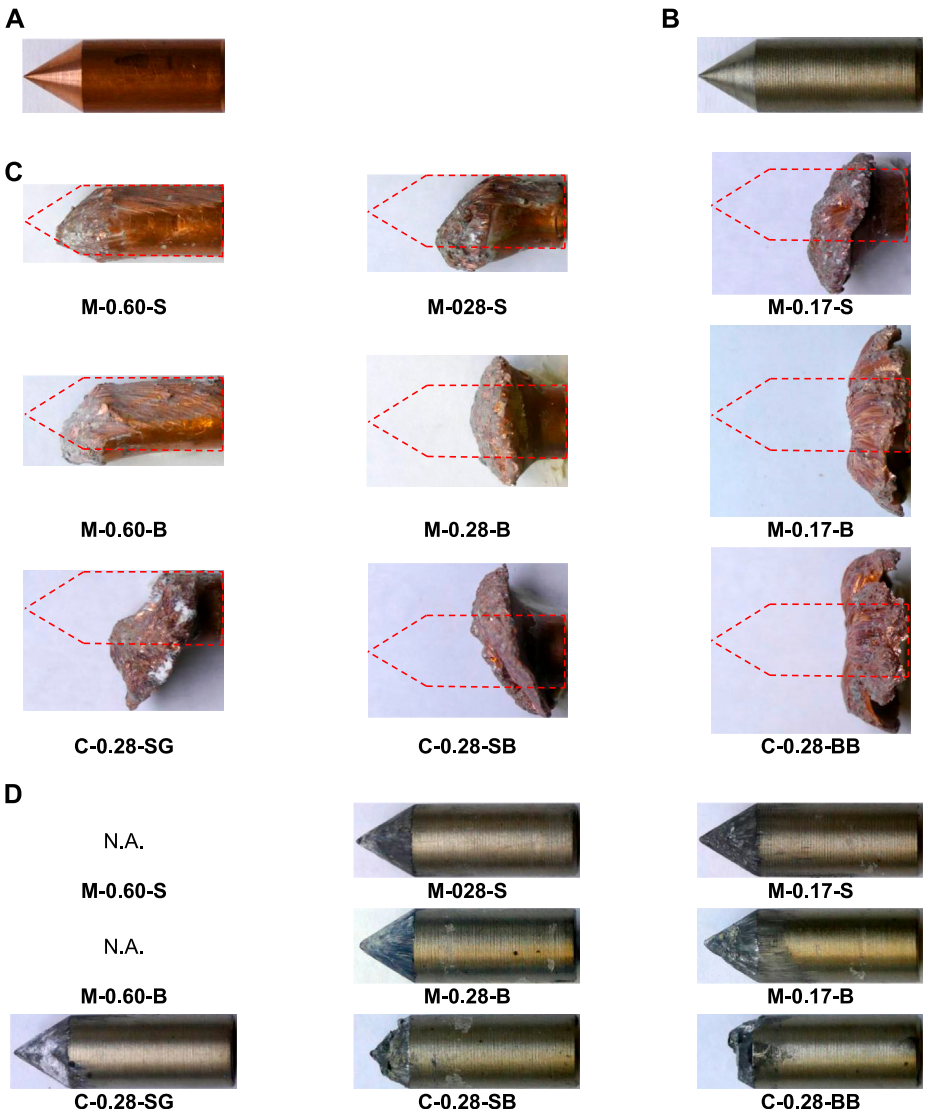


**FIGURE 4 |** Images of **(A)** original copper projectile, **(B)** original steel projectile, **(C)** post-HVPI test copper projectiles, and **(D)** post-HVPI test steel projectiles..

specimens with HR15T scale following (Wang et al., 2016; Zhang et al., 2020a; Zhang et al., 2020b). Since the typical depth of indentation in a hardness test is smaller than 1 mm, an effective hardness was proposed as an overall characterization of a cement composite's hardness (Wang et al., 2016). It can be calculated using **Eq. 1** as defined below.

$$H_{eff} = \frac{l_{ca}}{l_{ca}+l_m}H_{ca} + \frac{l_m}{l_{ca}+l_m}H_m \qquad (1)$$
$$l_m = \sqrt[3]{V_m},\ l_{ca} = \sqrt[3]{V_{ca}}$$

where $H_m$ and $H_{ca}$ are the measured hardness values of mortar and coarse aggregate, respectively; $l_m$ and $l_{ca}$ are the equivalent lengths of mortar and aggregate, respectively; $V_m$ and $V_{ca}$ are the volume fractions of mortar and coarse aggregate, respectively. More details regarding the effective hardness can be found in Wang et al. (2016). Note that for mortars without coarse aggregate, their effective hardness indices are equal to the measured hardness values.

HVPI tests were conducted using a light gas gun as shown in **Figure 1A**. A 300 × 170 × 150-mm block was placed in a steel jip and aligned such that a projectile would strike perpendicularly against the center of the front surface of each specimen. A pair of laser sensors was set up to determine the actual striking velocity of a projectile. Conical nosed projectiles weighting 7.9 g with a diameter of 8 mm were used. In contrast to the ASSAB XW-42 steel used in our previous work (Zhang et al., 2021b), copper with a purity of 99.5% was selected for the deformable projectile based on a series of preliminary studies. The properties of 99.5% copper and ASSAB XW-42 steel are provided in **Table 3**. Considering the higher density of copper (8,940 kg/m$^3$) compared with steel (7,700 kg/m$^3$), a slightly shorter shank

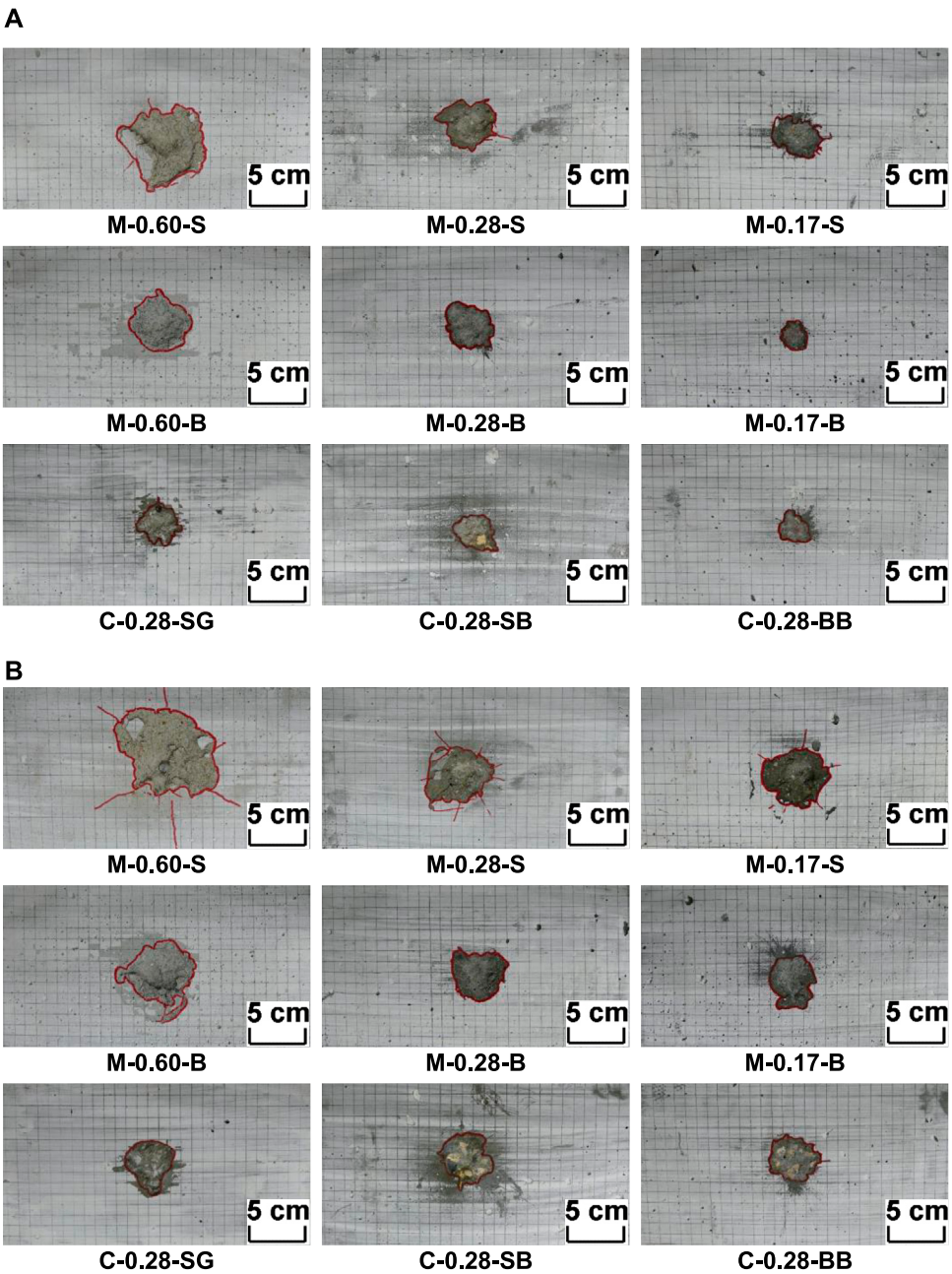


**FIGURE 5 |** Damage of cement composites after impact tests **(A)** deformable projectile and **(B)** non-deformable projectile.

length for the copper projectile was designed to ensure the same initial impact energy (**Figures 1B** and **C**). It should be noted that such slight difference in projectile length has a negligible influence on the performance of cement composites subjected to HVPI (Li et al., 2005). A polypropylene plastic sabot weighting 1.7 g was attached to the projectile to ensure a proper fit into the 12.7 mm barrel of the light gas gun. Compressed helium gas was utilized to propel the projectile at the pressure of approximately 35 bar to achieve the designed striking velocity of 400 m/s. The HVPI tests were conducted at an age of approximately 91 days. A set of new projectile, sabot, and specimen was utilized for each HVPI test.

The damage to the cement composites induced by the HVPI was quantified based on the depth of penetration (DOP), equivalent crater diameter (CD), and crater volume (CV), as illustrated in **Figure 2**. DOP is the distance from the impact face to the deepest point of a crater. CD is the diameter of an equivalent circle possessing an identical area with the spalling crater, which was determined by counting the 10 × 10-mm grids drew on the front face prior to HVPI test. CV is determined as the

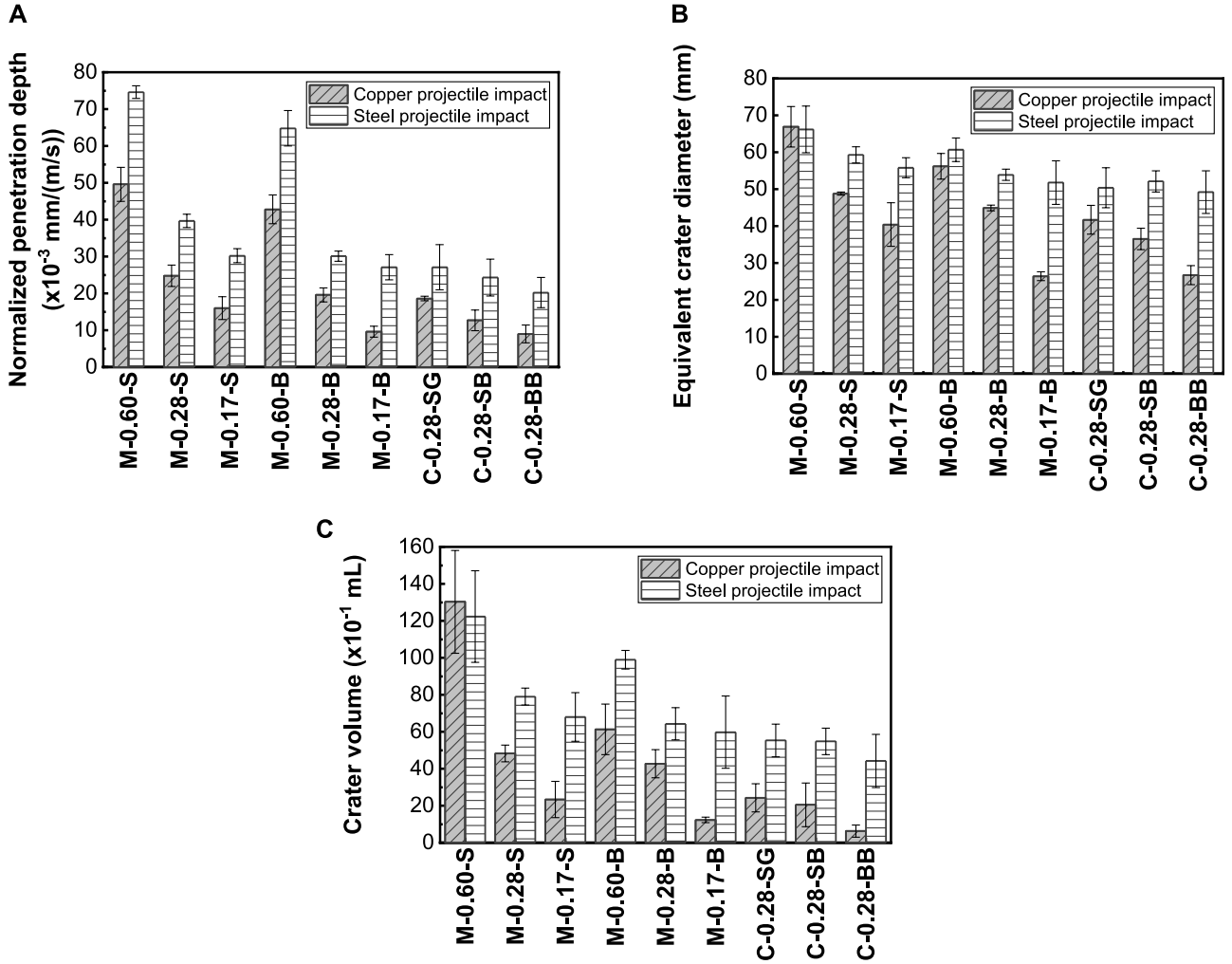


**FIGURE 6 |** Comparison of the normalized damage characteristics of cement composites, **(A)** DOP, **(B)** CD, and **(C)** CV.

sand volume needed to fill up a crater. The constituent (mortar or coarse aggregate) upon which the projectile struck against influences the characteristics of corresponding damage. To minimize the variation of experimental results because of the relatively small diameter of projectile, three and four replicates were tested for the mortar and concrete mixtures, respectively. Note that the practical limitation of small projectile size was also recognized in (Gold et al., 1996; Gomez and Shukla, 2001; Zhang et al., 2005; Bludau et al., 2006; Werner et al., 2013; Máca et al., 2014; Nia et al., 2014; Wu et al., 2015a; Peng et al., 2016; Song et al., 2019). In total, thirty 300 × 170 × 150-mm specimens were tested. The average values together with corresponding standard deviations are reported.

The damage to the projectiles was characterized by its change of length ($\gamma_l$), diameter ($\gamma_d$), and mass ($\gamma_m$) following (Xiao et al., 2010; Kong et al., 2017; Zhang et al., 2020b), and can be calculated using **Eqs 2–4**, respectively, as defined below.

$$\gamma_l = |(l_0 - l_r)/l_0| \tag{2}$$

$$\gamma_d = |(d_0 - d_r)/d_0| \tag{3}$$

$$\gamma_m = |(m_0 - m_r)/m_0| \tag{4}$$

where $l_0$ and $l_r$ are the original and residual projectile lengths, respectively; $d_0$ and $d_r$ are the original and residual projectile diameters, respectively; $m_0$ and $m_r$ are the original and residual projectile masses, respectively. An example on the measurement of original and residual projectile lengths and diameters is illustrated in **Figure 3**.

## RESULTS AND DISCUSSION

### Influence of Deformable Nature of Projectile on the Damage Characteristics of Cement Composites

The damage characteristics of cement composites and projectiles after HVPI tests are summarized in **Tables 4** and **5**, respectively. Note that

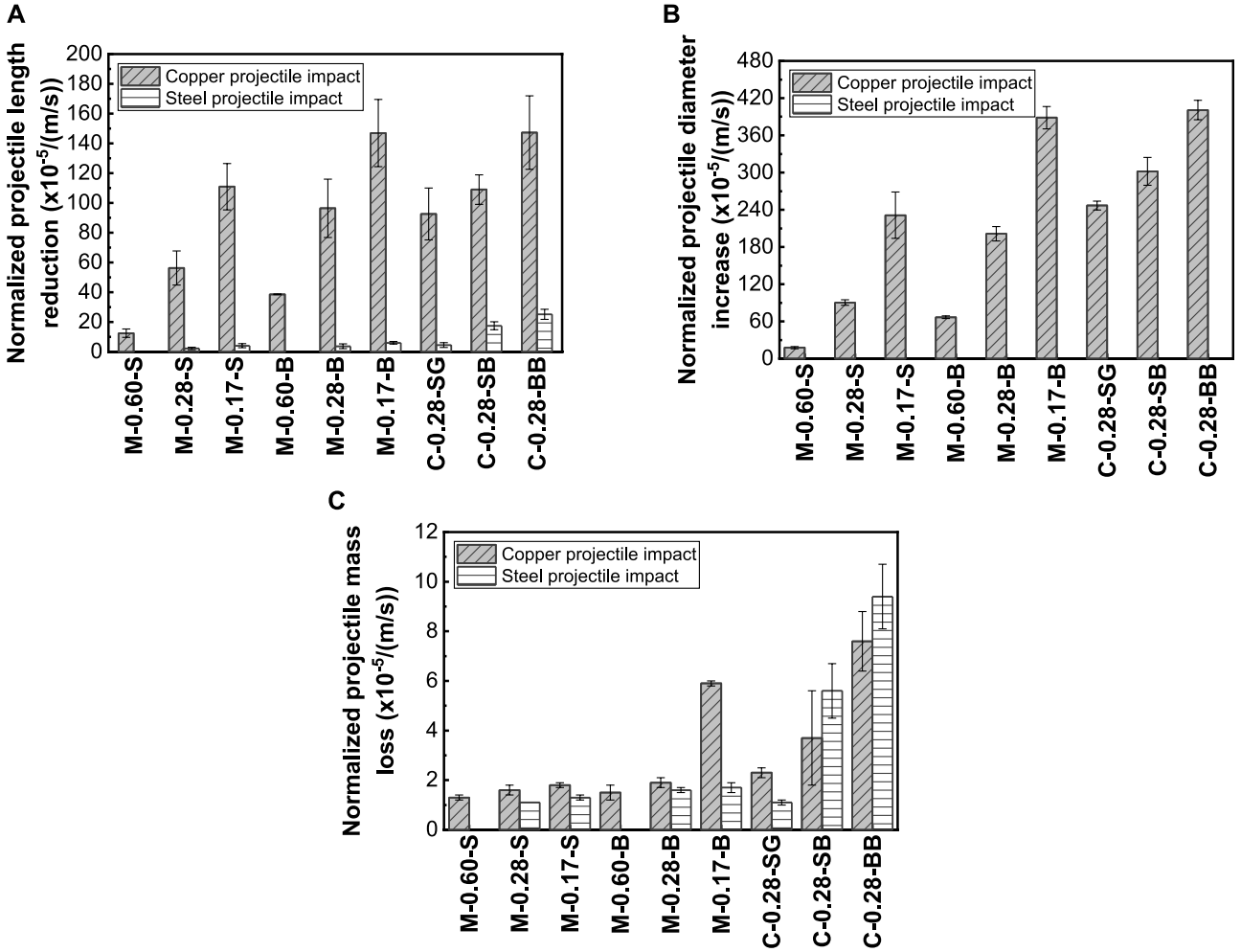


**FIGURE 7 |** Comparison of the normalized damage characteristic of projectiles, **(A)** length reduction, **(B)** diameter increase, and **(C)** mass loss.

the results of our earlier work (Zhang et al., 2021b) using steel projectiles are also included for comparison purpose. The test conditions in this study and that earlier work (Zhang et al., 2021b) are essentially the same such as the projectile nose shape (conical), mass (7.8 g), diameter (8.0 mm), striking velocity (approximately 400 m/s), and specimen dimension (300 × 170 × 150-mm). There is a slight difference in the projectile length due to the difference in densities of copper and steel (see *Test Methods*). The major difference lies in the nature of projectiles. **Figure 4** presents the original and post-HVPI test images of the projectiles which indicates the deformable and non-deformable nature of copper and steel projectiles, respectively. Substantial length reduction, diameter increase, and mass loss occurred for all the copper projectiles whereas the steel projectiles essentially maintained the original conditions except for minor scratch or deformation. It is worth pointing out that the steel projectiles impacting C-0.28-SB and C-0.28-BB also demonstrated appreciable deformation and damage which is most likely due to the direct collision with coarse CBA. However, for simplicity, copper and steel projectiles will be referred to as deformable and non-deformable projectiles in the following analyses and discussions. The steel projectiles striking against M-0.60-S and M-0.60-B were fully embedded in the targets and thus were not retrieved. Therefore, these images are not available.

The measured striking velocities varied between 380 and 435 m/s, although the designed striking velocity was set as 400 m/s. The slight difference in actual striking velocities may affect the corresponding damage characteristics. Indeed, the experimental study by Zhang et al. (2005) found a linear relationship between the DOPs and projectile striking velocities ranging from 250 to 650 m/s. In contrast, the CDs and CVs appeared unaffected by the striking velocities. This is consistent with those reported in (Maalej et al., 2005; Feng et al., 2018). Therefore, the DOPs are normalized with respect to the striking velocities in the following analyses and discussions, but the CDs and CVs are not adjusted. Normalization was also conducted when assessing the projectile length reduction, diameter increase, and mass loss for the same reason (Zhang et al., 2020b). The post-HVPI test images of cement composites subjected to the deformable and non-deformable projectiles are provided in

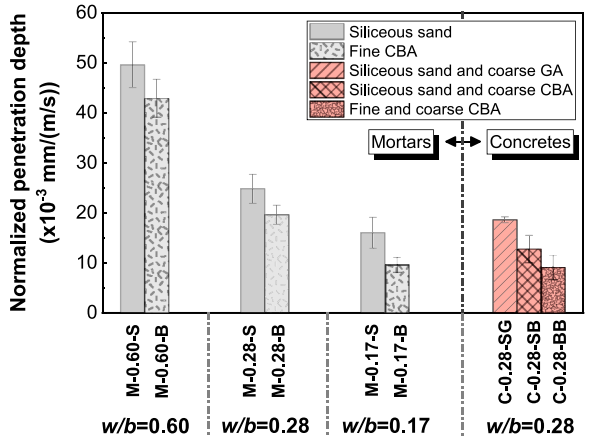


**FIGURE 8 |** Effect of CBA on the DOP of cement composites subjected to deformable copper HVPI.

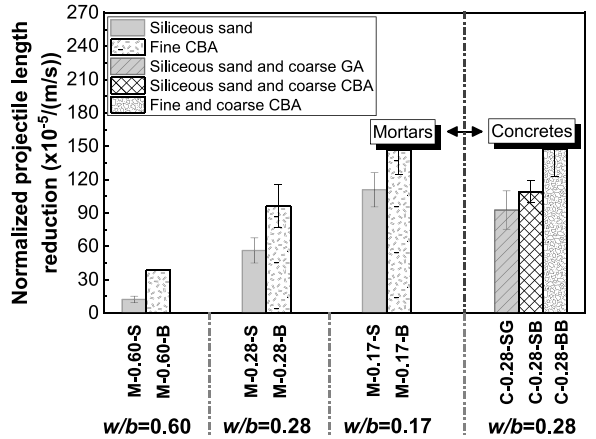


**FIGURE 9 |** Effect of CBA on the normalized length reduction of deformable copper projectile.

**Figure 5**. It can be observed that the damage of cement composites is largely localized and neither scabbing nor perforation is observed.

**Figure 6** compares the damage characteristics of investigated cement composites. It is observed that for the same target under the given set of impact conditions, the DOPs, CDs, and CVs resulting from the impact of deformable (copper) projectiles are much smaller than those caused by the impact of non-deformable (steel) projectiles. **Figure 7** shows the damage characteristics of investigated projectiles. The length reduction, diameter increase, and mass loss of deformable (copper) projectiles after the HVPI tests are significantly greater compared to those of non-deformable (steel) projectiles under similar impact conditions. When a projectile deforms during HVPI, part of the kinetic energy is consumed by its deformation and less kinetic energy will be available for the penetration process (Ohno et al., 1992). For a given impact condition, the larger the projectile deformation, the less severe the damage caused by the projectile. This explains the smaller DOPs, CDs, and CVs resulting from the impact of deformable (copper) projectiles compared to that caused by the non-deformable (steel) projectiles.

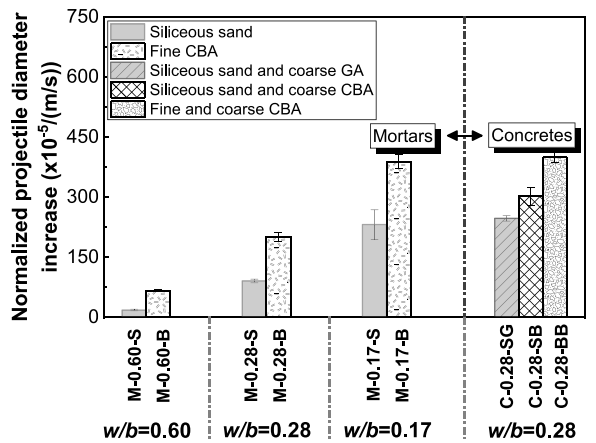


**FIGURE 10 |** Effect of CBA on the normalized diameter increase of deformable copper projectile.

## Effect of CBA on the Damage Characteristics of Cement Composites

### Effect of CBA on the Depth of Penetration

It can be observed from **Figure 8** that when subjected to deformable HVPI, the inclusion of fine CBA in mortars (M-0.60-B, M-0.28-B, and M-0.17-B) decreases the DOPs by 14–40% in comparison to the counterparts using siliceous sand (M-0.60-S, M-0.28-S, and M-0.17-S). The inclusion of coarse CBA in concrete (C-0.28-SB) leads to a 32% decrease of the DOP compared with that using coarse GA (C-0.28-SG). These observations clearly demonstrate that replacing the conventional aggregates (siliceous sand or coarse GA) with CBA (either fine or coarse) is beneficial for reducing the DOP. In addition, the mixed use of coarse and fine CBA (C-0.28-BB) exhibits a further DOP reduction of 52% and 30% compared to that containing no CBA (C-0.28-SG) or coarse CBA only (C-0.28-SB), respectively.

The stress in a specimen subjected to HVPI increases rapidly, which drives a large number of micro-cracks into rapid propagation. In contrast to the quasi-static loading in which sufficient time is allowed for micro-cracks to seek the path of least resistance [e.g., interfacial transition zone between aggregate and matrix (Wu et al., 2020a)], the micro-cracks under impact loading are generally forced to propagate directly through the aggregate particles, instead of the weaker phase such as interfacial transition zone (Zielinski, 1984; Bischoff and Perry, 1991; Zhang et al., 2005; Wang et al., 2016; Wu et al., 2020a; Wu et al., 2020b; Zhong et al., 2021; Zhang et al., 2021a; Wu et al., 2021). Since the compressive strength of CBA is considerably higher than that of GA [more than 2000 MPa for CBA as reported in (Wu et al., 2015a) vs. 238.5 MPa for GA as given in **Table 1**], it thus has better capability of arresting

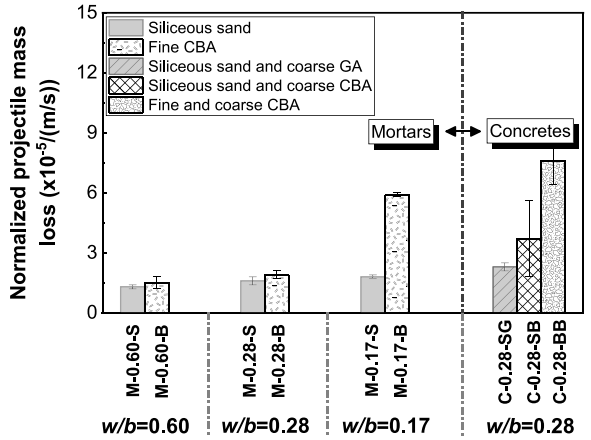


**FIGURE 11 |** Effect of CBA on the normalized mass loss of deformable copper projectile.

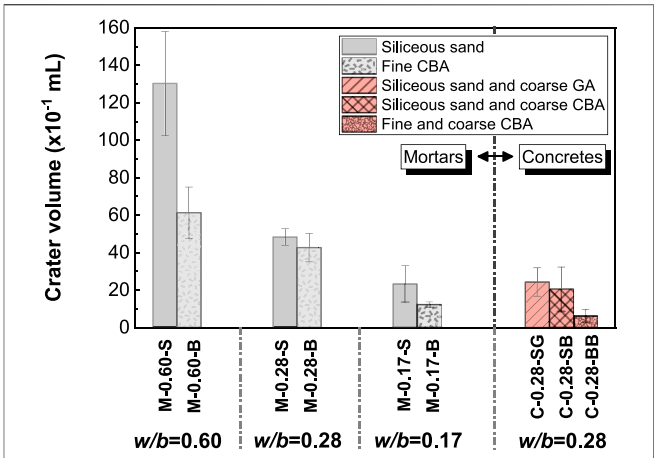


**FIGURE 13 |** Effect of CBA on the CV of cement composites subjected to deformable copper HVPI.

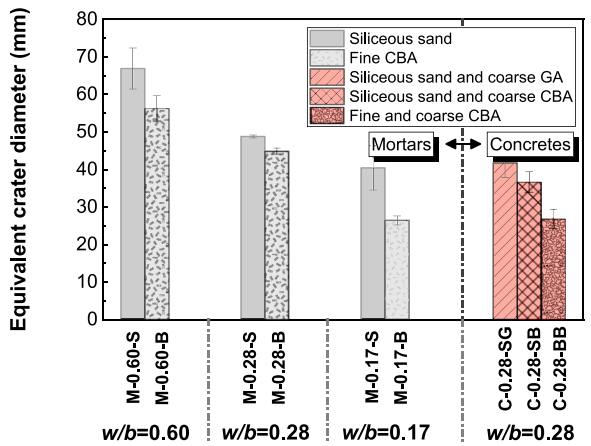


**FIGURE 12 |** Effect of CBA on the CD of cement composites subjected to deformable copper HVPI.

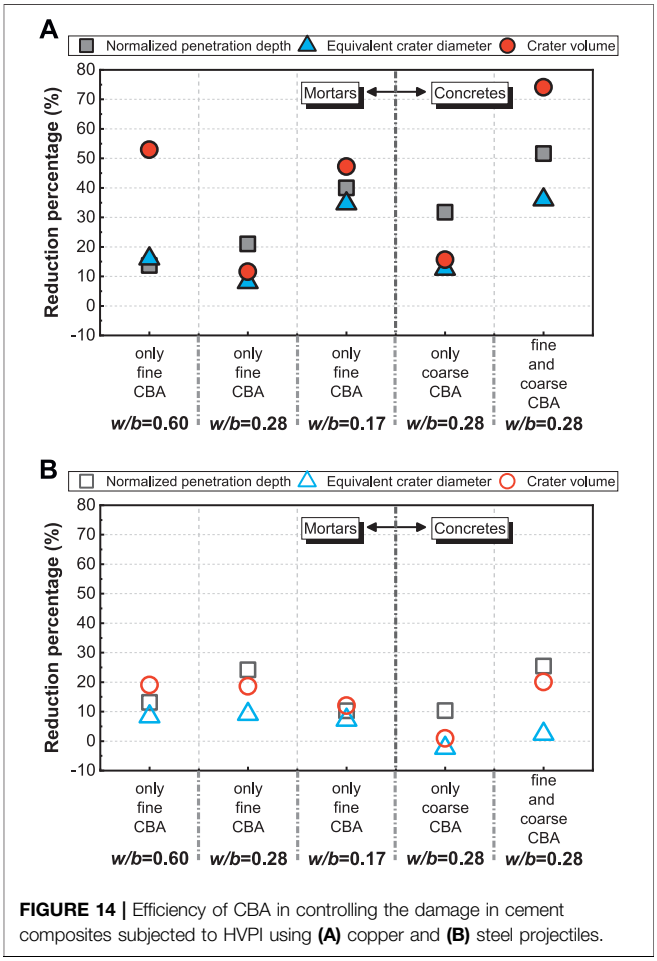


**FIGURE 14 |** Efficiency of CBA in controlling the damage in cement composites subjected to HVPI using **(A)** copper and **(B)** steel projectiles.

the micro-crack propagation under impact loading. In addition, it was reported by Quek et al. (2010) that CBA has higher energy absorption capacity in comparison to GA when crushed during impact. Larger amount of kinetic energy of the penetrating projectile is absorbed by the crush of CBA, leaving less energy available for the process of penetration. Consequently, significantly improved resistance to HVPI in terms of the DOP was observed. Another explanation is the additional friction between the penetrating projectile and CBA which also dissipates the impact energy as experimentally confirmed by (Zhang et al., 2020a).

The visually observed damages to the deformable projectiles as shown in **Figure 4** are qualitative evidences to the aforementioned mechanisms contributing to the reduced DOP due to the presence of CBA. It is further quantified by examining the retrieved projectiles in terms of the length reduction, diameter increase, and mass loss as illustrated in **Figures 9–11**, respectively. As shown in **Figure 9**, the inclusion of fine CBA in mortars (M-0.60-B, M-0.28-B, and M-0.17-B) leads to the higher projectile length reduction by 35–200% in comparison to the counterparts using

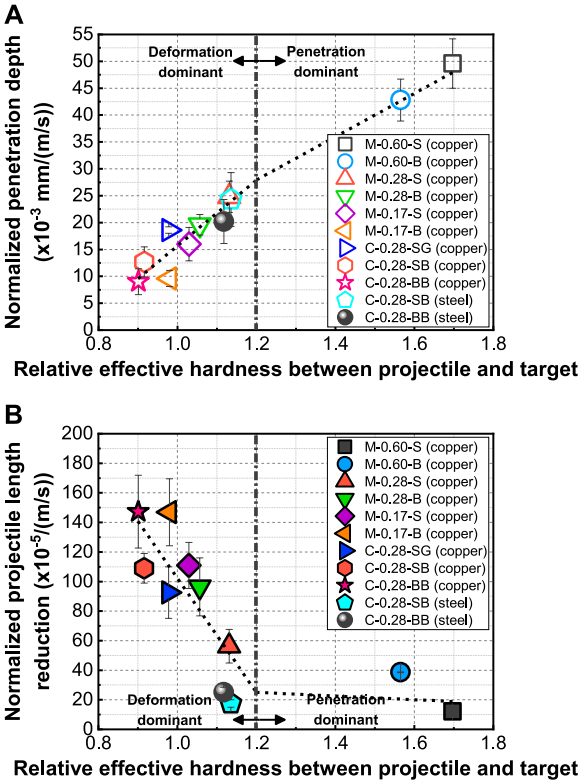


**FIGURE 15 |** Variation of **(A)** the normalized DOP and **(B)** the projectile length reduction with respect to the REH.

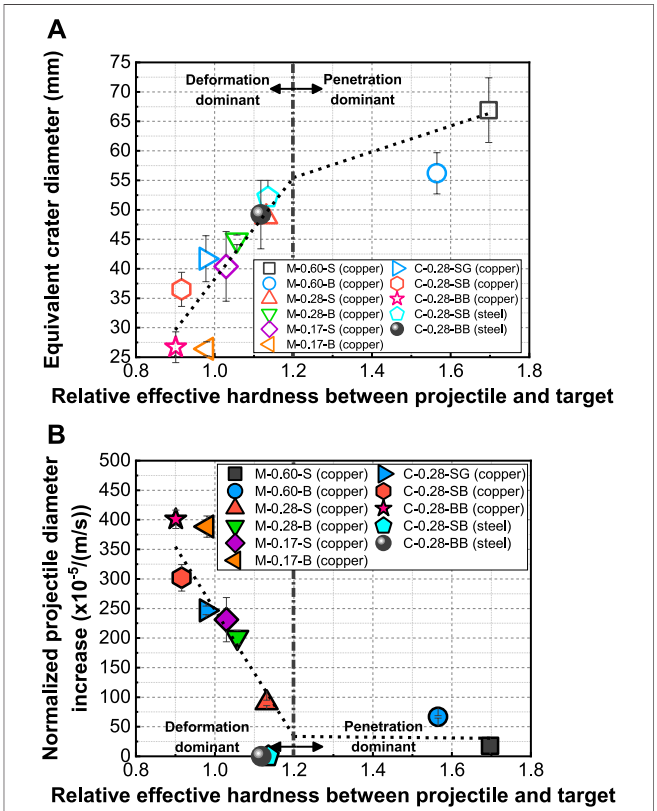


**FIGURE 16 |** Variation of **(A)** the CD and **(B)** the projectile diameter increase with respect to the REH.

siliceous sand (M-0.60-S, M-0.28-S, and M-0.17-S). The incorporation of coarse CBA in concrete (C-0.28-SB) increases the projectile length reduction by about 20% compared to those using coarse GA (C-0.28-SG). The combined incorporation of both fine and coarse CBA in concrete (C-0.28-BB) leads to 60% and 35% increase of projectile length reduction compared to the concretes without CBA (C-0.28-SG) or with coarse CBA only (C-0.28-SB), respectively. The normalized changes in the diameter and mass for the retrieved projectiles are presented in **Figures 10** and **11**, respectively. More severe increase in the diameter and mass loss was observed for projectiles striking against the mixtures with either fine or coarse CBA alone and their combination. The trends in the damage characteristics of the retrieved projectiles are consistent with the DOPs and supports the mechanisms discussed in the previous paragraph.

## Effect of CBA on the Equivalent Crater Diameter

Incorporation of either fine or coarse CBA alone or their combination is also effective in controlling the CD but to a lower extent compared to its influence on the DOP. As observed in **Figure 12**, there is an 8–35% reduction in the CDs for mortars incorporating fine CBA (M-0.60-B, M-0.28-B, and M-0.17-B) compared to those using siliceous sand (M-0.60-S, M-0.28-S, and M-0.17-S). The reduction in CD is 12% for concretes using coarse CBA (C-0.28-SB) compared to the counterpart incorporating coarse GA (C-0.28-SG). The combined incorporation of both fine and coarse CBA in concrete (C-0.28-BB) results in a 36% and 26% reduction of the CD compared to those containing no CBA (C-0.28-SG) or coarse CBA only (C-0.28-SB), respectively. The significantly higher compressive strength and energy absorption capacity of CBA could act as barriers to crack propagation during HVPI as discussed in *Effect of CBA on the Depth of Penetration*. Therefore, smaller CDs were observed. The reduced CDs could also be explained, at least partially, by the deformable nature of the projectiles. Part of the kinetic energy was consumed due to the deformation (**Figures 9–11**) of projectiles themselves or friction between projectiles and CBA (**Figure 4**), resulting in less kinetic energy available for penetration. Consequently, the CDs were reduced.

## Effect of CBA on the Crater Volume

**Figure 13** illustrates the influence of incorporating CBA on the CV of cement composites subjected to deformable copper HVPI. Using either fine or coarse CBA alone or their combination all results in reduction in CV. The incorporation of fine CBA in mortars (M-0.60-B, M-0.28-B, and M-0.17-B) decreases the CVs by 12–53% in comparison to the counterparts incorporating siliceous sand (M-0.60-S, M-0.28-S, and M-0.17-S). There is a 16% reduction of the CV by replacing coarse GA (C-0.28-SG) with coarse CBA (C-0.28-SB). Furthermore, with the mixed use of both fine and coarse CBA

(C-0.28-BB), a pronounced reduction of 74% was achieved compared to that without any CBA (C-0.28-SG). Since the CV in a cement composite specimen is dependent on its DOP and CD (Zhang, 2020; Zhang et al., 2021b; Zhong et al., 2021), the reduction of CV due to the incorporation of CBA can be expected considering the reduced DOP and CD (see *Effect of CBA on the Depth of Penetration of Cement Composites* and *Effect of CBA on the Equivalent Crater Diameter of Cement Composites*, respectively).

## Further Discussion

### Efficiency of CBA in Controlling the Different Damage Characteristics of Cement Composites

The efficiency of the incorporation of CBA (both fine and coarse) in controlling the DOP, CD, and CV of cement composites is of great importance for the design of protective structures. The efficiency was unveiled by assessing the percentage reduction of the damage characteristics as presented in **Figures 14A** and **B** for HVPI tests using deformable (copper) and non-deformable (steel) projectiles, respectively. In general, it is more effective in decreasing the DOP and CV than the CD, regardless if fine or coarse CBA alone or their combination were incorporated. However, the most effective approach is the mixed use of fine and coarse CBA which shows the greatest reduction in all damage characteristics. It is also found that the efficiency of CBA in controlling the corresponding damage characteristics of cement composites is different when subjected to deformable (copper) and non-deformable (steel) projectile impact. **Figure 14B** presents the relative reduction of DOP, CD, and CV of the same cement composites tested under the same conditions (e.g., projectile nose shape, diameter, mass, and striking velocities) presented in **Figure 14A** except for the non-deformable nature of the projectiles. By comparing **Figures 14A,B**, it is clear that the beneficial effect of CBA on the resistance of cement composites to HVPI is less significant when struck by the non-deformable (steel) projectile (typically within 20%) compared to that impacted by the deformable (copper) projectile (typically above 20% and up to 80%).

### Dependency of the Damage Characteristics of Cement Composites on the Relative Effective Hardness

The experimental study by Zhong et al. (2021) found that the effective hardness and energy absorption capacity under direct tension can be used to characterize the resistance of a variety of advanced cement composites subjected to HVPI in terms of DOP and CV, respectively. Recently, Zhang et al. (2021b) reported a close relationship between DOP and effective hardness for a wide range of cement composites including those utilized CBA and concluded that the reduction of CD and CV could be, at least partially, attributed to the increased splitting tensile strength of cement composites. However, non-deformable projectiles were used in those studies. It is still not clear which material properties can best reflect the contribution of CBA to the resistance of cement composites subjected to HVPI using deformable projectiles. High-intensity pressure is generated at the contact face between a projectile and target upon impact. The penetrating projectile may deform to different extents, depending on the relative properties of the projectile and target as well as the striking velocity (Gold et al., 1996; Xiao et al., 2010; Rakvåg et al., 2013). A part of the projectile kinetic energy can be consumed by the deformation of projectile itself.

It was reported in (Zhang et al., 2020b) that the relative effective hardness (REH) is a good indicator for the actual effect of the competing phenomena of penetration and deformation at a given striking velocity. The REH is defined as the ratio of the effective hardness of projectile to that of cement composites. The hardness values of the copper and steel projectiles provided by the suppliers were determined using HRB and HRC scales, respectively, while the hardness values of the cement composites in this study were measured using HR15T scale following the recommendation in (Callister and Rethwisch, 2012; Zhang et al., 2020a). For consistency, the hardness values of the copper and steel projectiles were also measured using HR15T scale in our laboratory as shown in **Table 3**. Note that the REH is calculated based on the measured hardness values of projectiles and cement composites in terms of HR15T scale.

The variation of the DOP and projectile length reduction with the REH for the deformable projectile impact, including all deformable copper projectiles and some steel projectiles with appreciable deformation (i.e., steel projectiles struck against C-0.28-SB and C-0.28-BB specimens), is presented in **Figure 15**. In general, the DOP increases with the increase of REH, whereas the projectile length reduction generally decreases with the increase of REH. There exists a critical REH of 1.2 beyond which the rate of increase in DOP decreased and the reduction in projectile length dropped significantly. This means that once the effective hardness of the projectile is greater than 1.2 times that of the cement composites, the penetration mechanism is dominant whereas the deformation phenomenon dictates the penetration process when the REH is smaller than this critical value.

The variation of the CD, as well as the projectile diameter increase, with respect to the REH for all deformable copper projectiles and some steel projectiles with appreciable deformation (i.e., steel projectiles struck against C-0.28-SB and C-0.28-BB specimens) is presented in **Figure 16**. Under the given set of impacting conditions, the CD generally increases with the increase of REH, whereas the projectile diameter change generally decreases with the increase of REH. As discussed in *Effect of CBA on the Crater Volume*, since the CV of a target specimen is associated with the DOP and CD (Zhang et al., 2021b), the reduction of CV in cement composites against the impact of deformable projectiles may also be reflected by the reduced REH with the use of CBA.

## CONCLUSION

This study provides a systematic experimental investigation on the influence of both fine and coarse calcined bauxite aggregate (CBA) on the resistance of cement composites subjected to deformable projectile impact at a designed velocity of 400 m/s.

Mixtures with Ø100 × 200-mm cylindrical compressive strengths varying between 37.9 and 210.2 MPa were proportioned and subjected to projectile impact. Conical-nosed projectiles made from copper with a purity of 99.5% weighting 7.8 g and possessing a diameter of 8.0 mm were adopted for the projectile impact tests. The damage to a cement composite is quantified based on the depth of penetration (DOP), equivalent crater diameter (CD), and crater volume (CV), while the damage to a projectile is characterized based on the length reduction, diameter increase, and mass loss. The main conclusions are summarized as follows:

1) The use of either fine or coarse CBA improves the resistance of cement composites against deformable projectile impact in terms of the DOP, CD, and CV compared to those using conventional siliceous sand or coarse granite aggregate (GA). The combined use of fine and coarse CBA further reduces the damage characteristics of cement composites compared to the solely use of fine or coarse CBA. The CBA is more effective in decreasing the DOP and CV in comparison to the CD.
2) Replacing of conventional aggregate with CBA causes more severe damage to the deformable projectiles in terms of length reduction, diameter increase, and mass loss. The mixed use of fine and coarse CBA leads to more severe damage to the deformable projectiles compared to those using either fine or coarse CBA alone.
3) The mitigated damage to the cement composites and more severe damage to the deformable projectiles could be explained by the significantly higher compressive strength and energy absorption capacity of CBA. This is also attributable, at least partly, to the friction between the deformable projectile and CBA.
4) The relative effective hardness (REH) between deformable projectile and target is a good indicator for the actual effect of the competing phenomena of penetration and deformation. The penetration mechanism is dominant when the REH is greater than 1.2, whereas the deformation mechanism is dominant when the REH is smaller than 1.2.

## DATA AVAILABILITY STATEMENT

The original contributions presented in the study are included in the article, further inquiries can be directed to the corresponding author.

## AUTHOR CONTRIBUTIONS

FZ: Formal analysis, Investigation, Writing—original draft. RZ: Formal analysis, Investigation, Writing—review & editing.

## ACKNOWLEDGMENTS

The authors appreciate the time and valuable comments from the reviewers that have helped improve the quality of this paper. The authors acknowledge the financial support from the National University of Singapore and Southeast University.

## REFERENCES

ASTM C39 (2017). *Standard Test Method for Compressive Strength of Cylindrical Concrete Specimens*. West Conshohocken, PA: ASTM International.

ASTM C127 (2015). *Standard Test Method for Relative Density (Specific Gravity) and Absorption of Coarse Aggregate*. West Conshohocken, PA: ASTM International.

ASTM C469 (2014). *Standard Test Method for Static Modulus of Elasticity and Poisson's Ratio of Concrete in Compression*. West Conshohocken, PA: ASTM International.

Bischoff, P. H., and Perry, S. H. (1991). Compressive Behaviour of Concrete at High Strain Rates. *Mater. Struct.* 24 (6), 425–450. doi:10.1007/bf02472016

Bludau, C., Keuser, M., and Kustermann, A. (2006). Perforation Resistance of High-Strength Concrete Panels. *ACI Struct. J.* 103 (2), 188–195. doi:10.14359/15176

British Standards BS 812-110 (1990). *Testing Aggregates - Part 110: Methods for Determination of Aggregate Crushing Value (ACV)*. London: British Standards Institution.

Cai, Z., Liu, F., Yu, J., Yu, K., and Tian, L. (2021). Development of Ultra-high Ductility Engineered Cementitious Composites as a Novel and Resilient Fireproof Coating. *Construct. Build. Mater.* 288, 123090. doi:10.1016/j.conbuildmat.2021.123090

Callister, W. D., Jr, and Rethwisch, D. G. (2012). *Fundamentals of Materials Science and Engineering: An Integrated Approach*. Fourth Edition ed. Hoboken, NJ, USA: John Wiley & Sons.

Dancygier, A. N., and Yankelevsky, D. Z. (1999). Effects of Reinforced Concrete Properties on Resistance to Hard Projectile Impact. *ACI Struct. J.* 96 (2), 259–269.

Dancygier, A. N., Yankelevsky, D. Z., and Jaegermann, C. (2007). Response of High Performance Concrete Plates to Impact of Non-deforming Projectiles. *Int. J. Impact Eng.* 34 (11), 1768–1779. doi:10.1016/j.ijimpeng.2006.09.094

Feng, J., Song, M., Sun, W., Wang, L., Li, W., and Li, W. (2018). Thick Plain Concrete Targets Subjected to High Speed Penetration of 30CrMnSiNi2A Steel Projectiles: Tests and Analyses. *Int. J. Impact Eng.* 122, 305–317. doi:10.1016/j.ijimpeng.2018.09.005

Gold, V. M., Vradis, G. C., and Pearson, J. C. (1996). Concrete Penetration by Eroding Projectiles: Experiments and Analysis. *J. Eng. Mech.* 122 (2), 145–152. doi:10.1061/(asce)0733-9399(1996)122:2(145)

Gomez, J. T., and Shukla, A. (2001). Multiple Impact Penetration of Semi-infinite Concrete. *Int. J. Impact Eng.* 25 (10), 965–979. doi:10.1016/s0734-743x(01)00029-x

Kœchlin, P., and Potapov, S. (2009). Classification of Soft and Hard Impacts—Application to Aircraft Crash. *Nucl. Eng. Des.* 239 (4), 613–618. doi:10.1016/j.nucengdes.2008.10.016

Kong, X. Z., Wu, H., Fang, Q., Zhang, W., and Xiao, Y. K. (2017). Projectile Penetration into Mortar Targets with a Broad Range of Striking Velocities: Test and Analyses. *Int. J. Impact Eng.* 106, 18–29. doi:10.1016/j.ijimpeng.2017.02.022

Li, Q. M., Reid, S. R., Wen, H. M., and Telford, A. R. (2005). Local Impact Effects of Hard Missiles on Concrete Targets. *Int. J. Impact Eng.* 32 (1), 224–284. doi:10.1016/j.ijimpeng.2005.04.005

Maalej, M., Quek, S. T., and Zhang, J. (2005). Behavior of Hybrid-Fiber Engineered Cementitious Composites Subjected to Dynamic Tensile Loading and Projectile Impact. *J. Mater. Civ. Eng.* 17 (2), 143–152. doi:10.1061/(asce)0899-1561(2005)17:2(143)

Máca, P., Sovják, R., and Konvalinka, P. (2014). Mix Design of UHPFRC and its Response to Projectile Impact. *Int. J. Impact Eng.* 63, 158–163. doi:10.1016/j.ijimpeng.2013.08.003

Nia, A. A., Zolfaghari, M., Khodarahmi, H., Nili, M., and Gorbankhani, A. H. (2014). High Velocity Penetration of Concrete Targets with Eroding Long- Rod

Projectiles; an Experiment and Analysis. *Int. J. Prot. Struct.* 5 (1), 47–63. doi:10.1260/2041-4196.5.1.47

Ohno, T., Uchida, T., Matsumoto, N., and Takahashi, Y. (1992). Local Damage of Reinforced Concrete Slabs by Impact of Deformable Projectiles. *Nucl. Eng. Des.* 138 (1), 45–52. doi:10.1016/0029-5493(92)90277-3

Peng, Y., Wu, H., Fang, Q., Liu, J. Z., and Gong, Z. M. (2016). Impact Resistance of Basalt Aggregated UHP-SFRC/fabric Composite Panel against Small Caliber Arm. *Int. J. Impact Eng.* 88, 201–213. doi:10.1016/j.ijimpeng.2015.10.011

Quek, S. T., Lin, V. W. J., and Maalej, M. (2010). Development of Functionally-Graded Cementitious Panel against High-Velocity Small Projectile Impact. *Int. J. Impact Eng.* 37, 928–941. doi:10.1016/j.ijimpeng.2010.02.002

Rakvåg, K. G., Børvik, T., Westermann, I., and Hopperstad, O. S. (2013). An Experimental Study on the Deformation and Fracture Modes of Steel Projectiles during Impact. *Mater. Des.* 51, 242–256. doi:10.1016/j.matdes.2013.04.036

Riedel, W., Nöldgen, M., Straßburger, E., Thoma, K., and Fehling, E. (2010). Local Damage to Ultra High Performance Concrete Structures Caused by an Impact of Aircraft Engine Missiles. *Nucl. Eng. Des.* 240 (10), 2633–2642. doi:10.1016/j.nucengdes.2010.07.036

Song, D., Tan, Q., Zhan, H., Liu, F., and Jiang, Z. (2019). Experimental Investigation on the Cellular Steel-Tube-Confined Concrete Targets against Projectile Impact. *Int. J. Impact Eng.* 131, 94–110. doi:10.1016/j.ijimpeng.2019.05.004

Wang, S., Le, H. T. N., Poh, L. H., Feng, H., and Zhang, M.-H. (2016). Resistance of High-Performance Fiber-Reinforced Cement Composites against High-Velocity Projectile Impact. *Int. J. Impact Eng.* 95, 89–104. doi:10.1016/j.ijimpeng.2016.04.013

Werner, S., Thienel, K.-C., and Kustermann, A. (2013). Study of Fractured Surfaces of Concrete Caused by Projectile Impact. *Int. J. Impact Eng.* 52, 23–27. doi:10.1016/j.ijimpeng.2012.09.005

Wu, H., Fang, Q., Chen, X. W., Gong, Z. M., and Liu, J. Z. (2015). Projectile Penetration of Ultra-high Performance Cement Based Composites at 510-1320 m/s. *Construct. Build. Mater.* 74, 188–200. doi:10.1016/j.conbuildmat.2014.10.041

Wu, H., Fang, Q., Gong, J., Liu, J. Z., Zhang, J. H., and Gong, Z. M. (2015). Projectile Impact Resistance of Corundum Aggregated UHP-SFRC. *Int. J. Impact Eng.* 84, 38–53. doi:10.1016/j.ijimpeng.2015.05.007

Wu, Z., Zhang, J., Fang, Q., Yu, H., and Haiyan, M. (2021). Mesoscopic Modelling of Concrete Material under Static and Dynamic Loadings: A Review. *Construct. Build. Mater.* 278, 122419. doi:10.1016/j.conbuildmat.2021.122419

Wu, Z., Zhang, J., Yu, H., and Ma, H. (2020). 3D Mesoscopic Investigation of the Specimen Aspect-Ratio Effect on the Compressive Behavior of Coral Aggregate concrete. *Compos. B. Eng.* 198, 108025. doi:10.1016/j.compositesb.2020.108025

Wu, Z., Zhang, J., Yu, H., Ma, H., Chen, L., Dong, W., et al. (2020). Coupling Effect of Strain Rate and Specimen Size on the Compressive Properties of Coral Aggregate concrete: A 3D Mesoscopic Study. *Compos. B. Eng.* 200, 108299. doi:10.1016/j.compositesb.2020.108299

Xiao, X., Zhang, W., Wei, G., and Mu, Z. (2010). Effect of Projectile Hardness on Deformation and Fracture Behavior in the Taylor Impact Test. *Mater. Des.* 31 (10), 4913–4920. doi:10.1016/j.matdes.2010.05.027

Yankelevsky, D. Z. (2017). Resistance of a Concrete Target to Penetration of a Rigid Projectile - Revisited. *Int. J. Impact Eng.* 106, 30–43. doi:10.1016/j.ijimpeng.2017.02.021

Zhang, F., Poh, L. H., and Zhang, M.-H. (2020). Critical Parameters for the Penetration Depth in Cement-Based Materials Subjected to Small Caliber Non-deformable Projectile Impact. *Int. J. Impact Eng.* 137, 103471. doi:10.1016/j.ijimpeng.2019.103471

Zhang, F., Poh, L. H., and Zhang, M.-H. (2021). Effect of Bauxite Aggregate in Cement Composites on Mechanical Properties and Resistance against High-Velocity Projectile Impact. *Cem. Concr. Compos.* 118, 103915. doi:10.1016/j.cemconcomp.2020.103915

Zhang, F., Poh, L. H., and Zhang, M.-H. (2020). Resistance of Cement-Based Materials against High-Velocity Small Caliber Deformable Projectile Impact. *Int. J. Impact Eng.* 144, 103629. doi:10.1016/j.ijimpeng.2020.103629

Zhang, F. (2020). Resistance of Cement-Based Materials against High-Velocity Projectile Impact. Ph.D. thesis. Singapore: National University of Singapore.

Zhang, F., and Zhong, R. (2021). A Parametric Study on the High-Velocity Projectile Impact Resistance of UHPC Using the Modified K&C Model. *J. Build. Eng.*, 103514. doi:10.1016/j.jobe.2021.103514

Zhang, J., Chen, C., Li, X., Chen, X., and Zhang, Y. (2021). Dynamic Mechanical Properties of Self-Compacting Rubberized Concrete under High Strain Rates. *J. Mater. Civ. Eng.* 33 (2), 04020458. doi:10.1061/(asce)mt.1943-5533.0003560

Zhang, M. H., Shim, V. P. W., Lu, G., and Chew, C. W. (2005). Resistance of High-Strength Concrete to Projectile Impact. *Int. J. Impact Eng.* 31 (7), 825–841. doi:10.1016/j.ijimpeng.2004.04.009

Zhang, T., Wu, H., Huang, T., Sheng, J. H., Fang, Q., and Zhang, F. J. (2018). Penetration Depth of RC Panels Subjected to the Impact of Aircraft Engine Missiles. *Nucl. Eng. Des.* 335, 44–53. doi:10.1016/j.nucengdes.2018.04.025

Zhong, R., Zhang, F., Poh, L. H., Wang, S., Le, H. T. N., and Zhang, M.-H. (2021). Assessing the Effectiveness of UHPFRC, FRHSC and ECC against High Velocity Projectile Impact. *Cem. Concr. Compos.* 120, 104013. doi:10.1016/j.cemconcomp.2021.104013

Zielinski, A. (1984). Fracture of Concrete under Impact Loading. *Struct. Impact Crashworthiness* 2, 654–665.

**Conflict of Interest:** The authors declare that the research was conducted in the absence of any commercial or financial relationships that could be construed as a potential conflict of interest.

frontiers in Materials

ORIGINAL RESEARCH
published: 20 December 2021
doi: 10.3389/fmats.2021.811110

# Mechanical and Self-Healing Performances of Crumb Rubber Modified High-Strength Engineered Cementitious Composites

*Yu Jiangtao*[1,2], *Jiang Fangming*[2], *Xing Qiong*[1], *Yang Qi*[3]* *and Li Mi*[4]*

[1]School of Civil Engineering, Architecture and Environment, Hubei University of Technology, Wuhan, China, [2]College of Civil Engineering, Tongji University, Shanghai, China, [3]Qinghai Transportation Planning and Design Research Institute Co., Ltd., Xining, China, [4]Shanghai Tiangu Housing Inspection Company, Ltd., Shanghai, China

High-strength engineered cementitious composite (HS-ECC) reinforced with polyethylene (PE) fiber characterizes wider crack widths than the conventional polyvinyl alcohol fiber-reinforced ECC (PVA-ECC), weakening the self-healing potential of HS-ECC. The properties of HS-ECC are tailored by introducing crumb rubber (CR), as artificial flaws can lower the matrix toughness and the crack width, leading to an enhanced self-healing potential of HS-ECC. In this study, CR is used to entirely replace silica sand (SS) with three equivalent aggregate-to-binder ratios of 0.2, 0.4, and 0.6, and two CR particle sizes (i.e., CR1 and CR2) are also considered to investigate the effects on density, compressive properties, and tensile performances of HS-ECC. Although CR substitution of SS influences adversely the mechanical strengths of HS-ECC, it can reduce the HS-ECC matrix fracture toughness, activate more microcracks, and reduce the crack width. Moreover, CR-modified HS-ECC specimens featuring the smallest crack width were preloaded to three specific strain levels, including 0.5%, 1.0%, and 2.0%, and then experienced wet–dry conditioning to exhibit effective mechanical and non-mechanical property recovery. The further hydration of binder materials enhances the interfacial bond stress and thus retains the mechanical performances of self-healed HS-ECC, which is expected to improve the practical application and benefit the sustainability of HS-ECC.

**Keywords: high-strength engineered cementitious composite, lightweight, crumb rubber, self-healing, tensile properties, sustainability**

OPEN ACCESS

***Edited by:***
*Xiangming Zhou,*
*Brunel University London,*
*United Kingdom*

***Reviewed by:***
*Zhigang Zhang,*
*Chongqing University, China*
*Lili Kan,*
*University of Shanghai for Science and Technology, China*

***Correspondence:**
*Li Mi*
*Limivip@163.com*
*Yang Qi*
*yangq8327@gmail.com*

***Specialty section:***
*This article was submitted to Structural Materials, a section of the journal Frontiers in Materials*

***Received:*** *08 November 2021*
***Accepted:*** *22 November 2021*
***Published:*** *20 December 2021*

***Citation:***
*Jiangtao Y, Fangming J, Qiong X, Qi Y and Mi L (2021) Mechanical and Self-Healing Performances of Crumb Rubber Modified High-Strength Engineered Cementitious Composites. Front. Mater. 8:811110. doi: 10.3389/fmats.2021.811110*

## INTRODUCTION

Concrete, as the most extensively used building material in the world featuring intrinsic brittleness, is prone to cracking during its service life, which negatively impacts its mechanical performance and leads to potential safety risks to infrastructure. The presence of cracks simultaneously offers pathways for an aggressive agent to penetrate through and causes steel bar corrosion and concrete erosion, which lower the durability and service life of a concrete structure and increase maintenance costs, making concrete infrastructure unsustainable. Therefore, a concrete material that has self-healing capability at cracked locations is highly desirable.

Previous research has identified the required conditions for self-healing in concrete materials, including the presence of specific chemical components such as unhydrated cement grains (Reinhardt and Jooss, 2003), exposure to various environmental conditions (i.e., underwater

immersion and cyclic wet–dry exposures) (Jacobsen et al., 1996; Edvardsen, 1999), and small crack widths (Jacobsen et al., 1996; Reinhardt and Jooss, 2003). The first two criteria can be easily satisfied, while the third criterion requiring the crack width below 150 μm and preferably below 50 μm is the most challenging in the design of self-healing concrete materials (Jacobsen et al., 1996; Aldea et al., 2000).

Engineered cementitious composite (ECC) is an outstanding high-performance fiber-reinforced concrete whose characteristics are systematically tailored according to the micromechanics. ECC exhibits well-distributed microcracks and tensile strain capacity of above 3% with a fiber volume fraction of no more than 2%. The crack width of polyvinyl alcohol (PVA) fiber-reinforced ECC (PVA-ECC) usually stabilizes at approximately 60 μm at the loading stage. The tiny crack of PVA-ECC as an intrinsic material property enables its self-healing capability in different environmental conditions (Yang et al., 2009; Kan and Shi, 2012; Zhang et al., 2014; Zhang and Zhang, 2017; Li et al., 2020; Dong et al. 2021; Yu et al., 2021). Thus, the long-term ductility and durability of PVA-ECC after cracking can be improved by the achievement of self-healing capability, resulting in a sustainable building material. However, the tensile strength of PVA-ECC falls in the range of 3–6 MPa with a compressive strength of less than 60 MPa (Reinhardt and Jooss, 2003; Yu et al., 2017), which are lower and may hinder its application in practical engineering.

High-strength ECC (HS-ECC) reinforced by ultra-high-molecular-weight polyethylene fiber (PE fiber) featuring both high mechanical strengths and high tensile ductility has been developed recently (Ranade et al., 2013; Curosu et al., 2017; Yu et al., 2018; Lei et al., 2019; Yu et al., 2020a). The compressive strength of HS-ECC ranges from 80 to over 150 MPa, and the tensile strength is in the range of 8–20 MPa. Besides, the tensile strain capacity of HS-ECC could reach 8.0% depending on the fiber types and fiber parameters (fiber volume, fiber length, and diameter) (Chen et al., 2018; Zhu et al., 2018; Li et al., 2019; Cai et al., 2021). Nevertheless, the crack width of HS-ECC is 120–200 μm, which is much wider than that of PVA-ECC because of the hydrophobicity of PE fiber and high matrix fracture toughness (Li et al., 2019), influencing adversely the self-healing potential of HS-ECC (Zhang and Zhang, 2017).

The rubber industry is developing at an alarming rate, while the improper disposal methods of scrap rubber, such as burning and landfill, have raised increasing environmental concerns. Using crumb rubber (CR) to replace partial fine aggregates in cementitious materials is an environmentally sustainable disposal method that is worthy of research. Despite the limited study on the use of CR in ECC, a consensus has been achieved that the addition of CR can enhance the tensile strain capacity and the cracking resistance of ECC by decreasing the toughness of the matrix (Huang et al., 2013; Zhang et al., 2015; Zhang et al., 2020b; Adesina and Das, 2021). Zhang et al. (2020b) found that cracks could be more easily triggered and the crack width could be reduced with CR addition to benefit the self-healing capacity of PVA-ECC. Accordingly, CR acting in artificial flaws within the matrix might also improve the crack robustness, reduce the crack width and density of HS-ECC, and modify its self-healing capacity, which has not been stressed before and remains to be fully clarified.

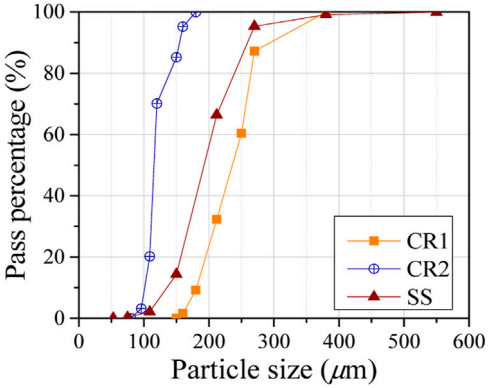


**FIGURE 1 |** Particle size distributions.

The objective of this research is to experimentally study the effects of CR particles on mechanical performance and self-healing capacity of lightweight HS-ECC under cyclic wet–dry conditioning. CR as a fine aggregate in HS-ECC was used to totally substitute silica sand (SS) by equal volume with three different aggregate/binder ratios (i.e., $a/b$ = 0.2, 0.4, and 0.6). In addition, CR with two particle sizes (i.e., CR1 and CR2) was adopted under $a/b$ = 0.4 to study the influence of particle size on the tensile behavior of HS-ECC. The HS-ECC specimen characterized with the smallest crack width (i.e., CR2-0.4) was selected to conduct the further self-healing tests. The CR2-0.4 specimen was preloaded to three certain tensile strains including 0.5%, 1.0%, and 2.0% and experienced 7 wet–dry cycles before reloading. The degree of self-healing capacity of HS-ECC was evaluated by resonant frequency (RF) and tensile performance after recovery.

# EXPERIMENTAL PROGRAM

## Mixture Preparation

The binder materials used for HS-ECC consists of three parts, including ordinary Portland cement, silica fume (SF), and fly ash (FA). These binder materials along with a low water-to-binder ratio ($w/b$) could generate sufficient C-S-H gel and homogenize the matrix to produce a high compressive strength under normal curing conditions. A polycarboxylate-based superplasticizer (SP) was used to gain proper mixture flowability. SS used as an aggregate had average and maximum particle sizes of 150 and 270 μm, respectively. CR with the density of 900 kg/m$^3$ and two-particle size distributions (i.e., CR1 and CR2) was employed to totally replace SS in the HS-ECC by volume. The particle size distributions of SS and CR are shown in **Figure 1**. It is clear that the particle size of CR was comparable with that of SS, and CR2 was finer while CR1 was coarser than SS. CR having lower bond stress to the matrix can be considered as an artificial flaw in HS-ECC.

**TABLE 1 |** Mix proportion of HS-ECC.

| Mix ID | Cement (kg/m$^3$) | SF (kg/m$^3$) | FA (kg/m$^3$) | SS (kg/m$^3$) | CR (kg/m$^3$) | Water (kg/m$^3$) | SP (kg/m$^3$) | Fiber (kg/m$^3$) | *a/b* |
|---|---|---|---|---|---|---|---|---|---|
| SS-0.4 | 625.0 | 125.0 | 680.0 | 575.0 | 0 | 270.0 | 30.0 | 20 | 0.4 |
| CR1-0.2 | 719.0 | 143.8 | 782.3 | — | 109.7 | 310.6 | 17.3 | 20 | 0.2 |
| CR1-0.4 | 625.0 | 125.0 | 680.0 | — | 191.7 | 270.0 | 30.0 | 20 | 0.4 |
| CR1-0.6 | 557.2 | 111.4 | 606.2 | — | 255.0 | 240.0 | 26.7 | 20 | 0.6 |
| CR2-0.4 | 625.0 | 125.0 | 680.0 | — | 191.7 | 270.0 | 30.0 | 20 | 0.4 |

*Note. The solid content of SP is 40%.*
*HS-ECC, high-strength engineered cementitious composite; SF, silica fume; FA, fly ash; SS, silica sand; CR, crumb rubber; SP, superplasticizer.*

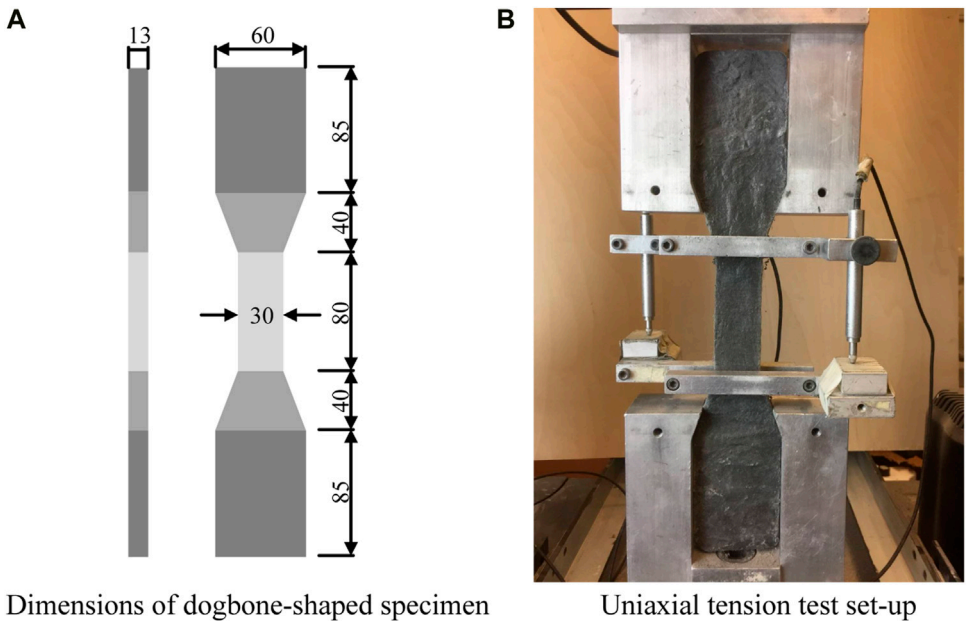


**FIGURE 2 |** Specimen dimensions and test setup. **(A)** Dimensions of dog bone-shaped specimen. **(B)** Uniaxial tension test set-up.

High-strength PE fiber with a nominal tensile strength of 2,400 MPa was used as the reinforcement in HS-ECC. The diameter and length of PE fiber were 24 and 18 mm, respectively, resulting in an aspect ratio (i.e., $L_f/d_f$) of 750, leading to a larger effective fiber/matrix interface area and a higher fiber-bridging capacity at the same fiber content (Naaman and Najm, 1991; Lin and Li, 1997). The PE fiber content was constant at 2% by volume for all the mixtures.

In order to study the influence of CR particles on the mechanical properties and self-healing capacity of HS-ECC, five HS-ECC mixtures were adopted in this study as listed in **Table 1**. The equivalent aggregate-to-binder (*a*/*b*) ratios of HS-ECC with CR totally substituting SS by an equal volume of 0.2–0.6 were considered. In addition, the effect of CR particle sizes (i.e., CR1 and CR2) on the tensile properties of HS-ECC was investigated at an equivalent *a*/*b* ratio of 0.40.

All HS-ECC mixtures were prepared under the same mixing process. The solid materials, including cement, SF, FA, and CR/SS, were firstly mixed for 30 s. Then, water and SP were added slowly and mixed with the solid ingredients at low speed for 5 min, followed by a high speed mixing for 1 min. Finally, fibers were gradually added in two batches and mixed at high speed until uniform distribution was achieved. The specimens were covered with plastic sheets after casting and were demolded after 24 h. The specimens were cured at room temperature (20°C ± 1°C and 40% ± 5% RH) until 28 days.

## Mechanical Testing Procedure

A direct tensile test was conducted (50-kN loading machine with a loading rate of 0.5 mm/min) to determine the full-range uniaxial tensile performance of HS-ECC, including the tensile strength, strain capacity, and crack patterns. The geometry of the dog bone-shaped specimen (**Figure 2A**) was designed to ensure that most of the cracks occur in the central gauge region (JSCE, 2008). A pair of linear variable displacement transducers (LVDTs) was attached with a gauge length of approximately 80 mm to measure the extension as shown in **Figure 2B**. During the test, multiple cracks penetrating through the thickness of the specimen accompanied with the strain-hardening behavior were observed.

**TABLE 2 |** Testing scheme of HS-ECC.

| Mix ID | Number of specimens | | |
|---|---|---|---|
| | Compression | Tension | Matrix three-point bending |
| SS-0.4, CR1-0.2, CR1-0.4, CR1-0.6, CR2-0.4 | 3 | 5 | 6 |
| CR2-0.4-0.5, 1.0, 2.0% | N/A | 5 | N/A |

*Note. HS-ECC, high-strength engineered cementitious composite.*

The compressive strengths of HS-ECC at 28 days were determined by using 50.8 mm (2 in.) of cube specimens and were calculated by averaging three specimens. CR particles acting as artificial flaws could reduce the fracture toughness of HS-ECC matrix (without fiber), and the three-point bending tests were conducted to determine the fracture toughness of HS-ECC matrix. The dimensions of the specimen were 40 mm × 40 mm × 180 mm with a span/depth ratio of 4.0 and a prefabricated crack depth/specimen depth of 0.3. The detailed testing scheme is shown in **Table 2**.

## Self-Healing Testing Procedure

The HS-ECC mixture incorporating CR particles featuring sufficiently small crack widths under direct tension (i.e., CR2-0.4) was selected for the self-healing test. The CR2-0.4 specimens were preloaded to three tensile strain values of 0.5%, 1.0%, and 2.0% to produce different damage levels as listed in **Table 2**. When the preset tensile strain values were reached, the specimens were unloaded and the crack widths were measured prior to wet–dry cycle conditioning. Afterward, the pre-cracked CR2-0.4 specimens were cured under wet–dry cycles, which is an accelerated testing method to simulate actual outdoor environments. One wet–dry cycle of the specimens includes submersion in water at 20°C ± 1°C for 48 h and then drying in laboratory air at 20°C ± 1°C and 40% ± 5% RH for 48 h. Water was replaced after each cycle. After undergoing 7 wet–dry cycles (28 days in total), the cured specimens were retested until failure. The tensile mechanical properties and crack patterns were employed to assess the self-healing capacity of HS-ECC with CR substitution.

In addition to the uniaxial tension test, longitudinal RF measurements (ASTM, 2019) were carried out on dog bone-shaped specimens to verify the presence of damage and quantify the extension of autogenous self-healing in HS-ECC according to the changes in RF. The RF values of the intact and pre-damaged CR2-0.4 specimens after each wet–dry curing were recorded. The change of RF can be regarded as an indicator to assess the damage degree of pre-damaged HS-ECC specimens and the recovery extension of self-healed HS-ECC specimens.

# RESULTS AND DISCUSSION

## Compressive Strength, Density, and Fracture Toughness

The compressive strength of HS-ECC at 28 days is demonstrated in **Figure 3**. As expected, the total substitution of SS with CR particles has demonstrated a significantly adverse effect on the compressive strength. Compared with the reference mixture of HS-ECC using SS as aggregate (i.e., SS-0.4) whose compressive strength is 86.6 MPa, the compressive strength of HS-ECC when SS is entirely replaced by CR by equal volume (i.e., CR1-0.4) reduces to 39.6 MPa with a 54.3% reduction. Besides, a higher amount of CR leads to a more obvious reduction in the compressive strength as shown in **Figure 3**. For instance, the compressive strength of CR-modified HS-ECC decreases from 60.0 to 30.8 MPa as the equivalent $a/b$ ratio increases from 0.2 to 0.6. The loss of the compressive strength of HS-ECC with CR substitution can be attributed to the lower stiffness of CR particle compared with SS, the increment of closed pores within the matrix caused by CR addition (Oikonomou and Mavridou, 2009), and the weak interfacial bond between the CR and around the cementitious matrix. Moreover, comparing the compressive strength of CR1-0.4 and CR2-0.4 in **Figure 3**, it is evident that the negative impact on the compressive strength due to CR substitution can be diminished to a certain degree by using CR with a smaller particle size (i.e., CR2-0.4). It is also clear that all the CR-modified HS-ECC mixtures could be utilized for structural applications, as the compressive strengths are higher than 30 MPa.

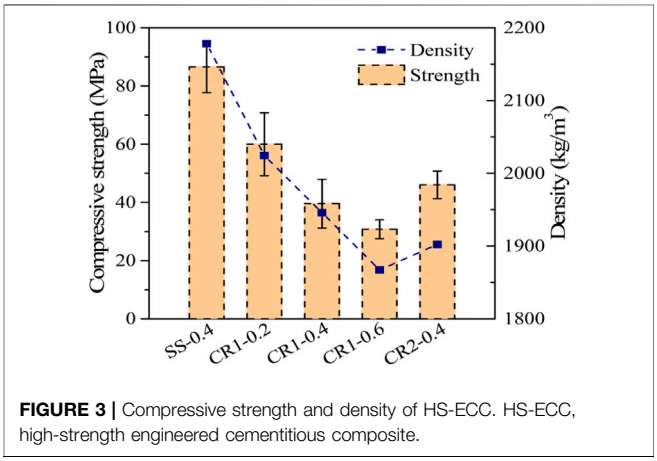


**FIGURE 3 |** Compressive strength and density of HS-ECC. HS-ECC, high-strength engineered cementitious composite.

The density of HS-ECC mixtures is also drawn in **Figure 3**. The incorporation of CR as a complete replacement of SS reduces the density of HS-ECC, and the density is positively correlated to the compressive strength of HS-ECC in general. It is noted from **Figure 3** that the density value decreases from 2,024 kg/m$^3$ of CR1-0.2 to 1,867 kg/m$^3$ of CR1-0.6 with a 7.7% reduction as the proportion of CR increases. Although CR2-0.4 with a smaller CR particle size exhibits a higher compressive strength, it has a

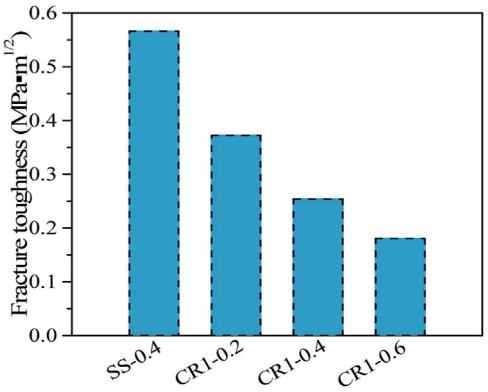


**FIGURE 4 |** Fracture toughness of HS-ECC. HS-ECC, high-strength engineered cementitious composite.

slightly lower density than CR1-0.4 with a larger CR particle size. In accordance with American Concrete Institute (ACI) committee report (American Concrete Institute, 2003), the density of lightweight cementitious composites for structural applications should be 1,120–1,920 kg/m$^3$ with a compressive strength at 28 days of more than 40 MPa. Thus, HS-ECC mixtures produced with 100% CR2 at an *a*/*b* ratio of 0.4 (i.e., CR2-0.4) can be classified as lightweight cementitious composites because their density is 1,902 kg/m$^3$ and compressive strength is 50.0 MPa.

According to the results of the three-point bending test, the fracture toughness of HS-ECC matrix with different CR proportions is obtained and shown in **Figure 4**. It can be found that the fracture toughness of HS-ECC matrix decreases steadily with the increase of CR proportion. Similar to the compressive strength, the fracture toughness of HS-ECC decreases sharply from 0.57 MPa·m$^{1/2}$ of SS-0.4 to 0.25 MPa·m$^{1/2}$ of CR1-0.4 when CR was used to completely replace SS by equal volume. Besides, the fracture toughness decreases gradually from 0.37 to 0.18 MPa·m$^{1/2}$ when the equivalent *a*/*b* ratio increases from 0.2 to 0.6. Designed based on the micromechanical model, two criteria (strength and energy criterion) should be satisfied to achieve the strain-hardening performance and multi-cracking states of ECC (Li and Leung, 1992). In order to achieve high tensile ductility and saturated multiple microcracks, the size and distribution of internal flaws should be tailored (Zhang et al., 2021). Reducing the critical flaw size by introducing artificial flaws such as CR whose interfacial bond stress with a cementitious matrix is relatively low can be regarded as an effective way to reduce matrix fracture toughness and thus activate more microcracks (Li and Wang, 2006; Zhang et al., 2020a), which could benefit the self-healing capacity of HS-ECC.

## Tensile Mechanical Properties

**Figure 5** presents the tensile stress–strain curves of HS-ECC specimens with different CR contents. All the HS-ECC specimens exhibit robust strain-hardening performance under uniaxial tension. The tensile strain capacities of all HS-ECC specimens at peak stress are higher than 6%, as well as the tensile elongations at breakage are higher than 12%. As shown in **Figures 5A–E**, it is clear that the substitution of SS by CR has a dramatic influence on the full-range tensile stress–strain curve of HS-ECC. Comparing **Figures 5A,B**, it is clear that the incorporation of CR with a larger particle size (i.e., CR1) than SS by equal volume decreases the peak tensile strength of HS-ECC distinctly while increasing the tensile strain capacity slightly. Besides, the replacement of SS by CR with a smaller particle size (i.e., CR2) than SS by equal volume as shown in **Figures 5A,E** affects marginally both the peak tensile strength and tensile strain capacity of HS-ECC. However, the CR2-0.4 specimen exhibits an obvious secondary hardening stage with a higher modulus as observed in **Figure 5E**. It might be because CR2 with a finer particle size introduces more artificial flaws into the matrix, and the majority of the cracks are activated in the first hardening stage, exhibiting obvious fluctuation. Then, limited cracks are newly generated in the secondary hardening stage, and slip-hardening behavior is observed to be accompanied by crack opening. Moreover, it also suggests that the increased proportion of CR (i.e., *a*/*b* increases from 0.2 to 0.6) benefits the performance of HS-ECC in terms of tensile ductility, whereas it has an adverse effect on the tensile strength as illustrated in **Figures 5B–D**.

The key tensile parameters of HS-ECC, including the peak and initial cracking stress ($\sigma_{tu}$ and $\sigma_{tc}$), the tensile strain capacity ($\varepsilon_{tu}$), the strain energy density ($g_{se}$), and the fracture energy ($G_f$), are summarized in **Table 3**. The definition and calculation method of $g_{se}$ and $G_f$ can be referred to in previous research (Yu et al., 2020b). Put simply, the strain energy density is the area enclosed by the strain-hardening branch of the tensile stress–strain curve, representing the energy dissipation capacity during the strain-hardening process, whereas the fracture energy is approximately equal to the area under the descending stage of the load–displacement curve, reflecting the energy dissipation capacity after crack localization during the strain-softening process.

The critical tensile parameters of HS-ECC are presented in **Figure 6**. The peak tensile strength of HS-ECC decreases from 11.73 MPa of SS-0.4 to 6.71 MPa of CR1-0.4 when CR1 is used to completely replace SS by equal volume (**Figure 6A**). CR particles with a larger particle size inside HS-ECC are enclosed by the matrix and loosen the matrix structure (Wang et al., 2020), and the peak tensile strength can be reasonably reduced. Besides, the larger particle size of CR1 compared with SS may disturb the fiber dispersion, resulting in the reduction of interfacial bond stress between PE fiber and matrix, leading to a further decrease in the peak tensile stress. Nevertheless, the peak tensile strength of HS-ECC with CR2 substitution (i.e., CR2-0.4) generates a comparable peak tensile strength with SS-0.4. This might be because CR2 has a finer and more irregular particle size than SS, alleviating the negative influences introduced by CR substitution. Moreover, it is noted from **Figure 6A** that with the increase of CR1 proportion, the peak tensile strength of HS-ECC reduces from 8.75 MPa of CR1-0.2 to 4.60 MPa of CR1-0.6 with a 47.4% reduction, which is mainly caused by the weakened matrix structure. Similarly, the reduced initial tensile stress of HE-ECC with CR particle

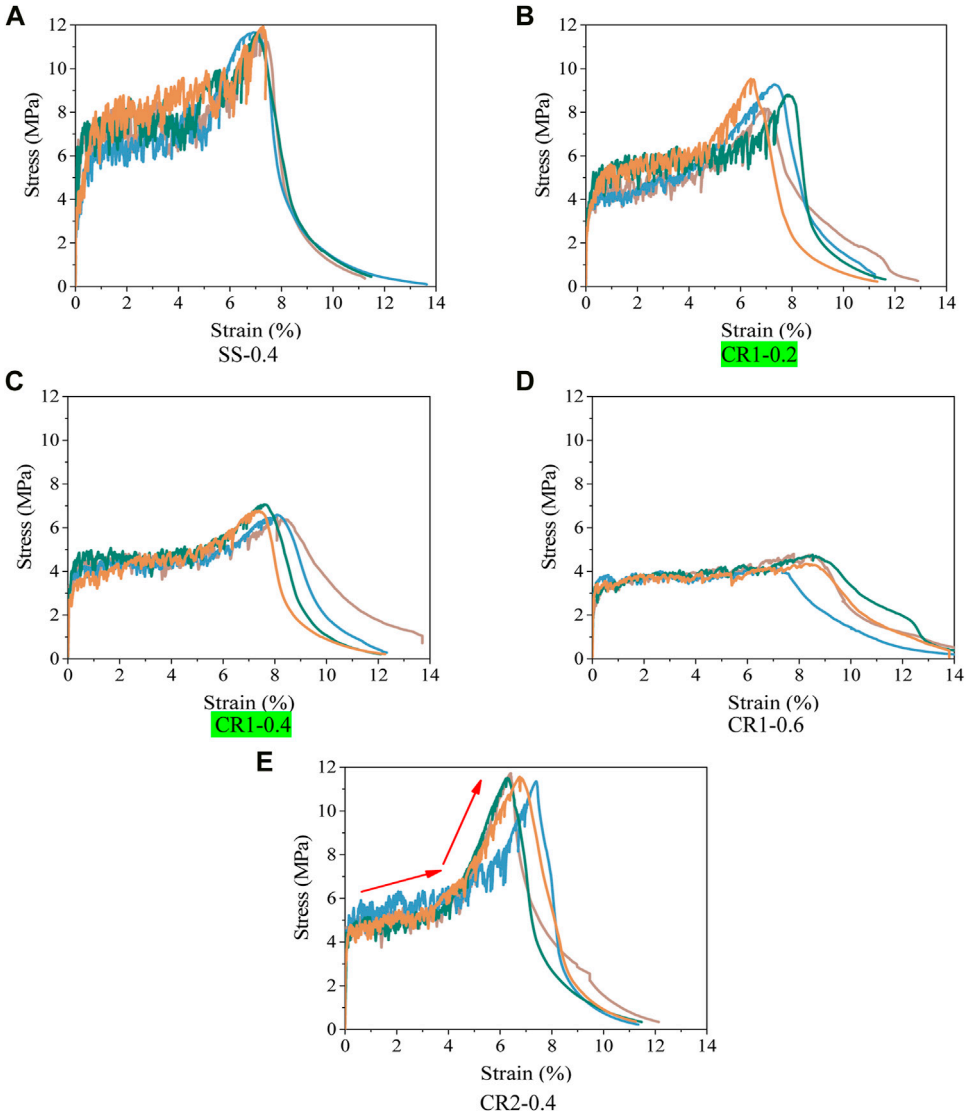


**FIGURE 5 |** Tensile stress–strain curves of HS-ECC. **(A)** SS-0.4. **(B)** CR1-0.2. **(C)** CR1-0.4. **(D)** CR1-0.6. **(E)** CR2-0.4. HS-ECC, high-strength engineered cementitious composite.

**TABLE 3 |** Critical mechanical parameters of HS-ECC.

| Mix ID | $\sigma_{tc}$ (MPa) | $\sigma_{tu}$ (MPa) | $\varepsilon_{tu}$ (%) | $g_{se}$ (kJ/m$^3$) | $G_f$ (kJ/m$^2$) | $G_f/\sigma_{tu}$ |
|---|---|---|---|---|---|---|
| SS-0.4 | 4.36 | 11.73 | 7.14 | 565.8 | 14.84 | 1.27 |
| CR1-0.2 | 3.40 | 8.75 | 7.36 | 427.6 | 9.87 | 1.13 |
| CR1-0.4 | 3.09 | 6.71 | 7.76 | 369.5 | 11.84 | 1.76 |
| CR1-0.6 | 2.89 | 4.60 | 7.63 | 294.3 | 12.04 | 2.62 |
| CR2-0.4 | 4.13 | 11.39 | 6.67 | 421.7 | 15.06 | 1.32 |

*Note. HS-ECC, high-strength engineered cementitious composite.*

substitution could be contributed to the decrease in matrix fracture toughness.

As shown in **Figure 6B**, the influence of CR substitution and CR proportion on the tensile strain capacity of HS-ECC is slight. The strain capacity of SS-0.4 is 7.14%, and this value increases mildly to 7.76% of CR1-0.4. It is noted from **Figure 6C** that the strain energy density shares a similar trend with that of the tensile strength (**Figure 6A**). The strain energy density of SS-0.4 (i.e., 565.8 kJ/m$^3$) is approximately 1.5 times that of CR1-0.4 (i.e., 369.5 kJ/m$^3$) due to the decrease of tensile stress. Moreover,

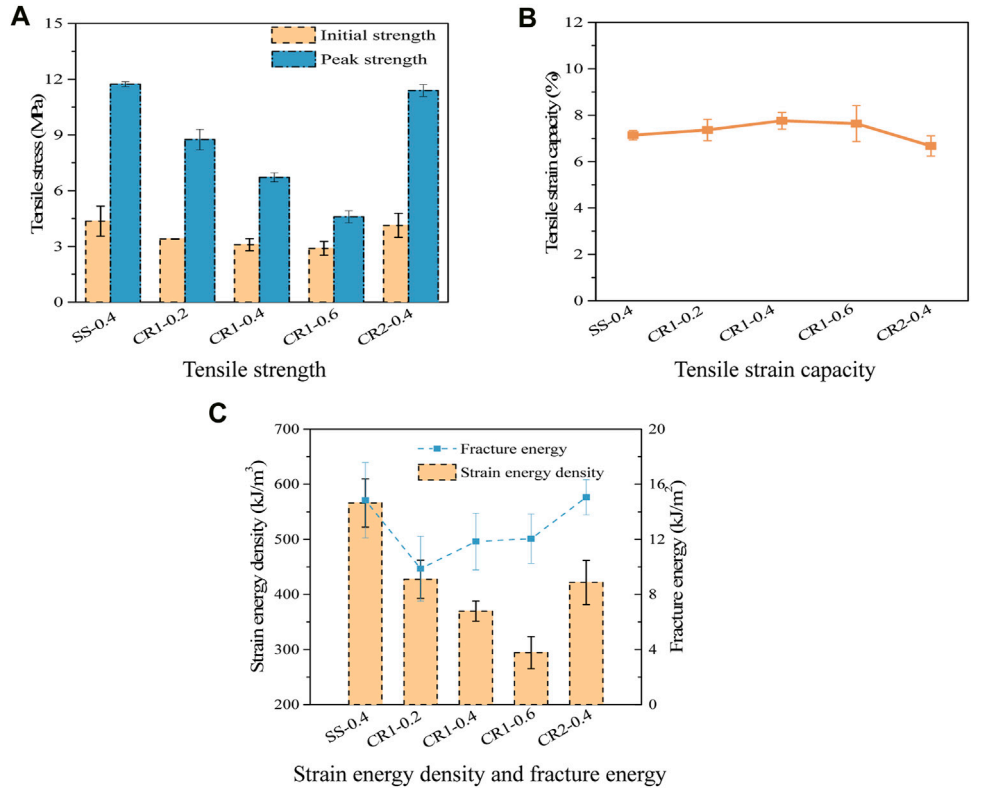


**FIGURE 6 |** Tensile mechanical parameters of HS-ECC. **(A)** Tensile strength. **(B)** Tensile strain capacity. **(C)** Strain energy density and fracture energy. HS-ECC, high-strength engineered cementitious composite.

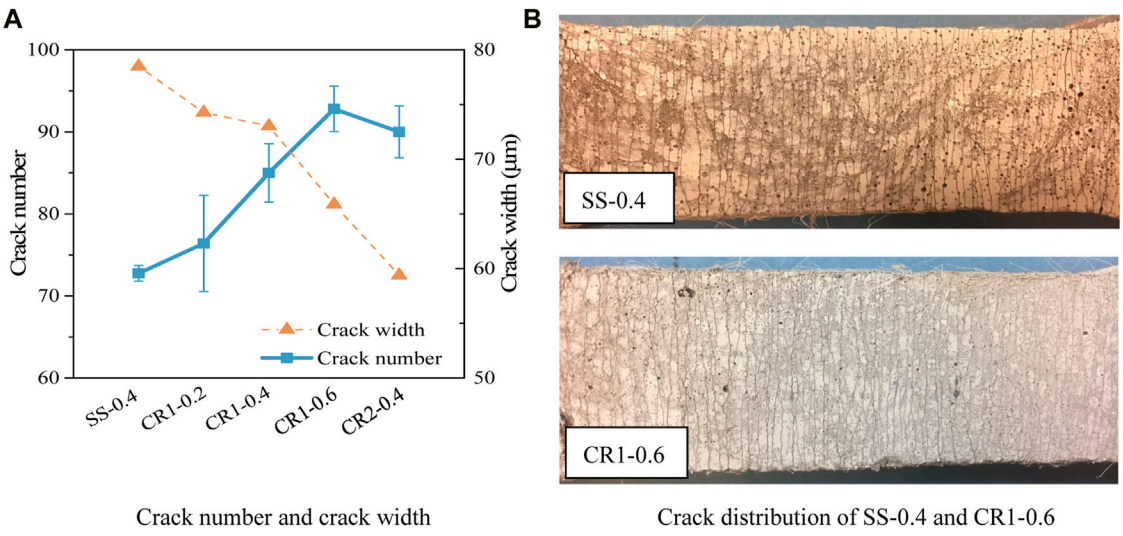


**FIGURE 7 |** Crack parameters of HS-ECC. **(A)** Crack number and crack width. **(B)** Crack distribution of SS-0.4 and CR1-0.6. HS-ECC, high-strength engineered cementitious composite.

the fracture energy of HS-ECC decreases as SS is entirely replaced by CR1 by equal volume, which is caused by the much lower peak tensile strength of CR1-0.4 (**Figure 6C**). Normalizing the fracture energy by the peak tensile strength (i.e., $G_f/\sigma_{tu}$) as listed in **Table 3**, it is noted that the larger $G_f/\sigma_{tu}$ ratio combined with the lower fracture energy as well as the lower peak tensile strength

**TABLE 4 |** Crack parameters of preloaded CR2-0.4

| Pre-tensile strain (%) | Crack number | Crack width (μm) |
|---|---|---|
| 0.5 | 9 | 43 |
| 1.0 | 17 | 48 |
| 2.0 | 27 | 59 |

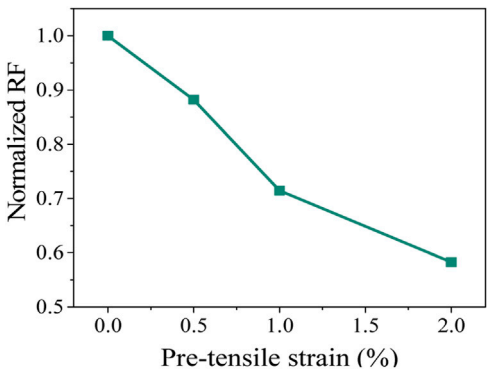


**FIGURE 8 |** Normalized RF of pre-damaged CR2-0.4. RF, resonant frequency.

values of CR1-0.4 compared with that of SS-0.4 indicates a gentler descending branch and a better energy consumption capacity after crack localization of HS-ECC with CR substitution. Additionally, it is also found from **Table 3** that the $G_f/\sigma_{tu}$ ratio increases from 1.13 to 2.62 gradually as CR1 proportion improves from 0.2 to 0.6, demonstrating the positive influence of CR addition on energy absorption capacity and ductility after crack localization.

## Crack Patterns

**Figure 7A** shows the crack number and crack width of CR-modified HS-ECC. It should be stressed that the crack number increases obviously from 73 to 85 when CR1 is used to totally replace SS. Simultaneously, with the increase of CR1 proportion from 0.2 to 0.6, the activated crack number of HS-ECC improves gradually from 76 to 93 with a 22.4% increment. As observed in **Figure 7B**, the crack distributions of CR1-0.6 are more saturated than those of SS-0.4. Nevertheless, an opposite trend with CR1 proportion is observed for the crack width in general. The average crack width of HS-ECC using SS as a fine aggregate is approximately 80 μm. This value decreases to 73 μm when CR1 is used to replace SS by equal volume, and the refining effect on crack width can be further enhanced to reduce the crack width to 59 μm when CR2 with a smaller particle size is adopted. Apparently, the replacement of SS by CR can activate more microcracks as well as reduce the crack width by introducing artificial flaws and decreasing the matrix fracture toughness as shown in **Figure 4**, enhancing the self-healing potential of HS-ECC.

## Self-Healing Properties of High-Strength Engineered Cementitious Composite

### Properties of Pre-Damaged CR2-0.4

The high-strength lightweight CR2-0.4 specimens exhibiting the smallest average crack width of 59 μm corresponding to the peak stress are selected to further explore the self-healing properties of HS-ECC. **Table 4** summarizes the crack pattern of the CR2-0.4 specimens preloaded to three strain levels, i.e., 0.5%, 1.0%, and 2.0%. The crack number increases with the increase of preloaded strain level from 9% at 0.5% to 27% at 2.0%, and a similar trend is observable in the average crack width at the loading stage that grows from 43 to 59 μm.

The normalized RF for the pre-cracked CR2-0.4 specimens preloaded to strain levels of 0.5%, 1.0%, and 2.0% is plotted in **Figure 8**. With the increase of pre-strain level, the normalized RF value decreases and expresses an almost linear relationship. The normalized RF gradually decreases from 0.88 at a pre-tensile strain of 0.5% to 0.58 at a pre-tensile strain of 2.0%. The increased

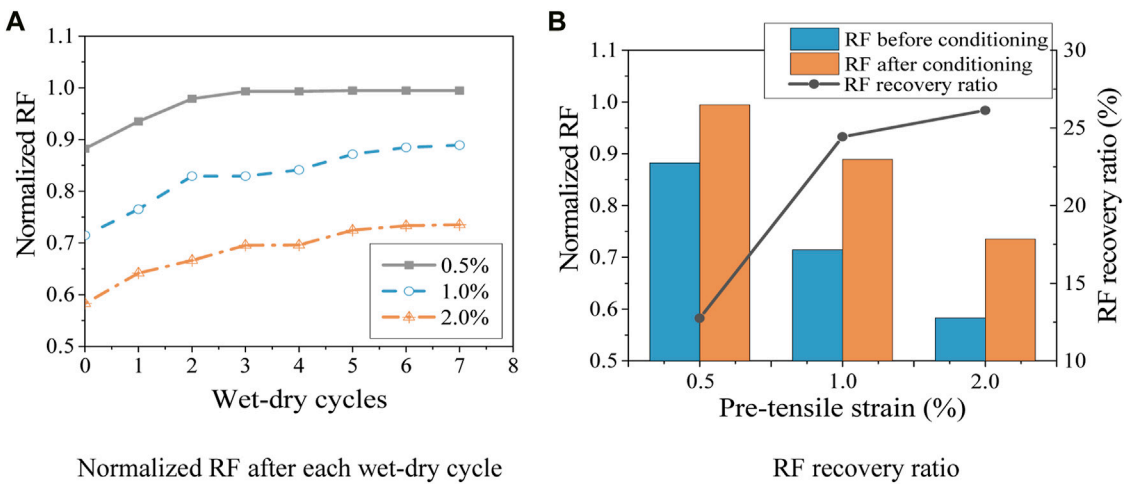


**FIGURE 9 |** RF of CR2-0.4 after wet–dry cycles. **(A)** Normalized RF after each wet–dry cycle. **(B)** RF recovery ratio. RF, resonant frequency.

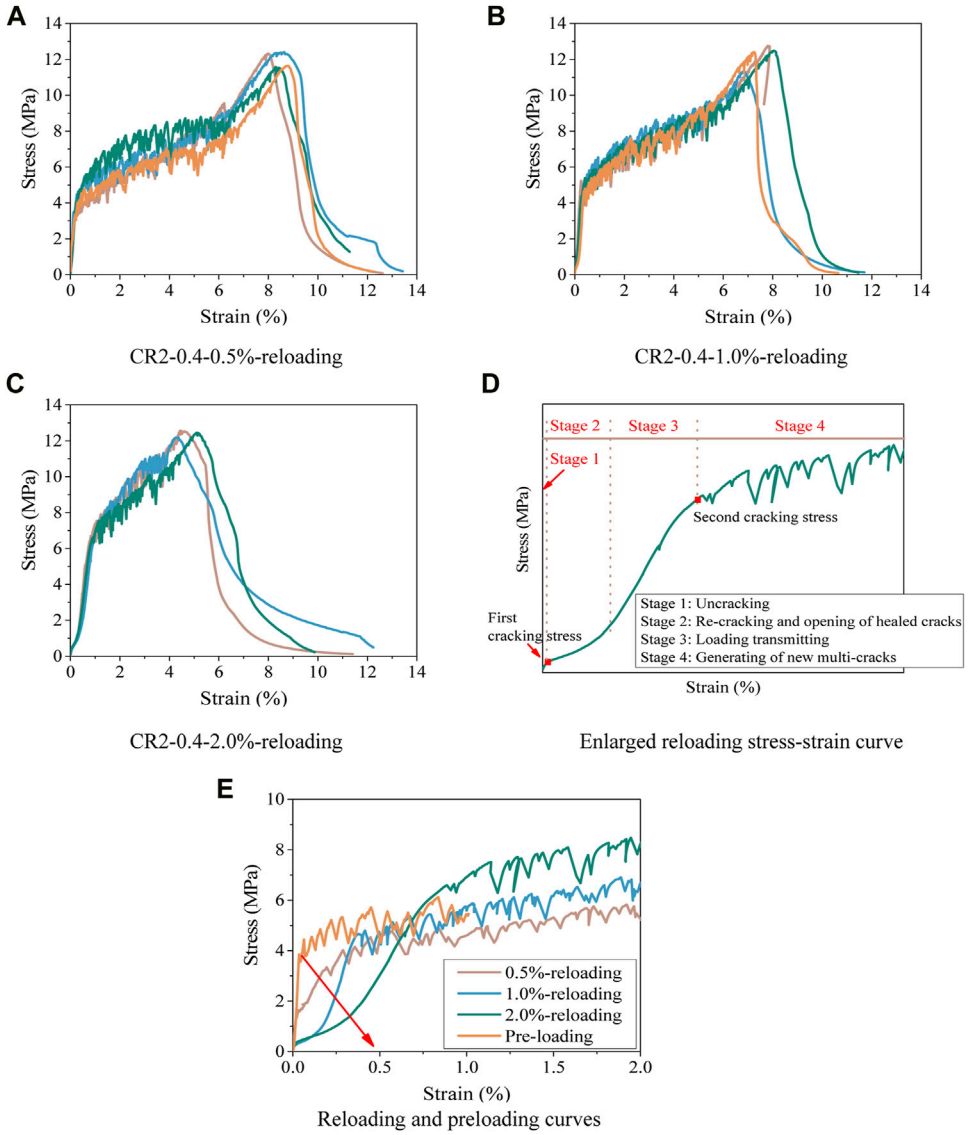


**FIGURE 10 |** Stress–strain curves of self-healed CR2-0.4 specimens. **(A)** CR2-0.4-0.5%-reloading. **(B)** CR2-0.4-1.0%-reloading. **(C)** CR2-0.4-2.0%-reloading. **(D)** Enlarged reloading stress–strain curve. **(E)** Reloading and preloading curves.

crack number as well as the enlarged crack width could be the reason for the decrease of RF.

## Resonant Frequency Recovery

The normalized RF recovery of the pre-cracked CR2-0.4 specimens before and after every wet–dry cycle is recorded and plotted in **Figure 9A**. At least three specimens are prepared to monitor the RF recovery. The RF of the CR2-0.4 specimens is normalized by the value of uncracked (virgin) specimens. Therefore, a high RF ratio represents a high recovery degree, which can be attributed to further hydration during the wet–dry conditioning regimes. Apparently, the CR2-0.4 specimens preloaded to a higher damage level show a lower RF both before and after wet–dry cycles. It is clear from **Figure 9A** that RF recovery mainly happens in the first 2–5 wet–dry cycles. After 7 wet–dry cycles, the normalized RF of the CR2-0.4 specimens regains beyond 99%, 89%, and 73% for 0.5%, 1.0%, and 2.0% pre-strained specimens, respectively. For the CR2-0.4 specimens preloaded to a lower strain level (i.e., 0.5%), the tighter distributed cracks with tinier crack widths (i.e., 43 μm) are more easily filled with healing products, and the RF can recover up to almost 100% of the uncracked specimen after only 2–3 cyclic wet–dry exposures. Nonetheless, for the CR2-0.4 specimens with more severe damage (i.e., a pre-tensile strain of 2.0% with a crack width of 59 μm), the hydration products generated during the wet–dry cycles accumulated at the microcrack surface might hinder the further hydration inside the microcrack, leading to a lower RF after healing. Moreover, the RF value for the CR2-0.4 specimens pre-damaged mildly tends to be faster compared with those pre-damaged seriously.

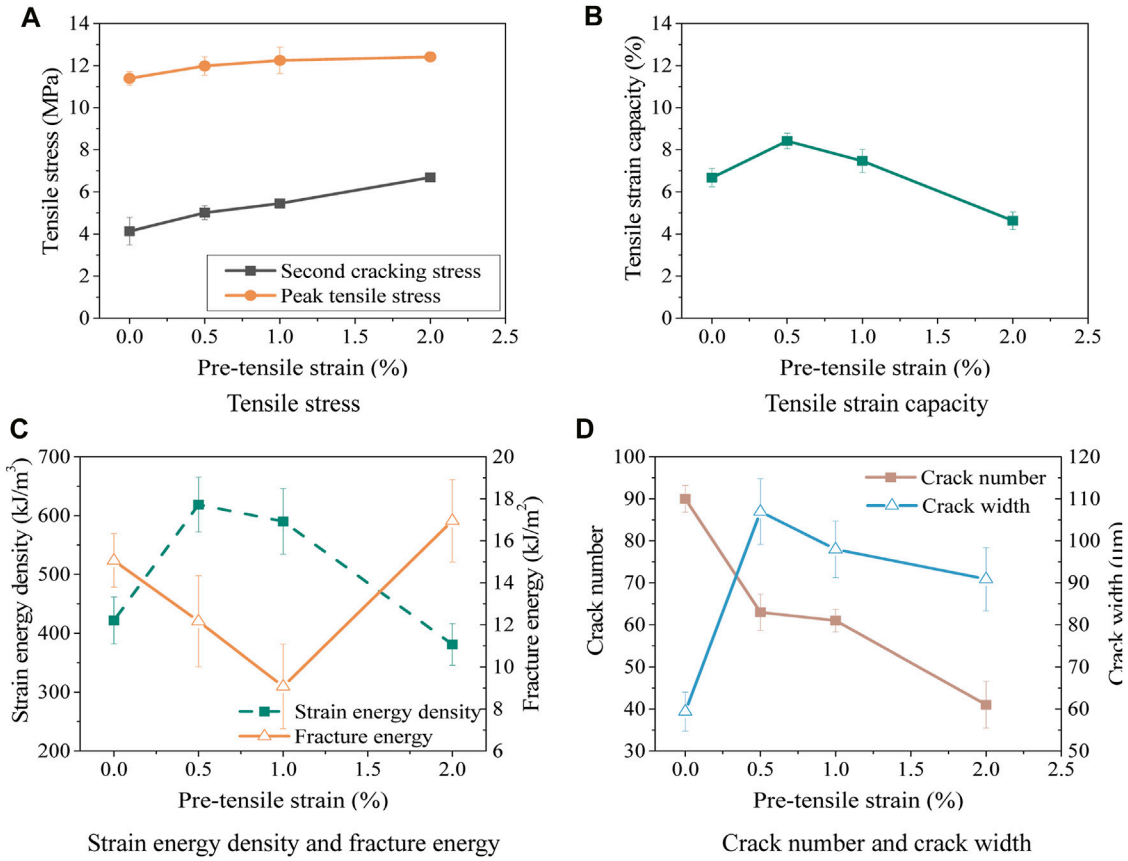


**FIGURE 11 |** Tensile parameters of reloading CR2-0.4 specimens. **(A)** Tensile stress. **(B)** Tensile strain capacity. **(C)** Strain energy density and fracture energy. **(D)** Crack number and crack width.

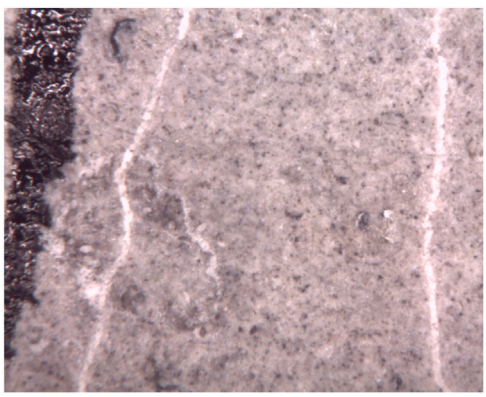

**FIGURE 12 |** Self-healing CR2-0.4-0.5% specimen surface after 7 wet–dry conditioning.

The extent of the RF recovery ratio of the CR2-0.4 specimens after 7 wet–dry cycles for three pre-strain levels is shown in **Figure 9B**. The ratio of RF recovery increases with the increase of preloading strain levels, meaning that the opportunity of crack healing can be enhanced by experiencing more damage in the form of crack numbers. Although the RF recovery ratio of the CR2-0.4 specimen pre-stretched to 2.0% tensile strain is relatively high (i.e., 26.1%), its self-healing capacity after curing conditioning is inadequate with an RF value of 73.5% of the intact one due to the wider crack width.

## Tensile Mechanical Performance Recovery

The reloading tensile stress–strain curves of the self-healed CR2-0.4 specimens preloaded to three tensile strains, including 0.5%, 1.0%, and 2.0%, are plotted in **Figures 10A–C**. All the pre-damaged and self-healed CR2-0.4 specimens exhibit significant strain-hardening performance as virgin specimens. It is worth noting that the residual strain induced during the preloading stage is neglected in the reloading stress–strain curves, expressing a conservative record of the tensile strain capacities of the self-healed specimens. As can be seen from **Figures 10A–C**, the reloaded CR2-0.4 specimens express a similar tensile strength whereas decreased tensile strain capacity with the increasing pre-damage level. The maintained tensile strength can be because water can penetrate through the cracks and the continued hydration can enhance the fiber/matrix interfacial bond during the self-healing process. Thus, the more pre-formed the cracks are, the higher the tensile strength recovery. Besides, as can be seen from the local enlarged stress–strain curve in **Figure 10D**, the reloading tensile process can be divided into four stages. Stage

1 with higher stiffness indicates that the self-healed matrix filled by the re-hydration products is uncracked; Stage 2 with much lower stiffness relates to the re-cracking and opening of the self-healed cracks, which offers less resistance to load; Stage 3 exhibits higher stiffness compared with Stage 2, more and more fibers re-engaged to bridge the cracks and transmit tensile load; and further loading causes Stage 4 features with the strain-hardening process. Further, the enlarged preloading stress–strain curves of the virgin CR2-0.4 specimen and the reloading curves of the self-healed CR2-0.4 specimens after wet–dry cycles are compared in **Figure 10E**. It is stressed that the stiffness of Stage 3 of reloading specimens, which is defined as the recovery stiffness of the self-healed specimens in this study, reduces with the increasing pre-tensile strain due to the aggravation of initial damage. As expected, the stiffness of the virgin CR2-0.4 specimen is much higher than the recovery stiffness of self-healed specimens during reloading (**Figure 10E**).

**Figure 11** compares the tensile parameters of the virgin CR2-0.4 specimens and those of reloaded specimens. It is noted from **Figure 11A** that not only the peak tensile stress but also the second cracking stress (**Figure 10D**) increases with higher pre-tensile strain. The peak tensile stress of virgin specimens is 11.39 MPa, and this value increased to 12.41 MPa of the specimen with a 2% pre-strain. This could be attributed to the further hydration of unreacted cementitious materials during the wet–dry curing process, leading to an improvement in the interfacial fiber/matrix bond stress, which causes a higher ultimate strength of the self-healed specimens. Accordingly, a full tensile strength recovery can be achieved after self-healing of the pre-damaged CR2-0.4 specimens. In addition, the second cracking stress represents a more obvious increment from 4.13 MPa of the virgin specimen to 6.69 MPa with an increase of 38.3% as the pre-damage level increases to 2.0%, demonstrating the effective tensile loading transition capacity of the pre-cracked location. Moreover, the first cracking stress of all the self-healed CR2-0.4 specimens is quite small at approximately 0.3–0.5 MPa as shown in **Figures 11A–C**, indicating that self-healing products are relatively weak as compared with the original matrix.

The tensile strain capacity of the reloaded CR2-0.4 specimens reduces from 8.42% at 0.5% pre-strain to 4.63% at 2.0% pre-strain (**Figure 11B**). Similarly, the crack number also decreases obviously from 63 to 41 with a 34.9% reduction within the same pre-damage level range as shown in **Figure 11D**. Both phenomena can be attributed to the improvement in matrix toughness caused by the further hydration of the matrix. However, it should be noted from **Figure 11B** that the tensile strain capacities of the reloaded CR2-0.4 specimens with relatively small tensile strain levels of 0.5% and 1.0% are higher than those of the virgin specimen, which could contribute to the wider crack width.

Comparing **Figures 11B,C**, it can be seen that the strain energy density shares a similar trend with that of strain capacity, which increases obviously from 421.7 kJ/m$^3$ of the virgin specimen to 618.7 kJ/m$^3$ of CR2-0.4-0.5% (i.e., 11% increase) and then gradually decreases to 381.1 kJ/m$^3$ as the pre-damage level increases to 2.0%. On the contrary, the fracture energy decreases from 15.06 kJ/m$^2$ of the virgin CR2-0.4 specimens to 12.17 kJ/m$^2$ of CR2-0.4-0.5% and further reduces to 9.07 kJ/m$^2$ of CR2-0.4-1.0% due to the sharper descending branch. The above results confirm the self-healing capacity of HS-ECC material in the form of rehabilitation of tensile properties to some degree.

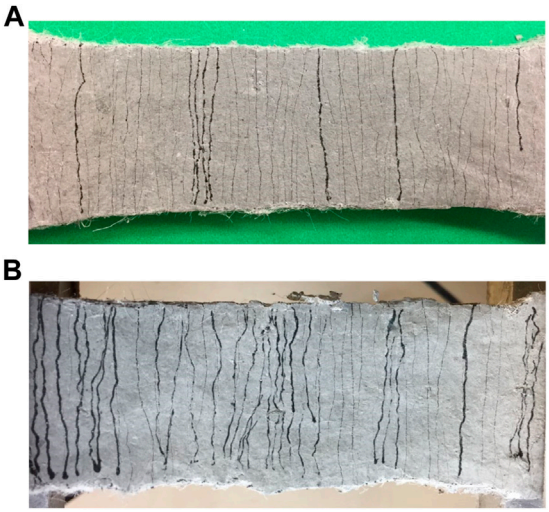


**FIGURE 13 |** Comparison of crack pattern for CR2-0.4 specimens before and after curing and reloading: **(A)** 0.5% pre-tensile strain and **(B)** 2.0% pre-tensile strain.

After self-healing, the white residue products along the crack lines after wet–dry conditioning can be observed in **Figure 12**. As mentioned before, the average crack width for the CR2-0.4 specimens preloaded to 0.5% tensile strain is about 43 μm as listed in **Table 4**. According to previous research, the majority of self-healed products are a combination of calcium carbonate crystals and calcium silicate hydrate gels (Kan and Shi, 2012).

The crack patterns for the CR2-0.4 specimens preloaded to 0.5% and 2.0% strain capacity and after curing and reloading are compared in **Figure 13**. The black lines were marked to represent cracks formed during the preloading stage. New cracks seem to follow and propagate along the pre-formed and self-healed cracks, indicating that self-healing products have a weaker structure than the original hydrated cementitious matrix. Thus, cracks are prone to generate and reopen on the previous crack location, resulting in an extremely small first cracking stress and low stiffness of Stage 2 in **Figure 10D**. At the same time, new cracks and crack paths are also observed to develop adjacent to previously self-healed cracks on new locations, resulting in Stage 3 and Stage 4 in **Figure 10D** and resuming the multiple cracking behaviors of self-healed HS-ECC specimens. Certainly, the self-healed cracks are capable to transmit the tensile load effectively to cause new cracking, demonstrating the recovery of mechanical properties through the self-healing process.

## CONCLUSION

A sustainable lightweight HS-ECC is developed by substituting SS completely by CR in this study, and the self-healing behavior of a

series of CR-modified HS-ECC specimens preloaded to three certain tensile strains including 0.5%, 1.0%, and 2.0% is investigated. CR as a fine aggregate in HS-ECC replaces SS entirely with three equivalent aggregate/binder ratios (i.e., $a/b$ = 0.2, 0.4, and 0.6) and two-particle sizes (i.e., CR1 and CR2) at $a/b$ = 0.4. According to the uniaxial tensile test results, the HS-ECC specimen that exhibits the smallest crack width (i.e., CR2-0.4) is selected to further conduct the self-healing tests. The rate and extent of self-healing behavior of the CR2-0.4 specimens are evaluated by RF and tensile performances after wet–dry conditioning. The detailed conclusions are summarized as follows.

1. The density and compressive strength of HS-ECC decrease with the increase of CR1 proportion. Particularly, CR2-0.4 using smaller CR particle exhibits a higher compressive strength while a lower density than that of CR1-0.4 with a larger CR particle size and can be classified as a lightweight cementitious composite.
2. All the HS-ECC specimens exhibit obvious strain-hardening performance under uniaxial tension. The peak tensile stress and initial tensile stress of HS-ECC decrease as the proportion of CR increases (i.e., $a/b$ from 0.2 to 0.6). Nevertheless, the peak tensile strength of HS-ECC with finer CR2 substitution generates a comparable peak tensile strength with the control specimen using SS as a fine aggregate. Besides, the influence of CR substitution and proportion on the tensile strain capacity of HS-ECC is irrelevant. Moreover, HS-ECC with CR substitution indicates a gentler descending branch and a better energy consumption capacity after crack localization.
3. CR acting as artificial flaws can reduce the HS-ECC matrix fracture toughness, activate more microcracks, and reduce crack widths, benefitting the self-healing potential of HS-ECC. Particularly, CR2-0.4 with the smallest crack width of 59 μm corresponding to the peak stress, which is comparable with the value of PVA-ECC, is selected to further study the self-healing properties of HS-ECC.
4. CR2-0.4 specimens have been proven to exhibit effective self-healing ability from both the mechanical and non-mechanical aspects. The majority of the RF recovery happens before the first 2–5 wet–dry cycles, and the recovery rate for the CR2-0.4 specimens with milder pre-damage is faster than that of those pre-damaged more seriously.
5. All the self-healed CR2-0.4 specimens have strain-hardening behavior with newly formed multi-cracks. The tensile stress–strain curves of the self-healed CR2-0.4 specimens can be divided into four stages according to the significant stiffness differences, representing distinct load transferring mechanisms. The further hydration of binder materials can enhance the interfacial bond stress and thus retain the mechanical performance, especially the tensile strength of the self-healed CR2-0.4 specimens. Further investigation on the self-healing performance of HS-ECC at loading status is warranted.

## DATA AVAILABILITY STATEMENT

The raw data supporting the conclusion of this article will be made available by the authors, without undue reservation.

## AUTHOR CONTRIBUTIONS

YJ: conceptualization and writing of original draft. XQ: methodology. JF: investigation and data curation. YQ: data curation. LM: Investigation and data curation.

## REFERENCES


Adesina, A., and Das, S. (2021). Performance of Engineered Cementitious Composites Incorporating Crumb Rubber as Aggregate. *Construction Building Mater.* 274, 122033. doi:10.1016/j.conbuildmat.2020.122033

Aldea, C.-M., Song, W.-J., Popovics, J. S., and Shah, S. P. (2000). Extent of Healing of Cracked normal Strength concrete. *J. Mater. Civ. Eng.* 12 (1), 92–96. doi:10.1061/(asce)0899-1561(2000)12:1(92)

American Concrete Institute (2003). *ACI Committee Report 213R-03 Structural Lightweight Aggregate concrete*. Detroit: American concrete institute.

ASTM (2019). *ASTM C215-19, Standard Test Method for Fundamental Transverse, Longitudinal, and Torsional Resonant Frequencies of Concrete Specimens*. West Conshohocken, PA: ASTM International.

Cai, Z., Liu, F., Yu, J., Yu, K., and Tian, L. (2021). Development of Ultra-high Ductility Engineered Cementitious Composites as a Novel and Resilient Fireproof Coating. *Construction Building Mater.* 288, 123090. doi:10.1016/j.conbuildmat.2021.123090

Chen, Y., Yu, J., and Leung, C. K. Y. (2018). Use of High Strength Strain-Hardening Cementitious Composites for Flexural Repair of concrete Structures with Significant Steel Corrosion. *Construction Building Mater.* 167, 325–337. doi:10.1016/j.conbuildmat.2018.02.009

Curosu, I., Liebscher, M., Mechtcherine, V., Bellmann, C., and Michel, S. (2017). Tensile Behavior of High-Strength Strain-Hardening Cement-Based Composites (HS-SHCC) Made with High-Performance Polyethylene, Aramid and PBO Fibers. *Cement Concrete Res.* 98, 71–81. doi:10.1016/j.cemconres.2017.04.004

Dong, F., Wang, H., Jiang, F., Xing, Q., and Yu, J. (2022). In-Plane Shear Behavior of Masonry Panels Strengthened With Ultra-High Ductile Concrete (UHDC). *Eng. Struct.* 252, 113609. doi:10.1016/j.engstruct.2021.113609

Edvardsen, C. (1999). "Water Permeability and Autogenous Healing of Cracks in concrete," in *Innovation in concrete Structures: Design and Construction* (London: Thomas Telford Publishing), 473–487.

Hammond, G. P., and Jones, C. I. (2008). Embodied Energy and Carbon in Construction Materials. *Proc. Inst. Civil Eng. - Energ.* 161 (2), 87–98. doi:10.1680/ener.2008.161.2.87

Huang, X., Ranade, R., Ni, W., and Li, V. C. (2013). On the Use of Recycled Tire Rubber to Develop Low E-Modulus ECC for Durable concrete Repairs. *Construction Building Mater.* 46, 134–141. doi:10.1016/j.conbuildmat.2013.04.027

Jacobsen, S., Marchand, J., and Boisvert, L. (1996). Effect of Cracking and Healing on Chloride Transport in OPC concrete. *Cement Concrete Res.* 26 (6), 869–881. doi:10.1016/0008-8846(96)00072-5

JSCE (2008). *Recommendations for Design and Construction of High-Performance Fiber Reinforced Cement Composites with Multiple Fine Cracks*. Tokyo, Japan: Japan Society of Civil Engineers, 1–16.

Kan, L.-l., and Shi, H.-s. (2012). Investigation of Self-Healing Behavior of Engineered Cementitious Composites (ECC) Materials. *Construction Building Mater.* 29, 348–356. doi:10.1016/j.conbuildmat.2011.10.051

Lei, D.-Y., Guo, L.-P., Chen, B., Curosu, I., and Mechtcherine, V. (2019). The Connection between Microscopic and Macroscopic Properties of Ultra-high

Strength and Ultra-high Ductility Cementitious Composites (UHS-UHDCC). *Composites B: Eng.* 164, 144–157. doi:10.1016/j.compositesb.2018.11.062

Li, L., Cai, Z., Yu, K., Zhang, Y. X., and Ding, Y. (2019). Performance-based Design of All-Grade Strain Hardening Cementitious Composites with Compressive Strengths from 40 MPa to 120 MPa. *Cement and Concrete Composites* 97, 202–217. doi:10.1016/j.cemconcomp.2019.01.001

Li, V. C., Bos, F. P., Yu, K., McGee, W., Ng, T. Y., Figueiredo, S. C., et al. (2020). On the Emergence of 3D Printable Engineered, Strain Hardening Cementitious Composites (ECC/SHCC). *Cement Concrete Res.* 132, 106038. doi:10.1016/j.cemconres.2020.106038

Li, V. C., and Leung, C. K. Y. (1992). Steady-State and Multiple Cracking of Short Random Fiber Composites. *J. Eng. Mech.* 118 (11), 2246–2264. doi:10.1061/(asce)0733-9399(1992)118:11(2246)

Li, V. C., and Wang, S. (2006). Microstructure Variability and Macroscopic Composite Properties of High Performance Fiber Reinforced Cementitious Composites. *Probabilistic Eng. Mech.* 21 (3), 201–206. doi:10.1016/j.probengmech.2005.10.008

Lin, Z., and Li, V. C. (1997). Crack Bridging in Fiber Reinforced Cementitious Composites with Slip-Hardening Interfaces. *J. Mech. Phys. Sol.* 45 (5), 763–787. doi:10.1016/s0022-5096(96)00095-6

Naaman, A. E., and Najm, H. (1991). Bond-slip Mechanisms of Steel Fibers in concrete. *Mater. J.* 88 (2), 135–145.

Oikonomou, N., and Mavridou, S. (2009). Improvement of Chloride Ion Penetration Resistance in Cement Mortars Modified with Rubber from Worn Automobile Tires. *Cement and Concrete Composites* 31 (6), 403–407. doi:10.1016/j.cemconcomp.2009.04.004

Ranade, R., Li, V. C., Stults, M. D., Heard, W. F., and Rushing, T. S. (2013). Composite Properties of High-Strength, High-Ductility Concrete. *ACI Mater. J.* 110 (4), 413–422. doi:10.1016/j.optmat.2013.06.025

Reinhardt, H.-W., and Jooss, M. (2003). Permeability and Self-Healing of Cracked concrete as a Function of Temperature and Crack Width. *Cement concrete Res.* 33 (7), 981–985. doi:10.1016/s0008-8846(02)01099-2

Wang, J., Guo, Z., Yuan, Q., Zhang, P., and Fang, H. (2020). Effects of Ages on the ITZ Microstructure of Crumb Rubber concrete. *Construction Building Mater.* 254, 119329. doi:10.1016/j.conbuildmat.2020.119329

Yang, Y., Lepech, M. D., Yang, E.-H., and Li, V. C. (2009). Autogenous Healing of Engineered Cementitious Composites under Wet-Dry Cycles. *Cement Concrete Res.* 39 (5), 382–390. doi:10.1016/j.cemconres.2009.01.013

Yu, K.-Q., Lu, Z.-D., Dai, J.-G., and Shah, S. P. (2020). Direct Tensile Properties and Stress-Strain Model of UHP-ECC. *J. Mater. Civ. Eng.* 32 (1), 04019334. doi:10.1061/(asce)mt.1943-5533.0002975

Yu, K.-Q., Yu, J.-T., Dai, J.-G., Lu, Z.-D., and Shah, S. P. (2018). Development of Ultra-high Performance Engineered Cementitious Composites Using Polyethylene (PE) Fibers. *Construction Building Mater.* 158, 217–227. doi:10.1016/j.conbuildmat.2017.10.040

Yu, K., Ding, Y., Liu, J., and Bai, Y. (2020). Energy Dissipation Characteristics of All-Grade Polyethylene Fiber-Reinforced Engineered Cementitious Composites (PE-ECC). *Cement and Concrete Composites* 106, 103459. doi:10.1016/j.cemconcomp.2019.103459

Yu, K., Mcgee, W., Ng, T. Y., Zhu, H., and Li, V. C. (2021). 3D-printable Engineered Cementitious Composites (3DP-ECC): Fresh and Hardened Properties. *Cement Concrete Res.* 143, 106388. doi:10.1016/j.cemconres.2021.106388

Yu, K., Wang, Y., Yu, J., and Xu, S. (2017). A Strain-Hardening Cementitious Composites with the Tensile Capacity up to 8. *Construction Building Mater.* 137, 410–419.

Zhang, Z., Ma, H., and Qian, S. (2015). Investigation on Properties of ECC Incorporating Crumb Rubber of Different Sizes. *Act* 13 (5), 241–251. doi:10.3151/jact.13.241

Zhang, Z., Qian, S., and Ma, H. (2014). Investigating Mechanical Properties and Self-Healing Behavior of Micro-cracked ECC with Different Volume of Fly Ash. *Construction Building Mater.* 52, 17–23. doi:10.1016/j.conbuildmat.2013.11.001

Zhang, Z., Yang, F., Liu, J., and Wang, S. P. (2020a). Eco-Friendly High Strength, High Ductility Engineered Cementitious Composites (ECC) With Substitution of Fly ash by Rice Husk Ash. *Cem. Concr. Res.* 137, 106200.

Zhang, Z., Qin, F., Ma, H., and Xu, L. (2020b). Tailoring an Impact Resistant Engineered Cementitious Composite (ECC) by Incorporation of Crumb Rubber. *Construction Building Mater.* 262, 120116. doi:10.1016/j.conbuildmat.2020.120116

Zhang, Z., Liu, S., Yang, F., Weng, Y., and Qian, S. Z. (2021). Sustainable High Strength, High Ductility Engineered Cementitious Composites (ECC) With Substitution of Cement by Rice Husk Ash. *J. Cleaner Prod.* 317, 128379. doi:10.1016/j.jclepro.2021.128379

Zhang, Z., and Zhang, Q. (2017). Self-healing Ability of Engineered Cementitious Composites (ECC) under Different Exposure Environments. *Construction Building Mater.* 156, 142–151. doi:10.1016/j.conbuildmat.2017.08.166

Zhu, H., Wan, K. T., Satekenova, E., Zhang, D., Leung, C. K. Y., and Kim, J. (2018). Development of Lightweight Strain Hardening Cementitious Composite for Structural Retrofit and Energy Efficiency Improvement of Unreinforced Masonry Housings. *Construction Building Mater.* 167, 791–812. doi:10.1016/j.conbuildmat.2018.02.033

**Conflict of Interest:** YQ was employed by the company Qinghai Transportation Planning and Design Research Institute Co., Ltd. LM was employed by Shanghai Tiangu Housing Inspection Company, Ltd.

The remaining authors declare that the research was conducted in the absence of any commercial or financial relationships that could be construed as a potential conflict of interest.

frontiers in Materials

ORIGINAL RESEARCH
published: 20 December 2021
doi: 10.3389/fmats.2021.801452

# Bond–Slip Law Between Steel Bar and Different Cement-Based Materials Considering Anchorage Position Function

*Jie Xiao[1], Xiang Long[2], Ming Ye[2], Haibo Jiang[1]*, Lingfei Liu[3], Fan Mo[1], Dejun Deng[1] and Zikang Huang[1]*

[1]School of Civil and Transportation Engineering, Guangdong University of Technology, Guangzhou, China, [2]Yuexiu Transport Infrastructure Co., Ltd., Hongkong, China, [3]School of Transportation, Civil Engineering & Architecture/Foshan University, Foshan, China

The bond performance between steel bar and cement-based materials was the prerequisite for the two materials to work together, and previous studies showed that the bond behavior of the steel bars and cement-based materials will vary with the kinds of cement-based materials. For this reason, this paper adopted 12 direct pullout test specimens including three types of concrete and two types of steel bars. The strain of the steel bar at six measuring points was measured with a strain gauge. Based on the measured strain and free end slip of the steel bars, the distribution of steel stress, bond stress, and relative slip and the bond slip relation along the anchorage length were obtained and analyzed for different concrete and different steel bars. Based on these test results of steel strain and relative slip at six measuring points, the anchorage position function could be established in consideration of anchorage position, which was conducive to the establishment of an accurate bond–slip relationship. In addition, the anchorage length of the steel bar in Engineered Cementitious Composites (ECC) calculated from the equilibrium equation of critical limit state is only half of the anchorage length calculated in the current Code for Design of Concrete Structures (GB 50010-2010) in China. It is suggested to establish the critical anchorage length formula suitable for ECC in future studies.

**Keywords: bond-behavior, engineered cementitious composite, pull-out tests, anchorage position function, critical anchorage length**

OPEN ACCESS

***Edited by:***
*Kequan Yu,*
*Tongji University, China*

***Reviewed by:***
*Lei Wang,*
*Xi'an University of Architecture and Technology, China*
*Biao Hu,*
*Shenzhen University, China*

****Correspondence:***
*Haibo Jiang*
*hbjiang@gdut.edu.cn*

***Specialty section:***
*This article was submitted to Structural Materials, a section of the journal Frontiers in Materials*

***Received:*** *25 October 2021*
***Accepted:*** *15 November 2021*
***Published:*** *20 December 2021*

***Citation:***
*Xiao J, Long X, Ye M, Jiang H, Liu L, Mo F, Deng D and Huang Z (2021) Bond–Slip Law Between Steel Bar and Different Cement-Based Materials Considering Anchorage Position Function. Front. Mater. 8:801452. doi: 10.3389/fmats.2021.801452*

## INTRODUCTION

Cement-based materials are widely used in civil buildings, bridges, tunnels, and other fields because of its advantages of convenient supply of raw material, low cost, good durability, and so on (Fu et al., 2021; Lei et al., 2021; Lam et al., 2021; Wang et al., 2020; Wang et al., 2021a; Wang et al., 2021b; Zhang et al., 2021). As one of the advanced cement-based materials, Engineered Cementitious Composites (ECC) has received more and more attention from both engineers and researchers because of its superior strain-hardening behavior, crack control capability, and ductile property (Cai et al., 2021; Hu et al., 2019; Xiong et al., 2021a; Xiong et al., 2021b; Yu et al., 2021; Yu et al., 2017; Zhou et al., 2019). Experimental studies have confirmed that the ultimate tensile strain of ECC could exceed 3%, which is about 100–300 times as large as that of ordinary concrete and 5-10 times as large

as that of steel bar (Li et al., 2002; Xu and Wang 2008). The bond performance between steel reinforcement and cement-based materials was the prerequisite for the two materials to work together and played an important role in ensuring reliable force transfer from the steel reinforcement to surrounding cement-based materials. Effective bonding between the steel bar and the cement-based material is essential for the two materials to work stably and cooperatively. Poor bonding performance will weaken the load-bearing capacity of the component, which will lead to structural failure.

Over the past years, many scholars have carried out some investigations on the bond performance of steel bars in ECC. Wang et al. (2015) carried out pullout tests to evaluate the influences of the properties of matrix materials on the bond behaviors between BFRP bars and cementitious materials and found that the bond strength of the ECC specimen was higher than that of the cement mortar specimen under the same cover thickness and embedment length. Lee et al. (2016) found that the bond strength between steel reinforcement and ECC could be significantly higher than that between steel reinforcement and normal concrete. Deng et al. (2018) carried out direct pullout tests of the steel bar in ECC by changing the bar diameter, bar shape, cover thickness, fiber volume content, and ECC strength and found that the ultimate bond strength of ECC and steel bars is better than the extreme bond strength of ordinary concrete and steel bars. Deng et al. (2018) also built the position function and proposed an accurate bond–slip relationship according to the distribution of bond stress along the anchorage length. Cai et al. (2020) investigated the bond–slip performance of steel reinforcement embedded in ECC as well as concrete and found that the bond strength between steel reinforcement and ECC was higher than that between steel reinforcement and concrete due to the superior tensile ductility of ECC. Xiao et al. (2021) carried out an direct pullout experiment to explore the influence of rebar diameter and type, cover layer thickness, embedment length, and fiber volume content on the bond behavior of the rebar embedded in ECC and found that as the embedment length increased, the bond stress distribution in the bonded section became increasingly nonuniform. Huang et al. (2020) examined the variation in bond stress along the anchorage length of glass fiber reinforced polymer (GFRP) bar tendons *via* strain gauges attached to the GFRP bars and established a more accurate bond stress and slip constitutive model of the GFRP bars and concrete. Hossain et al. (2020) performed pullout tests on specimens with different parameters such as bar type, bar diameter, embedded length, and concrete types to study the bond strength between GFRP bars and ECC and found that the bond strengths of GFRP bars embedded in the ECC were larger than that embedded in the normal concrete. As the foundation of finite element analysis and engineering design of reinforced concrete, the bond–slip relationship between steel bar and concrete will directly affect the reliability of analysis results. Krstulovic-opara et al. (1994) found that the bond performance was significantly affected by the tensile strength and strain capacity of the matrix. Therefore, compared with traditional cement-based materials such as concrete and fiber-reinforced concrete, the bond performance of steel bar in ECC may be quite different.

**TABLE 1 |** Mix proportion used for the three types of concrete (by weight).

| Concrete type | ECC | NSC | SFRC |
|---|---|---|---|
| Cement/kg·m$^{-3}$ | 383.7 | 473.6 | 383.7 |
| Fly ash/kg·m$^{-3}$ | 895.3 | — | 895.3 |
| Silica sand/kg·m$^{-3}$ | 455 | — | 455 |
| Superplasticizer/kg·m$^{-3}$ | 10.12 | 6.16 | 10.12 |
| PVA fiber/kg·m$^{-3}$ | 26 | — | — |
| Steel fiber/kg·m$^{-3}$ | — | — | 13 |
| Water/kg·m$^{-3}$ | 303 | 184.6 | 303 |
| River sand/kg·m$^{-3}$ | — | 694.3 | — |
| Gravel/kg·m$^{-3}$ | — | 1,047.5 | — |
| Cube compressive strength/MPa | 48 | 50 | 75 |

In the past few years, many studies have been conducted on the bond performance of deformed steel bars in concrete under service periods. According to the test results, various bond strength models and bond stress–slip constitutive models have been proposed assuming that the bonding stress is uniformly distributed over the embedded length, and the average bond stress is equal to the applied load divided by the contact area between the steel bar and the surrounding concrete (Zhao and Jin 2002). However, in practical engineering, the distribution of bond stress is different along the anchorage length. Therefore, it is necessary to take this difference into account to establish a more accurate bond–slip relationship. Previous studies have shown that the tensile strength and strain capacity of the matrix had a major impact on the bonding performance (Krstulovic-Opara et al., 1994; Choi et al., 2017). Therefore, the bond behavior of the steel bars in ECC may be different from the bond behavior of the steel bars in traditional brittle materials (such as concrete and fiber-reinforced concrete). For this reason, this paper adopted twelve direct pullout test specimens including three types of concrete and two types of steel bars. The strain of the steel bar at six measuring points was measured with strain gauges. Bonding stress could be calculated by these strains of the steel bar. Based on these test results of steel strain and relative slip at six measuring points, an accurate bond–slip relationship could be established in consideration of anchorage position.

# EXPERIMENTAL PROGRAM

## Materials

Engineered cementitious composites (ECC), normal strength concrete (NSC), and steel fiber-reinforced concrete (SFRC) were constituted with the mixture formulations provided in **Table 1**. The ECC and SFRC both contained Ordinary Portland cement (P.O 42.5R), Class I high-calcium fly ash, silica sand, superplasticizer, and water. The difference between the ECC and SFRC is that polyvinyl alcohol (PVA) fiber is used in ECC, while steel fiber concrete contains steel fiber. The characteristics of PVA fiber and steel fiber used in this study are listed in **Table 2**. The NSC contained Ordinary Portland cement (P.O. 42.5R), river sand, gravel, water, and

**TABLE 2 |** Characteristics of PVA fiber and steel fiber.

| Fiber type | Density/g·cm$^{-3}$ | Diameter/mm | Length/mm | Nominal tensile strength/MPa | Elongation at rupture/% | Young's modulus/GPa |
|---|---|---|---|---|---|---|
| PVA fiber | 1.3 | 0.04 | 12 | 1,600 | 6 | 40 |
| Steel fiber | 7.8 | 0.22 | 13 | 2,850 | 3.5 | 206 |

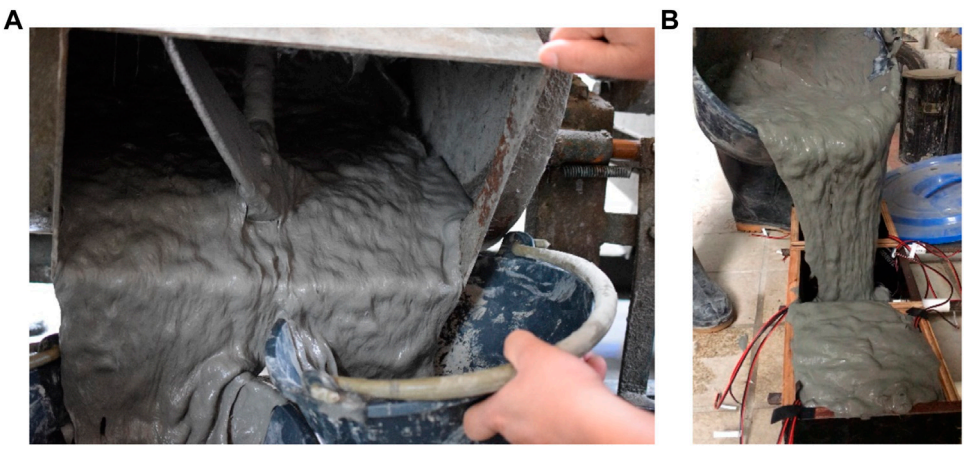


**FIGURE 1 |** Production process of ECC specimens: **(A)** ECC material that has been stirred and **(B)** specimen casting.

superplasticizer. The 28-day average compressive strengths of ECC, NSC, and SFRC are 48, 50, and 75 MPa, respectively.

A common horizontal concrete mixer with a volume of 30 l was used to mix the components and prepare cement-based material samples, as shown in **Figure 1**. The dispersion of PVA fibers in the ECC is a key factor in achieving ideal mechanical properties. In this paper, the clusters of PVA fibers purchased from the market were placed in a plastic mold with a diameter of 150 mm and a height of 300 mm, and then the plastic mold was turned upside down on a smooth wooden board. Then, a demolding gun connected to the demolding air pump was inserted into the small hole at the bottom of the plastic mold, which can make PVA fibers evenly dispersed under the action of the airflow, as shown in **Figure 2**. The steel fibers were also evenly added into the SFRC mixture during the mixing process in order to avoid the congestion of the steel fibers. In order to test the tensile properties of ECC material, fresh ECC mixtures were poured into standard-size dog bone specimens, as shown in **Figure 3A**. The results of the tensile performance test showed that the ultimate tensile strain of ECC used in this paper exceeds 3% and met the requirements of ECC, as shown in **Figure 3B**. The design value of the tensile strength $f_{ty}$ of the ECC concrete was 4.58 MPa, and the testing and calculation procedures can be found in the literature (Xiao et al., 2021).

## Specimen Design

The pullout test is one of the most widely used test methods on investigating the bond performance between steel bar and cement-based materials due to the convenience of specimen manufacturing, the simple operation of test apparatus, and the easy analysis of the test results. In this paper, the pullout test was employed to study the bond performance between steel bar and cement-based materials. Direct pullout test specimen is to embed a steel bar horizontally into the concrete cube along its central axis. In order to ensure that the thickness of the protective layer is sufficient to make the failure mode of the specimen result in pullout failure, the side length of the concrete cube was designed to be 160 mm. A PVC pipe with a length of 60 mm was placed in the nonbonded region in the concrete cube, and the PVC pipe was filled with polyurethane foam to avoid concrete flowing into it during casting. The steel bar extends 50 mm from the free end and 360 mm from the loading end, and the length of the bond region was 100 mm, as shown in **Figure 4**. The experiment was divided into four groups, each of which consisted of three identical test specimens. The type of concrete used in the first three groups was different, and the type of steel bar used in the last group was different. Within the 100-mm anchorage length of each specimen, six strain gauges were pasted at equal intervals, each about 20 mm apart, as shown in **Figure 4**. The symbol E-C16 represents that the concrete of the specimen was ECC and the steel bar was ribbed steel bar with a diameter of 16 mm. The symbol E-C16R denoted that the concrete of the specimen was ECC and the steel bar was a plain round bar with a diameter of 16 mm. The symbol P-C16 meant that the concrete of the specimen was normal concrete and the steel bar was ribbed steel bar with a diameter of 16 mm. The symbol SF-C16 indicated that the concrete of the specimen was SFRC and the steel bar was ribbed steel bar with a diameter of 16 mm. The yield

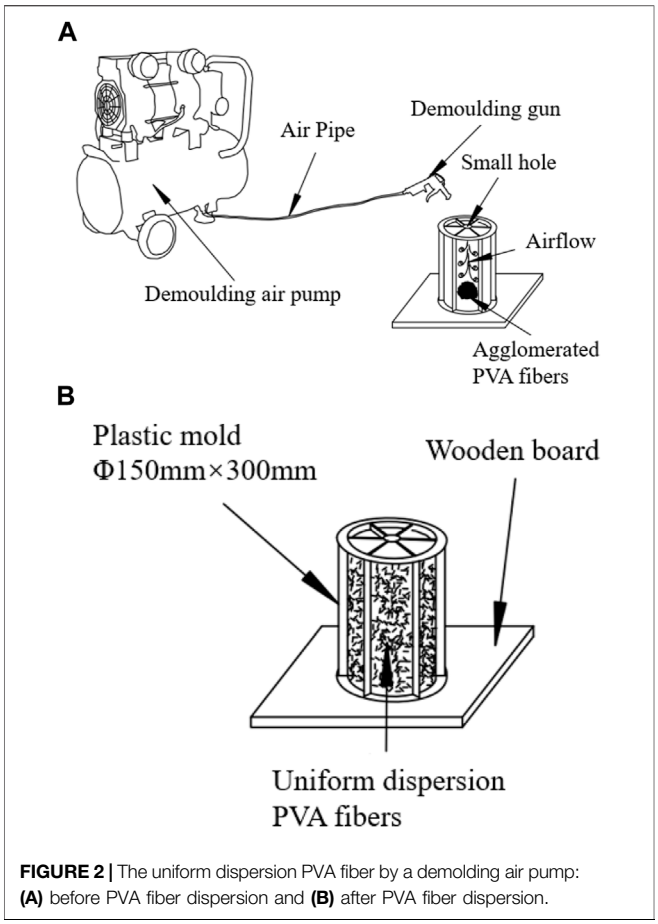


**FIGURE 2 |** The uniform dispersion PVA fiber by a demolding air pump: **(A)** before PVA fiber dispersion and **(B)** after PVA fiber dispersion.

strength of the ribbed steel bar was 415.06 MPa and the yield strength of the plain round bar was 252.99 MPa and the testing data can be found in the literature (Xiao et al., 2021).

## Experiment setup

The pullout test was carried out on the experimental machine shown in **Figure 5**. The concrete specimens with the embedded steel bar were placed in a self-made steel frame, which consisted of two 25-mm-thick square steel plates. The two square steel plates were connected to each other by four 20-mm-diameter steel rods located at the corners. The distance between the two steel plates was set to 50 cm to ensure there was sufficient space for the installation of linear variable differential transformers (LVDTs). There was a 30-mm-diameter hole in the center of the steel frame bottom plate to allow the steel bar to pass through. A universal testing machine with a maximum tensile force of 1,000 kN was adopted to apply the pullout load. The pullout load was applied at a rate of 0.5 mm/min in displacement loading mode until failure. Assuming that the bond stress is uniformly distributed along the longitudinal direction, the formula below can be used to calculate the average bond strength between steel bar and concrete:

$$\tau = \frac{P}{\pi d l_a} \tag{1}$$

where P denotes the pullout force, d represents the diameter of the steel bar, and $l_a$ means the length of the bond region. As shown in **Figure 5**, the BC segment was the bond region of the steel bar. The MM section was the upper surface of the concrete cubes close to the free end. The NN section was the lower surface of the concrete cubes close to the loading end. Two LVDTs were symmetrically mounted on the MM section to test the average displacement of the MM section $S_M$. An LVDT was placed at the free end of the steel bar (section AA) to test its displacement $S_A$. The TDS-530 data acquisition system was employed to obtain the test data. The net slip of the free end of the steel bar could be expressed as follows:

$$S_F = \frac{S_A - S_M}{2} \tag{2}$$

Since the BF segment was long and near the loading end, the loading force was large, and the deformation generated could not be ignored. Therefore, the deformation of the BF segment should be taken into consideration when calculating the net slip of the loading end. The deformation of the steel bar in segmented BF could be expressed as

$$\Delta S_{BF} = \frac{P}{E_S A_S} L_{BF} \tag{3}$$

where $E_S$ denotes the elastic modulus of the steel bar, $A_S$ represents the cross-sectional area of the rebar, $L_{BF}$ denotes the initial length of the steel bar in segment BF, and P refers to the pullout load. If $S_Z$ represented the displacement of the loading end of the universal testing machine, the net slip of the steel bar at the loading end can be expressed as follows:

$$S_L = S_Z - \Delta S_{BF} \tag{4}$$

Therefore, the average relative slip of the steel bar and the matrix along the anchorage section could be expressed as follows:

$$S = \frac{S_F + S_L}{2} \tag{5}$$

# EXPERIMENTAL RESULTS AND DISCUSSION

## Bond Stress-Slip Curves

The relationship of bond stress and slip was one of the most important experimental results for studying the bond performance between steel bars and concrete. The stress–slip relationships of the pullout tests of the four groups of the specimens in this paper are shown in **Figure 6**. For ordinary concrete P-C16, when the slip increased to about 1.5 mm, the tensile force slowly approached the ultimate load, and when the bond stress reached the maximum value, the concrete split due to the hoop tensile force exceeded the tensile strength of the concrete. The width of the cracks formed was relatively large in the form of brittle failure. For the SFRC SF-C16, the failure mode of SF-C16 was different from the failure mode of P-C16. Although there was a large crack the same as P-C16, the concrete of SF-

C16 specimen did not split with brittle sound, forming a shear failure mode. In addition, the phenomenon of some steel fibers sinking was observed during casting of the concrete specimens, so the bond strength was lower than the results of other scholars, and the slip was lower than that of P-C16, which may be that the fiber sinking reduced the bond performance of steel bar and SFRC. Compared with P-C16 and SF-C16, the crack forms of specimen E-C16 were different. Although the failure mode was also shear failure, the surface of ECC specimen would find fine and intensive cracks that were hard to be observed by the naked eyes. The cracks were radially distributed from the center to the edge, and the number of the cracks on the surface of E-C16 was much more than that on the surface of P-C16 and SF-C16. This is attributed to that ECC had excellent crack control capability and ductile property. However, the shear strength of the pullout test ECC specimen E-C16R with a plain round bar was relatively small. At the initial stage, the shear stress of E-C16R was mainly supported by the chemical adhesion. Once the slip reached a certain value, the bond stress would decrease, and the slip would increase. The steel bar would be pulled out from the ECC, and it was difficult to find cracks on the surface of the specimen E-C16R, indicating that the bond performance was poor.

## The Distribution of Steel Stress Along the Anchorage Length

Since the strains of the steel bar under different loading levels could be measured by the strain gauges attached to the steel bar, the stress distribution of the steel bar along the anchorage length could be calculated, as shown in **Figure7**. The steel tension gradients of E-C16 and SF-C16 were the same, and their steel tension force started from 6 to 30 kN. The steel tension gradients of P-C16 were twice those of E-C16 and SF-C16 and the steel tension force of P-C16 started from 12 to 60 kN. As the bond strength of the specimen E-C16R was small, the tensile force of the steel bar was small as well and the steel tension force of E-C16R started from 1.5 to 3.5 kN. It is shown in **Figure 7** that the stress distribution curves of the steel bars along the anchorage length were similar in the four types of specimens. The stresses of the steel bars were relatively gentle at the loading end and free end, but relatively steep in the middle. As the load increased, the stress of the steel bar at the loading end increased, but the free end did not change much. The comparison between the specimen E-C16 and SF-C16 showed that the gradient of the steel bar stress variation of E-C16 was smaller than that of SF-C16. This meant that the steel bar stress of E-C16 was relatively stable with the variation of the anchoring position. The stresses of the steel bars of E-C16 at the free end were obviously larger than those of SF-C16 with the increase in the reinforcement pulling force. This showed that the PVA fibers played a good bridge effect on the concrete matrix. When the tension force of the steel bar was the same, the stress of the steel bar in P-C16 at each anchorage position was larger than that in E-C16 and SF-C16. The stress gradient of the steel bar in P-C16 was relatively obvious, which indicated that the bond strength of P-C16 was relatively high. With the increase in the tension force of the steel bar, the stress of the steel bar in E-C16R showed a great change at the loading end, while the stress of the steel bar at the distance of 60 mm from the loading end decreases almost to zero. Such an obvious change indicated that the anchorage performance of E-C16R was significantly lower than that of the ribbed steel bar.

## The Distribution of Bond Stress Along the Anchorage Length

In this paper, the strain gauge pasted on the surface of the steel bar was used to measure the strain of the steel bar at six measurement points along the bond region. Then the bond stress at each measurement point instead of the average stress of each interval was directly calculated according to the calculation method adopted in reference Xu and Wang (2008). Assuming that the strain of the steel bar was smoothly distributed in the bond region, and the bond region was divided into five sections by the measurement points, and the length of each section was h, the following formulas can then be obtained:

$$\varepsilon(x_i + h) = \varepsilon(x_i) + h\varepsilon'(x_i) + \frac{h^2}{2!}\varepsilon''(x_i) + \frac{h^3}{3!}\varepsilon'''(x_i) + o(h^4) \quad (6)$$

$$\varepsilon(x_i - h) = \varepsilon(x_i) - h\varepsilon'(x_i) + \frac{h^2}{2!}\varepsilon''(x_i) - \frac{h^3}{3!}\varepsilon'''(x_i) + o(h^4) \quad (7)$$

**Eq. 7** is subtracted from **Eq. 6**:

$$\varepsilon'(x_i) = \frac{\varepsilon(x_i + h) - \varepsilon(x_i - h)}{2h} - \frac{h^2}{6}\varepsilon'''(x_i) + o(h^3) \quad (8)$$

Add **Eqs 6**, **7** to obtain:

$$\varepsilon''(x_i) = \frac{\varepsilon(x_i + h) + \varepsilon(x_i - h)}{h^2} + o(h^2) \quad (9)$$

Take the derivative of **Eq. 9** and substitute it into the right-hand side of **Eq. 8**:

$$\varepsilon'(x_i) = \frac{\varepsilon(x_i + h) - \varepsilon(x_i - h)}{2h} - \frac{1}{6}\left(\varepsilon'_{i+1} + \varepsilon'_{i-1} - 2\varepsilon'_i\right) + o(h^3) \quad (10)$$

Ignore the error term and arrange $\delta\varepsilon_i = \varepsilon_{i+1} - \varepsilon_{i-1}$ to obtain the following formula:

$$\dot{\varepsilon_{i-1}} + 4\dot{\varepsilon_i} + \dot{\varepsilon_{i+1}} = \frac{3}{h}(\varepsilon_{i+1} - \varepsilon_{i-1}) = \frac{3}{h}\delta\varepsilon_i \quad (11)$$

The following formula can be obtained from the microsegment equilibrium of the steel bar, as shown in **Figure 8**:

$$\dot{\varepsilon_i} = \tau_i \frac{\pi d}{E_s A_s} = \frac{4\tau_i}{E_s d} \quad (12)$$

Substitute **Eq. 12** into **Eq. 11** to obtain the following formula:

$$\tau_{i-1} + 4\tau_i + \tau_{i+1} = \frac{3E_s d}{4h}\delta\varepsilon_i \quad (13)$$

Considering that its boundary conditions were $\tau_0 = \tau_n = 0$, the bond stress could be obtained through the following equations:

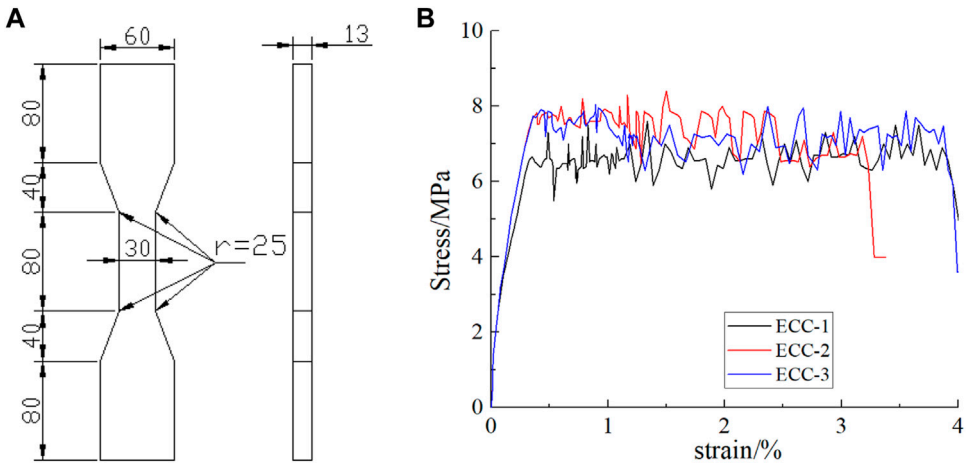


**FIGURE 3 |** Design and tensile property of the adapted ECC in the experiment: **(A)** dimension of dog-bone specimen (Unit mm) and **(B)** tensile stress–strain curves of ECC.

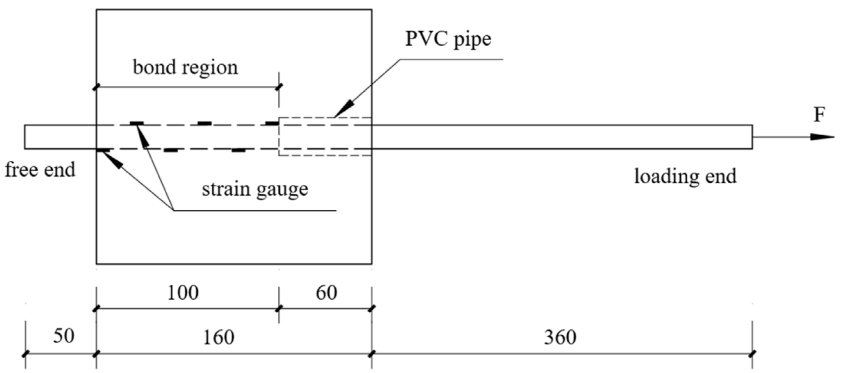


**FIGURE 4 |** Details of test specimen (Unit: mm).

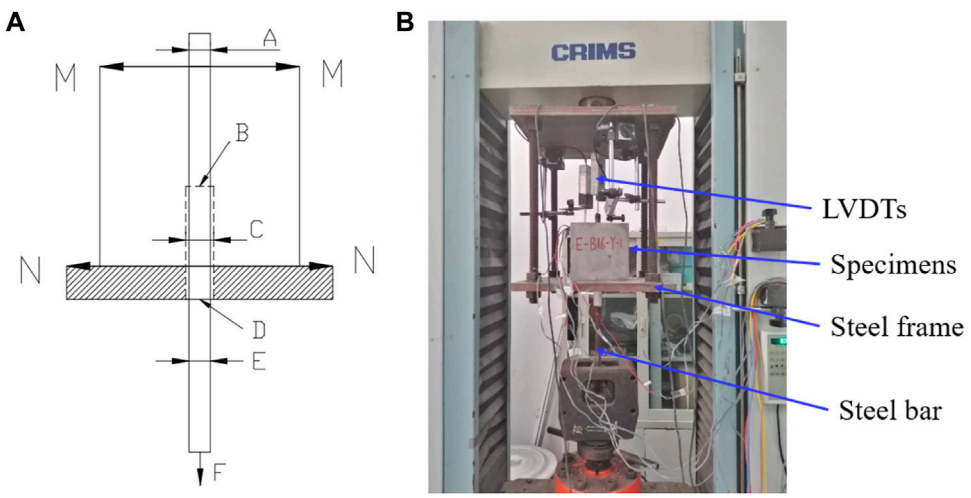


**FIGURE 5 |** Schematic diagram of loading apparatus and measurement position: **(A)** diagrammatic view and **(B)** photograph.

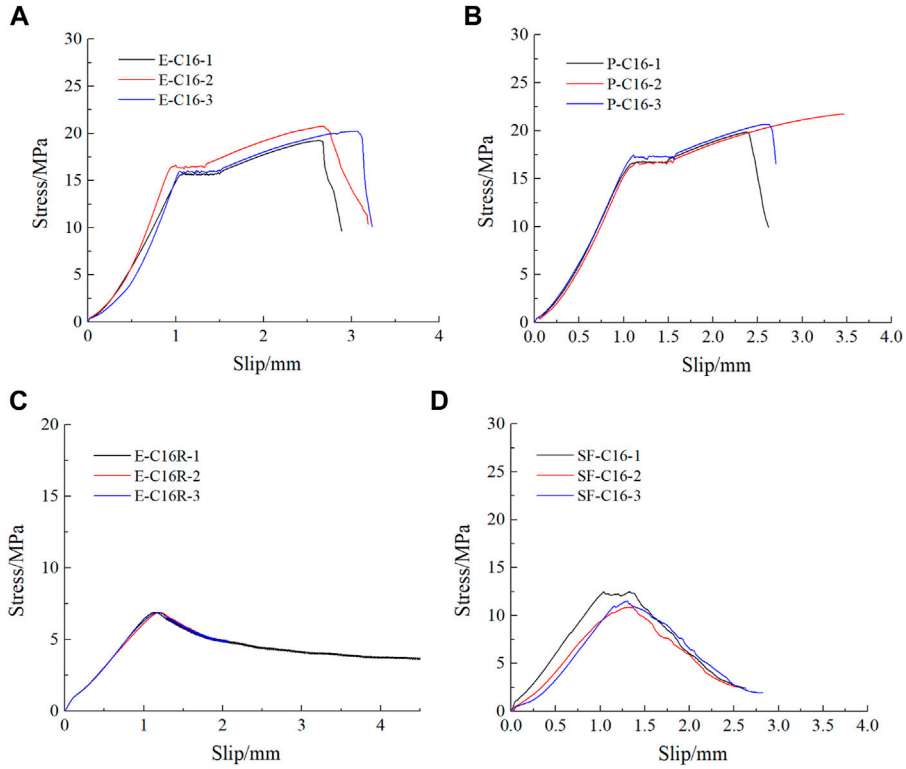


**FIGURE 6 |** Bond–slip curve: **(A)** E-C16, **(B)** P-C16, **(C)** E-C16R, and **(D)** SF-C16.

$$\begin{bmatrix} 4 & 1 & & & & & & \\ & 1 & 4 & 1 & & & & \\ & & & \cdots & \cdots & & & \\ & & & & 1 & 4 & 1 & \\ & & & & & 1 & 4 & \end{bmatrix} \begin{Bmatrix} \tau_1 \\ \tau_2 \\ \tau_3 \\ \cdots \\ \tau_i \\ \cdots \\ \tau_{n-2} \\ \tau_{n-1} \end{Bmatrix} = \frac{3E_s d}{4h} \begin{Bmatrix} \delta\varepsilon_1 \\ \delta\varepsilon_2 \\ \delta\varepsilon_3 \\ \cdots \\ \delta\varepsilon_i \\ \cdots \\ \delta\varepsilon_{n-2} \\ \delta\varepsilon_{n-1} \end{Bmatrix} \quad (14)$$

where $E_s$ represents the elasticity modulus of steel bar, d denotes the diameter of steel, and $\tau_i$ and $\varepsilon_i$ denote the bond stress and steel strain, respectively, at pint i. **Equation 14** was a three-diagonal array equation that can be solved by the chase method. No matter how the measurement points of steel bar were arranged within the bond region, the equations could always form a strictly diagonally dominant matrix. Therefore, the numerical solution to the equations always existed and the bond stress of each strain measurement point can be calculated by software for calculation.

Through **Eq. 14**, the bond stress under different uniaxial tensile loads was calculated. If these bond stresses were added up along the anchorage length, the bond stress multiplied by the circumference of the steel bar should be equal to the load applied to the steel bar at the loading end. If there was any difference between the two forces, the negative of the difference value should be adjusted according to the principle of equal distribution. Then, a smooth curve was used to express the general trend of the variations of the bond stress along the anchorage length, so that the area under the curve of bond stress distribution multiplied by the circumference of the steel bar was equal to the load applied to the steel bar at the loading end, and the curve of the distribution of bond stress along the anchorage length was obtained, as shown in **Figure 9**. The distance from the free end was defined as the X-coordinate, and the calculated stress in each strain recording point was defined as the Y-coordinate.

As is shown in **Figure 9**, no matter what kind of specimens, the distribution of bond stress along the anchorage length had a similar trend. That is, at each tensile load level, the stress along the anchorage length increased from the free end to the loading end. There were also some differences in the distribution of bond stress along the anchorage length for different specimens. For specimen E-C16, with the increase of the load applied to the steel bar at the loading end, the position of the maximum bond stress gradually approached the free end, and the stress in the middle of the anchorage position gradually became plump, indicating that the PVA fiber played a good bridging role. For specimen P-C16, at the initial stage of loading, the position of the maximum bond stress was close to the loaded end, but with the increase in the load applied to the steel bar at the loaded end, the stress at 60 mm away from the loaded end became plump and bore most of the tension force, gradually becoming the maximum bond stress. For specimen SF-C16, with the increase in tension force, the

bond stress peak values of the specimen appeared at 20 and 60 mm away from the loading end. The peak points of the bond stress moved right with the increase in the tensile force. It was speculated that the good connection of steel fiber left and right hooks made the concrete work well together. For specimen E-C16R, the peak points of the bond stress mainly appeared at 40 mm away from the loading end, and the peak value of its bond stress at each tensile load level was far less than that of the specimen with the ribbed steel bar.

## The Distribution of Relative Slip Along the Anchorage Length

From the measured slip of the loading end and the free end, the slip between steel bar and cement-based material at any position in the anchorage length could be calculated. It meant that this slip could be determined by the displacement difference between reinforcing bar and cement-based material at each point. In the test, the strain of the steel bar $\varepsilon_{si}$ at each measuring point had been obtained by the method of the internal strain gauge, so the elongation of the steel bar micro-segment was $\Delta l_{si} = \varepsilon_{si}\Delta l$ ($\Delta l$ was the spacing between strain gauges 20 mm). The average stress $\sigma_{ci}$ and strain $\varepsilon_{ci}$ of cement-based material around the steel bar can be calculated by the balance of micro-segments. Therefore, the micro-segment deformation of cement-based material was

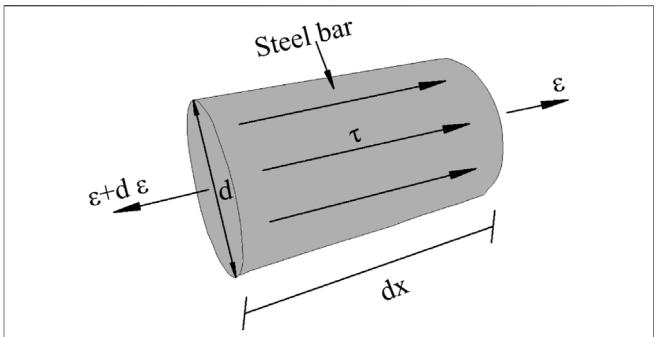


**FIGURE 8 |** The microsegment equilibrium of steel bar.

$\Delta l_{ci} = \varepsilon_{ci}\Delta l$. However, the stress distribution of cement-based materials in the cross section was not uniform. The stress at the steel bar interface was large, and the stress away from the steel bar interface was small. Meanwhile, the change in stress along the cross section varied related to the anchorage position. This change in trend was very obvious when near the loading end, but this changing trend was gentle when near the free end. Therefore, the inhomogeneous deformation coefficient $\gamma_c$ (the ratio of the interface strain to the average strain of the section) was introduced to consider this effect.

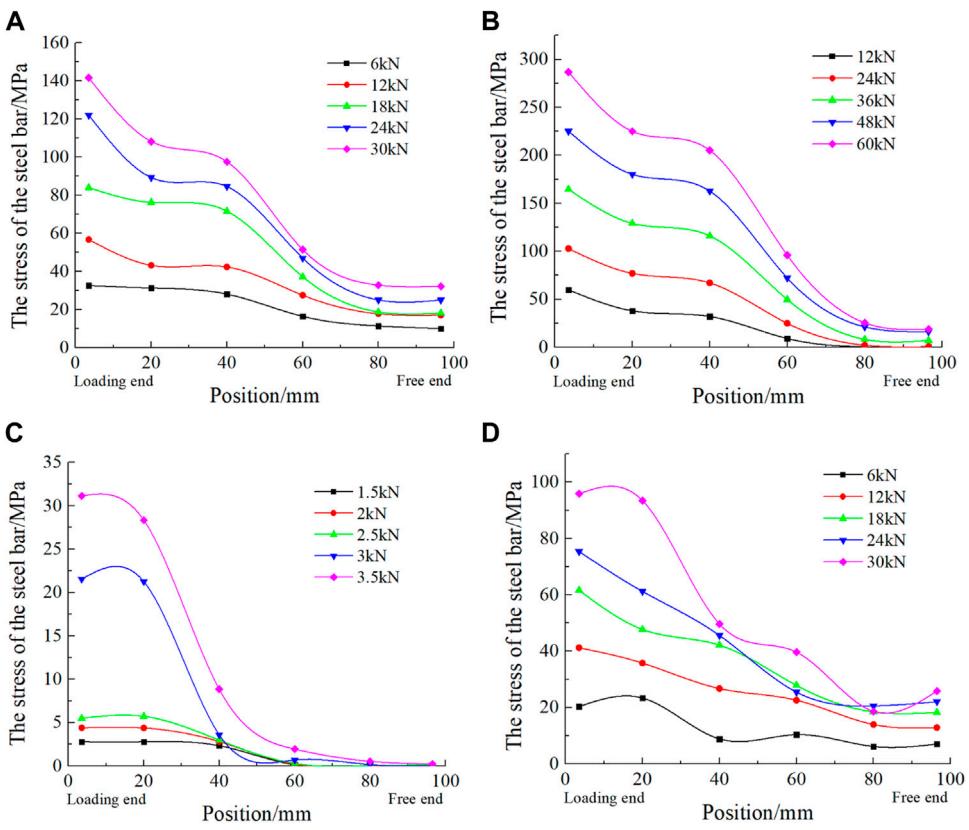


**FIGURE 7 |** Distribution rule of the stress of the steel bar along the anchorage length: **(A)** E-C16, **(B)** P-C16, **(C)** E-C16R, and **(D)** SF-C16.

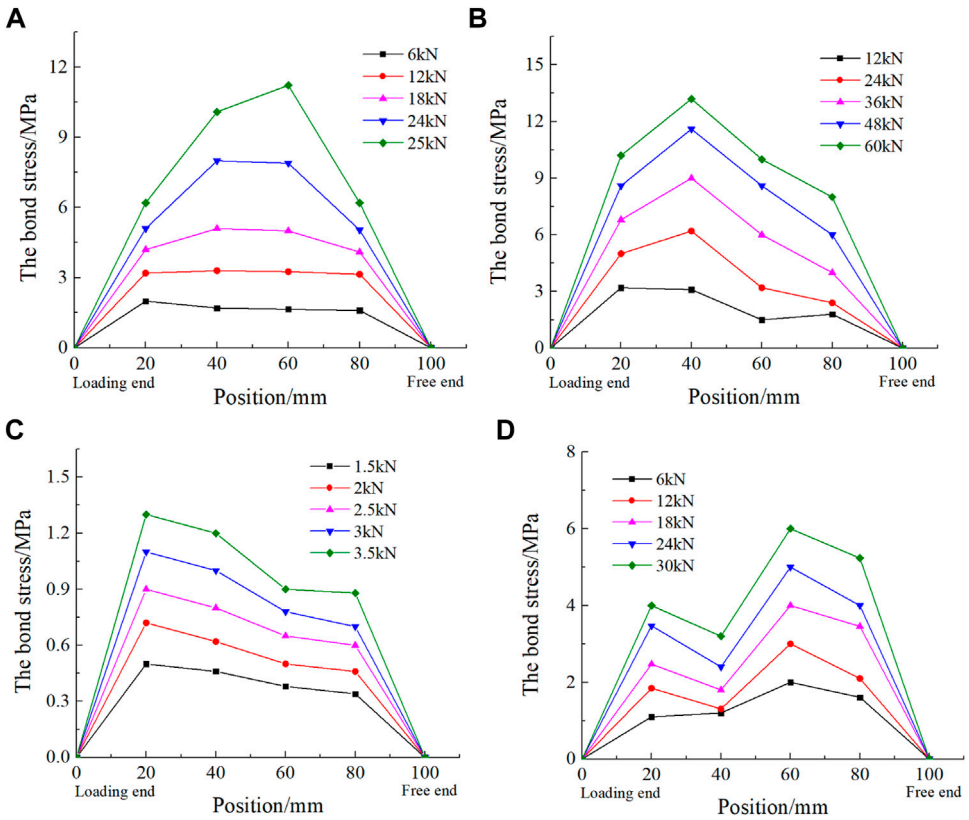


**FIGURE 9 |** The relationship between bond stress and anchorage position: **(A)** E-C16, **(B)** P-C16, **(C)** E-C16R, and **(D)** SF-C16.

After obtaining the deformation of each microsegment and the deformation of the cement-based materials, the nonuniform deformation coefficient $\gamma_c$ can be calculated according to the relative slip of the loading end $s_l$ and the relative slip of the free end $s_f$.

$$s_l = s_f + \sum_{i=1}^{n} (\Delta l_{si} + \gamma_c \Delta l_{ci}) \tag{15}$$

The relative slip $s_x$ between the steel bar and cement-based materials at x mm away from the free end could be expressed by **Eq. 16**:

$$s_x = s_f + \sum_{i=1}^{m} (\Delta l_{si} + \gamma_c \Delta l_{ci}), \quad m = \frac{x}{h} \tag{16}$$

where x is the distance away from the free end and h is the length of the bond region. According to the above method, the relative slip of the steel bar and cement-based materials at each point within the anchorage length could be calculated under any load, as shown in **Figure 10**.

According to the result as shown in **Figure 10**, in the case of 12 and 24 kN, the relative slip fitting of the SFRC SF-C16 was very smooth, indicating that the adhesion force of the free end of the steel bar was lost at the early stage of the experiment and the shear lag effect was not obvious. However, for normal concrete specimens P-C16, the slip at the loading end was larger than that at the free end, and the shear lag effect occurred. For the E-C16 member with high toughness, the concrete integrity became better due to the connection between aggregates through PVA fiber with good hydrophilicity. The difference between the relative slip of the loading end and the relative slip of the free end was not particularly obvious, which indicated that ECC had good toughness and high ductility. Compared with specimen E-C16, it was obvious that the bond performance of E-C16R was very poor. Although the difference between the relative slip of the loading end and the relative slip of the free end was also not particularly obvious in the early stage, at the moment of the failure, the difference between the relative slip of the loading end and the relative slip of the free end became larger and the shear lag effect occurred.

## The Variation of the Bond Slip Relation Along the Anchorage Length

Since the bond stress between steel bar and cement-based materials along the anchorage length would vary with the position, it was impossible to measure every strain of the steel bar along the anchorage length. In this paper, the bond–slip relationship was studied according to the anchorage points glued with strain gauges. Assuming that there was a bond–slip relationship at each measuring point, each specimen had a bond–slip relationship at the anchorage positions of 20, 40, 60,

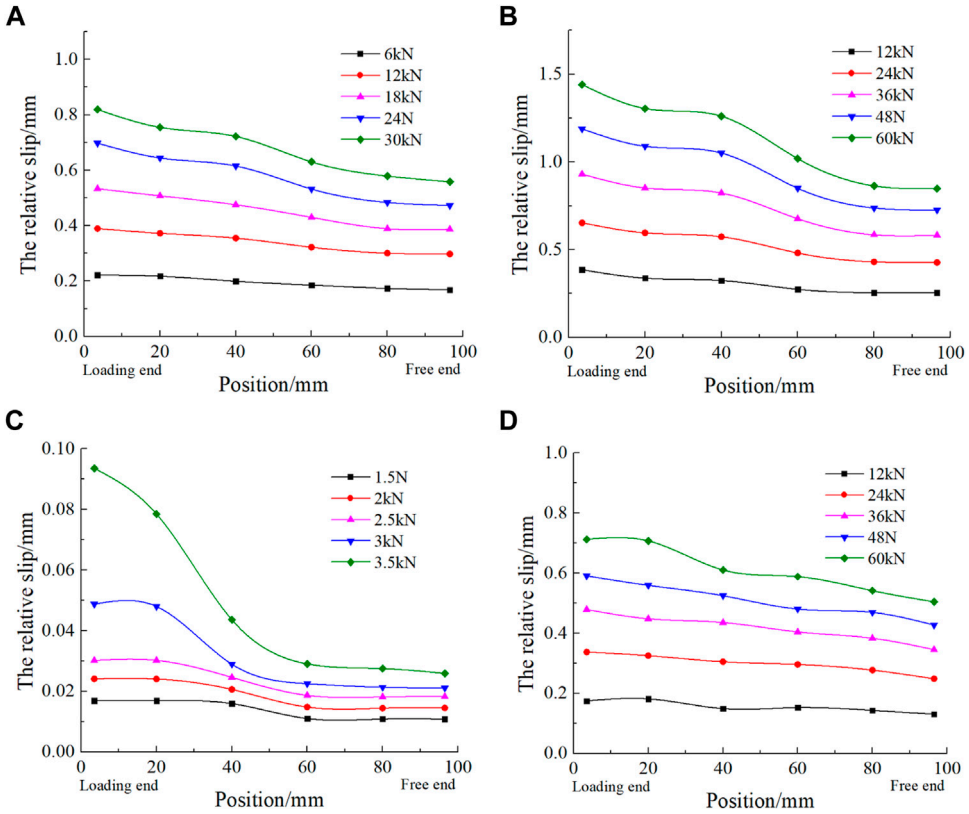


**FIGURE 10 |** Relationship between slip and position: **(A)** E-C16, **(B)** P-C16, **(C)** E-C16R, and **(D)** SF-C16.

**TABLE 3 |** The fitting result for the bond-slip relation of specimens E-C16.

| Anchorage position | Fitting parameters | | | | Correlation coefficient |
|---|---|---|---|---|---|
| X/mm | a | b | c | d | $R^2$ |
| 20 | 0.214 | 2.462 | 6.370 | −1.126 | 0.954 |
| 40 | 0.318 | 5.459 | 1.733 | 0.383 | 0.929 |
| 60 | 0.588 | −7.134 | 61.658 | −50.275 | 0.935 |
| 80 | 0.161 | −11.754 | 7473.358 | −120112.9 | 0.881 |

and 80 mm. According to the bond stress and its corresponding slip at each point along the anchorage length of the steel bar under all levels of load mentioned above, the bond–slip expressions at different positions could be fitted. After several trial calculations, it was found that the bond–slip relation at different anchorage points could be fitted by a cubic polynomial as follows:

$$\tau = a + bs + cs^2 + ds^3 \tag{17}$$

where $\tau$ is the bond stress and its unit was MPa, and s is the bond–slip and its unit was mm. a, b, c, and d are the fitting parameters. The fitting result for the bond–slip relation of specimens E-C16, P-C16, E-C16R, and SF-C16 at the anchorage positions of 20, 40, 60, and 80 mm are listed in **Tables 3–6**, respectively. It can be seen from the data in these four tables that the cubic polynomial could fit the experimental data well. All the correlation coefficients were above 0.9, and all the variances were very small.

**TABLE 4 |** The fitting result for the bond–slip relation of specimens P-C16.

| Anchorage position | Fitting parameters | | | | Correlation coefficient |
|---|---|---|---|---|---|
| X/mm | a | b | c | d | $R^2$ |
| 20 | 0.013 | 14.792 | −18.491 | 9.589 | 0.931 |
| 40 | 0.249 | 4.079 | 8.717 | −3.980 | 0.976 |
| 60 | 0.357 | 7.650 | 23.006 | −8.930 | 0.995 |
| 80 | −0.035 | −0.406 | 10.315 | −2.595 | 0.944 |

**TABLE 5 |** The fitting result for the bond–slip relation of specimens E-C16R.

| Anchorage position | Fitting parameters | | | | Correlation coefficient |
|---|---|---|---|---|---|
| X/mm | a | b | c | d | $R^2$ |
| 20 | 0.01 | 12.78 | −127.93 | 884.79 | 0.996 |
| 40 | 0.02 | 11.65 | 687.08 | −1254.79 | 0.988 |
| 60 | 0.01 | 18.61 | 255.55 | −5835.06 | 0.856 |
| 80 | 0.01 | 1.52 | 1052.63 | −28606.01 | 0.866 |

**TABLE 6 |** The fitting result for the bond–slip relation of specimens SF-C16.

| Anchorage position | Fitting parameters | | | | Correlation coefficient |
|---|---|---|---|---|---|
| X/mm | a | b | c | d | $R^2$ |
| 20 | 0.148 | 4.360 | 3.903 | −3.578 | 0.926 |
| 40 | 0.144 | 10.922 | −34.235 | 40.498 | 0.947 |
| 60 | 0.189 | 13.923 | −19.990 | 22.622 | 0.966 |
| 80 | 0.173 | 12.783 | −29.680 | 42.245 | 0.899 |

**Figure 11** shows the bond slip curves of each specimen at different positions along the anchorage length in the loading process. It can be seen from the figure that the bond stress was not uniformly distributed at different anchorage points, but varied, obeying the cubic polynomial. Therefore, it was necessary to use the bonding test to establish the bond slip constitutive relation considering the influence of anchorage position.

## Anchorage Position Function

The anchorage position function was a relative function that described the relative magnitude of the bond stiffness at different positions. Generally, the following methods were used to obtain the following: according to the abovementioned, the curve of the variation law of steel stress along the anchorage length was obtained firstly, and then the distribution of bond stress along the anchorage length was obtained by the stress of the steel bar. Next, the curve of the variation law of the relative slip along the anchorage length was drawn, and finally the distribution curve of bond stress $\tau$ at different anchorage positions under all slips was obtained. On the basis of these curves, the abscine value was divided by the anchorage length L, and the ordinate value was divided by its average bond stress, which was transformed into a normalized curve, and then the anchorage position function $\psi(x)$ was obtained by statistical regression. On the basis of **Figure 12**, the test data was simplified by a standardized method. The bond stress of each specimen at different anchorage positions was fitted; the fitting data results are listed in **Tables 7**, **8**, where a, b, c, d, e, and f are the fitting coefficients and $R^2$ and S are the

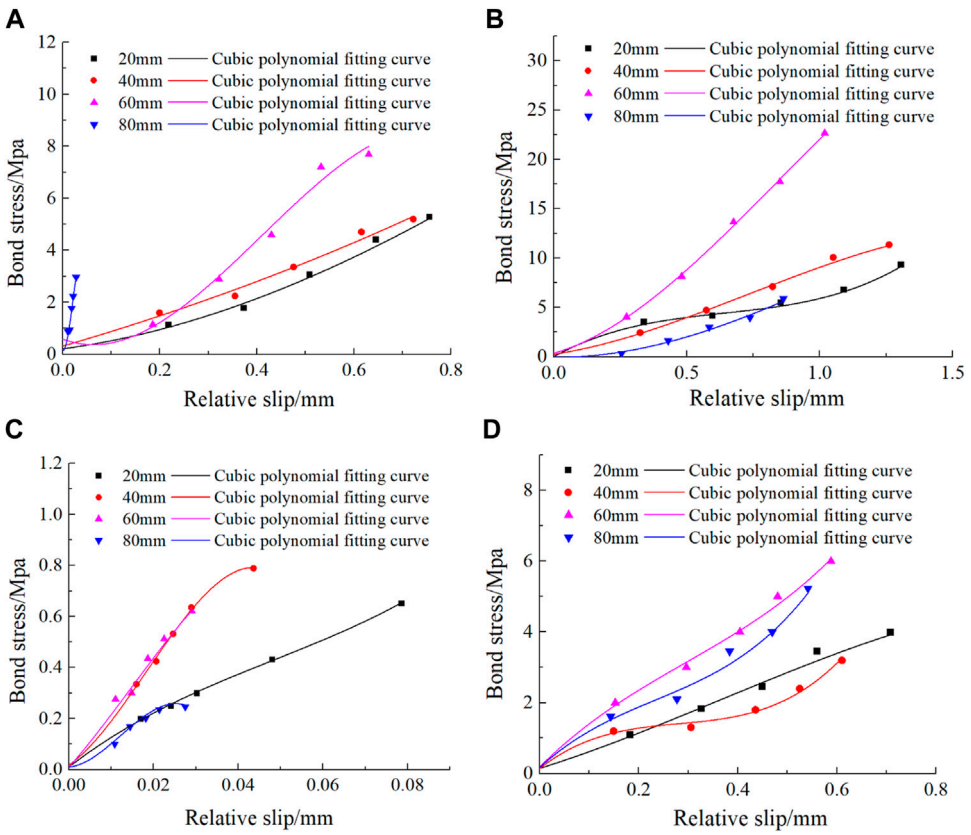


**FIGURE 11 |** The relationship between bond stress and relative slip at different anchorage positions: **(A)** E-C16, **(B)** P-C16, **(C)** E-C16R, and **(D)** SF-C16.

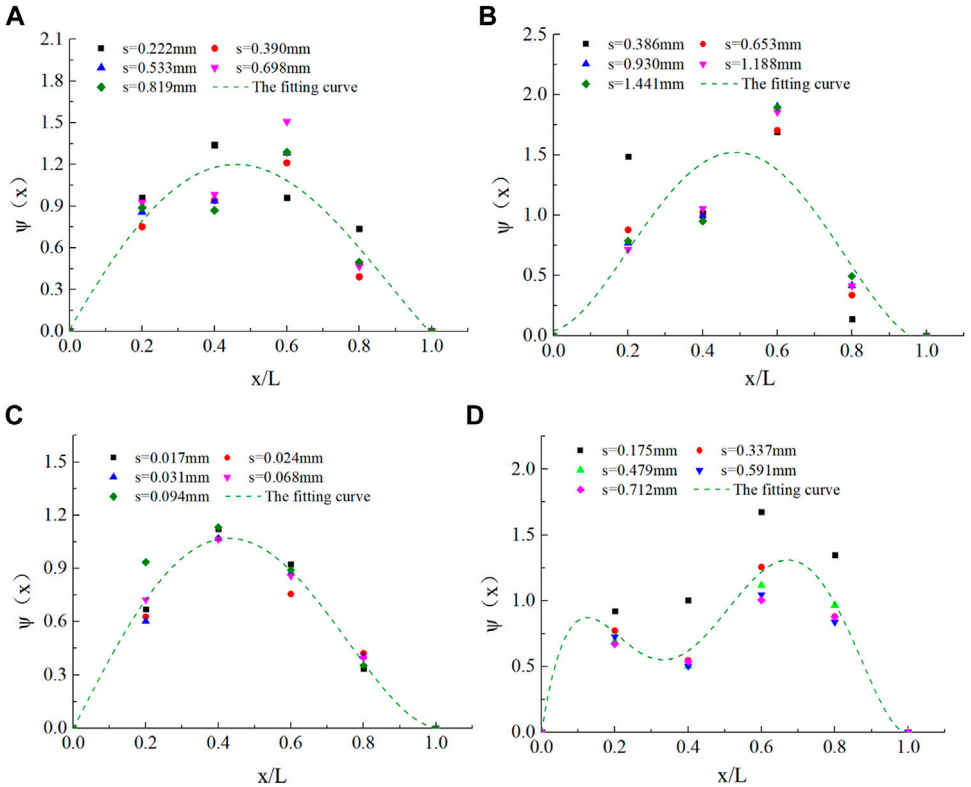


**FIGURE 12 |** Position function: **(A)** E-C16, **(B)** P-C16, **(C)** E-C16R, and **(D)** SF-C16.

**TABLE 7 |** The fitting results of specimens E-C16R, E-C16, and P-C16 at different anchorage positions.

| Specimens type | Fitting parameters | | | | | Correlation coefficient |
|---|---|---|---|---|---|---|
| | a | b | c | d | e | $R^2$ |
| E-C16 | 0.016 | 4.52 | −1.893 | −7.143 | 4.483 | 0.885 |
| P-C16 | 0.043 | 0.687 | 21.33 | −45.06 | 22.96 | 0.738 |
| E-C16R | −0.003 | 3.997 | 0.373 | −12.472 | 8.108 | 0.977 |

**TABLE 8 |** The fitting results of specimens SF-C16 at different anchorage positions.

| Specimens type | Fitting parameters | | | | | | Correlation coefficient |
|---|---|---|---|---|---|---|---|
| | a | b | c | d | e | fact | R2 |
| SF-C16 | 0 | 17.64 | −119.27 | 312.51 | −338.13 | 127.26 | 0.880 |

correlation coefficients and variance, respectively. According to correlation coefficient $R^2$, the fitting effect of the four polynomials was good for the three kinds of specimens E-C16R, E-C16, and P-C16, and their fitting correlation coefficient R2 was above 0.85, but the fitting effect of the four polynomials was poor for specimens SF-C16. Therefore, this paper adopted the fifth-degree polynomial to fit the test results of SF-C16 with the variance of 0.

According to **Tables 7**, **8**; **Figure 12** above, the anchorage position functions of four different kinds of specimens could be obtained. The anchorage position function of the specimens E-C16 is as follows:

$$\psi_E(x) = 0.016 + 4.52\left(\frac{x}{L}\right) - 1.893\left(\frac{x}{L}\right)^2 - 7.143\left(\frac{x}{L}\right)^3 + 4.483\left(\frac{x}{L}\right)^4 \quad (18)$$

The anchorage position function of the specimens P-C16 is as follows:

$$\psi_P(x) = 0.043 - 0.687\left(\frac{x}{L}\right) + 21.33\left(\frac{x}{L}\right)^2 - 45.06\left(\frac{x}{L}\right)^3 + 22.96\left(\frac{x}{L}\right)^4 \quad (19)$$

The anchorage position function of the specimens E-C16R is as follows:

$$\psi_{ER}(x) = -0.003 + 3.997\left(\frac{x}{L}\right) + 0.373\left(\frac{x}{L}\right)^2 - 12.472\left(\frac{x}{L}\right)^3 + 8.108\left(\frac{x}{L}\right)^4 \quad (20)$$

The anchorage position function of the specimens SF-C16 is as follows:

$$\psi_{SF}(x) = 17.64\left(\frac{x}{L}\right) - 119.27\left(\frac{x}{L}\right)^2 + 312.51\left(\frac{x}{L}\right)^3 - 338.13\left(\frac{x}{L}\right)^4 + 127.26\left(\frac{x}{L}\right)^5 \quad (21)$$

Since the number of test specimens was limited, the anchorage position function of the steel bars and cement-based materials discussed herein was mainly for comparison, and by comparison, the expression function varied with the change of cement-based materials. The bond–slip relation obtained by the pullout test could not reflect the influence of bond position, but in fact, the bond–slip constitutive relation varied with anchorage position. In order to describe this variation, an anchorage position function could be determined on the basis of the basic bond–slip relationship that was already known, and the bond–slip constitutive relation along anchorage length was expressed by multiplying the basic bond–slip relationship with the anchorage position function. The basic bond–slip relation adopted the average bond–slip constitutive relation $\tau = \varphi(s)$, then the bond–slip constitutive relation between steel bar and cement-based materials could be accurately described as:

$$\tau(s, x) = \varphi(s) \cdot \psi(x) \quad (22)$$

where $\tau(s, x)$ denotes the bond constitutive relation that varied with anchorage position. $\varphi(s)$ represents the average bond–slip relationship measured through the pullout test. $\psi(x)$ is the anchorage position function, which could be taken according to **Eqs 18–21**.

## Anchorage Length of the Steel Bar in ECC

There are two kinds of failure modes for the steel bar embedded in ECC under the tension force F: one is failure due to the steel bar being pulled apart; the other is failure due to the interface between the steel bar and ECC being sheared off. For the determined steel bar and ECC, the yield stress of the steel bar is a determined value, while the anchorage force applied by the ECC on the steel bar increases with the increase of the anchoring length La. When the anchorage length increases to a certain value, the anchorage force can be equal to the yield force of the steel bar, which means the anchorage failure occurs simultaneously with the yield of the steel bar. This particular anchorage length is called the "critical anchorage length." The state in which the anchorage force is equal to the yield force of the steel bar is called "anchorage limit state." It can be seen that the critical anchorage length is actually the minimum anchorage length that the steel bar cannot be pulled out in ECC when the tension force F reaches the yield force of the steel bar. The anchorage limit state is the state that the yield stress of the steel bar and the ultimate bond stress between the steel bar and ECC reach at the same time. Assume that under the critical limit state, the critical anchorage length of the steel bar in ECC is $l_{cr}$. The tensile force of the steel bar is F and the yield strength of the steel bar is $f_y$. The diameter of the steel bar is d, and the bond stress of the interface between the steel bar and ECC is $\tau_u$, then the anchorage force applied by ECC on the steel bar can be calculated as follows:

$$F = \pi d l_{cr} \tau_u \quad (23)$$

The relation between the force F applied on the steel bar and the yield strength of the steel bar $f_y$ can be calculated as follows:

$$F = \frac{\pi d^2}{4} f_y \quad (24)$$

The calculation formula of critical anchorage length $l_{cr}$ can be obtained from the equality of the above two expressions:

$$l_{cr} = \frac{f_y d}{4\tau_u} \quad (25)$$

In this paper, the diameter of the ribbed steel bar is 16 mm, the yield strength of the ribbed steel bar is 400 MPa, and the design value of ECC's tensile strength is 4.58 MPa. By substituting these values into **Eq. 25**, the critical anchorage length of the ribbed steel bar in ECC can be calculated to be 97 mm ($l_a \approx 6$ days).

However, in the current Code for Design of Concrete Structures (GB 50010-2010) in China, when making full use of the tensile strength of the steel bar, the anchorage length of tensile steel bar should be calculated as follows:

$$l_a = \alpha \frac{f_y}{f_t} d \quad (26)$$

where α is called the shape coefficient of the steel bar, $f_t$ is called the design value of the tensile strength of the concrete, and $f_y$ is called the design value of the tensile strength of the steel bar. In this paper, the shape coefficient of the ribbed steel bar α is 1.4, the design value of the tensile strength of the ECC $f_t$ is 4.58 MPa, and the design value of the tensile strength of the steel bar $f_y$ is 400 MPa. In this paper, the critical anchorage length of the ribbed steel bar with a diameter of 16 mm in ECC can be calculated to be 195.68 mm ($l_a$ = 12.23 days) by substituting each of the above values into **Eq. 26**. It could be seen that it was safe and conservative to use **Eq. 26** to calculate the anchorage length of the steel bar in ECC. Through the pullout test, we also found that when the anchorage length reached 100 mm, some of the steel bars reached the yield point. Therefore, in order to facilitate engineering application, it is suggested to establish the critical anchorage length formula suitable for ECC in future studies.

## CONCLUSION

In this paper, experimental results for the influence of concrete type and steel bar type on the bond performance between steel bar and cement-based materials through the pullout test were presented and discussed. From this investigation, the following conclusions can be drawn:

1) Compared with failure modes of the pull-out specimens containing normal concrete (P-C16) and SFRC (SF-C16), it was found that fine and intensive cracks that were hard to be observed by naked eyes appeared on the surface of the pullout specimens containing ECC (E-C16). These cracks of E-C16 were radially distributed from the center to the edge, and the number of the cracks on the surface was much more than that on the other two specimens. This showed that ECC had excellent crack control capability and ductile property.
2) The strain of the steel bar at six measuring points was measured with strain gauge. Based on the measured strain and free end slip of the steel bars, the distribution of steel stress, bond stress, and relative slip and the bond slip relation along the anchorage length were obtained and analyzed for different concrete and different steel bars. Anchorage position function was established in consideration of anchorage position, which was conducive to the establishment of an accurate bond–slip relationship.
3) It was safe and conservative to use the calculation formula of critical anchorage length in the current Code for Design of Concrete Structures (GB 50010-2010) in China to calculate the critical anchorage length of the steel bar in ECC. It is suggested to establish the critical anchorage length formula suitable for ECC in future studies.

## AUTHOR'S NOTE

Yuexiu Transport Infrastructure Co., Ltd. is mainly engaged in the investment, construction and operation management of toll highways, bridges and ports in Guangdong province and other high-growth provinces of China. In order to extend the service life of the bridge deck and substructure and to reduce material consumption over the life of the bridge and highway, all the authors participated the project on engineered cementitious composite materials and expect to particularly replace the traditional concrete expansion joints.

## DATA AVAILABILITY STATEMENT

The original contributions presented in the study are included in the article/supplementary material; further inquiries can be directed to the corresponding author.

## AUTHOR CONTRIBUTIONS

JX, XL, and HJ conceived and designed the study. MY, LL, FM, and DD performed the experiments. JX, MY, and ZH wrote the paper. JX, XL, and HJ reviewed and edited the manuscript. All authors contributed to the article and approved the submitted version.

## FUNDING

The research presented was funded by the National Natural Science Foundation of China (51778150) and the National Natural Science Foundation of China (51808133), Natural Science Foundation of Guangdong Province in China (2016A030313699), and Guangzhou Municipal Science and Technology Project China (201804010422).

## ACKNOWLEDGMENTS

The authors would like to thank the National Natural Science Foundation of China for funding this project. The laboratory of school of civil and transportation engineering at Guangdong University of Technology is also gratefully acknowledged for providing all the resources required for this work.

## REFERENCES

Cai, J., Pan, J., Tan, J., and Li, X. (2020). Bond Behaviours of Deformed Steel Rebars in Engineered Cementitious Composites (ECC) and concrete. *Construction Building Mater.* 252, 119082. doi:10.1016/j.conbuildmat.2020.119082

Cai, Z., Liu, F., Yu, J., Yu, K., and Tian, L. (2021). Development of Ultra-high Ductility Engineered Cementitious Composites as a Novel and Resilient Fireproof Coating. *Construction Building Mater.* 288, 123090. doi:10.1016/j.conbuildmat.2021.123090

Choi, W.-C., Jang, S.-J., and Yun, H.-D. (2017). Bond and Cracking Behavior of Lap-Spliced Reinforcing Bars Embedded in Hybrid Fiber Reinforced Strain-Hardening Cementitious Composite (SHCC). *Composites B: Eng.* 108, 35–44. doi:10.1016/j.compositesb.2016.09.086

Deng, M., Pan, J., and Sun, H. (2018). Bond Behavior of Steel Bar Embedded in Engineered Cementitious Composites under Pullout Load. *Construction Building Mater.* 168, 705–714. doi:10.1016/j.conbuildmat.2018.02.165

Fu, C., Fang, D., Ye, H., Huang, L., and Wang, J. (2021). Bond Degradation of Non-uniformly Corroded Steel Rebars in concrete. *Eng. Structures* 226, 111392. doi:10.1016/j.engstruct.2020.111392

Hossain, K. M. A., Alam, S., Anwar, M. S., and Julkarnine, K. M. Y. (2020). Bond Strength of Fibre-Reinforced Polymer Bars in Engineered Cementitious Composites. *Proc. Inst. Civil Eng. - Construction Mater.* 173 (1), 1–13. doi:10.1680/jcoma.17.00020

Hu, B., Zhou, Y., Xing, F., Sui, L., and Luo, M. (2019). Experimental and Theoretical Investigation on the Hybrid CFRP-ECC Flexural Strengthening of RC Beams with Corroded Longitudinal Reinforcement. *Eng. Structures* 200, 109717. doi:10.1016/j.engstruct.2019.109717

Huang, H., Yuan, Y., Zhang, W., Hao, R., and Zeng, J. (2020). Bond Properties between GFRP Bars and Hybrid Fiber-Reinforced concrete Containing Three Types of Artificial Fibers. *Construction Building Mater.* 250, 118857. doi:10.1016/j.conbuildmat.2020.118857

Krstulovic-Opara, N., Watson, K. A., and Lafave, J. M. (1994). Effect of Increased Tensile Strength and Toughness on Reinforcing-Bar Bond

Behavior. *Cement and Concrete Composites* 16 (2), 129–141. doi:10.1016/0958-9465(94)90007-8

Lam, L., Huang, L., Xie, J.-H., and Chen, J.-F. (2021). Compressive Behavior of Ultra-high Performance concrete Confined with FRP. *Compos. Structures* 274, 114321. doi:10.1016/j.compstruct.2021.114321

Lee, S. W., Kang, S.-B., Tan, K. H., and Yang, E.-H. (2016). Experimental and Analytical Investigation on Bond-Slip Behaviour of Deformed Bars Embedded in Engineered Cementitious Composites. *Construction Building Mater.* 127, 494–503. doi:10.1016/j.conbuildmat.2016.10.036

Lei, W., Zeng, X., Yang, H., and Lv, X. (2021). Investigation and Application of Fractal Theory in Cement-Based Materials: A Review. *Fractal Fractional* 5 (4), 247. doi:10.3390/fractalfract5040247

Li, V. C., Wu, C., Wang, S. X., Ogawa, A., and Saito, T. (2002). Interface Tailoring for Strain-Hardening Polyvinyl Alcohol Engineered Cementitious Composite (PVA-ECC). *ACI Mater. J.* 99 (5), 463–472. doi:10.1016/S0042-207X(02)00187-2

Wang, H., Sun, X., Peng, G., Luo, Y., and Ying, Q. (2015). Experimental Study on Bond Behaviour between BFRP Bar and Engineered Cementitious Composite. *Construction Building Mater.* 95, 448–456. doi:10.1016/j.conbuildmat.2015.07.135

Wang, L., Guo, F., Lin, Y., Yang, H., and Tang, S. W. (2020). Comparison between the Effects of Phosphorous Slag and Fly Ash on the C-S-H Structure, Long-Term Hydration Heat and Volume Deformation of Cement-Based Materials. *Construction Building Mater.* 250, 118807. doi:10.1016/j.conbuildmat.2020.118807

Wang, L., Jin, M., Zhou, S., Tang, S., and Lu, X. (2021a). Investigation of Microstructure of C-S-H and Micro-mechanics of Cement Pastes under NH4NO3 Dissolution by 29Si MAS NMR and Microhardness. *Measurement* 185, 110019. doi:10.1016/j.measurement.2021.110019

Wang, L., Li, G., Li, X., Guo, F., and Tang, S. (2021b). Influence of Reactivity and Dosage of MgO Expansive Agent on Shrinkage and Crack Resistance of Face Slab concrete. *Cement and Concrete Composites* 125, 104333. doi:10.1016/j.cemconcomp.2021.104333

Xiao, J., Long, X., Ye, M., Jiang, H., Liu, L., and Zhai, K. (2021). Experimental Study of Bond Behavior between Rebar and PVA-Engineered Cementitious Composite (ECC) Using Pull-Out Tests. *Front. Mater.* 8, 15. doi:10.3389/fmats.2021.633404

Xiong, Y., Xu, G., Wu, D., Fang, S., and Tang, Y. (2021a). Investigation of Using the Ceramic Polishing brick Powder in Engineered Cementitious Composites. *J. Building Eng.* 43, 102489. doi:10.1016/j.jobe.2021.102489

Xiong, Y., Yang, Y., Fang, S., Wu, D., and Tang, Y. (2021b). Experimental Research on Compressive and Shrinkage Properties of ECC Containing Ceramic Wastes under Different Curing Conditions. *Front. Mater.* 8, 1. doi:10.3389/fmats.2021.727273

Xu, S., and Wang, H. (2008). Experimental Study on Bond-Slip between Ultra High Toughness Cementitious Composites and Steel Bar. *Eng. Mech.* 25 (11), 53–061. doi:10.1016/S1872-5791(08)60058-5

Yu, K., McGee, W., Ng, T. Y., Zhu, H., and Li, V. C. (2021). 3D-printable Engineered Cementitious Composites (3DP-ECC): Fresh and Hardened Properties. *Cement Concrete Res.* 143, 106388. doi:10.1016/j.cemconres.2021.106388

Yu, K. Q., Wang, Y. C., Yu, J. T., and Xu, S. L. (2017). A Strain-Hardening Cementitious Composites with the Tensile Capacity up to 8. *Construction Building Mater.* 137, 410–419. doi:10.1016/j.conbuildmat.2017.01.060

Zhang, J., Huang, J., Fu, C., Huang, L., and Ye, H. (2021). Characterization of Steel Reinforcement Corrosion in concrete Using 3D Laser Scanning Techniques. *Construction Building Mater.* 270, 121402. doi:10.1016/j.conbuildmat.2020.121402

Zhao, Y., and Jin, W. (2002). Test Study on Bond Stress-Slip Relationship of concrete and Steel Bar. *J. Building Structures* 23 (1), 32–37. doi:10.1007/BF02960786

Zhou, Y., Fu, H., Li, P., Zhao, D., Sui, L., and Li, L. (2019). Bond Behavior between Steel Bar and Engineered Cementitious Composite (ECC) Considering Lateral FRP Confinement: Test and Modeling. *Compos. Structures* 226, 111206. doi:10.1016/j.compstruct.2019.111206

**Conflict of Interest:** XL and MY were employed by the company Yuexiu Transport Infrastructure Co., Ltd.

The remaining authors declare that the research was conducted in the absence of any commercial or financial relationships that could be construed as a potential conflict of interest.

**Publisher's Note:** All claims expressed in this article are solely those of the authors and do not necessarily represent those of their affiliated organizations, or those of the publisher, the editors, and the reviewers. Any product that may be evaluated in this article, or claim that may be made by its manufacturer, is not guaranteed or endorsed by the publisher.

frontiers in Materials

ORIGINAL RESEARCH
published: 14 February 2022
doi: 10.3389/fmats.2022.832579

# Experimental Study on Seismic Performance of Confined Masonry Walls With Window Openings Strengthened by Using Hybrid-Fiber Modified Reactive Powder Concrete

*Guo-an Liu[1], Xin Wang[1,2]*, Zhe Yang[1], Lei-yu Wang[3], Yun-wen Zhou[4] and Guo-bin Chen[3]*

*[1]School of Civil Engineering, Shandong Jianzhu University, Jinan, China, [2]Key Laboratory of Building Structural Retrofitting and Underground Space Engineering of Ministry of Education, Jinan, China, [3]Engineering Research Institute of Appraisal and Strengthening of Shandong Jianzhu University CO., LTD, Jinan, China, [4]Shandong Dawei Design Group CO., LTD, Jinan, China*

Unreinforced masonry structures are vulnerable to seismic action, especially with window openings. Therefore, a strengthening technique needs to be proposed to improve the seismic performance of the confined masonry walls with window openings. In this study, hybrid fibers modified reactive powder concrete (HFMRPC) with good composite action to masonry walls were obtained through material tests. Then, the HFMRPC material was used as a coating to strengthen or repair the confined masonry walls with window openings by single-sided full coverage, double-sided full coverage, single-sided coverage in piers, and double-sided coverage in piers. To investigate the effect of HFMRPC coating on strengthening or repairing the confined masonry walls with window openings. Seven half-scale masonry walls were tested under in-plane quasi-static horizontal loading. The results indicated that the retrofitting technology using HFMRPC coating could effectively enhance the load-bearing capacity, energy dissipation capacity of the strengthened and repaired masonry walls and delay their stiffness degradation. Among the above-mentioned strengthening methods, the strengthening in piers significantly enhanced the ductility and energy dissipation of the specimens, and the double-sided full coverage enhanced the load-bearing capacity and stiffness of the specimens. Finally, a simplified analysis method was proposed to calculate the shear bearing capacity of the strengthened or repaired confined masonry walls with window openings based on theoretical analysis and test results.

**Keywords: confined masonry wall with window opening, hybrid-fiber modified reactive powder concrete, retrofitting, cyclic loading, seismic behavior**

OPEN ACCESS

***Edited by:***
*Kequan Yu,*
*Tongji University, China*

***Reviewed by:***
*Fangyuan Dong,*
*Tongji University, China*
*Xiaodan Teng,*
*Guangxi University, China*

****Correspondence:***
*Xin Wang*
*wangxin@sdjzu.edu.cn*

***Specialty section:***
*This article was submitted to Structural Materials, a section of the journal Frontiers in Materials*

***Received:*** *10 December 2021*
***Accepted:*** *03 January 2022*
***Published:*** *14 February 2022*

***Citation:***
*Liu G-a, Wang X, Yang Z, Wang L-y, Zhou Y-w and Chen G-b (2022) Experimental Study on Seismic Performance of Confined Masonry Walls With Window Openings Strengthened by Using Hybrid-Fiber Modified Reactive Powder Concrete. Front. Mater. 9:832579. doi: 10.3389/fmats.2022.832579*

## INTRODUCTION

As one of the primary structural forms with a long history, masonry structure is widely used in mainland China. In recent years, two major earthquakes, i.e., Wenchuan Earthquake in 2008 and Yushu Earthquake in 2010, happened in mainland China. Due to the various anisotropy and brittleness of brick, existing masonry structures have a greater vulnerability in earthquakes and are severely damaged under strong earthquake effects (Tai et al., 2011). Meanwhile, any masonry

opening can seriously weaken the shear bearing capacity, ductility, and initial stiffness, which changes the failure pattern of masonry walls (Shariq et al., 2008). Therefore, masonry walls with window openings were severely damaged under earthquakes. An effective strengthening technique is needed to improve the seismic performance of masonry structures, especially for those with window openings.

Different kinds of Fiber-reinforced polymers (FRP) materials are widely used to reinforce masonry walls are proved to be an effective reinforcement method (Foraboschi, 2016; Guerreiro et al., 2018; Kalali and Kabir, 2012). Masonry walls reinforced with FRP can effectively improve the in-plane shear strength (Konthesingha et al., 2013; Leal-Graciano et al., 2020). The integrity of the masonry wall can be maintained under large deformation caused by the lateral displacement, and the collapse of the wall is also delayed, which enhances the deformation capacity and energy dissipation of the masonry wall (El-Diasity et al., 2015). However, organic binders (epoxy resin, etc.) are applied to FRP during strengthening construction. Hence, there are problems of poor behavior in bond at high temperature and its irreversibility and limitations such as incompatibility and poor coordination between FRP and masonry substrates (Bui et al., 2015). It will not only cause damage to human health but also be detrimental to the environment. Some progress attempts have been made to use inorganic matrices instead of FRP bonding as the strengthening method to solve these problems. A composite system consisting of continuous multiaxial hybrid fibers embedded in the mortar-based matrix was proposed and denominated Textile Reinforced Mortar (TRM). Internationally, the inorganic composite systems reinforced by textile are also named Textile Reinforced Concrete/Cement (TRC) (Bisby et al., 2011; Cheng et al., 2020), Fiber Reinforced Cementitious Matrix/Mortar (FRCM) (Del Zoppo et al., 2019a; Mercedes et al., 2020), Cementitious Matrix Grid (CMG) (Prota et al., 2006), Composite Reinforced Mortar (CRM) (Del Zoppo et al., 2019b), or Inorganic Matrix-Grid (IMG) (Augenti et al., 2011; Parisi et al., 2013). The research has shown that the application of TRM is served as an alternative to the application of FRP. Since TRM was proven effective in strengthening concrete specimens, it was also introduced into strengthening masonry structures (Papanicolaou et al., 2007; Papanicolaou et al., 2008). The brittle failure of masonry walls can be improved by using the TRM strengthening method, which ensures the integrity at the failure and increases the ultimate load of the strengthened masonry wall (Dong et al., 2020; Garcia-Ramonda et al., 2020). With the growing awareness of environmental protection, more researchers have started to use green and sustainable plant fibers such as flax, hemp, coir, sisal, and jute as reinforcement materials in inorganic composites, which can be served as alternatives to traditional inorganic fibers and are more friendly to the environment (Ferrara et al., 2020). However, the construction procedure of the TRM system is complicated, which requires a smooth application of mortar before laying the single or multiple layers of fibers on the wall surface. The lateral strength of the masonry structures strengthened with the TRM system is lower than that of those strengthened with FRP. Meanwhile, there is still some uncertainty about the long-term durability of TRM composite systems in freeze-thaw cycles, hygrothermal environments, and alkaline environments (Al-Lami et al., 2020).

Engineered cementitious composite (ECC) is a material with strain hardening properties and multiple crack development under the tensile and shear loading. The tensile and shear properties of the specimens are improved due to the "bridge effect" of the fibers within the ECC (Cai et al., 2021; Ding et al., 2022; Li and Leung, 1992). Many researchers have used ECC to strengthen masonry walls, and test results indicated that the stiffness, ductility, and energy dissipation capacity of the masonry structures strengthened with ECC can be effectively improved (Deng and Yang, 2020; Dong et al., 2022a; Dong et al., 2022b; Niasar et al., 2020). Although the shear strength of the masonry structure continues to be increased as the thickness of ECC coating, the increased rate of the shear strength gradually decreases (Lin et al., 2014). In addition, with the increasing thickness of the masonry wall, the retrofitting effect of ECC coating becomes less and less obvious (van Zijl and De Beer, 2019). Compared with the other strengthening methods, constructing the additional plaster coating is relatively simple, which effectively shortens the construction period and reduces the damage to the external facade and the initial wall. Furthermore, the application of the plaster coating can also guarantee minimal interference to the use of the current building during construction. Therefore, an effective plastered strengthening material for masonry structures that need to be developed is significant. Reactive powder concrete (RPC) coating has been used to strengthen and repair the confined masonry walls (Wang et al., 2019). The in-plane seismic behavior of the masonry walls strengthened with RPC coating was improved significantly. Due to the interaction between RPC coating and the masonry wall, the bond between the mortar and brick interface was enhanced, and the restriction between the concrete frame and masonry wall was also improved (Wang et al., 2021).

In this paper, a retrofitting technology using hybrid fibers modified reactive powder concrete (HFMRPC) was used to strengthen or repair the confined masonry walls with window openings. A mixed proportion of HFMRPC material with moderate compressive strength but an excellent surface bond property with brick was developed. Then, seven half-scale confined masonry walls with window openings were constructed, and six of them were strengthened or repaired with HFMRPC coating. Subsequently, the unstrengthened, strengthened, and repaired masonry walls were tested under the in-plane quasi-static lateral loading. The effectiveness of the HFMRPC strengthening technology was evaluated in terms of seismic performance parameters such as the load-carrying capacity, failure mode, crack development, displacement ductility, stiffness, and energy dissipation of the masonry walls. In addition, a simplified calculation method for the shear resistance of the confined masonry walls with window openings was proposed based on the theoretical analysis and test results.

**TABLE 1 |** Mix proportions of HFMRPC.

| Mixture | Cement | Sliver sand | Silica fume | Fly ash | Mineral powder | Steel fiber (vol %) | PP fiber (vol %) | water | Water reducer agent (%) | Fluidity (mm) |
|---|---|---|---|---|---|---|---|---|---|---|
| 1 | 1 | 2.08 | 0.3 | 0.4 | 0.3 | 1.50 | 0.50 | 0.80 | 0.00 | 149 |
| 2 | 1 | 2.08 | 0.3 | 0.4 | 0.3 | 1.50 | 0.50 | 0.38 | 0.30 | 152 |
| 3 | 1 | 2.08 | 0.3 | 0.4 | 0.3 | 1.50 | 0.50 | 0.48 | 0.20 | 138 |
| 4 | 1 | 2.08 | 0.3 | 0.4 | 0.3 | 1.50 | 0.50 | 0.58 | 0.10 | 132 |
| 5 | 1 | 2.08 | 0.3 | 0.4 | 0.3 | 1.50 | 0.50 | 0.58 | 0.20 | 158 |
| 6 | 1 | 2.08 | 0.3 | 0.4 | 0.3 | 1.50 | 0.50 | 0.58 | 0.30 | 177 |

# MATERIALS AND METHODS

## Characterization of HFMRPC and Mixture Proportion

Traditional RPC is characterized by high strength, toughness, and fluidity. Compared with the traditional RPC, the compressive strength of brick is much less. If the difference of compressive strength between the bricks and the strengthening materials is too great, it is neither economic nor conducive to the coordination of the two materials. Furthermore, due to the high fluidity of RPC, it is difficult to be used as plastering without using molds when strengthening masonry structures. Based on the above problems, the traditional RPC needs to be modified according to the design theory of RPC. The modified RPC (i.e., HFMRPC) can be adapted to the characteristics of the masonry wall, and it has a good bond with the masonry wall to ensure the better integrity of the strengthened structure under seismic action. Therefore, the strength and fluidity of the modified RPC need to be reduced while its ductility and adhesion need to be increased.

In this study, the hybrid-fiber modified reactive powder concrete (HFMRPC) matrix consists of ordinary Portland cement, medium river sand, fly ash, mineral powder, and silica fume. Then, steel fibers (diameter: 0.2 mm, length: 13 mm), polypropylene (PP) fibers (diameter: 45 μm, length: 18–20 mm), and high-efficiency polycarboxylate water reducer agent (water-reducing rate ≥35%) were also added to the matrix. The fluidity, adhesion, and compressive strength were used as the screening conditions for the mixture to ensure the composite action of HFMRPC coating and brick wall. Different mix proportions were designed to explore the effect of the water-cement ratio and water reducer agent on the HFMRPC material. The mixed proportions of HFMRPC in this study are listed in **Table 1**.

## Preparation and Mechanical Characterization of HFMRPC

First, the raw materials, including cement, medium river sand, mineral powder, silica fume, and fly ash, were put into the mixer and mixed in turn. Then, it was followed by the even addition of steel fibers and PP fibers to the mixture. During the mixed process, the fiber agglomeration should be prevented. The dry materials should be pre-mixed for more than 4 min to ensure that all materials were well mixed. Finally, the water and water reducer agent were added, and then the mixture was stirred again for more than 4 min. After the HFMRPC was well stirred, three cubes (100 mm × 100 mm × 100 mm) were prepared for each batch. After 24 h of natural curing, the tested cubes were demolded. Then, after 28 days of natural curing, the average compressive strength of the three cubes for each batch was measured.

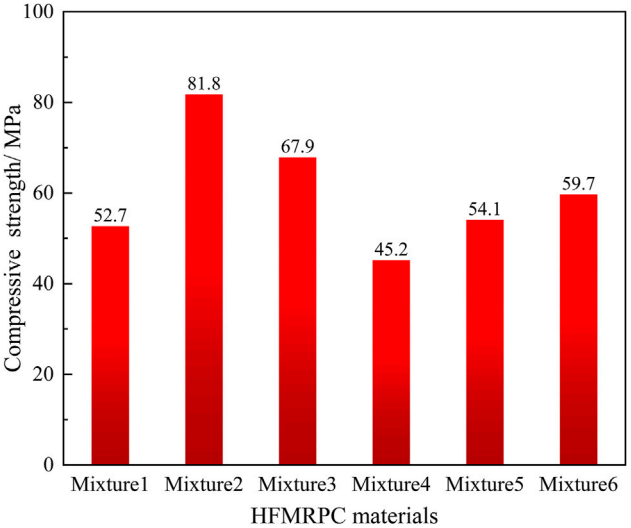


**FIGURE 1 |** Compressive strength of the HFMRPC materials with various mix proportions.

The compressive strengths of the HFMRPC materials with various mix proportions are shown in **Figure 1**, and the fluidity of each mixture is listed in **Table 1**. The required strength of the reinforcing material is not high as the strength of brick is relatively low. However, fluidity and viscosity are the key factors to achieve plastering. The viscosity was gradually increased as the fluidity was decreased. By comparing the mixtures 4, 5, and 6, it can be found that at the same water-binder ratio, the flowability and compressive strength of the mixtures increased with the increase of the water reducer agent, while their viscosity was reduced. When comparing the mixtures 2, 3, and 4, the compressive strength decreased significantly with the increase of the water-binder ratio. In

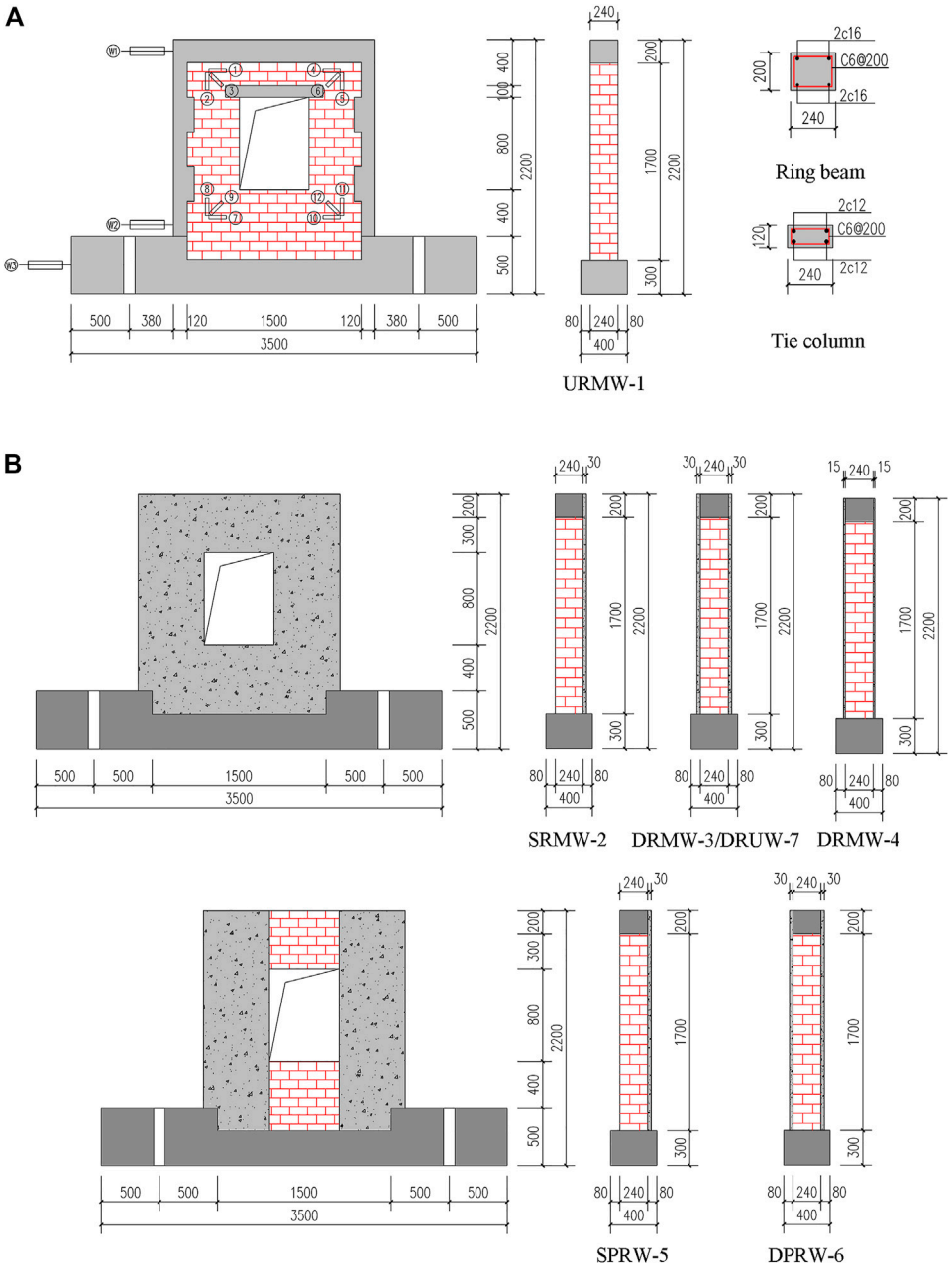


**FIGURE 2 |** Details of the tested wall (unit: mm) **(A)** the layout, reinforcement, and facades of tested walls **(B)** strengthening methods for the tested walls.

addition, the addition of fiber to the matrix resulted in a decrease in flowability but an improvement in viscosity. Therefore, the compressive strength of HFMRPC was reduced by increasing the water-binder ratio, and the difference in compressive strength between the brick and HFMRPC was also decreased. Also, with the reduction of the water reducer agent, the flowability and compressive strength of HFMRPC was reduced, but its viscosity was increased, which can be applied on the surface of masonry walls by using hand-trowel. Finally, mixture four was selected for strengthening and repairing the masonry structures based on the test results.

## Description of Masonry Walls

Seven half-scale masonry walls consisting of a ring beam, two confining columns, a reinforced concrete footing, and a masonry wall with a window were constructed. Two-bolt holes were reserved in the reinforced concrete footings of the brick walls, and then they were firmly anchored to the strong laboratory floor with 100 mm-diameter high strength bolts. The bolts can avoid any uplift and slip when the horizontal displacement loading was applied. All the brick walls were constructed by an experienced bricklayer with a typical bond pattern and the same construction, which included the low-strength mortars, clay bricks, and uneven

**TABLE 2 |** Strengthening methods for the tested walls.

| Specimen | Strengthening method | The thickness of HFMRPC coating (mm) | Source of specimen |
|---|---|---|---|
| URMW-1 | None | 0 | Initial |
| SRMW-2 | Single-sided full coverage | 30 | |
| DRMW-3 | Double-sided full coverage | 30 | |
| DRMW-4 | Double-sided full coverage | 15 | |
| SPRW-5 | Single-sided coverage in piers | 30 | |
| DPRW-6 | Double-sided coverage in piers | 30 | |
| DRUW-7 | Double-sided full coverage | 30 | Tested URMW-1 |

mortar joints. These construction technologies were intentionally used to construct the confined masonry walls because these walls were widely applied in the countryside of mainland China.

The details of the tested walls are shown in **Figure 2**. The aspect ratio of the seven walls was 1:1. Specimen URMW-1 was the controlled specimen without any strengthened measure. Specimen SRMW-2 was strengthened with overall HFMRPC coating only on one side to prevent the indoor space from being occupied. Specimen DRMW-3 was strengthened with the overall HFMRPC coating on both sides. Specimen DRMW-4 was strengthened in the same way as the specimen DRMW-3, and only the thickness of the HFMRPC coating was different. Specimen SPRW-5 was single-side strengthened with HFMRPC coating only in the piers. Specimen DPRW-6 was double-side strengthened with HFMRPC coating only in the piers to improve the local rigidity of the masonry wall. Specimen DRUW-7 was repaired and strengthened with HFMRPC coating after the URMW-1 was tested. The differences in strengthening methods are shown in **Table 2**. Before the test, white latex paint was applied on the surface of the specimens for a better observation of the cracks during cyclic loading.

The first procedure for strengthening the masonry wall was to deal with its surface. After the strength of the mortar reached to the standard of use, all the loose cement mortar and dust were removed from the surface of the masonry wall that was required to be strengthened. After that, the polished specimens were got wet by sprinkling water and then placed in a ventilated place until the dry surface with a saturated condition was reached. Finally, HFMRPC coating with various thicknesses was smeared on the uneven masonry surface. When repairing the specimen URMW-1 after being tested, the crushed bricks were first removed, and then the dislodged and broken mortar joints were also cleared, and then the same procedure was taken as that for strengthening the other specimens. Furthermore, it was worth noting that the hole joints generated from removing the broken bricks and mortar in the masonry walls should be first filled with HFMPRC plastering. Finally, the specimens were strengthened with the HFMRPC coating. The 28-days outdoor curing was recommended before the strengthened specimens were used. Furthermore, the strengthened specimens should be kept moist during the first week of the curing process to prevent the cracking caused by the shrinkage of the coating.

## Material Properties

The mechanical properties of the bricks, cement mortar, reinforcing bars, HFMRPC, and concrete used in this study were determined according to the standardized testing procedures. The confined masonry walls were built using sintered clay bricks with the standard dimension of 240 mm × 115 mm × 53 mm (length × height × thickness). Furthermore, all the HFMRPC cubes, mortar cubes, and concrete cubes were made from the same batch of materials and cured under the same conditions when the masonry walls were constructed. The measured compressive strengths of the bricks, cement mortar, HFMRPC, and concrete used in this study are listed in **Table 3**.

## Test Setup, Loading System, and Instrumentation

In this study, the seven half-scale specimens were tested in the Engineering Structure Disaster Prevention and Mitigation Laboratory of Shandong Architectural University, China. The actual force boundary conditions of the wall were simulated by the loading system, which included the constant vertical loading and the lateral cyclic loading with a displacement-controlled loading protocol. A 50 kN hydraulic jack (MTS) installed on the ring beam was used to impose the horizontal cyclic loading with displacement control. After the specimen was installed, a distribution steel beam was placed on the top of the specimen. A vertical load of 200 kN was applied on the top center of the distribution steel beam using a 100 t on a hydraulic jack to simulate a constant vertical compressive stress of 0.5 MPa transmitted from the gravity load. During the test, the vertical load was kept constant. The setup used for the quasi-static cyclic test is shown in **Figure 3**.

The horizontal loading pattern is shown in **Figure 4**. The displacement loading was divided into four stages, in which each level of displacement loading was cycled twice. The positive and negative displacements were the push and pull directions, respectively, as shown in **Figure 3**. The first stage was the elastic stage, and the displacement increment was chosen to start from 0.2 mm until the specimen was cracked to observe the development of the cracking process. The second stage was the elastic-plastic stage after cracking until the specimen yielded, and the displacement increment was increased to 0.4 mm. Subsequently, the third stage was the plastic stage after yielding until the peak load, and the displacement increment was changed to a higher level of 0.8 mm. Finally, the displacement increment in the fourth stage was turned into 1.6 mm after the peak load, and the bearing capacity continued to be decreased. According to the Chinese code (JGJ/T 101—2015), the test was

**TABLE 3 |** Compressive strength of the materials.

| Test units | Clay brick | Cement mortar | HFMRPC | Concrete |
|---|---|---|---|---|
| Compressive strength (MPa) | 7.42 | 1.90 | 45.2 | 35.50 |

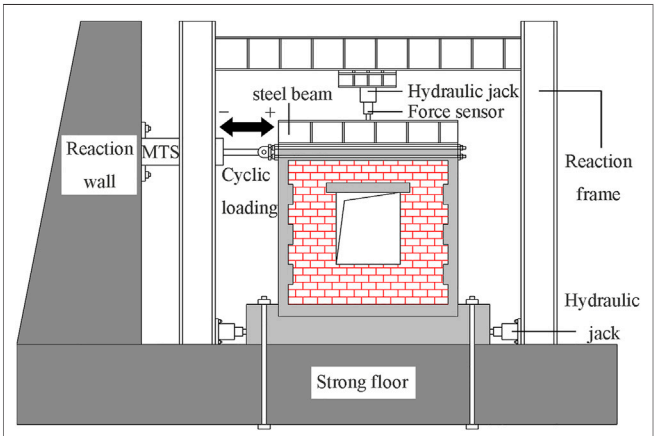


**FIGURE 3 |** Schematic diagram of the test setup.

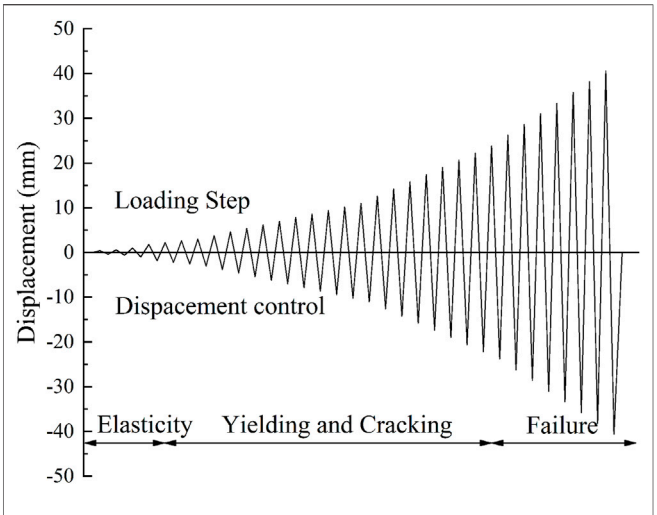


**FIGURE 4 |** Horizontal loading pattern.

loaded until the horizontal bearing capacity of the specimen dropped to 85% of the peak load.

The applied loads and displacements at the critical locations of the specimens were measured with two load cells and four linear variable displacement transducers (LVDTs), among which the lateral load was calibrated by a load cell installed in the MTS actuator. Another load cell was connected to the vertical hydraulic jack to guarantee the constant vertical load. The LVDT W1 was used to calibrate the horizontal displacement applied by the MTS actuator, which represented the horizontal displacement of the ring beam. The LVDT W2 was used to measure the horizontal displacement at the bottom of the specimen. The LVDT W3 was used to measure any possible slippage of the reinforced concrete footings relative to the strong laboratory floor. The LVDT W4 was placed at the middle of the ring beam to measure the displacement out-of-plane. The top of the specimen can move freely in-plane and out-of-plane, monitored in real-time by LVDT W4. During the test, the value of W4 was found to be small. Hence, the effect of out-of-plane bending on the specimen was negligible. The schematic layout of the displacement measurement points can be seen in **Figure 2A**. All LDVTs were connected to a computer-controlled data acquisition system. The visible crack patterns were continuously monitored after each load level was applied and marked on the specimens.

# EXPERIMENTAL OBSERVATIONS

## Failure Mode and Cracking Pattern

The failure mode and crack pattern for the unreinforced specimen URMW-1 are shown in **Figure 5**. The first crack in URMW-1 appeared at the upper corner of the window due to the stress concentration and then developed along the mortar joints. With increasing displacement, the cracks appeared at the bottom of the constructional columns, and the cracks at the window corners were gradually extended towards the diagonal direction in a stepped pattern. When the peak load was reached, the mortars continued to be spalled from bricks, and bricks in piers were crushed. Finally, the URMW-1 failed with the crushing of the piers and the column toe after the major shear cracks penetrated the edge of the constructional column. Meanwhile, the window was deformed, and an apparent inward convex from the window frame was observed. The failure mode for URMW-1 was a typical diagonal compression failure, which showed the characteristic of brittle damage. It indicated that the physical characteristics of bricks and the bonding capacity between bricks and mortar had an essential effect on the seismic bearing capacity for the URMW-1.

**Figure 6** shows the failure mode and crack pattern for the single-side strengthened specimen SRMW-2. The first crack in SRMW-2 appeared in the mortar at the window corner on the unreinforced side. With increasing displacement, the window corners on both sides cracked successively and formed a stepped crack extending to the diagonal. When reached the failure displacement, the coating was partially separated from the edge of the constructional column. Moreover, the concrete at the bottom of the constructional column was crushed. The failure mode for SRMW-2 was a typical shear slip failure, and the brittle characteristic was significantly improved compared with URMW-1. The failure mode on both sides of the SRMW-2 was similar, where the shear failure developed from the diagonal cracks in the HFMRPC coating and the mortar joints

**FIGURE 5 |** Failure mode and crack pattern for URMW-1 at ultimate displacement.

**FIGURE 6 |** Failure mode and crack pattern for SRMW-2 at ultimate displacement.

near the window corner. On one side of the SRMW-2 that was not reinforced, the mortar joints were less damaged than URMW-1, mainly because the HFMRPC coating enhanced the bond between the brick and mortar and provided restraint and protection to the brick wall. It demonstrated that the bonding property between the coating and the brick wall was well under the horizontal cyclic loading, and both of them deformed collaboratively to bear the shear force together.

As shown in **Figure 7**, the failure mode and crack pattern for specimens DRMW-3 and DRMW-4 were similar to specimen SRMW-2, both of which were typical shear slip failures with no significant improvement in the characteristics of brittle damage compared with the URMW-1. Both specimens were damaged with diagonal cracks on the coating, where the steel fibers were pulled out, and the PP fibers were broken. Meanwhile, at the edge of the sides of the constructional columns, there were only fine cracks, but no spalling occurred between the coatings and the brick walls. Furthermore, it was found that the bricks near the cracks were severely damaged after the coating was removed. The brick chips were bonded in the removal coating, indicating a good bond between the brick walls and coatings. The maximum width of the crack in DRMW-4 was wider than that in DRMW-3 at the time of failure. It indicated that the extent of the damage for the specimen was decreased with the increase of coating thickness. In brief, the integrity and stiffness were evenly increased due to the restriction of the double-sided coating. Hence, it resulted in a more even distribution of shear stress and made a pivotal contribution to improving the bearing capacity.

The failure mode and crack patterns for specimens SPRW-5 and DPRW-6 are shown in **Figure 8**. The first crack in both specimens appeared at the junction of the spandrels and the coating. As the loading continued, the shearing cracks of the

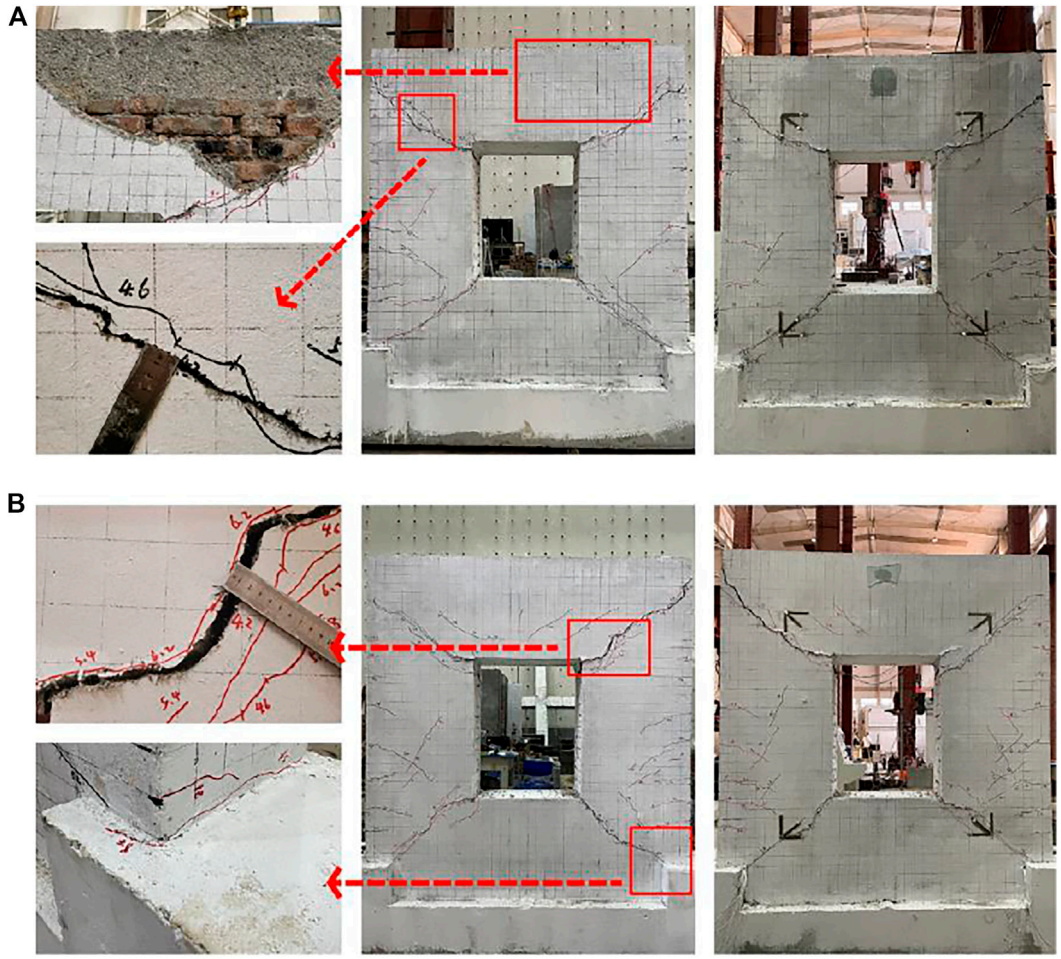


**FIGURE 7 |** Failure mode and crack pattern for DRMW-3 and DRMW-4 at ultimate displacement **(A)** DRMW-3 **(B)** DRMW-4.

spandrel developed diagonally along the mortar joints, and the concrete lintel beam on the upper part of the window also cracked. When the specimens reached the ultimate displacement, the spandrels were severely damaged and formed a characteristic "X-type" crack pattern on the side reinforced with the coating. Meanwhile, the edge of the coatings on the spandrels was separated from the wall. However, the piers on both sides were relatively intact due to the protection of the coating.

A mixed failure mode was observed in the specimens SPRW-5 and DRMW-6. It included a shear failure in the spandrels and a flexural failure in the piers. The two specimens exhibited the characteristic of ductile damage, showing a different failure mode from the other specimens. The two strengthening methods significantly increased the stiffness difference between the piers and spandrels. Therefore, it can be regarded that the strengthened piers were similar to two rigid columns, which were connected by a ring beam that was similar to a coupling beam in the shear wall. The damage to the specimens was caused by the generation of plastic hinges on the edge of the ring beam. Eventually, a rocking mechanism was generated on the rupture plane. This failure mode can consume a part of the earthquake energy in advance, which the seismic capacity of the spandrels was maximized, and the ductility of the specimens was also improved effectively.

In **Figure 9**, a shear slip failure was observed in the repaired specimen DRUW-7, the same as the specimen DRMW-3. The initial cracks developed from the four corners of the window and progressed along with the coating towards the diagonal direction in a stepped pattern. Eventually, the cracks at the bottom corner of the coating joined the shear crack at the bottom of the constructional columns, and the DRUW-7 failed. The brick, mortar joints, and concrete of the specimen URMW-1 had been damaged after the test. The constructional column at the bottom was also penetrated completely by shear cracks. Therefore, the damage extent of the DRUW-7 was more severe than that of the DRMW-3. The window of the URMW-1 developed significant plastic deformation at the time of failure, but after being repaired with HFMPRC coating, the shear stress was better redistributed due to the restraining effect of the coating, which prevented the continuous deformation of the window.

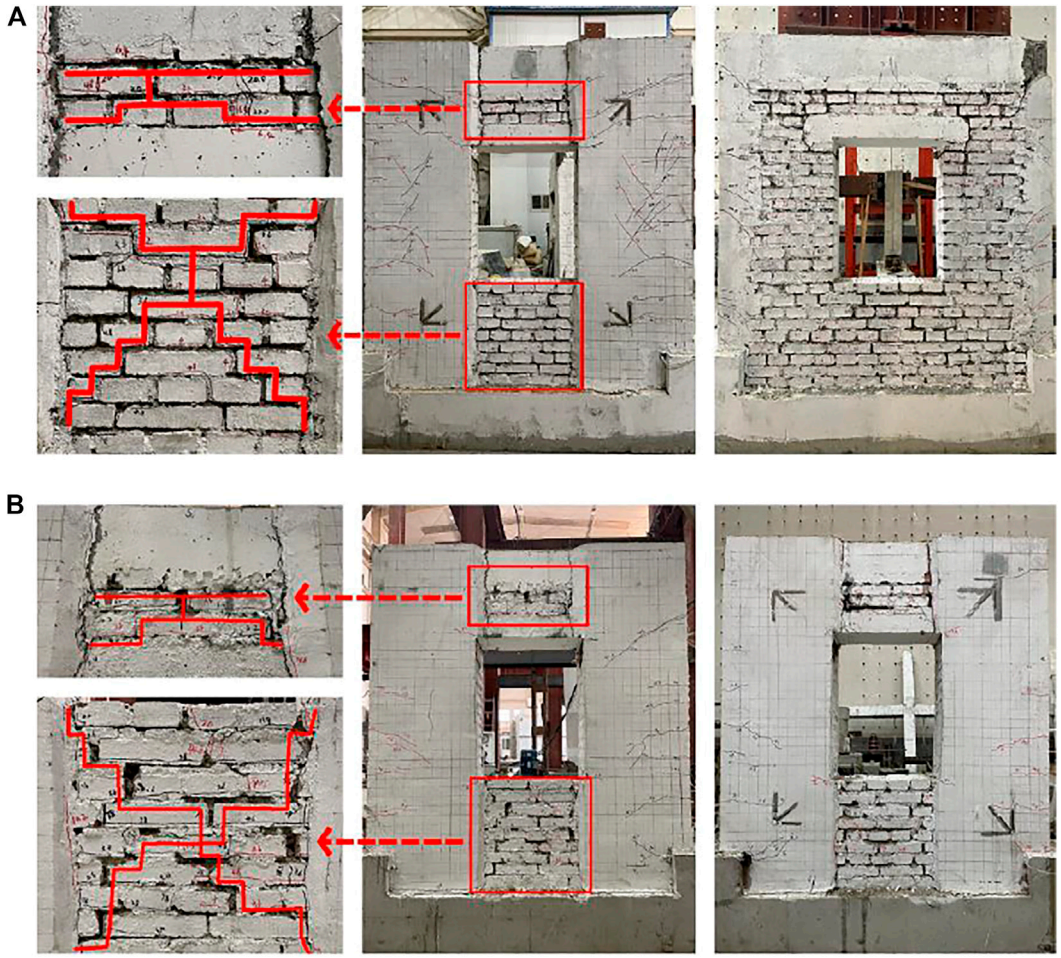


**FIGURE 8 |** Failure mode and crack pattern for SPRW-5 and DPRW-6 at ultimate displacement **(A)** SPRW-5 **(B)** DPRW-6.

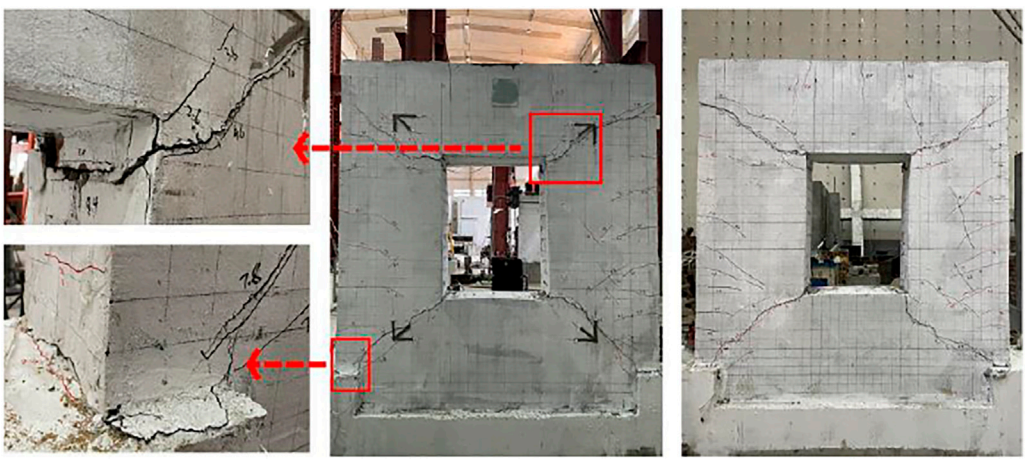

**FIGURE 9 |** Failure mode and crack pattern for DRUW-7 at ultimate displacement.

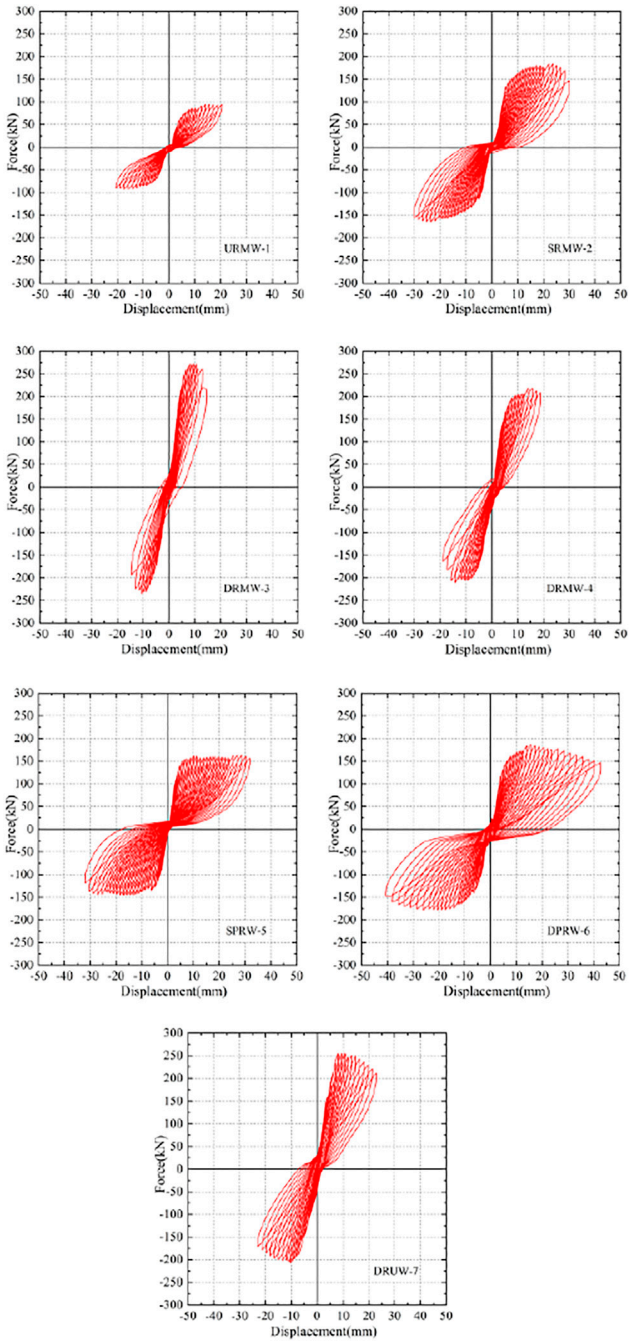


**FIGURE 10 |** Hysteresis curves.

## Hysteretic Curves of Load-Displacement

The hysteretic curves of all specimens are shown in **Figure 10**. No significant strength and stiffness degradation were observed in the second cycle of each displacement loading. Hence, the hysteretic curves of the first cycle in each displacement loading step were selected for comparative analysis. Before each specimen cracked, the hysteresis curves were almost linear, while the shape of the hysteresis curves curved significantly after cracking. The specimens reached the peak load after a smooth rising period. Due to the continuous development of shear cracks during the loading process, the hysteretic curves of the specimens showed an inverse "S" shape at the failure.

Due to the fragility of the bricks and the existence of window openings in the wall, the elastic deformation capacity of the controlled specimen URMW-1 was the lowest. Hence, a noticeable pinching effect in its hysteretic curve was observed. The URMW-1 experienced the most severe damage when the peak load was reached and produced a relatively large residual deformation and a significant slip. Nevertheless, the pinching behavior of the hysteretic curves was mitigated for all the strengthened specimens compared with the URMW-1. Although specimen SRMW-2 was only strengthened on one side by HFMRPC coating, the whole specimen remained intact after the failure. As the double-sided full coverage reinforcement increased the stiffness and integrity significantly, the pinching behavior of the hysteresis curve in specimen DRMW-3 was improved most obviously. Compared with the other specimens, the bearing capacity of specimen DRMW-3 was the highest, but it decreased fastest after reaching the peak load. The stiffness difference between the spandrels and piers in specimens SPRW-5 and DPRW-6 was increased through the strengthening in piers. Therefore, the earthquake-resistant behavior of the wall was fully exerted. This reinforcement decreased the bearing capacity at a flat rate, and the ductility was significantly improved. The hysteresis response of the repaired specimen DRUW-7 did not perform as well as the strengthened specimen DRMW-3, but it was significantly improved compared with the unstrengthened specimen URMW-1.

In summary, the hysteresis response of the strengthened or repaired specimens was effectively enhanced by using the proposed HFMRPC strengthening technique.

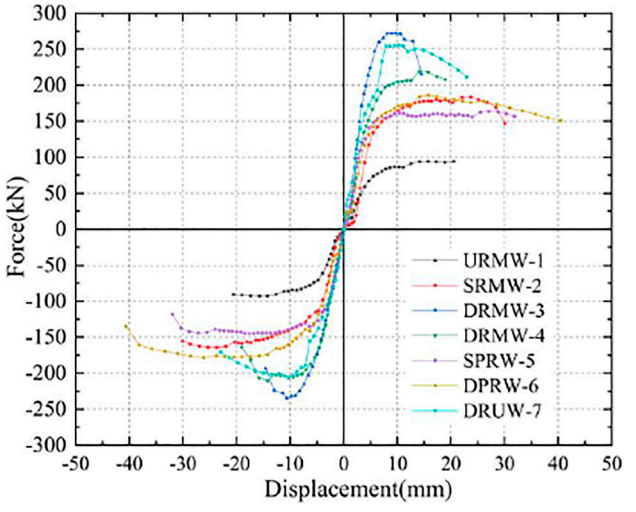


**FIGURE 11 |** Skeleton curves of load-displacement.

**TABLE 4 |** Critical load values of the specimens.

| Specimen | Cracking load $P_{cr}$ (kN) | Improvement | Peak load $P_u$ (kN) | Improvement | $P_{cr}/P_u$ |
|---|---|---|---|---|---|
| URMW-1 | 7.0 | — | 93.5 | — | 0.07 |
| SRMW-2 | 10.5 | 49.6% | 173.4 | 85.5% | 0.06 |
| DRMW-3 | 47.8 | 582.9% | 254.4 | 172.1% | 0.19 |
| DRMW-4 | 38.4 | 448.6% | 214.9 | 130.4% | 0.18 |
| SPRW-5 | 19.2 | 174.3% | 152.9 | 63.5% | 0.13 |
| DPRW-6 | 29.2 | 317.1% | 182.0 | 94.7% | 0.16 |
| DRUW-7 | 50.4 | 620.0% | 231.4 | 147.5% | 0.22 |

# RESULTS AND DISCUSSION

## Skeleton Curves of Load-Displacement

The skeleton curves of each specimen are compared in **Figure 11**. All specimens were in the linear elastic stage at the beginning of loading. Due to the different ways to strengthen the specimens using HFMRPC coating, the duration of the linear elastic stage was also related to the stiffness of the specimens. Hence, the improvement in the stiffness and the duration of the linear elastic stage were also different. Moreover, the horizontal load of the strengthened specimens was much higher than that of the unstrengthened specimen URMW-1 at the same horizontal displacement.

Afterward, the specimens entered the elastic-plastic stage, where the slope of the skeleton curves and the stiffness gradually decreased, while the bearing capacity continued to be increased until the specimens reached the peak load. After reaching the peak load, the bearing capacity of all specimens started to decrease, among which, the bearing capacity of specimen URMW-1 continued to be decreased and was severely damaged. The specimens SRMW-2, DRMW-3, and DRMW-4 had severe cracking in the coating along the diagonal direction from the window corner, and the constructional columns were penetrated by the through-length shear cracks, which led to a sudden decline in the bearing capacity of the specimens. Compared with other specimens, the bearing capacity of specimens SPRW-5 and DPRW-6 was not much different from the single-sided reinforcement specimen SRMW-2, but their strength decreased slowly. It was mainly due to the large stiffness difference between the piers and spandrels after the piers were reinforced with the HFMPRC coating. The reinforcement method in piers enabled a full function of the spandrels and improved the deformation capacity of the specimens, which led to a slight decrease of the bearing capacity until the ductile failure occurred.

As shown in **Table 4**, the cracking load ($P_{cr}$) and peak load ($P_u$) of specimens were compared. When the specimens were reinforced with HFMRPC coating, the cracking and peak loads increased to different extents. Compared with the specimen URMW-1, the cracking load of specimen SRMW-2 was improved by 49.6%, while the improved extent for the cracking load of the other strengthened specimens ranged from 174.3 to 620.0%. In terms of peak load, the ultimate bearing capacity of the strengthened specimens SRMW-2, SRRW-5, and DPRW-6 increased by 85.5, 63.5, and 94.7%, respectively, while the improvement in the ultimate bearing capacity of the specimens DRMW-3 and DRMW-4 were much more significant (by 172.1 and 130.4%, respectively). The thickness of the coating in specimen SRMW-2 was the same as the total thickness of the coating in specimen DRMW-4. In contrast, the bearing capacity of specimen DRMW-4 was significantly higher than that of specimen SRMW-2, which indicated that the effect of double-sided coating reinforcement was particularly remarkable to enhance the bearing capacity. After the specimen DRUW-7 was repaired with the HFMRPC coating, its cracking load was almost the same as the reinforced specimen DRMW-3. However, due to the existing damage in the bricks, mortar joints, and concrete, the peak load of the specimen DRUW-7 was lower than specimen DRMW-3, and the peak load was only improved by 147.5% compared with the specimen URMW-1. It indicated that the HFMRPC coating had a strong composite restraint effect on the specimens and protected brick walls, which significantly enhanced the seismic bearing capacity of the specimens. In particular, the double-sided full coverage reinforcement showed the most significant effect on improving composite restraint effect and bearing capacity.

## Displacement Ductility

Displacement ductility is an important parameter that reflects the deformation capacity of the specimen after yielding under the action of seismic force. The ductility coefficient ($\mu_{0.85}$) reflects the plastic deformation capacity and failure form of the specimen, which is calculated by the ultimate displacement divided by the yield displacement. A higher ductility coefficient indicates that the structure has a stronger plastic deformation ability and its failure form is a ductile failure, which results in better deformation capacity and energy dissipation capacity for the structure under earthquakes.

To accurately quantify the seismic performance of specimens, the displacements values at critical stages and the ductility coefficient of the seven specimens are listed in **Table 5**. In the study, the value of cracking displacement for the specimens is determined by the displacement value corresponding to the first visible crack. The yield displacement of the specimens is determined by the "Park Method." The peak displacement was determined by the displacement value corresponding to the maximum load on the skeleton curve. The ultimate displacement was determined by the displacement value corresponding to the load drops to 85% of the peak load.

**TABLE 5 |** Critical displacements of the specimens.

| Specimen | Cracking displacement $\Delta_{cr}$ (mm) | | Yield displacement $\Delta_y$ (mm) | | Peak displacement $\Delta_p$ (mm) | | Ultimate displacement $\Delta_{\mu 0.85}$ (mm) | | $\mu_{0.85}$ | $\mu_{0.85}$ | $\bar{\mu}0.85$ |
|---|---|---|---|---|---|---|---|---|---|---|---|
| | Push | Pull | Push | Pull | Push | Pull | Push | Pull | Push | Pull | Avg |
| URMW-1 | 0.46 | −0.53 | 6.91 | −6.21 | 20.5 | −15.7 | 20.5 | −20.6 | 2.97 | 3.32 | 3.14 |
| SRMW-2 | 1.06 | −1.16 | 7.76 | −8.74 | 23.7 | −23.7 | 30.1 | −30.0 | 3.88 | 3.43 | 3.66 |
| DRMW-3 | 1.56 | −1.42 | 5.71 | −6.84 | 8.93 | −10.6 | 14.5 | −14.6 | 2.54 | 2.13 | 2.34 |
| DRMW-4 | 1.36 | −1.42 | 6.98 | −5.74 | 14.1 | −14.2 | 18.9 | −19.0 | 2.72 | 3.31 | 3.01 |
| SPRW-5 | 0.57 | −0.62 | 5.03 | −4.56 | 27.0 | −17.6 | 31.9 | −32.0 | 6.34 | 7.01 | 6.68 |
| DPRW-6 | 1.06 | −1.16 | 7.07 | −7.67 | 15.8 | −20.6 | 38.1 | −40.6 | 5.39 | 5.29 | 5.34 |
| DRUW-7 | 1.06 | −1.16 | 8.26 | −8.43 | 10.3 | −10.3 | 22.9 | −23.0 | 2.77 | 2.73 | 2.75 |

As shown in **Table 5**, the displacement ductility worked out at the peak load varies from 2.13 to 7.01. The minimum ductility coefficient was obtained in the double-sided full coverage specimen DRMW-3, while the maximum ductility coefficient was obtained in the single-sided coverage in piers specimen SPRW-5, 112.7% higher than that of URMW-1. Compared with specimen URMW-1, the ductility coefficients of specimens SRMW-2 and DPRW-6 increased by 16.6and 70.1%, respectively, while the specimens DRMW-3, DRMW-4, and DRUW-7 decreased by 25.5, 4.1, and 12.4%, respectively. The higher ductility coefficients of the specimens SPRW-5 and DPRW-6 were that the reinforcement in piers of the specimen could increase the stiffness ratio between the spandrels and piers, which resulted in adequate damage in spandrels and thus delayed the failure displacement. The ductility coefficients of specimens DRMW-3, DRMW-4, and DRUW-7 were lower than the specimen URMW-1. It was attributed to the stiffness being increased by the double-sided full coverage reinforcement. Hence, the cracking load was significantly increased, resulting in the advanced peak displacement. After reaching the peak displacement, the shear cracks in the coating developed faster, which led to the shear force being transferred from the coating to the masonry wall and the constructional column. Therefore, the bearing capacity of the three specimens decreased faster, and the failure of three specimens was earlier. It was worth noting that the strengthened coating of specimen DRMW-3 was thicker than that of specimen DRMW-4. Although the yield displacements of the two specimens were almost the same, the peak and failure displacements of specimen DRMW-3 were lower than that of specimen DRMW-4. It indicated that as the thickness of the HFMRPC coating increased, the peak and failure displacements were earlier to be reached, and it was more prone to brittle failure. Due to the increased yield displacement of specimen SRMW-2, the improvement in ductility coefficient was slight, and the push direction was only 3.3% higher than that of specimen URMW-1. The damaged area of specimen DRUW-7 was repaired with HFMRPC material. Due to the high ductility of the repaired material, the ductility of the repaired specimen DRUW-7 was improved by 17.5% compared with the reinforced specimen DRMW-3. It demonstrated that compared with other reinforcement methods, the way of reinforcement in piers could effectively improve the ductility of specimens.

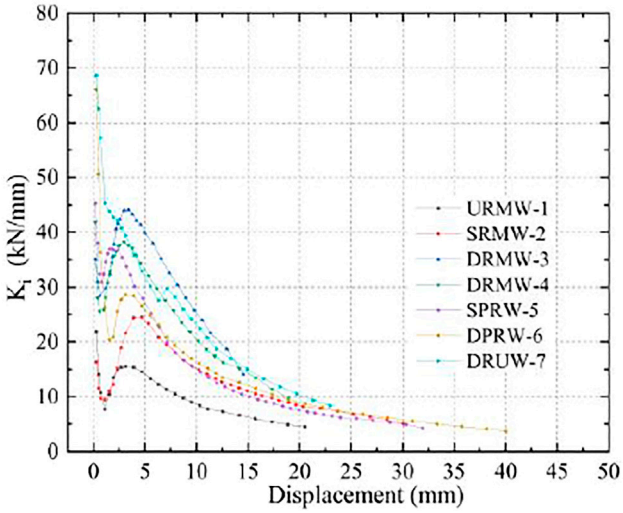


**FIGURE 12 |** Stiffness degradation curves.

## Stiffness Degradation

Stiffness degradation is essentially a phenomenon that the ability to resist deformation is gradually weakened due to the accumulation of internal structural damage under the action of cyclic loading. The stiffness degradation curve reflects the changing pattern of stiffness and the difficulty of resisting deformation at each specimen stage, such as cracking, damage, and destruction. The cyclic stiffness for the first cycle can be calculated approximately by **Equation. 1**:

$$K_i = \frac{F_i^+ - (F_i^-)}{\Delta_i^+ - (\Delta_i^-)} \tag{1}$$

The stiffness degradation for all the tested specimens was compared in **Figure 12**. When cracks were observed in the walls, the secant stiffness decreased significantly. In the later stages of loading, the stiffness degradation tended to be slow, and the reduction rate slowed down for all specimens. The specimen DRMW-3 strengthened with double-sided full coverage reinforcement showed a more significant residual stiffness at the failure time. Compared with specimen URMW-1, specimen SRMW-2 improved only by 57.9%, while the peak

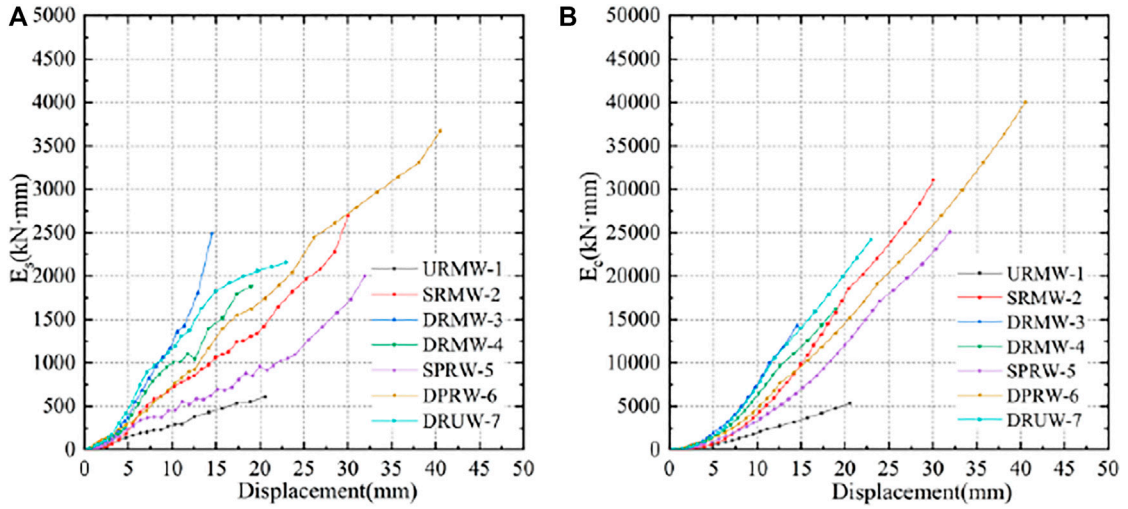


**FIGURE 13 |** Energy dissipation **(A)** single-cycle dissipated energy **(B)** cumulative dissipated energy.

stiffness of specimens DRMW-3, DRMW-4, SPRW-5, DPRW-6, and DRUW-7 improved by 184.1, 146.1, 145.1, 226.6, and 302.9%, respectively. Therefore, due to the strong composite restraint provided by the HFMRPC coating, each reinforcement method could enhance the stiffness of the specimens. Among them, the double-sided full coverage reinforcement had a significant effect on the improvement of stiffness, which can be enhanced with the increased thickness of the coating. The decreasing trend of the stiffness degradation curves for the specimen SPRW-5 and DPRW-6 tended to be significantly flat, which indicated that the two reinforcement methods effectively improved the brittle failure of specimens. Compared with the single-sided and double-sided strengthening of each reinforcement method, the latter significantly enhanced the peak stiffness and substantially enhanced the resistance to deformation. In summary, double-sided full coverage reinforcement can significantly improve the stiffness of masonry walls, but the improvement to brittle failure was not noticeable. The other reinforcement methods changed the damage mode from brittle damage to ductile damage and improved the stiffness of the specimens.

## Energy Dissipation

The energy dissipation in each cycle is defined by the area enclosed within the load-displacement hysteretic curve, which reflects the seismic performance of the masonry structure in the elastic-plastic state. Five energy dissipation parameters were calculated based on the hysteretic curves, including energy dissipation at yield displacement ($E_y$), energy dissipation at peak displacement ($E_p$), energy dissipation at failure displacement ($E_f$), single-cycle energy dissipation ($E_s$), and cumulative energy dissipation ($E_c$) to evaluate the energy dissipation capacity of tested specimens at different stages. The area enclosed by the hysteretic curve of the first cycle in each horizontal displacement loading step was the single-cycle energy dissipation, and the cumulative dissipation energy was calculated by the total sum of single-cycle energy dissipation.

The single-cycle energy dissipation and the cumulative dissipation energy are plotted in **Figure 13**, and the energy dissipation at each stage of the specimens was compared in **Table 6**. The energy dissipation capacity in all stages of the specimens was significantly improved by strengthening with HFMPRC coating. The ranking for the cumulative energy dissipation using different strengthening methods: URMW-1 < DRMW-3 < DRMW-4 < DRUW-7 < SPRW-5 < SRMW-2 < DPRW-6. Since it required a larger displacement and loading cycle for the unreinforced specimen URMW-1 to dissipate the same energy, URMW-1 suffered the most severe damage. The energy dissipation at yield displacement for specimen DRMW-3 was significantly higher than that of the other strengthened specimens because the stiffness and strength were significantly increased by using double-sided full coverage reinforcement, which enhanced the areas of the hysteretic curves (i.e., energy dissipation capacity). Compared with the other specimens, although DRMW-3 consumed the most energy in single-cycle energy dissipation, it reached the peak and failure displacement at the earliest time. Hence it consumed the least cumulative dissipation energy at the peak and failure displacement. The specimen DPRW-6 that adopted the double-sided coverage in piers reinforcement showed the advantage of high ductility, and it also experienced the largest elastic-plastic deformation. Therefore, the energy dissipation of DPRW-6 in the later stage of the loading period was significantly higher than that of the other specimens.

# SIMPLIFIED ANALYTICAL MODEL AND PREDICTION OF SHEAR CAPACITY

The transmission of lateral force across the masonry wall leads to an uneven distribution of stress within that masonry wall. With the increase of lateral force, the stress distribution is changed, and the failure in masonry walls occurs when the bricks reach their shear or compression strength. In this study, the confined

**TABLE 6 |** Cumulative energy dissipation in each stage of the specimens.

| Specimen | Cumulative dissipated energy | | | Improvement | | |
|---|---|---|---|---|---|---|
| | $E_y$ (kN·mm) | $E_p$ (kN·mm) | $E_f$ (kN·mm) | $E_y$ | $E_p$ | $E_f$ |
| URMW-1 | 863.1 | 4,200.1 | 5,362.9 | — | — | — |
| SRMW-2 | 2,345.9 | 22,036.0 | 31,059.6 | 171.8% | 424.7% | 479.2% |
| DRMW-3 | 3,195.1 | 7,216.0 | 14,298.1 | 270.2% | 71.8% | 166.6% |
| DRMW-4 | 2,216.8 | 11,061.0 | 16,255.5 | 156.8% | 163.4% | 203.1% |
| SPRW-5 | 940.1 | 14,969.7 | 25,105.8 | 8.9% | 256.4% | 368.1% |
| DPRW-6 | 2,442.1 | 11,821.3 | 40,067.3 | 182.9% | 181.5% | 647.1% |
| DRUW-7 | 5,534.8 | 7,841.9 | 24,215.7 | 541.3% | 86.7% | 351.5% |

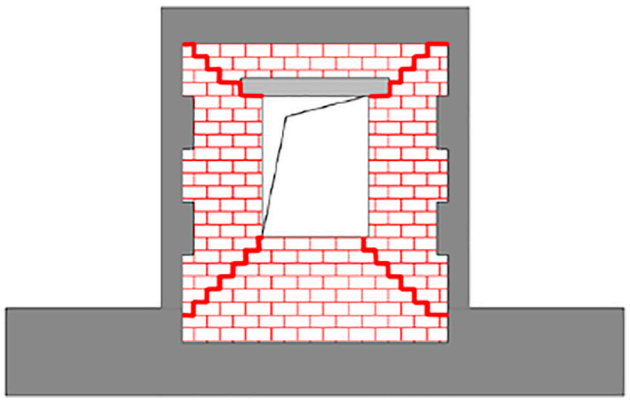

**FIGURE 14 |** Crack pattern of specimens.

masonry walls with window openings are simplified and analyzed through the equivalent diagonal strut concept. The effect of masonry walls on the overall dynamic response of the masonry structure is considered by replacing the masonry wall with two diagonal struts served in compression. The maximum shear strength of the confined masonry wall with window opening is predicted based on the diagonal strut mechanism.

The total shear strength ($V_{max}$) of the confined masonry walls with window openings retrofitted with HFMRPC coating consists of three components: the shear strength provided by masonry wall ($V_{man}$), the shear strength provided by constructional column ($V_{con}$), and the shear strength contributed by HFMRPC coating ($V_{coa}$ and $V'_{coa}$). Thus, the final shear capacity can be calculated by **Equation (2)**:

$$V_{max} = V_{man} + V_{coa} + V'_{coa} + V_{con} \tag{2}$$

## Contribution of the Masonry Wall and Constructional Columns to Shear Strength

Masonry structures are generally subjected to the combined effect of the vertical pressure caused by gravity loads and the shear forces caused by in-plane horizontal seismic action. Based on the test phenomena, the crack development pattern is shown in **Figure 14**. The shear resistance of the masonry wall is provided by the interaction between the brick and mortar, which includes the bond shear strength and friction. The typical stepped shear crack is approximately simplified as a single shear crack across the joint at the bottom. The vertical component of the stepped crack is in tension, and its contribution to the shear strength can thus be neglected. Referring to the code for design of masonry structures (GB 50003-2011), the shear bearing capacity of the confined masonry walls with window opening can be calculated as follows:

$$V_{man} = R_{man}\left(F_{mv} + \alpha_{man}\mu\sigma_{man}\right)A_{man} \tag{3}$$

$$\mu = 0.26 - 0.082\sigma_{man}/f \tag{4}$$

$$\mu = 0.23 - 0.065\sigma_{man}/f \tag{5}$$

Where $\alpha_{man}$ is the correction factor for different types of masonry and a value for brick used in the test is taken as 0.64; $\mu$ is the influence coefficient of shear-compression composite force, which can be determined according to the value of the permanent load partial factor $\gamma_G$; **Eqs 4, 5** are used to calculate the value of $\mu$ when $\gamma_G$ is taken as 1.2 and 1.35, respectively; $f$ and $F_{mv}$ are the design values of compressive strength and shear strength for bricks, respectively; $\sigma_{man}$ is the average compressive stress in the horizontal section of the masonry wall; $A_{man}$ is the horizontal cross-sectional area of the masonry wall; $R_{man}$ is the reduction factor of the masonry structure.

In the case of the window opening in the masonry wall, the overall shear strength of the masonry wall is directly reduced. Meanwhile, the synergistic working performance between different components in the wall is weakened, and the shear strength is thus indirectly weakened. Therefore, it is necessary to consider the reduction of the shear strength for the openings in the masonry structure by using the strength reduction factor $R_{D1}$ (Al-Chaar, 2002). With the horizontal displacement increased, the elastic limit of the masonry wall is exceeded, and severe damage occurs locally. Before the specimen is repaired, the damage of mortar joints and bricks needs to be visually inspected. The corresponding damage reduction factor $R_{D2}$ is used according to the damage condition to consider the effect on the bearing capacity of the repaired specimen DRUW-7. It should be noticed that the reduction factor only considers the reduction in strength of the masonry wall caused by the opening, which does not represent the possible stress distribution. Therefore, only the reduction factor is recommended to assess the bearing capacity of the overall structure. The reduction factors $R_{man}$ and $R_{D1}$ should be calculated as follows:

$$R_{D1} = 0.6\left(\frac{A_{oa}}{A_{pa}}\right)^2 + 1.6\left(\frac{A_{oa}}{A_{pa}}\right) + 1 \quad (6)$$

$$R_{man} = R_{D1} \times R_{D2} \quad (7)$$

where $A_{oa}$ is the area of the openings, $A_{pa}$ is the area of the masonry wall. For the undamaged masonry walls, the damage reduction factor $R_{D2}$ is taken as 1. Based on Al-Chaar et al.'s research, the height-to-thickness ratio of specimen DRUW-7 is less than 21, and its masonry wall is subjected to moderate damage. Therefore, the value of the damage reduction factor $R_{D2}$ is taken as 0.7.

If the spacing between construction columns is less than 3 m, the beneficial effect of the tie columns on the masonry structure should be taken into account. The contribution of the construction columns to the shear strength for masonry structures can be calculated as follows:

$$V_{con} = \lambda_{con}\left(0.7 f_t bh + 1.25 f_{yv}\frac{A_{sv}}{s}h_{con}\right) \quad (8)$$

Where $f_t$ is the tensile strength of concrete cube; $b$ and $h$ are the section length and width of the constructional column, respectively; $f_{yv}$ is the tensile strength of stirrups; $A_{sv}$ and $s$ are the cross-sectional area and stirrup spacing, respectively; $h_{con}$ is the effective height of construction column in the calculation unit. In addition, Yang JJ et al. found that the constructional columns are commonly insufficient developed, the ultimate efficiency of the construction column should be taken into account. When the spacing between construction columns is less than 3m, the value of reduction factor $\lambda_{con}$ for shear bearing capacity of the construction columns is taken as 0.28 (Guo et al., 2019; Yang et al., 1998).

## Contribution of HFMRPC Coating to Shear Strength

The contribution of HFMRPC coating to the shear strength can be calculated using the diagonal mechanism (Wang et al., 2021). For specimens SRMW-2, DRMW-3, DRMW-4, and DRUW-7, the HFMRPC coating can provide tensile strength to prevent diagonal cracking. Hence, the tensile strength provided by the coating can contribute to the shear strength of the masonry wall. For specimens SPRW-5 and DPRW-6, the HFMRPC coating can provide the tensile stress perpendicular to the cross-sectional direction to enhance the shear strength of the specimens. In summary, the shear strength contributed by the HFMRPC coating is calculated as follows:

$$V_{coa} = \alpha f_{coa} A_c \sin\theta \quad (9)$$

where $\alpha$ is the tensile stress distribution factor of HFMRPC coating, and its value is taken as 0.7 for all the specimens; $\theta$ is the angle between the direction of the main crack and the horizontal. Hence, $\sin\theta$ is the horizontal component of the tensile strength of the coating; the value of $\theta$ for specimens SRMW-2, DRMW-3, DRMW-4, and DRUW-7 are taken as 45°, and the value of $\theta$ for specimens SPRW-5 and DPRW-6 are taken as 70°; $f_{coa}$ and $A_c$ are the tensile strength of HFMRPC coating, and the cross-sectional area developed along the cracking direction, respectively.

Furthermore, the HFMRPC coating can also provide constraints for the construction columns (Wang et al., 2021). The shear strength provided from this restraint force for the masonry wall is calculated as follows:

$$V'_{coa} = 0.5 n f_{coa} t_{coa} h'_{coa} \quad (10)$$

Where $n$ is the number of reinforced surfaces, $t_{coa}$ is the thickness of the HFMRPC coating, $h'_{con}$ is equal to the one-third height of the construction column.

## Validation of the Proposed Model

The shear bearing capacity of all specimens was calculated by the equations mentioned above, and the tested and calculated results are shown in **Table 7**. It can be seen that except for the specimen DRMW-4 (its shear strength is underestimated by 20%), the calculated results for the other specimens are generally in close agreement with the test results. The underestimation is mainly due to construction errors resulting in the thickness of the coating being thicker than 15 mm. The average value, standard deviation, and coefficient of variation of the ratio between the calculated and test results for all the tested walls are 0.90, 0.06, and 6.59%, respectively. Therefore, the simplified analytical model proposed in this study can be used to calculate the shear strength for confined masonry walls with window openings strengthened by HFMRPC coating.

# CONCLUSION

In this study, seven confined masonry walls with window openings were tested to investigate the effectiveness of the in-plane strengthened or repaired technologies by using HFMRPC coatings. The conclusions drawn from the experimental and theoretical results are summarized as follows:

(1) A HFMRPC mixture was selected through material tests for strengthening or repairing. In contrast to the other mixtures, the selected mixtures four exhibited the lowest compressive strength and the smallest fluidity. Meanwhile, the viscosity of mixtures four allowed it to be plastered on the surface of masonry walls by hand-trowel.

(2) The failure mode of unreinforced specimen URMW-1 was a diagonal compression failure, while the failure modes of other reinforced specimens were shear slip failure, except for the failure modes of specimens SPRW-5 and DPRW-6, which were mixed failure modes of shear failure in the spandrels and flexural failure in the piers.

(3) Compared with the control specimen URMW-1, the cracking load and peak load of the strengthened specimens were increased, among which the double-sided full coverage had the most significant effect on the increase of bearing capacity. The cracking load of the strengthened specimens was increased within the range of 49.6% (specimen SRMW-2) to 582.9% (specimen DRMW-3), while the peak loads increased from 63.5% (SPRW-5) to 172.1% (DRMW-3).

(4) The improvements of ductility coefficients were 16.6, 112.7, and 70.1% for specimens SRMW-2, SPRW-5, and DPRW-6 compared with the control specimen URMW-1. The reinforcement in piers increased the stiffness difference between the piers and spandrels, which can significantly

**TABLE 7 |** Comparison of shear strength between calculated and tested values.

| Specimen | Shear strength | | $V_{Cal}/V_{Exp}$ | $V_{Cal}/V_{Exp}$ | | |
|---|---|---|---|---|---|---|
| | Tested strength $V_{Exp}$ (kN) | Calculated strength $V_{Cal}$ (kN) | | Average value | Standard deviation | Coefficient of variation (%) |
| URMW-1 | 93.5 | 84.5 | 0.90 | 0.91 | 0.06 | 6.59 |
| SRMW-2 | 173.4 | 159.4 | 0.92 | | | |
| DRMW-3 | 254.4 | 234.2 | 0.92 | | | |
| DRMW-4 | 214.9 | 171.8 | 0.80 | | | |
| SPRW-5 | 152.9 | 135.3 | 0.88 | | | |
| DPRW-6 | 182.0 | 186.1 | 1.02 | | | |
| DRUW-7 | 231.4 | 208.9 | 0.90 | | | |

increase the ductility of the specimens SPRW-5 and DPRW-6. However, the displacement ductility of the double-sided full coverage specimens was decreased than that of the URMW-1. The displacement ductility of specimens DRMW-3 and DRMW-4 decreased by 25.5 and 4.1%, respectively, which indicated that the peak displacement was reduced and the failure displacement was advanced by using the double-sided full coverage reinforcement method. When the coating was thicker, the ductility coefficient was reduced more significantly.

(5) The peak stiffnesses of the strengthened specimens were increased due to the strong composite restraint effect between the HFMRPC coating and specimen. The peak stiffnesses of the strengthened specimens were increased, ranging from 57.9% (SRMW-2) to 226.6% (DPRW-6) compared to the control specimen URMW-1. The energy dissipation in all stages of strengthened specimens was significantly increased compared with the URMW-1. The energy dissipation at yield displacement increased 156.8% (DRMW-4) to 270.2% (DRMW-3) except for specimen SPRW-5 (8.9%). The peak displacement energy dissipation and damage displacement energy dissipation can be enhanced within the range of 71.8–424.7% and 166.6–647.1%, respectively.

(6) Compared with the control specimen URMW-1, the cracking load, peak load, peak stiffness, and energy dissipation of the repaired specimen DRUW-7 were increased by 620.0, 147.5, 302.9, and 351.5%, respectively. Although the ductility coefficient was 12.4% lower than that of the URMW-1, it was 17.5% higher than that of the specimens DRMW-3 strengthened by double-sided full coverage.

(7) A simplified model was proposed for the shear bearing capacity of confined masonry walls with window openings strengthened by HFMRPC coating.

## DATA AVAILABILITY STATEMENT

The original contributions presented in the study are included in the article/Supplementary Material, further inquiries can be directed to the corresponding author.

## AUTHOR CONTRIBUTIONS

G-aL: Conceptualization, Validation, Formal analysis, Investigation, Data curation, Writing-original draft, Writing-review, and editing. XW: Methodology, Resources, Investigation, Project administration, Funding acquisition, Writing-review, and editing. ZY: Formal analysis, Data curation, Writing-original draft. L-yW: Formal analysis, Data curation. Y-wZ: Formal analysis, Data curation. G-bC: Supervision. All authors have read and agreed to the published version of the manuscript.

## FUNDING

This study received funding from the National Natural Science Foundation of China with Grant (No. 51878395), the Key Laboratory of Building Structural Retrofitting and Underground Space Engineering of Ministry of Education "Experimental Study on Seismic Performance of Confined Masonry Walls with Window Openings Strengthened by MRPC". The authors declare that this study received funding from Engineering Research Institute of Appraisal and Strengthening of Shandong Jianzhu University CO., LTD (No.H19230Z). The funder was not involved in the study design, collection, analysis, interpretation of data, the writing of this article or the decision to submit it for publication.

## REFERENCES

Al-Chaar, G. (2002). *Evaluating Strength and Stiffness of Unreinforced Masonry Infill Structures*.

Al-Lami, K., D'Antino, T., and Colombi, P. (2020). Durability of Fabric-Reinforced Cementitious Matrix (FRCM) Composites: A Review. *Appl. Sci.* 10, 1714. doi:10.3390/app10051714

Augenti, N., Parisi, F., Prota, A., and Manfredi, G. (2011). In-Plane Lateral Response of a Full-Scale Masonry Subassemblage with and without an Inorganic Matrix-Grid Strengthening System. *J. Compos. Constr.* 15, 578–590. doi:10.1061/(ASCE)CC.1943-5614.0000193

Bisby, L., Stratford, T., Smith, J., and Halpin, S. (2011). "FRP versus Fiber Reinforced Cementitious Mortar Systems at Elevated Temperature," in Proceeding of the 10th International Symposium on Fiber-Reinforced Polymer Reinforcement for Concrete Structures 2011, FRPRCS-10, Tampa, FL, United States, Dec 2011 (American Concrete Institute, ACI Special Publication), 863–881. doi:10.1021/acssuschemeng.7b02363

Bui, T.-L., Si Larbi, A., Reboul, N., and Ferrier, E. (2015). Shear Behaviour of Masonry walls Strengthened by External Bonded FRP and TRC. *Compos. Structures* 132, 923–932. doi:10.1016/j.compstruct.2015.06.057

Cai, Z., Liu, F., Yu, J., Yu, K., and Tian, L. (2021). Development of Ultra-high Ductility Engineered Cementitious Composites as a Novel and Resilient

Fireproof Coating. *Construction Building Mater.* 288, 123090. doi:10.1016/J.CONBUILDMAT.2021.123090

Cheng, S., Yin, S., and Jing, L. (2020). Comparative Experimental Analysis on the In-Plane Shear Performance of brick Masonry walls Strengthened with Different Fiber Reinforced Materials. *Construction Building Mater.* 259, 120387. doi:10.1016/j.conbuildmat.2020.120387

Del Zoppo, M., Di Ludovico, M., Balsamo, A., and Prota, A. (2019a). Experimental In-Plane Shear Capacity of Clay Brick Masonry Panels Strengthened with FRCM and FRM Composites. *J. Composites Construction* 23, 04019038. doi:10.1061/(ASCE)CC.1943-5614.0000965

Del Zoppo, M., Di Ludovico, M., Balsamo, A., and Prota, A. (2019b). In-plane Shear Capacity of Tuff Masonry walls with Traditional and Innovative Composite Reinforced Mortars (CRM). *Construction Building Mater.* 210, 289–300. doi:10.1016/j.conbuildmat.2019.03.133

Deng, M., and Yang, S. (2020). Experimental and Numerical Evaluation of Confined Masonry walls Retrofitted with Engineered Cementitious Composites. *Eng. Structures* 207, 110249. doi:10.1016/j.engstruct.2020.110249

Ding, Y., Yu, K., and Li, M. (2022). A Review on High-Strength Engineered Cementitious Composites (HS-ECC): Design, *Mechanical Property and Structural Application*. *Structures* 35, 903–921. doi:10.1016/J.ISTRUC.2021.10.036

Dong, F. Y., Li, Z. H., Yu, J. T., Jiang, F. M., and Wang, H. P. (2022a). Shaking-Table Test on a Two-Story Timber-Framed Masonry Structure Retrofitted with Ultra-high Ductile Concrete. *J. Struct. Eng.* 148, 1. doi:10.1061/(ASCE)ST.1943-541X.0003164

Dong, F., Wang, H., Jiang, F., Xing, Q., and Yu, J. (2022b). In-plane Shear Behavior of Masonry Panels Strengthened with Ultra-high Ductile concrete (UHDC). *Eng. Structures* 252, 113609. doi:10.1016/j.engstruct.2021.113609

Dong, Z., Deng, M., Zhang, Y., Zhang, C., and Ma, P. (2020). Out-of-plane Strengthening of Unreinforced Masonry walls Using Textile Reinforced Mortar Added Short Polyvinyl Alcohol Fibers. *Construction Building Mater.* 260, 119910. doi:10.1016/j.conbuildmat.2020.119910

El-Diasity, M., Okail, H., Kamal, O., and Said, M. (2015). Structural Performance of Confined Masonry walls Retrofitted Using Ferrocement and GFRP under In-Plane Cyclic Loading. *Eng. Structures* 94, 54–69. doi:10.1016/j.engstruct.2015.03.035

Ferrara, G., Caggegi, C., Martinelli, E., and Gabor, A. (2020). Shear Capacity of Masonry walls Externally Strengthened Using Flax-TRM Composite Systems: Experimental Tests and Comparative Assessment. *Construction Building Mater.* 261, 120490. doi:10.1016/j.conbuildmat.2020.120490

Foraboschi, P. (2016). Effectiveness of Novel Methods to Increase the FRP-Masonry Bond Capacity. *Composites B: Eng.* 107, 214–232. doi:10.1016/j.compositesb.2016.09.060

Garcia-Ramonda, L., Pelá, L., Roca, P., and Camata, G. (2020). In-plane Shear Behaviour by diagonal Compression Testing of brick Masonry walls Strengthened with basalt and Steel Textile Reinforced Mortars. *Construction Building Mater.* 240, 117905. doi:10.1016/j.conbuildmat.2019.117905

Guerreiro, J., Ferreira, J. G., Proença, J., and Gago, A. (2018). Strengthening of Old Masonry walls for Out-Of-Plane Seismic Loading with a Cfrp Reinforced Render. *Exp. Tech.* 42, 355–369. 13. doi:10.1007/s40799-018-0239-0

Guo, Z., Zheng, S., Xu, Z., and Sun, W. (2019). Experimental Study on Seismic Performance of Ungrouted Confined Concrete Masonry Walls with Unbonded Tendons. *Int. J. Civ Eng.* 17, 333–346. doi:10.1007/s40999-017-0275-7

Kalali, A., and Kabir, M. Z. (2012). Experimental Response of Double-Wythe Masonry Panels Strengthened with Glass Fiber Reinforced Polymers Subjected to diagonal Compression Tests. *Eng. Structures* 39, 24–37. doi:10.1016/j.engstruct.2012.01.018

Konthesingha, K. M. C., Masia, M. J., Petersen, R. B., Mojsilovic, N., Simundic, G., and Page, A. W. (2013). Static Cyclic In-Plane Shear Response of Damaged Masonry walls Retrofitted with NSM FRP Strips - an Experimental Evaluation. *Eng. Structures* 50, 126–136. doi:10.1016/j.engstruct.2012.10.026

Leal-Graciano, J. M., Quiñónez, B., Rodríguez-Lozoya, H. E., Pérez-Gavilán, J. J., and Lizárraga-Pereda, J. F. (2020). Use of GFRP as Retrofit Alternative for Confined Masonry walls with Window Opening Subjected to In-Plane Lateral Load. *Eng. Structures* 223, 111148. doi:10.1016/j.engstruct.2020.111148

Li, V. C., and Leung, C. K. Y. (1992). Steady-State and Multiple Cracking of Short Random Fiber Composites. *J. Eng. Mech.* 118, 2246–2264. doi:10.1061/(asce)0733-9399(1992)118:11(2246)

Lin, Y.-W., Wotherspoon, L., Scott, A., and Ingham, J. M. (2014). In-plane Strengthening of clay brick Unreinforced Masonry Wallettes Using ECC Shotcrete. *Eng. Structures* 66, 57–65. doi:10.1016/j.engstruct.2014.01.043

Mercedes, L., Bernat-Maso, E., and Gil, L. (2020). Analytical Model for Masonry walls Strengthened with Vegetal Fabric Reinforced Cementitious Matrix (FRCM) Composites and Subjected to Cyclic Loads. *Mater. Struct.* 53, 1–14. doi:10.1617/s11527-020-01583-9

Niasar, A. N., Alaee, F. J., and Zamani, S. M. (2020). Experimental Investigation on the Performance of Unreinforced Masonry wall, Retrofitted Using Engineered Cementitious Composites. *Construction Building Mater.* 239, 117788. doi:10.1016/j.conbuildmat.2019.117788

Papanicolaou, C. G., Triantafillou, T. C., Karlos, K., and Papathanasiou, M. (2007). Textile-reinforced Mortar (TRM) versus FRP as Strengthening Material of URM walls: In-Plane Cyclic Loading. *Mater. Struct.* 40, 1081–1097. doi:10.1617/s11527-006-9207-8

Papanicolaou, C. G., Triantafillou, T. C., Papathanasiou, M., and Karlos, K. (2008). Textile Reinforced Mortar (TRM) versus FRP as Strengthening Material of URM walls: Out-Of-Plane Cyclic Loading. *Mater. Structures* 41, 143–157. doi:10.1617/s11527-007-9226-0

Parisi, F., Iovinella, I., Balsamo, A., Augenti, N., and Prota, A. (2013). In-plane Behaviour of Tuff Masonry Strengthened with Inorganic Matrix-Grid Composites. *Composites Part B: Eng.* 45, 1657–1666. doi:10.1016/j.compositesb.2012.09.068

Prota, A., Marcari, G., Fabbrocino, G., Manfredi, G., and Aldea, C. (2006). Experimental In-Plane Behavior of Tuff Masonry Strengthened with Cementitious Matrix-Grid Composites. *J. Compos. Constr.* 10, 223–233. doi:10.1061/(asce)1090-0268(2006)10:3(223)

Shariq, M., Abbas, H., Irtaza, H., and Qamaruddin, M. (2008). Influence of Openings on Seismic Performance of Masonry Building walls. *Building Environ.* 43, 1232–1240. doi:10.1016/j.buildenv.2007.03.005

Tai, J. J., Deng, J. H., Chen, F., and Wei, J. B. (2011). Characterization of Surface Rupture and Structural Damage in Hongkou Town during Wenchuan Earthquake. *J. Earthquake Tsunami* 05, 363–387. doi:10.1142/s1793431111001145

Van Zijl, G. P., and De Beer, L. (2019). Sprayed Strain-Hardening Cement-Based Composite Overlay for Shear Strengthening of Unreinforced Load-Bearing Masonry. *Adv. Struct. Eng.* 22, 1121–1135. doi:10.1177/1369433218807686

Wang, X., Li, S., Wu, Z., Bu, F., and Wang, F. (20192019). Experimental Study on Seismic Strengthening of Confined Masonry Walls Using RPC. *Adv. Mater. Sci. Eng.* 2019, 1–13. doi:10.1155/2019/5095120

Wang, X., Xie, Q., Wu, Z., Bu, F., and Wang, F. (2021). Experimental Study on Seismic Performance of Strengthening Masonry wall Using Hybrid Fiber-Reinforced Reactive Powder concrete. *Earthquake Spectra* 37, 1785–1805. doi:10.1177/8755293020988012

Yang, J., Gao, Y., and Tong, Z. J. J. O. B. S. (1998). *Analysis of Shear Strength of Concrete Block Masonry with Ring Beams and Constructional Columns*. (in Chinese).

**Conflict of Interest:** Authors L-yW, and G-bC were employed by the Engineering Research Institute of Appraisal and Strengthening of Shandong Jianzhu University CO., LTD. Author Y-wZ was employed by Shandong Dawei Design Group CO., LTD.

The remaining authors declare that the research was conducted in the absence of any commercial or financial relationships that could be construed as a potential conflict of interest.

# Advantages of publishing in Frontiers

**OPEN ACCESS**
Articles are free to read for greatest visibility and readership

**FAST PUBLICATION**
Around 90 days from submission to decision

**HIGH QUALITY PEER-REVIEW**
Rigorous, collaborative, and constructive peer-review

**TRANSPARENT PEER-REVIEW**
Editors and reviewers acknowledged by name on published articles

**Frontiers**
Avenue du Tribunal-Fédéral 34
1005 Lausanne | Switzerland

**Visit us:** www.frontiersin.org
**Contact us:** frontiersin.org/about/contact

**REPRODUCIBILITY OF RESEARCH**
Support open data and methods to enhance research reproducibility

**DIGITAL PUBLISHING**
Articles designed for optimal readership across devices

**FOLLOW US**
@frontiersin

**IMPACT METRICS**
Advanced article metrics track visibility across digital media

**EXTENSIVE PROMOTION**
Marketing and promotion of impactful research

**LOOP RESEARCH NETWORK**
Our network increases your article's readership